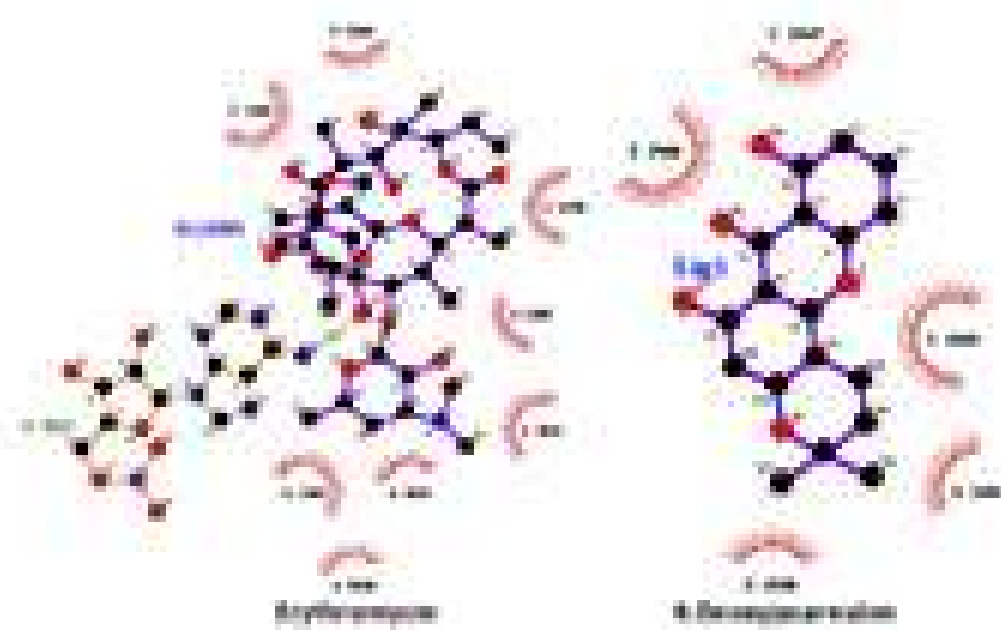


Indonesian Journal of Chemistry

Vol. 20, No. 4, August 2020



Approved by SCOPUS and DOAJ
for publication

Magnetic Mesoporous Silica Composite for Enhanced Preconcentration of Selected Organophosphorus Pesticides in Fruits

Nur Husna Zainal Abidin, Wan Nazihah Wan Ibrahim*, Nor Suhaila Mohamad Hanapi, and Nor'ashikin Saim

Faculty of Applied Sciences, Universiti Teknologi MARA, 40450 Shah Alam, Selangor, Malaysia

* **Corresponding author:**

email: wannazihah@salam.uitm.edu.my

Received: January 23, 2019

Accepted: June 12, 2019

DOI: 10.22146/ijc.42935

Abstract: In the present work, MCM-41 coated magnetic particles (Fe_3O_4 -MCM-41) composite was synthesized and employed as an effective adsorbent in magnetic solid phase extraction (MSPE) of three selected organophosphorus pesticides (OPPs) namely chlorpyrifos, diazinon and parathion methyl from grape and strawberry samples prior to high performance liquid chromatography with UV detection (HPLC-UV). The synthesized sorbent was physicochemically and morphologically characterized via Fourier transform infrared spectroscopy (FT-IR), field emission scanning electron microscopy (FESEM), transmission electron microscopy (TEM), X-ray diffraction (XRD) and N_2 adsorption analysis. The main parameters on the extraction efficiency of selected OPPs, including extraction time, desorption solvent, desorption time, and sorbent dosage, were thoroughly optimized. Compared to MCM-41 sorbent, the newly synthesized Fe_3O_4 -MCM-41 adsorbent shows a linear response (0.1 - 5.00 mg L^{-1}) with good determination coefficients ranging from 0.9900 to 0.9980 , low limits detection (LODs), 0.02 - 0.15 mg L^{-1} and low limit quantifications (LOQs), 0.06 - 0.40 mg L^{-1} . The precision as relative standard deviation (%RSD) of the proposed MSPE method was studied at low and high concentration (0.1 - 5.0 mg L^{-1}) based on intra-day (1.0 to 6.0% , $n = 3$) and inter-day (1.0 to 7.0% , $n = 3$), respectively. Fruit matrices were used to assess the field applicability of the sorbents. Comparatively, Fe_3O_4 -MCM-41 achieved excellent percent recovery (85 - 120%) compared to the MCM-41 (70 - 110%). The result revealed that the Fe_3O_4 -MCM-41 composite was efficient sorbent with good capability for the preconcentration of selected OPPs from fruit samples.

Keywords: MCM-41; Fe_3O_4 -MCM-41; organophosphorus pesticides; magnetic solid phase extraction

■ INTRODUCTION

In recent years, the pesticide has been remarkably increased in usage for better agricultural practices, transparency, and traceability in the production and marketing of conventional food. Generally, organophosphorus pesticides (OPPs) are widely used as insecticides in agriculture activities, which lead to extensive contamination of water, atmosphere soil as well as agriculture products and eventually in derivate food commodities [1] due to their desirable properties such as biodegradable and short persistence in the environment [2]. Particularly, fruit commodities contaminated by

OPPs, including grape, tomato, strawberry, apple, and pineapple [3-6], are becoming the hottest issue for environmental researchers because it can threaten human health. Grape and strawberry are usually freshly consumed without peeling, which risks harmful to human health because some of them have high acute toxicity due to the prevention of neural impulse transmission by their inhibitions of acetyl cholinesterase function in the nervous system [7]. Due to the high toxicity at low concentration, European Union (EU) have established maximum residue limits (MRLs) of various pesticides in grape and strawberry samples in the range of 0.01 to 0.05 mg L^{-1} [8]. Consequently, due to the

exceeded permitted level by regulation as well as well-known toxicity of OPPs pesticides and their degraded products, effective extraction coupled with appropriate clean-up and enrichment steps are necessary prior to instrument analysis [9-11].

Several techniques including, liquid-liquid extraction (LLE) [12], solid phase extraction (SPE) [13], solid phase microextraction (SPME) [14], micro solid phase extraction (μ -SPE) [15] and dispersive solid phase extraction (DSPE) [16] have been successfully applied to remediate the pesticides and their degraded products from the various matrices. Comparatively, the SPE method offers good recovery, short extraction time, high enrichment factor, less organic solvent consumption, and reasonable cost is eminent as an advantageous and genuine method [17-19]. However, there are several limitations encountered of this method, including a large amount of eluent, time-consuming, due to the limited rate of diffusion and mass transfer and limited efficiencies of the target analytes from large breakthrough volume [18]. Thus, the development of novel SPE models by applying magnetic nanoparticles as the SPE sorbent known as magnetic solid phase extraction (MSPE) are highly sensible.

In recent years, magnetic solid phase extraction (MSPE) a pioneering technique for sample preparation as well as performed a great interest in order to improve the stability, sensitivity, compatibility, and good extraction efficiency. It is a new mode of SPE based on the adoption of magnetic or magnetizable adsorbents which can be readily isolated from the sample matrix by an external magnet without any filtration or centrifugation [21-22]. Notably, magnetic sorbents are uniformly dispersed into suspension by vortexing or shaking to enhance the interfacial area between sorbent and analytes, which give high extraction efficiency in a short time [20,22].

Hitherto, Fe_3O_4 nanoparticles have been widely used as a sorbent in MSPE due to its high magnetic saturation, low toxicity, and simple preparation process [23]. However, as their high surface area (10 to $450 \text{ m}^2 \text{ g}^{-1}$), the unprotected metal oxide nanoparticles have a great tendency to aggregates, less surface interaction and easily oxidized [23,25]. These drawbacks can overcome through

functionalization or coating with different compounds for pre-concentration trace level of organic pollutants [24-26]. To date, silica/magnetite nanocomposites have been particularly devoted, since the protective layer afforded by silica can screen the dipolar magnetic attraction between magnetite particles, which favor the dispersion and prevent them from leaching in the acidic environment [27].

In this regard, mesoporous silica such as MCM-41 (Mobil Composition of Matter Number 41), and SBA-15 (Santa Barbara Amorphous-15) are solid materials, as well as consist of a honeycomb-like porous structure with hundreds of free mesopores that are able to accommodate relatively with high coverage of bioactive molecules. Their tremendous features, include high surface area ($700\text{--}1500 \text{ m}^2 \text{ g}^{-1}$), large pore volume ($> 0.7 \text{ cm}^3 \text{ g}^{-1}$), tunable pore size with a narrow distribution, and good chemical and thermal stability of these materials, make them potentially suitable for various application in different fields of technology including drug delivery system [28], catalysis [29], sensing [30] and removal/preconcentration of organic pollutants [30-32]. Furthermore, a huge density of silanol groups on the pore wall allows a variety of functional groups to be incorporated for increasing selectivity [34]. A literature survey reveals that the application of silica embedded magnetite system has been aroused widespread in environmental analysis. For instance, octadecyl moieties derivatized Fe_3O_4 for polycyclic aromatic hydrocarbons from environmental samples [20] $\text{Fe}_3\text{O}_4@\text{SiO}_2\text{-C18}$ magnetic composite materials for extraction of organophosphorus pesticides [35], $\text{Fe}_3\text{O}_4@\text{SiO}_2@\text{PMMA}$ for enrichment peptides and proteins [36] and MCM-41 embedded Fe_3O_4 nanoparticles for the extraction and determination of selective antidepressant drugs in biological fluids [23].

There have been significant advances in magnetic nanoparticles applied as sorbents for magnetic solid phase extraction to the best of our knowledge, relatively few published works address the investigation of the potential use of mesoporous silica coated magnetic nanoparticles as a sorbent for magnetic solid phase extraction in organic pollutants agriculture crops. In

view of the aforementioned, the main aim of this study was to investigate the synthesis of Fe_3O_4 -MCM-41 as an efficient sorbent for magnetic solid phase extraction (MSPE). Therefore, the extraction performance of sorbent was evaluated for MSPE to extract three OPPs (chlorpyrifos, diazinon and parathion methyl) in strawberry and grape samples prior to high performance liquid chromatography UV detection (HPLC-UV). To accomplish this purposed, the parameters affecting the extraction recoveries were investigated, and the related optimized values were obtained.

■ EXPERIMENTAL SECTION

Materials

Analytical grade acetonitrile and methanol were obtained from Merck (Darmstadt, Germany), hydrochloric acid 37%, ammonium hydroxide NH_4OH 25%, were provided from Sigma Aldrich (USA). Pesticide standard of chlorpyrifos, diazinon, and parathion methyl prepared in methanol were purchased from Sigma Aldrich (purity assay in range of 98–101%). A stock solution (1000 mg L^{-1}) of each pesticide was prepared in methanol, then a 100 mg/L intermediary standard mixture stock was achieved. For the synthesis of MCM-41 and Fe_3O_4 -MCM-41, cetyltrimethylammonium bromide (CTABr) and Ludox colloidal (30%) were purchased from Sigma-Aldrich. $\text{FeCl}_2 \cdot 4\text{H}_2\text{O}$ and FeCl_3 were obtained from Merck (Germany). Potassium dihydrogen phosphate (KH_2PO_4), sodium hydroxide (NaOH) and phosphoric acid were obtained from Merck (Darmstadt, Germany).

Chromatographic Conditions

The chromatographic analysis for pesticides was performed on a ZORBAX Eclipse C_{18} column ($5 \mu\text{m} \times 2.1 \times 100 \text{ mm}$) from Agilent Technologies, (USA), consisting of a quaternary pump and UV-Vis Detector. Analyte peaks were detected using Agilent UV-Vis detector at a selected wavelength of 210 nm . The mobile phase consisted of acetonitrile and phosphate buffer (pH 4.5; 1 mM) at the ratio of 60:40 v/v. The flow rate was programmed at 0.2 mL min^{-1} and the injection ($0.2 \mu\text{L}$) into the HPLC system was carried out manually using microsyringe Hamilton Company (California, USA).

Procedure

Preparation of MCM-41 and Fe_3O_4 -MCM-41

The MCM-41 was prepared according to the previous study [37-38] with minor modifications. Briefly, sodium silicate (solution A) was prepared by mixing 33.80 mL of Ludox (30%) with 3.03 g sodium hydroxide (NaOH) in 37.5 mL double distilled water at $80 \text{ }^\circ\text{C}$ for 2 h with stirring. Another solution (solution B) was prepared separately by mixing 9.60 g of cetyltrimethylammonium bromide (CTABr) and 0.50 g of ammonium hydroxide (NH_4OH) in 75.0 mL of distilled water, followed by stirring at $80 \text{ }^\circ\text{C}$ until a clear solution was obtained. Both solutions, A and B, were mixed in polypropylene bottle to give a gel with a composition of $6 \text{ SiO}_2:\text{CTABr}:1.5 \text{ Na}_2\text{O}:0.15 (\text{NH}_4)_2\text{O}:250\text{H}_2\text{O}$, followed by vigorous stirring. The resulting gel was kept in an air oven for crystallization at $100 \text{ }^\circ\text{C}$ for 24 h. The gel then was cooled to room temperature, and the pH of the gel was adjusted approximately to 10.2 by adding 25 wt.% acetic acid. The heating and pH adjustment were repeated twice. The solid product was filtered, washed, neutralized and dried overnight at $100 \text{ }^\circ\text{C}$. Finally, the solid product was calcined at $550 \text{ }^\circ\text{C}$ in the furnace.

Fe_3O_4 -MCM-41 (Fig. 1) was prepared by following the reported procedure with minor modification [39]. Briefly, Fe_3O_4 -MCM-41 was prepared by mixing 0.5 g of MCM-41 in 100 mL doubled distilled water and 1 mmol $\text{FeCl}_2 \cdot 4\text{H}_2\text{O}$ and 2 mmol FeCl_3 were added to this solution. Then, the solution mixture was vigorously stirred

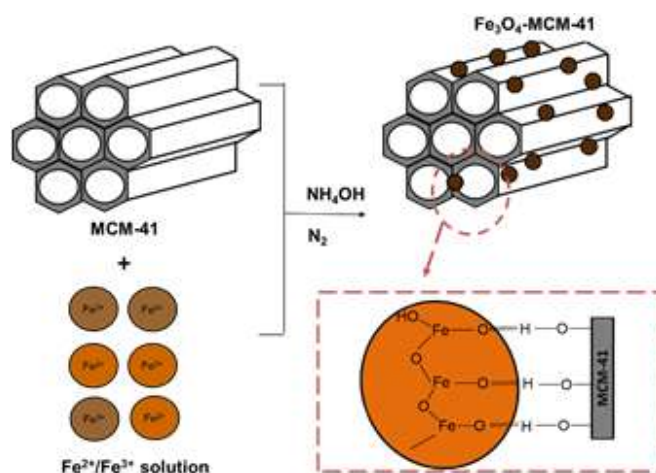


Fig 1. Synthesis route of Fe_3O_4 -MCM-41 [40]

and degassed with nitrogen. During the stirring solution, 10 mL aqueous ammonium hydroxide solution was added dropwise. Once the solution became black, and it was continued stirring for another 1 h. Finally, the solution was centrifuged with doubled distilled water until the pH becomes neutral. Then, the synthesized Fe_3O_4 -MCM-41 was dried in a vacuum desiccator at room temperature.

The characterization of synthesized MCM-41 and Fe_3O_4 -MCM-41 was performed by Fourier transform infrared (FTIR), X-ray diffraction (XRD), field emission scanning electron microscopy (FESEM), and nitrogen adsorption-desorption isotherms. A Perkin Elmer 8300 Series KBr-Fourier transform infrared spectrometer (KBr-FTIR) was used KBr pellets method in the range from 4000 to 400 cm^{-1} for recording the FTIR spectra. Surface morphology and size of synthesized materials were studied using JEOL JEM-2300 field emission scanning electron microscopy (Tokyo, Japan) after coating the sample with a gold film, using a voltage 20 kV. Transmission electron microscopy (TEM) was performed using a JEM-2100F microscope (200 kV). XRD analysis was carried out on (Rigaku) with $\text{CuK}\alpha$ radiation ($\lambda = 1.5406 \text{ \AA}$, 30 Kv, 30 mA) to investigate the internal array of the composite. The specific surface area and averaged pore size of the prepared materials were determined using Brunauer-Emmett-Teller (BET) surface area analyzer (Belsorp-mini II, Japan). The sample was evacuated at (300 °C and in nitrogen flow for 6 h). The surface area was obtained from the linear of Brunauer-Emmett-Teller (BET) method using adsorption data in the relative pressure range from 0.05 to 0.2. The pore size distribution was calculated from the adsorption branch of the isotherm using the Barrett-Joyner-Halenda (BJH) model.

Real sample preparation

Grape and strawberry were chosen as real model samples, and the sample preparation procedure was implemented based on the reported procedure [41]. Then, 1000 μL of the standard solution of pesticides (1 mg L^{-1}) in real samples was spiked into real samples (10 g of each) and kept at room temperature for 1 h. Afterward, 10 mL of distilled water and 10 mL of methanol were added into it and was mashed using a laboratory mixer followed by homogenization using ultra-sonicator (4000 rpm) for

5 min. Finally, the solution was filtered using filter paper two times. The same procedure was conducted for unspiked samples without the addition of the standard solution of the pesticides. Finally, the filtered solutions (spiked and unspiked) were subjected to the proposed procedure.

Extraction procedures for selected organophosphorus pesticides

Optimization of MSPE parameters. Different parameters include types of extraction time, desorption solvent, desorption time, and sorbent dosage were optimized during the MSPE. Initially, 10 mL of sample volume, 50 mg of sorbent, and 15 min extraction time were used for extraction of the selected chlorinated pesticides. The organophosphorus pesticides were eluted using 0.5 mL of different types of solvents.

Magnetic solid phase extraction (MSPE). The prepared of Fe_3O_4 -MCM-41 composite was studied as MSPE sorbent for the enhanced preconcentration of the targeted pesticides from fruit samples [42]. Briefly, an optimum weight of the sorbent Fe_3O_4 -MCM-41 (50 mg) was added into 10 mL of treated samples spiked with known variable amounts of selected pesticides. The mixture was shaken (250 rpm) for 15 min at room temperature by orbital shaker to achieve a homogenous dispersion solution. With the aid of an external magnet, the sample solution was be removed, and the trapped analytes were eluted with 500 μL of acetone under ultrasonication for 5 min. Finally, the magnet was again placed to the vial, and the eluate was evaporated under the mild nitrogen stream, and the resultant residue was reconstituted with 0.1 mL acetone. An aliquot (2 μL) of final extract sample was injected into the HPLC/UV. Simplified schematic of the analytical procedure of MSPE is illustrated in Fig. 2.

MCM-41-DSPE procedure

A synthesized MCM-41 was optimized with important extraction parameters such as type of solvent, desorption time, sorbent dosage, extraction time. Acetone, acetonitrile, methanol, and ethyl acetate with 0.5 mL was used to optimize the effect of the solvent on MCM-41-DSPE. Comparatively, high extraction efficiency was achieved using 0.5 mL acetone at different

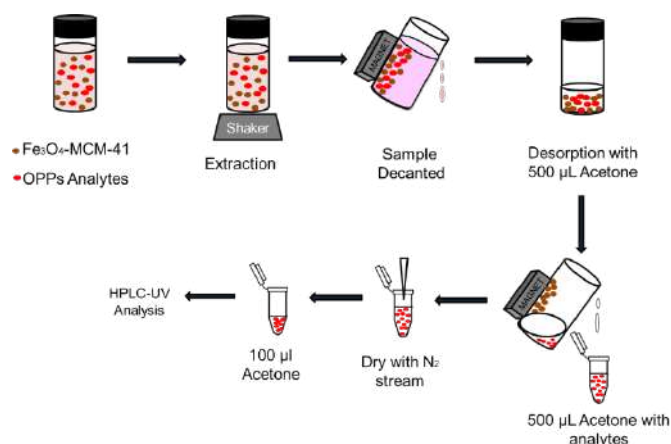


Fig 2. Schematic illustration of magnetic solid phase extraction using Fe_3O_4 -MCM-41 sorbent

desorption time (1 to 10 min). On the basis of the results, 0.5 mL of acetone at 5 min desorption time was selected as optimized desorption time. In order to improve the preconcentration factor, the sorbent dosage was also optimized (30 to 100 mg). The maximum extraction efficiency was obtained with 50 mg of sorbent dosage and thus was selected as the optimized sorbent dosage. The best result was achieved at 15 min extraction time.

■ RESULTS AND DISCUSSION

Characterization FTIR Analysis

FTIR analyses were employed to ascertain functional groups performed in Fe_3O_4 , MCM-41, and Fe_3O_4 -MCM-41 sorbents. Major adsorption bands shown in prepared sorbents were summarized in Table 1. As shown in Fig. 3, a large, broad band in all samples between 3450 and 3330 cm^{-1} corresponds O–H stretching vibration mode of silanol groups and the band at 1639 cm^{-1} is assigned to bending mode of O–H and the adsorbed

water [42-43]. The typical adsorption peaks at 1077, 800 and 460 cm^{-1} , which ascribed to the presence of asymmetric Si–O–Si stretching, symmetric Si–O–Si stretching and Si–O–Si vibration, appear in the infrared spectra of MCM-41 and Fe_3O_4 -MCM-41, respectively [45-47]. Furthermore, the adsorption peak shown in pristine Fe_3O_4 at 599 cm^{-1} (Fig. 3(b)) indicated the Fe–O stretching [45-46]. The Fe_3O_4 -MCM-41 particles show characteristics peaks at 464 and 1636 cm^{-1} , which slightly decreased with the appearance of the Fe–O–Si covalent bonding due to OH condensation [44]. Consequently, changes of some characteristic peaks confirmed the Fe_3O_4 nanoparticles were successfully anchored on the surface of MCM-41.

X-ray Diffraction

XRD patterns of MCM-41 and Fe_3O_4 -MCM-41 are shown in Fig. 4(a) and 4(b), respectively. The diffractogram of MCM-41 exhibited Bragg peaks at low

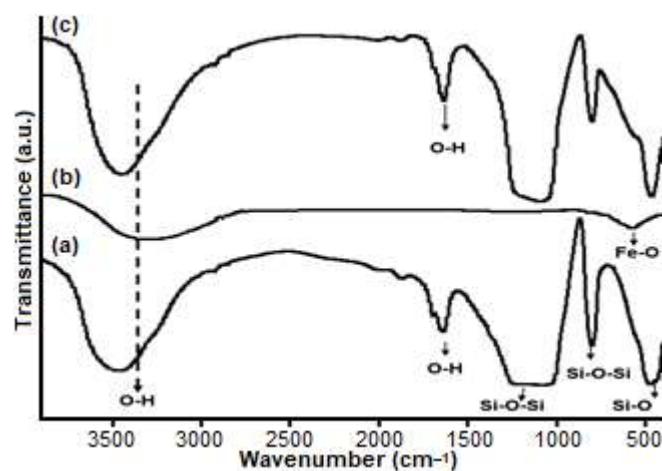


Fig 3. FTIR spectra of (a) MCM-41, (b) Fe_3O_4 and (c) Fe_3O_4 -MCM-41

Table 1. Comparison of FTIR absorption bands of MCM-41 and Fe_3O_4 -MCM-41

Adsorption stretching bands	Wavelength (cm^{-1})		
	MCM-41	Fe_3O_4	Fe_3O_4 -MCM-41
O–H stretching	3453	3330	3450
O–H bending	1639	-	1636
Asymmetric Si–O–Si	1077	-	1096
Symmetric Si–O–Si	800	-	798
Si–O–Si	459	-	463
Fe–O	-	599	-

angles between 0.967 – 1.865° , indexed as (100), (110) and (200) in the hexagonal system (Fig. 4(a)). These peaks are typical of these materials and arise from the quasiregular arrangement of the mesopores in the bulk material [50]. However, the obtained XRD pattern appeared only one broad peak at 2θ of 0.967° due to (100), and two extremely weak peaks between 1.203 and 1.865° due to (110) and (200) planes, being indicative of a material which does not exhibit long-range mesopores ordering [51]. Meanwhile, the broad diffraction peaks of 2θ at 20 – 30° shown in the angle XRD pattern of Fe_3O_4 -MCM-41 are the characteristics from the amorphous silica template (Fig. 4(b)). The diffraction peaks appeared at 2θ of 35.7 , 43.3 , 56.4 , and 63.1° were assigned to (311), (400), (511) and (440) reflections, respectively, which are indexed to the spinel structure of pure stoichiometric Fe_3O_4 (JCPDS Card No. 19-0629) [39]. The characteristic peaks of the existence of magnetite particles in Fe_3O_4 -MCM-41 exhibited the same textural property as MCM-41, which confirmed that mesoporosity was preserved after synthesis of Fe_3O_4 nanoparticles.

Morphology Property

The surface morphology of synthesized of MCM-41 and Fe_3O_4 -MCM-41 were analyzed via field emission scanning electron microscopy (FESEM) and transmission electron microscopy (TEM). The micrographs are illustrated in Fig. 5 and 6. The FESEM micrograph of

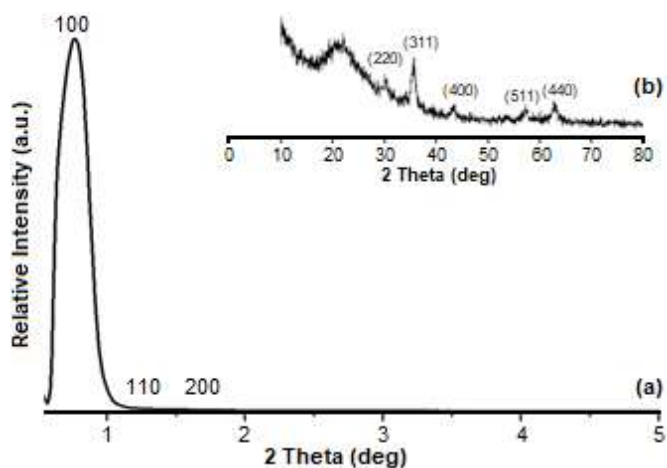


Fig 4. XRD patterns of (a) MCM-41 (b) Fe_3O_4 -MCM-41 composite

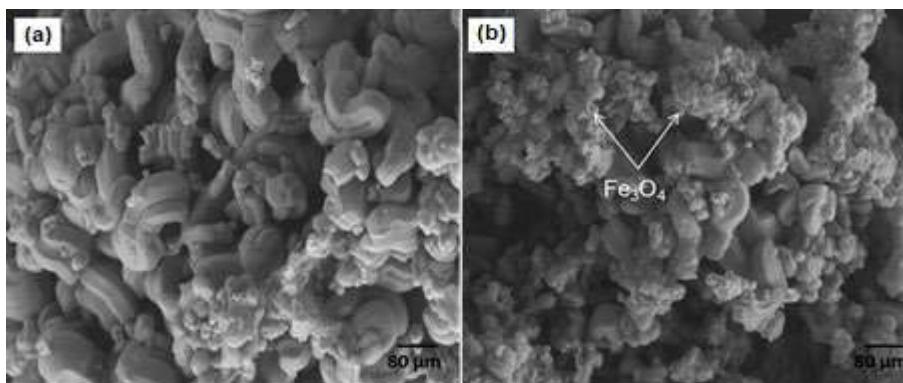


Fig 5. Micrograph image of (a) MCM-41 and (b) Fe_3O_4 -MCM-41 observed at 5 K magnification

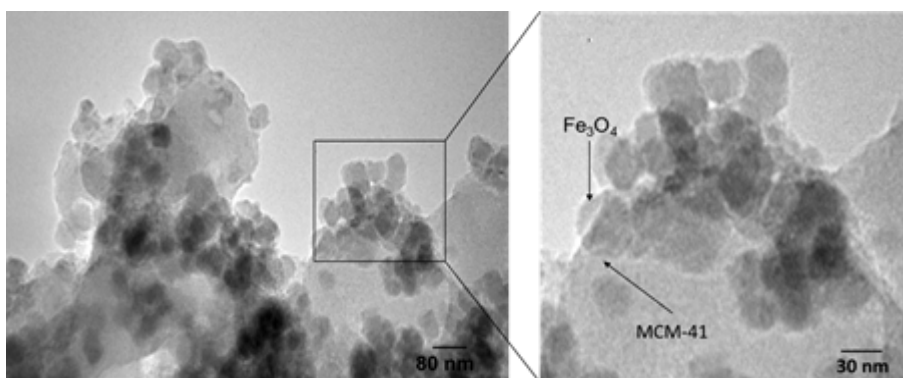


Fig 6. TEM images of Fe_3O_4 -MCM-41

MCM-41 in Fig. 5(a), showed loosely agglomerated particles with a rod-like shape, with uniform pore size about 3.83 nm, which is a good agreement with narrow size distribution (BJH) determined by nitrogen adsorption-desorption measurement [52]. After dispersing with Fe_3O_4 , Fig. 5(b) clearly shows that the distribution of magnetite particles on the surface of MCM-41 unnoticeable coating. Besides, the particle sizes are difficult to measure due to the agglomeration of magnetite particles on the surface of MCM-41. In order to indicate the iron oxide nanoparticles on the surface of mesoporous silica, a detailed TEM analysis was performed. TEM images are shown in Fig. 6, the iron oxide nanoparticles dispersed and appeared as dark dot-like objects on the surface of mesoporous silica with an average diameter approximately about 13 nm. Besides some particles could be seen in partially aggregated due to the existence of magnetic interaction between particle [27]. Thus, the TEM analysis gives evidence that the ordered mesoporous structure is maintained after dispersing.

Nitrogen Desorption Adsorption Isotherm

The isotherm of nitrogen adsorption-desorption and the corresponding pore size distribution curve of various prepared samples are presented in Fig. 7. Apparently, all samples exhibit a typical type IV physisorption curves which indicate the pattern of

mesopores materials (2–50 nm) according to the classifications of the IUPAC (Fig. 7(a)). The samples also display clear H1 type hysteresis loop with rapid in nitrogen uptake $p/p_0 = (0.4-1.0)$, which is due to monolayer adsorption of nitrogen to the walls of the mesopores. Furthermore, the samples also demonstrated a narrow pore size distribution by the BJH method, as shown by the inset in Fig. 7(b). The pore size distribution centered near (3.83 nm) for MCM-41 and Fe_3O_4 -MCM-41 (3.39 nm), respectively, suggest that the pore size is predominantly composed of mesopores and concentrated in the small size range. Fe_3O_4 -MCM-41 composite contributes a small pore size compared to the pure mesoporous due to the magnetite particles (Fe_3O_4) occupy on the mesopore free space intrachannels of MCM-41 partially [40]. This makes this composite a promising candidate for the incorporation and subsequent analysis under appropriate conditions.

The effective adsorption functional groups in the MCM-41 and Fe_3O_4 -MCM-41 pores is studied by the expressive of surface area, size, and pore volume, as presented in Table 1. A sensible difference was observed for the BET specific surface of MCM-41 ($436 \text{ m}^2 \text{ g}^{-1}$) and Fe_3O_4 -MCM-41 ($293 \text{ m}^2/\text{g}$), respectively. From the results obtained, it can be concluded that the pore size of distribution in this study can be varied within 3.83 nm to 13 nm due to the irregular pore and surface area of prepared materials. However, this pore size is sufficient

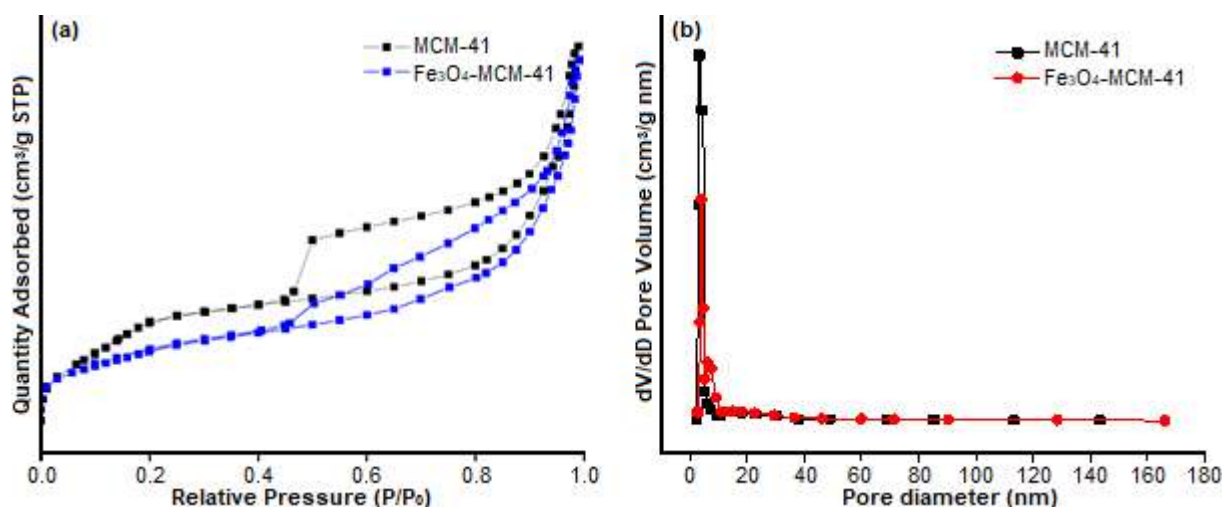


Fig 7. (a) N_2 adsorption isotherms, (b) Pore size distribution of pure MCM-41 and Fe_3O_4 -MCM-41 composite

Table 2. N₂ adsorption results

Sample	S _{BET} (m ² g ⁻¹)	D _p (nm)	V _p (cm ³ g ⁻¹)
MCM-41	436	11.27	0.533
Fe ₃ O ₄ -MCM-41	293	10.70	0.465

S_{BET} = Specific area; D_p = Mean pore diameter; V_p = Mean pore volume

enough for the sorption of targeted pesticides. Details results for sorption studies will be discussed in subtopic analytical performance.

Optimization of MSPE Procedure

A batch-wise MSPE was investigated to assess the extraction efficiency of the synthesized Fe₃O₄-MCM-41 sorbent for the selected organophosphorus pesticides. In order to optimize extraction conditions, several main parameters including desorption solvent, extraction time, desorption time and sorbent dosage were studied in one variable at a time (OVAT), which ensures the variable responsible for any effect observed is clearly identified.

Effect of extraction time

As an equilibrium extraction step is concerned, a parameter plays imperative rules on the extraction

efficiency. The effect of extraction time on the extraction efficiency of OPPs using Fe₃O₄-MCM-41 was performed to achieve the highest sensitivity and recovery. Extraction was investigated at different shaking time from 5 to 20 min. The extraction efficiency depends on the mass transfer between Fe₃O₄-MCM-41 and analytes in the sample solution. As illustrated in Fig. 8(a), there was a rapid increase in extraction efficiency of all analytes when the extraction time was prolonged from 5 to 15 min, and the peak areas remained nearly constant or decreased when the extraction time was further increased to 20 min. This phenomenon might be due to the back-extraction of analytes from the adsorbent into the sample solution [53]. Thus, 15 min was selected as the optimum extraction time for subsequent extractions.

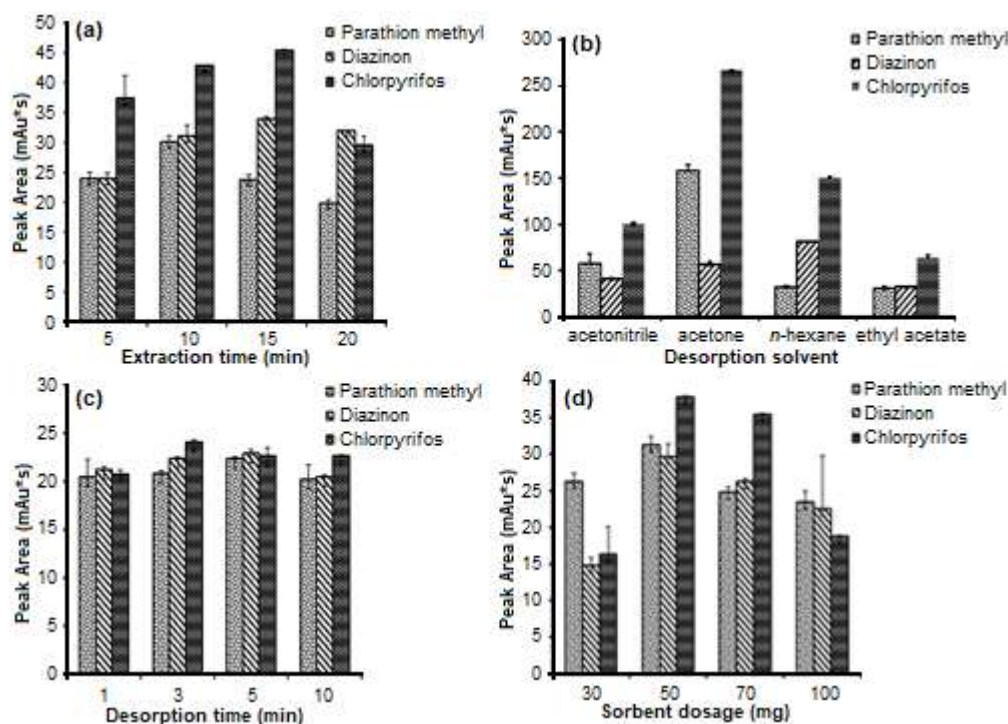


Fig 8. Effect of (a) extraction time, (b) desorption solvents, (c) desorption time and (d) sorbent dosage on OPPs pesticide extraction efficiency

Effect of desorption solvent

The selection of an appropriate desorption solvent plays a vital role in the MSPE process to ensure high recovery and sensitivity on method performance [11]. In general, the selection of desorption solvent, the polarity of solvents, the solubility of analytes relies on its compatibility of the analytical instrument should be considered. Due to the selected of OPPs relatively mid-polar and they were adsorbed strongly on Fe_3O_4 -MCM-41 surface, thus only polar solvent can disrupt the interaction and desorbed the analytes. Hence, four organic solvents of different polarity, namely, acetonitrile, acetone, ethyl acetate, and hexane, respectively, were performed to elute the adsorbed analyte from the magnetic Fe_3O_4 -MCM-41 sorbent. These solvents have different polarities, with ethyl acetate being the most polar solvent and *n*-hexane being the most non-polar solvent. It is obviously shown in Fig. 8(b) that the *n*-hexane provided good response and satisfactory efficiency towards non-polar chlorpyrifos and diazinon.

Particularly, the Fe_3O_4 -MCM-41 could not be dispersed well in *n*-hexane, which impeded the effective desorption of analytes from sorbent, but *n*-hexane is a non-polar solvent, and it provide hydrophobic interactions with selected non-polar OPPs, which similar in chemical characteristics. Otherwise, the acetone gave the highest response towards polar parathion methyl and as well as satisfactory efficiency was also obtained for the non-polar OPPs due to its highest desorption ability, and it is the least viscous solvent compared to the other three solvents except for diazinon whose response was lower than parathion methyl and chlorpyrifos. Hence, 500 μL of acetone was selected for the desorption of polar and non-polar compounds throughout the entire study as a desorption solvent.

Effect of desorption time

Desorption time is regarded as the time that is required to desorb all the analytes from the sorbent. In order to study the effect of desorption time (Fig. 8(c)), the process was performed with the aid of an ultrasonicator at different durations in the range 1 min to 10 min. It can be observed that the peak area increased with desorption time to reach a maximum at 5 min. Beyond this point

(10 min), no significant increase peak area was observed due to the analytes being re-adsorbed by the sorbent [54]. Therefore, 5 min was adequate and acceptable to elute all the absorbed analytes fully.

Effect of sorbent dosage

The optimization of the mass of the sorbent is one of critical condition that provides a sufficient capacity to retain both the analyte and any contaminants that may be also be retained during the loading procedure [17]. In order to achieve the highest extraction recovery, the effect of sorbent dosage was assessed by changing the mass of sorbent in the range of 30 to 100 mg to extract the selected OPPs pesticides (Fig. 8(d)). This graph clarified that the peak area ratio of the extracted OPPs remarkably increased up to 50 mg of the sorbent. However, when 70 mg of sorbent was used, no additional enhancement of the peak area was observed. The decrease in response could be due to the saturation of the active site on the adsorbent that has been exceeded. Thus, 50 mg of sorbent was adopted for subsequent analysis.

Extraction Performance of Fe_3O_4 , MCM-41, and Fe_3O_4 -MCM-41

Comparative studies were performed in order to compare the extraction performance of the newly synthesized of Fe_3O_4 , MCM-41 and Fe_3O_4 -MCM-41 sorbents for pre-concentration of four pesticides of different polarity organophosphorus pesticides (chlorpyrifos, diazinon, and parathion-methyl). Fig. 9 illustrates that the Fe_3O_4 showed unsatisfactory (< 10%) towards the all selected OPPs studied as evidence by the extraction recoveries observed. However, when Fe_3O_4 -MCM-41 particles were utilized as a sorbent, relatively higher extraction recoveries (> 70%) of OPPs pesticides were obtained [23]. The capability of Fe_3O_4 -MCM-41 exhibited the highest extraction recoveries due to the analyte was adsorbed on the active site of MCM-41, and this possibility might be due to the hydrogen bonding interaction between the silanol groups of MCM-41 with different anionic sites (O, N, S, and Cl) of the selected OPPs [55].

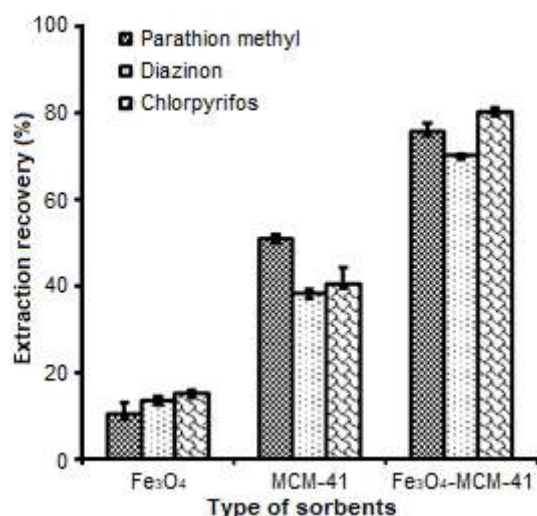


Fig 9. Comparison of extraction performance (based on extraction recoveries) of three different sorbents for the OPPs pre-concentration. Condition for extractions: sample volume 10 mL, mass of sorbent 50 mg, concentration of analytes 1 mg L⁻¹, extraction time 15 min, desorption time 3 min and 0.5 mL acetone as desorption solvent

Analytical Performance

Quantitative analysis of MSPE method based on Fe₃O₄-MCM-41 as sorbent was validated under the optimized conditions using different analytical parameters such as linearity, the limit of detection (LOD), the limit of quantification (LOQ), precision and accuracy. Matrix match calibration was performed by spiking

different concentrations of the selected pesticides into the strawberry and grape samples. The linearity of the MSPE technique for OPPs pesticides using MCM-41 and Fe₃O₄-MCM-41 was performed in the range from 0.1–5.00 mg L⁻¹ for strawberry and grape samples. Good linearity with a high value of the coefficient of determination (R^2) was higher than 0.9900 in the linear range (Table 3). The LOD ($S/N = 3$) obtained for all pesticides in the range 0.02–0.15 mg L⁻¹ and the LOQ ($10 \times S/N$) in the range 0.06–0.40 mg L⁻¹. However, the obtained LOD for Fe₃O₄-MCM-41 is appreciably lower as compared to the MCM-41. Besides, LOD obtained for Fe₃O₄-MCM-41 was well below the maximum residue limits (MRLs) real-life range of grape and strawberry (10 mg L⁻¹) set by EU for each pesticide. Thus, the proposed MSPE method based on Fe₃O₄-MCM-41 is highly efficient for the determination of these selected pesticides in fruit samples.

Repeatability and reproducibility of the proposed MSPE method were investigated using intraday and interday measurements. Relative standard deviation (%RSD) were assessed at low and high concentrations (0.1–5.0 mg L⁻¹) with triplicate analyses on the same day and over three different days ($n = 3$) using fruits samples, respectively. Acceptable results based on RSD% were obtained in the range from 1.0 to 6.0% ($n = 3$) and 1.0 to 7.0% ($n = 3$) for intraday and interday precision respectively (Table 4).

Table 3. Statistical results of MSPE method for selected pesticides, including linear range, correlation coefficients (R^2), the limit of detection (LOD), the limit of quantification (LOQ) of MCM-41 and Fe₃O₄-MCM-41 of OPPs spiked in fruits samples ($n = 3$)

	Fe ₃ O ₄ -MCM-41				MCM-41			
	Linearity (mg L ⁻¹)	LOD (mg L ⁻¹)	LOQ (mg L ⁻¹)	R^2	Linearity (mg L ⁻¹)	LOD (mg L ⁻¹)	LOQ (mg L ⁻¹)	R^2
Strawberry								
Chlorpyrifos	0.1-5.00	0.02	0.06	0.9955	0.1-5.00	0.12	0.38	0.9942
Diazinon	0.1-5.00	0.12	0.39	0.9935	0.1-5.00	0.15	0.40	0.9950
Parathion methyl	0.1-5.00	0.12	0.38	0.9940	0.1-5.00	0.10	0.22	0.9912
Grapes								
Chlorpyrifos	0.1-5.00	0.04	0.13	0.9966	0.1-5.00	0.11	0.22	0.9945
Diazinon	0.1-5.00	0.04	0.12	0.9960	0.1-5.00	0.13	0.36	0.9971
Parathion methyl	0.1-5.00	0.06	0.19	0.9980	0.1-5.00	0.14	0.34	0.9960

Table 4. Study of repeatability and reproducibility of the MSPE method based on intraday and interday precisions

Analyte	MSPE precision			
	Intraday %RSD (n = 3)		Interday %RSD (n = 3)	
	Spiked in fruits samples (mg L ⁻¹)			
	0.1	5.00	0.1	5.00
Grapes				
Chlorpyrifos	74.9 (3.2)	125.2 (1.2)	95.8 (6.4)	100.89 (0.3)
Diazinon	75.9 (2.7)	95.2 (4.3)	70.7 (1.4)	122.08 (4.5)
Parathion methyl	75.5 (1.9)	92.9 (4.1)	76.1 (2.1)	114.5 (1.2)
Strawberry				
Chlorpyrifos	73.8 (4.6)	107.7 (0.8)	72.6 (5.8)	100.63 (1.1)
Diazinon	74.50 (5.8)	69.94 (3.8)	92.6 (6.4)	88.48 (4.2)
Parathion methyl	79.4 (4.3)	108.1 (4.4)	70.9 (6.6)	73.76 (3.4)

Reusability of the adsorbent was carried out by evaluating the extraction performance of Fe₃O₄-MCM-41 for different extraction-desorption cycles. In order to investigate the regeneration of the sorbent, the used of sorbent was washed subsequently with acetone respectively after each extraction, and then the dried

sorbent was used in the subsequent analysis. The result indicates that Fe₃O₄-MCM-41 could be used repeatedly at least three times without a significant decrease in extraction recoveries (> 90%) and its magnetic property. These results show the adsorbent is stable for repeated used, which is favorable for MSPE based method.

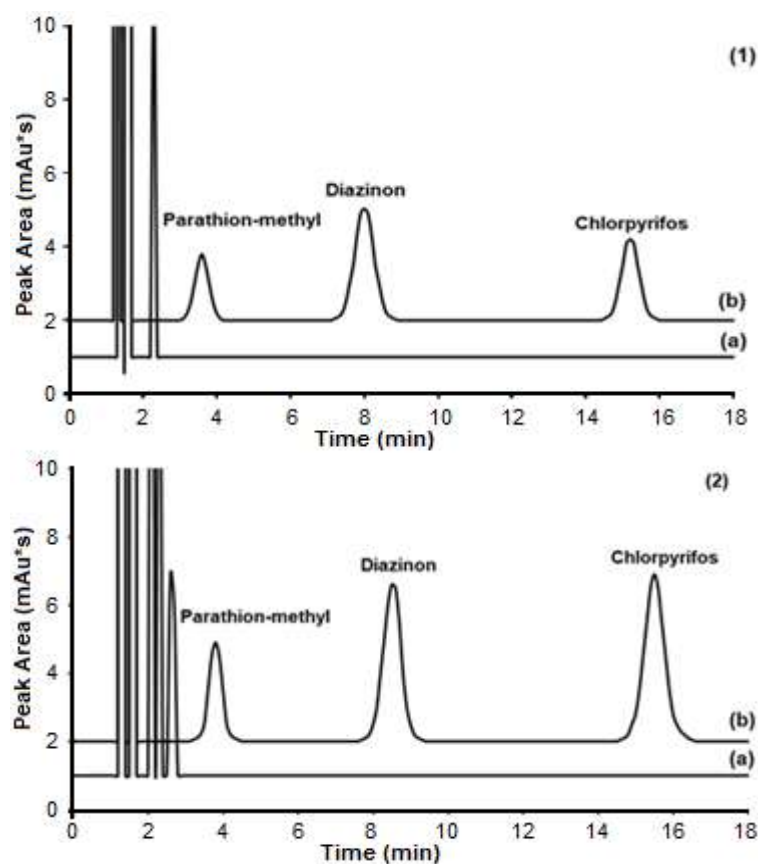
**Fig 10.** HPLC-UV chromatogram for the (a) unspiked (1 mg L⁻¹) and (b) spiked of real samples of (1) grape and (2) strawberry

Table 5. Recovery and RSD% of OPPs analysis in grape and strawberry samples using developed MCM-41 and Fe₃O₄-MCM-41

Sorbent	Sample	Spiked level (mg L ⁻¹)	% Recovery (RSD%, n=3)		
			Chlorpyrifos	Diazinon	Parathion methyl
MCM-41	Strawberry	0	nd	nd	nd
		1	110.7 (5.7)	101.4 (2.0)	108.9 (5.2)
	Grapes	0	nd	nd	nd
		1	112.4 (4.6)	107.2 (0.7)	73.3 (4.8)
Fe ₃ O ₄ -MCM-41	Strawberry	0	nd	nd	nd
		1	101.8 (1.8)	83.5 (3.0)	109.6(4.3)
	Grapes	0	nd	nd	nd
		1	118.3 (5.5)	108.8 (1.3)	115.3 (1.2)

Table 6. Comparison of the current study with other recent solid-based extraction techniques that used for determination of OPPs in fruits and vegetable sample preparation

Adsorbent	Method	Detector	Matrix	LODs	Recovery (%)	References
Fe ₃ O ₄ -MCM-41	MSPE	HPLC-UV	Fruits	0.02 mg L ⁻¹	85-120	This study
MG@SiO ₂ -TMSPEdc	MSPE	GC-μECD	Fruits	0.20 μg kg ⁻¹	82-113	[56]
Fe ₃ O ₄ @G-TEOS-MTMOS	MSPE	GC-ECD	Water	1.44 pg mL ⁻¹	83-105	[57]
Fe ₃ O ₄ @SiO ₂ @GO-PEA	MSPE	GC-NPD	Water and vegetables	0.02 μg L ⁻¹	94.6-104.2	[58]
C-G/Fe ₃ O ₄	SPME	HPLC-UV	Water	5.0 ng L ⁻¹	>70	[59]
GCB/PSA/Fe ₃ O ₄	DSPE	GC-MS	Vegetables	1.30 ng L ⁻¹	70.3-114.1	[60]
Molecular imprinted polymer	SPE	GC-MS	Fruits	0.83 μg L ⁻¹	89.7-99.7	[61]
PDMS-TEOS	SBSE	GC-TCD	Vegetables	0.06 ng mL ⁻¹	70-85	[62]

Organophosphorus Pesticides (OPPs), limit of detection (LOD), magnetic solid phase extraction (MSPE), solid phase microextraction (MSPE), dispersive solid phase extraction (DSPE), solid phase extraction (SPE), stir bar sorptive extraction (SBSE), high-performance liquid chromatography-ultraviolet detector (HPLC-UV), gas chromatography-electron capture detector (GC-ECD), gas chromatography mass spectrometry (GC-MS), gas chromatography thermal conductivity (GC-TCD)

Real Sample Analysis

In order to assess the applicability of the proposed Fe₃O₄-MCM-41, MSPE method OPPs pesticides were isolated to strawberry and grape as real model samples. Prior to that, the real samples were treated in accordance with the procedure in preparing samples and were then spiked with the OPP standard solution with level 1 mg L⁻¹. Each sample was analyzed three times using the HPLC/UV. The same process was applied to unspiked samples. The obtained HPLC chromatograms for strawberry and grape samples (spiked and unspiked) are illustrated in Fig. 10(1) and 10(2). It was shown that the unspiked samples for the selected pesticides were not detected. Besides, Table 5 shown good recoveries of the method were observed in the range of 85–120% with good repeatability %RSD (< 10%, n = 3) for the selected

pesticides in both strawberry and grape samples. Additionally, RSDs for triple extraction was more than 10% for the analyte in the real samples.

Comparison with Other Methods

Literature research of analytical performances on the determination of OPPs pesticide in various samples was conducted to compare the properties of the proposed method with those of the reputed studies. As illustrated in Table 6, the developed MSPE method offers LOD better than SPE, DSPE, and comparable with that of SPME and MSPE methods which demonstrated considerable lower LODs. However, the LODs of the current MSPE procedure is lower than MLRs (10 mg L⁻¹) and offers an easier and faster procedure for the simultaneous extraction of selected pesticides from fruit samples.

■ CONCLUSION

The combined advantages of the large surface area of MCM-41 and magnetic properties of Fe₃O₄ make the successfully synthesized Fe₃O₄-MCM-41 a promising sorbent for microextraction of OPPs pesticides in fruit samples. Outstanding relative recovery (85–120%) and low LOD (0.04–0.20 mg L⁻¹) with method precision (RSD%) of (2.6 to 9.0%, n = 3) for selected OPPs in real samples were achieved. These results proved that the newly synthesized of Fe₃O₄-MCM-41 is a versatile adsorbent for the preconcentration of OPPs pesticides as compared to those of MCM-41. The field studies also supported the effectiveness of this new magnetic nanocomposite adsorbent which could be used and has good potential for the extraction of selected pesticides from real fruit samples.

■ ACKNOWLEDGMENTS

The authors wish to thank Universiti Teknologi MARA for the facilitation and the Ministry of Education Malaysia for their financial supports through vote number 600-IRMI/FRGS 5/3 (039/2017) (FRGS/1/2017/STG01/UITM/02/8).

■ REFERENCES

- [1] Nodeh, H.R., Wan Ibrahim, W.A., Kamboh, M.A., and Sanagi, M.M., 2015, Dispersive graphene-based silica coated magnetic nanoparticles as a new adsorbent for preconcentration of chlorinated pesticides from environmental water, *RSC Adv.*, 5 (93), 76424–76434.
- [2] Farajzadeh, M.A., Mogaddam, M.R.A., Aghdam, S.R., Nouri, N., and Bamorowat, M., 2016, Application of elevated temperature-dispersive liquid-liquid microextraction for determination of organophosphorus pesticides residues in aqueous samples followed by gas chromatography-flame ionization detection, *Food Chem.*, 212, 198–204.
- [3] Sanusi, A., Guillet, V., and Montury, M., 2004, Advanced method using microwaves and solid-phase microextraction coupled with gas chromatography-mass spectrometry for the determination of pyrethroid residues in strawberries, *J. Chromatogr. A*, 1046 (1-2), 35–40.
- [4] Ravelo-Pérez, L.M., Hernández-Borges, J., and Rodríguez-Delgado, M.Á., 2008, Multi-walled carbon nanotubes as efficient solid-phase extraction materials of organophosphorus pesticides from apple, grape, orange, and pineapple fruit juices, *J. Chromatogr. A*, 1211 (1-2), 33–42.
- [5] Lambropoulou, D.A., and Albanis, T.A., 2003, Headspace solid-phase microextraction in combination with gas chromatography-mass spectrometry for the rapid screening of organophosphorus insecticide residues in strawberries and cherries, *J. Chromatogr. A*, 993 (1-2), 197–203.
- [6] Soler, C., Mañes, J., and Picó, Y., 2005, Comparison of liquid chromatography using triple quadrupole and quadrupole ion trap mass analyzers to determine pesticide residues in oranges, *J. Chromatogr. A*, 1067 (1-2), 115–125.
- [7] Maroni, M., Colosio, C., Ferioli, A., and Fait, A., 2000, Biological monitoring of pesticide exposure: A review. Introduction, *Toxicology*, 143 (1), 5–118.
- [8] European Commission, *EU Pesticides database*, <https://ec.europa.eu/food/plant/pesticides/eu-pesticides-database/public/?event=homepage&language=EN>, accessed on 07 January 2019.
- [9] Ahmadi, K., Abdollahzadeh, Y., Asadollahzadeh, M., Hemmati, A., Tavakoli, H., and Torkaman, R., 2015, Chemometric assisted ultrasound leaching-solid phase extraction followed by dispersive-solidification liquid-liquid microextraction for determination of organophosphorus pesticides in soil samples, *Talanta*, 137, 167–173.
- [10] Alves, A.C.H., Gonçalves, M.M.P.B., Bernardo, M.M.S., and Mendes, B.S., 2011, Determination of organophosphorus pesticides in the ppq range using a simple solid-phase extraction method combined with dispersive liquid-liquid microextraction, *J. Sep. Sci.*, 34 (18), 2475–2481.
- [11] Wan Ibrahim, W.A., Veloo, K.V., and Sanagi, M.M., 2012, Novel sol-gel hybrid methyltrimethoxysilane-tetraethoxysilane as solid

- phase extraction sorbent for organophosphorus pesticides, *J. Chromatogr. A*, 1229, 55–62.
- [12] Timofeeva, I., Shishov, A., Kanashina, D., Dzema, D., and Bulatov, A., 2017, On-line in-syringe sugaring-out liquid-liquid extraction coupled with HPLC-MS/MS for the determination of pesticides in fruit and berry juices, *Talanta*, 167, 761–767.
- [13] García, M.D.G., Dahane, S., Arrabal-Campos, F.M., Viciano, M.M.S., García, M.A., Fernández, I., and Galera, M.M., 2017, MCM-41 as novel solid phase sorbent for the pre-concentration of pesticides in environmental waters and determination by microflow liquid chromatography-quadrupole linear ion trap mass spectrometry, *Microchem. J.*, 134, 181–190.
- [14] Saraji, M., Jafari, M.T., and Mossaddegh, M., 2016, Carbon nanotubes@silicon dioxide nanohybrids coating for solid-phase microextraction of organophosphorus pesticides followed by gas chromatography-corona discharge ion mobility spectrometric detection, *J. Chromatogr. A*, 1429, 30–39.
- [15] Della Pelle, F., Di Crescenzo, M.C., Sergi, M., Montesano, C., Di Ottavio, F., Scarpone, R., Scortichini, G., and Compagnone, D., 2016, Micro-solid-phase extraction (μ -SPE) of organophosphorous pesticides from wheat followed by LC-MS/MS determination, *Food Addit. Contam. A*, 33 (2), 291–299.
- [16] Hou, X., Lei, S.R., Qiu, S.T., Guo, L.A., Yi, S.G., and Liu, W., 2014, A multi-residue method for the determination of pesticides in tea using multi-walled carbon nanotubes as a dispersive solid phase extraction absorbent, *Food Chem.*, 153, 121–129.
- [17] Pavlović, D.M., Babić, S., Horvat, A.J.M., and Kaštelan-Macan, M., 2007, Sample preparation in the analysis of pharmaceuticals, *TrAC, Trends Anal. Chem.*, 26 (11), 1062–1075.
- [18] Samsidar, A., Siddiquee, S., and Shaarani, S.M., 2018, A review of extraction, analytical and advanced methods for determination of pesticides in environment and foodstuffs, *Trends Food Sci. Technol.*, 71, 188–201.
- [19] Šafaříková, M., and Šafařík, I., 1999, Magnetic solid-phase extraction, *J. Magn. Magn. Mater.*, 194 (1-3), 108–112.
- [20] Bai, L., Mei, B., Guo, Q.Z., Shi, Z.G., and Feng, Y.Q., 2010, Magnetic solid-phase extraction of hydrophobic analytes in environmental samples by a surface hydrophilic carbon-ferromagnetic nanocomposite, *J. Chromatogr. A*, 1217 (47), 7331–7336.
- [21] Krisbiantoro, P.A., Santosa, S.J., and Kunarti, E.S., 2017, Synthesis of fulvic acid-coated magnetite (Fe_3O_4 -FA) and its application for the reductive adsorption of $[\text{AuCl}_4]^-$, *Indones. J. Chem.*, 17 (3), 453–460.
- [22] Suyanta, Sutarno, Nuryono, Rusdiarso, B., Kunarti, E.S., Kusumastuti, H., and Kurnia, L., 2019, Superparamagnetic nanocomposite of magnetite-chitosan using oleic acid as anti agglomeration and glutaraldehyde as crosslinkage agent, *Indones. J. Chem.*, 19 (1), 133–142.
- [23] Kamaruzaman, S., Sanagi, M.M., Yahaya, N., Wan Ibrahim, W.A., Endud, S., and Wan Ibrahim, W.N., 2017, Magnetic micro-solid-phase extraction based on magnetite-MCM-41 with gas chromatography-mass spectrometry for the determination of antidepressant drugs in biological fluids, *J. Sep. Sci.*, 40 (21), 4222–4233.
- [24] Li, X.S., Zhu, G.T., Luo, Y.B., Yuan, B.F., and Feng, Y.Q., 2013, Synthesis and applications of functionalized magnetic materials in sample preparation, *TrAC, Trends Anal. Chem.*, 45, 233–247.
- [25] Krížek, M., Pechoušek, J., Tuček, J., Šafařová, K., Medřík, I., and Machala, L., 2012, Iron oxide nanoparticle powders with high surface area, *AIP Conf. Proc.*, 1489 (1), 88–94.
- [26] Zhu, L., Pan, D., Ding, L., Tang, F., Zhang, Q., Liu Q., and Yao, S., 2010, Mixed hemimicelles SPE based on CTAB-coated $\text{Fe}_3\text{O}_4/\text{SiO}_2$ NPs for the determination of herbal bioactive constituents from biological samples, *Talanta*, 80 (5), 1873–1880.
- [27] de Souza, K.C., Andrade, G.F., Vasconcelos, I., de Oliveira Viana, I.M., Fernandes, C., and de Sousa,

- E.M.B., 2014, Magnetic solid-phase extraction based on mesoporous silica-coated magnetic nanoparticles for analysis of oral antidiabetic drugs in human plasma, *Mater. Sci. Eng., C*, 40, 275–280.
- [28] Manzano, M., Aina, V., Areán, C.O., Balas, F., Cauda, V., Colilla, M., Delgado M.R., and Vallet-Regí, M., 2008, Studies on MCM-41 mesoporous silica for drug delivery: Effect of particle morphology and amine functionalization, *Chem. Eng. J.*, 137 (1), 30–37.
- [29] Duan, X., Qian, G., Zhou, X., Chen, D., and Yuan, W., 2012, MCM-41 supported CoMo bimetallic catalysts for enhanced hydrogen production by ammonia decomposition, *Chem. Eng. J.*, 207–208, 103–108.
- [30] Takeuchi, R., Shoji, A., and Sugawara, M., 2013, A solid phase-based nanopore sensing system for biomolecules using lipid-loaded mesoporous silica MCM-41 and a fluorescent dye, *Sens. Actuators, B*, 181, 29–37.
- [31] Sayari, A., Hamoudi, S., and Yang, Y., 2005, Applications of pore-expanded mesoporous silica. 1. Removal of heavy metal cations and organic pollutants from wastewater, *Chem. Mater.*, 17 (1), 212–216.
- [32] Koesnarpadi, S., Santosa, S.J., Siswanta, D., and Rusdiarso, B., 2017, Humic acid coated Fe₃O₄ nanoparticle for phenol sorption, *Indones. J. Chem.*, 17 (2), 274–283.
- [33] Muflikhah, M., Rusdiarso, B., Putra, E.G.R., and Nuryono, 2017, Modification of silica coated on iron sand magnetic material with chitosan for adsorption of Au(III), *Indones. J. Chem.*, 17 (2), 264–273.
- [34] Yokoi, T., Yoshitake, H., and Tatsumi, T., 2004, Synthesis of mesoporous silica by using anionic surfactant, *Stud. Surf. Sci. Catal.*, 154, 519–527.
- [35] Maddah, B., and Shamsi, J., 2012, Extraction and preconcentration of trace amounts of diazinon and fenitrothion from environmental water by magnetite octadecylsilane nanoparticles, *J. Chromatogr. A*, 1256, 40–45.
- [36] Chen, H., Deng, C., and Zhang, X., 2010, Synthesis of Fe₃O₄@SiO₂@PMMA core-shell-shell magnetic microspheres for highly efficient enrichment of peptides and proteins for MALDI-ToF MS analysis, *Angew. Chem. Int. Ed.*, 49 (3), 607–611.
- [37] Kamaruzaman, S., Sanagi, M.M., Endud, S., Wan Ibrahim, W.A., and Yahaya, N., 2013, MCM-41 solid phase membrane tip extraction combined with liquid chromatography for the determination of non-steroidal anti-inflammatory drugs in human urine, *J. Chromatogr. B*, 940, 59–65.
- [38] Taib, N.I., Endud, S., and Katun, M.N., 2011, Functionalization of mesoporous Si-MCM-41 by grafting with trimethylchlorosilane, *Int. J. Chem.*, 3 (3), 2–10.
- [39] Bhuyan, D., Saikia, M., and Saikia, L., 2015, Magnetically recoverable Fe₃O₄@SBA-15: An improved catalyst for three component coupling reaction of aldehyde, amine, and alkyne, *Catal. Commun.*, 58, 158–163.
- [40] Liu, Y., Qiu, J., Jiang, Y., Liu, Z., Meng, M., Ni, L., Qin, C., and Peng, J., 2016, Selective Ce(III) ion-imprinted polymer grafted on Fe₃O₄ nanoparticles supported by SBA-15 mesopores microreactor via surface-initiated RAFT polymerization, *Microporous Mesoporous Mater.*, 234, 176–185.
- [41] Hou, M., Zang, X., Wang, C., and Wang, Z., 2013, The use of silica-coated magnetic graphene microspheres as the adsorbent for the extraction of pyrethroid pesticides from orange and lettuce samples followed by GC-MS analysis, *J. Sep. Sci.*, 36 (19), 3242–3248.
- [42] Mahpishanian, S., Sereshti, H., and Baghdadi, M., 2015, Superparamagnetic core-shells anchored onto graphene oxide grafted with phenylethyl amine as a nano-adsorbent for extraction and enrichment of organophosphorus pesticides from fruit, vegetable and water samples, *J. Chromatogr. A*, 1406, 48–58.
- [43] Kiselev, A.V., Lygin, V.I., and Starodubceva, R.V., 1972, Spectral and energetic aspects of water adsorption by Li-, Na-, K- and Cs-X zeolites, *J. Chem. Soc., Perkin Trans. 1*, 68 (0), 1793–1798.
- [44] Ulu, A., Noma, S.A.A., Koytepe, S., and Ates, B., 2018, Magnetic Fe₃O₄@MCM-41 core-shell

- nanoparticles functionalized with thiol silane for efficient l-asparaginase immobilization, *Artif. Cells Nanomed. Biotechnol.*, 46 (Suppl. 2), 1035–1045.
- [45] Alam, N., and Mokaya, R., 2008, Crystalline mesoporous silica materials from layered silicate precursors, *J. Mater. Chem.*, 18, 1383–1391.
- [46] Hui, K.S., and Chao, C.Y.H., 2006, Synthesis of MCM-41 from coal fly ash by a green approach: Influence of synthesis pH, *J. Hazard. Mater.*, 137 (2), 1135–1148.
- [47] Fellenz, N.A., De Berti, I.O.P., Soldati, A.L., Stewart, S.J., Marchetti, S.G., and Bengoa, J.F., 2015, Changes on structural and magnetic properties of maghemite nanoparticles during their coverage with MCM-41, *Ceram. Int.*, 41 (10), 15057–15066.
- [48] Abdollahi-Alibeik, M., and Rezaeipoor-Anari, A., 2016, Fe₃O₄@B-MCM-41: A new magnetically recoverable nanostructured catalyst for the synthesis of polyhydroquinolines, *J. Magn. Magn. Mater.*, 398, 205–214.
- [49] Arica, T.A., Ayas, E., and Arica, M.Y., 2017, Magnetic MCM-41 silica particles grafted with poly(glycidylmethacrylate) brush: Modification and application for removal of direct dyes, *Microporous Mesoporous Mater.*, 243, 164–175.
- [50] Kumar, D., Schumacher, K., du Fresne von Hohenesche, C., Grün, M., and Unger, K.K., 2001, MCM-41, MCM-48 and related mesoporous adsorbents: Their synthesis and characterisation, *Colloids Surf., A*, 187-188, 109–116.
- [51] Grün, M., Unger, K.K., Matsumoto, A., and Tsutsumi, K., 1999, Novel pathways for the preparation of mesoporous MCM-41 materials: control of porosity and morphology, *Microporous Mesoporous Mater.*, 27 (2-3), 207–216.
- [52] Teo, H.T., Siah, W.R., and Yuliati, L., 2016, Enhanced adsorption of acetylsalicylic acid over hydrothermally synthesized iron oxide-mesoporous silica MCM-41 composites, *J. Taiwan Inst. Chem. Eng.*, 65, 591–598.
- [53] See, H.H., Sanagi, M.M., Wan Ibrahim, W.A., and Naim, A.A., 2010, Determination of triazine herbicides using membrane-protected carbon nanotubes solid phase membrane tip extraction prior to micro-liquid chromatography, *J. Chromatogr. A*, 1217 (11), 1767–1772.
- [54] Lee, T.P., Saad, B., Ng, E.P., and Salleh, B., 2012, Zeolite Linde Type L as micro-solid phase extraction sorbent for the high performance liquid chromatography determination of ochratoxin A in coffee and cereal, *J. Chromatogr. A*, 1237, 46–54.
- [55] Amani, M.A., Latifi, A.M., Tahvildari, K., and Karimian, R., 2017, Removal of diazinon pesticide from aqueous solutions using MCM-41 type materials: isotherms, kinetics, and thermodynamics, *Int. J. Environ. Sci. Technol.*, 15 (6), 1301–1312.
- [56] Nodeh, H.R., Wan Ibrahim, W.A., Kamboh, M.A., and Sanagi, M.M., 2017, New magnetic graphene-based inorganic-organic sol-gel hybrid nanocomposite for simultaneous analysis of polar and non-polar organophosphorus pesticides from water samples using solid-phase extraction, *Chemosphere*, 166, 21–30.
- [57] Nodeh, H.R., Sereshti, H., Gaikani, H., Kamboh, M.A., and Afsharsaveh, Z., 2017, Magnetic graphene coated inorganic-organic hybrid nanocomposite for enhanced preconcentration of selected pesticides in tomato and grape, *J. Chromatogr. A*, 1509, 26–34.
- [58] Mahpishanian, S., and Sereshti, H., 2016, Three-dimensional graphene aerogel-supported iron oxide nanoparticles as an efficient adsorbent for magnetic solid phase extraction of organophosphorus pesticide residues in fruit juices followed by gas chromatographic determination, *J. Chromatogr. A*, 1443, 43–53.
- [59] Razmi, H., and Jabbari, M., 2015, Development of graphene-carbon nanotube-coated magnetic nanocomposite as an efficient sorbent for HPLC determination of organophosphorus pesticides in environmental water samples, *Int. J. Environ. Anal. Chem.*, 95 (14), 1353–1369.
- [60] Luo, Y.B., Zheng, H.B., Jiang, X.Y., Li, X., Zhang, H.F., Zhu, F.P., Pang, Y.Q., and Feng, Y.Q., 2015, Determination of pesticide residues in tobacco

- using modified QuEChERS procedure coupled to on-line gel permeation chromatography-gas chromatography/tandem mass spectrometry, *Chin. J. Anal. Chem.*, 43 (10), 1538–1544.
- [61] Wan Ibrahim, W.A., Wan Ismail, W.N., and Sanagi, M.M., 2013, Selective and simultaneous solid phase extraction of polar and non-polar organophosphorus pesticides using sol-gel hybrid silica-based sorbent, *Jurnal Teknologi*, 62 (3), 83–87.
- [62] Guan, H., Brewer, W.E., Garris, S.T., and Morgan, S.L., 2010, Disposable pipette extraction for the analysis of pesticides in fruit and vegetables using gas chromatography/mass spectrometry, *J. Chromatogr. A*, 1217 (12), 1867–1874.

Synthesis of Zinc Oxide Nanoparticles for Oil Upgrading and Wax Deposition Control: Effect of Calcination Temperature

Siti Nurliyana Che Mohamed Hussein^{1,*}, Fatin Syahirah Mohamed Fuad¹, and Marina Ismail²

¹Faculty of Chemical Engineering, Universiti Teknologi MARA (UiTM), 40450 Shah Alam, Selangor Darul Ehsan, Malaysia

²Academy of Language Studies, Universiti Teknologi MARA (UiTM), 40450 Shah Alam, Selangor Darul Ehsan, Malaysia

* **Corresponding author:**

tel: +6012-5283517

email: siti.nurliyana@uitm.edu.my

Received: February 4, 2019

Accepted: October 25, 2019

DOI: 10.22146/ijc.43317

Abstract: In this study, ZnO nanoparticles were synthesized using a sol-gel method for oil upgrading and wax deposition control. The synthesized ZnO nanoparticles were used to measure viscosity and wax deposition in the heavy crude oil and to investigate the effectiveness of the nanoparticles in the reduction of viscosity and wax deposition control of the heavy crude oil. This study investigated the effect of calcination temperature on ZnO nanoparticles during synthesis towards viscosity reduction and wax deposition control. ZnO nanoparticles were calcined at different temperatures ranging from 300 to 900 °C. The calcined ZnO nanoparticles were characterized using X-ray diffraction (XRD), Field Emission Scanning Electron microscope (FESEM), and Energy-dispersive X-ray spectroscopy (EDX) for its structure, size, shape, and morphology. The characterization results showed a hexagonal wurtzite structure of ZnO nanoparticles. The physical properties and rheology of heavy crude oil were characterized by using Electronic Rheometer and cold finger method to analyze the viscosity, shear rate, and wax deposition of the heavy crude oil for performance study. Decreased in crystallite size from 15.59 to 12.84 nm was observed with increasing calcination temperature from 300 to 400 °C, and a further increase of calcination temperature from 400 to 900 °C, the crystallite size increased from 12.84 to 41.58 nm. The degree viscosity reduction (DVR %) of heavy crude oil was observed to increase by 41.7%, with decreasing ZnO nanoparticles size from 30.11 nm to 12.84 nm. The optimum calcination temperature was 400 °C. Wax deposition decreases by 32.40% after the addition of ZnO nanoparticles into heavy crude oil.

Keywords: zinc oxide (ZnO); nanoparticles; calcination; wax content; viscosity reduction

■ INTRODUCTION

Wax deposition in heavy crude oil has always brought a significant impact on the petroleum industry, especially in the transportation and production section. There are various effects of wax deposition in heavy crude oil that we should be concerned about, for example, non-Newtonian flow characteristics of the fluid, increased pumping power, decreased flow rate, or even to the total blockage of the pipeline [1]. Wax precipitation induced by the viscosity of heavy crude oil that increases can cause flow line pressure to drop, leading to low flow rates [2]. In turn, this makes conditions for wax deposition in the pipes more favorable. Serious wax deposition in heavy crude oil needs extra attention since it may cause harm

not only to the transportation and production section, but also to the petroleum economy as well. There are many advanced technology and chemicals for wax prevention and removals, such as wax crystal modifiers and dispersants. However, these methods have disadvantages, such as cost and limited to one well [1]. ZnO nanotechnology has introduced a more effective solution for the petroleum industry as it provided simple and cheaper technology. Hence, it has become a major interest nowadays to reduce wax deposition from the heavy crude oil, to avoid its bad effect on the petroleum industry as well as to the environment.

Wax deposition in pipelines is commonly caused by several factors such as temperature, flow rate, oil

composition, and shear rate [3]. Generally, wax precipitation and deposition are related to the wax content of heavy crude oil. As the temperature increases, the viscosity of the crude oil decreases. In oil composition, the API gravity plays an important role in the petroleum industry as it is related to the wax deposition [4]. A high API gravity shows that crude oil has low wax content. An API gravity that is greater than 10 indicates light crude oil, whereas an API gravity of less than 10 indicates heavy crude oil [5]. Basically, the heavier the crude oil, the higher wax content.

In this study, the focus will be given on the heavy crude oil from the petroleum industry, such as in transportation and production. It is well known that this heavy crude oil releases a higher significant deposition of wax content. The wax that is present in the heavy crude oil primarily consists of paraffin hydrocarbons (C_{18} – C_{36}) known as paraffin wax and naphthenic hydrocarbons (C_{30} – C_{60}) [6]. The factor that leads to wax deposition problems depends on the type of oil and the molecular composition of the wax molecules. The waxes in crude oils are often more challenging to control because the alkane chains are often longer in the crude oil [7].

Currently, various conventional methods have been used to remove the wax precipitate in heavy crude oil, such as thermal techniques, chemical techniques, mechanical techniques, and thermo-chemical packages [1]. However, these conventional methods have some downside with their process in removing or preventing the wax precipitate from heavy crude oil [8]. For example, electric heaters can cause an increase in maintenance costs, and the availability of electrical power is limited, while chemical techniques, such as dispersants, could lead to harmful erosion [1].

Numerous transition metals have been used in many applications such as iron and zinc because of its heat and electric conductivity [9]. In addition, these metals are commonly used as catalytic agents due to their ability to change their state or absorb other substances on their surface and activate them in the process [9].

Numerous methods have been described in research to synthesize ZnO nanoparticles, such as the sol-gel method, co-precipitation, and spray pyrolysis [10].

However, in this study, the sol-gel process was more preferred than the other methods because of its low cost and simple [11].

■ EXPERIMENTAL SECTION

Materials

Crude oil obtained from Kemaman Bitumen Company Sdn. Bhd. (KBC) was used as received for characterization and rheological tests to analyze its properties. Zinc acetate dihydrate ($Zn(CH_3COO)_2 \cdot 2H_2O$), oxalic acid ($C_2H_4O_4 \cdot 2H_2O$), and ethanol (C_2H_5OH) 95% AR Grade obtained from Vchem Laboratory Chemicals, ammonia solution acquired from Daejung Chemicals. The other chemicals such as hydrochloric acid (HCl), methanol (CH_3OH), *n*-heptane (C_7H_{16}), and toluene (C_7H_8) also obtained from the Vchem Laboratory Chemicals.

Instrumentation

High-Resolution X-ray Diffractometer (PANalytical X'Pert PRO MRD) was used to analyze the crystallinity of the zinc oxide nanoparticles. Energy Dispersive X-ray Spectroscopy (EDX) was used in this study to verify the elemental composition of nanoparticles sample. The surface morphology of ZnO nanoparticles was determined using Field Emission scanning electron microscopy (FESEM). The rheological measurement was carried out using a Rheometer Paar Physica MCR300.

Procedure

Characterization of crude oil

The sample of crude oil studied in this work was obtained from Kemaman Bitumen Company (KBC) Sdn Bhd. Table 1 shows the physical properties and composition of crude oil in weight percentage (%) of the sample crude oil that was obtained from KBC. The density of crude oil was determined by using Eq. (1) and Eq. (2) where S.G., ρ_{oil} , and ρ_{water} are the specific gravity, oil density, and water density, respectively. The API gravity of crude oil refers to the density of the fluid after the gas been liberated from the fluid at ambient pressure and reservoir temperature [12]. Crude oil gained from the KBC was considered heavy crude oil because of API

Table 1. Physical properties and composition of crude oil

Physical properties	
Density (kg/m ³)	999
Specific gravity, SG	0.999
API°	11
Viscosity at 40 °C (cP)	17,751
Color	Black
Cloud Point (°C)	12
Composition	
	Wt.%
Saturates	3.0
Aromatic	63.4
Resin	12.9
Asphaltenes	20.7

and density value of mostly heavy oil ranging between 10° to 22° API and 920 to 1000 kg/m³ [13].

$$\text{API}^\circ = \frac{141.5}{\text{S.G.}} - 131.5 \quad (1)$$

$$\text{S.G.} = \frac{\rho_{\text{oil}}}{\rho_{\text{H}_2\text{O}}} \quad (2)$$

Synthesis of zinc oxide nanoparticles

ZnO nanoparticles were prepared under constant processing conditions of pH, zinc acetate, oxalic acid ratio, and drying temperature by using a sol-gel method. Zinc acetate [Zn (CH₃COOH)₂·2H₂O], oxalic acid [C₂H₂O₄], and ethanol [CH₃CH₂OH] were used as precursor materials for the preparation of ZnO nanoparticles [10,14]. In addition, the effect of calcination temperature was studied during the synthesis of ZnO nanoparticles by varying its temperature from 300 to 900 °C [15-16]. For the preparation of ZnO nanoparticles with molar ratios of 1:2 of zinc acetate and oxalic acid, 2 g of zinc acetate was added to the 100 mL of ethanol solution (+ 10% volume of water) in 500 mL glass beaker in a water bath at 65 °C under reflux condition for 30 min. An amount of 1.64 g of oxalic acid powder was added to the 100 mL of ethanol solution in 500 mL glass beaker at 45 °C under 700 rpm speed for 30 min. Then, the oxalic acid solution was slowly added by using a burette to the zinc acetate solution in 500 mL glass beaker under vigorous stirring at 1000 rpm [10,17]. The final pH of the reactant was kept at 3 by adding a required amount of hydrochloric acid and ammonia solution, respectively. Then, the solution was kept undisturbed for a while till

white precipitates were seen in the solution and filter the precipitate by using a vacuum pump. The precipitate was dried at 80 °C for 2 h in a sintering boat which was put in a drying oven, and then calcined at 300 °C for 2 h in a sintering boat in the furnace to obtain a smoother powder [11]. The calcination of the ZnO precipitate was repeated but at different calcination temperatures between 400 to 900 °C.

Characterization of ZnO nanoparticles

The X-ray diffraction analysis was carried out for the synthesized ZnO nanoparticles by using a High-Resolution X-ray Diffractometer (PANalytical X'Pert PRO MRD) with Cu K α radiation ($\lambda = 1.54060 \text{ \AA}$) over the angle 2θ range of 10°–90° [10]. X-ray diffraction was used to analyze the crystallinity of zinc oxide nanoparticles. The XRD patterns indicate the formation of the crystal structure. The diffraction angle used for the ZnO nanoparticles sample was from 10° to 90°. In this study, the intensity peaks and diffraction angle of calcined ZnO at 300 to 900 °C were investigated to determine the effect of calcination temperature on the crystallite size of ZnO nanoparticles.

Other than XRD, field-emission scanning electron microscope (FESEM) and energy dispersive X-ray (EDX) were also used to study the characteristic of these nanoparticles by analyzing their morphological structure and composition element of the ZnO nanoparticles. The morphological structure of ZnO nanoparticles was determined by using a high-resolution scanning electron (Zeiss, Supra40VP) with the magnification of 10,000.

The crystallite size of ZnO nanoparticles was then estimated by using the Debye-Scherrer formula given in Eq. (3), where 0.89 is Scherrer's constant, λ is the wavelength of X-rays, θ is the Bragg diffraction angle, and B is the full width at half-maximum (FWHM) of the diffraction peak [18].

$$D = \frac{0.89\lambda}{B \cos\theta} \quad (3)$$

Rheological measurements

ZnO nanoparticles (0.4 g) was added to the heavy crude oil. The tests were performed at a different temperature ranging between 30, 45, and 60 °C. This

experiment was run in a controlled condition: shear rate between 0 and 500 s^{-1} at $24.85 \text{ }^\circ\text{C}$. Shear rate and apparent viscosity values were obtained every 10 sec, resulting in 28 points, respectively. For performance study, the effect of ZnO nanoparticle's size and temperature at a higher shear rate on the viscosity reduction of heavy crude oil were investigated by using this equipment.

■ RESULTS AND DISCUSSION

Characterization of Synthesized Zinc Oxide Nanoparticles

X-ray diffraction (XRD)

XRD was used to characterize the crystalline nature of the ZnO nanoparticles. Fig. 1 shows XRD patterns of ZnO nanoparticles calcined at different temperatures ranging from 300 to $900 \text{ }^\circ\text{C}$. The presence of high-intensity peaks corresponds to the (100), (002), and (101) lattice plane confirms the formation of the hexagonal wurtzite structure of the ZnO nanoparticles. The peaks gained in this study perfectly matches with the standard peaks of ZnO powder diffraction (JCPDS 36-1451). All the diffraction peaks of ZnO nanoparticles at different calcination temperatures were observed at 2θ : 31.95° , 34.7° , 36.4° , 47.8° , 56.9° , 63.1° , 66.5° , 68.1° , and

69.3° , that attributed to the (100), (002), (101), (102), (110), (103), (200), (112), and (201) crystal planes of the hexagonal ZnO powder. Fig. 1 suggests that, with an increase in calcination temperature, the intensity of diffraction peaks increases, which indicates the strengthening of the ZnO phase [11].

The obtained crystallite size of ZnO nanoparticles was tabulated in Table 2. The decrease in crystallite size from 15.59 to 12.84 nm was observed with an increase in calcination temperature from 300 to $400 \text{ }^\circ\text{C}$. However, the crystallite size continued to increase from 12.84 to 41.58 nm by a further increase in calcination temperature from 400 to $800 \text{ }^\circ\text{C}$. The average crystallite size of ZnO nanoparticles was found to be 25.42 nm. The decrease in crystallite size at low temperature indicates the restructuring process, whereas the increase in calcination temperature with an increase in crystallite size suggests the strengthening of the ZnO nanoparticles phase [11]. In addition, by referring to Fig. 1, the spectrum became sharper, and diffraction peak became narrower with the increase in the temperature from 400 to $800 \text{ }^\circ\text{C}$, indicating that the crystallite ZnO nanoparticles formation has been established due to growth rate between the crystallographic planes [16,19-21].

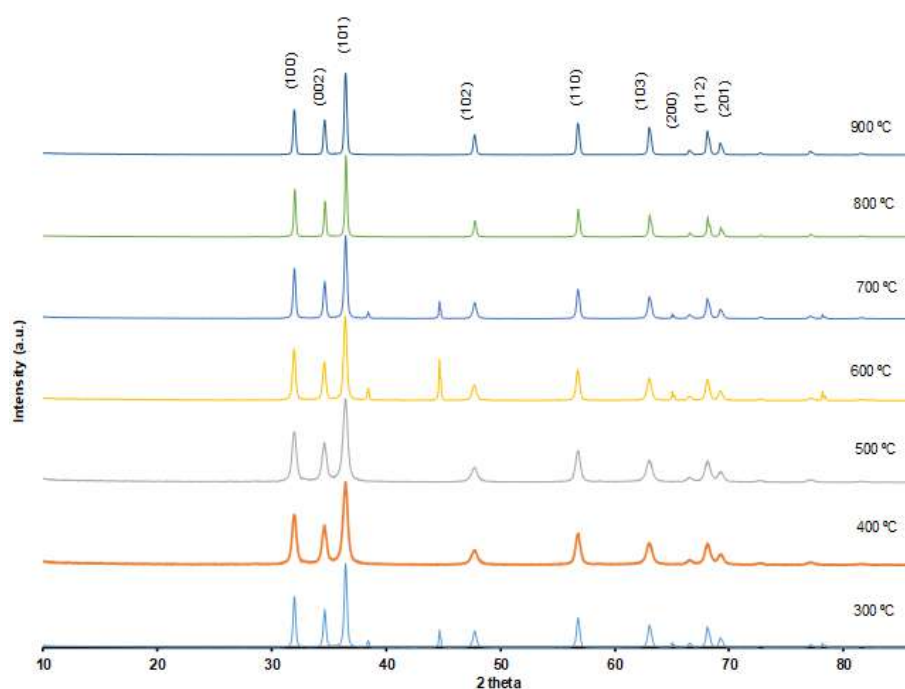


Fig 1. XRD patterns of the ZnO nanoparticles calcined at 300, 400, 500, 600, 700, 800, and $900 \text{ }^\circ\text{C}$.

Table 2. XRD analysis of ZnO nanoparticles: Full width at half-maximum (B) and size (nm) for each degree

Temperature (°C)	Position 2θ (°)	Full width at half-maximum (B)	Size (nm)
300	36.4	0.56	15.59
400	36.4	0.68	12.84
500	36.4	0.47	18.58
600	36.4	0.34	25.68
700	36.4	0.29	30.11
800	36.4	0.21	41.58
900	36.4	0.26	33.58

Energy dispersive X-ray spectroscopy (EDX)

EDX was used in this study to verify the elemental composition of the nanoparticles synthesized by using the sol-gel method. Table 3 shows the weight and atomic percentage of EDX of the ZnO element, which suggests the good purity of the ZnO powder. Therefore, the experimental synthesis of zinc oxide nanoparticles sample was successful due to the presence of zinc and oxygen elements, respectively.

These results show that the final product was pure ZnO nanoparticles. According to Al-Hada et al. [19], by using zinc nitrate as a precursor, the atomic percentages of Zn and O were approximately 50.13% and 49.87%. From this comparison, it showed that the precursor of zinc acetate produces a higher atomic percentage of Zn than precursor zinc nitrate. However, the value of the atomic percentage of Zn and O between both precursors did not create a huge difference.

Effect of Calcination Temperature on Size of Zinc Oxide Nanoparticles

Fig. 2 shows the crystallite size of the ZnO as a function of calcination temperature ranging between 300 to 900 °C. As calcination temperature increases from 300 to 400 °C, the crystallite size of ZnO decreases. The decrease in the crystallite size of ZnO from 15.59 to 12.84 nm was due to the structural rearrangement, which indicates a restructuring process [10-11]. However, the crystallite size of ZnO tends to increase from 12.84 to 41.58 nm with increasing calcination temperature from 400 to 800 °C, which implies the strengthening of the ZnO phase. This was because of the increment of the crystallite

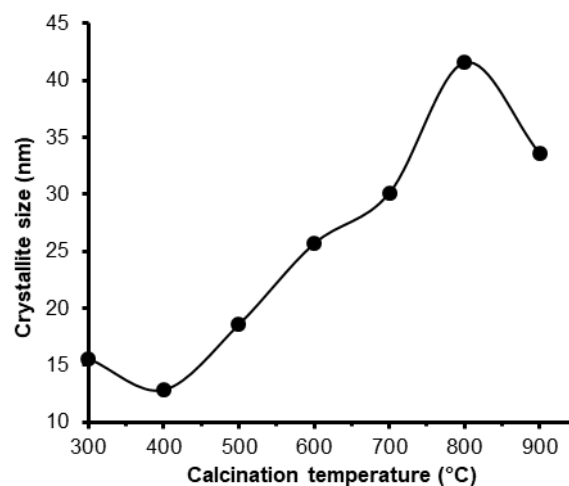
volume to the surface ratio [11,19]. The minimum crystallite size of ZnO in this study was achieved at a temperature of 400 °C, whereas the maximum one was achieved at 800 °C.

Effect of Calcination Temperature on the Morphology of the Nanoparticles

Fig. 3 shows FESEM images of the ZnO nanoparticles at different calcination temperature. Fig. 3(a) reveals that the synthesized sample has nanoparticles appearance with a rod-like morphology structure at lower temperature. Fig. 3(b) shows that the length of the

Table 3. Weight and atomic percentage of EDX of ZnO element

Element	Wt.%	Atomic %
O	22.59	45.61
Zn	77.41	54.39

**Fig 2.** Variation in crystallite size with varying calcination temperatures.

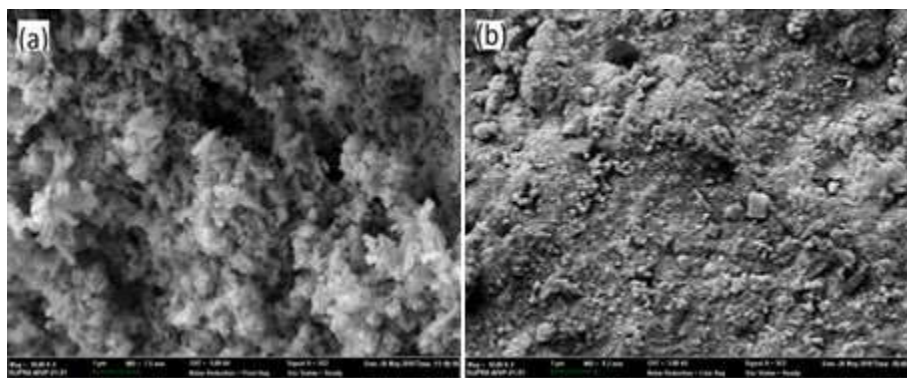


Fig 3. FESEM images of ZnO nanoparticles at calcination temperature of (a) 400 °C and (b) 500 °C.

structure was reduced with the increase in the calcination temperature. The results are consistent with previous research stated that ZnO nanoparticles product started to crumble and overlapped in a proportional relation with the increase of calcination temperature [19-20,22].

Effect of Nanoparticle Size towards Viscosity Reduction

To further investigate the effect of the calcination temperature of the ZnO nanoparticles on the heavy crude oil, the reduction of viscosity of heavy crude oil was carried out. Fig. 4 shows the viscosity of the heavy crude oil in the presence of ZnO nanoparticles at different nanoparticle sizes at 30 °C and shear rate between 0 and 80 s⁻¹. This indicates that the addition of ZnO nanoparticles into the heavy crude oil will reduce the viscosity of the

heavy crude oil. The nanoparticle sizes evaluated in this study were 12.84, 18.58, 25.68, 30.11, 33.58, and 41.58 nm. It was observed that the viscosity of heavy crude oil decreased with a decrease in nanoparticle sizes. The highest viscosity reduction of heavy crude oil obtained at 12.84 nm. As particle size increases, a decrease in performance was noticed [23]. This is due to fewer active sites available for nanoparticles to attach to heavy crude oil components [24].

The degree of viscosity reduction (DVR) was calculated by Eq. (4), where μ_{H_2O} and μ_{np} were the crude oil before and after additional nanoparticle values, measured at a shear rate between 0 and 80 s⁻¹, respectively. Fig. 5 indicates the degree of viscosity reduction of heavy crude oil with the presence of the ZnO nanoparticles with different sizes, at 30 °C and shear

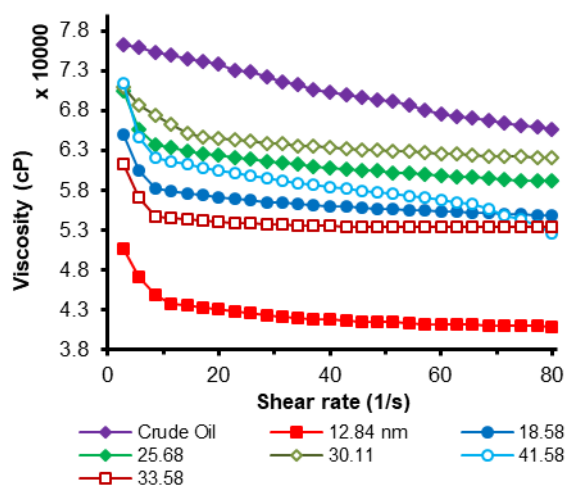


Fig 4. Viscosity of heavy crude oil in the presence of ZnO nanoparticles at different nanoparticles size at 30 °C and shear rate between 0 and 80 s⁻¹

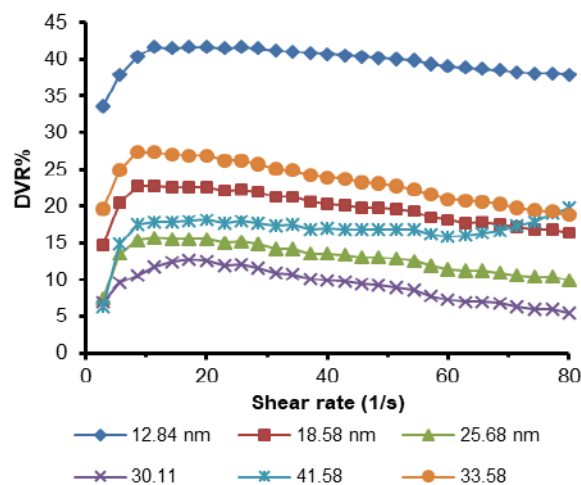


Fig 5. The degree of viscosity reduction of heavy crude oil with the presence of the ZnO nanoparticles with different sizes, at 30 °C and shear rate between 0 and 80 s⁻¹

rate between 0 and 80 s⁻¹. The values of DVR indicate that the optimal nanoparticle size at which the biggest change in viscosity obtained was 12.84 nm for all shear rates. The lowest degree of viscosity reduction was 5.5%, which occurred at 30.11 nm, while the highest degree of viscosity reduction was 41.7% at 12.84 nm. However, increasing the shear rate from 10 to 80 s⁻¹ slightly reduced the DVR%.

$$\text{DVR \%} = \left(\frac{\mu_{\text{HO}} - \mu_{\text{np}}}{\mu_{\text{np}}} \right) \times 100 \quad (4)$$

Effect of Temperature and High Shear Rate on Heavy Crude Oil

Temperature plays an important role in viscosity control of heavy crude oil, as increasing the temperature will reduce the viscosity of the oil. Fig. 5 shows that ZnO nanoparticles at 12.84 nm exhibit the best performances due to the higher percentage in viscosity reduction. Therefore, in this analysis of temperature and high shear rate effect, nanoparticles with a size of 12.84 nm were chosen to be evaluated at three different temperatures at high shear rates. The temperatures of 30, 45, and 60 °C were evaluated respectively, at shear rates between 0 and 500 s⁻¹. Fig. 6 displays the rheological responses for heavy crude oil both with and without additional ZnO nanoparticles at 30, 45, and 60 °C, at shear rates between 0 and 500 s⁻¹. The DVR for 30, 45, and 60 °C, and at shear rates between 0 and 500 s⁻¹ are presented.

The rheological responses of heavy crude oil with additional ZnO nanoparticles at 30, 45, and 60 °C shows the degree of viscosity reduction for heavy crude oil where the highest DVR was 71%. Therefore, increase in the shear rate from 0 to 500 s⁻¹ with increase in the temperature at 30, 45, and 60 °C will decrease the DVR. The rheological behavior of heavy crude oil at 60 °C shows the minor changes in viscosity values between presence and absence of ZnO nanoparticles. Fig. 6 indicates that at temperature 30 °C, the DVR tends to increase up to 71% with increasing shear rate from 100 to 400 s⁻¹. However, at temperatures of 45 and 60 °C, the DVR tends to decrease with an increase in shear rate from 100 to 400 s⁻¹. From this observation, it can be concluded that the optimum temperature of this performance was at 45 °C, where the

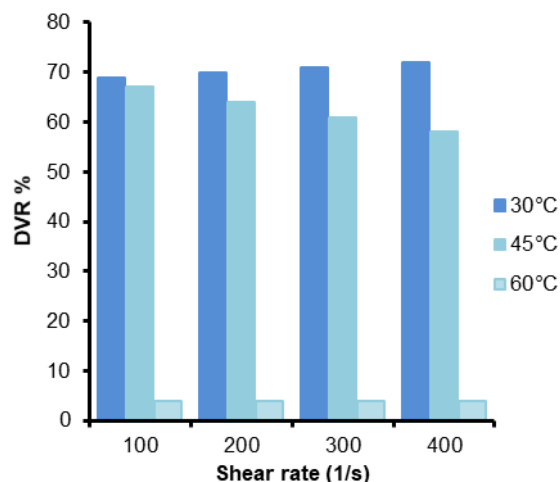


Fig 6. Degree of viscosity reduction at shear rates between 0 and 500 s⁻¹ at different temperatures of 30, 45 and 60 °C

DVR was reduced nearly to 0% with further increase in the temperature. As the temperature increases, so does the rate of reaction of ZnO nanoparticles towards heavy crude oil. However, very high temperatures can denature the ZnO nanoparticles and change both the chemical and physical properties of the ZnO nanoparticles.

CONCLUSION

ZnO nanoparticles were successfully synthesized by using the sol-gel method at different calcination temperatures from 300 to 900 °C. The effect of calcination temperature on the structure and crystallite size of ZnO nanoparticles at different temperatures was studied by using XRD, FESEM, and EDX. The XRD results approved the presence of the formation of the hexagonal wurtzite structure of ZnO nanoparticles. The crystallinity increased with increasing calcination temperature. The crystallite size decreased (15.59 to 12.84 nm) with an increase in calcination temperature from 300 to 400 °C. Further increase in calcination temperature from 400 to 800 °C resulted in an increase in the crystallite size from 12.84 to 41.58 nm. The synthesized sample was then used for viscosity reduction for oil upgrading, and it showed that nanoparticles at the size of 12.84 nm gave the best performances for viscosity reduction compared to the others.

■ ACKNOWLEDGMENTS

The author would like to thank Malaysian Ministry of Higher Education and Universiti Teknologi MARA (UiTM) for the Fundamental Research Grant Scheme (FRGS). (Project No.: 600-IRMI/FRGS 5/3 (048/2019)). Special thanks to Kemaman Bitumen Complex (KBC) for their supply of heavy oil to realize this research.

■ REFERENCES

- [1] Sousa, A.L., Matos, H.A., and Guerreiro, L.P., 2019. Preventing and removing wax deposition inside vertical wells: A review, *J. Pet. Explor. Prod. Technol.*, 9 (3), 2091–2107.
- [2] Subramanie, P.A.P., Padhi, A., Ridzuan, N., and Adam, F., 2019, Experimental study on the effect of wax inhibitor and nanoparticles on rheology of Malaysian crude oil, *J. King Saud Univ. Eng. Sci.*, In Press, Corrected Proof.
- [3] Mansourpoor, M., Azin, R., Osfouri, S., and Izadpanah, A.A., 2019, Experimental investigation of wax deposition from waxy oil mixtures, *Appl. Petrochem. Res.*, 9 (2), 77–90.
- [4] Quan, Q., Wang, W., Wang, P., Yang, J., Gao, G., Yang, L., and Gong, J., 2016, Effect of oil temperature on the wax deposition of crude oil with composition analysis, *Braz. J. Chem. Eng.*, 33 (4), 1055–1061.
- [5] Meyer, R.F., 1987, Prospects for heavy crude oil development, *Energy Explor. Exploit.*, 5 (1), 27–55.
- [6] Fan, K., Huang, Q., Li, S., and Yu, W., 2017, The wax deposition rate of water-in-crude oil emulsions based on the laboratory flow loop experiment, *J. Dispersion Sci. Technol.*, 38 (1), 8–18.
- [7] Abdurrahman, M., Ferizal, F.H., Husna, U.Z., and Pangaribuan, L., 2018, Possibility of wax control techniques in Indonesian oil fields, *AIP Conf. Proc.*, 1941(1), 020001.
- [8] White, M., Pierce, K., and Acharya, T., 2018, A review of wax-formation/mitigation technologies in the petroleum industry, *SPE Prod. Oper.*, 33 (3), 476–485.
- [9] Khan, I., Saeed, K., and Khan, I., 2019, Nanoparticles: Properties, applications and toxicities, *Arabian J. Chem.*, 12 (7), 908–931.
- [10] Khan, R.N., Ali, N., Riaz, S., and Naseem, S., 2015, Effect of calcination on properties of cobalt doped ZnO nanoparticles, *Mater. Today: Proc.*, 2 (10, Part B), 5765–5770.
- [11] Ashraf, R., Riaz, S., Kayani, Z.N., and Naseem, S., 2015, Effect of calcination on properties of ZnO nanoparticles, *Mater. Today: Proc.*, 2 (10, Part B), 5468–5472.
- [12] Jain, D., and Bihani, A.D., 2014, Crude oil viscosity correlations: A novel approach for Upper Assam Basin, *PetroTech 2014: The 11th International Oil and Gas Conference and Exhibition*, New Delhi, India, 12–14 January 2014.
- [13] Santos, R.G., Loh, W., Bannwart, A.C., and Trevisan, O.V., 2014, An overview of heavy oil properties and its recovery and transportation methods, *Braz. J. Chem. Eng.*, 31 (3), 571–590.
- [14] Hasnidawani, J.N., Azlina, H.N., Norita, H., Bonnia, N.N., Ratim, S., and Ali, E.S., 2016, Synthesis of ZnO nanostructures using sol-gel method, *Procedia Chem.*, 19, 211–216.
- [15] He, L., Tong, Z., Wang, Z., Chen, M., Huang, N., and Zhang, W., 2018, Effects of calcination temperature and heating rate on the photocatalytic properties of ZnO prepared by pyrolysis, *J. Colloid Interface Sci.*, 509, 448–456.
- [16] Mornani, E.G., Mosayebian, P., Dorrnian, D., and Behzad, K., 2016, Effect of calcination temperature on the size and optical properties of synthesized ZnO nanoparticles, *J. Ovonic Res.*, 12 (2), 75–80.
- [17] Patil, S., and Raut, S.J., 2012, Synthesis and characterization of ZnO nanoparticles and 50% ZnO-bentonite nanocomposite, *Int. J. Chem. Sci.*, 10 (2), 1124–1132.
- [18] Sunitha, S., Rao, A., and Jayabalan, K., 2015, Synthesis of novel cobalt doped zinc oxide/carbon nano composite for the photocatalytic degradation of acid blue 113, *Orient. J. Chem.*, 31 (1), 107–112.
- [19] Al-Hada, N.M., Saion, E.B., Shaari, A.H., Kamarudin, M.A., Flaifel, M.H., Hj Ahmad, S., and Gene, S.A., 2014, A facile thermal-treatment route to synthesize ZnO nanosheets and effect of calcination temperature, *PLoS One*, 9 (8), e103134.

- [20] Ismail, A.M., Menazea, A.A., Kabary, H.A., El-Sherbiny, A.E., and Samy, A., 2019, The influence of calcination temperature on structural and antimicrobial characteristics of zinc oxide nanoparticles synthesized by sol-gel method, *J. Mol. Struct.*, 1196, 332–337.
- [21] Getie, S., Belay, A., Chandra Reddy, A.R., and Belay, Z., 2017, Synthesis and characterizations of zinc oxide nanoparticles for antibacterial applications, *J. Nanomed. Nanotechnol.*, S8, 004.
- [22] Al-Hada, N.M., Saion, E.B., Shaari, A.H., Kamarudin, M.A., and Gene, S.A., 2013, The influence of calcination temperature on the formation of zinc oxide nanoparticles by thermal-treatment, *Appl. Mech. Mater.*, 446-447, 181–184.
- [23] Ekaputra, A.A., Sabil, K.M., Hosseinipour, A., and Bin Saaid, I., 2014, Impacts of viscosity, density and pour point to the wax deposition, *J. Appl. Sci.*, 14 (23), 3334–3338.
- [24] Patel, H., Shah, S., Ahmed, R., and Ucan, S., 2018, Effects of nanoparticles and temperature on heavy oil viscosity, *J. Pet. Sci. Eng.*, 167, 819–828.

Adsorption-Desorption Profile of Methylene Blue Dye on Raw and Acid Activated Kaolinite

Nurul Ain Safiqah Md Sandollah¹, Sheikh Ahmad Izaddin Sheikh Mohd Ghazali¹,
Wan Nazihah Wan Ibrahim², and Ruhaida Rusmin^{1,*}

¹Faculty of Applied Sciences, Universiti Teknologi MARA, Negeri Sembilan Branch, Kuala Pilah Campus, 72000 Kuala Pilah, Negeri Sembilan, Malaysia

²Faculty of Applied Sciences, Universiti Teknologi MARA, 40450 Shah Alam, Selangor, Malaysia

* **Corresponding author:**

tel: +606-4832100

email: ruhaida@uitm.edu.my

Received: February 12, 2019

Accepted: August 1, 2019

DOI: 10.22146/ijc.43552

Abstract: The efficiencies of raw (RK) and acid activated (0.5 M AAK) kaolinite clay minerals to remove methylene blue (MB) dyes in aqueous solution were investigated and compared. The 0.5 M AAK was prepared by treatment of RK in dilute 0.5 M HCl aqueous solution under reflux. Kaolinite adsorbents were characterized and their MB removal performances were evaluated via the batch method. MB desorption from spent kaolinites was investigated at pH 4 to 8. The MB removal was increased with increasing initial dye concentration, agitation speed and adsorbent dosage in 60 min reaction time at pH 6. Both kaolinites showed high MB removal (up to 97%). The Freundlich model has the best-fit equilibrium adsorption isotherm model for RK and 0.5 M AAK. The kinetic data for both adsorbents showed strong agreement with the pseudo second order kinetic model ($r^2 > 0.98$). Nevertheless, the spent RK adsorbent demonstrated a significant higher MB retention than 0.5 M AAK in desorption experiments. Kaolinite clays have great potential as cost-effective materials for dyes removal in wastewater treatment.

Keywords: kaolinite; activation; removal; dyes; desorption

■ INTRODUCTION

The application of synthetic azo dyes as a commercial colorant has greatly expanded in recent years, catalyzed by the rapid growth of textile industries in the global market. In most industries, synthetic azo dyes offer advantages over natural dyes due to their simple preparation method, more diverse structure and higher stability [1]. Nevertheless, improper discharge of azo dye, such as Methylene Blue (MB) into water sources could pose negative health and environmental impacts because of their toxicity and persistency against degradation agents [2]. Therefore, it is of great importance to ensure the necessary effluent treatment was performed to avoid the deterioration of water quality. Methylene Blue (chemical formula of $C_{16}H_{18}ClN_3S$) is a polar hydrophobic azo dye belongs to the phenothiazine family, which are commonly used in garment manufacturing, health, and chemical industries. Previously, various types of adsorbents

such as activated carbon, fly ash, red mud, etc. for removing MB from aqueous solution have been reported [3]. Although the activated carbon is so far being considered as the most common adsorbent for dyes removal, its expensive preparation cost and regeneration issues have limited their application and are economically unfavorable [4].

Clay minerals are colloid particles built from the interaction of rocks, soils, and sediments. Clay minerals are known as hydrated aluminium silicates that consist of a layered structure made up of tetrahedral sheets that link to an octahedral sheet by sharing of apical oxygen [5]. The detailed structure of clay minerals has been widely discussed elsewhere [6-7]. Naturally, clay minerals have the ability to remove toxic compounds from the environment and reducing the dispersion of pollutants in soil and water [5,8]. These materials are considered as suitable alternative materials over expensive commercial activated carbon due to their

abundance, low cost, environmentally friendly, multiple ion exchange properties and less toxicity [8].

Kaolinite is categorized as a 1:1 (1 tetrahedral sheet and 1 octahedral sheet) class of clay minerals with non-swelling properties [5] and chemical composition of $\text{Al}_2\text{Si}_2\text{O}_5(\text{OH})_4$. In Malaysia, kaolinite resources exist mainly in the states of Johor, Perak, and Pahang, with the estimated annual production of over 500,000 tons in 2013 [9]. Even though kaolinite clays are abundant in Malaysia, this natural resource is still limitedly used in wastewater treatment studies. Thus, the performance of kaolinite clays in removing dyes remains underexplored and warrants detail assessment.

Surface modification of raw kaolinite is usually necessary as this clay is less reactive and has a smaller specific surface area as compared to other clay minerals (e.g. bentonite) [10]. So far, the acid activation technique has been the most useful, cheap, simple and common method for modifying the kaolinite to achieve desirable attributes [11]. Acid activation is defined as the treatment of clay minerals with inorganic acids at a particular temperature in order to increase the acidity, surface area, and porosity of the clays [11]. Although concentrated acid was reported to produce better results in terms of high surface area and porosity [12], the highly acidic leachant is potentially hazardous, less ergonomic and could pose an environmental concern if untreated. Low concentration of acid (less than 2 M) was recommended to ensure no significant alteration of clay's basic structure [13]. Furthermore, it is recently reported that low acid concentration is already sufficient for higher adsorption towards pollutant, as demonstrated by the activated kaolinite prepared from dilute acid (0.5 M H_2SO_4) used to remove Crystal Violet and Brilliant Green dyes [14]. In another research, a 0.5 M HNO_3 acid was used to activate Moroccan Clay that yields a high adsorption capacity (500 mg/g) towards Methylene Blue [15]. To the best of our knowledge, acid activation of kaolinite using dilute hydrochloric acid has not been thoroughly discussed in the literature. Hence, this study aims to use dilute inorganic acid in treating kaolinite and evaluate its performance against raw kaolinite in removing Methylene Blue (MB) in aqueous solution. The MB adsorption is

investigated under various experimental parameters (e.g. pH, adsorbent loading, time and initial concentration) to assess their adsorption characteristics and deduce the reaction mechanism. This study also aims to give an insight into the suitability of spent kaolinite to be recycled for water treatment application as an approach to support environment sustainability. For this purpose, the MB retention stability in spent kaolinites is studied through the desorption experiment to assess its regeneration capabilities. The findings of this study will provide an insight into the potential of kaolinites as a cost-effective and efficient adsorbent for water remediation technologies.

■ EXPERIMENTAL SECTION

Materials

Kaolinite clay mineral (purchased from MyLab Supplier, Malaysia) was used without further purification. Methylene blue (C.I. 52015, from Merck) was purchased from R&M Chemicals. Hydrochloric acid (HCl, 37%) and sodium hydroxide (NaOH, 96%) were supplied by R&M Chemicals and of analytical grade.

Instrumentation

X-ray powder diffraction (XRD) pattern in the 2θ range 10° to 90° was recorded with Panalytical model Empyrean (Panalytical, Almelo, Netherlands) operating at 40 kV and 35 mA using Cu K α radiation ($\lambda = 1.54059 \text{ \AA}$). The Fourier transformed infrared spectroscopy (FTIR) spectra were recorded on Perkin-Elmer infrared spectrophotometer using ATR mode with a resolution of 4 cm^{-1} in the range of $4000\text{--}650 \text{ cm}^{-1}$. Zeta potential analysis was performed using a Zetasizer 1600 Zeta Potential and Size Analyzer (Malvern Instrument). A 0.05% (m/v) kaolinite suspension (prepared at pH 4, 6 and 8) was prepared and analyzed in duplicates at 25°C .

Procedure

Acid activation of kaolinite

Acid activation of raw kaolinite was performed according to a previous report [16]. A 20.0 g of raw kaolinite (RK) was refluxed at 70°C with 0.5 M HCl for 3 h. The resulting materials were centrifuged and washed with water several times until all Cl^- was

removed as confirmed by the AgNO_3 test. Then, the products were oven-dried at 60°C until a constant weight was obtained. The acid activated kaolinite was labelled as 0.5 M AAK (kaolinite treated with 0.50 M HCl).

Adsorption experiment

Methylene Blue (MB) stock solution (100 ppm) was first prepared by dissolving accurate weight of MB in deionized water and then diluted to pre-determined concentration (20, 30, 40, 50 and 70 ppm). MB adsorption experiments on raw and activated kaolinites were carried out through a batch method at 25°C in a 15 mL centrifuge tube at various experimental parameters. Experiments were performed at pH 4, 6, and 8 (adjusted using 0.01 M NaOH or HCl) to evaluate the influence of pH. The contact time was varied from 10 to 180 min until equilibrium was reached. The effect of initial concentration was studied in concentration range up to 70 ppm (mg/L). Meanwhile, the effect of adsorbent loading was investigated using a 0.01, 0.03 and 0.05 g/mL loading. The kinetic study was performed at the optimized condition at the initial concentration of 50 ppm. The removal percentage at different agitation speed (1000, 1500, and 2500 rpm) was also tested. The aliquots were centrifuged at 2500 rpm and the concentration of MB in the supernatant before and after adsorption were determined using UV-Vis spectrophotometer [T80+, PG instrument Ltd] at wavenumber 668 nm.

The removal percentage of MB by kaolinite was calculated using Eq. (1):

$$\text{Removal percentage (\%)} = \frac{[\text{MB}]_{\text{initial}} - [\text{MB}]_{\text{final}}}{[\text{MB}]_{\text{initial}}} \times 100\% \quad (1)$$

Desorption experiment

Desorption experiment was performed using spent kaolinites (RK and 0.5 M AAK) previously used in treating a 50 mg/L MB aqueous solution (performed at the optimized condition of pH = 6, loading = 0.05 g/mL, and agitation speed = 2500 rpm). The spent kaolinites were placed in deionized water at pH 4, 6 and 8 (adjusted using 0.1 M HCl or 0.1 M NaOH) under agitation. Desorption process was performed in 60 min and the supernatant was collected through centrifugation. The concentration of desorbing MB was determined using the UV-Vis spectrometer. The MB desorption percentage was calculated according to Eq. (2):

$$\text{Percent desorption (\%)} = \frac{[\text{MB}]_{\text{desorbed}}}{[\text{MB}]_{\text{adsorbed}}} \times 100\% \quad (2)$$

RESULTS AND DISCUSSION

Characterization

The XRD patterns of raw and activated kaolinites are shown in Fig. 1. The important characteristic peaks of kaolinite were located at 2θ of 12.6° and 24.9° associated with [001] reflection [17]. Other peaks at 34.8° , 35.9° , and 38.5° were also associated with kaolinite. These

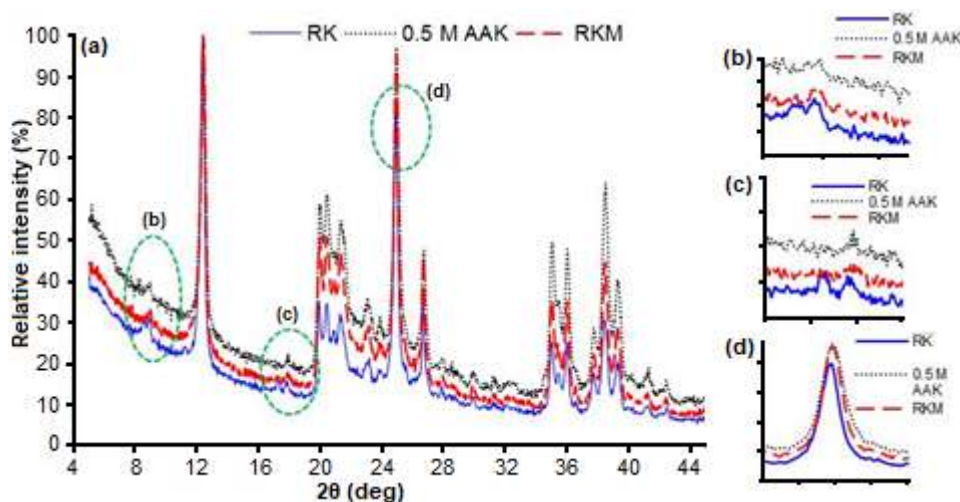


Fig 1. XRD diffractogram of raw (RK), 0.5 M AAK and raw kaolinite loaded with MB (RKM)

sharp and intense peaks indicate kaolinite as the dominant minerals present with a high degree of crystallinity. A trace of illite ($2\theta = 8.5$ and 17.1°) (Fig. 1(b-c)) as impurities was noticed [10]. The illite peak was almost diminished in 0.5 M AAK diffractogram denoting dissolution of this mineral due to acid attack. Neither alteration in the diffraction pattern nor peak shifting was observed in the acid activated kaolinite (0.5 M AAK) (Fig. 1(d)). To elucidate the possible interaction of MB-kaolinite, the XRD pattern of the spent raw kaolinite loaded with MB (assigned as RKM) was acquired (Fig. 1). No significant variation (i.e. peak shifting or broadening) with respect to the RK diffractogram was observed. This shows that the MB interacts only on the surface of the kaolinite without any intercalation on the clay's interlayer.

The FTIR spectra of raw and activated kaolinites are shown in Fig. 2(a). Kaolinite has typically four distinct absorption bands of the hydroxyl group in the range of $3700\text{--}3620\text{ cm}^{-1}$ [18-19]. The interlayer hydroxyl stretching mode of Al-OH was located at 3653 and 3667 cm^{-1} (out-of-plane vibration) as well as at 3697 cm^{-1} (symmetric stretching). The band at 3620 cm^{-1} is representing the stretching vibration of the internal hydroxyl group of Al-OH lying between the tetrahedral and octahedral sheets [20]. The Si-O-Si/Al asymmetric and symmetric stretching could be observed at 1033 and 790 cm^{-1} , respectively [7]. The bands at 913 and 938 cm^{-1} were attributed to the OH deformation modes of inner and surface hydroxyls groups, respectively [7]. Whereas the band located at 755 cm^{-1} was ascribed to the Si-O vibration of the clay sheet [7]. All these bands confirmed the presence of kaolinite, which is in agreement with the

XRD patterns described earlier. The differences in IR spectra of activated kaolinites were closely examined in the OH stretching region (3700 to 3650 cm^{-1}) (Fig. 2(a), inset). A slight broadening of the Al-OH stretching band at 3697 cm^{-1} was observed in the 0.5 M AAK (Fig. 2(a), inset). This observation suggested a minor perturbation occurred in the kaolinite octahedral sheets caused by cation leaching during acid activation [14].

Meanwhile, the zeta potential analysis (Fig. 2(b)) showed that both RK and 0.5 M AAK had a negative surface charge at pH range 4 to 8, as usually observed for clay mineral materials [8]. This negative surface charge was contributed by the protonation/deprotonation of the surface hydroxyl group (aluminol or silanol) of the broken edge of kaolinite's plane. At pH 6, the 0.5 M AAK showed a much more negative surface charge compared to RK; which could lead to a higher electrostatic interaction with the cationic MB.

Adsorption Experiment

Effect of initial pH solution on the adsorption of MB

During the adsorption process, the pH of aqueous solution plays an important role [21], as pH variation could; i) alter the metals ion speciation, ii) raise ionic competition due to excess of a proton (H^+) or hydroxyl ion (OH^-), and iii) affect surface properties of the adsorbate. Furthermore, clay mineral like kaolinite has two types of surfaces called basal surfaces (i.e. interlayer surfaces) and a more complex edge surfaces (i.e. broken surfaces) [17]. The basal surfaces are pH-independent whereas edge surface sites (consist of dangling bonds like Al-O, Si-O and Mg-O) are usually pH dependent (amphoteric). Thus, any changes of pH will result in the

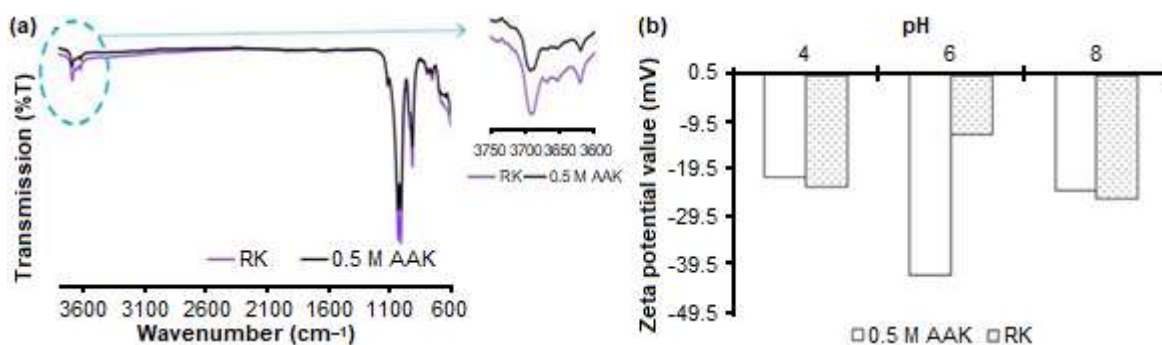


Fig 2. FTIR spectra (a) and zeta potential value (b) of raw and activated kaolinite

protonation/de-protonation of active surface functional groups leading to a different complexing capability towards organic substances [5].

The MB removal by all adsorbents was lowest at pH 4, whereas experiments performed at pH 6 recorded the highest percentage (Fig. 3(a)). Based on the zeta potential measurement, it was deduced that the cationic MB could potentially interact with the negative charge of the kaolinite through the electrostatic interaction [10]. Hence, in acidic suspension (pH 4), the excess H^+ may compete with cationic MB for the active sites of kaolinite [10]. The acidic pH also induces the protonation of the surface functional groups of the kaolinite which in turn reduce the clay's attraction towards cationic MB due to repulsive electrostatic forces.

During acid activation, the H^+ ions (from acids in the activation process) might preferably be adsorbed on the negative surface of the clay hence altering the surface charge [5]. Yet, in this study, the removal percentage of 0.5 M AAK (96.8%) was quite similar to the performance of the RK (95.3%), contradicting with trends observed in previous research findings [22] and a more recent

publication [23]. Meanwhile, at high pH (pH 8), less competition by H^+ resulted in more removal of MB (Fig. 3(a)). As deprotonation of MB in alkaline aqueous solution is considered not possible [24], the slight decrease in MB removal at alkaline pH hence is likely attributed by the changes in surface chemistry of the clays. Similar finding on the reduction of removal efficiencies of MB by kaolinite at the working condition of $pH > 7$ was also reported by previous researchers [25]. Thus pH 6 was chosen as the optimum pH for the subsequent experiment as this pH provides the highest removal efficiency. We deduced that the slightly higher removal percentage of 0.5 M AAK was governed by the removal of impurities (e.g. illite) [14] that allowed more exposed active sites, in accordance with the XRD diffractogram discussed previously. Furthermore, the 0.5 M AAK demonstrated more negative zeta potential value at this pH (Fig. 2(b)), thus allowing stronger interaction with MB as compared to the RK.

Effect of time on the adsorption of MB

Results demonstrated that the MB removal was gradually increased at reaction time increment (Fig. 3(b)).

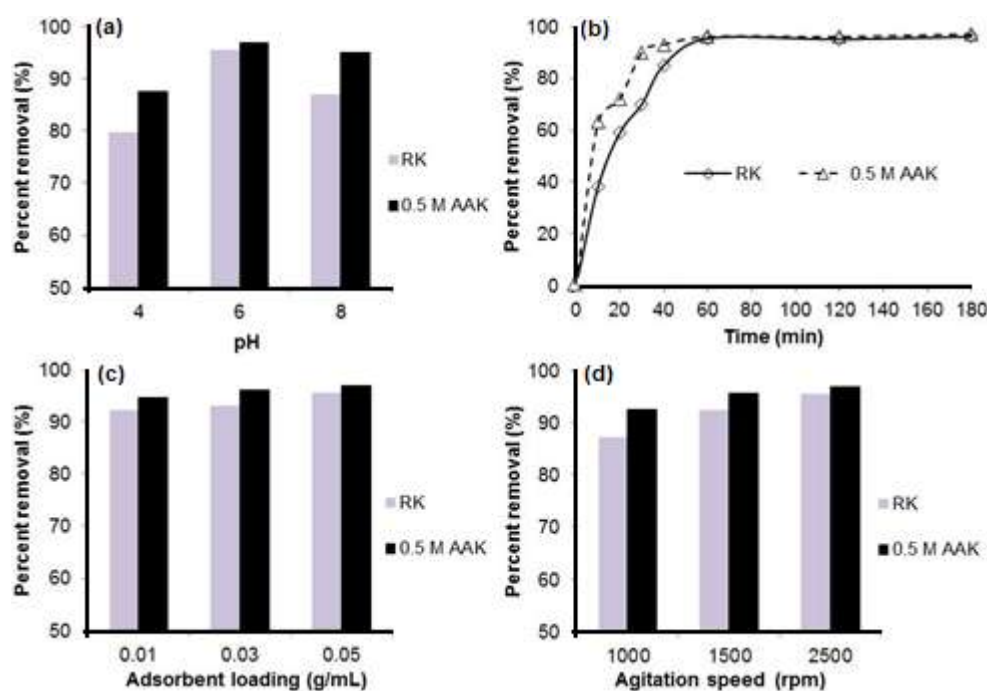


Fig 3. Effect of (a) pH; (b) time; (c) loading; and (d) agitation speed, on % removal of MB (performed at temperature = 25 °C, agitation speed = 2500 rpm, adsorbent loading = 0.05 g/mL, initial concentration = 50 mg/L, where appropriate)

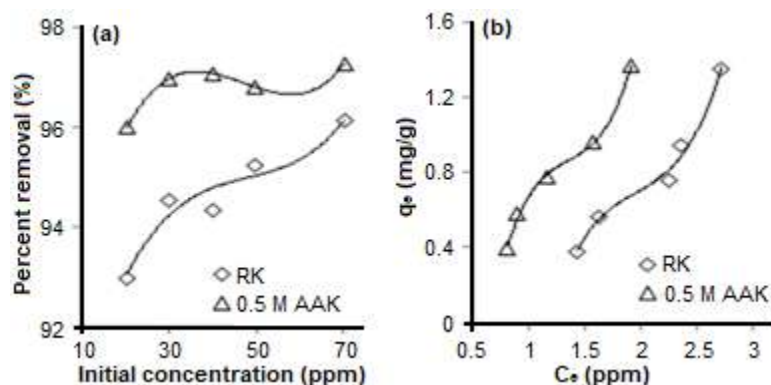


Fig 4. Effect of initial concentration towards MB removal (a), adsorption isotherm for RK and 0.5 M AAK (b)

The removal rate of RK and 0.5 M AAK was considered fast, as more than 60% dye was successfully removed at the earliest of 20 min initial time (Fig. 3(b)). Overall, the equilibrium was attained after 60 min and the MB removal remained constant henceforth. The fast MB uptake by all kaolinites indicated a strong interaction between MB and active sites on the kaolinite surface [4].

Effect of adsorbent loading on the adsorption of MB

For all adsorbents, the removal of MB was enhanced as the adsorbent dosage was increased (Fig. 3(c)). These findings were ascribed to more availability of surface active sites of the adsorbent. The sufficient active sites will allow more MB to be deposited and adsorbed [25]. The removal percentage of RK and 0.5 M AAK was maintained at above > 90% for all adsorbent loading. This implies that both adsorbents have abundance active sites with high affinity towards MB.

Effect of agitation speed on the adsorption of MB

Agitation is one of the important parameters in adsorption phenomena as it influences the distribution of the solute in the bulk solution and reduces the mass transfer effect. The MB removal efficiency was enhanced with the increase in agitation speed (Fig. 3(d)). At 2500 rpm, up to 96% of MB was successfully removed (Fig. 3(d)). High agitation speed may provide more energy to minimize the mass transfer phenomenon [26] and promote the more interfacial area of contact between adsorbent (clay)-adsorbate (MB). Hence, a higher removal percentage in an allocated time can be achieved.

Effect of initial concentration on the adsorption of MB

A high initial dye concentration provides a sufficient driving force to overcome the mass transfer resistance between the aqueous and solid phases [27]. It was observed that at an initial concentration of 20 ppm, more than 90% MB removal was recorded by all adsorbents (Fig. 4(a)). The maximum adsorption capacity attained for RK and 0.5 M AAK at an initial concentration of 20 to 70 ppm was 1.35 and 1.37 mg/g, respectively (Fig. 4(b)).

Adsorption isotherm

To determine the best-fit adsorption isotherm model in describing the MB adsorption, the adsorption data were fitted into four models; namely Langmuir, Freundlich, Dubinin–Radushkevich (D–R) and Temkin model (Table 1). The Langmuir isotherm model works based on the assumption of a monolayer and uniform energies of adsorption. The Langmuir constant (K_L) and the maximum adsorption capacity (q_{max}) were respectively obtained from the slope and the intercept of a linearised Langmuir equation, shown by Eq. (3):

$$\frac{C_e}{q_e} = \frac{1}{(q_{max}K_L)} + \frac{C_e}{q_{max}} \quad (3)$$

where q_e and C_e is the adsorbed amount of MB (mg/g) and concentration of MB (mg/L) at equilibrium, respectively [10].

Meanwhile, the Freundlich isotherm model assumes a heterogeneous surface site with multilayer

adsorption, and could be expressed by the following relationship (Eq. (4)):

$$\log q_e = \log K_f + \frac{1}{n} \log C_e \quad (4)$$

K_f is the Freundlich constant (L/g), meanwhile, the $1/n$ denotes the adsorption intensity [28].

Temkin model [29] takes into account the adsorbing species-adsorbent interactions at the solid/liquid interface equilibrium. The intercept and slope of q_e plotted versus $\ln C_e$ in the following Temkin equation (Eq. (5)):

$$q_e = B_T \ln A_T + B_T \ln C_e \quad (5)$$

which will give the value of A_T associated with the Temkin isotherm equilibrium binding constant (L/g), and B_T which depicts the Temkin isotherm constant, respectively. The B_T value could be derived to calculate the b constant, related to the heat of adsorption (kJ/mol), through Eq. (6):

$$B_T = \frac{RT}{b} \quad (6)$$

The Dubinin–Radushkevich (D–R) isotherm model does not follow the Langmuir model assumption on a homogenous surface or a constant adsorption potential. Rather, the D-R isotherm focuses on describing the physical and chemical features of adsorption of a single solute system. The linearized D–R isotherm is expressed as:

$$\ln q_e = \ln q_{\max} - \beta \varepsilon^2 \quad (7)$$

where β is the coefficient related to the mean free energy of adsorption [4] per mol of the adsorbate (mol^2/J^2). The q_{\max} and β were calculated from the slope and intercept of the linear plot of $\ln q_e$ versus ε^2 . The ε is the Polanyi potential expressed as:

$$\varepsilon = RT \ln \left(1 + \frac{1}{C_e} \right) \quad (8)$$

in which R (J/mol K) is the gas constant and T (K) is the absolute temperature. The value of β is related to sorption energy E (kJ/mol) and is expressed by the relationship:

$$E = \frac{1}{(2\beta)^{0.5}} \quad (9)$$

The E value which falls in the range of 1–8 kJ/mol indicates the main mechanism of adsorption is physical adsorption, a value between 8 to 16 kJ/mol is related to ion-exchange, whereas chemisorption is predicted for E value in the range of 20–40 kJ/mol [30].

Meanwhile, error analysis was performed using squares of the errors (SSE), residual root mean square error (RMSE), and Chi-square test, x^2 , to evaluate the fitness of the isotherm data with the regression coefficient, r^2 , determined from the linearized model.

$$\text{SSE} = \sum_{i=1}^n (q_{e,\text{meas}} - q_{e,\text{calc}})^2 \quad (10)$$

$$\text{RMSE} = \sqrt{\frac{1}{n} \sum_{i=1}^n (q_{e,\text{meas}} - q_{e,\text{calc}})^2} \quad (11)$$

$$\text{Chi-square, } x^2 = \frac{\sum_{i=1}^n (q_{e,\text{meas}} - q_{e,\text{calc}})^2}{q_{e,\text{meas}}} \quad (12)$$

where $q_{e,\text{meas}}$, and $q_{e,\text{calc}}$ is the equilibrium adsorption capacity (mg/g) that is measured experimentally and calculated from the isotherm adsorption model, respectively, while n is referred to the number of experimental observations.

The adsorption data of both RK and 0.5 M AAK poorly fit the linearized Langmuir isotherm and gives an unusual negative value of K_L and q_{\max} (Table 1). This showed the linearized Langmuir isotherm is unsuitable to be used to describe the adsorption process for both adsorbents.

On the other hand, both the empirical data of RK and 0.5 M AAK is well-fitted with the Freundlich adsorption isotherm model ($r^2 > 0.94$) (Table 1) thus allowing a fair comparison on adsorption isotherm properties between both adsorbents. A good agreement with the Freundlich isotherm model indicated a multilayer and heterogeneous adsorption. The typical value of $1/n$ is usually ranged from 0 to 1, however, the $1/n$ values obtained from the Freundlich model were above 1 (Table 1). This suggested that cooperative adsorption may occur raised by attractive adsorbate–adsorbate interaction. The binding of an MB molecule to one site on kaolinite may synergically facilitate the adsorption of subsequent molecules towards the active sites. Previous studies on the adsorption of dyes had also reported similar findings [26,31]. Furthermore, these results were in accordance with the S-type adsorption isotherm (according to classification by Giles et al. [32]

Table 1. Parameters of adsorption isotherm model for all adsorbents

Isotherm model/Adsorbent	RK	0.5 M AAK
Langmuir		
q_{\max} (mg/g)	-1.125	-2.786
K_L (L/mg)	-0.1707	-1.3282
r^2	0.7724	0.3518
SSE	0.0223	1.2410
RMSE	0.1492	1.1140
Chi-square (x^2)	0.0299	1.2553
Freundlich		
1/n	2.4014	1.2814
K_f (L/g)	0.1289	0.5834
r^2	0.9441	0.9452
SSE	0.0318	0.0236
RMSE	0.1783	0.1536
Chi-Square (x^2)	0.0427	0.0300
D-R		
q_{\max} (mg/g)	2.077	1.906
E (kJ/mol)	0.707	1.118
r^2	0.9221	0.9551
SSE	0.3341	0.3530
RMSE	0.5780	0.5941
Chi-square (x^2)	2.4754	2.7423
Temkin		
A_T (L/g)	0.906	1.849
B_T	1.3074	1.009
b (kJ/mol)	1.895	2.455
r^2	0.8782	0.9520
SSE	0.0683	0.0269
RMSE	0.2613	0.1640
Chi-square (x^2)	0.0767	0.0292

observed from the plot of adsorption data from both adsorbents (Fig. 4(b)). This type of adsorption isotherm is particularly experienced when the adsorbate has large hydrophobic components, like most dyes [31]. At very low concentration, dye-kaolinite interaction was small and in a concave shape, probably due to the competition with solvent (water). But as the MB concentration increased, the amount of adsorption was enhanced (Fig. 4(b)). The empirical data for the Freundlich isotherm model also demonstrated a small SSE, RMSE and Chi-square x^2 value. A small error value indicates the close fitness of the measured experimental data with the

theoretical value calculated from each model [33].

Meanwhile, the empirical data of RK demonstrated less fitness to D-R and Temkin isotherm, as compared to 0.5 M AAK (Table 1). D-R isotherm is used to differentiate between the physical or chemical adsorption. The theoretical E value from the D-R model (Table 1) for both RK and 0.5 M AAK implies that the adsorption is governed by physisorption as the $E < 8$ kJ/mol [30]. The theoretical q_{\max} value (1.906 mg/g) obtained from the D-R isotherm was in close agreement with the experimental value obtained by the 0.5 M AAK (1.37 mg/g). Temkin isotherm is less suitable to describe the RK adsorption ($r^2 < 0.9$) but showed good fit with 0.5 M AAK ($r^2 > 0.95$) with small x^2 value. A positive value of b retrieved from the Temkin isotherm model suggested that the adsorption is of endothermic process. The heat of adsorption is also less than 8 kJ/mol indicating a physical adsorption process, which is in good agreement with the findings obtained from the D-R isotherm previously.

Kinetics

The kinetic studies were performed and fitted through the pseudo first order and second order model. The linear form of the pseudo first order model (known as Lagergren model) [34] is expressed by:

$$\log(q_e - q_t) = \log q_e - \frac{K_1 t}{2.303} \quad (13)$$

where q_t and q_e are the amounts of MB adsorbed in mg/g at time t (min) and at equilibrium, respectively. K_1 is assigned to the pseudo first order adsorption rate constant (min^{-1}) obtained from the slope of the plots of $\log(q_e - q_t)$ versus t .

Meanwhile, the pseudo second order model [35] assumes chemisorption as the rate limiting step and could be expressed by the Eq. (14):

$$\frac{t}{q_t} = \frac{1}{h} + \frac{1}{q_e} t \quad (14)$$

where h is the initial sorption rate (mg/g.min). The values of q_e and h were calculated from the slope and intercept of the linear plot of t/q_t against t , respectively. In addition, the pseudo second order constant, K_2 (g/mg.min) is derived from the relationship in Eq. (15):

$$h = K_2 q_e \quad (15)$$

The pseudo second order kinetic model demonstrated the best fit ($r^2 > 0.98$ and smaller SSE, RMSE and x^2) to the adsorption data for both RK and 0.5 M AAK compared to pseudo first order model (Table 2). Therefore, chemisorption is deduced to be the rate limiting step for MB adsorption by both kaolinite adsorbents [28].

Desorption Experiments

Desorption studies are important in order to investigate the retention stability of adsorbent-adsorbate and validate their reliability for regeneration purpose. Strong adsorbent-pollutant interaction is necessary to ensure no leaching of adsorbed pollutant occurred during the treatment process. On the other hand, if the research emphasizes towards generating a cost-effective treatment, efficient desorption (or recoveries) of a pollutant from spent adsorbent is the first crucial step to allow the adsorbent to be regenerated. Interestingly, although both adsorbents showed almost similar removal percentage of MB during adsorption (95.3 and 96.8% for RK and 0.5 M AAK, respectively), their desorption profile exhibit a distinctive pattern. The 0.5 M AAK showed less desorption percentage than RK at pH 8, but the trend was reversed at pH 4 and 6 (Fig. 5). It was proposed that activation may cause protonated surface sites as a consequence of H^+ (from HCl) interaction with clay's surface during activation [22]. Furthermore acid activation may induce changes in pore structure and size distribution [22]. The protonated surface of 0.5 M AAK and broad band of pore size hence create less retention capability to hold the adsorbed MB molecules, causing a greater MB released during desorption studies. Besides, the prevalence of H^+ ions in the acidic solution (especially at pH 4) may be exchangeable with the MB deposited on kaolinite's surface and trigger the desorption of MB into the solution [36].

Meanwhile, at pH 8, deprotonation by excessive hydroxyl ions (OH^-) on part of 0.5 M AAK surface was predicted. This deprotonation may cause charge delocalization and concurrently strengthen MB-kaolinite retention. Hence less embedded MB was released towards the aqueous solution during desorption. It was also proposed that the low desorption percentage of dyes in

Table 2. Kinetic analysis on the adsorption of MB by RK and 0.5 M AAK (performed at initial [MB] = 50 mg/L, agitation speed 2500 rpm, at 0.05 g/mL loading, at 25 °C)

Kinetic model/Adsorbent	RK	0.5 M AAK
<i>Pseudo first order</i>		
q_e (mg/g)	0.5652	0.2412
k_1 (min^{-1})	0.0404	0.0324
r^2	0.7127	0.7180
SSE	1.9027	1.4078
RMSE	1.3794	1.1865
Chi-square (x^2)	1.9959	1.2863
<i>Pseudo second order</i>		
q_e (mg/g)	1.0933	1.0054
k_2 ($g\ mg^{-1}\ min^{-1}$)	0.0641	0.1939
h ($g\ mg^{-1}\ min^{-1}$)	0.0801	0.2120
r^2	0.9896	0.9975
SSE	0.0167	0.0121
RMSE	0.1294	0.1101
Chi-square (x^2)	0.0289	0.0162

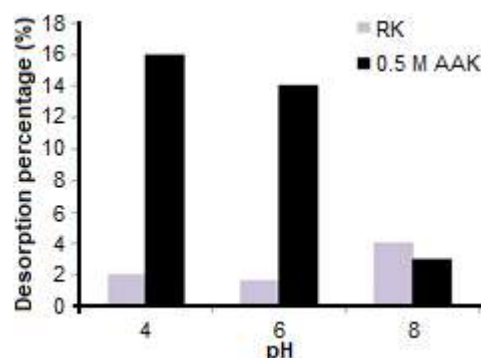


Fig 5. MB desorption efficiency (%) by spent kaolinites

highly alkaline eluent could probably be due to new complexes that were formed [36]. As the MB desorption percentage in RK was less than 5%, it can be concluded that the kaolinite-MB retention on RK was stronger and irreversible as compared to the 0.5 M AAK. Nevertheless, for the purpose of regeneration and adsorbent recycling, 0.5 M AAK is a more promising material as the loaded MB is easier to be leached out from the spent clays during desorption process.

CONCLUSION

Acid activation provides a simple and inexpensive approach for kaolinite modification. The 0.5 M AAK gave

higher removal percentage (up to 97%) but of similar performance against raw kaolinite. The removal of MB by kaolinites in aqueous water is achieved via physisorption while the rate limiting step is governed by the chemisorption. High adsorbent loading, initial concentration, and agitation speed have enhanced the MB removal percentage. While the MB removal performance between RK and 0.5 M AAK was analogous, the findings from the desorption experiment showed that the kaolinite-MB retention in the spent RK was irreversible and more stable against pH influence. Hence, the forthcoming regeneration process of spent acid-activated kaolinite for re-use in water treatment is expected to be more feasible as compared to raw clays. Overall, kaolinite has shown a promising application in treating dyes from contaminated water.

■ ACKNOWLEDGMENTS

The authors would like to thank Universiti Teknologi MARA, Negeri Sembilan branch for technical facilities and financial support through internal funding, also the anonymous reviewers for their feedback to improve the manuscript.

■ REFERENCES

- [1] Bafana, A., Devi, S.S., and Chakrabarti, T., 2011, Azo dyes: Past, present and the future, *Environ. Rev.*, 19, 350–371.
- [2] Kallel, F., Chaari, F., Bouaziz, F., Bettaieb, F., Ghorbel, R., and Chaabouni, S.E., 2016, Sorption and desorption characteristics for the removal of a toxic dye, methylene blue from aqueous solution by a low cost agricultural by-product, *J. Mol. Liq.*, 219, 279–288.
- [3] Rafatullah, M., Sulaiman, O., Hashim, R., and Ahmad, A., 2010, Adsorption of methylene blue on low-cost adsorbents: A review, *J. Hazard. Mater.*, 177 (1-3), 70–80.
- [4] Rida, K., Bouraoui, S., and Hadnine, S., 2013, Adsorption of methylene blue from aqueous solution by kaolin and zeolite, *Appl. Clay Sci.*, 83-84, 99–105.
- [5] Bergaya, F., and Lagaly, G., 2006, “Chapter 1 General introduction: Clays, clay minerals, and clay science” in *Handbook of Clay Science*, 1st Ed., Eds. Bergaya, F., Theng, B.K.G., and Lagaly, G., Elsevier Science, Netherlands, 1–18.
- [6] Zhou, C.H., and Keeling, J., 2013, Fundamental and applied research on clay minerals: From climate and environment to nanotechnology, *Appl. Clay Sci.*, 74, 3–9.
- [7] Madejova, J., and Komadel, P., 2001, Baseline studies of the clay minerals society source clays: Infrared methods, *Clays Clay Miner.*, 49 (5), 410–432.
- [8] Rusmin, R., Sarkar, B., Biswas, B., Churchman, J., Liu, Y., and Naidu, R., 2016, Structural, electrokinetic and surface properties of activated palygorskite for environmental application, *Appl. Clay Sci.*, 134, 95–102.
- [9] Shi, L., 2017, “The mineral industry of Malaysia” in *Minerals Yearbook 2014: Metals and Minerals*, Vol. I, U.S. Geological Survey, Reston, VA, 16.1–16.7.
- [10] Gao, W., Zhao, S., Wu, H., Deligeer, W., and Asuha, S., 2016, Direct acid activation of kaolinite and its effects on the adsorption of methylene blue, *Appl. Clay Sci.*, 126, 98–106.
- [11] Komadel, P., 2016, Acid activated clays: Materials in continuous demand, *Appl. Clay Sci.*, 131, 84–99.
- [12] Hai, Y., Li, X., Wu, H., Zhao, S., Deligeer, W., and Asuha, S., 2015, Modification of acid-activated kaolinite with TiO₂ and its use for the removal of azo dyes, *Appl. Clay Sci.*, 114, 558–567.
- [13] Wu, P., and Ming, C., 2006, The relationship between acidic activation and microstructural changes in montmorillonite from Heping, China, *Spectrochim. Acta, Part A*, 63 (1), 85–90.
- [14] Sarma, G.K., Gupta, S.S., and Bhattacharyya, K.G., 2019, Removal of hazardous basic dyes from aqueous solution by adsorption onto kaolinite and acid-treated kaolinite: Kinetics, isotherm, and mechanistic study, *SN Appl. Sci.*, 1, 211.
- [15] El Mouzdahir, Y., Elmchaouri, A., Mahboub, R., Gil, A., and Korili, S.A., 2010, Equilibrium modeling for the adsorption of methylene blue from aqueous solutions on activated clay minerals, *Desalination*, 250 (1), 335–338.
- [16] Vanaamudan, A., Pathan, N., and Pamidimukkala, P., 2014, Adsorption of Reactive Blue 21 from

- aqueous solutions onto clay, activated clay, and modified clay, *Desalin. Water Treat.*, 52 (7-9), 1589–1599.
- [17] Hu, P., and Yang, H., 2013, Insight into the physicochemical aspects of kaolins with different morphologies, *Appl. Clay Sci.*, 74, 58–65.
- [18] Frost, R.L., 1997, The structure of the kaolinite minerals FT-Raman study, *Clay Miner.*, 32 (1), 65–77.
- [19] Saikia, B.J., and Parthasarathy, G., 2010, Fourier transform infrared spectroscopic characterization of kaolinite from Assam and Meghalaya, Northeastern India, *J. Mod. Phys.*, 1, 206–210.
- [20] Panda, A.K., Mishra, B.G., Mishra, D.K., and Singh, R.K., 2010, Effect of sulphuric acid treatment on the physico-chemical characteristics of kaolin clay, *Colloids Surf., A*, 363, 98–104.
- [21] Ullah, Z., Hussain, S., Gul, S., Khan, S., and Bangash, F.K., 2016, Use of HCl-modified bentonite clay for the adsorption of Acid Blue 129 from aqueous solutions, *Desalin. Water Treat.*, 57 (19), 8894–8903.
- [22] Bhattacharyya, K.G., and Gupta, S.S., 2011, Removal of Cu(II) by natural and acid-activated clays: An insight of adsorption isotherm, kinetic and thermodynamics, *Desalination*, 272 (1-3), 66–75.
- [23] Chicinaş, R.P., Bedelea, H., Stefan, R., and Măicăneanu, A., 2018, Ability of a montmorillonitic clay to interact with cationic and anionic dyes in aqueous solutions, *J. Mol. Struct.*, 1154, 187–195.
- [24] Mills, A., Hazafy, D., Parkinson, J., Tuttle, T., and Hutchings, M.G., 2011, Effect of alkali on methylene blue (C.I. Basic Blue 9) and other thiazine dyes, *Dyes Pigm.*, 88 (2), 149–155.
- [25] Tehrani-Bagha, A.R., Nikkar, H., Mahmoodi, N.M., Markazi, M., and Menger, F.M., 2011, The sorption of cationic dyes onto kaolin: Kinetic, isotherm, and thermodynamic studies, *Desalination*, 266 (1-3), 274–280.
- [26] Berrios, M., Martín, M.Á., and Martín, A., 2012, Treatment of pollutants in wastewater: Adsorption of methylene blue onto olive-based activated carbon, *J. Ind. Eng. Chem.*, 18 (2), 780–784.
- [27] Vimonses, V., Lei, S., Jin, B., Chow, C.W.K., and Saint, C., 2009, Kinetic study and equilibrium isotherm analysis of Congo Red adsorption by clay materials, *Chem. Eng. J.*, 148 (2-3), 354–364.
- [28] Auta, M., and Hameed, B.H., 2013, Acid modified local clay beads as an effective low-cost adsorbent for dynamic adsorption of methylene blue, *J. Ind. Eng. Chem.*, 19 (4), 1153–1161.
- [29] Temkin, M.J., and Pyzhev, V., 1940, Recent modification to Langmuir isotherms, *Acta Physicochim. URSS*, 12, 217–222.
- [30] Desta, M.B., 2013, Batch sorption experiments: Langmuir and Freundlich isotherm studies for the adsorption of textile metal ions onto Teff Straw (*Eragrostis tef*) agricultural waste, *J. Thermodyn.*, 2013, 375830.
- [31] Gómez, V., Larrechi, M.S., and Callao, M.P., 2007, Kinetic and adsorption study of acid dye removal using activated carbon, *Chemosphere*, 69 (7), 1151–1158.
- [32] Giles, C.H., MacEwan, T.H., Nakhwa, S.N., and Smith, D., 1960, Studies in adsorption. Part XI. A system of classification of solution adsorption isotherms, and its use in the diagnosis of adsorption mechanisms and in the measurement of specific surface areas of solids, *J. Chem. Soc.*, 14, 3973–3993.
- [33] Zamri, T.K.A.T.M., Munaim, M.S.A., and Wahid, Z.A., 2017, Regression analysis for the adsorption isotherms of natural dyes onto bamboo yarn, *Int. Res. J. Eng. Technol.*, 4 (6), 1699–1703.
- [34] Yuh-Shan, H., 2004, Citation review of Lagergren kinetic rate equation on adsorption reactions, *Scientometrics*, 59, 171–177.
- [35] Ho, Y.S., 2006, Review of second-order models for adsorption systems, *J. Hazard. Mater.*, 136 (3), 681–689.
- [36] Daneshvar, E., Vazirzadeh, A., Niazi, A., Kousha, M., Naushad, M., and Bhatnagar, A., 2017, Desorption of Methylene blue dye from brown macroalgae: Effects of operating parameters, isotherm study, and kinetic modeling, *J. Cleaner Prod.*, 152, 443–453.

Cytotoxic Activity of 2-O- β -glucopyranosil Cucurbitacin D from Benalu Batu (*Begonia* sp.) Growing in Morowali, Central Sulawesi

Muhammad Sulaiman Zubair^{1,*}, Walied Mohamed Alarif², Mohamed Ali Ghandourah², Syariful Anam¹, and Ibrahim Jantan³

¹Department of Pharmacy, Science Faculty, Tadulako University, Jl. Soekarno Hatta Tondo, Palu 94118, Indonesia

²Department of Marine Chemistry, Marine Science Faculty, King Abdul Aziz University, Jeddah 21589, Saudi Arabia

³School of Pharmacy, Taylor's University, Lakeside Campus, Jl. Taylors No. 1, Subang Jaya 47500, Selangor, Malaysia

* **Corresponding author:**

tel: +62-451-486221

email: sulaiman_zubair80@yahoo.co.id

Received: February 16, 2019

Accepted: June 30, 2019

DOI: 10.22146/ijc.43626

Abstract: Benalu batu (*Begonia* sp.) had been used traditionally as an anticancer medicinal plant by Wana tribe in Morowali, Central Sulawesi. This study aims to evaluate the cytotoxic activity of 2-O- β -glucopyranosil cucurbitacin D, isolated from the ethyl acetate soluble fraction of Benalu batu (*Begonia* sp.) and to determine its action on apoptosis induction. Benalu batu (*Begonia* sp.) herb was extracted by maceration using ethanol 96% as a solvent. Vacuum liquid column chromatography and preparative thin layer chromatography have been applied on fractionation and isolation of the compound. The structure elucidation was performed by extensive analysis of 1D/2D nuclear magnetic resonance (NMR) and Mass Spectrophotometer (MS). Cytotoxic activity against human breast adenocarcinoma (MCF-7) and human colon colorectal carcinoma (HCT-116) cell lines were performed by 5-diphenyltetrazolium bromide (MTT) method. Annexin V-FITC assay was employed to determine the apoptosis induction. 2-O- β -glucopyranosil cucurbitacin D showed potent cytotoxic activity against MCF-7 and HCT-116 with the IC₅₀ of 19.913 and 0.002 μ g/mL, respectively. Annexin V-FITC assay clearly exhibited the cytotoxic mechanism on MCF-7 and HCT-116 via apoptosis induction with a significant percentage of early and late apoptosis of 75.8 and 78.4%, respectively. This study reveals the potential cytotoxic activity of 2-O- β -glucopyranosil cucurbitacin D isolated from Benalu batu and its mechanism via apoptosis induction.

Keywords: *Begonia* sp.; 2-O- β -glucopyranosil cucurbitacin D; cytotoxic; MCF-7; HCT-116

■ INTRODUCTION

Medicinal plants were abundant in Indonesia and used by local people to traditionally treat several diseases. Moreover, medicinal plants were also a rich source for discovering new drugs, and after research and development, they can lead to being a potent drug which can be used in clinical practice. More than 60% of the drugs available in the market were derived from natural source [1-3].

Begoniaceae, a plant family with approximately 1600 species, widely distributed along with subtropical

and tropical areas over the world [4]. Our literature survey found that only about 10 species of *Begonia* plants were studied up to now regarding the chemical composition and biological activity study. Most of the compounds reported from *Begonia* species are flavonoids, triterpenoids, steroids, and their glycosides along with alkaloid [5]. The biological activity was ranging from antibacterial [6-7], antioxidant [8], anti-hyperglycemic [9], antiviral to cytotoxic activities [10-12].

Benalu batu (*Begonia* sp.) was traditionally used as an ethnomedicinal plant by Wana tribe in Morowali, Central Sulawesi, to treat several diseases, such as tumor,

cancer, asthma, dry cough, lumbago, kidney failure, ulcer, laxatives, waging irregular menstruation, urolithiasis, tuberculosis, diabetes, eczema, and gout. Our previous study has established the anticancer activity of the methanol extract of this herb plant against breast and cervical cancer cell lines (T47D and HeLa cells) [13]. In our interest to investigate the phytochemical anticancer agents from this herb plant, a preliminary *in silico* docking study to early identify the predictive potential natural product compounds type from *Begonia* species have been performed. An alkaloid, a steroidal glycoside, flavonoid glycoside, and triterpenoid glycoside were recommended compounds that might have possible action to inhibit the proliferation of cancer cells [5]. This study reports the isolation and structure elucidation of one of the targeted compounds, a terpenoid glycoside, assigned as 2-O- β -glucopyranosil cucurbitacin D (Fig. 1) from ethyl acetate soluble fraction of *Benalu batu* (*Begonia* sp.). To the best of our knowledge, this is the first report of bioactive compound reported from *Benalu batu* (*Begonia* sp.), and it confirmed the presence of cucurbitacin type compounds on *Begonia* species. Cytotoxic activity and apoptosis assay of the isolated compound on several types of cancer cell lines were also evaluated.

■ EXPERIMENTAL SECTION

Materials

The whole plant (herb) of *Benalu batu* (*Begonia* sp.), which grows in the mountain, was collected from Morowali, Central Sulawesi, on April 2014. The plant was still identified by Wisnu H. Ardi (Taxonomist) at Bogor Botanic Garden, Bogor, Indonesia and deposited as a dried specimen (BSP 00020414) at Phytochemistry Laboratory, Department of Pharmacy, Tadulako University.

Instrumentation

TLC aluminium sheets 20 × 20 cm silica gel 60 F₂₅₄ was used. Silica gel 60 (Merck) for vacuum liquid column chromatography (230–400 mesh) was used. Preparative precoated TLC glass plates SIL G-25 UV₂₅₄, 0.25 mm silica gel and Sephadex LH-20 (Sigma, St. Louis, USA) were used for isolation and purification of the compounds. Spots

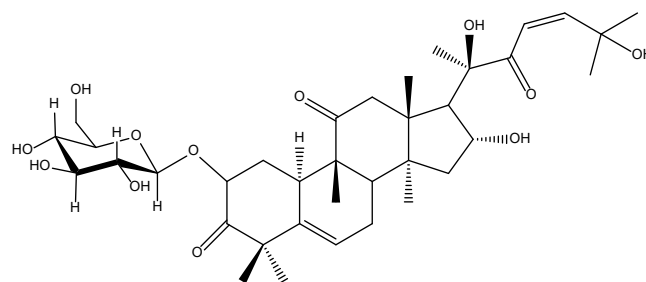


Fig 1. 2-O- β -glucopyranosil cucurbitacin D

on TLC were visualized by using spraying reagent of methanol-sulphuric acid and *p*-anisaldehyde-sulphuric acid for terpenoid detection. Nuclear magnetic resonance (NMR) were recorded for 1D and 2D on Avance^{III} Bruker WM 600 MHz for ¹H and 150 MHz for ¹³C. Chemical shifts are given δ (ppm) relative to TMS as internal standard, and deuterated chloroform was used as solvents. Electron impact mass spectra were determined at 70 eV using a Kratos GCMS-25 instrument.

Procedure

Extraction and isolation

The herb plant was dried in the shade at room temperature. The dried simplicia (250 g) was extracted with ethanol 96% (3 × 0.8 L, 24 h for each batch) at room temperature. The solvent was removed in a vacuum until reached a residue (15 g) referred to as crude ethanol extract. The ethanol extract (10 g) was suspended in water and successively partitioned with *n*-hexane and ethyl acetate to obtain *n*-hexane and ethyl acetate soluble fraction. The ethyl acetate fraction (3 g) was chromatographed on silica gel (60–120 mesh), and the packed column was eluted by employing gradient system of the solvent of *n*-hexane 100%, *n*-hexane/ethyl acetate mixture, followed by ethyl acetate/methanol mixture and methanol 100%. Forty fractions of 50 mL each were collected. Similar fractions were collected together according to TLC pattern in eight fractions (F1–F8). The fourth fraction, which is detected to contain terpenoid, was continued to further isolation using successive TLC preparative with a solvent system of methanol: chloroform (8:2) as a mobile phase. A spot with R_f 2.40 (purple color with H₂SO₄/MeOH) was taken to give the compound (5.6 mg).

Compound

Identification of 2-O- β -glucopyranosil cucurbitacin D was determined by using the spectroscopic method on MS, 1D/2D NMR and comparison with the literature. The chemical structure of isolated compounds can be seen in Fig. 1.

2-O-B-glucopyranosil cucurbitacin D. Gummy material, HRESIMS (positive-ion mode), $m/z = 679.8068$ $[M + H]^+$ (Calc. for $C_{36}H_{55}O_{12}$, 679.3610).

1H NMR (600 MHz, $CDCl_3$): δ H 7.088 (1H, d (10.8), H-24), 6.806 (1H, d (10.8), H-23), 5.716 (1H, br s, H-6), 4.834 (1H, br s, H-2), 4.431 (1H, br s, H-1'), 4.256 (s, OH-20), 3.941 (2H, m, H-6'), 3.936 (d (3.0), OH-16), 3.780 (1H, m, H-16), 3.650 (1H, m, H-5'), 3.569 (1H, m, H-4'), 3.548 (s, OH-25), 3.488 (1H, m, H-3'), 3.417 (1H, m, H-2'), 3.337 (1H, d (9), Ha-12), 2.902 (1H, br d (7.2), H-10), 2.668 (1H, d (9), Hb-12), 2.367 (1H, d (8.4), H-17), 2.353 (1H, m, Ha-1), 2.315 (1H, d(4.8), Hb-7), 1.997 (1H, m, H-8), 1.993 (1H, d(4.8), Ha-7), 1.957 (1H, m, H-15a), 1.626 (1H, m, H-15b), 1.450 (1H, m, Hb-1), 1.384 (3H, s, H-21), 1.357 (3H, s, H-28), 1.259 (3H, s, H-27), 1.236 (3H, s, H-29), 1.227 (3H, s, H-26), 1.127 (3H, s, H-30), 1.011 (3H, s, H-19), 0.951 (3H, s, H-18).

^{13}C NMR (150 MHz, $CDCl_3$): δ C 216.452 (C-11), 212.155 (C-3), 202.591 (C-22), 156.748 (C-24), 140.222 (C-5), 119.944 (C-6), 118.218 (C-23), 102.969 (C-1'), 79.600 (C-2), 78.901 (C-20), 77.204 (C-16), 76.425 (C-5'), 76.257 (C-3'), 73.839 (C-2'), 71.271 (C-25), 70.255 (C-4'), 61.988 (C-6'), 50.815 (C-4), 50.612 (C-14), 50.335 (C-9), 48.820 (C-12), 48.390 (C-17), 47.824 (C-13), 42.374 (C-8), 34.770 (C-1), 34.581 (C-15), 33.917 (C-10), 29.686 (C-28), 29.234 (C-27), 28.069 (C-26), 24.034 (C-21), 22.679 (C-7), 21.310 (C-29), 19.656 (C-18), 19.183 (C-19), 18.148 (C-30).

Cytotoxic activity

The cytotoxic activity was performed by MTT colorimetric assay as described in our previous study [14]. About 1.0 mg of compound were dissolved by 1.0 mL of RPMI-1640 medium to obtain stock solutions of 1000 μ g/mL. Then, the sample was diluted to desired concentrations of 6.25, 12.5, 25, and 50 μ g/mL using dimethylsulphoxide (DMSO) in which the DMSO concentration in each sample was 1% v/v. The cancer cells

of human breast adenocarcinoma (MCF-7) and human colon colorectal carcinoma (HCT-116) were batch cultured for 10 d, then seeded in 96 well plates of 1×10^4 cells/well in fresh complete growth medium in 96-well flat bottom culture plates at 37 °C using incubator in 5% CO_2 humidified atmosphere (CelCulture, Esco Medical ApS, Denmark). After 24 h incubation, the medium (without serum) was added and cells were incubated for 48 h either alone (negative control) or with different concentrations of the sample. Then, the cells were added with 10 μ L/well of MTT (5 mg/mL) and incubated again for 4 h in an incubator at 37 °C in 5% CO_2 humidified atmosphere. The reaction was stopped by adding 100 μ L dimethylsulfoxide (DMSO) and the plate was then placed for 15 min in the shade room. The absorbance of each well was read at 550 nm wavelength in Elisa Reader (Infinite M200 pro NanoQuant, Tecan, Switzerland), using wells without cells as blanks. All experiments were performed in triplicate. Anticancer drugs of doxorubicin and fluorouracil were used as a positive standard. The effect of compounds on the proliferation of cancer cells was expressed as the % cytoviability, using the following formula:

$$\% \text{ Cytoviability} = \frac{\text{Absorbance of treated cells}}{\text{Absorbance of control cells}} \times 100\%$$

The probit analysis on SPSS 17.0 (SPSS Inc., Chicago IL, USA) was used to calculate the IC_{50} by plotting the series of concentration and the percentage of cytoviability.

Annexin V-FITC apoptosis assay

Briefly, 1×10^5 of cells lines (MCF-7 and HCT-116) were treated with 5.0 μ L annexin V-FITC and 5.0 μ L propidium iodide (PI) using the apoptosis detection kit (BD Biosciences, San Jose, CA) according to the manufacturer's protocol. Flow cytometry on FACScanto II (BD Biosciences, San Jose, CA) was used to analyze the binding of Annexin V-FITC and PI without gating restrictions using 10,000 cells. Logarithmic amplification of both the FL1 (FITC-A) and the FL2 (PI-A) channels were performed to obtain the data. CellQuest software was used for analysis the quadrant of coordinate dot plots. The photomultiplier voltage and compensation setting adjustment to eliminate the

spectral overlap between the FL1 and the FL2 signals was done by using the unstained cells.

■ RESULTS AND DISCUSSION

Cytotoxic Activity

The result of the cytotoxic activity of 2-O- β -glucopyranosil cucurbitacin D can be seen in Fig. 2. It clearly showed that 2-O- β -glucopyranosil cucurbitacin D has ability to inhibit the proliferation of both MCF-7 and HCT-116 cell lines. However, the inhibition on HCT-116 was higher than on MCF-7, where at the concentration of 25 $\mu\text{g/mL}$, the percentage of cell viability on HCT-116 was 6.88% compared to MCF-7 (48.26%). Therefore, the IC_{50} of 2-O- β -glucopyranosil cucurbitacin D on HCT-116 was also higher than on MCF-7 with the value of 0.002 and 19.913 $\mu\text{g/mL}$, respectively (Table 1).

Annexin V-FTIC Apoptosis Assay

The result of annexin V-FTIC of 2-O- β -glucopyranosil cucurbitacin D can be seen in Fig. 3. It clearly showed that the significant percentage of early and late apoptosis of 2-O- β -glucopyranosil cucurbitacin D on HCT-116 and MCF-7 was 78.4 and 75.8%, respectively.

Compound 2-O- β -glucopyranosil cucurbitacin D was isolated as a gummy material. Liebermann-Burchard test supported that the compound is a terpenoid. Moreover, it gave a reddish spot on a TLC plate after spraying with *p*-anisaldehyde as well. The analysis of HRESI-MS at m/z 679.3610 $[\text{M} + \text{H}]^+$ supporting the molecular structure of glycosidal triterpenoid with the molecular formula of $\text{C}_{36}\text{H}_{54}\text{O}_{12}$ that can be suggested to have 10 degrees of unsaturation. The ^{13}C NMR spectral data exhibited 36 signals of a carbon atom which is categorized by DEPT into eight methyls, six methylene,

twelve methines, and ten quaternary carbons. The presence of glucopyranosil moiety was supported by the resonance of an anomeric carbon at 102.969 ppm, together with four methines at 76.425, 76.257, 73.839, 70.255 ppm and one methylene carbon at 61.988 ppm. Three carbonyl carbons observed at 216.452, 212.155, and 202.591 ppm supporting the skeleton of cucurbitacin triterpenoid skeleton attached by single monosaccharide moiety. The carbonyl group was assigned to C2, C11, and C22, respectively. Moreover, four olefinic carbon signals (118.218, 119.944, 140.222 and 156.748) supported the main skeleton of cucurbitacin type triterpenoid by suggesting the presence of trisubstituted double bond at C5-C6 and a disubstituted double bond at C23-C24.

The ^1H NMR revealed the skeleton of cucurbitacin type triterpenoid in the form of a glycosidic compound, proven by the presence of eight methyl singlet signal in the area between 0.951–1.384 ppm, the vicinal coupling of AB system between H-23, resonating at 6.806, and H-24

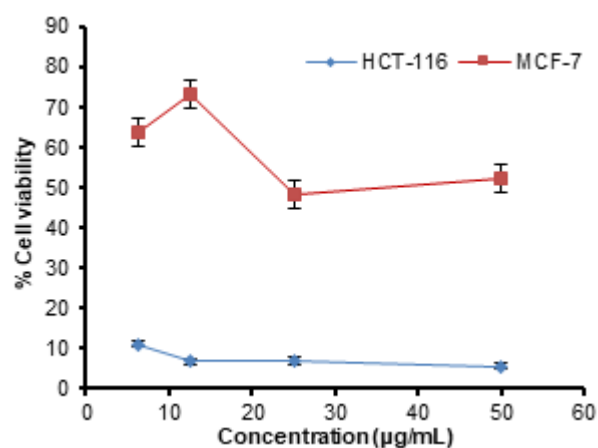


Fig 2. The percentage of cell viability of 2-O- β -glucopyranosil cucurbitacin D on MCF-7 and HCT-116

Table 1. Cytotoxic activity of 2-O- β -glucopyranosil cucurbitacin D

Compound	IC_{50} ($\mu\text{g/mL}$)	
	MCF-7	HCT-116
2-O- β -glucopyranosil cucurbitacin D	19.2 \pm 5.094	0.002 \pm 0.019
Doxorubicin ^a	0.02 \pm 0.038	-
Fluorouracil ^b	-	21.7 \pm 4.019

^aDoxorubicin was used as a positive control on MCF-7, ^bFluorouracil was used as a positive control on HCT-116, Data are presented as mean \pm standard deviation, SD

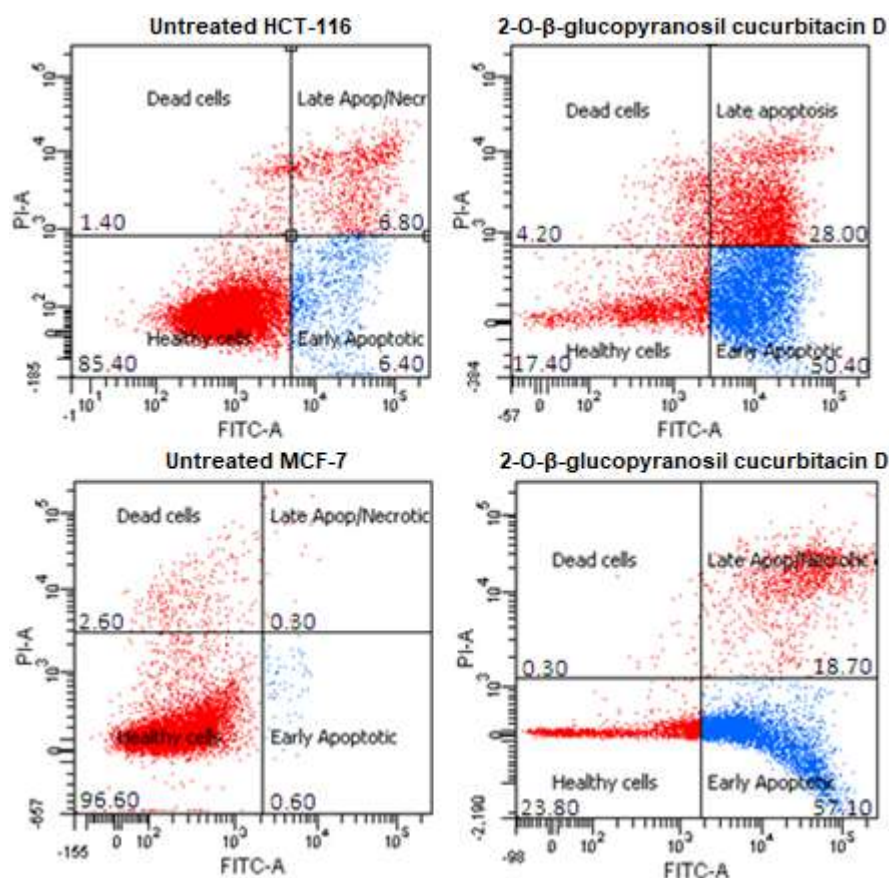


Fig 3. Effect of 2-O-β-glucopyranosil cucurbitacin D on HCT-116 and MCF-7 on annexin V-FITC-positive staining. The four quadrants identified as LL (healthy cells); LR (early apoptotic); UR (late apoptotic) and UL (necrotic)

at 7.088, where its J value of 10.8, suggesting the stereochemistry for C-23-24 is Z configuration [15]. A broad singlet proton signal at 5.716, assigned for C6. A typical triplet signal at 3.780 for H-16, a characteristic of geminal coupling of H-12 as two duplets at 2.668 and 3.337 ($J = 9$ Hz), an upfield shift at 4.834 for H-2, which are attributed by the glycosidic linkage of this position and also from carbonyl group at C-3. A single monosaccharide moiety was revealed by an anomeric proton at 4.431, together with five signals of oxygenated carbon in the range of 3.417–3.941.

Cucurbitacin type triterpenoid was mostly encountered in the cucurbitaceae family plant. However, the presence of this compound was also reported from the genus of Begoniaceae. Among the begoniaceae plants, only *Begonia heraclifera* and *Begonia nantoensis* were reported to contain cucurbitacin type compounds [11-12]. Therefore, this compound, 2-O-B-glycopyranosil

cucurbitacin D, found for the first time in *Benalu batu* (*Begonia* sp.), can be a marker compound for the species of *Begonia*.

The cytotoxic activity of cucurbitacin type compounds was intensively studied. Cucurbitacin B, cucurbitacin E, and cucurbitacin I have been reported to inhibit the cell proliferation of human breast cancer [16-18]. Cucurbitacin B, cucurbitacin D, and dihydrocucurbitacin D inhibited the growth of human nasopharyngeal carcinoma (KB) cells, murine embryonic fibroblasts (313) cells, human prostate carcinoma (PC-3) cells, murine methylcholanthrene-induced fibrosarcoma (MethA) cells [11]. Cucurbitacin B and dihydrocucurbitacin B inhibited the cell proliferation of mouse embryonic fibroblast (NIH3T3) and virally transformed form (KA3IT) [19]. In the form of glycoside, cucurbitacin I glycoside and cucurbitacin E glycoside has been reported to inhibit Hepatoma Cell

Line (HepG2) and mice-bearing tumor of Ehrlich's ascites carcinoma (EAC) [20]. This fact showed the potential anticancer activity for this type of compounds.

2-O- β -glycopyranosil cucurbitacin D exhibited potent cytotoxic activity against MCF-7 and HCT-116 cancer cell lines with the IC₅₀ of 19.913 and 0.002 μ g/mL, respectively. This result encourages us to further study its mechanism on apoptosis induction. Both cell lines were stained by annexin A and gave a proper indication on early and late apoptosis, as shown in Fig. 3. The result showed that there is a significant increase in the percentage of annexin V-FITC-positive apoptotic cells (early + late apoptotic) on HCT-116 and MCF-7 when compared to the untreated cells (Fig. 4). Therefore, it can be concluded that 2-O- β -glycopyranosil cucurbitacin D inhibited the cell proliferation of HCT-116 and MCF-7 via apoptosis induction. Some studies had reported cucurbitacin type compounds could induce apoptosis mechanism, such as cucurbitacin D exhibit anticancer activity in human breast cancer by inhibiting Stat3 and Akt signaling and cucurbitacin B induces apoptosis by inhibition of the JAK/STAT pathway [21-22]. Therefore, 2-O- β -glycopyranosil cucurbitacin D might also induce apoptosis in this same mechanism.

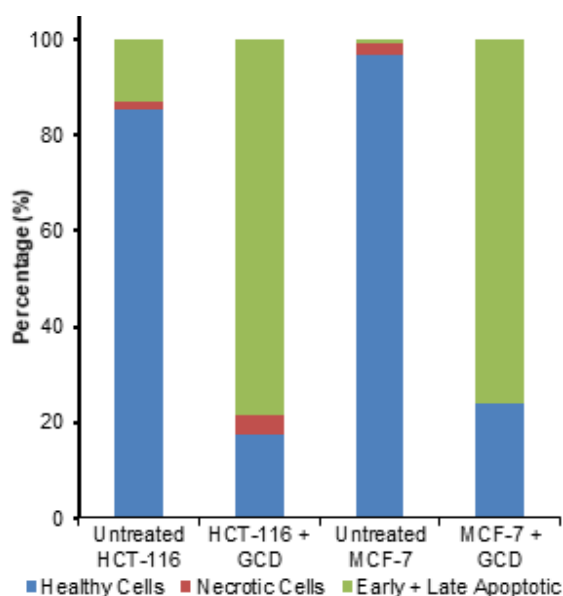


Fig 4. The percentage of healthy cells, necrotic cells and early + late apoptotic cells on HCT-116 and MCF-7 cell lines after exposed by 2-O- β -glucopyranosil cucurbitacin D (GCD)

CONCLUSION

2-O- β -glycopyranosil cucurbitacin D was successfully isolated for the first time from *Benalu batu* (*Begonia* sp.). This result indicated that the presence of cucurbitacin type triterpenoid could be a marker compound for *Begonia* plant species. It exhibited potent cytotoxic activity against HCT-116 and MCF-7 as well via apoptosis induction.

ACKNOWLEDGMENTS

The author acknowledges the Ministry of Research, Technology and Higher Education, Republic of Indonesia, for supporting this study through a grant of INSINAS 2015 (RD-2015-0106).

REFERENCES

- [1] Harvey, A.L., Eldrada-Ebel, R., and Quinn, R.J., 2015, The re-emergence of natural products for drug discovery in the genomics era, *Nat. Rev. Drug Discovery*, 14 (2), 111–129.
- [2] Dias, D.A., Urban, S., and Roessner, U.A., 2012, Historical overview of natural products in drug discovery, *Metabolites*, 2 (2), 303–333.
- [3] Newman, D.J., and Cragg, G.M., 2012, Natural product as sources of new drugs over the 30 years from 1981 to 2010, *J. Nat. Prod.*, 75 (3), 311–335.
- [4] Ding, B., Nakamura, K., Kono, Y., Ho, M.J., and Peng, C.I., 2014, *Begonia jinyunensis* (Begoniaceae, section *Platycentrum*), a new palmately compound leaved species from Chongqing, China, *Bot. Stud.*, 55, 62.
- [5] Zubair, M.S., Anam, S., Khumaidi, A., Susanto, Y., Hidayat, M., and Ridhay, A., 2016, Molecular docking approach to identify potential anticancer compound from Benalu batu (*Begonia* sp.), *AIP Conf. Proc.*, 1755 (1), 080005.
- [6] Ramesh, N., Viswanathan, M.B., Saraswathy, A., Balakrishna, K., Brindha, P., and Lakshmanaperu malsamy, P., 2002, Phytochemical and antimicrobial studies of *Begonia malabarica*, *J. Ethnopharmacol.*, 79 (1), 129–132.
- [7] Jeeva, S., and Antonisamy, J.M., 2012, Anti-bacterial and phytochemical studies on methanolic

- extracts of *Begonia floccifera* Bedd. flower, *Asian Pac. J. Trop. Biomed.*, 2 (1), S151–S154.
- [8] Kalpanadevi, V., and Mohan, V.R., 2012, *In vitro* antioxidant studies of *Begonia malabarica* Lam. and *Begonia floccifera* Bedd, *Asian Pac. J. Trop. Biomed.*, 2 (3), S1572–1577.
- [9] Pandikumar, P., Babu, N.P., and Ignacimuthu, S., 2009, Hypoglycemic and antihyperglycemic effect of *Begonia malabarica* Lam. in normal and streptozotocin induced diabetic rats, *J. Ethnopharmacol.*, 124 (1), 111–115.
- [10] Doskotch, R.W., and Hufford, C.D., 1970, Hexanor-cucurbitacin D, a degraded cucurbitacin from *Begonia tuberhybrida* var. *alba*, *Can. J. Chem.*, 48, 1787–1788.
- [11] Frei, B., Heinrich, M., Herrmann, D., Orjala, J.E., Schmitt, J., and Sticher, O., 1998, Phytochemical and biological investigation of *Begonia heracleifolia*, *Planta Med.*, 64 (4), 385–386.
- [12] Wu, P.L., Lin, F.W., Wu, T.S., Kuoh, C.S., Lee, K.H., and Lee, S.J., 2004, Cytotoxic and anti-HIV principles from the rhizomes of *Begonia nantoensis*, *Chem. Pharm. Bull.*, 52 (3), 345–349.
- [13] Anam, S., Yuliet, Ritna, A., Dwimurti, F., Rismayanti, D., and Zubair, M.S., 2014, Aktivitas sitotoksik ekstrak metanol Benalu batu (*Begonia* sp.): Ethnomedicine suku Wana Sulawesi Tengah, *Indones. J. Pharm. Sci.*, 12 (1), 10–16.
- [14] Zubair, M.S., Anam, S., and Lallo, S., 2016, Cytotoxic activity and phytochemical standardization of *Lunasia amara* Blanco wood extract, *Asian Pac. J. Trop. Biomed.*, 6 (11), 962–966.
- [15] Theodore, C.M., Lorig-Roach, N., Still, P.C., Johnson, T.A., Draskovic, M., Schwochert, J.A., Napfen, C.N., Crews, M.S., Barker, S.A., Valeriote, F.A., Lokey, R.S., and Crews, P., 2015, Biosynthetic products from a nearshore-derived gram negative bacterium enable reassessment of the kailuin depsipeptides, *J. Nat. Prod.*, 78 (3), 441–452.
- [16] Duangmano, S., Sae-Lim, P., Suksamrarn, A., Domann, F.E., and Patmasiriwat, P., 2012, Cucurbitacin B inhibits human breast cancer cell proliferation through disruption of microtubule polymerization and nucleophosmin/B23 trans location, *BMC Complement. Altern. Med.*, 12, 185.
- [17] Lopez-Haber, C., and Kazanietz, M.G., 2013, Cucurbitacin I inhibits Rac1 activation in breast cancer cells by a reactive oxygen species-mediated mechanism and independently of Janus tyrosine kinase 2 and P-Rex1, *Mol. Pharmacol.*, 83 (5), 1141–1154.
- [18] Kong, Y., Chen, J., Zhou, Z., Xia, H., Qiu, M.H., and Chen, C., 2014, Cucurbitacin E induces cell cycle G2/M phase arrest and apoptosis in triple negative breast cancer, *PLoS One*, 9 (7), e103760.
- [19] Ayyad, S.E.N., Abdel-Lateff, A., Basaif, S.A., and Shier, T., 2011, Cucurbitacins-type triterpene with potent activity on mouse embryonic fibroblast from *Cucumis prophetarum*, cucurbitaceae, *Pharmacogn. Res.*, 3 (3), 189–193.
- [20] Ayyad, S.E.N., Abdel-Lateff, A., Alarif, W.M., Patacchioli, F.R., Badria, F.A., and Ezmirly, S.T., 2012, *In vitro* and *in vivo* study of cucurbitacins-type triterpene glucoside from *Citrullus colocynthis* growing in Saudi Arabia against hepatocellular carcinoma, *Environ. Toxicol. Pharmacol.*, 33 (2), 245–251.
- [21] Ku, J.M., Hong, S.H., Kim, H.I., Lim, Y.S., Lee, S.J., Kim, M., Seo, H.S., Shin, Y.C., and Ko, S.G., 2018, Cucurbitacin D exhibits its anti-cancer effect in human breast cancer cells by inhibiting Stat3 and Akt signaling, *Eur. J. Inflammation*, 16, 1–9.
- [22] Thoennissen, N.H., Iwanski, G.B., Doan, N.B., Okamoto, R., Lin, P., Abbasi, S., Song, J.H., Yin, D., Toh, M., Xie, W.D., Said, J.W., and Koeffler, H.P., 2009, Cucurbitacin B induces apoptosis by inhibition of the JAK/STAT pathway and potentiates antiproliferative effects of gemcitabine on pancreatic cancer cells, *Cancer Res.*, 69 (14), 5876–5884.

Isolation and Antibacterial Activity by *in vitro* and *in silico* Approach of 6-Deoxyjacareubin Compound from *Garcinia latissima* Miq. Fruit

Neneng Siti Silfi Ambarwati¹, Berna Elya², Amarila Malik², Yuditya Artha², Islamudin Ahmad³, Azminah Azminah⁴, Muhammad Hanafi^{5,6,*}, and Hanita Omar⁷

¹Faculty of Engineering, Universitas Negeri Jakarta, Jl. Rawamangun Muka, East Jakarta 13220, Indonesia

²Faculty of Pharmacy, Universitas Indonesia, UI Depok Campus, Depok 16424, West Java, Indonesia

³Department of Pharmaceutical Sciences, Faculty of Pharmacy, Mulawarman University, Jl. Kuaro, Gn. Kelua, Samarinda 75119, East Kalimantan, Indonesia

⁴Faculty of Pharmacy, Universitas Surabaya, Jl. Raya Kalirungkut, Surabaya 60293, East Java, Indonesia

⁵Research Centre for Chemistry–Indonesian Institute of Sciences, Kawasan PUSPIPTK Serpong, Tangerang Selatan 15314, Banten, Indonesia

⁶Faculty of Pharmacy, Pancasila University, Jl. Srengseng Sawah, Jagakarsa, South Jakarta 12640, Indonesia

⁷Chemistry Division, Centre for Foundation Studies in Science, University of Malaya, Kuala Lumpur, Malaysia

* Corresponding author:

email: hanafi124@yahoo.com

Received: February 17, 2019

Accepted: October 7, 2019

DOI: 10.22146/ijc.43641

Abstract: The previous research showed that the fraction C from active extract of *Garcinia latissima* Miq. fruit was active against *Bacillus subtilis*. This study aims to isolate and identify the active compound as an antibacterial agent from the fraction C. Fraction C was purified by recrystallization using chloroform and n-hexane solvents and then isolated using preparative-thin layer chromatography-silica gel 60 GF₂₅₄ to give a yellow compound. The antibacterial activity was determined using microdilution with thiazolyl blue tetrazolium bromide indicator against *B. subtilis* American Type Culture Collection 6633. The isolate was identified using UV-Vis, IR, MS, Proton Nuclear Magnetic Resonance (¹H-NMR) and carbon NMR (¹³C-NMR), and NMR-2D techniques including HMQC and HMBC. Based on the spectroscopic analysis and literature review, the compound was identified as 6-deoxyjacareubin, which is a new compound from *Garcinia latissima* Miq. The 6-deoxyjacareubin showed antibacterial activity with MIC value of 156.25 ppm and was categorized as a weak antibacterial agent because the MIC value was more than 100 ppm. According to *in silico* approach to the docking study, 6-deoxyjacareubin showed similar hydrophobic interaction with several amino acid residues including C2565, C2589, G2484, U2590, and U5588 between a native ligand.

Keywords: 6-deoxyjacareubin; antibacterial; *Bacillus subtilis*; *Garcinia latissima* Miq.

■ INTRODUCTION

Humans have a dependence on herbal medicines in treating various diseases. Herbal medicines have been used long before the discovery of modern synthetic drugs, as traditional medicines that have always been a part of human traditions and cultures [1]. The sources of traditional medicine can be obtained from plants, including abundant native Indonesian plants [2].

Therefore, these plants need to be investigated further so that native Indonesian plants can continue to be main sources of traditional medicine [2].

One of the important part of medicine for human is their antimicrobial activity [3]. The use of antibiotics has reached an alarming level of resistance. The emergence of toxicity and the reduced effectiveness of using synthetic drugs are other problems that must be

resolved [4]. Therefore, it is necessary to do research to look for compounds from natural ingredients that have antibacterial activity [4]. This study is to test the antimicrobial activity on native Indonesian plants. The qualitative methods of the antimicrobial test include bioautography and diffusion methods, while the quantitative method of antimicrobial test is performed by the dilution method so that the minimum inhibitory concentration value can be obtained [5].

Garcinia latissima Miq. (Clusiaceae) is a plant that grows in tropical and subtropical regions. The fruit of this plant is sweet, sour and rich in nutrition. A previous study showed that 2% of the *G. latissima* Miq. fruit ethyl acetate extract in dimethyl sulfoxide (DMSO) gave inhibition zone diameter against *B. subtilis* of 9.62 mm and the minimum inhibitory concentration (MIC) against *B. subtilis* of the extract was 2500 ppm [6]. The extract was fractionated by column chromatography. Fraction C had the highest activity from 11 fractions (FA-K). The result of the activity test against *B. subtilis* from the previous study of the fraction C 2% in DMSO provided inhibition zone diameter of 9.46 mm and MIC of 1250 ppm [7].

In this study, isolation of fraction C was performed as well as antibacterial test of the isolated result. The presence of pharmacophore groups in the active compound can be used as antibacterial treatment against *B. subtilis* [8]. The positive control that was used as an antibacterial agent against *B. subtilis* was erythromycin that works by inhibiting protein synthesis [9]. The mechanism of erythromycin in the system was observed by the formation of a peptide bond with a ribosomal 50S subunit of bacteria (1:1) thereby inhibiting peptidyl transferase activity present in the 23S rRNA in the 50S subunit [10]. rRNA 23S consists of six domains, two of which are peptidyl transferase sites that are domains V and II connected by 5S rRNA [11]. Erythromycin binds specifically to adenine 2058 in domain V to inhibit the synthesis of a nascent 50S ribosomal subunit from *B. subtilis* [11]. This causes the distribution mRNA to be inhibited and affects the binding of peptidyl tRNA [10]. Molecular docking studies can further find more effective antibacterial agents [8].

6-Deoxyjacareubin isolated from *Calophyllum zeylanicum*, and *Kielmeyera speciosa* woods (Guttiferae) was reported to have antimicrobial activity [12]. 6-Deoxyjacareubin compound has been reported to be isolated from *Calophyllum inophyllum* L. [13]. *Calophyllum inophyllum* stem bark methanol extract acts as an antibacterial agent against *Pseudomonas aeruginosa*, *Staphylococcus aureus* and *Staphylococcus epidermidis* at 25 µg/mL concentration and against *Bacillus licheniformis*, *Bacillus subtilis*, *Escherichia coli* and *Klebsiella pneumoniae* at 50 µg/mL concentration [14]. Oil from *C. inophyllum* L. has an antibacterial activity against Gram negative bacteria [15].

■ EXPERIMENTAL SECTION

Materials

The fruits of *G. latissima* Miq. were obtained from Bogor Botanical Gardens and has been identified by the center for plant conservation Bogor Botanical Garden, Indonesian Institute of Sciences (LIPI).

The chemical materials used in this study were *n*-hexane, ethyl acetate, methanol, distilled water, glacial acetic acid, thin layer chromatography-silica gel 60 GF₂₅₄, silica gel G₆₀, H₂SO₄, AlCl₃, nutrient agar, cetrinide, Thiazolyl blue tetrazolium bromide, p.a. solvents such as *n*-hexane, ethyl acetate, ethanol, chloroform, dichloromethane, methanol, and acetone.

n-Hexane, ethyl acetate, methanol, and distilled water were from Brataco Chemica, the p.a. solvents were purchased from Smart Laboratory, glacial acetic acid was purchased from Merck, thin layer chromatography-silica gel 60 GF₂₅₄, silica gel G₆₀, H₂SO₄, AlCl₃, nutrient agar, and cetrinide was purchased from Merck, while Thiazolyl blue tetrazolium bromide was purchased from BBI Life Sciences.

Instrumentation

The equipment used in the study were a rotary evaporator, column chromatography equipment, thin layer chromatography equipment, vials and bottles, micro pipet, UV-Vis spectrophotometer, analytical balance, glasswares, CAMAG UV cabinet 4, electric stove,

Memmert oven, refrigerator, infra-red spectrophotometer, nuclear magnetic resonance spectroscopy, High Performance Liquid Chromatography–Mass Spectrometry–Mass Spectrometry, microplate 96-well and Memmert incubator.

Procedure

Extraction, fractionation, and isolation processes

The extraction process of *G. latissima* fruits (8.9 kg) by successive maceration (by three solvents: *n*-hexane, ethyl acetate, and methanol) was performed according to the study by Ambarwati et al. [6]. Moreover, the *G. latissima* fruits ethyl acetate extract (157 g) was fractionated. The fractionation was conducted using column chromatography according to the study by Ambarwati et al. [7] and resulted in 11 fractions (A-K).

The material used for the isolation was the fraction C of ethyl acetate extract of *G. latissima* Miq. fruits (1.53 g). Fraction C was separated on silica gel column chromatography (CC) (305 mm × 23 mm i.d) with *n*-hexane/ethyl acetate (100:0–0:100, v/v) as eluents and then purified by recrystallization and thin layer chromatography-silica gel. The recrystallization of fraction C was processed by modifying the non-polar solvent (hexanes) and the semi-polar solvent (ethyl acetate). And then, fraction C was purified further using preparative thin-layer chromatography (*p*-TLC) method. From the purification, 6-deoxyjacareubin was obtained and then identified using thin-layer chromatography with *n*-hexane-chloroform (1:4, v/v) as the mobile system. The retention factor (*R_f*) value of the isolate obtained from thin-layer chromatography with *n*-hexane-chloroform was 0.4.

Antibacterial activity

The antibacterial activity of the compound was evaluated against *B. subtilis* ATCC 6633 which was taken from the laboratory of Microbiology, Faculty of Pharmacy, Universitas Indonesia. The bacterial cultures were developed by selective nutrient agar at 37 °C for 24 h [1]. The nutrient broth was used for the preparation of inoculum of the bacteria, and nutrient agar was used for the screening method. The antibacterial activity test against *B. subtilis* was carried out by microdilution

method using yellow indicator tetrazolium salt (MTT) so that the MIC value (in triplicates) is obtained.

In silico molecular study

Crystal structure of peptidyl transferase was downloaded from the RCSB protein data bank complexed with erythromycin (PDB ID: 1JZY) [16]. The macromolecule enzyme was reduced by removing several of the nonessential residues to minimize the macromolecule size. Docking method was validated by re-docking the co-crystallized ligand (erythromycin) into the same active site of the enzyme using AutoDock Tools, and the results were determined by values of Root Mean Square Deviation (RMSD). Subsequently, the ligand (6-deoxyjacareubin) was optimized by adding charge using Antechamber and docked into the same active site. Gasteiger charge was added to both ligands; free binding energy values were calculated and analyzed. The ligand-residue interaction was visualized using LigPlot to observe involved residue which contributed to the values of binding affinity.

RESULTS AND DISCUSSION

The 6-deoxyjacareubin compound obtained was observed as yellow needles crystals (16.8 mg) which were obtained from chloroform solution. The molecular formula was determined to be C₁₈H₁₄O₅ from its quasi-molecular ion peak at *m/z* 311.43 [M+H]⁺ (molecular-weight or exact mass was calculated 310.0841) in the Liquid Chromatography–Mass Spectrometry spectra which are shown in Fig. 1.

The results of the UV isolate spectrum (Fig. 2) showed that the isolate using chloroform solvent, had the maximum λ absorption, at 308 and 329 nm. The maximum wavelength (329 nm) indicates that the compound contained a conjugated unsaturated ketone. The unsaturated conjugated bond is a single and double bond that alternate each other [17]. The maximum wavelength of 308 nm indicates the presence of a substituted benzene ring, the xanthone framework [18].

The hydroxyl group (–OH) was detected in the IR spectrum at 3425 cm⁻¹ (shown in Fig. 3). The absorption bands at 2900 and 2800 cm⁻¹ indicate the vibration of the

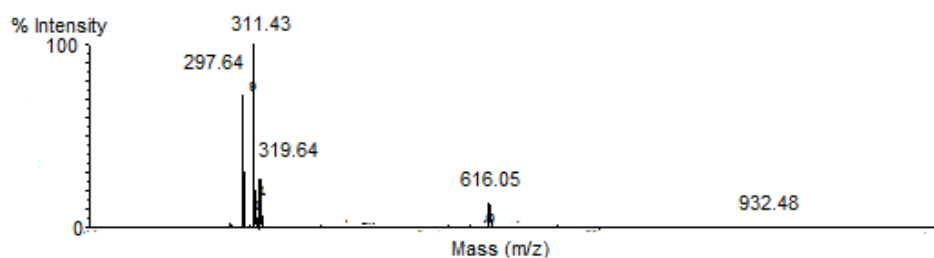


Fig 1. The Liquid chromatography-mass spectrometry spectra of compound 1

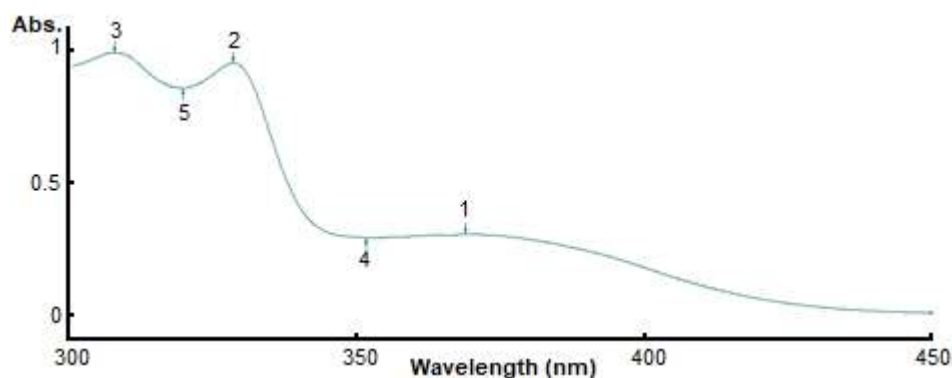


Fig 2. The UV spectrum of compound 1

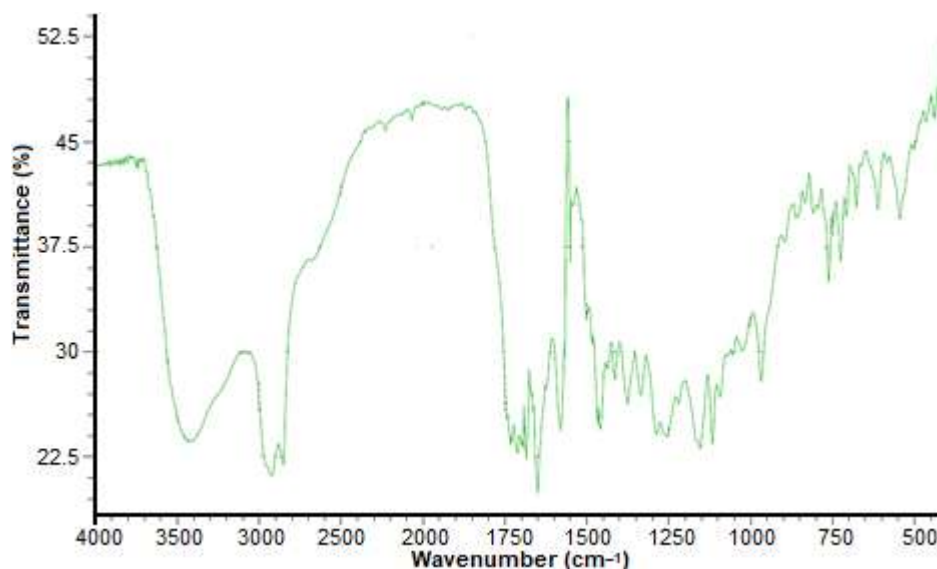


Fig 3. The IR spectrum of compound 1

CH (CH, CH₂, CH₃). The presence of an absorption band at 1680 cm⁻¹ indicates the vibration of the phenyl group [18]. From these infra-red spectra data, it is estimated that these compounds contain hydroxyl groups, phenyl groups, and CH, CH₂, or CH₃ groups.

The ¹H-NMR spectrum showed a specific peak in the aliphatic region at δ_H 1–2 ppm (Fig. 4). There is also a peak that characterizes a xanthone derivative of a dimethyl

group present at δ_H 1.49 (s, 6H) and two doublet protons (as a chromene) at δ_H 5.78 (d, *J* = 10.4 Hz) and δ_H 7.06 (d, *J* = 10.4 Hz) [19]. A coupling constant *J* value (in Hz) in NMR proton provides information in measuring the interaction of proton pairs. Protons in an ortho relationship show large coupling (8–12 Hz, but normally about 10); protons with a meta relationship show a small coupling (2–6 Hz). Furthermore, there is one singlet

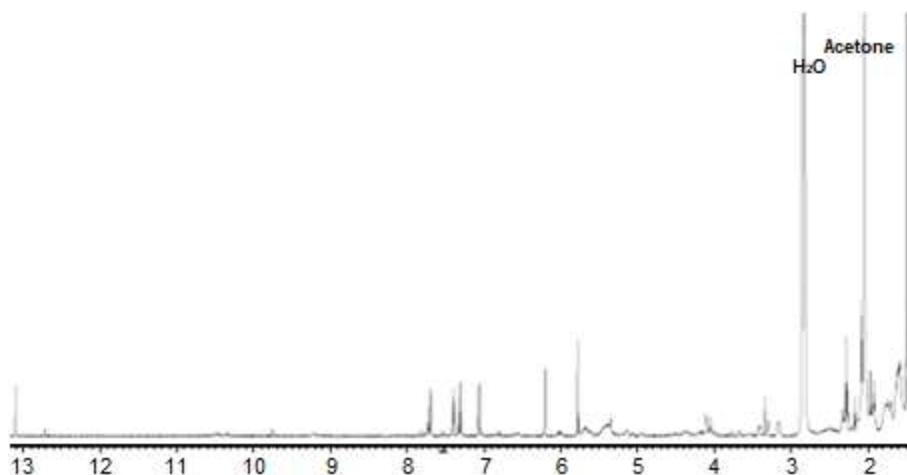


Fig 4. The spectrum of H-NMR

Table 1. ¹H-NMR and ¹³C-NMR data compound 1 compared with 6-deoxyjacareubin

No	Compound 1 (in acetone-d6)		6-Deoxyjacareubin (in acetone-d6) [19]	
	δ ¹³ C-NMR	δ ¹ H-NMR (m, J in Hz)	δ ¹³ C-NMR	δ ¹ H-NMR (m, J in Hz)
1	116.0	7.0 (dd, 8.4; 2.0)	116.7	7.66 (dd, 7.8, 1.6)
1a	122.6	-	-	-
2	121.9	7.31 (t, 8, 4)	122.6	7.27 (t, 7.8)
3	122.6	7.39 (dd, 8.4, 2.0)	122.6	7.35 (dd, 7.8, 1.6)
4	146.8	-	144.3	-
4a	147.5	-	-	-
5	99.9	6.21 (s)	-	6.40 (s)
5a	164.2	-	-	-
6	153.0	-	159.5	-
7	104.5	-	106.3	-
8	162.3	13.1 (s)	162.7	13.33 (s)
9	182.5	-	-	-
9a	102.7	-	-	-
10	116.5	7.06 (d, 10.4)	-	6.69 (d, 10.1)
11	128.4	5.75 (d, 10.4)	-	5.76 (d, 10.2)
12	78.3	-	-	-
13, 14	28.2	1.50 (6H, s)	-	1.48 (6H, s)

proton at δ_H 6.21 (s) and aromatics with an ABC system appearing at δ_H 7.39 (dd); 7.31 (t) and 7.71 (dd). The presence of particular groups in the highly downfield region of δ_H 13.10 (s), is also a characteristic that this compound is thought to be a xanthone derivative [19]. The ¹H-NMR and ¹³C-NMR data compound were compared with 6-deoxyjacareubin (chromenoxantone group) [20]; see Table 1. We concluded this structure to be as described in Fig. 5.

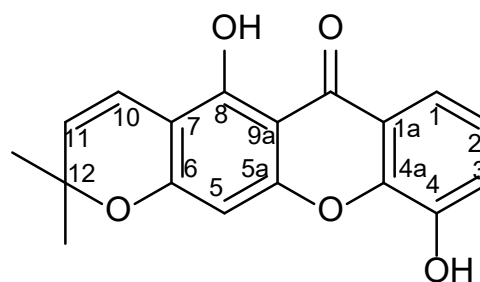


Fig 5. The structure of compound 1

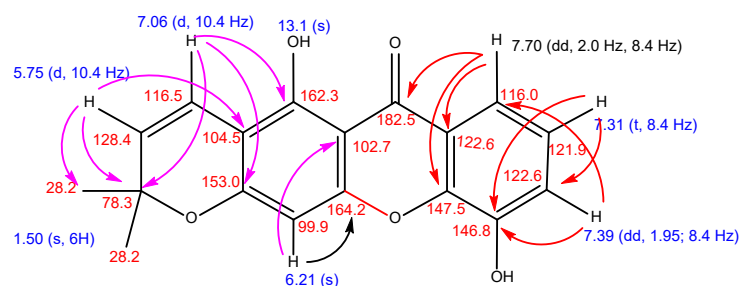


Fig 6. The HMBC correlation the compound 1

The assignments of all carbons were confirmed by the HMBC experiment. In the HMBC spectrum, the long-range correlation from the aromatic proton signal at δ_H 5.75 (d, $J = 10.4$ Hz) to the carbon signals at δ_C 28.2 (13,14- CH_3), 78.3 (C-12), 104.5 (C-7) indicated 6,6-dimethyl-3,6-dihydro-2H-pyran at C-7 of the phenol. The cross-peaks between 6.21 (1H, s), δ_C 102.7 (C-9a) and 164.2 (C-5a) suggested the connection of but-1-ene in the phenolic unit. The position of 6,6-dimethyl-3,6-dihydro-2H-pyran was determined by the correlations of the proton signal at δ_H 7.06 (1H, d, $J = 10.4$ Hz) with the carbon signals at δ_C 78.3 (C-12), 153.0 (C-6), and 162.3 (C-8). The position of the phenolic group was determined by the correlations of the proton signal at δ_H 7.31 (1H, t, $J = 8.4$ Hz) with the carbon signals at δ_C 122.6 (C-3), 146.8 (C-4) and the correlations of the proton signal at δ_H 7.39 (1H, dd, $J = 2.0, 8.4$ Hz) with the carbon signals at δ_C 116.0 (C-1) and 146.8 (C-4). The cross-peaks between 7.70 (1H, dd, $J = 2.0, 8.4$ Hz) and δ_C 122.6 (C-1a), 147.5 (C-4a), and 182.5 (C-9) suggested the connection of the phenolic group with the pyran unit. The HMBC correlation is thoroughly illustrated in Fig. 6.

Antibacterial Activity

The test result of the antibacterial activity with microdilution method of 6-deoxyjacareubin is shown in Fig. 7. The MIC of 6-deoxyjacareubin and erythromycin against *B. subtilis* respectively were 156.25 and 25 ppm. The 6-deoxyjacareubin MIC value was greater than the positive-controls (erythromycin) MIC value, which means that the sensitivity of 6-deoxyjacareubin against *B. subtilis* was lower than erythromycin.

The mechanism of inhibiting bacteria by antibacterial compounds is by damaging the cell walls of the bacteria.

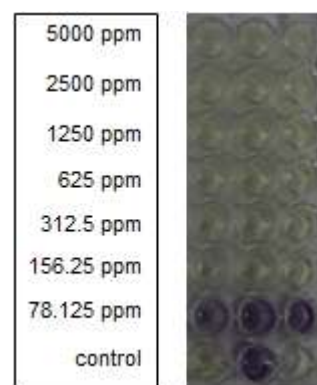


Fig 7. The result of MIC the compound (6-deoxyjacareubin) test using the microdilution method with an indicator of tetrazolium salt (MTT)

Molecules of nucleic acid and protein are also changed after the damaging of the cell wall. The damage also inhibit the works of enzymes, by inhibiting the synthesis of nucleic acid and protein from the bacterial cells which leads to its death [21].

The test of MIC isolate against *B. subtilis* bacteria resulted with a MIC value of 156.25 ppm, while the value of MIC from the ethyl acetate extract of the fruit (fraction C) is 1250 ppm (obtained from previous research). Those results show that the isolate is more active than the fraction. The isolate is a polyphenol compound that can inhibit hydrolytic enzymes (protease) which are found in microbes [22]. The protease enzyme is a proteolytic enzyme that catalyzes the termination of peptide bonds in proteins that has a role in cell growth [23].

6-Deoxyjacareubin is a chromenoxanthone compound [24]. The xanthone compound is a compound that has a tricyclic aromatic system with an anthraquinone base structure and is also known as an anti-bacterial agent [25]. Xanthone compounds contain

Table 2. Calculated estimated binding free energy and inhibition constant in docking of 6-deoxyjacareubin to erythromycin

No	Compound	Binding free energy		Inhibition constant	
1	Erythromycin (redocking)	RMSD 2.00 Å -5.75 kcal/mol		RMSD 2.00 Å 61.27 μM	
2	6-Deoxyjacareubin	Best rank -5.66 kcal/mol	Best cluster 6/10 = -5.66 kcal/mol	Best rank 70.87 μM	Best cluster 70.87 μM

two benzenes with O atoms and ketones, have lipophilic properties and some of these compounds have been studied as anti-*B. subtilis* [26].

The isolate with a MIC value of 156.25 ppm shows that anti-bacterial activity against *B. subtilis* is low since the value of MIC > 100 ppm [27]. This also corresponds with the fraction C activity from the fruit's ethyl acetate extract that has a value of 1250 ppm. The value from fraction C shows that it has a low activity against *B. subtilis* since the value of MIC > 625 ppm [27].

In Silico

The ligand stability is defined by RMSD value obtained from docking studies. Ligand stability is determined by RMSD value which describes the different coordinates to the best docking score. In this study, the ligand exhibited RMSD value of below 2.00 Å. Thus it shows that by using reduced macromolecule, the ligand was able to maintain the coordinate stability by showing similar coordinates within 10 runs of docking. Further molecular dynamic study is required to understand the properties of reduced macromolecule [28].

The affinity and inhibition constant (k_i) were -5.75 kcal/mol and 61.27 μM, respectively. 6-Deoxyjacareubin resulted in lower affinity compared to the cocrystal structure of erythromycin with binding energy and inhibition constant of -5.66 kcal/mol and 70.87 μM, respectively. Docking results of 6-deoxyjacareubin showed interaction with several residues in concordance to the residues bonded with erythromycin. These residues included U2588, C2589, G2484, and U2590, indicating similar activity of 6-deoxyjacareubin with erythromycin. The table of calculated estimated binding free energy and inhibition constant in the docking of 6-deoxyjacareubin to

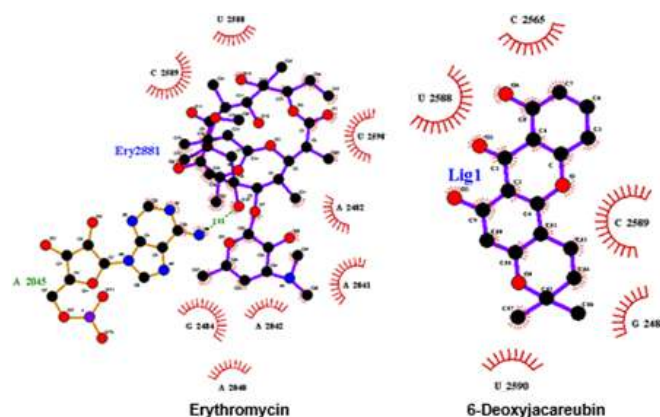


Fig 8. The interaction between erythromycin and 6-deoxyjacareubin with amino acids on the A2042 PDB receptor using the LigPlot program was illustrated

erythromycin can be seen in Table 2 [17].

Erythromycin involved hydrogen bonding with A2042 which was not shown on deoxyjacareubin. The hydrogen bonding might have contributed to erythromycin affinity which was slightly higher than deoxyjacareubin. Both ligands exhibited similar hydrophobic interaction with several residues. The interaction between erythromycin and 6-deoxyjacareubin with amino acids on the A2042 PDB receptor using the LigPlot program is illustrated in Fig. 8.

CONCLUSION

Deoxyjacareubin compounds were isolated from the ethyl acetate extract of *G. latissima* Miq. fruit, and acted as an antibacterial agent against *B. subtilis* with a MIC value of 156.25 ppm. According to the docking study, 6-deoxyjacareubin showed similar hydrophobic interaction with several amino acid residues (including C2565, C2589, G2484, U2590, and U5588) between a native ligand.

■ ACKNOWLEDGMENTS

The research was supported by the Ministry of Research, Technology and Higher Education of the Republic of Indonesia with the contract number: 1/SP2H/DRPM/LPPM-UNJ/III/2019.

■ REFERENCES

- [1] Kochuthressia, K.P., Britto, S.J., Jaseentha, M.O., and Raphael, R., 2012, In vitro antimicrobial evaluation of *Kaempferia galanga* L. rhizome extract, *Am. J. Biotechnol. Mol. Sci.*, 2 (1), 1–5.
- [2] Sholikhah, E.N., 2016, Indonesian medicinal plants as sources of secondary metabolites for pharmaceutical industry, *J. Med. Sci.*, 48 (4), 226–239.
- [3] Nascimento, G.G.F., Locatelli, J., Freitas, P.C., and Silva, G.L., 2000, Antibacterial activity of plant extracts and phytochemicals on antibiotic-resistant bacteria, *Braz. J. Microbiol.*, 31 (4), 247–256.
- [4] Dzotam, J.K., and Kuete, V., 2017, Antibacterial and antibiotic-modifying activity of methanol extracts from six Cameroonian food plants against multidrug-resistant enteric bacteria, *BioMed Res. Int.*, 2017, 1583510.
- [5] Valgas, C., de Souza, S.M., Smânia, E.F.A., and Smania, Jr.A., 2007, Screening methods to determine antibacterial activity of natural products, *Braz. J. Microbiol.*, 38 (2), 369–380.
- [6] Ambarwati, N.S.S., Elya, B., Malik, A., and Hanafi, M., 2017, Phytochemical and antimicrobial studies on *Garcinia latissima* Miq. fruits extract, *Asian J. Pharm. Clin. Res.*, 10 (7), 230–232.
- [7] Ambarwati, N.S.S., Malik, A., Listari, A.T., Nirwana, Elya, B., and Hanafi, M., 2017, Antibacterial activity of fractions of ethyl acetate extract of *Garcinia latissima* Miq. fruits, *Asian J. Pharm. Clin. Res.*, 10 (17), 81–84.
- [8] Bhakiaraj, D., Elavarasan, T., and Gopalakrishnan, M., 2014, Synthesis, spectral analysis, antimicrobial evaluation and molecular docking studies of some novel 3,5-dichloro-2,6-diarylpiperidin-4-ones, *Der Pharma Chem.*, 6 (5), 243–250.
- [9] Lin, J.T., Connelly, M.B., Amolo, C., Otani, S., and Yaver, D.S., 2005, Global transcriptional response of *Bacillus subtilis* to treatment with subinhibitory concentrations of antibiotics that inhibit protein synthesis, *Antimicrob. Agents Chemother.*, 49 (5), 1915–1926.
- [10] Champney, W.S., and Burdine, R., 1995, Macrolide antibiotics inhibit 50S ribosomal subunit assembly in *Bacillus subtilis* and *Staphylococcus aureus*, *Antimicrob. Agents Chemother.*, 39 (9), 2141–2144.
- [11] Pechère, J.C., and Kaplan, E.L., 2004, *Streptococcal Pharyngitis: Optimal Management*, Karger Medical and Scientific Publishers, Basel, Switzerland.
- [12] Harborne, J.B., Baxter, H., and Moss, G.P., 1999, *Phytochemical Dictionary A Handbook of Bioactive Compounds from Plants*, 2nd Ed., CRC Press, Boca Raton, Florida.
- [13] Iinuma, M., Tosa, H., Tanaka, T., and Yonemori, S., 1994, Two new xanthenes in the underground part of *Calophyllum inophyllum*, *Heterocycles*, 37 (2), 833–838.
- [14] Oo, W.M., 2018, Pharmacological properties of *Calophyllum inophyllum* – Updated review, *Int. J. Photochem. Photobiol.*, 2 (1), 28–32.
- [15] Lim, T.K., 2012, *Edible Medicinal and Non-Medicinal Plants*, Springer, Netherlands.
- [16] Schlünzen, F., Zarivach, R., Harms, J., Bashan, A., Tocilj, A., Albrecht, R., Yonath, A., and Franceschi, F., 2001, Structural basis for the interaction of antibiotics with the peptidyl transferase centre in eubacteria, *Nature*, 413 (6858), 814–821.
- [17] Dewick, P.M., 2006, *Essentials of Organic Chemistry for Students of Pharmacy, Medicinal Chemistry and Biological Chemistry*, 1st Ed., Wiley, Hoboken, New Jersey.
- [18] Wu, Y.P., Zhao, W., Xia, Z.Y., Kong, G.H., Lu, X.P., Hu, Q.F., and Gao, X.M., 2013, Three novel xanthenes from *Garcinia paucinervis* and their anti-TMV activity, *Molecules*, 18 (8), 9663–9669.
- [19] Yi, B., Hu, L., Mei, W., Zhou, K., Wang, H., Luo, Y., Wei, X., and Dai, H., 2010, Antioxidant phenolic compounds of cassava (*Manihot esculenta*) from

- Hainan, *Molecules*, 16 (12), 10157–10167.
- [20] Hostettmann, K., Marston, A., and Hostettmann, M., 1998, *Preparative Chromatography Techniques Applications in Natural Product Isolation*, 2nd Ed., Springer-Verlag, Berlin Heidelberg.
- [21] Kurniawati, P.T., Soetjipto, H., and Limantara, L., 2007, Antioxidant and antibacterial activities of bixin pigment from annatto (*Bixa orellana* L.) seeds, *Indones. J. Chem.*, 7 (1), 88–92.
- [22] Su, P.W., Yang, C.H., Yang, J.F., Su, P.Y., and Chuang, L.Y., 2015, Antibacterial activities and antibacterial mechanism of *Polygonum cuspidatum* extracts against nosocomial drug-resistant pathogens, *Molecules*, 20 (6), 11119–11130.
- [23] Gupta, R., Beg, Q.K., and Lorenz, P., 2002, Bacterial alkaline proteases: Molecular approaches and industrial applications, *Appl. Microbiol. Biotechnol.*, 59 (1), 15–32.
- [24] Hostettmann, K., and Hostettmann, M., 1989, “Xanthones” in *Methods in Plant Biochemistry*, vol. 1, Eds. Harborne, J.B., Academic Press, London, 493–508.
- [25] Narasimhan, S., Maheshwaran, S., Abu-Yousef, I.A., Majdalawieh, A.F., Rethavathi, J., Das, P.E., and Poltronieri, P., 2017, Anti-bacterial and anti-fungal activity of xanthones obtained via semi-synthetic modification of α -mangostin from *Garcinia mangostana*, *Molecules*, 22 (2), 275.
- [26] Fukai, T., Oku, Y., Hou, A.J., Yonekawa, M., and Terada, S., 2004, Antimicrobial activity of hydrophobic xanthones from *Cudrania cochinchinensis* against *Bacillus subtilis* and methicillin-resistant *Staphylococcus aureus*, *Chem. Biodivers.*, 1 (9), 1385–1390.
- [27] Awouafack, M.D., McGaw, L.J., Gottfried, S., Mbouangouere, R., Tane, P., Spiteller, M., and Eloff, J.N., 2013, Antimicrobial activity and cytotoxicity of the ethanol extract, fractions and eight compounds isolated from *Eriosema robustum* (Fabaceae), *BMC Complem. Altern. Med.*, 13, 289.
- [28] Liu, K., and Kokubo, H., 2017, Exploring the stability of ligand binding modes to proteins by molecular dynamics simulations: A cross-docking study, *J. Chem. Inf. Model.*, 57 (10), 2514–2522.

Study of the Synthesis of Zirconia Powder from Zircon Sand obtained from Zircon Minerals Malaysia by Caustic Fusion Method

Istikamah Subuki^{1,*}, Mimi Fazzlinda Mohsin¹, Muhammad Hussain Ismail², and Fazira Suriani Mohamed Fadzil⁴

¹Faculty of Chemical Engineering, Universiti Teknologi MARA, 40450 Shah Alam, Selangor, Malaysia

²Faculty of Mechanical Engineering, Universiti Teknologi MARA, 40450 Shah Alam, Selangor, Malaysia

³Industrial Centre of Innovation Nanotechnology, SIRIM Industrial Research, Lot 34, Jl. Hi-Tech 2/3, Kulim Hi-Tech Park, 09000 Kulim, Kedah, Malaysia

* **Corresponding author:**

email: istikamah@uitm.edu.my

Received: March 4, 2019

Accepted: August 9, 2019

DOI: 10.22146/ijc.43936

Abstract: The zircon powder from Zircon Minerals Malaysia is a pure premium grade zircon sand milled 1.5 μm that contain ZrSiO_4 , ZrO_2 , HfO_2 , SiO_2 , Al_2O_3 , TiO_2 , and Fe_2O_3 . The monoclinic zirconia powders were synthesized from the zircon sand of Zircon Minerals Malaysia, by caustic fusion method at calcination temperatures between 500 °C to 800 °C. The as-synthesized zirconia was characterized through X-Ray diffraction (XRD), scanning electron microscopy (SEM), thermogravimetric and differential thermal analysis (TG-DTA), and X-Ray fluorescence (XRF) techniques. The XRD results show two monoclinic phases of microcrystalline zirconia. Zirconia that was calcined at 600 °C obtained the highest value of ZrO_2 , which was 54.48%; followed by zirconia calcined at 700, 800, and 500 °C, which obtained the ZrO_2 values of 53.58, 52.41, and 51.53%, respectively, based on the XRF analysis. As-synthesized zirconia showed monoclinic phases where the surface areas were 0.0635g, 0.135, 0.0268, and 0.0288 m^2/g , for zirconia calcined at temperatures of 500, 600, 700, and 800 °C, respectively. The surface structure of the powder that had been calcined at 600 °C showed similarities with the commercial zirconia. The similarities of the synthesized zirconia and commercial zirconia showed that the zirconia powder could be synthesized using zircon sand by caustic fusion method, even though the content of zirconia was lower compared to that of the commercial zirconia powder.

Keywords: zirconia; zircon sand; monoclinic; caustic fusion method

■ INTRODUCTION

Zirconia (ZrO_2) powder is a white crystalline known as zirconium oxide. This powder is chemically inert and can withstand high temperatures, corrosion, and thermal shock [1]. The condition of the zirconia can either be in natural form or processed form. Zirconium oxide is the condition when the zirconia is in the natural form, known as mineral baddeleyite. The zirconia is calcined to high temperatures to produce zirconia oxide. Many researchers are interested in studying the zirconia powder because it is widely used in ceramic materials and many applications, such as in dentistry, scaffold bone tissue engineering, and

enamels [2]. The melting point of the natural zirconia as mineral baddeleyite is high, which is 2715 °C, and its boiling point is 4300 °C, which makes the toughness of the zirconia very high [3]. Zirconia has unique properties because of its complex and temperature-dependent phase transition. Pure zirconia exists in three crystal phases: monoclinic, cubic, and tetragonal, depending on the temperature [4]. The material can have sharp edges and a very smooth surface when the powder is in fine grain size. However, the weakness of the zirconia in its physical characteristics is shown during phase change, when it is heated [5]; the addition of stabilizers can overcome this problem. Yttria partially stabilized zirconia

exists when the yttrium oxide is added as a stabilizer, making it one of the solutions in solving this problem [6].

There are several methods to produce zirconia powder, such as hydrothermal oxidation, thermal decomposition, precipitation, and hydrolysis [7]. The method used to produce different characteristics of zirconia powder is based on the desired product. The best result obtained for zirconia powder is using chemical routes, but it is not an economical method for industrial manufacturing compared to the conventional milling method [8]. However, the high-quality nanometer-sized powder is obtainable using the technology of precipitation. Nevertheless, these powders are relatively expensive even though it produces high purity zirconia. Zircon can be used to overcome the problem because zircon is the main mineral precursor. Zircon is the main type of heavy mineral species, and it can be found at the beach along the coast of Brazil [9]. In industrial minerals, zircon is commercially important. The use of zircon in the production of zirconia is quickly increasing because it is capable of resisting high temperatures and chemical attacks, creating good refractory for furnaces, steel ladles, and foundry sand used [10]. The production of zirconia is simple, and it requires low capital and operational cost by concentrating the zircon through caustic fusion [11-12]. These facts show that the caustic method is essential for compound production. The fusion method is generally used to synthesize the zirconia from zircon. In this method, different chemicals can be used, such as sodium hydroxide, and calcium carbonate. However, sodium hydroxide is commonly used in caustic fusion method for the production of zirconium oxide or zirconia. Thus, in this study, to synthesize the zirconia powder, zircon sand will be used to produce high purity and economical zirconia by using caustic fusion method.

■ EXPERIMENTAL SECTION

Materials

Table 1 shows the chemical composition of Australian Zircon sand obtained from the Zircon Minerals Malaysia. The commercial zirconia powder was obtained from Vistee Technology Services.

Table 1. Chemical composition of zircon sand

Name of substances	Composition percent (%)
Zirconia + Hafnia (ZrO ₂ + HfO ₂)	64.2
Silica (SiO ₂)	33.8
Alumina (Al ₂ O ₃)	0.90
Titania (TiO ₂)	0.14
Iron Oxide (Fe ₂ O ₃)	0.06

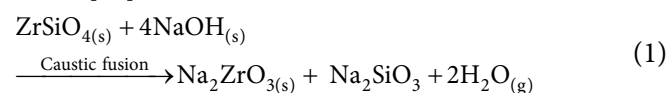
Instrumentation

Analysis were conducted to evaluate the physical and chemical characterizations of all of the synthesized zirconia powders. The thermal behavior of the powders was analyzed by thermogravimetric and differential thermal analysis (Mettler Toledo TGA/DSC SDTA851). The powders were then heated from room temperature to 1000 °C at a heating rate of 10 °C/min in a flowing nitrogen atmosphere. Ultima IV Rigaku X-Ray diffractometer was used at a scan speed of 2 °C/min over a scan range between 10°–90° to examine the phase that is present in the powder. The particle size distribution of the powder was measured using Malvern Instrument type Mastersizer 2000. Brunauer–Emmett–Teller (BET) analysis was used to measure the specific surface area, and X-Ray fluorescence (XRF) PAN Analytical Axios was used to determine the chemical composition in the powder. The surface structure of the powders was assessed using a scanning electron microscopy (SEM) image (Zeiss LEO 1525).

Procedure

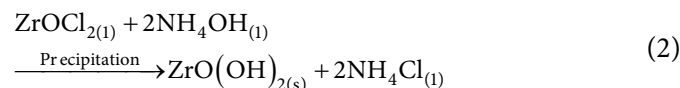
Synthesis of zirconia powder

The zirconia was synthesized by using the caustic fusion method. NaOH was weighed at 30 g and zircon at 33 g [13]. The weight was determined by calculating the number of moles according to the chemical reaction below [13]:

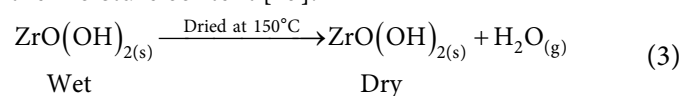


Next, the acid leaching method was used to produce ZrOCl₂ by dissolving the mixture in 120 mL of 5 M HCl solution. The process was conducted at 85 °C for 30 min. Then, the ZrOCl₂ produced was reacted with

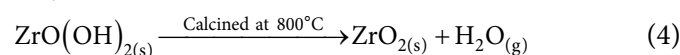
NH_4OH 1 M until the pH of the solution becomes 9 to obtain the $\text{Zr}(\text{OH})_4$.



The process was done by stirring at 90 °C. The $\text{Zr}(\text{OH})_2$ was produced after 24 h, and then filtered and washed using hot water to get a pH solution of 7. Before the zirconia powder was obtained by the calcination process, the residue was heated at 150 °C for 3 h to remove the moisture content [13].



The calcination process was done at 800 °C for 5 h and repeated with different temperatures which were 500, 600, and 700 °C.



■ RESULTS AND DISCUSSION

Thermal Analysis

Fig. 1 shows the TG-DTA curves of the hydrous zirconia, $\text{ZrO}(\text{OH})_2$ after it was dried at 150 °C. The TG-DTA curve exhibited several endothermic peaks below 1000 °C which indicates that the samples obtained would

be denatured at a temperature of 765.8 °C. However, the sample structures illustrate that the samples calcined at more than 700 °C had started to melt, as shown in Fig. 7(c), and hardened when they were cooled at room temperature. Based on the DSC curves, the melting point of $\text{ZrO}(\text{OH})_2$ was 59.94 °C. The melting point of $\text{ZrO}(\text{OH})_2$ should be 318 °C [13]. This result showed that the presence of impurity components added during the synthesis of $\text{ZrO}(\text{OH})_2$, such as ammonium ion, had accelerated the degradation of the polymeric network, while the chloride ions that had affected the thermal stability of caustic fusion were not significant, compared to the ammonium ions.

Crystallization

Fig. 2 shows XRD patterns of the samples that were prepared at different temperatures in the calcination process, which ranged from 500 to 800 °C for both the synthesized and commercial zirconia powders. The X-Ray diffractogram showed two monoclinic phases of nanocrystalline zirconia 28.1° (111), 31.4° (111) (JCPDS card no.78-1807) and tetragonal 30.2° (101), 50.2° (112) and 60.2° (211) (JCPDS card 79-2769) [14].

In Fig. 2(b) to (e), based on the samples used, the X-Ray pattern on the line of the synchrotron beam showed

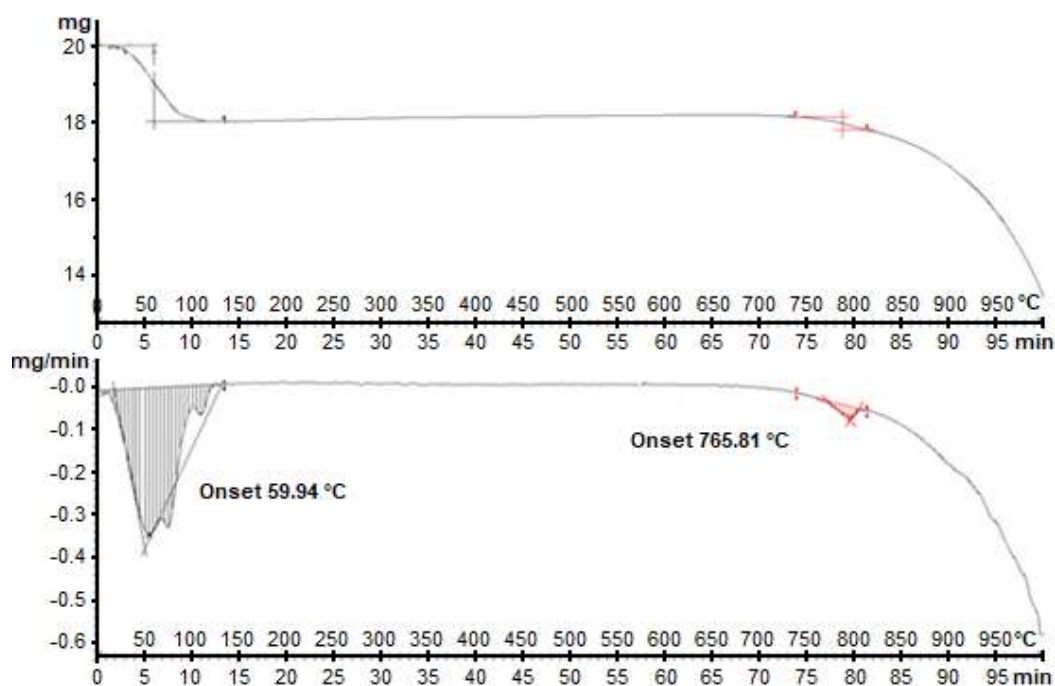


Fig 1. TG-DTA curves of the hydrous zirconia, $\text{ZrO}(\text{OH})_2$ precipitated after dried at 150 °C

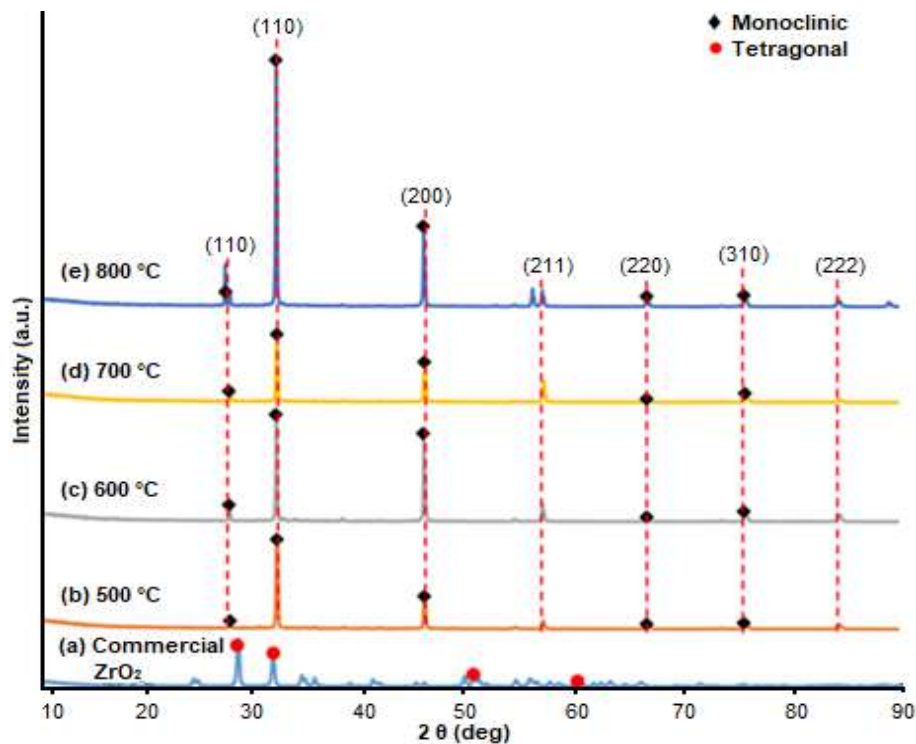


Fig 2. XRD patterns for commercial zirconia and hydrous zirconia, $ZrO(OH)_2$ after calcination at various temperature

that the synthesized zirconia was a nearly pure monoclinic zirconia (> 95%) [15]. The synthesized zirconia did not possess the tetragonal structure because the calcination temperature was not above 1170 °C, based on the XRD pattern obtained. Fig. 3 shows the three crystallographic structures that occurred in pure zirconia [18]. First, the monoclinic form that remained stable until 1170 °C. Second, the tetragonal form that remained stable between 1170 and 2370 °C. Third, the cubic form that remained stable above 2370 °C. The volumetric expansion of 3–5% is related to both martensitic natures in considerable technological importance in the changes of zirconia from tetragonal to monoclinic structure [16]. Afterwards, the significant effect of calcination on the phase purity of the zirconia powder was determined. Thirty two percent of the total zirconia was in the monoclinic phase and above 1170 °C, in which it will totally change to the tetragonal form. Then, during the calcination process, the presence of cations was resulted from the migration of cations when the existing diffusion pathway was inactivated or not fully in the crystalline phase. This is because the transformation process is indicated by the endothermic peak and is irreversible [17].

However, the preparation of synthesized zirconia can affect its structure. The material was prepared using zircon sand and produced at a pH of 10 when the precipitation was formed, which means it was able to obtain a high percentage of monoclinic form. A medium pH range (8–11) could produce monoclinic zirconia, while a low pH (3–5) and high pH range (13–14) produces tetragonal phase based on previous researches [15]. This is because the initial zirconium species are well detached,

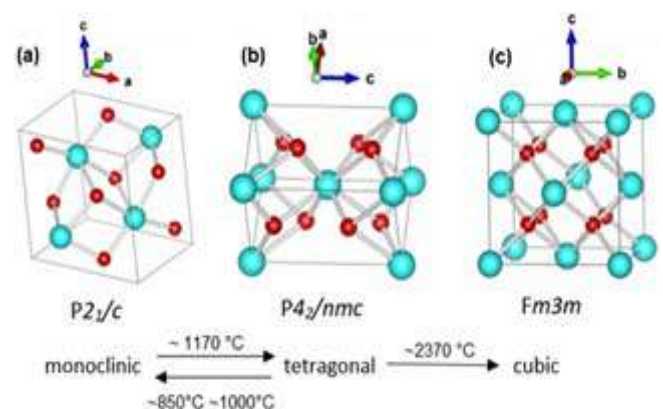


Fig 3. Zirconia phase transformations. As the temperature increases, the zirconia transforms from (a) monoclinic to (b) tetragonal to (c) cubic [18]

and could probably be because it is a monoatomic species of the zirconium [15]. The application for monoclinic structure can be used for components in refractory materials, molten metal filters, additive to mixed oxide systems, and nozzles and stoppers of transfer/holding ladles.

Meanwhile, the commercial zirconia contained tetragonal zirconia at a high percentage. The commercial zirconia had fully changed from the monoclinic to tetragonal form since the thermal treatment of the commercial zirconia was above 1170 °C. Within the temperature of 1170 to 2300 °C, the zirconia was in a stable tetragonal form [19-20]. The effect of pH can be the main factor for the zirconia produced in the tetragonal phase because it can be obtained at either a low pH (3–5) or high pH (13–14) range [15].

Particle Size and Morphology

The particle size distribution parameters of the synthesized zirconia powder are shown in Fig. 4. Usually, the most significant aspect in the particle size distribution is the three-point distribution, nominated as D_{10} , D_{50} , and D_{90} using Eq. (5).

$$S_w = \frac{2.56}{\log_{10} \left(\frac{D_{90}}{D_{10}} \right)} \quad (5)$$

The ideal condition of the value S_w can either be less than 2 or greater than 7, showing a very broad ($S_w = 2$ or $D_{90} = 19D_{10}$) or very narrow distribution ($S_w = 7$ or $D_{90} = 2.3D_{10}$) [21]. Based on the results tabulated in Table 2, the synthesized particle width distributions were 4.52, 2.26, 2.81, and 5.53, where they correspond to a broad distribution because their S_w was less than 7. For the commercial zirconia, the S_w value was 2.49. The particle

width distribution and specific surface area of zirconia and commercial zirconia at 600 °C were almost similar, which were 0.1350 and 0.1310 m^2/g , respectively. The results obtained from this analysis showed that the zirconia powder could be synthesized by using zircon sand. By using commercial zirconia as an indicator, it is possible to determine if the powder produced is similar to the commercial one or otherwise.

Fig. 5 shows that the increase of temperature made the particle size distribution less narrow, except for the synthesis of zirconia at a temperature of 600 °C. Calcination temperature influences the size of the zirconia and densification of the samples. However, in this result, the value of the specific surface area was not consistent. The smaller the size, the larger the specific surface area. The particle size of the powder is directly dependent on the calcination temperature because at high temperatures, shrinkage is likely to occur on the zirconia [22]. From the observation made, the lower the calcination temperature, the narrower the distribution.

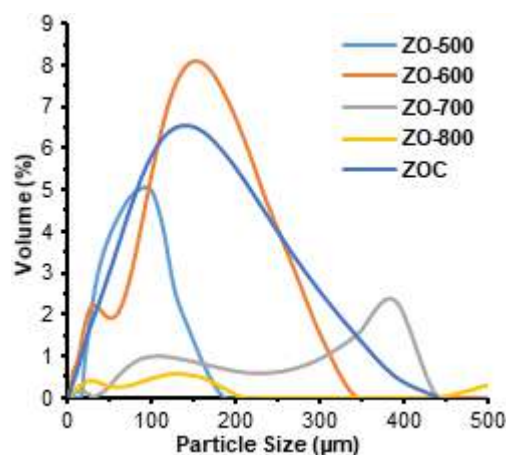


Fig 4. Particle size distribution for synthesized zirconia powder of different temperatures of calcination

Table 2. Parameter of the particle size distribution

ZrO ₂ powder	Particle size (µm)			Particle width distribution (S_w)	Specific surface area (m^2/g)
	D_{10}	D_{50}	D_{90}		
ZrO ₂ 500 °C	38.725	121.380	142.802	4.52	0.0635
ZrO ₂ 600 °C	21.928	153.055	299.111	2.26	0.1350
ZrO ₂ 700 °C	190.251	930.022	1546.454	2.81	0.0268
ZrO ₂ 800 °C	507.257	993.615	1473.014	5.53	0.0288
Commercial ZrO ₂	23.645	110.514	252.177	2.49	0.1310

Primary distribution of the particles are broaden with the equivalent of decreasing volume fraction, as the calcination temperature increases [22]. In Fig. 5, the influence of the particle size on the phase of zirconia is shown when the calcination had been completed to produce zirconia. The calcination temperature had affected the size of the distribution in which the highest surface area was obtained at calcination temperature of 600 °C. This is probably because the zirconia was defined as amorphous zirconia due to its high surface area and the presence of small particles, as well as the presence of the surfactant that can be induced [23]. However, the particle size is probably the influencing factor because the embryonic nuclei is responsible for the nature of the phase obtained. Improvement on the digested zirconia had increased its resistance to thermal calcination of up to 800 °C when compared to the undigested zirconia. As the time of digestion increased, the loss in the surface area decreased with calcination temperature up to 800 °C [24]. Hence, the smallest particle size width was 2.26, which was synthesized zirconia at 600 °C, that also had the largest specific surface area of 0.1350 m²/g, in which it is almost similar to that of the commercial zirconia at 0.1310 m²/g.

In the BET analysis, the specific surface area, S_{BET} , and pore distribution were determined. In Table 3, parameters of the BET analysis of the synthesized zirconia are stated.

The highest BET surface area of the synthesized zirconia was 1.8915 m²/g, which was calcined at 700 °C, and the lowest surface area was 0.6811 m²/g at 600 °C. For the total volume in pores, the highest was 0.00439 m³/g, belonging to the synthesized zirconia at 600 °C, and the lowest was 0.00147 m³/g. However, as the calcination temperature increased, the total area in pores of the synthesized zirconia also increased.

Fig. 6 shows the surface area against the pore width of the synthesized zirconia calcined at 500, 600, 700, and

800 °C. The pore width widened with increasing calcination temperature, except for the synthesized zirconia calcined at 600 °C. The pore width reached the largest value with an incremental surface area when the synthesized zirconia was calcined at 600 °C. The graph pattern for the synthesized zirconia at 600, 700, and 800 °C were unimodal, and for the synthesized zirconia at 500 °C, it was bimodal. The synthesized powders contained voids or pores. In addition, the particle's slow growth is a direct influence to its loose porous structure

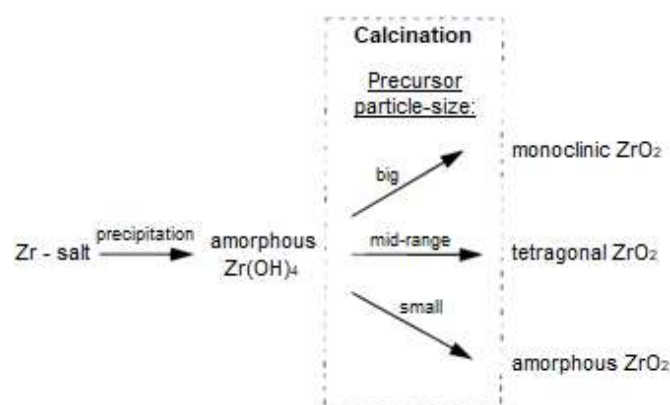


Fig 5. Influence of the precursor particle size on the phase of zirconia [23]

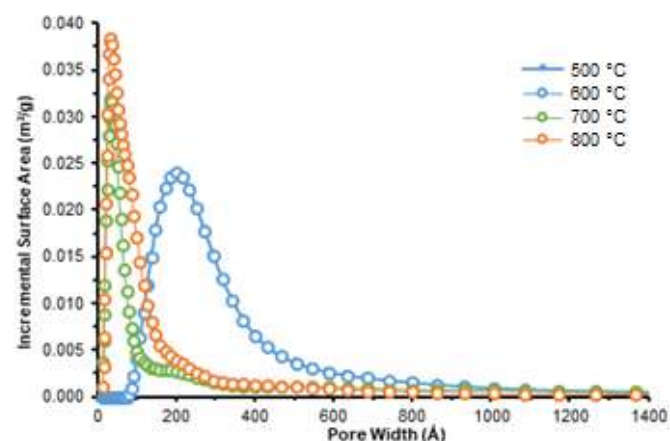


Fig 6. Surface area against pore width of synthesized zirconia at different calcination temperatures

Table 3. Parameter of the BET analysis

ZrO ₂ Powder	BET surface area, S_{BET} (m ² /g)	Total area in pores (m ² /g)	Total volume in pores (m ³ /g)
ZrO ₂ 500 °C	1.0721	0.239	0.00147
ZrO ₂ 600 °C	0.6811	0.329	0.00439
ZrO ₂ 700 °C	1.8915	0.546	0.00205
ZrO ₂ 800 °C	1.5074	0.750	0.00268

and the ability to sustain its amorphous nature during calcination of up to 500 °C [25]. At 600 °C, the intermediate temperature for zirconia transformed the phase from an amorphous to crystalline nature of t-zirconia, and at 800 °C, stabilization was found for t-zirconia with a porous structure [25]. An assumption can be made that ceramics with spherical shape and large pores had caused the presence of particles with hollow spherical shape in the source powder since the average size of the powder corresponds to large pores with an average size in calcined materials [26].

Table 4 indicates the chemical composition of ZrO₂ samples at different calcination temperatures and also the composition of commercial zirconia. The results showed that the synthesized zirconia could produce the highest amount of ZrO₂ at a temperature of 600 °C, which was 54.48%. The amount of Na₂O in synthesized zirconia was too large. However, the amount of Na substance in zirconia is detrimental to its strength and ionic conductivity, which is an important characteristic of zirconia-based materials [27]. The importance of zirconia containing a high amount of Na can also be seen in when it is used in the thermal barrier, making the high content of sodium in powders acceptable [27]. This can be correlated to the chemical composition of zircon sand in Table 1. The composition of zirconium ions inside the

sand was not pure, due to the presence of other substances which affect the purity of the synthesized zirconia.

Fig. 7 shows the SEM images for the surface and topography of zirconia, synthesized at different calcination temperatures, and also images of commercial zirconia. The structure in Fig. 7(a) showed an amorphous-like structure because it is unlikely to be crystalline. Meanwhile, the differences in Fig. 7(c) and 7(d) are that the shape of the agglomerated powder was reduced when the temperature of calcination increased. Furthermore, Fig. 7(b) showed a similarity in shape with that in Fig. 7(e). The powders calcined at 600 °C had the same shape as commercial zirconia. Based on this observation, the synthesis of zirconia powder can be performed using zircon sand when calcined at 600 °C. However, the structure of zirconia calcined at more than

Table 4. Chemical composition of ZrO₂ samples

Samples	XRF Chemical Composition (wt.%)			
	ZrO ₂	Na ₂ O	SiO ₂	CaO
ZrO ₂ 500 °C	51.53	43.77	7.59	0.18
ZrO ₂ 600 °C	54.48	46.40	7.86	0.23
ZrO ₂ 700 °C	53.58	41.20	12.09	0.30
ZrO ₂ 800 °C	52.41	35.72	16.33	0.36
Commercial ZrO ₂	100	-	-	-

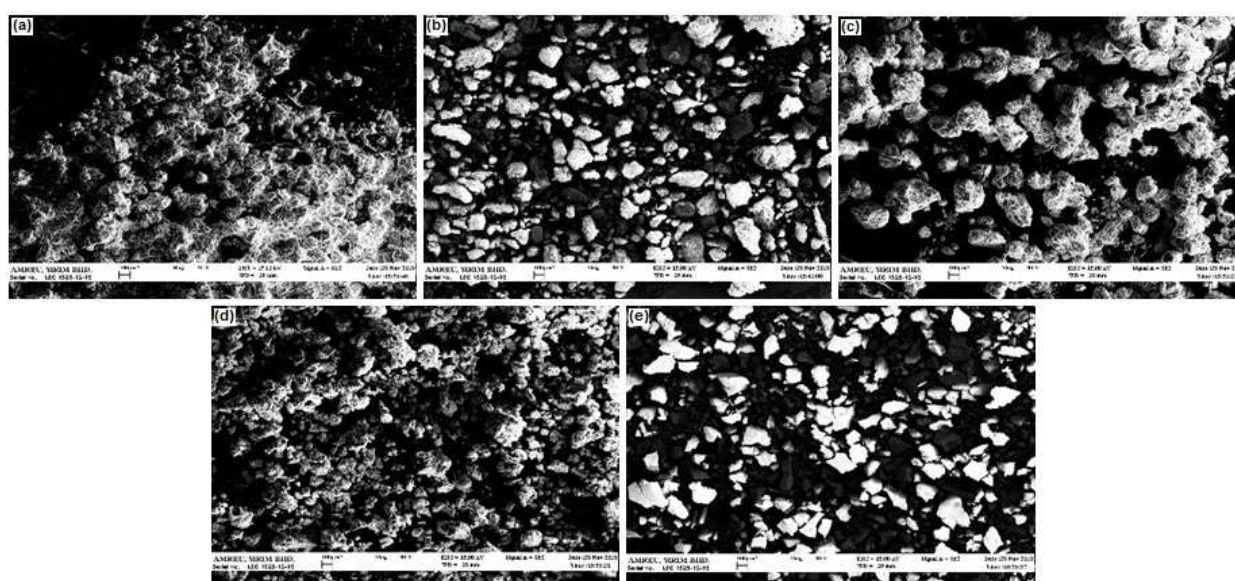


Fig 7. SEM images of (a) synthesized zirconia at 500 °C, (b) synthesized zirconia at 600 °C, (c) synthesized zirconia at 700 °C, (d) synthesized zirconia at 800 °C, and (e) commercial zirconia

700 °C showed that the structure becomes denatured because it will start to melt at that temperature.

Based on a previous study, the calcination of local zircon sand from Indonesia using the same method of synthesis, which is the caustic fusion method, at calcination temperature of higher than 500 °C gives good ionic conductivity [13]. The slopes of zirconia calcined between 600 to 700 °C showed the greatest ionic conductivity based on their researches [13]. However, in this study, the synthesis of the zirconia differs from what was performed in the previous study. In the present study, the synthesis of zirconia was conducted using different raw materials, which was the zircon sand supplied from Zircon Minerals Malaysia Sdn. Bhd. However, the same method of synthesis was successfully applied to synthesize the zirconia. The results obtained showed that zirconia calcined at 600 °C had produced an almost similar structure with commercial zirconia. In addition, other characteristics, such as the surface area and pore volume of the synthesized zirconia, were the greatest when compared with other zirconia.

■ CONCLUSION

The synthesized zirconia powder can be produced from a caustic fusion method using the raw material of zircon sand. Based on the results using the XRD analysis, BET, SEM, and by investigating the particle size of the synthesized zirconia powder, it was shown that the obtained powder had achieved almost similar characteristics to that of the commercial powder. However, the structure of the synthesized and commercial zirconia based on the XRD analysis was different in which the synthesized zirconia was in a monoclinic structure, while the commercial zirconia was in tetragonal. The SEM images, showed that the structures were the same for both powders. This is proven from observing the particle size width and specific surface area, where results for both powders were almost the same. Hence, the synthesis of zirconia powder using the zircon sand supplied from Zircon Minerals Malaysia Sdn. Bhd. was successful.

■ ACKNOWLEDGMENTS

The authors would like to express gratitude for the financial support given under the Fundamental Research Grant Scheme (FRGS, 600-RMI/FRGS 5/3 (457/2019)

from Universiti Teknologi MARA (UiTM), Malaysia. The authors would also like to extend our appreciation to the Zircon Minerals Malaysia for providing the Australian Zircon Sand as a raw material for this project.

■ REFERENCES

- [1] Sommers, A., Wang, Q., Han, X., T'Joen, C., Park, Y., and Jacobi, A., 2010, Ceramics and ceramic matrix composites for heat exchangers in advanced thermal systems—A review, *Appl. Therm. Eng.*, 30 (11-12), 1277–1291.
- [2] Gerhardt, L.C., and Boccaccini, A.R., 2010, Bioactive glass and glass-ceramic scaffolds for bone tissue engineering, *Materials*, 3 (7), 3867–3910.
- [3] Mihai, L.L., Parlatescu, I., Gheorghe, C., Andreescu, C., Bechir, A., Pacurar, M., and Cumpata, C.N., 2014, *In vitro* study of the effectiveness to fractures of the aesthetic fixed restorations achieved from zirconium and alumina, *Rev. Chim.*, 65 (6), 725–729.
- [4] Bocanegra-Bernal, M.H., and de la Torre, S.D., 2002, Phase transitions in zirconium dioxide and related materials for high performance engineering ceramics, *J. Mater. Sci.*, 37 (23), 4947–4971.
- [5] Daou, E.E., 2014, The zirconia ceramic: Strengths and weaknesses, *Open Dent. J.*, 8, 33–42.
- [6] Della Bona, A., Pecho, O.E., and Alessandretti, R., 2015, Zirconia as a dental biomaterials, *Materials*, 8 (8), 4978–4991.
- [7] Sōmiya, S., and Akiba, T., 1999, Hydrothermal zirconia powders: A Bibliography, *J. Eur. Ceram. Soc.*, 19 (1), 81–87.
- [8] Kljajević, L., Matović, B., Radosavljević-Mihajlović, A., Rosić, M., Bosković, S., and Devečerski, A., 2011, Preparation of ZrO₂ and ZrO₂/SiC powders by carbothermal reduction of ZrSiO₄, *J. Alloys Compd.*, 509 (5), 2203–2215.
- [9] Yamagata, C., Andrade, J.B., Ussui, V., de Lima, N.B., and Paschoal, J.O.A., 2008, High purity zirconia and silica powders via wet process: Alkali fusion of zircon sand, *Mater. Sci. Forum*, 591-593, 771–776.
- [10] Götsch, T., Wallisch, W., Stöger-Pollach, M., Klötzer, B., and Penner, S., 2016, From zirconia to yttria: Sampling the YSZ phase diagram using

- sputter-deposited thin films, *AIP Adv.*, 6 (2), 025119.
- [11] Rahmawati, F., Permadani, I., Soepriyanto, S., Syarif, D.G., and Herald, E., 2014, Double steps leaching and filtration in caustic fusion method to produce zirconia from local zircon concentrate, *Proceedings of the 2014 International Conference on Physics and its Applications (ICOPIA-14)*, 99–102.
- [12] Rahmawati, F., Permadani, I., Herald, E., Syarif, D.G., and Soepriyanto, S., 2016, Structure and morphological analysis of various composition of yttrium doped-zirconia prepared from local zircon sand, *J. Phys. Conf. Ser.*, 776 (1), 012050.
- [13] Apriany, K., Permadani, I., Syarif, D.G., Soepriyanto, S., and Rahmawati, F., 2016, Electrical conductivity of zirconia and yttrium-doped zirconia from Indonesian local zircon as prospective material for fuel cells, *IOP Conf. Ser.: Mater. Sci. Eng.*, 107, 012023.
- [14] Gusain, D., Singh, P.K., and Sharma, Y.C., 2016, Kinetic and equilibrium modelling of adsorption of cadmium on nano crystalline zirconia using response surface methodology, *Environ. Nanotechnol. Monit. Manage.*, 6, 99–107.
- [15] Srinivasan, R., De Angelis, R.J., Ice, G., and Davis, B.H., 1991, Identification of tetragonal and cubic structures of zirconia using synchrotron x-radiation source, *J. Mater. Res.*, 6 (6), 1287–1292.
- [16] Oliveira, A.P., and Torem, M.L., 2001, The influence of precipitation variables on zirconia powder synthesis, *Powder Technol.*, 119 (2-3), 181–193.
- [17] Gauna, M.R., Conconi, M.S., Gómez, S., Suárez, G., Aglietti, E.F., and Rendtorff, N.M., 2015, Monoclinic-tetragonal zirconia quantification of commercial nanopowder mixtures by XRD and DTA, *Ceram.-Silik.*, 59 (4), 318–325.
- [18] Brog, J.P., Chanez, C.L., Crochet, A., and Fromm, K.M., 2013, Polymorphism, what it is and how to identify it: A systematic review, *RSC Adv.*, 3 (38), 16905–16931.
- [19] Ning, S., Zhan, P., Xie, Q., Li, Z., and Zhang, Z., 2013, Room-temperature ferromagnetism in undoped ZrO₂ thin films, *J. Phys. D: Appl. Phys.*, 46 (44), 445004.
- [20] Simione, D., Baldinozzi, G., Gosset, D., Dutheil, M., Bulou, A., and Hansen, T., 2003, Monoclinic to tetragonal semireconstructive phase transition of zirconia, *Phys. Rev. B*, 67 (6), 064111.
- [21] Zauner, R., 2006, Micro powder injection moulding, *Microelectron. Eng.*, 83 (4-9), 1442–1444.
- [22] Yaqub, A., Savaniu, C., Janjua, N., and Irvine, J., 2013, Preparation via a solution method of La_{0.2}Sr_{0.25}Ca_{0.45}TiO₃ and its characterization for anode supported solid oxide fuel cells, *J. Mater. Chem. A*, 1 (45), 14189–14197.
- [23] Stichert, W., and Schüth, F., 1998, Influence of crystallite size on the properties of zirconia, *Chem. Mater.*, 10 (7), 2020–2026.
- [24] Chuah, G.K., and Jaenicke, S., 1997, The preparation of high surface area zirconia – Influence of precipitating agent and digestion, *Appl. Catal., A*, 163 (1-2), 261–273.
- [25] Nayak, N.B., and Nayak, B.B., 2016, Temperature-mediated phase transformation, pore geometry and pore hysteresis transformation of borohydride derived in-born porous zirconium hydroxide nanopowders, *Sci. Rep.*, 6, 26404.
- [26] Buyakova, S., Sablina, T., and Kulkov, S., 2015, Porosity and mechanical properties of zirconium ceramics, *AIP Conf. Proc.*, 1688 (1), 030009.
- [27] Manivasakan, P., Rajendran, V., Rauta, P.R., Sahu, B.B., and Panda, B.K., 2011, Synthesis of monoclinic and cubic ZrO₂ nanoparticles from zircon, *J. Am. Ceram. Soc.*, 94 (5), 1410–1420.

Preparation of Ammonia Dealuminated Metakaolinite and Its Adsorption against Bixin

Winda Rahmalia¹, Jean-François Fabre², Thamrin Usman^{1,*}, and Zéphirin Mouloungui^{2,3}

¹Department of Chemistry, Faculty of Mathematics and Natural Sciences, Tanjungpura University, Jl. Prof. Dr. H. Hadari Nawawi, Pontianak 78124, West Kalimantan, Indonesia

²Université de Toulouse, INP-ENSIACET, Laboratoire de Chimie Agro-industrielle (LCA), 4 Allée Emile Monso, 31030 Toulouse, France

³INRA, UMR 1010 CAI, F-31030 Toulouse, France

* Corresponding author:

tel: +62-561-577963

email: thamrin_usman@untan.ac.id

Received: April 3, 2019

Accepted: August 30, 2019

DOI: 10.22146/ijc.44706

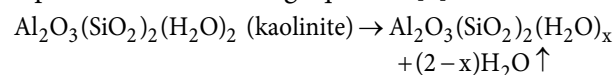
Abstract: This study aims to prepare dealuminated metakaolinite which has a high surface area by using NH_4OH as an activator. The natural kaolinite sample was treated at $600\text{ }^\circ\text{C}$ for 6 h in order to obtain metakaolinite. A dealuminated metakaolinite was then prepared by the repeated activation method using concentrated ammonia (5 M NH_4OH) at room temperature. Depending on the nature of each type of material, natural kaolinite, NH_4OH treated kaolinite, metakaolinite and NH_4OH treated metakaolinite were characterized using X-ray diffraction (XRD), Fourier-transform infrared spectroscopy (FTIR), scanning electron microscopy-energy dispersive spectroscopy (SEM-EDS), and Brunauer-Emmett-Teller (BET-N_2) measurements. XRD and FTIR results confirmed that structural transformation from kaolinite to metakaolinite had occurred. According to SEM-EDS data, the activation of metakaolinite by NH_4OH allowed the dealumination of metakaolinite. The increase in the Si/Al ratio was almost twice as high as in kaolinite. BET-N_2 analysis showed that the specific surface area and the total pore volume increased significantly after activation. Its adsorption properties were tested against bixin. Bixin adsorption on dealuminated metakaolinite followed pseudo-second order kinetic where $k_2 = 0.20\text{ g/mg min}$. The adsorption isotherm followed the Langmuir model where $q_m = 0.72\text{ mg/g}$.

Keywords: ammonia; adsorption; bixin; metakaolinite

■ INTRODUCTION

Kaolinite [$\text{Al}_2\text{Si}_2\text{O}_3(\text{OH})_4$] is a mineral clay that is relatively inexpensive. It is effective as a support material. This behavior is governed by the extent and nature of the outer surface, the interspace, and the crystal structure that can be modified by appropriate processing techniques [1-3]. Acidic or alkaline activation has been widely studied as a chemical treatment to improve the characteristics of natural kaolinite. However, activation from natural kaolinite shows that improving the properties of kaolinite by chemical processes is difficult because of the high passivity of this material. Thus, it was not significantly affected by acidic or alkaline treatments, even under concentrated solution conditions [4-7].

Due to the passivity of kaolinite, acidic or alkaline activation was also studied from metakaolinite. It is a metastable phase obtained by calcination of kaolinite, which has been reported to be more reactive in chemical treatments. Metakaolinites are obtained by calcination of kaolinite at temperatures between 500 and $900\text{ }^\circ\text{C}$ [5,8]. This transformation occurs by losing its structural water and a reorganization of the structure. Only a small part of AlO_6 octahedron is maintained, while the rest is transformed into much more reactive tetra and pentacoordinate units. This process of dehydroxylation is presented in following equation [5].



The calcination conditions of kaolinite strongly influence the reactivity of the solids obtained. The best conditions for obtaining a highly reactive metakaolinite were discussed by various authors who reported calcination values between 600 and 800 °C [5,9-10]. Calcination at higher temperatures leads to the formation of mullite and cristobalite. In this study, we used the calcination temperature of 600 °C according to the adapted protocol written by Belver et al. [5].

Rahmalia et al. [6] previously studied the characterization of HCl and KOH treated kaolinite and their adsorption properties against bixin (Fig. 1). The results showed that there was only little change in the kaolinite structure after treatment. However, the activation of kaolinite using alkaline solutions allowed the increase of the adsorption capacity of bixin, both isotherms adsorptions, and kinetics. Bixin was chosen in this study because it is a carotenoid dye that is widely used in industry, cosmetics, pharmaceutical products, as food coloring, textile dye [11-14], sensitizer in the solar cell [15-17] and photodynamic therapy [18]. The double bonds structure of bixin renders it unstable to light, temperature, and oxygen exposure [19-20]. Incorporating bixin into the surface or interlayer space of clay minerals is one of the efforts to increase its stability [21-22].

In line with the development of environmentally friendly technologies, NH_4OH is a less toxic alternative to KOH. KOH strongly attacks cell constituents by dissolving keratin, hydrolyzing lipids, and degrading proteins. The destructive effect of KOH on the eyes is particularly serious. The effect of NH_4OH is less severe. The corrosive effects of NH_4OH cause destruction of single tissues, while KOH causes severe tissue destruction [23]. NH_4OH enters the nitrogen cycle. It is produced in the soil by bacterial methods. NH_4OH is also produced naturally from the decomposition of organic matter [24]. So we used NH_4OH in this work. Since the alkaline properties of NH_4OH are almost the same as KOH, it is advantageous to develop a new activator which has less toxicity, and is believed to also improve surface properties of natural kaolinite.

Although the bixin adsorption rate on kaolinite is faster when acetone acts as a solvent, it is preferred to use

dimethyl carbonate (DMC) since it can increase the adsorptive capacity of bixin on kaolinite [6]. Most properties of DMC make it a truly green reagent [25]: (1) DMC is a non-toxic compound. Since the mid-1980s, it is no longer produced from phosgene, but rather by oxidative catalytic carbonylation of methanol with oxygen. In addition to improving the safety of the procedure, this manufacturing process avoids phosgene contamination and eliminates the need for inorganic salts as by-products. (2) DMC is classified as a flammable liquid just like methanol, and has no irritant or mutagenic effects, either by contact or by inhalation. Therefore, it can be handled safely without the special precautions required for toxic and mutagenic methyl halides. (3) DMC has a versatile and flexible chemical reactivity that depends on experimental conditions.

Thus, the objective of this work is the activation of metakaolinite using concentrated NH_4OH solution to obtain the metakaolinite with better properties. The treatment of kaolinite using concentrated NH_4OH was also done for comparative study. The parameters studied are the properties of kaolinite and metakaolinites after activation and its adsorption characteristics against bixin.

■ EXPERIMENTAL SECTION

Materials

Bixin crystals containing 88.11% *cis*-bixin and 11.75% *di-cis*-bixin and an unknown compound (0.14%) were obtained by the extraction and purification processes described by Rahmalia et al. [26]. Natural kaolinite ($\text{Al}_2\text{O}_3 \cdot 2\text{SiO}_2 \cdot 2\text{H}_2\text{O}$), CAS Number 1318-74-7, was supplied by Sigma-Aldrich (Germany), together with analytical grade ammonium hydroxide (NH_4OH , NH_3 , 28.0–30.0%) and dimethyl carbonate (99%) were supplied by Sigma-Aldrich, Germany.

Procedure

Preparation and activation of metakaolinite by NH_4OH

The kaolinite was calcined at 600 °C in an oven to give the corresponding metakaolinite. The calcination was carried out under an air atmosphere in a programmable furnace, with a program for heating from

room temperature to the calcination temperature by $10\text{ }^{\circ}\text{C min}^{-1}$ and maintaining the calcination temperature for 6 h. The metakaolinite obtained was named K_{Cal} . Activation was performed by adding 10 g of K_{Cal} in 100 mL of a 5 M NH_4OH solution. The mixture was stirred on a vibrating table continuously (300 rpm) for 6 h at room temperature. The suspension was filtered and the residue was washed using distilled water until neutral and dried in an oven at $103\text{ }^{\circ}\text{C}$ for 24 h. This process was repeated 3 times to optimize the activation process. The final product obtained was called K_{CA} . The activation of kaolinite without calcination was also done by a similar method, and the final product obtained was called K_{A} . K_{A} , K_{Cal} , and K_{CA} were characterized by XRD, FTIR, SEM-EDS, and BET-N_2 .

Adsorption of bixin on KB and KCA

The adsorption process was carried out by adopting the experiment optimum condition of Rahmalia et al. [6]. Stock solutions of bixin (20 mg/L) were prepared in dimethyl carbonate. Solutions at the required concentrations (3–18 mg/L) were prepared by dilution of the stock solution. The adsorbent (0.05 g) was then added to a solution of 5 mL of bixin (3–18 mg/L). The mixtures were stirred on a vibrating table continuously (300 rpm) at room temperature ($\sim 22\text{ }^{\circ}\text{C}$). Samples were taken after 4 h (predetermined equilibrium time) and small aliquots of the supernatant were removed and diluted to an appropriate concentration, if necessary. The absorption spectrum was determined immediately with a Shimadzu UV-1800 UV-visible spectrophotometer. Concentrations of bixin in the solutions were determined by a UV-visible spectrophotometer calibrated at 456 nm dimethyl carbonate [27]. For contact time studies, the residual concentration of 5 mL of bixin solution (10 mg/L) with kaolinite (0.1 g) was determined at various time points from 5 to 360 min. The experiments were performed in triplicate and mean values were reported.

RESULTS AND DISCUSSION

Characteristics of Dealuminated Metakaolinite

The XRD diffractograms (Fig. 1) show the amorphous patterns for K_{Cal} and K_{CA} . The calcination process resulted in significant crystallographic transformations of kaolinite.

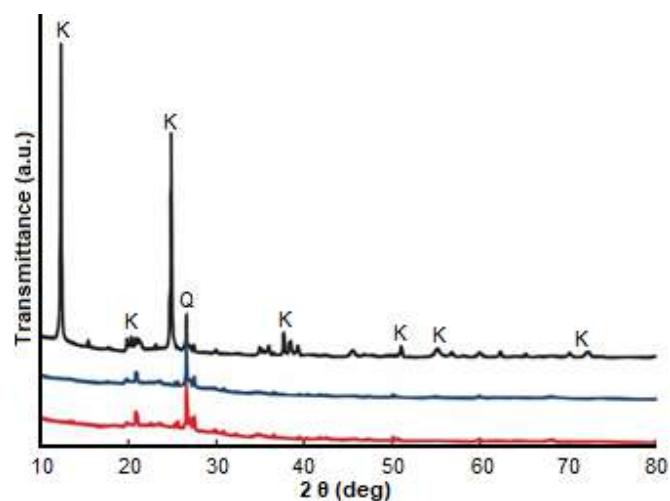


Fig 1. XRD diffractograms of K_{A} (black), K_{Cal} (blue), and K_{CA} (red)

Two intense diffraction reflections at 2θ values of 12.3 and 24.9° which were observed at K_{A} had disappeared, while peaks attributed to quartz (2θ of 21.22 and 27.45°) remained unchanged. A diffractogram for K_{A} showed no significant difference with respect to kaolinite before activation as reported in Rahmalia et al. [6]. The calcination product patterns are similar to those reported for metakaolinites [5,9]. Since the activation of metakaolinite was performed at room temperature, the XRD pattern of K_{CA} did not show significant variations from K_{Cal} . This indicates that treatment with NH_4OH at room temperature leads to very small alterations in the crystal structure of metakaolinite. However, the International Centre for Diffraction Data (ICDD) shows that K_{CA} (PDF 01-076-5970) contains a small amount of sodium aluminum silicon oxide. It is the precursor component of zeolite formation. This mineral is not present in the K_{Cal} . This result shows that NH_4OH has the ability to convert metakaolinite to zeolite although activation was performed at room temperature.

FTIR analysis (Fig. 2) confirm the transformation of kaolinite during calcination and activation. The FTIR spectra patterns of K_{A} showed no significant differences between kaolinite before and after treatment, indicating an absence of significant change in the kaolinite samples. The FTIR spectrum of natural kaolinite published by Rahmalia et al. [6] was also presented for comparison. The FTIR spectrum of natural kaolinite characteristic bands

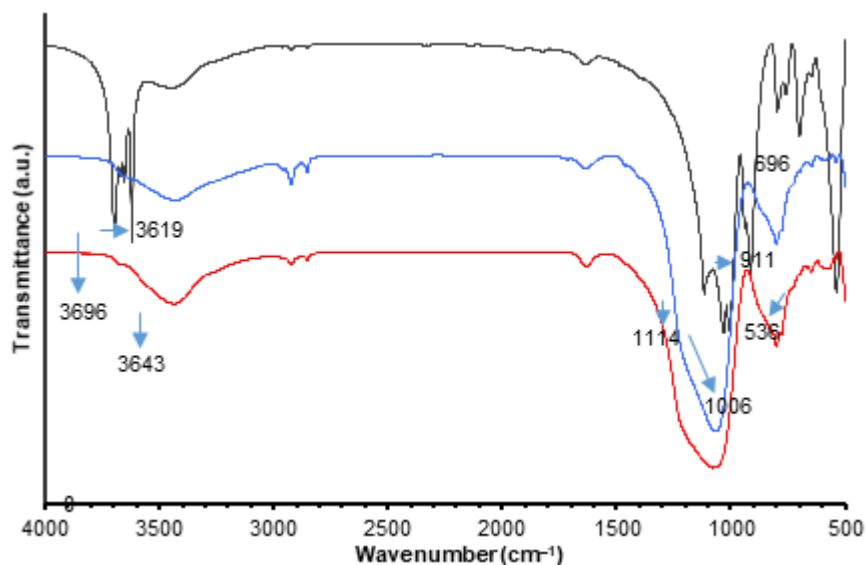


Fig 2. The FTIR spectra of K_A (black), K_{Cal} (blue), K_{CA} (red)

of kaolinite: at 3696, 3669, 3652, and 3619 cm^{-1} correspond to the stretching of inner-surface-hydroxyl groups, at 3443 cm^{-1} corresponds to stretching of the hydroxyl group of water, 1631 cm^{-1} corresponds to the O–H deformation of water, 1114 cm^{-1} corresponds to Si–O stretching (longitudinal mode), 1030, and 1006 cm^{-1} correspond to in-plane Si–O stretching, 937 cm^{-1} corresponds to the –OH deformation of inner-surface hydroxyl groups, 911 cm^{-1} corresponds to Al–OH deformation, 794 cm^{-1} corresponds to Si–O vibration, 755 and 696 cm^{-1} correspond to Si–O perpendicular vibrations, 536 cm^{-1} corresponds to Al–O–Si deformation, 468 cm^{-1} corresponds to Si–O–Si deformation, and 428 cm^{-1} corresponds to Si–O deformation.

The calcination process of kaolinite caused the almost complete disappearance of the water and hydroxyl bands. The stretching of inner-surface-hydroxyl groups bands at 3696, 3669, 3652 and 3619 cm^{-1} , and the –OH deformation of inner-surface hydroxyl groups band at 937 cm^{-1} also disappeared. This proves that the dehydroxylation process occurred. The significant decrease in Al–OH deformation band at 911 cm^{-1} and Al–O–Si deformations at 536 cm^{-1} indicates that the evolution of octahedral Al^{3+} coordination in the kaolinite structure towards coordination tetrahedral in metakaolinite was observed.

The spectrum of metakaolinite shows a very simple spectrum, consisting of three broad bands centered at 1079, 777, and 470 cm^{-1} . The first corresponds to the

vibrations of the tetrahedral sheet, clearly showing the deformation of this sheet during calcination. The second band corresponds to silica or free quartz, unaffected by calcination. Finally, the third band corresponds to the structural flexural vibrations. The simplification of this region also shows the structural deformation of kaolinite in metakaolinite.

Glukhovskiy et al. [28] proposed a general mechanism for the alkaline activation of materials consisting mainly of silica and reactive alumina. The mechanism of the Glukhovskiy model is composed of joint destruction-coagulation-condensation-crystallization reactions. The first step is a decomposition of the Si–O–Si and Al–O–Si covalent bonds, which occurs as the pH of the alkaline solution increases. These groups are therefore transformed into a colloidal phase. Then, an accumulation of destruction products occurs, which often interacts with each other to form a coagulated structure, which leads to the third phase, the generation of a condensed and crystallized structure. In another study, Steinerova [29] reported that metakaolinite in a strong alkaline medium allows hydrolysis of metakaolinite source components and their disintegration during which bridging oxygen (BOS) converts to non-bridging oxygen (NBOs) precursors release ($\text{BOS} \rightarrow \text{NBOs}$), leading to a solution of the hydrated units of SiO_4 and AlO_4 . As a consequence, we did not observe any significant

differences between the IR spectra of K_{CA} and K_{Cal} . On the other hand, the Al–O–Si deformation band at 536 cm^{-1} completely disappeared, followed by the decrease in intensity of the Si–O–Si band at 468 cm^{-1} .

Alkaline attack on the structure of metakaolinite produces a release of silicate and aluminate species in solution, with 5 or 6 Al coordinates converted into 4-coordinations during dissolution. In this case, the release of Al may be faster than that of Si [30]. This can be explained by the decrease in the percentage of Al in metakaolinite after activation as observed by elemental analysis using SEM-EDS (Table 1). According to SEM-EDS data, the activation of metakaolinite by NH_4OH allowed the dealumination of metakaolinite. The increase in the Si/Al ratio was almost twice as high as in natural kaolinite, K_A and K_{Cal} .

Table 2 shows that monolayer volume, surface area, and total pore volume decreased during calcination due to particle aggregation when water molecules were removed from the structure. Meanwhile the average pore diameter showed an increase, indicating that the high temperature calcination process also allowed pore opening by minimizing organic contaminations of natural kaolinite. The specific surface area and the total pore volume increased significantly after treatment for K_{CA} because of the reorganization of the K_{Cal} structure. These results show that metakaolinite is more reactive under treatment compared to natural kaolinite. NH_4OH is capable of activating kaolinite by increasing slightly the surface area and average pore diameter of K_A . NH_4OH was capable of dealuminating metakaolinite by increasing the surface area by up to 16 times more than natural kaolinite. It is

probably due to the ability of concentrated NH_4OH to dissolve aluminic and silicic part of metakaolinite.

Due to the change in chemical composition, the mapping of the elements was conducted for natural kaolinite and K_{CA} using SEM-EDS with a magnification of $2000\times$ to know their distributions of chemical elements. The results of the analyses are shown in Fig. 3. It is found that the elements of O, N, Mg, Al, Si, and K of natural kaolinite were homogeneously distributed. After calcination followed by activation, a new phase was observed forming more pores. Activation by NH_4OH led to the formation of pore domains that were larger in the clusters site of chemical elements such as O, Si, and Al. This figure also shows the change in the distribution of the chemical elements of Na, Mg, and K but less important.

Adsorption of Bixin on Dealuminated Metakaolinite

For the comparison study with respect to natural kaolinite, HCl treated kaolinite, and KOH treated kaolinite, that Rahmalia et al. [6] had studied previously, we carried out the adsorption of bixin on K_A and K_{CA}

Table 1. SEM-EDS analysis data

Element	wt. %			
	Natural kaolinite [11]	K_A	K_{Cal}	K_{CA}
O	56.9	58.0	53.3	56.0
Na	0.42	0.45	0.29	0.37
Mg	0.15	0.26	0.31	0.19
Al	18.4	18.2	19.8	13.7
Si	23.1	22.5	24.5	28.1
K	0.79	0.38	0.72	0.83
Fe	0.22	0.22	0.22	0.23
Si/Al	1.26	1.23	1.24	2.06

Table 2. BET- N_2 analysis data

Kaolinites		Natural kaolinite [11]	K_A	K_{Cal}	K_{CA}
Weight of sample (g)		0.21	0.22	0.21	0.19
Saturation vapor pressure (kPa)		99.22	99.78	97.18	97.14
	Volume of monolayer, V_m ($\text{cm}^3\text{ STP g}^{-1}$)	1.76	1.88	1.64	28.57
BET	Constant of energy, C (first layer)	42.94	35.99	122.07	2877.50
Parameters	Surface area BET, a_s BET ($\text{m}^2\text{ g}^{-1}$)	7.65	8.15	7.13	124.33
Analysis	Total pore volume, $p/p_0 = 0.99$ ($10^{-2}\text{ cm}^3\text{ g}^{-1}$)	3.62	2.89	2.34	7.43
	Average pore diameter, d_p (nm)	8.20	14.17	13.16	2.39

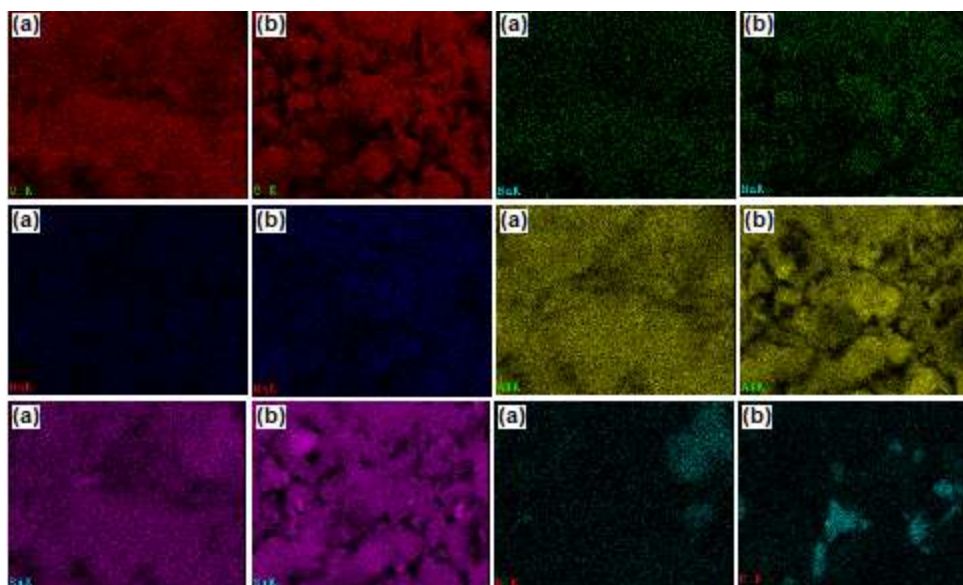


Fig 3. Cartography of elements of natural kaolinite (a) and K_{CA} (b)

using dimethyl carbonate as the solvent. The effect of contact time showed that bixin in dimethyl carbonate needed 240 min to wait for equilibrium (Fig. 4). The result was the same when natural kaolinite, HCl treated kaolinite, and KOH treated kaolinite were used as adsorbents.

The absorption spectrum of the supernatant solution of bixin in dimethyl carbonate before and after adsorption by K_A and K_{CA} for 240 min is shown in Fig. 5. In contrast to the adsorption properties of bixin on natural kaolinite and treated kaolinite, the spectrum of bixin after adsorption on K_{CA} showed a small red displacement (bathochromic). It appeared in the visible region and gave a maximum absorbance at 462 nm, moving 6 nm with respect to the bixin spectrum before adsorption (456 nm), and is associated with the position of the 0–1 band of vibrations. This behavior is an advantage in bixin applications as a photosensitizer. That is, less energy is needed for the bixin to be excited from HOMO to LUMO compared to bixin adsorbed on natural kaolinite and treated kaolinite.

In order to explain the design of an adsorption system and the interaction between bixin and metakaolinite in this study, we used the most common types of isotherms, which are the Langmuir and Freundlich models. They are the best models to explain the trend of adsorption based on the essence of adsorbents saturated with adsorbate after

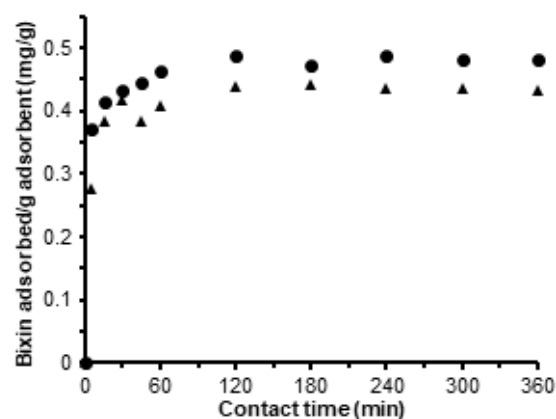


Fig 4. Effect of contact time on adsorption of bixin using K_A (▲) and K_{CA} (●)

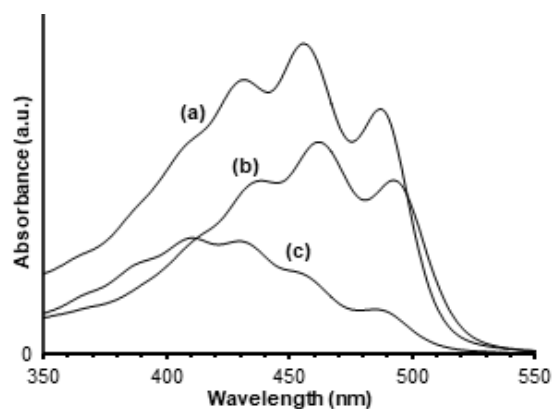


Fig 5. Supernatant solution absorption spectrum of bixin in dimethyl carbonate before (a) and after adsorption on K_A (b) and K_{CA} (c)

enough contact time. Freundlich isotherm is applicable to adsorption processes that occur on heterogenous surfaces. This isotherm gives an expression which defines the surface heterogeneity and the exponential distribution of active sites and their energies. The linear form of the Freundlich isotherm is as follows [31]:

$$\log q_e = \log K_f + \frac{1}{n} \log C_e \quad (1)$$

where q_e is the amount of the adsorbate at equilibrium (mg/g), C_e is the equilibrium concentration of the adsorbate on the adsorbent (mg/L), K_f is adsorption capacity (L/mg) and $1/n$ is adsorption intensity; it also indicates the relative distribution of the energy and the heterogeneity of the adsorbate sites.

In the Langmuir model, the mass of solute adsorbed per unit mass of adsorbent increases linearly with solute concentration at low surface coverage, approaching an asymptote as the adsorption sites become saturated. Eq. (2) is based on three important assumptions: (1) the energy of adsorption is identical for all sites and is independent of surface coverage, (2) adsorption occurs only at localized sites, with no interaction between adjoining adsorbed molecules, and (3) the sorption maximum represents monolayer coverage. The linear form of the Langmuir Eq. (2) can be expressed as follows [32]:

$$\frac{C_e}{q_e} = \frac{1}{K_L \cdot q_m} + \left(\frac{1}{q_m} \right) C_e \quad (2)$$

where K_L is Langmuir constant related to adsorption capacity (mg/g), which can be correlated with the variation of the suitable area and porosity of the adsorbent which implies that large surface area and pore volume will result in higher adsorption capacity, and q_m is maximum adsorption capacity (mg/g).

Table 3 shows that the equilibrium data did not correspond to the Freundlich equation for K_A and K_{CA} in dimethyl carbonate. The poor fit of these models was demonstrated by the very low correlation coefficient ($r^2 < 0.95$) and the values of $n > 1$. The Langmuir equation gave a better fit, with $r^2 > 0.95$. This indicates the presence of a homogeneous active site and the coverage of the adsorbent surface with a monolayer of bixin. Depending on the values of q_m , the bixin adsorption on K_{CA} is favorable compared to K_A . This is predictable as the adsorption capacity of adsorbents increased with an increase in the specific surface area of BET.

The adsorption kinetics (k_1 and k_2) were also calculated for K_A and K_{CA} as well as the correlation coefficient, the values of q_{e1} and q_{e2} (calculation) and q_e (experiment) by using the Lagergren's pseudo-first order and pseudo-second order models to investigate the

Table 3. Adsorption parameters for the adsorption of bixin on K_A and K_{AC}

Adsorption isotherm parameters		K_A	K_{AC}
Freundlich	K_f (L/mg)	0.36	0.60
	N	0.14	8.76
	r^2	0.42	0.30
Langmuir	K_L (mg/g)	7.89	6.16
	q_m (mg/g)	0.47	0.72
	r^2	0.99	0.98
Adsorption kinetic parameters		K_A	K_{AC}
Pseudo-first order	q_e exp (mg/g)	0.44	1.43
	q_{e1} (mg/g)	0.19	0.46
	k_1 (10^{-2}) (1/min)	3.57	10.4
	r^2	0.84	0.73
Pseudo-second order	q_{e2} (mg/g)	0.44	1.41
	h (10^{-2}) (mg/g min)	20.1	39.9
	k_2 (mg/g.min)	1.05	0.20
	r^2	0.99	0.99

dynamics of the bixin adsorption process. The pseudo-first order model assumes that the rate of change of solute uptake over time is directly proportional to the difference in saturation concentration and the amount of solid uptake over time. In most cases, the adsorption reaction involves diffusion across a boundary (3) [33]. The adsorption process with chemisorption controls the rate, according to the pseudo-second order model (4) [34].

$$\log(q_e - q_t) = \log q_e - k_1 \cdot \frac{t}{(2.303)^t} \quad (3)$$

$$\frac{t}{q_t} = \frac{1}{(k_2 q_e^2)} + \left(\frac{1}{q_m} \right) \cdot t \quad (4)$$

where k_1 is pseudo first order adsorption rate constant (1/min) and k_2 is pseudo second order adsorption rate constant (g/mg min). Values of k_1 and k_2 were calculated from the intercept of the corresponding plots of $\log(q_e - q_t)$ against t and t/q_t against t .

As seen in this table, the values of the correlation coefficients for the pseudo-second-order rate equation were found to be higher than those of the pseudo-first-order rate equation. Although the r^2 values for plots are in the range of 0.7329 after applying the pseudo-first order model, the calculated q_{e1} values obtained from this model do not give reasonable values because they are very small relative to the values of the experimental q_e . The values of q_{e2} and q_e were close in agreement with the other values for the pseudo-second order model. These results confirm that the bixin adsorption process on both K_A and K_{CA} follow the pseudo-second-order kinetic model. These results prove that adsorption occurs in this experiment by chemisorption [35].

■ CONCLUSION

The treatment of metakaolinite with NH_4OH is a good method for producing the dealuminated metakaolinite with a very large surface area. The nature of the adsorption process depends on the physical and chemical characteristics of the adsorbents, as well as on the conditions of the system. The product obtained can also slightly decrease the energy required to excite the electrons of the bixin from HOMO to LUMO. It can also increase the capacity of kaolinite to adsorb bixin to almost twice the amount of activated kaolinites without an initial

calcination phase. Finally, dimethyl carbonate has potential to be a good solvent for increasing the adsorptive capacity of bixin on kaolinite.

■ ACKNOWLEDGMENTS

This study received financial support from the Ministry of Research Technology and the Higher Education Republic of Indonesia (KEMENRISTEK DIKTI) through the National Competitive Research (217/SP2H/LT/DRPM/2019) and Tanjungpura University through DIPA research (1945/UN22.8/KP/2018). We thank Cedric Charvillat (*Centre Inter-universitaire de Recherche et d'Ingénierie des Matériaux*), Gwénaëlle Raimbeaux (*Laboratoire de Genie Chimique*), and Deni Ferdian (Universitas Indonesia) for assistance with the analysis of kaolinite samples, by XRD, BET- N_2 , and EDS, respectively.

■ REFERENCES

- [1] Frost, R.L., Makó, É., Kristóf, J., and Klopogge, J.T., 2002, Modification of kaolinite surface through mechanochemical treatment—a mid-IR and near-IR spectroscopic study, *Spectrochim. Acta, Part A*, 58 (13), 2849–2859.
- [2] Frost, R.L., Kristóf, J., Makó, É., and Horváth, E., 2003, A DRIFT spectroscopic study of potassium acetate intercalated mechanochemically activated kaolinite, *Spectrochim. Acta, Part A*, 59, 1183–1194.
- [3] Khan, T.A., Khan, E.A., and Shahjahan, 2015, Removal of basic dyes from aqueous solution by adsorption onto binary iron-manganese oxide coated kaolinite: Nonlinear isotherm and kinetics modeling, *Appl. Clay Sci.*, 107, 70–77.
- [4] Kumar, S., Panda, A.K., and Singh, R.K., 2013, Preparation and characterization of acid and alkaline treated kaolin clay, *Bull. Chem. React. Eng. Catal.*, 8 (1), 61–69.
- [5] Belver, C., Bañares-Muñoz, M.A., and Vicente, M.A., 2002, Chemical activation of kaolinite under acid and alkaline conditions, *Chem. Mater.*, 14 (5), 2033–2043.
- [6] Rahmalia, W., Fabre, J.F., Usman, T., and Mouloungui, Z., 2018, Adsorption characteristics of

- bixin on acid- and alkali-treated kaolinite in aprotic solvents, *Bioinorg. Chem. Appl.*, 2018, 3805654.
- [7] Yahaya, S., Jikan, S.S., Badarulzaman, N.A., and Adamu, A.D., 2017, Effect of acid treatment on the SEM-EDX characteristics of kaolin clay, *Path Sci.*, 3 (9), 4001–4005.
- [8] Mackenzie, R.C., 1970, *Differential Thermal Analysis*, Vol. I, Academic Press, London.
- [9] Ilić, B.R., Mitrović, A.A., and Miličić, L.R., 2010, Thermal treatment of kaolin clay to obtain metakaolin, *Hem. Ind.*, 64 (4), 351–356.
- [10] Varga, G., 2007, The structure of kaolinite and metakaolinite, *Épitöanyag*, 59, 6–9.
- [11] Cardarelli, C.R., Benassi, M.T., and Mercadante, A.Z., 2008, Characterization of different annatto extracts based on antioxidant and colour properties, *LWT Food Sci. Technol.*, 41 (9), 1689–1693.
- [12] Das, D., Maulik, S.R., and Bhattacharya, S.C., 2007, Dyeing of wool and silk with *Bixa orellana*, *Indian J. Fibre Text. Res.*, 32 (3), 366–372.
- [13] dos Santos, G.C., Mendonça, L.M., Antonucci, G.A., dos Santos, A.C., Antunes, L.M.G.A., and Bianchi, M.L.P., 2012, Protective effect of bixin on cisplatin-induced genotoxicity in PC12 cells, *Food Chem. Toxicol.*, 50 (2), 335–340.
- [14] Venugopalan, A., Giridhar, P., and Ravishankar, G.A., 2011, Food, ethanobotanical and diversified applications of *Bixa orellana* L.: A scope for its improvement through biotechnological mediation, *Indian J. Fundam. Appl. Life Sci.*, 1 (4), 9–31.
- [15] Gómez-Ortíz, N.M., Vázquez-Maldonado, I.A., Pérez-Espadas, A.R., Mena-Rejón, G.J., Azamar-Barrios, J.A., and Oskam, G., 2010, Dye-sensitized solar cells with natural dyes extracted from achiote seeds, *Sol. Energy Mater. Sol. Cells*, 94 (1), 40–44.
- [16] Hiendro, A., Hadari, F., Rahmalia, W., and Wahyuni, N., 2012, Enhanced performance of bixin-sensitized TiO₂ solar cells with activated kaolinite, *IJERI*, 4 (1), 40–44.
- [17] Ruiz-Anchondo, T., Flores-Holguín, N., and Glossman-Mitnik, D., 2010, Natural carotenoids as nanomaterial precursors for molecular photovoltaics: A computational DFT study, *Molecules*, 15 (7), 4490–4510.
- [18] Olson, M., and Allen, N.D., 2012, *Natural photodynamic agents and their use*, Patent, EP2214495A4.
- [19] Montenegro, M.A., Rios, A.O., Mercadante, A.Z., Nazareno, M.A., and Borsarelli, C.D., 2004, Model studies on the photosensitized isomerization of bixin, *J. Agric. Food Chem.*, 52 (2), 367–373.
- [20] Rios, A.O., Borsarelli, C.D., and Mercadante, A.Z., 2005, Thermal degradation kinetics of bixin in an aqueous model system, *J. Agric. Food Chem.*, 53 (6), 2307–2311.
- [21] Kohno, Y., Inagawa, M., Ikoma, S., Shibata, M., Matsushima, R., Fukuhara, C., Tomita, Y., Maeda, Y., and Kobayashi, K., 2011, Stabilization of a hydrophobic natural dye by intercalation into organo-montmorillonite, *Appl. Clay Sci.*, 54 (3-4), 202–205.
- [22] Rahmalia, W., 2009, Synthesis of kaolinite-bixin organoclay and their photostability test, *Thesis*, Magister of Biology, Christian University of Satya Wacana, Salatiga, Indonesia.
- [23] Picot, P.A., and Grenouillet, P., 1995, *Safety in the Chemistry and Biochemistry Laboratory*, Eds. Prokopetz, A.T., and Walters, D.B., Wiley-VCH, Inc., New York.
- [24] Portejoie, S., Martinez, J., and Landmann, G., 2002, L'ammoniac d'origine agricole: Impacts sur la santé humaine et animale et sur le milieu naturel, *INRA Prod. Anim.*, 15 (3), 151–160.
- [25] Tundo, P., and Selva, M., 2002, The chemistry of dimethyl carbonate, *Acc. Chem. Res.*, 35 (9), 706–716.
- [26] Rahmalia, W., Fabre, J.F., and Mouloungui, Z., 2015, Effect of cyclohexane/acetone ratio on bixin extraction yield by accelerated solvent extraction method, *Procedia Chem.*, 14, 455–464.
- [27] Rahmalia, W., Fabre, J.F., Usman, T., and Mouloungui, Z., 2014, Aprotic solvents effect on the UV-visible absorption spectra of bixin, *Spectrochim. Acta, Part A*, 131, 455–460.

- [28] Glukhovskiy, V.D., Rostovskaja, G.S., and Rumyna, G.V., 1980, High strength slag alkaline cement, *Proceedings of the 7th International Congress on the Chemistry of Cement*, Paris, 3, 164–168.
- [29] Steinerova, M., 2010, Microporous inorganic polymers based on metakaolinite and their open porosity structure of 10-20 nm in diameter, *The 2nd International Conference NANOCON 2010*, Olomouc, Czech Republic, 12–14 October 2010.
- [30] Li, C., Sun, H., and Li, L., 2010, A review: The comparison between alkali-activated slag (Si + Ca) and metakaolin (Si + Al) cement, *Cem. Concr. Res.*, 40 (9), 1341–1349.
- [31] Freundlich, H., 1906, Adsorption in solution, *Z. Phys. Chem.*, 57, 385–470.
- [32] Langmuir, I., 1916, The constitution and fundamental properties of solids and liquids, Part I. Solids, *J. Am. Chem. Soc.*, 38 (11), 2221–2295.
- [33] Lagergren, S., 1898, About the theory of so-called adsorption of soluble substances, *Kungl. Svenska Vetenskapsakad. Handl.*, 24 (4), 1–39.
- [34] Ho, Y.S., and McKay, G., 1999, Pseudo-second order model for sorption processes, *Process Biochem.*, 34 (5), 451–465.
- [35] Vimonses, V., Lei, S., Jin, B., Chow, C.W.K., and Saint, C., 2009, Adsorption of congo red by three Australian kaolins, *Appl. Clay Sci.*, 43 (3-4), 465–472.

Electrical and Thermal Conductivity of Cyclic Natural Rubber/Graphene Nanocomposite Prepared by Solution Mixing Technique

Vivi Purwandari^{1,2}, Saharman Gea^{3,*}, Basuki Wirjosentono³, Agus Haryono⁴,
I Putu Mahendra¹, and Yasir Arafat Hutapea³

¹Postgraduate School, Department of Chemistry, Faculty of Mathematics and Natural Sciences, Universitas Sumatera Utara, Jl. Bioteknologi No. 1, Medan 20155, Indonesia

²Department of Chemistry, Universitas Sari Mutiara, Jl. Kapten Muslim, Medan 20124, Indonesia

³Department of Chemistry, Faculty of Mathematics and Natural Sciences, Universitas Sumatera Utara, Jl. Bioteknologi No. 1, Medan 20155, Indonesia

⁴Research Center for Chemistry, Indonesian Institute of Sciences, Kawasan PUSPIPTEK, Serpong 15314, South Tangerang, Banten, Indonesia

* **Corresponding author:**

tel: +62-85297978578

email: s.gea@usu.ac.id

Received: April 4, 2019

Accepted: September 4, 2019

DOI: 10.22146/ijc.44791

Abstract: Thermal and electrical conductivity studies of Cyclic Natural Rubber nanocomposite with graphene 1 and 2 phr (G1 and G2), and modified 1 and 2 graphenes (mG1 and mG2) have been carried out. Graphene was activated with cetrimonium bromide (CTAB), was isolated from Sawahlunto coal (Bb) by the Hummer modification method. The nanocomposite was fabricated through the mixing solution method using xylene as a solvent. The characterizations of nanocomposites, which were performed by Fourier Transform Infrared (FT-IR) and X-Ray Diffraction (XRD) reveal an interaction between graphene, CTAB, and the CNR matrix. Furthermore, the results of Scanning Electron Magnetic (SEM) and Transmission Electron Microscopy (TEM) analysis indicate that the particle size becomes smaller, and the particle distribution is more in accordance with CTAB. Thermal analysis of nanocomposites using Differential Scanning Calorimeter (DSC) showed an increase in thermal conductivity from 3.0084 W/mK to 3.5569 W/mK. Analysis of electrical conductivity using the Two-Point Probe shows 2 phr mG (mG2) capable of increasing electrical conductivity from 0.1170×10^{-4} S/cm to 0.2994×10^{-4} S/cm.

Keywords: CNR; graphene; coal; CTAB; electrical conductivity

■ INTRODUCTION

The addition of a small amount of graphene to the polymer matrix was found to increase the electrical conductivity of nanocomposites significantly [1-2]. The electrical conductivity of the nanocomposite can be increased by chemically reducing GO [3-4]. Pure graphene is not compatible with all types of organic polymers, and composites obtained have inhomogeneous morphology.

On the other hand, the surface functionalization of graphene can increase the dispersion of graphene into the polymer matrix and also increase the interaction between phases between graphene and the polymer matrix [5-6].

Graphene functionalization has good solubility in organic solvents and good interface interaction with organic polymers [6]. Another reason for graphene functionality significance is that hydrophobic graphene usually forms irreversible agglomeration and produces graphite through van der Waals bonds. This phenomenon has the effect of reducing the surface area of graphene and reducing the electrical properties of graphene [7].

Kim et al. showed an increase in dispersion between styrene butadiene (SBR) latex and multi-layer graphene/CTAB. Multi-layer graphene is more effective

and stably dispersed in the SBR matrix by CTAB because of the electrostatic attraction between fillers and negatively charged colloidal SBR particles [7]. Based on this, CTAB-graphene functionalization is used to enhance interface interactions in the matrix [8-9].

CNR has weak adhesion properties to polar surfaces [10-11] as a non-electrically conductive material, and it has a great potency to develop CNR as a conductive paint. Many previous studies employed natural rubber nanocomposite as a matrix and graphene or functionalized graphene as a filler [12-14], but for graphene fillers obtained from Sawahlunto coal, it has never been reported before. Cyclic Natural Rubber (CNR) has also never been reported as a matrix with graphene fillers. This study used CNR as an insulator as a matrix and graphene from Sawahlunto coal as a nanofiller. The resulting nanocomposite is expected to be a conductive paint resin.

Therefore, the aim of this research is to prepare and evaluate the electrical and thermal conductivity of CNR/graphene composite by looking at the effect of the amount of graphene and modification of graphene, which is added as nanofiller.

■ EXPERIMENTAL SECTION

Materials

Materials used were natural graphite (coal) from Sawahlunto River Parambahan village of Stone Tanjung District of Talawi Cit, Central Sawahlunto, West Sumatra, Indonesia. The Cyclic Natural Rubber (CNR) obtained from PTPN III, Sumatera Utara – Indonesia. Sulfuric acid 98%, sodium nitrate, potassium permanganate, hydrochloric acid 36%, hydrogen peroxide, CTAB were all of analytical-grade and obtained from Sigma-Aldrich (USA), demineralized water and xylene were purchased from Bratachem, Medan-Indonesia.

Procedure

Synthesis of graphene oxide and graphene from Sawahlunto coal

The fine powder of Sawahlunto coal was placed in an oven at 125 °C for 24 h. The powder was converted into GO by the oxidation process. The amount of 1 g of graphite Sawahlunto coal (g-Bb) and 50 mg of sodium

nitrate was introduced into 70 mL of sulphuric acid (98 wt.%), the reaction was placed in the ice bath. After that, as many as 3 g of KMnO_4 was added into the solution gradually. The solution was stirred for 2 h, and it was diluted using deionized water. The 30% of hydrogen peroxide was added into the previous solution until the color was turned into bright yellow. It indicated that the oxidation process of graphite was perfectly done. The mixture was filtrated and washed with dilute HCl to remove the other mineral. The pH of the previous solution was neutralized using deionized water. The obtained graphite oxide dispersion was treated using ultrasonication with frequency 50–60 Hz for 90 min [7,15-16]. The brown color of water dispersion indicated the presence of a stable Nano sheet's graphene oxide (GO-Bb). The reduction process of the exfoliation results (GO-Bb900) was performed using the 1% NaBH_4 in 0.2% NaOH. The mixture was stirred for 1 h, and 6 M HCl was added drop by drop until the air bubbles were disappeared. After that, the precipitate was formed and then washed with DM water until the pH was neutral. The precipitate was then dried at 100 °C for 12 h. Finally, the graphene powder was successfully manufactured from Sawahlunto coal (G-Bb900). The obtained graphene oxide (GO-Bb) and graphene (G-Bb) were evaluated using XRD, SEM, TEM and FT-IR analysis.

Graphene functionalization and nanocomposite preparation

Two gram of graphene oxide (GO-Bb) was dispersed in 100 mL of deionized water that assisted with ultrasonication. On the other side, 2 g of CTAB was dissolved in 100 mL of ethanol. Those two solutions were mixed and stirred for 24 h at room temperature. This treatment was continued with the addition of 10 mL of 1 wt.% NaBH_4 and 0.2 wt.% NaOH and stirred for 24 h. The obtained black powder (mG) was washed several times using a mixture of deionized water and ethanol with the ratio 1:1, and the powder was dried at 60 °C until the weight was constant [17-18]. The composite was prepared using solution mixing between CNR and mG. The amount of 1 and 2 phr mG was dispersed in 20 mL of xylene using ultra-sonication for 1 h. Then, as many as 10 g of CNR was added into that dispersion and stirred

until CNR was perfectly dissolved [13]. The solution was cast into an acrylic plate and dried at room temperature for 72 h. The obtained nanocomposites were labeled as m-G1 and m-G2 that referred to the addition of 1 and 2 phr of mG.

Characterization

The FT-IR spectra of the as-prepared GO and nanocomposite were determined using ATR-IR Bruker Alpha Platinum with the wavenumber range between 4000–500 cm^{-1} . The wide-angle X-Ray diffractogram of GO and nanocomposite was evaluate using Shimadzu 7000 with the source of irradiation $\text{K}\alpha$ Cu. The scan speed was 2°/min, and the range of 2θ was 7°–70°. The morphology and microstructure of GO and nanocomposite were determined using SEM JEOL 6510(LA), accelerating voltage of 20.00 kV, magnification $\times 2,500$ and TEM JEM-1400, accelerating voltage of 120 Volt, magnification 150,000, while the thermal conductivity was measured using DSC-60, flow rate 30 mL/min, scanning from 25 to 600 °C at the rate 15 °C/min. The measurement of GO and nanocomposite's electrical resistivity was conducted using a two-point probe.

RESULTS AND DISCUSSION

The Characterization of GO

Fig. 1(a) shows the diffractogram of graphite of (g-Bb), graphene oxide (GO-Bb), and graphene (G-Bb)

obtained from Sawahlunto coal. For the graphite, it shows a peak at 2θ of 24.58° with d -spacing 0.1776 nm. The graphene oxide shows a peak at different 2θ , around 11.08°, with the value of d -spacing of 0.4008 nm [18]. The shifting of a peak to the lower value of 2θ and the increase of the d -spacing value were caused by the presence of some functional group in graphene oxide, i.e., epoxy and carbonyl. The reduction process of graphene oxide was conducted using 1 wt.% NaBH_4 ; as a result, the signal is shifting to 24.0° of 2θ . This value of 2θ indicated that the graphene had been successfully obtained by the reduction process of graphene oxide. The increase of 2θ value in graphene also gives an impact on the decrease of d -spacing value to be 0.1894 nm due to the disappeared of epoxy and carbonyl group in graphene [19-21].

The FT-IR spectra of graphene oxide and graphene can be seen in Fig. 2(a). The particular peak of graphene oxide can be found at 3354, 2086, 1621, 1163 and 1040 cm^{-1} . The peak at 3354 cm^{-1} indicated the presence of hydroxyl group or van der Waals interaction between water and graphene oxide. The second peak at 2086 cm^{-1} confirmed the presence of vibration of C=O stretching from aldehyde, ketone, and ester. The C=C bonding of aromatic and aliphatic also can be found at 1621 cm^{-1} . The last peak was found in 1163 and 1040 cm^{-1} , which indicated the presence of C–O–C and C=C–H or Ar–H [22-24].

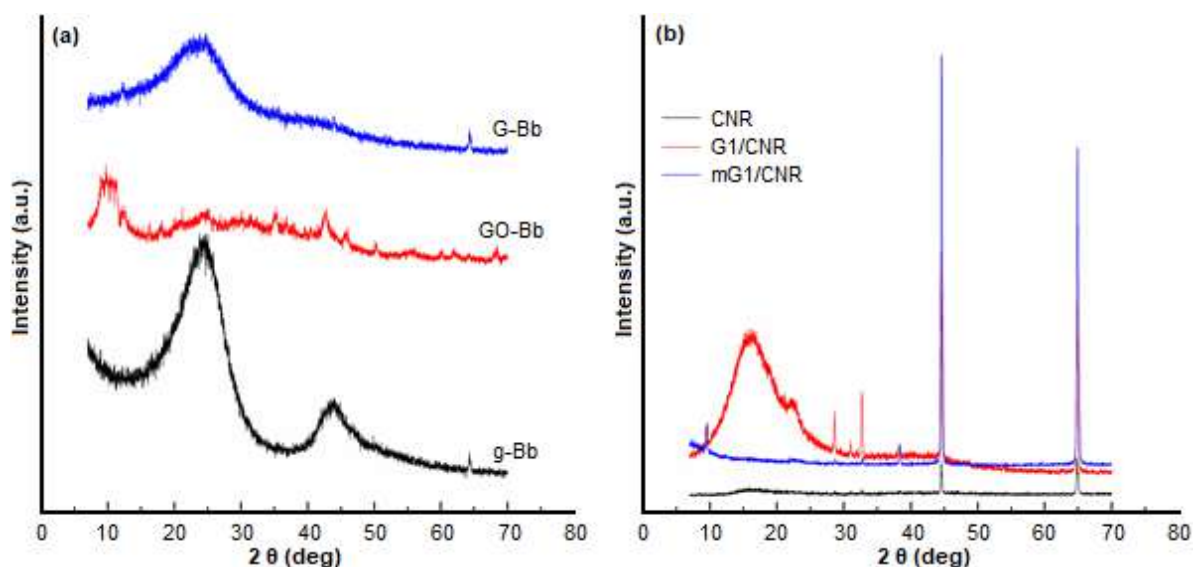


Fig 1. (a) Crystallographic of g-Bb, GO-Bb, G-Bb (b) Crystallographic of CNR, G1/CNR, and mG1/CNR

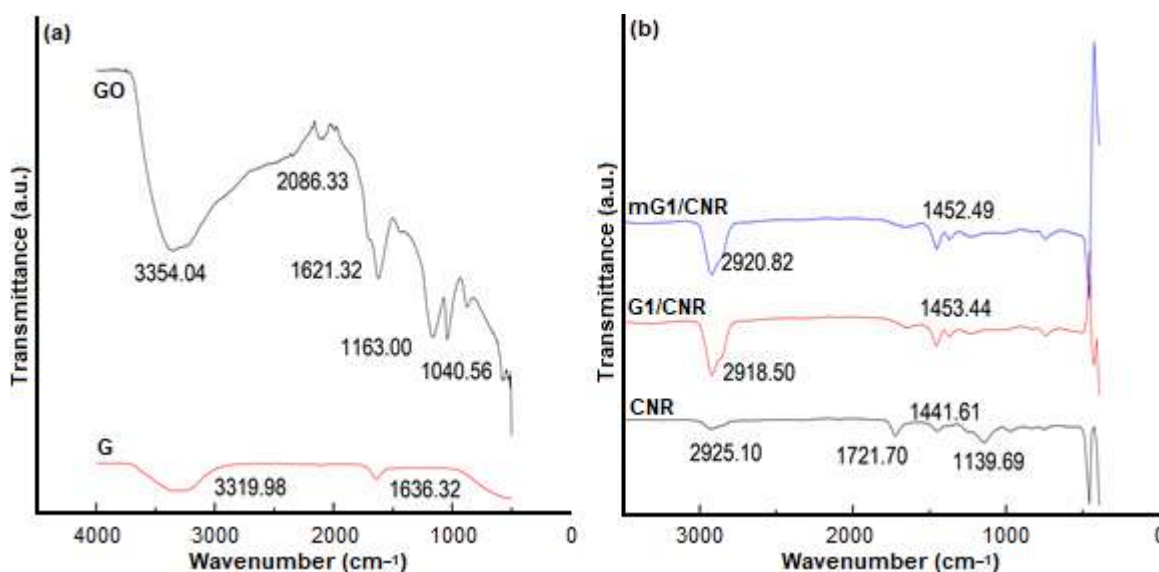


Fig 2. (a) FTIR spectra of GO-Bb and G-Bb, (b) FTIR spectra of CNR, G1/CNR, and mG1/CNR

Kumar et al. (2014) have already synthesized graphene from bituminous. The FT-IR of the reduced graphene oxide showed the functional group that contains oxygen almost disappeared. The particular peak of graphene in this research showed a similarity with the previous work, and it appears at 1600 cm⁻¹ that refers to the skeleton of graphite that was not perfectly oxidized [18].

Fig. 1 (b) showed the crystallographic of G1 and mG1 that dispersed in the CNR matrix. There is a shifting signal at 2θ of 24° and 14° that is caused by the graphene's intercalating in the non-polar matrix of CNR. In the nanocomposite mG/CNR, there is no particular signal of mG; it is dominated by the signal of material, which has a long carbon structure [25], i.e., CNR, but the presence of CNR increase the crystallinity of nanocomposite [26]. The other characteristic of nanocomposite was identified using FT-IR to show the functional group that presence in the material. Fig. 2(b) shows the FT-IR spectra of CNR, G1/CNR, and mG1/CNR; those spectra have a similar peak at 2920–2925 cm⁻¹ and 1441–1452 cm⁻¹ that indicated the presence of vibration of C–H stretching and C–H bending. The disappeared of the peak at 1139, and 1721 was interpreted as the formation of C–H and C=C that obtain from the interaction between graphene and CTAB [27].

Graphene modification was conducted reacting graphene oxide with CTAB, which was then reduced using NaBH₄. In a graphene peak of 1441 cm⁻¹, it shows

C–OH groups originating from unreduced graphene oxide and not bound to CTAB [28]. The spectra of mG1/CNR FTIR also showed almost the same peak, the presence of CTAB was also marked at peak 1453 cm⁻¹ [29]. Similarly, the two peaks of G1/CNR and mG1/CNR state that graphene modification only occurs on the surface of the graphene plane.

The dispersion of unmodified graphene and modified graphene in a CNR matrix were investigated using SEM and TEM (Fig. 3 and 4). SEM micrographs show that most xylene the matrix area is not filled with graphene filler (Fig. 3(a)) [29]. Modified graphene with CTAB has a better surface because mG looks more evenly spread on the CNR matrix.

Fig. 3 shows the nanocomposite microstructure, as shown in the picture, the particle of graphene (G) and modified graphene (mG) in the CNR's matrix has good distribution. Meanwhile, in Fig. 4, the particle of CNR and the nanocomposite is obtained as agglomer. The single particle size in the agglomer of CNR is 25 nm. However, after the addition of graphene or unmodified graphene, the particle size of a single particle of nanocomposite has changed to be 27 nm, and the addition of modified graphene has changed the particle size of a single particle of nanocomposite significantly, to be 6.2 nm. The increase of particle size after the addition of unmodified graphene is due to the incompatibility of

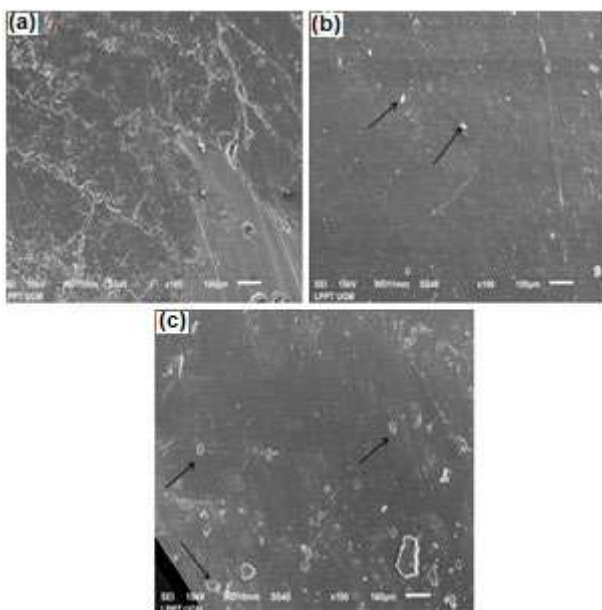


Fig 3. SEM images of (a) CNR, (b) G1/CNR, (c) mG1/CNR

those two materials. The effect of graphene surface modification using CTAB has a big impact on the enhancement of compatibility between graphene and CNR, evidenced by a significant change in the decrease in nanocomposite and graphene particle size well bound to the CNR matrix [3-4,27,29].

The Thermal and Electrical Conductivity of the Nanocomposite

Thermal conductivity

The differential scanning calorimetry has been used to measure the thermal property of nanocomposite. Based on the literature, graphene has good thermal conductivity; it was about $\sim 5000\text{W/mK}$ and has been utilized as a nanofiller in the polymer matrix to enhance the thermal conductivity property. Also, in the previous research graphene has been combined with natural rubber with a good thermal conductivity property [29].

Thermal DSC becomes one technique used to measure the thermal conductivity of solid material by measuring the curve slope. The equation below can be used to determine the thermal conductivity:

$$\text{Slope} = \frac{d\Delta P}{\Delta T_p} = \frac{2}{R} \quad (1)$$

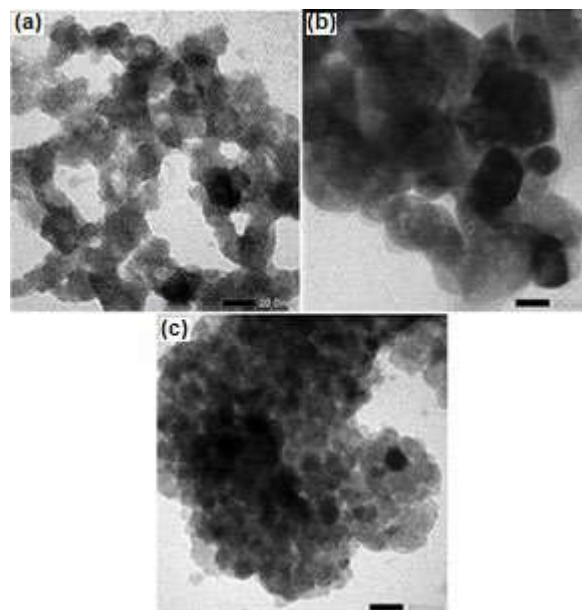


Fig 4. The TEM images of (a) CNR, (b) G1/CNR, (c) mG1/CNR with the 150,000 magnification

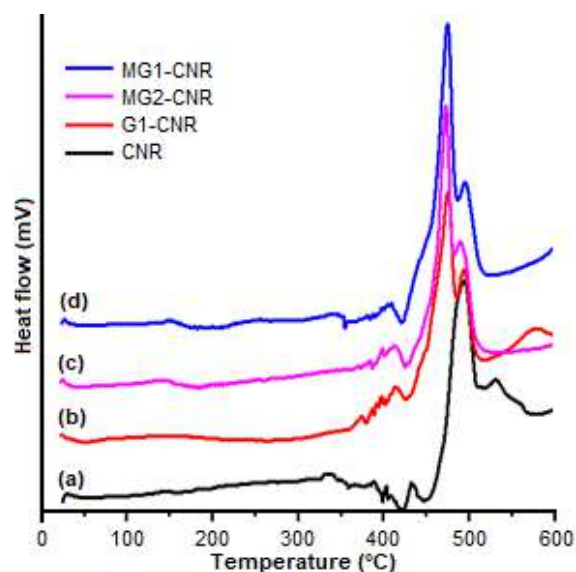


Fig 5. DSC and regression curve of (a) CNR, (b) G1/CNR, (c) mG1/CNR, (d) mG2/CNR

where ΔP is the differential value of heat flow after subtracted with the baseline, T_p is the temperature of DSC during measurement, and R is the total of resistance [30-31]. The thermal DSC and regression curve along with thermal conductivity of CNR matrix after the addition of unmodified and modified graphene can be seen in Fig. 5 and Fig. 6, respectively.

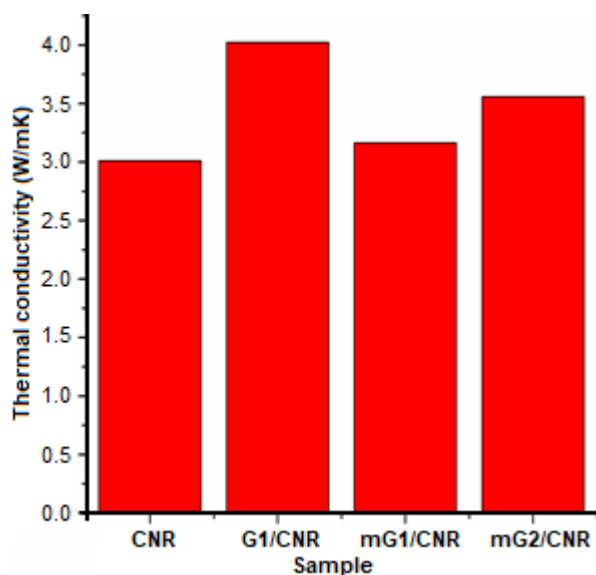


Fig 6. Thermal conductivity of CNR and nanocomposite measured by DSC

After the addition of unmodified graphene, the thermal conductivity value increased to 4.0203 W/mK, but after the addition of 1 phr of modified graphene, the value decreased to 3.1635 W/mK and observed an increase in being after the addition of 2 phr modified graphene. This decrease in thermal conductivity of graphene modification 1 phr (mG1/KAS) is due to the non-polar long alkyl group on CTAB [32].

The addition of unmodified graphene to the CNR matrix reduced the CNR Tg from 96.21 to 95.02 °C. Also, there was a slight decrease in Tg with modified graphene from 96.21 to 92.83 °C and 94.21 °C for 1 phr and 2 phr of mG. Furthermore, the Tg showed that modified graphene did not show a significant effect on changes in matrix Tg. However, the modified graphene Tg was much lower than the unmodified graphene. This is due to the fact that modified graphene is more integrated into the CNR matrix than unmodified graphene [31-32].

Electrical conductivity

The electrical conductivity is the ability of a material to conduct electricity. Graphene, with its electrical conductivity, is able to change the polymer property from an insulator to be a conductive material [29]. Fig. 7 shows the change of electrical conductivity after the addition of unmodified and modified graphene in the NR matrix, which is an insulator.

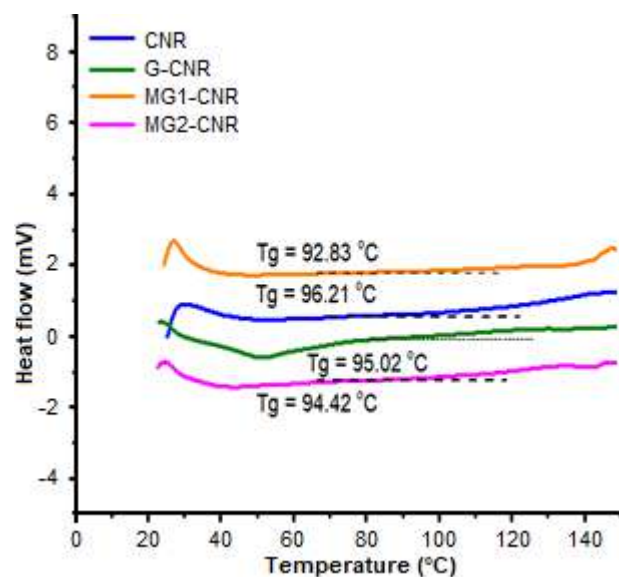


Fig 7. Glass transition temperature (Tg) of Nanocomposite

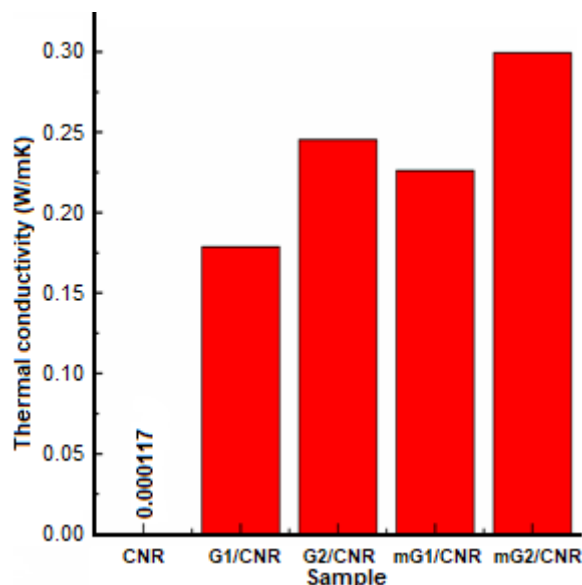


Fig 8. The result characterization of G/CNR and mG/CNR nanocomposite using *Two-Point Probe* method

Based on Fig. 8, the addition of 1 and 2 phr of unmodified graphene into the CNR matrix contribute to an increase in the thermal conductivity of CNR to be 0.1781 and 0.2453 $\times 10^{-6}$ S/cm. After the addition of modified graphene with the same concentration, it gave a value of 0.2262 and 0.2994 $\times 10^{-6}$ S/cm. Based on this value, unmodified and modified graphene changes the electrical property of CNR from an insulator to be

semiconductor [29]. This trend shows that the increase in electrical conductivity is depending on the concentration of unmodified and modified graphene. The low value of this electrical conductivity was caused by the presence of the agglomeration process between CNR and the unmodified and modified graphene (Based on TEM result) [33-34].

■ CONCLUSION

The fabrication of nanocomposites with Cyclic Natural Rubber (CNR) as a matrix, and graphene oxide (isolated from Sawahlunto coal) mixed with cetrimonium bromide (CTAB) cationic surfactant, which was then reduced with NaBH_4 with the solution mixing method was conducted and was proven to be able to increase the CNR/graphene nanocomposite functionalization. The nanocomposite electrical conductivity was measured by using the Two-point probe. The resulted non-polar CNR matrix with the addition of unmodified graphene filler and modified graphene was able to increase the electrical conductivity into semiconductor nanocomposite. By using Differential Scanning Calorimeter (DSC), it shows an increase in thermal conductivity with the addition of unmodified graphene and modified graphene from CNR.

■ ACKNOWLEDGMENTS

Authors would like to acknowledge KEMENRISTEK-DIKTI for financial support through Penelitian Disertasi Doktor grant scheme with the contract number of 033/K1.1/LT.1/2018.

■ REFERENCES

- [1] Chen, C., Yang, Q.H., Yang, Y., Lv, W., Wen, Y., Hou, P.X., Wang, M., and Cheng, H.M., 2009, Self-assembled free-standing graphite oxide membrane, *Adv. Mater.*, 21 (29), 3007–3011.
- [2] Yang, Y.J., and Li, W., 2014, CTAB functionalized graphene oxide/multiwalled carbon nanotube composite modified electrode for the simultaneous determination of ascorbic acid, dopamine, uric acid and nitrite, *Biosens. Bioelectron.*, 56, 300–306.
- [3] Phiri, J., Johansson, L.S., Gane, P., and Maloney T., 2018, A comparative study of mechanical, thermal and electrical properties of graphene-, graphene oxide- and reduced graphene oxide-doped microfibrillated cellulose nanocomposites, *Composites Part B*, 147, 104–113.
- [4] Wu, J., Huang, G., Li, H., Wu, S., Liu, Y., and Zheng, J., 2013, Enhanced mechanical and gas barrier properties of rubber nanocomposites with surface functionalized graphene oxide at low content, *Polymer*, 54 (7), 1930–1937.
- [5] Wu, X., Lin, T.F., Tang, Z.H., Guo, B.C., and Huang, G.S., 2015, Natural rubber/graphene oxide composites: Effect of sheet size on mechanical properties and strain-induced crystallization behavior, *eXPRESS Polym. Lett.*, 9 (8), 672–685.
- [6] Krishnamoorthy, K., Veerapandian, M., Yun, K., and Kim, S.J., 2013, The chemical and structural analysis of graphene oxide with different degrees of oxidation, *Carbon*, 53, 38–49.
- [7] Fauziyah, N., Sriatun, and Pardoyo, 2015, Adsorption of indigo carmine dye using cetyltrimethylammonium bromide (CTAB) surfactant modified zeolite, *JSM*, 23 (4), 121–126.
- [8] Kang, H., Zuo, K., Wang, Z., Zhang, L., Liu, L., and Guo, B., 2014, Using a green method to develop graphene oxide/elastomers nanocomposites with combination of high barrier and mechanical performance, *Compos. Sci. Technol.*, 92, 1–8.
- [9] Zhang, H.B., Zheng, W.G., Yan, Q., Yang, Y., Wang, J.W., Lu, Z.H., Ji, G.Y., and Yu, Z.Z., 2010, Electrically conductive polyethylene terephthalate/graphene nanocomposites prepared by melt compounding, *Polymer*, 51 (5), 1191–1196.
- [10] Siregar, A.M., Eddiyanto, Wirjosentono, B., and Siregar, A.Z., 2016, Oxidation degradation study and use of phenol and amina antioxidant compounds in natural rubber cyclical, *Intl. J. Sci. Technol. Res.*, 5 (5), 297–299.
- [11] Siregar, M.S., Thamrin, Wirjosentono, B., Eddiyanto, and Mendez, J.A., 2014, Grafting of maleic anhydride onto cyclized natural rubber by reactive processing: The effect of maleic anhydride concentrations, *Chem. Mater. Res.*, 6 (11), 15–21.
- [12] Liu, H., Li, Y., Dai, K., Zheng, G., Liu, C., Shen, C., Yan, X., Guo, J., and Guo, Z., 2015, Electrically

- conductive thermoplastic elastomer nanocomposites at ultralow graphene loading levels for strain sensor applications, *J. Mater. Chem. C*, 4 (1), 157–166.
- [13] Zhan, Y., Wu, J., Xia, H., Yan, N., Fei, G., and Yuan, G., 2011, Dispersion and exfoliation of graphene in rubber by an ultrasonically-assisted latex mixing and in situ reduction process, *Macromol. Mater. Eng.*, 296 (7), 590–602.
- [14] Powell, C., and Beall, G.W., 2015, Graphene oxide and graphene from low grade coal: Synthesis, characterization and applications, *Curr. Opin. Colloid Interface Sci.*, 20 (5-6), 362–366.
- [15] Purwandari, V., Gea, S., Wirjosentono, B., and Haryono, A., 2018, Synthesis of graphene oxide from the Sawahlunto-Sijunjung coal via modified hummers method, *AIP Conf. Proc.*, 2049, 020065.
- [16] Araby, S., Meng, Q., Zhang, L., Kang, H., Majewski, P., Tang, Y., and Ma, J., 2014, Electrically and thermally conductive elastomer/graphene nanocomposites by solution mixing, *Polymer*, 55 (1), 201–210.
- [17] Bian, J., Wei, X.W., Lin, H.L., Gong, S.J., Zhang, H., and Guan, Z.P., 2011, Preparation and characterization of modified graphite oxide/poly(propylene carbonate) composites by solution intercalation, *Polym. Degrad. Stab.*, 96 (10), 1833–1840.
- [18] Kumar, E.S., Sivasankar, V., Sureshbabu, R., Raghu, S., and Kalaivani, R.A., 2017, Facile synthesis of few layer graphene from bituminous coal and its application towards electrochemical sensing of caffeine, *Adv. Mater. Lett.*, 8 (3), 239–245.
- [19] Li, G., Yuan, J.B., Zhang, Y.H., Zhang, N., and Liew, K.M., 2018, Microstructure and mechanical performance of graphene reinforced cementitious composites, *Composites Part A*, 114, 188–195.
- [20] Sandhya, P.K., Jose, J., Sreekala, M.S., Padmanabhan, M., Kalarikkal, N., and Thomas, S., 2018, Reduced graphene oxide and ZnO decorated graphene for biomedical applications, *Ceram. Int.*, 44 (13), 15092–15098.
- [21] Gea, S., Sari, J.N., Bulan, R., Piliang, A., Amaturrahim, S.A., and Hutapea, Y.A., 2018, Chitosan/graphene oxide biocomposite film from pencil rod, *J. Phys. Conf. Ser.*, 970 (1), 012006.
- [22] Stobinski, L., Lesiak, B., Malolepszy, A., Mazurkiewicz, M., Mierzwa, B., Zemek, J., Jiricek, P., and Bieloshapka, I., 2014, Graphene oxide and reduced graphene oxide studied by the XRD, TEM and electron spectroscopy methods, *J. Electron. Spectrosc. Relat. Phenom.*, 195, 145–154.
- [23] Tang, Z., Liu, X., Hu, Y., Zhang, X., and Guo, B., 2017, A slurry compounding route to disperse graphene oxide in rubber, *Mater. Lett.*, 191, 93–96.
- [24] Gea, S., Barus, D.A., Sibarani, Y.S., Panindia, N., Sari, J.N., Sebayang, K., Ginting, H., and Hutapea, Y.A., 2018, The study on physical and mechanical properties of latex/graphene oxide composite film, *J. Phys. Conf. Ser.*, 1120 (1), 012052.
- [25] Lee, J.Y., Kumar, V., Tang, X.W., and Lee, D.J., 2017, Mechanical and electrical behavior of rubber nanocomposites under static and cyclic strain, *Compos. Sci. Technol.*, 142, 1–9.
- [26] Matos, C.F., Galembeck, F., and Zarbin, A.J.G., 2014, Multifunctional and environmentally friendly nanocomposites between natural rubber and graphene or graphene oxide, *Carbon*, 78, 469–479.
- [27] Kuila, T., Bose, S., Mishra, A.K., Khanra, P., Kim, N.H., and Lee, J.H., 2012, Chemical functionalization of graphene and its applications, *Prog. Mater. Sci.*, 57 (7), 1061–1105.
- [28] Camargo, P.H.C., Satyanarayana, K.G., and Wypych, F., 2009, Nanocomposites: Synthesis, structure, properties and new application opportunities, *Mater. Res.*, 12 (1), 1–39.
- [29] Park, W., Hu, J., Jauregui, L.A., Ruan, X., and Chen, Y.P., 2014, Electrical and thermal conductivities of reduced graphene oxide/polystyrene composites, *Appl. Phys. Lett.*, 104 (11), 113101.
- [30] Camirand, C.P., 2004, Measurement of thermal conductivity by differential scanning calorimetry, *Thermochim. Acta*, 417 (1), 1–4.
- [31] Mu, Q., and Feng, S., 2007, Thermal conductivity of graphite/silicone rubber prepared by solution intercalation, *Thermochim. Acta*, 462 (1-2), 70–75.
- [32] Shiu, S.C., and Tsai, J.L., 2014, Characterizing thermal and mechanical properties of graphene/epoxy nanocomposites, *Composites Part B*,

- 56, 691–697.
- [33] Kuilla, T., Bhadra, S., Yao, D., Kim, N.H., Bose, S., and Lee, J.H., 2010, Recent advances in graphene based polymer composites, *Prog. Polym. Sci.*, 35 (11), 1350–1375.
- [34] Imran, S.M., Kim, Y., Shao, G.N., Hussain, M., Choa, Y.H., and Kim, H.T., 2014, Enhancement of electroconductivity of polyaniline/graphene oxide nanocomposites through in situ emulsion polymerization, *J. Mater. Sci.*, 49 (3), 1328–1335.

Bioleaching Ability of Fungi Isolated from an Indonesian Sulfurous River Sediment

Serafica Btari Christiyani Kusumaningrum¹, I Wayan Warmada²,
Wahyu Wilopo², and Endah Retnaningrum^{3,*}

¹Graduate Student of Biology Faculty, Universitas Gadjah Mada,
Jl. Teknika Selatan, Sekip Utara, Yogyakarta 55281, Indonesia

²Department of Geological Engineering, Faculty of Engineering, Universitas Gadjah Mada,
Jl. Grafika No. 2, Yogyakarta 55281, Indonesia

³Faculty of Biology, Universitas Gadjah Mada,
Jl. Teknika Selatan, Sekip Utara, Yogyakarta 55281, Indonesia

* **Corresponding author:**

email: endahr@ugm.ac.id

Received: April 7, 2019

Accepted: February 22, 2020

DOI: 10.22146/ijc.44810

Abstract: The unique characteristics of sulfurous river sediment located in Ungaran, Indonesia, are a reservoir of novel fungi with manganese bioleaching properties. Fungi are known to produce metabolic organic acids that have a potential for the industrial application of leaching metal from the ores. This application has high advantages, including low cost, low energy, and creates minimal environmental damage. Therefore, this research was performed to analyze the manganese bioleaching activities of two fungal isolates (KA2B2 and KB4B) from Indonesian sulfurous river sediment on pyrolusite and determine their phenotypic characters. These activities were investigated in terms of changes in fungal biomass, soluble manganese concentration, pH reduction, and organic acid production during 16 days of leaching. Soluble manganese concentrations were measured by atomic absorption spectrometry (AAS), whereas organic acid concentrations were analyzed by high-performance liquid chromatography (HPLC). According to bioleaching investigations, KA2B2 strain was more efficient than KB4B1 strain in extracting manganese from 0.02 g/cm³ pyrolusite. It also produced higher levels of organic acids, such as oxalic acid and citric acid, than KB4B1 strain, proving that strain of KA2B2 could be used to extract manganese from pyrolusite. Based on the phenotypic characters, both strains were identified as genus *Penicillium*.

Keywords: pyrolusite; soluble manganese; oxalic acid; citric acid

■ INTRODUCTION

Manganese is an important heavy metal that serves several industrial purposes. Due to an increase in its demand for use in industrial products, the development of an effective and environmentally safe method of metal extraction is necessary. Recently, bioleaching has been reported as the most effective, low-cost, and promising green technology for metal extraction. This method involves the activities of microorganism groups, such as chemoautotrophic bacteria (sulfur-oxidizing bacteria), heterotrophic bacteria, and fungi [1-4]. Fungi are a ubiquitous group of microbial communities that play a

growing role as agents of geochemical change. Most previous research was conducted to isolate fungi from peculiar habitats such as acids, mine drainage, mining areas, the igneous oceanic crust, and rocks [5-8]. Fungal strains have been reported to extract several heavy metals such as gold, copper, nickel, and lithium by processes of bioleaching [9-11].

Fungal bioleaching processes, which are necessary for mining industry development, involve several mechanisms, including matrix solubilization, complex metal forming results from organic acids or amino acids excretion reaction, reduction of ferric iron mediated by oxalic acid, and metals bioaccumulation by fungal

mycelia. In addition, fungal bioleaching has advantages over bacterial bioleaching because fungi have a shorter lag phase during growth, the ability to tolerate toxic materials, a faster leaching rate, and capability to grow over a wide range of pH (from acidic to alkaline conditions) and in sulfurous environments [12-18].

A sulfurous river located in Ungaran, Indonesia, is one of the places that has the unique characteristics of a high sulfur concentration and a wide temperature range. In such sediment ecosystems, fungi can exhibit a variety of tolerance and survival mechanisms. These unique habitats can also serve as a reservoir of novel fungi with extraordinary properties. In consequent, the fungi with the potential for metal extraction could be isolated from these habitats. However, there is no recent study reported indigenous fungi from the Indonesian sulfurous river, which have potency for metals extraction. Therefore, in this study, fungi that have bioleaching ability were isolated from this habitat, and their phenotypic characters determined. Their manganese bioleaching ability was also investigated based on fungal growth, changes in pH values, manganese solubility, and organic acid production.

■ EXPERIMENTAL SECTION

Materials

The pyrolusite used in this research was collected and originated from Kliripan, Kulonprogo, Yogyakarta, Indonesia (7°51'48''S–110°07'00''E). The ore was dry ground to a mean particle diameter of 0.1–0.2 mm [19-20]. The mineralogical components of the ore samples were analyzed as 25% Mn, 30.4% Fe, and 34.0% S. These samples were subsequently used for bioleaching experiments. The second set of sediment samples were collected from the sulfurous river in Ungaran, Middle Java, Indonesia. These samples were kept at 4 °C and used only for isolating fungi.

Instrumentation

The pH of the leachate was measured by using a digital pH meter (Metrohm). Dissolved manganese was analyzed by using a flame atomic absorption spectrophotometer (Hitachi, Z-2000) [21]. The organic acid components were investigated using high-

performance liquid chromatography (HPLC, Knauer) equipped with a Zorbax C18 column (250 mm × 4.6 mm) and a detector with diode array at 210 nm. The mobile phase was composed of 0.01 mol/L $\text{KH}_2\text{PO}_4\text{-H}_3\text{PO}_4$ (pH 2.6) and 3% methanol (v/v) at 0.5 mL/min flow rate. Finally, to quantify organic acids, an external standard method has been used [22].

Procedure

Fungal isolation and screening

One gram of the second sample was diluted in 9 mL sterilized H_2O and was inoculated into sucrose liquid medium with a pulp density of pyrolusite of 0.02 g/cm³ (final pH: 6.0). The mixture was incubated at 30 °C with rotary shaking at 120 rpm. The sucrose liquid medium consisted of the following composition (g/L⁻¹): sucrose (100), NaNO_3 (1.5), KH_2PO_4 (0.5), $\text{MgSO}_4 \cdot 7\text{H}_2\text{O}$ (0.025), KCl (0.025), and yeast extract (1.6) [9]. After 7 days of incubation, it was plated on sucrose solid medium with a pulp density of pyrolusite of 0.02 g/cm³. This culture was incubated for 7 days until single colonies as pure cultures of the fungal strain were obtained. Sixteen pure strains were isolated from the second sample and then transferred into a sterilized liquid sucrose medium with a pulp density of pyrolusite of 0.02 g/cm³. Through analyzing shifts in media pH values, fungal strains were selected within 7 days based on their ability to significantly lower the pH of the medium from more than 7.3 to 3.0. These strains were selected for further experiments.

Bioleaching investigations

Two fungal strains selected (KA2B2 and KB4B1) were incubated on potato dextrose agar slants for 7 days. After incubation, their spores were washed from the cultures using a physiological saline sterile solution (9 g/L⁻¹ NaCl). Spores were enumerated under a microscope at 400× magnification using a hemocytometer of 1 mm depth, and their number was determined at about 10⁷ spores/mL with a physiological saline sterile solution [23].

One milliliter part of the spore suspension was inoculated into 100 mL of sterilized sucrose medium with a pulp density of pyrolusite of 0.02 g/cm³ in a 250 mL

Erlenmeyer flask. Each strain was incubated at 30 °C and 120 rpm for 16 days. On experimental days 0, 2, 4, 6, 8, 10, 12, 14, and 16, samples were collected from each flask, centrifuged for 10 min at 5000 rpm and filtered through a 0.42 µm Whatman membrane filter. The filtered samples were then measured for their value of pH, soluble manganese concentration, and organic acids. Whereas, the filter paper containing mycelia was then dried at 80 °C for 24 h for fungal biomass measurements.

Phenotypic characterization

Both strains were further observed for their phenotypic characters based on a macroscopic and microscopic investigation in two types of identification media: Czapek yeast auto lysate (CYA) and malt extract auto lysate (MEA). Fungal cultures were incubated following the recommended of previously mycology researches [24-25]. The macroscopic observations studied included the diameter of the colony, the color of obverse and reverse colonies, and the presence or absence of exudates. Whereas, microscopic characters of the fungal isolates were observed using an optical microscope.

Statistical analysis

The data were analyzed using a Statistical Analysis Systems (SAS 9.4, SAS Institute, Inc., Cary, NC, USA) software package. Statistical analysis differences between average values were analyzed using analysis of variance (ANOVA) and Duncan Multiple Range Test (DMRT) method, respectively. The results were reported as means of three replicates. Their mean values were then compared using a significance level of $p < 0.05$.

RESULTS AND DISCUSSION

In this investigation, two fungal cultures (strain KA2B2 and KB4B) were isolated and selected from the five strains for subsequent observations. These selections were evaluated by analyzing shifts in media pH values produced during acidolysis by fungal strains. As reported by previous researchers, the main mechanism of bioleaching by fungal strains is the acidolysis of organic acids [9,26]. Both filamentous fungal strains were observed to significantly lower the pH of the medium from more than 7.3 to 3.0 in 7 days.

Changes in Fungal Biomass, pH, and Manganese Concentration during the Bioleaching Process

Bioleaching experiments were conducted at pH 6 and 30 °C with a particle size of 0.1–0.2 mm and agitation at 120 rpm. The initial inoculum size was 10^7 spores/mL, the pulp densities of pyrolusite were 0.02 g/cm³ and the incubation time was 16 days. In this research, the two fungal strain *Penicillium* KA2B2 and *Penicillium* KB4B1 were selected and compared as bioleaching agents. Fig. 1 compares the changes in fungal biomass, pH, and yield of extracted manganese between the two strains during 16 days of bioleaching investigations.

Penicillium KA2B2 yielded larger biomass and had a shorter lag phase compared with *Penicillium* KB4B1. During 4 days of *Penicillium* KA2B2 growth, the biomass had a maximum value of 30 g/L, and the pH of the medium steadily decreased, reaching 1.5 on the 16th day. This increase in the biomass value and decrease in pH at the fourth day indicated that *Penicillium* KA2B2 was in its logarithmic growth phase. A similar trend of increasing biomass and declining pH values during the logarithmic growth phase of *Penicillium* KA2B2 was also observed in the culture of *Penicillium* KB4B1. In comparison, *Penicillium* KB4B1 took longer to reach the logarithmic growth phase, which was observed at 6 days' incubation. The maximum value of its fungal biomass was 18 g/L, and the minimum pH was 2.6.

The acidification phenomenon in both cultures led to manganese solubilization, as shown by the increase in their yield of leached manganese. *Penicillium* KA2B2 extracted as much as 25% of the manganese from pyrolusite under optimal conditions at 8 days' incubation. On the other hand, *Penicillium* KB4B1 extracted less (20%) manganese from pyrolusite under optimal conditions at 10 days' incubation. As reported by previous researchers, the phenomenon of culture acidification is caused by organic acids provided by strains, which are important in the metal bioleaching process. These acids could supply both protons and metal-complexing anions, leading to free metal cations released. The reactions between organic acids (oxalic acid,

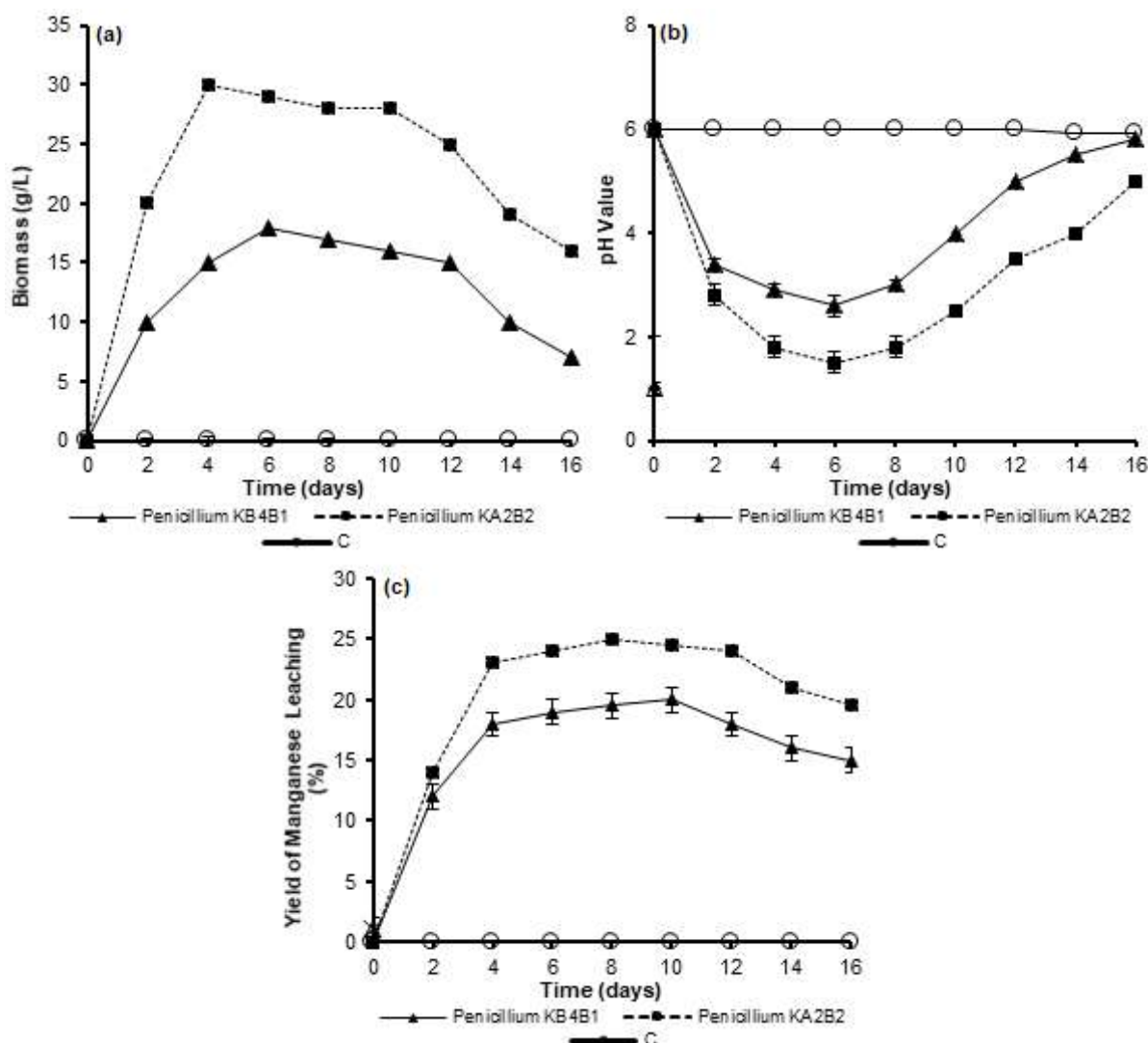
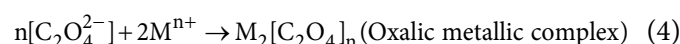
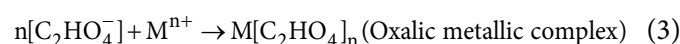
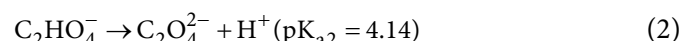
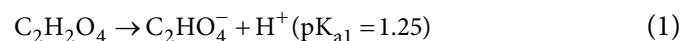


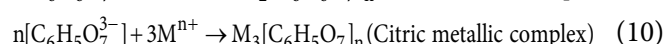
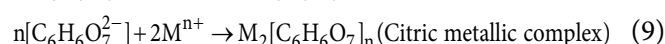
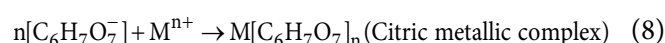
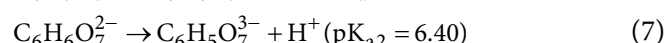
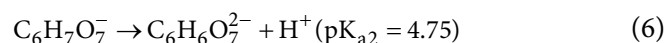
Fig 1. Changes in biomass (a); pH value (b); and manganese yield (c); between *Penicillium* KB4B1 and *Penicillium* KA2B2 at a pulp density of pyrolusite of 0.02 g/cm³ during 16 days of leaching

citric acid) and metallic ion (Mⁿ⁺) are described below [27-28].

The dissociation (1, 2) and complexation reactions (2, 3) of oxalic acid are:



Whereas the dissociation (5, 6, 7) and complexation reactions (8, 9, 10) of citric acid are:



Organic acid analysis by HPLC revealed that the *Penicillium* KA2B2 culture reached optimum production of citric acid and oxalic acid at 13.5 and 17 mmol/L, respectively. In contrast, the maximum production of citric acid and oxalic acid of *Penicillium* KB4B1 were 5 and 8 mmol/L, respectively (Fig. 2).

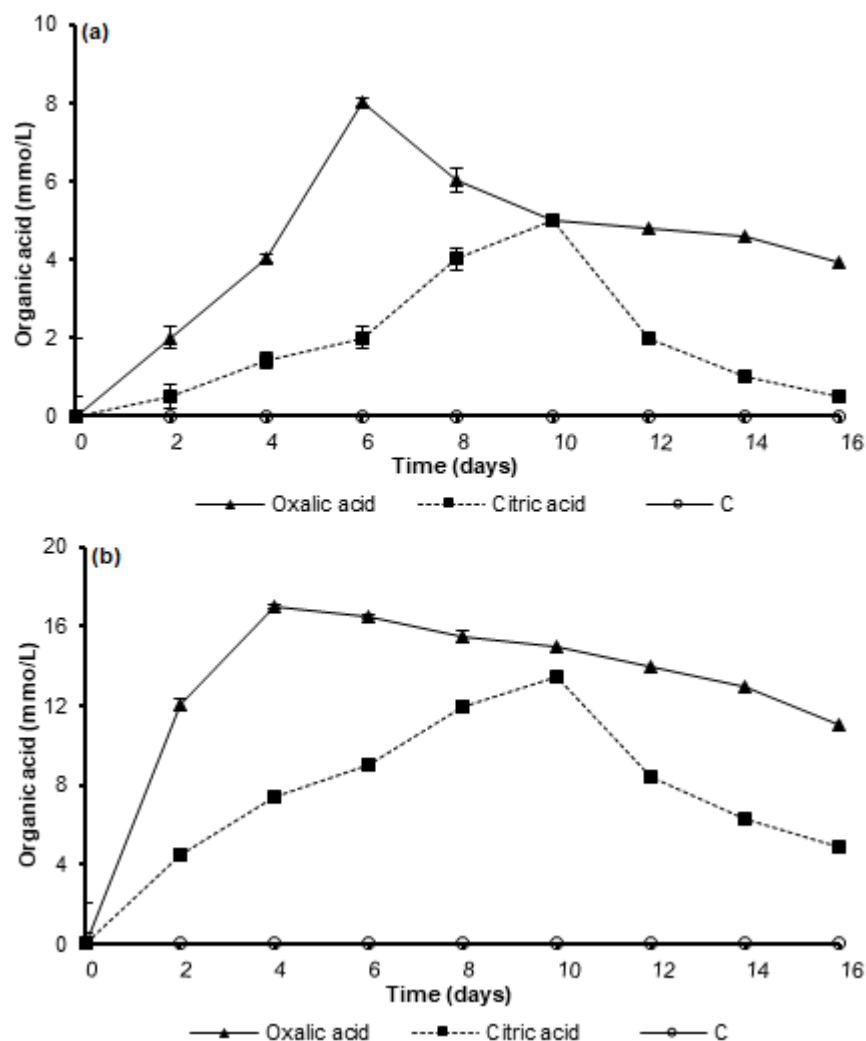


Fig 2. Organic acid production in *Penicillium* KB4B1 (a) and *Penicillium* KA2B2 (b) at pulp densities of pyrolusite of 0.02 g/cm³ in the 16-day leaching process

There were similar trends of oxalic acid and citric acid secretion in *Penicillium* KA2B2 and *Penicillium* KB4B1. Within the logarithmic growth phase of these fungi, the production of oxalic acid was highly increased, and then slowly decreased; however, a significant amount of oxalic acid remained in the medium at the end of the incubation. In contrast, the production of citric acid by both strains occurred within the stationary phase, which was characterized by a decreased rate of growth in these fungi. In comparison with pH measurements, it is clear that the increase in citric acid and oxalic acid secretion by the two strains occurred at pH values less than 3. When the pH of the medium measured was above pH 3, acid production was reduced.

Oxalic acid biosynthesis from glucose occurs when oxaloacetate is hydrolyzed to oxalate and acetate, catalyzed by cytosolic oxaloacetase, while citric acid is formed as an intermediate in a cycle of tricarboxylic acids involving a polysaccharide such as sucrose [29]. Therefore, sucrose present in the medium during the bioleaching experiment was used as a substrate by the strain for oxalic acid and citric acid biosynthesis. Glucose was first released from sucrose, then absorbed and catabolized to two molecules of pyruvate. In the following step, it was converted into oxaloacetate and acetyl-CoA, and finally, citric acid formed by condensation of these two precursors, which was then secreted from mitochondria and mycelia [30-32]. From

these results, it was clear that the increase in citric acid production by the cultures was followed by a reduction of the concentration of oxalic acid present in the cultures.

Compared to previous studies, both fungi were about 54% lower in extracting manganese than *Aspergillus niger* PTCC 5210 isolated from mining deposits in India [29]. Those fungi were also 22% lower in extracting metals than *Penicillium chrysogenum* Y5 isolated from heavy metal contaminated areas [33]. In this study, the low ability of metal extraction from both fungi due to the optimization processes of bioleaching has not been done. Optimization of the parameters that enhanced fungal bioleaching was related to their production of metabolic organic acids, including organic carbon, nitrogen, phosphorous, micronutrient ($MgSO_4$ and $MnSO_4$), and aeration.

Phenotypic Characters of Fungi

For phenotypic identification, fungal isolates were characterized according to previously researchers [24-25]. Macroscopic observations showed heterogeneity between the fungal isolates that being examined (Table 1). The data obtained exhibit that colony diameters of fungal strain KA2B2 varied over a wide range on different agar media: from 3.6 mm (CYA) to 14.3 mm (MEA). In addition, the examined fungal cultures displayed variations in surface and reverse colony colors. Strain KA2B2 had a green to the grey surface and orange to bright yellow colony color

on CYA. Its surface and reverse colony colors on MEA were green and orange to bright yellow, respectively.

Observation of fungal microscopic characters such as conidiophore branching and its elements are key to the identification of fungi. Two types of fungal conidiophores, metulae, phialides, conidia, and stipe characters, were observed (Table 2). Fungal strain KA2B2 had a mono-verticillate conidiophore branching pattern. The metulae had a compact terminal character. The type of fungal phialides was ampuliform. The conidia size was less than 10 μm , with a globose and smooth morphology. Fungal strain KB4B1 also had a mono-verticillate conidiophore branching pattern. The metulae had a tuberculate character. The fungal phialides were cylindrical and short with a wide neck. The conidia size was also less than 10 μm , with a globose and smooth morphology. Thus, based on both macroscopic and microscopic investigations, both of strain KA2B2 and KB4B1 was identified as genus *Penicillium*.

CONCLUSION

Penicillium KA2B2 isolated from Indonesian sulfurous river sediment is highly efficient for manganese extraction with a pulp density of pyrolusite of 0.02 g/cm^3 . The culture extracted manganese by producing oxalic acid and citric acid from the sucrose in the medium. These investigations indicate that oxalic acid

Table 1. Macroscopic characters of two selected fungi isolated from sulfurous river sediment

Strain	On CYA			On MEA		
	Surface colony color	Reverse colony color	Diameter (mm)	Surface colony color	Reverse colony color	Diameter (mm)
KA2B2	Green-gray	Orange to bright yellow	3.6	Green	Orange to bright yellow	14.3
KB4B1	Dark green	Green	33.3	Dark green	Yellow	33.3

Table 2. Microscopic characters of two selected fungi isolated from sulfurous river sediment

Strain	Conidiophore Branching Pattern	Metulae	Phialide	Conidia	Stipes
KA2B2	Mono-verticillate	compact terminal	Ampuliform	< 10 μm , globose, smooth-walled	Rather long, smooth-walled, vesiculate
KB4B1	Mono-verticillate	tuberculate	Cylindrical, short, and wide neck	< 10 μm , globose, smooth-walled	Relatively short

and citric acid contribute significantly to manganese leaching from pyrolusite. This strain is strongly recommended for further studies in field observations.

■ ACKNOWLEDGMENTS

This research was financially supported by KEMENRISTEK DIKTI Indonesia with the Research Implementation Letter No: 173/UN1/DITLIT/DITLIT/LT/2018. We express our thanks to technicians from Microbiology and Falitma Laboratory, Biology Faculty, and also *Laboratorium Penelitian Pusat Terpadu*, Universitas Gadjah Mada, Yogyakarta, Indonesia.

■ REFERENCES

- [1] Fonti, V., Dell'anno, A., and Beolchini, F., 2016, Does bioleaching represent a biotechnological strategy for remediation of contaminated sediments?, *Sci. Total Environ.*, 563-564, 302–319.
- [2] Pathak, A., Morrison, L., and Healy, M.G., 2017, Catalytic potential of selected metal ions for bioleaching, and potential techno-economic and environmental issues: A critical review, *Bioresour. Technol.*, 229, 211–221.
- [3] Gu, T., Rastegar, S.O., Mousavi, S.M., Li, M., and Zhou, M., 2018, Advances in bioleaching for recovery of metals and bioremediation of fuel ash and sewage sludge, *Bioresour. Technol.*, 261, 428–440.
- [4] Retnaningrum, E., and Wilopo, W., 2019, Pyrolusite bioleaching by an indigenous *Acidithiobacillus* sp. KL3 isolated from an Indonesian sulfurous river sediment, *Indones. J. Chem.*, 19 (3), 712–719.
- [5] Vázquez-Campos, X., Kinsela, A.S., Waite, T.D., Collins, R.N., and Neilan, B.A., 2014, *Fodinomyces uranophilus* gen. nov. sp. nov. and *Coniochaeta fodinicola* sp. nov., two uranium mine-inhabiting Ascomycota fungi from northern Australia, *Mycologia*, 106 (6), 1073–1089.
- [6] Ivarsson, M., Bengtson, S., and Neubeck, A., 2016, The igneous oceanic crust – Earth's largest fungal habitat?, *Fungal. Ecol.*, 20, 249–255.
- [7] Gadd, G.M., 2017, Fungi, rocks and minerals, *Elements*, 13 (3), 171–176.
- [8] Ferreira, P.C., Pupin, B., and Rangel, D.E.N., 2018, Stress tolerance of soil fungal communities from native Atlantic forests, reforestations, and a sand mining degraded area, *Fungal Biol.*, 122 (6), 400–409.
- [9] Madrigal-Arias, J.E., Argumedo-Delira, R., Alarcón, A., Mendoza-López, M.R., García-Barradas, O., Cruz-Sánchez, J.S., Ferrera-Cerrato, R., and Jiménez-Fernández, M., 2015, Bioleaching of gold, copper and nickel from waste cellular phone PCBs and computer gold finger motherboards by two *Aspergillus niger* strains, *Braz. J. Microbiol.*, 46 (3), 707–713.
- [10] Kim, M.J., Seo, J.Y., Choi, Y.S., and Kim, G.H., 2016, Bioleaching of spent Zn-Mn or Ni-Cd batteries by *Aspergillus* species, *Waste Manage.*, 51, 168–173.
- [11] Bahaloo-Horeh, N., Mousavi, S.M., and Baniasadi, M., 2018, Use of adapted metal tolerant *Aspergillus niger* to enhance bioleaching efficiency of valuable metals from spent lithium-ion mobile phone batteries, *J. Cleaner Prod.*, 197, 1546–1557.
- [12] Li, Q., Csetenyi, L., Paton, G.I., and Gadd, G.M., 2015, CaCO₃ and SrCO₃ bioprecipitation by fungi isolated from calcareous soil, *Environ. Microbiol.*, 17 (8), 3082–3097.
- [13] Grum-Grzhimaylo, A.A., Georgieva, M.L., Bondarenko, S.A., Debets, A.J.M., and Bilanenko, E.N., 2016, On the diversity of fungi from soda soils, *Fungal Divers.*, 76, 27–74.
- [14] Boldt-Burisch, K., and Naeth, M.A., 2017, Early colonization of root associated fungal communities on reclamation substrates at a diamond mine in the Canadian Sub-Arctic, *Appl. Soil Ecol.*, 110, 118–126.
- [15] Xu, H.B., Tsukuda, M., Takahara, Y., Sato, T., Gu, J.D., and Katayama, Y., 2018, Lithoautotrophical oxidation of elemental sulfur by fungi including *Fusarium solani* isolated from sandstone Angkor temples, *Int. Biodeterior. Biodegrad.*, 126, 95–102.
- [16] Gholipour, S., Mehrkesh, P., Azin, E., Nouri, H., Rouhollahi, A.A., and Moghimi, H., 2018, Biological treatment of toxic refinery spent sulfidic

- caustic at low dilution by sulfur-oxidizing fungi, *J. Environ. Chem. Eng.*, 6 (2), 2762–2767.
- [17] Şener, B., Aksoy, D.Ö., Çelik, P.A., Toptaş, Y., Koca, S., Koca, H., and Çabuk, A., 2018, Fungal treatment of lignites with higher ash and sulphur contents using drum type reactor, *Hydrometallurgy*, 182, 64–74.
- [18] Sutcliffe, B., Chariton, A.A., Harford, A.J., Hose, G.C., Greenfield, P., Midgley, D.J., and Paulsen, I.T., 2018, Diverse fungal lineages in subtropical ponds are altered by sediment-bound copper, *Fungal Ecol.*, 34, 28–42.
- [19] Mehta, K.D., Das, C., Kumar, R., Pandey, B.D., and Mehrotra, S.P., 2010, Effect of mechano-chemical activation on bioleaching of Indian Ocean nodules by a fungus, *Miner. Eng.*, 23 (15), 1207–1212.
- [20] Chiang, Y.W., Santos, R.M., Monballiu, A., Ghyselbrecht, K., Martens, J.A., Mattos, M.L.T., Van Gerven, T., and Meesschaert, B., 2013, Effects of bioleaching on the chemical, mineralogical and morphological properties of natural and waste-derived alkaline materials, *Miner. Eng.*, 48, 116–125.
- [21] Khayatian, G., Moradi, M., and Hassanpoor, S., 2018, MnO₂/3MgO nanocomposite for preconcentration and determination of trace copper and lead in food and water by flame atomic absorption spectrometry, *J. Anal. Chem.*, 73, 470–478.
- [22] Vilanova, L., Viñas, I., Torres, R., Usall, J., Buron-Moles, G., and Teixidó, N., 2014, Acidification of apple and orange hosts by *Penicillium digitatum* and *Penicillium expansum*, *Int. J. Food Microbiol.*, 178, 39–49.
- [23] Gillot, G., Jany, J.L., Poirier, E., Maillard, M.B., Debaets, S., Thierry, A., Coton, E., and Coton, M., 2017, Functional diversity within the *Penicillium roqueforti* species, *Int. J. Food Microbiol.*, 241, 141–150.
- [24] Pitt, J.I., and Hocking, A.D., 2009, *Fungi and Food Spoilage*, Springer, Boston, MA.
- [25] Visagie, C.M., Houbraken, J., Frisvad, J.C., Hong, S.B., Klaassen, C.H.W., Perrone, G., Seifert, K.A., Varga, J., Yaguchi, T., and Samson, R.A., 2014, Identification and nomenclature of the genus *Penicillium*, *Stud. Mycol.*, 78, 343–371.
- [26] Golmohammadzadeh, R., Faraji, F., and Rashchi, F., 2018, Recovery of lithium and cobalt from spent lithium ion batteries (LIBs) using organic acids as leaching reagents: A review, *Resour. Conserv. Recycl.*, 136, 418–435.
- [27] Qu, Y., Lian, B., Mo, B., and Liu, C., 2013, Bioleaching of heavy metals from red mud using *Aspergillus niger*, *Hydrometallurgy*, 136, 71–77.
- [28] Xu, T.J., Ramanathan, T., and Ting, Y.P., 2014, Bioleaching of incineration fly ash by *Aspergillus niger* – precipitation of metallic salt crystals and morphological alteration of the fungus, *Biotechnol. Rep.*, 3, 8–14.
- [29] Mohanty, S., Ghosh, S., Nayak, S., and Das, A.P., 2017, Bioleaching of manganese by *Aspergillus* sp. isolated from mining deposits, *Chemosphere*, 172, 302–309.
- [30] Panda, S.K., Mishra, S.S., Kayitesi, E., and Ray, R.C., 2016, Microbial-processing of fruit and vegetable wastes for production of vital enzymes and organic acids: Biotechnology and scopes, *Environ. Res.*, 146, 161–172.
- [31] Liu, J., Li, J., Shin, H., Liu, L., Du, G., and Chen, J., 2017, Protein and metabolic engineering for the production of organic acids, *Bioresour. Technol.*, 239, 412–421.
- [32] Yang, L., Lübeck, M., and Lübeck, P.S., 2017, *Aspergillus* as a versatile cell factory for organic acid production, *Fungal Biol. Rev.*, 31 (1), 33–49.
- [33] Xia, M.C., Bao, P., Liu, A.J., Zhang, S.S., Peng, T.J., Shen, L., Yu, R.L., Wu, X.L., Li, J.K., Liu, Y.D., Chen, M., Qiu, G.Z., and Zeng, W.M., 2018, Isolation and identification of *Penicillium chrysogenum* strain Y5 and its copper extraction characterization from waste printed circuit boards, *J. Biosci. Bioeng.*, 126 (1), 78–87.

Synthesis of Soluble Novel Polyacetylenes Containing Carbamate and Eugenol Moieties

Erwin Abdul Rahim

Department of Chemistry, Tadulako University, Jl. Sukarno-Hatta Km 9, Palu 94148, Central Sulawesi, Indonesia

* **Corresponding author:**

email: erwin_abdulrahim@yahoo.com

Received: May 4, 2019

Accepted: September 24, 2019

DOI: 10.22146/ijc.45603

Abstract: This study was aimed to synthesize a series of novel polyacetylenes containing carbamate and eugenol moieties. The polymerization of 1-(3,4-dimethoxyphenyl)propane-2-yl prop-2-ynylcarbamate (**1**), 1-(3,4-dimethoxyphenyl)propane-2-yl 3-ethynyl phenylcarbamate (**2**), 1-(3,4-dimethoxyphenyl)propane-2-yl 4-ethynylphenylcarbamate (**3**), (2S)-1-(3,4-dimethoxyphenyl)propane-2-yl 2-((prop-2ynoxy)carbonylamino)propanoate (**4**) in the presence of (nbd)Rh⁺[η⁶-C₆H₅B⁻(C₆H₅)₃] as catalyst have successfully produced corresponding polyacetylenes [poly(**1**)-poly(**4**)] in high yield. The molecular weight of the synthesized polyacetylenes ranged between 13,900–18,400 g/mol. In particular, the molecular weight of poly(**1**) could be increased by the addition of menthol. Practically, these polymers were found to have a stable helical structure and soluble in common organic solvents.

Keywords: polyacetylenes; carbamate; eugenol; Rh catalyst; helical structure

■ INTRODUCTION

Eugenol (4-allyl-2-methoxyphenol) has been recognized to approximately covering 80–90% of the clove oil weight. In fact, it is primarily produced and continued to grow in Indonesia [1-2]. In general, the eugenol compound has the molecular formula of C₁₀H₁₂O₂, which contains several functional groups, including allyl (-CH₂-CH=CH₂), phenol (-OH), and methoxy (-OCH₃). Those functional groups allow eugenol to be used as a raw material for the synthesis of other more valuable compounds. For instance, Miao et al. [3] have utilized eugenol as a bio-based heat-resistant epoxy resin. Deng et al. [4] have utilized eugenol as polymeric oil-absorbent microspheres. Meanwhile, Liu et al. [5] have applied eugenol as a bio-renewable thermosetting copolymer.

On the other hand, the helical polyacetylenes have been attracting interests due to their unique structure, chiroptical properties and potentials for being utilized in various critical applications, including as a stimuli-responsive chiral material, enantioselective catalysts, a chemical sensor, chiral discrimination, and optical crystalline material [6]. In poly(*N*-propargylamides) and poly(*N*-propargyl carbamates), the amide groups could stabilize the helical structure by an intramolecular hydrogen

bond as well as steric repulsion between their side chain(s) [7]. In other words, a combination of the steric repulsion and the strengthened intramolecular hydrogen bond will result in a far more stable helical structure.

A recent study demonstrated that poly(*N*-propargyl carbamates) containing eugenol scaffold has been successfully synthesized by using (nbd)Rh⁺[η⁶-C₆H₅B⁻(C₆H₅)₃] catalyst. In fact, the monomer is known to have a splitting methoxy group, where the corresponding polymer would have a moderate molecular weight. If recrystallization is conducted on the monomer until its methoxy group is not splitting anymore, molecular weight (*M_n*) and polydispersity index (PDI) of the monomer will significantly increase. The polymer can function as a smart material [8]. On the other hand, there is another possibility to increase the molecular weight and PDI of a novel derived eugenol having the methoxy group splitting. Shiotsuki et al. [9] revealed that the chiroptical properties of the amino acid based polyacetylenes strongly depend on their molecular weight. Therefore, this study was aimed to prepare novel polymers by introducing eugenol moiety to poly(*N*-propargyl carbamates) and phenylacetylene, which contain carbamate group. In general, this article reports the synthesis and characterization of novel polymers

from derived from eugenol, as a starting material, by utilizing $(\text{nb})\text{Rh}^+[\eta^6\text{-C}_6\text{H}_5\text{B}^-(\text{C}_6\text{H}_5)_3]$ as an effective catalyst in the polymerization of monosubstituted acetylene.

■ EXPERIMENTAL SECTION

Materials

Methyleugenol (4-allyl-2-methoxyphenyl) was provided by Indesso Co., Ltd. 1-(3,4-Dimethoxyphenyl)propane-2-ol was prepared by reacting methyl eugenol with formic acid, which would then be hydrolyzed with potassium hydroxide [10]. Besides, $(\text{nb})\text{Rh}^+[\eta^6\text{-C}_6\text{H}_5\text{B}^-(\text{C}_6\text{H}_5)_3]$ was prepared by reacting $[(\text{nb})\text{RhCl}]_2$ with $\text{NaB}(\text{C}_6\text{H}_5)_4$ [11]. While $[(\text{nb})\text{RhCl}]_2$ was provided by Aldrich, other reagents were commercially provided by Wako Pure Chemical Industries. In this study, tetrahydrofuran (THF) used for polymerization was purified by applying a standard purification procedure.

Instrumentation

The ^1H and ^{13}C NMR spectra were recorded in chloroform-*d* (CDCl_3) on a JEOL EX-400 spectrometer. The IR spectra, on the other hand, were measured by applying a Shimadzu FTIR-8100 spectrophotometer. Furthermore, the melting points were determined with a Yanaco micro melting point apparatus. Carlo Erba 1106 was applied in this study as an elemental analyzer, while Jasco J-810 spectropolarimeter was used to record Circular Dichroism (CD) spectra. The specific rotation $[\alpha]_D$ values were measured on a Jasco DIP-1000 digital polarimeter with a sodium lamp as the light source. The number-average molecular weight (M_n) and weight-average molecular weight (M_w) were estimated by using gel permeation chromatography (GPC) with Shodex K804, K805, and K806 columns eluted with THF as an eluent, polystyrene calibration, refractive-index, and UV detectors.

Procedure

Synthesis of monomers

1-(3,4-Dimethoxyphenyl)propane-2-yl prop-2-ynyl carbamate (1). First, 1-(3,4-dimethoxyphenyl)propane-2-ol (19.6 g, 0.1 mol, 1 equiv.) was added to a solution of tryphosgene (25 g, 0.1 mol 1 equiv.) in dry ether (200 mL) at 0 °C, and the resulting mixture was stirred at the same temperature for 1 h. Next, propargylamide (7.97 g, 0.1 mol,

1 equiv.) was added to the mixture, and the mixture was continuously stirred at 0 °C overnight. After that, a white precipitate was filtered off, and the filtrate was concentrated. Ethyl acetate (100 mL) was later added to the residue. The organic phase was washed with 2 M HCl, saturated with aqueous NaHCO_3 , dried over MgSO_4 , and then concentrated. In the end, monomer **1** was isolated and purified by applying column chromatography with silica gel as solid adsorbent, which was then eluted by using 3/2 (v/v) *n*-hexane/ethyl acetate to form a white solid. Yield: 25%; mp 90–93 °C; $[\alpha]_{D20} = 0^\circ$ ($c = 0.1$ g/dL in CDCl_3). ^1H NMR (400 MHz, CDCl_3 , δ): 1.21–1.37 (m, 3H, CH_3), 2.22 (s, 1H; $\equiv\text{CH}$), 2.53–2.89 (d, $J = 3.4$ Hz, 2H, $-\text{CH}_2\text{-Ar}$), 3.86 (d, $J = 3.4$ Hz, OCH_3), 4.17 (s, 1H, $-\text{NHCO}-$), 4.98–5.02 (m, 2H, $-\text{CH}-$), 6.23 (s, 1H, $-\text{CH}_2\text{-NH}-$), 6.71–6.80 (m, 3H, Ar); ^{13}C NMR (400 MHz, CDCl_3 , δ): 17.1, 19.0, 32.8, 42.3, 53.1, 56.3, 68.3, 71.6, 80.4, 114.9, 115.2, 121.6, 144.9, 147.7, 132.1, 157.5, 175.7; IR (KBr, cm^{-1}): 3320 (N-H), 3291 (H-C \equiv), 1660 (C=O); Anal. calcd. for $\text{C}_{18}\text{H}_{24}\text{N}_2\text{O}_5$: C, 64.97%; H, 6.91%; N, 5.05%; found: C 64.90%, H 6.93%, N 7.73%.

1-(3,4-Dimethoxyphenyl)propane-2-yl 3-ethynyl phenylcarbamate (2). This compound **2** was synthesized from 3-ethynylaniline in a similar manner to **1**. It was later isolated and purified by using column chromatography with silica gel as solid adsorbent, and then eluted by using 3/2 (v/v) hexane/ethyl acetate to form a colorless liquid.

Yield: 30%; bp 185 °C; $[\alpha]_{D20} = 0^\circ$ ($c = 0.1$ g/dL in CDCl_3); ^1H NMR (400 MHz, CDCl_3 , δ): 1.35–1.37 (d, 3H, CH_3), 2.66–2.92 (d, $J = 3.4$ Hz, 2H; $-\text{CH}_2\text{-Ar}$), 3.83 (d, $J = 12.7$ Hz, 6H; OCH_3), 4.05 (s, 1H, CH), 4.52 (s, 1H, CH), 6.74–7.81 (m, 7H, Ar), 9.86 (s, 1H, NH); ^{13}C NMR (400 MHz, CDCl_3 , δ): 21.1, 42.9, 56.1, 71.6, 81.4, 82.3, 112.5, 121.3, 121.4, 112.5, 121.4, 122.9, 126.4, 127.9, 128.5, 130.0, 135.5, 147.1, 152.3, 149.9; IR (CHCl_3 , cm^{-1}): 3322 (N-H), 3290 (H-C \equiv), 1661 (C=O); Anal. calcd. for $\text{C}_{20}\text{H}_{21}\text{NO}_4$: C, 70.78%, H 6.24%, N 4.13%; found: C 70.75%, H 6.25%, N 4.12%.

1-(3,4-Dimethoxyphenyl)propane-2-yl 4-ethynyl phenylcarbamate (3). This compound **3** was synthesized from 4-ethynylaniline in a similar manner to **1**. It was later isolated and purified by applying

column chromatography with silica gel as solid adsorbent, and then eluted by using 3/2 (v/v) hexane/ethyl acetate to form a brown solid.

Yield: 20%; mp/bp 20 °C; $[\alpha]_{D20} = 0^\circ$ ($c = 0.1$ g/dL in $CDCl_3$); 1H NMR (400 MHz, $CDCl_3$, δ): 1.35–1.37 (d, 3H, CH_3), 2.66–2.92 (d, $J = 3.4$ Hz, 2H; $-CH_2-Ar$), 3.83 (d, $J = 4.9$ Hz, 6H; OCH_3), 4.05 (s, 1H, CH), 4.52 (s, 1H, CH), 6.74–7.81 (m, 7H, Ar), 9.86 (s, 1H, NH); ^{13}C NMR (400 MHz, $CDCl_3$, δ): 21.1, 42.9, 56.1, 71.6, 81.4, 82.3, 112.5, 121.3, 121.4, 112.5, 121.4, 122.9, 126.4, 127.9, 128.5, 130.0, 135.5, 147.1, 152.3, 149.9; IR (KBr, cm^{-1}): 3323 (N-H), 3290 (H-C \equiv), 1660 (C=O); Anal. calcd. for $C_{20}H_{21}NO_4$: C, 70.78%, H 6.24%, N 4.13%; found: C 70.79%, H 6.26%, N 4.15%.

(2S)-1-(3,4-Dimethoxyphenyl)propane-2-yl 2-((prop-2-ynyl)carbonylamino)propanoate (4). This compound **4** was synthesized from (S)-2-amino-N-(prop-2-ynyl)propanamide in a similar manner to **1**, in which 1-(3-dimethylaminopropyl)-3-ethyl carbodiimide hydrochloride (EDC.HCl) was applied as a condensing agent. It was later isolated and purified by column chromatography with silica gel as solid adsorbent, and then eluted by using 3/2 (v/v) hexane/ethyl acetate to form a colorless liquid.

Yield: 25%; mp/bp 180 °C; $[\alpha]_{D20} = -7.5^\circ$ ($c = 0.1$ g/dL in $CDCl_3$); 1H NMR (400 MHz, $CDCl_3$, δ): 1.22–1.38 (m, 6H, CH_3), 2.66–2.92 (d, $J = 3.4$ Hz, 2H; $-CH_2-Ar$), 3.83 (d, $J = 4.9$ Hz, 6H; OCH_3), 4.05 (s, 1H, CH), 4.52 (s, 1H, CH), 6.74–7.81 (m, 7H, Ar), 9.86 (s, 1H, NH); ^{13}C NMR (400 MHz, $CDCl_3$, δ): 21.1, 42.9, 56.1, 71.6, 81.4, 82.3, 112.5, 121.3, 121.4, 112.5, 121.4, 122.9, 126.4, 127.9, 128.5, 130.0, 135.5, 147.1, 152.3, 149.9; IR ($CHCl_3$, cm^{-1}): 3323 (N-H), 3290 (H-C \equiv), 1660 (C=O); Anal. calcd. for $C_{18}H_{23}NO_6$: C, 61.88%, H 6.64%, N 4.01%; found: C, 61.89%, H 6.66%, N 4.02%.

Polymerization of monomers 1-4

In this process, a monomer solution ($[monomer] = 0.1$ M) in THF was added to $(nbd)Rh^+[\eta^6-C_6H_5B^-(C_6H_5)_3]$ solution ($[monomer]/[Rh] = 50$) under nitrogen, and it was kept at 30 °C for 1 h. The resulting solution was later poured into *n*-hexane (600 mL) to precipitate a polymer. Next, it was isolated by filtration, which was then dried under a reduced pressure to form a powder.

Polymerization with the addition of menthol

Menthol (1% weight) was added to the monomer solution ($[monomer] = 0.1$ M) in THF. Next, the mixture was added into $(nbd)Rh^+[\eta^6-C_6H_5B^-(C_6H_5)_3]$ solution ($[monomer]/[Rh] = 50$) under nitrogen atmosphere, and then kept at 30 °C for 1 h. The produced solution was later poured into *n*-hexane (600 mL) to precipitate a polymer. Then, it was isolated by using the filtration process, which was followed by a drying process under reduced pressure to form a powder.

Spectroscopic data of the polymers

Poly(1). 1H NMR (400 MHz, $CDCl_3$, δ): 1.09–1.33 (m, 3H, CH_3), 2.53–2.92 (m, 2H, $-CH_2-Ar$), 4.24 (s, 1H, $-NHCO-$), 4.89 (s, 1H, $-CH-CH_3$), 6.59–6.65 (m, 5H, $-CH=C$, NH, Ar); IR ($CHCl_3$): 3430 (N-H), 2980, 2950, 2650 (C=O), 1561.

Poly(2). 1H NMR (400 MHz, $CDCl_3$, δ): 1.35–1.37 (d, 3H, CH_3), 2.66–2.92 (d, $J = 3.4$ Hz, 2H; $-CH_2-Ar$), 3.83 (d, 6H; OCH_3), 4.05 (s, 1H, CH), 5.52 (s, 1H, NH), 6.74–7.81 (m, 7H, Ar); IR ($CHCl_3$): 3432 (N-H), 1733 (C=O), 1512.

Poly(3). 1H NMR (400 MHz, $CDCl_3$, δ): 1.35–1.37 (d, 3H, CH_3), 2.66–2.92 (d, $J = 3.4$ Hz, 2H; $-CH_2-Ar$), 3.83 (d, 6H; OCH_3), 4.05 (s, 1H, CH), 5.55 (s, 1H, NH), 6.74–7.81 (m, 7H, Ar); IR ($CHCl_3$): 3431 (N-H), 17.33 (C=O), 1514.

Poly(4). 1H NMR (400 MHz, $CDCl_3$, δ): 1.09–1.36 (m, 6H, CH_3), 2.64–2.86 (m, 2H, $-CH_2-CH-$), 3.79 (s, 8H, OCH_3 , $CH=CCH_2$), 4.24 (s, 1H, $-CH-NH-$), 4.68 (s, 1H, $-CH-CH_2-Ar$), 5.02 (s, 1H, $-NH$), 6.38 (s, 1H, $-CH=$), 6.65–6.70 (m, 3H, Ar); IR ($CHCl_3$): 3430 (N-H), 1732 (C=O), 1510.

RESULTS AND DISCUSSION

Synthesis of Monomers

The synthetic routes for novel monomers **1-4** was displayed in Fig. 1. First, eugenol derivative was transformed into monomers **1-4** in moderate yield. In addition to elemental analysis, the monomers were identified by 1H NMR and ^{13}C NMR in IR spectroscopy. Apparently, the IR spectra of all monomers showed absorbances from carbamates at 3300–3500 cm^{-1} (N-H) and 1661–1750 cm^{-1} (C=O). The characteristic absorption

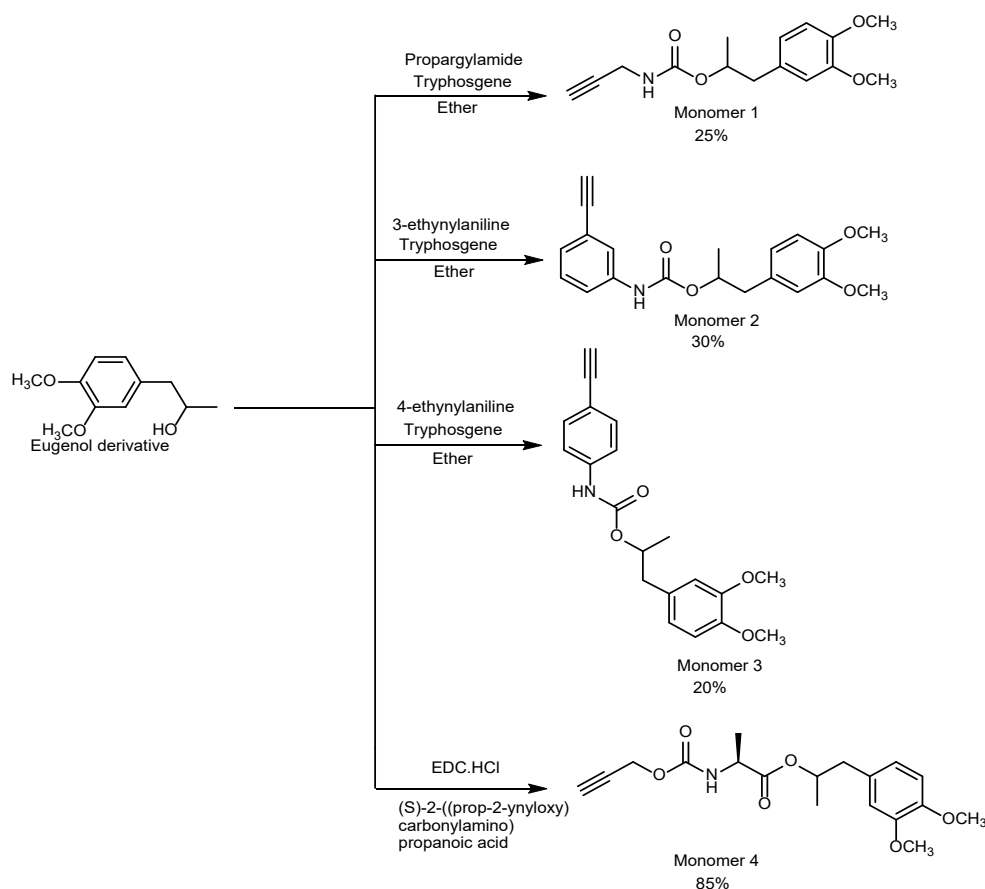


Fig 1. Synthesis of monomers 1-4

of H-C \equiv stretched appeared at 3290 cm⁻¹, while the absorption at 2169 cm⁻¹ showed C \equiv C stretching groups. Furthermore, confirmation of monomer 1-4 structures was conducted by applying ¹H NMR analysis. In fact, the hydrogen resonance at 2.20 ppm showed protons from triple-bond acetylene from monomers. In addition, resonance at about 1.50 and 4.80 ppm showed hydrogen atoms from CH₃ and CH from eugenol derivatives. The resonance at 3.3 ppm was experiencing splitting, which was typical for the methoxy group of eugenol derivative (Fig. 3). In addition, the ¹³C NMR shows the present peak for H-C \equiv , and elemental analyses indicated the monomers had been successfully synthesized.

Polymerization

The polymerization of monomers 1-4 by applying (nbd)Rh⁺[η^6 -C₆H₅B⁻(C₆H₅)₃] catalyst, which was particularly effective for the polymerization of monosubstituted acetylenes [12-19], gave the

corresponding poly (1)-(4) in very good yields (Fig. 2). Based on FTIR analysis, the disappearance of absorption for H-C \equiv and C \equiv C at 3390 and 2169 cm⁻¹, showed that triple-bonds from monomers to be completely polymerized. Moreover, the proton resonance of acetylene at 2.22 ppm was, in fact, not visible, showing that polymerization had taken place (Fig. 3). Other polymers poly(1-3)s showed a similar spectra. Practically, polymerizations of 1-4 with the application of Rh catalyst gave the corresponding polymers with molecular weights ranging from 13,900–18,400 g/mol (Table 1).

It is interesting to note that the molecular weight of poly(1) (13,900 g/mol) could be increased by the addition of menthol (Fig. 4). As a matter of fact, this study was the first to report the addition of menthol into (nbd)Rh⁺[η^6 -C₆H₅B⁻(C₆H₅)₃] catalyst to significantly increase molecular weight in high quantitative yield (\approx 99%). Monomer 1 was observed to be in a splitting methoxy group, hence the molecular weight of the resulting polymer could be

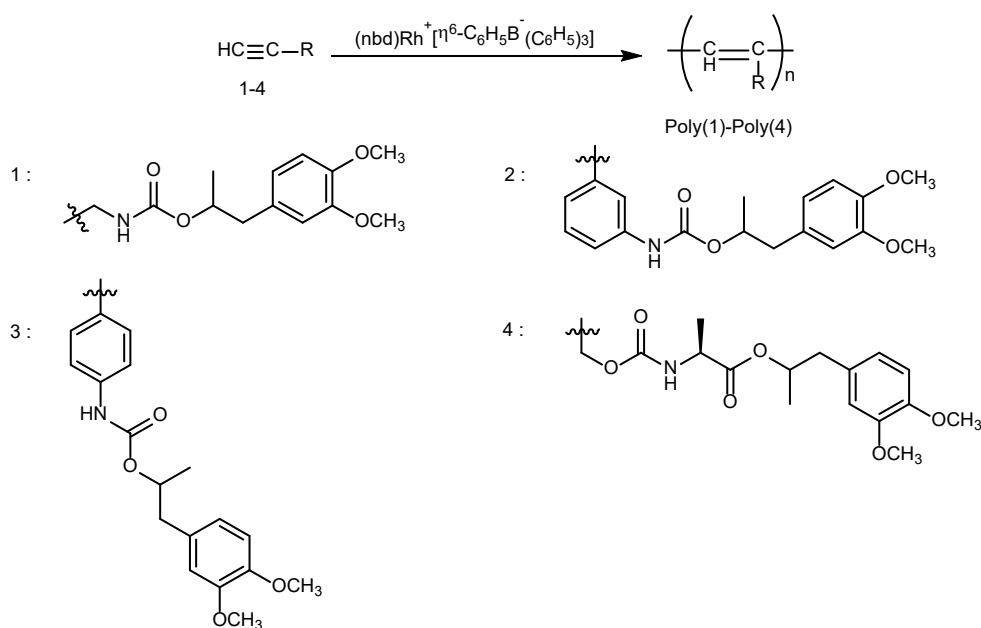


Fig 2. Synthesis of poly(1)-poly(4) using Rh catalyst

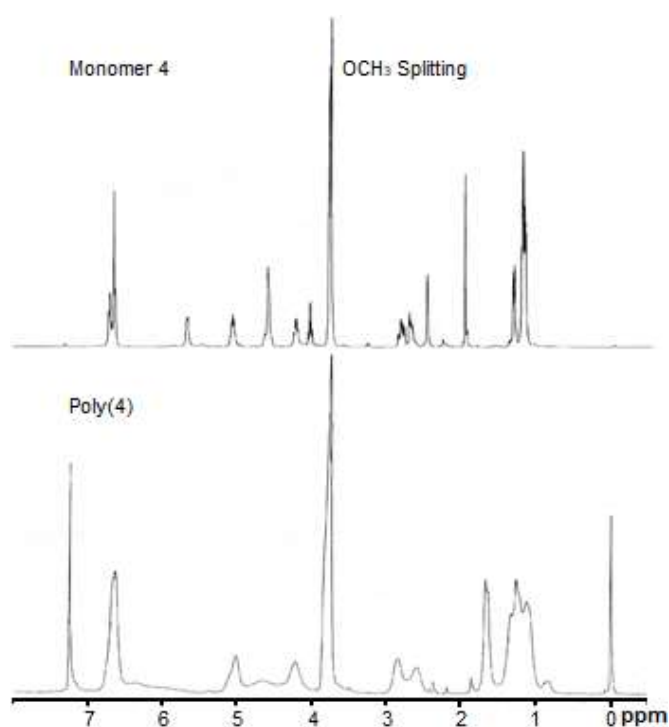


Fig 3. ^1H -NMR spectra of monomer 4 and poly(4)

technically increased. In the work of Rahim [8], the recrystallizing monomer to produce no splitting methoxy group had been proven to increase its molecular weight and PDI significantly. Practically, the addition of menthol may induce the recrystallization of monomer 1; hence, its

Table 1. Polymerization of 1-4 with the application of $[(\text{nbd})\text{Rh}^+[\eta^6\text{-C}_6\text{H}_5\text{B}^-(\text{C}_6\text{H}_5)_3]]^a$

Monomer	Polymer			
	Yield	M_n^c	M_w/M_n^c	$[\alpha]_D^{25}$ ^d
1	99	13,900	1.6	0
2	98	18,400	2.4	0
3	97	18,200	2.5	0
4	98	16,400	1.7	350

^a) polymerization conditions $\rightarrow [M]_0 = 0.1 \text{ M}$ in THF; $(\text{nbd})\text{Rh}^+[\eta^6\text{-C}_6\text{H}_5\text{B}^-(\text{C}_6\text{H}_5)_3] = 2 \text{ mM}$; $[M]_0/[\text{Rh}] = 50$; $T = 30 \text{ }^\circ\text{C}$; $t = 1 \text{ h}$

^b) *n*-hexane-insoluble part

^c) determined by GPC (THF elution and polystyrene standards)

^d) measured by polarimetry (concentration = 1 g/dL, CHCl_3)

molecular weight and PDI would significantly increase. From the technical point of view, it would be easier to synthesize the polymer, while the time required to conduct the synthesis would be faster compared to the typical method without recrystallization. In the current situation, rationales behind this finding have not been clear; hence, it requires further works.

Poly(*N*-propargylamides) and poly(*N*-propargyl carbamates) were found to be less stable, which unfortunately limited their applications [7]. In fact, applying an appropriate substituent would increase the stability of their helix. This study found that eugenol may be potentially used as the appropriate substituent. In

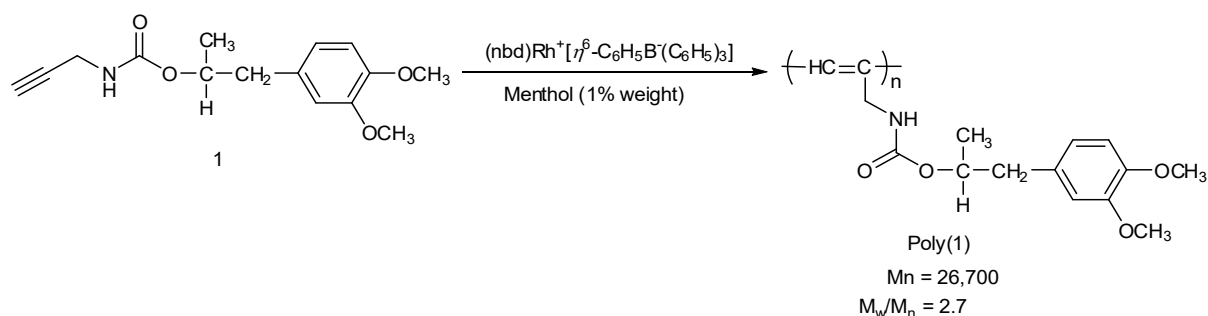


Fig 4. Synthesis of poly(1) in the presence of menthol

Table 2. Solubility of poly(1)-poly(4) in various solvent^a

Solvent	CH ₂ Cl ₂	CHCl ₃	THF	Acetone	Benzene	Toluene	DMF	DMSO	Hexane
Poly(1)	O	O	O	O	O	O	O	O	x
Poly(2)	O	O	O	O	O	O	O	O	x
Poly(3)	O	O	O	O	O	O	O	O	x
Poly(4)	O	O	O	O	O	O	O	O	x

^a O = soluble; x = insoluble (3.0 mg of polymer/1 mL of solvent)

general, the helix content could be tuned by adjusting temperature [9]. In this work, poly(4) showed a large specific rotation, which was indicated by a one-handed helical structure. Meanwhile, poly(1), poly(2), and poly(3) showed no specific rotation, which indicated their helical structures to have a racemic form. In fact, poly(1)-poly(3) were observed to contain eugenol moieties in a racemic form, resulting in 0 (zero) specific rotation. Meanwhile, poly(4) was revealed to contain an optically-active substituent (L-Alanine), and its main chain of polymer helix was stabilized by hydrogen bonding, hence resulting in a very large specific rotation ($[\alpha]_D = -350^\circ$).

Solubility of Polymers

Table 2 shows that poly(1)-poly(4) have very good solubility in various organic solvents. In other words, these polymers could completely dissolve in common solvents, including CH₂Cl₂, CHCl₃, THF, Acetone, Benzene, Toluene, DMF, and DMSO. However, they would not be soluble in *n*-hexane.

The solubility of monosubstituted polyacetylene was, in fact, dependent on their substituent. The poor solubility of monosubstituted polyacetylene could be attributed to the rigid structure and stronger hydrogen bonding strength. As an example, poly(*N*-propargylamides) containing azobenzene and fluorene moieties was not soluble in acetone, benzene, toluene, DMF, or hexane

[7,10]. Thus, polyacetylenes had various drawbacks in their applications. They were particularly insoluble in solvents, making it essentially impossible to process these materials [20]. To address the problem, this study demonstrated that the introduction of the eugenol derivative scaffold might improve the polymer solubility; hence, it would be easily processed.

CONCLUSION

Polymerization of a monomer containing carbamate and eugenol scaffolds in the presence of [(nbd)Rh⁺[η⁶-C₆H₅B-(C₆H₅)₃]] catalyst gave the corresponding polymers in high yields with the molecular weight ranging from 13,900–18,400 g/mol. Besides, adding menthol to the catalyst has successfully increased molecular weight of the polymers. The polymers were found to be soluble in common organic solvents and have a stable helical structure.

ACKNOWLEDGMENTS

The author thanks the Faculty of Mathematics and Natural Science, Tadulako University, Indonesia, for their support during this research.

REFERENCES

- [1] Rahim, E.A., Sanda, F., and Masuda, T., 2004, Synthesis and properties of novel polyacetylene

- containing eugenol moieties, *J. Macromol. Sci. Part A Pure Appl. Chem.*, 41 (2), 133–141.
- [2] Rahim, E.A., Sanda, F., and Masuda, T., 2004, Synthesis and properties of novel eugenol-based polymers, *Polym. Bull.*, 52 (2), 93–100.
- [3] Miao, J.T., Yuan, L., Guan, Q., Liang, G., and Gu, A., 2017, Biobased heat resistant epoxy resin with extremely high biomass content from 2,5-furandicarboxylic acid and eugenol, *ACS Sustainable Chem. Eng.*, 5 (8), 7003–7011.
- [4] Deng, J., Yang, B., Chen, C., and Liang, J., 2015, Renewable eugenol-based polymeric oil-absorbent microspheres: preparation and oil absorption ability, *ACS Sustainable Chem. Eng.*, 3 (4), 599–605.
- [5] Liu, K., Madbouly, S.A., and Kessler, M.R., 2015, Biorenewable thermosetting copolymer based on soybean oil and eugenol, *Eur. Polym. J.*, 69, 16–28.
- [6] Ohsawa, S., Sakurai, S., Nagai, K., Maeda, K., Kumaki, J., and Yashima, E., 2012, Amplification of macromolecular helicity of dynamic helical poly(phenylacetylene)s bearing non-racemic alanine pendants in dilute solution, liquid crystal and two-dimensional crystal, *Polym. J.*, 44, 42–50.
- [7] Zhang, J., Ren, X., Li, S., and Huang, W., 2014, Synthesis and conformational study of novel, stable, helical poly(*N*-propargylamides) containing dipole azobenzene chromophores in the side chain, *Polym. Bull.*, 71 (11), 2803–2818.
- [8] Rahim, E.A., 2018, Unique polymerization and new smart material of eugenol-based helical polymers, *Int. J. Sci. Res.*, 7 (11), 990–996.
- [9] Shiotsuki, M., Kumazawa, S., Onishi, N., and Sanda, F., 2011, Molecular weight dependence of helical conformation of amino acid-based polyphenyl acetylenes, *J. Polym. Sci., Part A: Polym. Chem.*, 49 (22), 4921–4925.
- [10] Rahim, E.A., Sanda, F., and Masuda, T., 2006, Synthesis and properties of optically active amino acid-based polyacetylenes bearing eugenol and fluorene moieties, *J. Polym. Sci., Part A: Polym. Chem.*, 44 (2), 810–819.
- [11] Schrock, R.R., and Osborn, J.A., 1970, π -Bonded complexes of the tetraphenylborate ion with rhodium(I) and iridium(I), *Inorg. Chem.*, 9 (10), 2339.
- [12] Masuda, T., 1997, "Acetylene polymerization" in *Catalysis in Precision Polymerization*, Eds. Kobayashi, S., Wiley, Chichester, 67–97.
- [13] Masuda, T., 1996, "Acetylenic polymer" in *Polymeric Material Encyclopedia*, Eds. Salamone, J.C., CRC Press, New York, 32–40.
- [14] Karim, S.M.A., Nomura, R., Kajii, H., Hidayat, R., Yoshino, K., and Masuda, T., 2000, Synthesis and properties of a soluble and widely conjugated polyethylene having antryl pendant, *J. Polym. Sci., Part A: Polym. Chem.*, 38 (S1), 4717–4723.
- [15] Sone, T., Asako, R., Masuda, T., Tabata, M., Wada, T., and Sasabe, H., 2001, Polymerization of *o*-trifluoromethyl(phenylacetylene) initiated by [Rh(norbornadiene)Cl]₂ and MoOCl₄-*n*-Bu₄Sn-EtOH catalysts. Formulation of order and disorder trans sequences, *Macromolecules*, 34 (6), 1586–1592.
- [16] Shiotsuki, M., Sanda, F., and Masuda, T., 2011, Polymerization of substituted acetylenes and features of the formed polymers, *Polym. Chem.*, 2 (5), 1044–1058.
- [17] Tabata, M., Sone, T., and Sadahiro, Y., 1999, Precise synthesis of monosubstituted polyacetylenes using Rh complex catalysts. Control of solid structure and π -conjugation length, *Macromol. Chem. Phys.*, 200 (2), 265–282.
- [18] Tabata, M., Mawatari, Y., Sone, T., Yonemoto, D., Miyasaka, A., Fukushima, T., and Sadahiro, Y., 2002, Synthesis of helical substituted polyacetylenes using rhodium complex catalyst-color control through the columnar formation, *Kobunshi Ronbunshu*, 59 (4), 168–177.
- [19] Kishimoto, Y., Itou, M., Miyatake, T., Ikariya, T., and Noyori, R., 1995, Polymerization of monosubstituted acetylenes with a zwitterionic Rhodium (I) complex, (nbd)Rh⁺[η 6-C₆H₅B⁻(C₆H₅)₃], *Macromolecules*, 28 (19), 6662–6666.
- [20] Rahim, E.A., and Sanda, F., 2019, Synthesis and functionality of eugenol-based polyacetylenes, *J. Phys. Conf. Ser.*, 1242, 012003.

Optimization and Characterization of Wood Vinegar Produced by *Shorea laevis* Ridl Wood Pyrolysis

Hasan Ashari Oramahi^{1*}, Tsuyoshi Yoshimura², Elvi Rusmiyanto³, and Kustiati³

¹Faculty of Forestry, University of Tanjungpura, Jl. Daya Nasional, Pontianak 78124, Indonesia

²Research Institute for Sustainable Humanosphere (RISH), Kyoto University, Uji, 611-0011 Kyoto, Japan

³Faculty of Mathematics and Natural Sciences, University of Tanjungpura, Jl. Prof. Dr. H. Hadari Nawawi, Pontianak 78124, Indonesia

* **Corresponding author:**

email: oramahi@fahutan.untan.ac.id

Received: May 14, 2019

Accepted: July 5, 2019

DOI: 10.22146/ijc.45783

Abstract: In this study, the Box-Behnken Design (BBD) was employed to investigate the effects of wood particle size, pyrolysis temperature, and pyrolysis time on the production of wood vinegar from the Indonesian “bengkirai” wood (*Shorea laevis* Ridl). Characterization of wood vinegar was conducted by gas chromatography-mass spectrometry (GC-MS). Three variable designs consisting of wood particle size (2.00, 2.38, and 3.36 mm), pyrolysis temperature (350, 400, and 450 °C), and pyrolysis time (105, 120, and 135 min) were employed in a BBD response surface methodology (RSM-BBD). RSM-BBD results suggested that maximum wood vinegar yield would be obtained with a wood particle size of 3.85 mm, pyrolysis temperature of 400 °C, and pyrolysis time of 93 min. In addition, the mathematical model indicated the maximum wood vinegar yield would be 30.31%. The main compounds in wood vinegar were acetic acid, 1-hydroxy-2-propanone, furfural, 2,3-pentanedione, phenol, 2-methoxy phenol, 2-methoxy-4-methyl phenol, 2,6-dimethoxy phenol, and 1,2,4-trimethoxybenzene.

Keywords: wood vinegar; *Shorea laevis*; response surface methodology; Box-Behnken design; pyrolysis temperature; wood particle size

■ INTRODUCTION

Wood vinegar, also known as pyroligneous acid, is a yellowish or dark brown condensate prepared from a wood or biomass carbonization process at a high temperature in the absence of oxygen [1]. Wood vinegar has been widely used as herbicide, insecticide, and fungicide [2-3]. For example, Hagner et al. [3] reported that wood vinegar from willow (*Salix* sp.) had insecticidal activity against *Rhopalosiphum padi*. Various studies have been reported about the effects of different types of wood, wood particle size (particle size), pyrolysis temperature and time on the yield of wood vinegar [4-7].

The wood types and pyrolysis temperature are primary factors for wood vinegar yield [7-8]. For example, Ma et al. [9] reported that wood vinegar yield from *Rosmarinus officinalis* leaves was 25%, whereas those from *Eucalyptus urograndis* and *Mimosa tenuiflora* wood

were 37.8 and 30.5%, respectively [10]. Ratanapisit et al. [11] found that the maximum wood vinegar yield from rubber wood at a pyrolysis temperature of 550 °C was 27.45%.

The response surface methodology (RSM) is a collection of mathematics- and statistics-based techniques that are useful for modeling and analysis of the effects of several independent variables, as well as the interactions between them. Its objectives are to optimize the response [12]. RSM has been successfully used to maximize wood vinegar yield from *Euphorbia rigida* [13] and palm kernel [14] by fast pyrolysis. Optimization of operating parameters and process of wood vinegar from *Acacia mangium* was studied by Crespo et al. [6], who found that optimum pyrolysis conditions were obtained at a temperature, heating rate, and particle size of 499.57 °C, 12 °C min⁻¹ and 0.46 mm, respectively, for

a yield of 33.13%. Ngo et al. [14] used the RSM to study the effect of feedstock feed rate, the particle size of biomass, the temperature of pyrolysis, and residence time on the fast pyrolysis of palm kernel; the optimal wood vinegar yield was 49.50%.

However, the wood vinegar made from *Shorea laevis* has not previously been tested for optimization of production and characterization. The Indonesian “bengkirai” wood has been used as a raw material in the home furniture industry, especially in West Kalimantan. The home furniture industry produces a huge volume of waste sawdust from wood. Therefore, the utilization of “bengkirai” sawdust to produce value-added materials would contribute to not only reducing waste but also to support local communities. The aim of this study was to predict the maximum yield of wood vinegar from the Indonesian “bengkirai” wood using the RSM-BBD. The chemical composition of wood vinegar was evaluated using gas chromatography-mass spectrometry (GC-MS).

EXPERIMENTAL SECTION

Materials

The material was collected from a home furniture industry in Pontianak, Indonesia, converted into wood meals by a Willey mill and then air dried until reaching a moisture content of 12.5%. The particle sizes of wood wastes were 2.00 mm (mesh number 10), 2.38 mm (mesh number 8), and 3.36 mm (mesh number 6).

Procedure

Pyrolysis of wood and experimental design

Pyrolysis of wood particles was conducted following the method described in Tranggono et al. [15] and Oramahi et al. [16]. The pyrolysis scheme in this study can be seen in Fig. 1. Particles were placed in a closed reactor that was then heated to the desired temperature of 350,

400, and 450 °C, for pyrolysis times of 105, 120, and 135 min, for 15 runs. The optimization procedure was designed based on a three-factor inscribed BBD with independent variables consisting of particle size: 2.00 mm, 2.38 mm, and 3.36 mm; pyrolysis temperature: 350, 400 and 450 °C; and pyrolysis time: 105, 120 and 135 min, using three levels of each variable for a total of 15 runs, as shown in Table 1 and 2.

BBD was applied to optimize wood-vinegar yield made from *Shorea laevis*. Particle size (X_1), pyrolysis temperature (X_2), and pyrolysis time (X_3) were the selected independent variables (Table 1). These variables were coded as a low, medium, or high for the RSM design points. As already mentioned, we used a BBD design for the experiment to regard the influence of the independent variables on the response [17-18].

For optimal point prediction, the second-order polynomial equation was:

$$Y = \beta_0 + \sum_{i=1}^k \beta_i X_i + \sum_{i=1}^k \beta_{ii} X_i^2 + \sum_{i,j} \beta_{ij} X_i X_j + \varepsilon \quad (1)$$

where X_i , X_j are the independent variables and β_0 , β_i , β_{ii} , and β_{ij} are the regression coefficients [18-19]. To examine the predictive value, both formula's minimum and maximum values were used for canonical analysis.

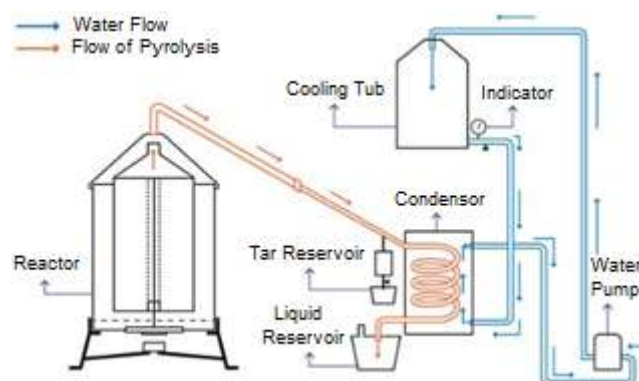


Fig 1. Pyrolysis device series scheme

Table 1. The level of the variable used for the Box-Behnken Design

Independent Variable	Symbol	Coded variable level		
		Low	Center	High
Wood particle size (mm)	X_1	-1	0	1
Pyrolysis temperature (°C)	X_2	2.00	2.38	3.36
Pyrolysis time (min)	X_3	350	400	450
		105	120	135

Table 2. The Box-Behnken design of the observed responses and predicted value for the wood vinegar yield from *Shorea laevis*

Run	X ₁	X ₂	X ₃	Wood vinegar yield (%)	
				Observed	Predicted
1	-1	-1	0	5.89	8.22
2	-1	1	0	30.89	32.10
3	1	-1	0	28.89	27.68
4	1	1	0	34.44	32.01
5	-1	0	-1	25.33	23.00
6	-1	0	1	26.00	24.69
7	1	0	-1	28.89	30.19
8	1	0	1	34.44	36.77
9	0	-1	-1	17.56	17.46
10	0	-1	1	23.33	22.21
11	0	1	-1	31.00	32.12
12	0	1	1	35.56	25.66
13	0	0	0	26.67	28.37
14	0	0	0	29.11	28.37
15	0	0	0	29.33	28.37

The ANOVA for the response of the surface quadratic model and the statistical significance of influence was analyzed by F-tests. The significance of each term was calculated using both the F-value and Prob > F values, and larger F-values indicated the term was significant [12,20].

Characterization of wood vinegar

Wood vinegar compound, retention time (RT), the relative percentage of the area from *S. laevis* Ridl were characterized using GC-MS (Shimadzu Manufacturing Co. Ltd, Kyoto, Japan, QP-210S). The GC-MS analysis conditions were as follows: capillary columns (DB-624); 30 m × 0.25 mm; temperature of injection: 250 °C; column temperature program: 60–200 °C and He flow rate: 40.0 mL/min. The GC-MS was arranged in the electron ionization mode at 70 eV with an interface temperature of 200 °C. Samples (1 µL) were injected into a column and kept at 60–200 °C with an increasing rate of 5 °C/min. The compounds were identified by comparison with the standard library data [16,21] and calculated by the integrated peak areas.

Statistical analysis

Statistica (version 6.0) and SAS (version 8.2, SAS

Institute Inc., NC, USA) were used for the analysis of the results of the BBD.

RESULTS AND DISCUSSION

Maximizing the Yield of Wood Vinegar from Indonesian “Bengkirai” Wood

To determine the best combination of particle size (X₁), pyrolysis temperature (X₂), and pyrolysis time (X₃) within the range of 2.00–3.36 mm, 350–450 °C, and 105–135 min, respectively, trials were designed based on a BBD. To maximize the wood vinegar yield, combinations of independent variables were selected (Table 2).

The stationer points in wood vinegar production were 3.85 mm for particle size (1.50), 400 °C for pyrolysis temperature (0.05), and 93 min for pyrolysis time (-1.82). The calculated maximum wood vinegar yield was 30.31%. Factors contributing to maximize wood vinegar yield were pyrolysis temperature and particle size [6]. The effect of pyrolysis time on wood vinegar yield was negligible in this study.

The higher wood vinegar yield at a higher temperature (Table 2) might have been due to the complete pyrolysis at these temperatures. Similar results were reported by Islam et al. [8] and Crespo et al. [6].

Crespo et al. [6] observed that wood vinegar yield from *Acacia mangium* ranged from 24.88–32.94% and that a high wood vinegar yield was obtained at higher temperatures of nearly 500 °C. In the present experiments, at the lower pyrolysis temperature of 350 °C, the sawdust could not be completely decomposed, so that lower wood vinegar yields were obtained. A pyrolysis temperature of 300 °C resulted in lower vinegar yield than that of 450 °C [8]. Wu et al. [22] reported that the highest wood vinegar yield from Chinese fir (*Cunninghamia lanceolata* (Lamb.) Hook) sawdust reached 25% in the pyrolysis temperature range of 350–450 °C, and that wood vinegar yield decreased to 21.22% with temperatures above 450 °C. The yield of wood vinegar from walnut shell increased from 3.46 to 17.66% with a pyrolysis temperature increase from 140 to 290 °C. The yield increase was mainly due to the increase of cellulose and lignin decomposition [23].

In addition, the lower particle size of 2.00 mm was likely to depress the oxygen supply, while at the higher particle size of 3.36 mm, wood particles could be completely decomposed and higher wood vinegar yields obtained. Islam et al. [8] reported that the wastepaper feedstock producing a maximum percentage of the mass of liquid were 45 and 52% for particle sizes 0–1 cm and 1–2 cm, respectively. The coefficient value (CV) was 0.176, representing a relatively good fit to response variables (Table 3).

The model regression coefficient of determination (R^2) was 0.9542 for wood vinegar yield, which indicated

95.42% of the variability could be explained by the model, leaving only 4.58% residual variability for wood vinegar yield. Sofina and Islam [24] obtained similar results, with higher variability by the model. Oramahi et al. [5] reported that the higher R^2 value showed that the model could be efficiently applied to predict wood vinegar yield. Table 3 shows that the main effects of the regression model were obtained by the t-test in the order of β_2 (7.42) > β_1 (5.09) > β_3 (2.18). This indicated that the X_2 (pyrolysis temperature) and X_1 (particle size) variables were the most important factors, with the strongest effect on wood vinegar yield. Meanwhile, X_3 (pyrolysis time) was not a significant factor in wood vinegar yield ($p < 0.05$).

As shown in Table 3, the coefficient of variation (CV=9.87%) was low, which indicated that the results had very high precision. Wang et al. [25] contended that the lower the CV value, the greater the reliability of the study. Fig. 2(a-c) show the three dimensional (3D) response surface curves of a graphical illustration of the effect of particle size, the temperature of pyrolysis, and pyrolysis time on wood vinegar yield.

As already mentioned, optimum conditions for particle size, pyrolysis temperature, and pyrolysis time were found to be 3.85 mm (1.50), 400 °C (0.05), and 93 min (-1.82), respectively. The ANOVA for the quadratic model (Table 4) indicated that the contribution of the linear model was significant ($p < 0.05$), while those of the quadratic and cross product were not.

Table 3. Regression coefficients of the predicted quadratic polynomial model

Sources of variation	Coefficient of polynomial	Error	t-value	Pr > t
Intercept	28.37	1.55	18.34	<0.000
X_1	4.82	0.95	5.09	0.004
X_2	7.03	0.95	7.42	0.000
X_3	2.07	0.95	2.18	0.081
$X_1 * X_1$	-0.77	1.39	-0.55	0.605
$X_2 * X_1$	-4.86	1.34	-3.64	0.015
$X_2 * X_2$	-2.57	1.39	-1.84	0.124
$X_3 * X_1$	1.22	1.34	0.91	0.404
$X_3 * X_2$	-0.30	1.34	-0.23	0.830
$X_3 * X_3$	-1.07	1.39	0.76	0.480

Coefficient of variation = 9.87%, $R^2 = 0.95$

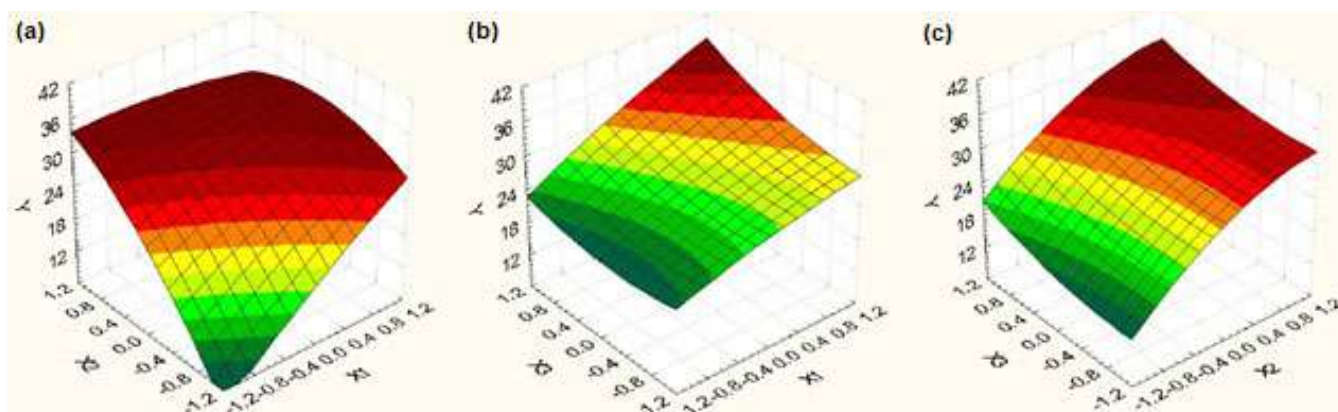


Fig 2. Response surface curve for wood vinegar yield showing the interaction between: (a) wood particle size (X_1 ; mm) and pyrolysis temperature (X_2 ; °C), (b) wood particle size (X_1 ; mm) and pyrolysis time (X_3 ; min), (c) pyrolysis temperature (X_2 ; °C) and pyrolysis time (X_3 ; min)

Table 4. Analysis of variances (ANOVA) for quadratic model

Regression	DF	Sum of squares	R^2	p -value (prob > F)
Linear	3	615.09	0.78	0.001
Quadratic	3	32.00	0.04	0.330
Cross product	3	109.90	0.13	0.064
Total model	9	747.98	0.95	0.007

The responses of the BBD fitted with a second-order polynomial equation to illustrate the wood vinegar yield is given as follows:

$$Y = 28.7 + 4.82X_1 + 7.03X_2 + 2.07X_3 - 0.77X_1^2 - 2.57X_2^2 - 4.86X_1 \cdot X_2 + 1.22X_1 \cdot X_3 - 0.30X_2 \cdot X_3 - 6.67X_3^2 \quad (2)$$

The Chemical Compound of Wood Vinegar from *Shorea laevis*

Table 5 shows the GC-MS analysis data for the wood vinegar obtained from *Shorea laevis* Ridl at a pyrolysis temperature of 400 °C (optimum condition). As may be seen in Table 5, the main chemical compounds of the wood vinegar were acetic acid (4.96%), 1-hydroxy-2-propanone (2.50%), furfural (27.80%), phenol (15.26%), mequinol (8.63%), 4-methylphenol (3.00%), and 2-methoxy-4-methyl phenol (4.28%). The amounts of acid and phenol content in wood vinegar were less than furfural. Thus it was assumed that pyrolysis temperature of 400 °C was optimal process condition for transforming the compound of wood vinegar to be furfural. In addition, the wood vinegar compound is affected by pyrolysis temperature, the particle size of wood and polymers of

wood namely cellulose, hemicellulose, and lignin in the raw material [26-28]. Wu et al. [22] found that the acids compound of wood vinegar decreased as pyrolysis temperature was raised from 250 to 350 °C, and the highest compound was 19.31% at 250 °C, whereas the acid compound decreased to 9.96% at 350 °C. However, for this study, the researcher focused only on wood vinegar obtained from *Shorea laevis* at a pyrolysis temperature of 400 °C which was characterized.

Nam et al. [29] stated that the main component of wood vinegar obtained from cotton stalk were acid, ketones, furans, and phenols. The furans and acids were furfural (30.54%) and acetic acid (29.42%), respectively. Meanwhile, Wei et al. [30] reported that the wood vinegar from walnut tree branches at 230–370 °C contained 32.68% phenols and 30.78% organic acid. The main acid was acetic acid, accounting for 22.62%. They reported that wood vinegar showed the strongest antimicrobial activities to *Phytophthora capsici*, *Colletotrichum orbiculare*, *Valsa mali*, *Cochliobolus sativus*, *Helminthosporium sativum*, and *Phytophthora infestan*. The phenol and organic acid were active compounds of

Table 5. The GC-MS analysis of wood vinegar obtained from *Shorea laevis* at the optimum temperature pyrolysis condition

No	RT	Wood vinegar compound	Area (% rel)
1	3.708	Acetone	4.56
2	3.883	Diazene	2.02
3	7.575	Propanal	1.30
4	7.918	Acetic acid	4.96
5	9.442	2,3-Pentanedione	1.05
6	9.589	1-Hydroxy-2-propanone	2.52
7	16.288	Furfural	27.80
8	19.346	Ethanone	1.22
9	21.424	2-Butanone	3.98
10	21.508	2-Propoxy butane	2.99
11	21.689	5-Methyl-2-furancarboxaldehyde	6.40
12	24.117	Phenol	15.26
13	26.258	Mequinol	8.63
14	27.165	4-Methyl phenol	3.00
15	29.776	2-Methoxy-4-methyl phenol	4.28
16	35.270	2,6-Dimethoxy phenol	0.89

wood vinegar for antimicrobial activity.

Zheng et al. [31] identified 25 chemical compounds by GC-MS analysis of wood vinegar prepared from giant reed (*Arundo donax* L.) at 300–600 °C. The main components were acetic acid, phenols, aldehyde, ketone, alcohol, and esters. Meanwhile, Theapparath et al. [32] obtained wood vinegar from *Garcinia mangostana* Linn., *Durio zibethinus* L., and *Lansium domesticum* Serr., and found the main components were an organic acid, phenols, and methoxyphenols. Pimenta et al. [33] reported that wood vinegar from *Eucalyptus urograndis* contained 93 compounds: phenolics, furans, pyrans, esters, aldehydes and ketones, and that the main components were phenolics. Nakai et al. [34] demonstrated that wood vinegar from solid wood and wood-base composites could inhibit the growth of a white-rot fungus, *T. versicolor*, and a brown-rot fungus, *F. palustris*. The higher phenolic compounds in wood vinegar may have contributed to the increased inhibition against fungal growth. Phenols and organic acids are important compounds in wood vinegar's antifungal and antimicrobial activities, as well as its termiticidal activity. Two kinds of wood vinegar from the hull of spina date seed (HSDS) and the shell of peanut (PS) had 32 major compounds, and phenolics were

dominant. The wood vinegar from HSDS and PS also showed antioxidant activity [35]. Hagner et al. [3] stated the pesticidal activity of wood vinegar obtained from willow (*Salix* sp.) and found total acid and acetic acid.

■ CONCLUSION

The pyrolysis temperature and particle size variables were the most important factors with the strongest effect on wood vinegar yield. Optimization by the RSM-BBD the pyrolysis conditions for the maximum wood vinegar yield for the Indonesian "bengkirai" wood (*Shorea laevis* Ridl) was 3.85 mm particle size, 400 °C pyrolysis temperature, and 93 min in pyrolysis time, for a yield of 30.31%. The predominant compounds in the wood vinegar were acetic acid, 1-hydroxy-2-propanone, furfural, 2,3-pentanedione, phenol, 2-methoxy phenol, 2-methoxy-4-methyl phenol, 2,6-dimethoxy phenol, and 1,2,4-trimethoxybenzene. Further study are still required, in particular, concerning the effectiveness of wood vinegar for plant protection.

■ ACKNOWLEDGMENTS

The authors would like to acknowledge the financial support of the Ministry of Research, Technology and Higher Education of Indonesia for

financially supporting this project in the fiscal year 2018, through a research grant International research collaboration and scientific publication. We also thank the director of the Research Institute for Sustainable Humanosphere, Kyoto University, Japan, for providing facilities for this study.

■ REFERENCES

- [1] Lee, S.H., H'ng, P.S., Lee, A.N., Sajap, A.S., Tey, B.T., and Salmiah, U., 2011, Production of wood vinegar from lignocellulosic biomass and their effectiveness against biological attacks, *J. Appl. Sci.*, 10 (20), 2440–2446.
- [2] Tiirikkala, K., Fagernäs, L., and Tiirikkala, J., 2010, History and use of wood pyrolysis liquids as biocide and plant protection product, *Open Agric. J.*, 4, 111–118.
- [3] Hagner, M., Tiirikkala, K., Lindqvist, I., Niemelä, K., Wikberg, H., Källi, A., and Rasa, K., 2018, Performance of liquids from slow pyrolysis and hydrothermal carbonization in plant protection, *Waste Biomass Valorization*, 1–12.
- [4] Pinto, F., Paradela, F., Gulyurtlu, I., and Ramos, A.M., 2013, Prediction of liquid yields from the pyrolysis of waste mixtures using response surface methodology, *Fuel Process. Technol.*, 116, 271–283.
- [5] Oramahi, H.A., Wahdina, Diba, F., and Yoshimura, T., 2015, Optimization of production of lignocellulosic biomass bio-oil from oil palm trunk, *Procedia Environ. Sci.*, 28, 769–777.
- [6] Crespo, Y.A., Naranjo, R.A., Quitana, Y.G., Sanchez, C.G., and Sanchez, E.M.S., 2017, Optimisation and characterisation of bio-oil produced by *Acacia mangium* Willd wood pyrolysis, *Wood Sci. Technol.*, 51 (5), 1155–1171.
- [7] Akhtar, J., and Amin, N.S., 2012, A review on operating parameters for optimum liquid oil yield in biomass pyrolysis, *Renewable Sustainable Energy Rev.*, 16 (7), 5101–5109.
- [8] Islam, M.N., Beg, M.R.A., and Islam, R.I., 2005, Pyrolytic oil from fixed bed pyrolysis of municipal solid waste and its characterization, *Renewable Energy*, 30 (3), 413–420.
- [9] Ma, C., Song, K., Yu, J., Yang, L., Zhao, C., Wang, W., Zu, G., and Zu, Y., 2013, Pyrolysis process and antioxidant activity of pyroligneous acid from *Rosmarinus officinalis* leaves, *J. Anal. Appl. Pyrolysis*, 104, 38–47.
- [10] de Souza Araújo, E., Pimenta, A.S., Feijó, F.M.C., Castro, R.V.O., Fasciotti, M., Monteiro, T.V.C., and de Lima, K.M.G., 2018, Antibacterial and antifungal activities of wood vinegar from the wood of *Eucalyptus urograndis* and *Mimosa tenuiflora*, *J. Appl. Microbiol.*, 124 (1), 85–96.
- [11] Ratanapisit, J., Apiraksakul, S., Rerngnarong, A., Chungsiriporn, J., and Bunyakarn, C., 2009, Preliminary evaluation of production and characterization of wood vinegar from rubberwood, *Songklanakarin J. Sci. Technol.*, 31 (3), 343–349.
- [12] Montgomery, D.C., 2008, *Design and analysis of experiments*, John Wiley & Sons, New York.
- [13] Kiliç, M., Pütün, E., and Pütün, A.E., 2014, Optimization of *Euphorbia rigida* fast pyrolysis conditions by using response surface methodology, *J. Anal. Appl. Pyrolysis*, 110, 163–171.
- [14] Ngo, T.A., Kim, J., and Kim, S.S., 2013, Fast pyrolysis of palm kernel cake using a fluidized bed reactor: Design of experiment and characteristics of bio-oil, *J. Ind. Eng. Chem.*, 19 (1), 137–143.
- [15] Tranggono, Suhardi, Setiadji, B., Darmadji, P., Supranto, and Sudarmanto, 1996, Identifikasi asap cair dari berbagai jenis kayu dan tempurung kelapa, *ITEPA*, 1 (2), 15–24.
- [16] Oramahi, H.A., Yoshimura, T., Diba, F., Setyawati, D., and Nurhaida, 2018, Antifungal and antitermitic activities of wood vinegar from oil palm trunk, *J. Wood Sci.*, 64 (3), 311–317.
- [17] Liu, Y., Wei, S., and Liao, M., 2013, Optimization of ultrasonic extraction of phenolic compounds from *Euryale ferox* seed shells using response surface methodology, *Ind. Crops Prod.*, 49, 837–843.
- [18] Yuan, Z., Xu, Z., Zhang, D., Chen, W., Zhang, T., Huang, Y., Gu, L., Deng, H., and Tian, D., 2018, Box-Behnken design approach towards optimization of activated carbon synthesized by co-

- pyrolysis of waste polyester textiles and $MgCl_2$, *Appl. Surf. Sci.*, 427, 340–348.
- [19] Srinivasa, P.C., Ravi, R., and Tharanathan, R.N., 2007, Effect of storage conditions on the tensile properties of eco-friendly chitosan films by response surface methodology, *J. Food Eng.*, 80 (1), 184–189.
- [20] Safari, M., Abdi, R., Adl, M., and Kafashan, J., 2018, Optimization of biogas productivity in lab-scale by response surface methodology, *Renewable Energy*, 118, 368–375.
- [21] Mun, S.P., and Ku, C.S., 2010, Pyrolysis GC-MS analysis of tars formed during the aging of wood and bamboo crude vinegar, *J. Wood Sci.*, 56 (1), 47–52.
- [22] Wu, Q., Zhang, S., Hou, B., Zheng, H., Deng, W., Liu, D., and Tang, W., 2015, Study on the preparation of wood vinegar from biomass residues by carbonization process, *Bioresour. Technol.*, 179, 98–103.
- [23] Zhai, M., Shi, G., Wang, Y., Mao, G., Wang, D., and Wang, Z., 2015, Chemical compositions and biological activities of wood vinegar from the walnut shell, *BioResources*, 10 (1), 1715–1729.
- [24] Sofina-E-Arab and Islam, M.A., 2015, Production of mahogany sawdust reinforced LDPE wood–plastic composites using statistical response surface methodology, *J. For. Res.*, 26 (2), 487–494.
- [25] Wang, X., Yang, G., Li, F., Feng, Y., and Ren, G., 2013, Response surface optimization of methane potentials in anaerobic co-digestion of multiple substrates: Dairy, chicken manure, and wheat straw, *Waste Manage. Res.*, 31 (1), 60–66.
- [26] Karagöz, S., Bhaskar, T., Muto, A., and Sakata, Y., 2005, Comparative studies of oil compositions produced from sawdust, rice husk, lignin and cellulose by hydrothermal treatment, *Fuel*, 84 (7-8), 875–884.
- [27] Fan, Y., Cai, Y., Li, X., Yin, H., Yu, N., Zhang, R., and Zhao, W., 2014, Rape straw as a source of bio-oil via vacuum pyrolysis: Optimization of bio-oil yield using orthogonal design method and characterization of bio-oil, *J. Anal. Appl. Pyrolysis*, 106, 63–70.
- [28] Mantilla, S.V., Gauthier-Maradei, P., Gil, P.Á., and Cárdenas, S.T., 2014, Comparative study of bio-oil production from sugarcane bagasse and palm empty fruit bunch: Yield optimization and bio-oil characterization, *J. Anal. Appl. Pyrolysis*, 108, 284–294.
- [29] Nam, H., and Capareda, S., 2015, Experimental investigation of torrefaction of two agricultural wastes of different composition using RSM (response surface methodology), *Energy*, 91, 507–516.
- [30] Wei, Q., Ma, X., and Dong, J., 2010, Preparation, chemical constituents and antimicrobial activity of wood vinegar from walnut tree branches, *J. Anal. Appl. Pyrolysis*, 87 (1), 24–28.
- [31] Zheng, H., Sun, C., Hou, X., Wu, M., Yao, Y., and Li, F., 2018, Pyrolysis of *Arundo donax* L. to produce pyrolytic vinegar and its effect on the growth of dinoflagellate *Karenia brevis*, *Bioresour. Technol.*, 247, 273–281.
- [32] Theapparath, Y., Khongthong, S., Rodjan, P., Lertwittayanon, K., and Faroongsarng, D., 2019, Physicochemical properties and in vitro antioxidant activities of wood vinegar prepared from brushwood biomass waste of Mangosteen, Durian, Rambutan, and Langsat, *J. For. Res.*, 30 (3), 1139–1148.
- [33] Pimenta, A.S., Fasciotti, M., Monteiro, T.V., and Lima, K.M., 2018, Chemical composition of wood vinegar obtained from *Eucalyptus* GG100 Clone, *Molecules*, 23 (2), 426.
- [34] Nakai, T., Kartal, S.N., Hata, T., and Imamura, Y., 2007, Chemical characterization of pyrolysis liquids of wood-based composites and evaluation of their bio-efficiency, *Build. Environ.*, 42 (3), 1236–1241.
- [35] Li, Z., Zhang, Z., Wu, L., Wang, J., Liu, Z., Zhang, Z., and Wang, Z., 2017, Preparation and characterization of two wood vinegar obtained from the hull of spina date seed and shell of peanut, *Chem. Res. Chin. Univ.*, 33 (3), 348–353.

Preparation and Powder XRD Analysis of Tris(2,2'-bipyridine)nickel(II) Trifluoroacetate

Kristian Handoyo Sugiyarto*, Isana Supiah Yosephine Louise, and Shinta Setya Wilujeng

Department of Chemistry Education, Universitas Negeri Yogyakarta, Jl. Colombo No. 1, Yogyakarta 55281, Indonesia

* Corresponding author:

email: sugiyarto@uny.ac.id

Received: June 9, 2019

Accepted: August 7, 2019

DOI: 10.22146/ijc.46483

Abstract: The complex containing Ni(II)-2,2'-bipyridin (bipy)-trifluoroacetate (TFA) was prepared by direct interaction of the corresponding precursors in an aqueous solution. AAS measurement for metal content, TGA-DTA analysis and electrical conductance suggest the ionic complex of $[\text{Ni}(\text{bipy})_3](\text{CF}_3\text{COO})_2 \cdot 6\text{H}_2\text{O}$. The magnetic moment of 3.13–3.17 BM indicates the paramagnetism corresponding to two unpaired electrons which is clearly higher than that of the spin only value (2.87 BM), and commonly observed due to the spin-orbit coupling in Ni(II). UV-Vis spectral property revealed the first two main ligand field bands centered at about 14200 and 18650 cm^{-1} , which are attributed to the spin-allowed transition, ${}^3\text{A}_{2g} \rightarrow {}^3\text{T}_{2g}$ and ${}^3\text{A}_{2g} \rightarrow {}^3\text{T}_{1g}(\text{F})$, respectively. The expected third band at higher energy seems to appear as a shoulder at 26500 cm^{-1} (378 nm), as it is masked by a strong intensity of charge transfer band centered at 31050 cm^{-1} . The infrared spectrum exhibits mode of vibrations of the functional groups of ligand and TFA. The powder diffractogram was refined by Le Bail method and found fit as monoclinic system of space group of $\text{P}2_1/\text{M}$, with figures of merit: $R_p = 3.62$, $R_{wp} = 5.76$, $R_{exp} = 3.48$, goodness of fitting (GOF) 2.745 and the derived Bragg R-Factor = 0.05.

Keywords: Rietica; Le Bail; bipy; trifluoroacetate; nickel(II)

■ INTRODUCTION

The chemistry of 2,2'-bipyridine (bipy) as a bidentate ligand has been well known for *tris-bipy* complex since long time ago [1]. However, the crystallographic aspects of the corresponding single crystals are scarcely reported. It is not surprising since the preparation of a single crystal suitable for refining the structural data of particular complex is sometimes quite complicated and even unsuccessful. Rietica is one of known programs of Le Bail to refine the lattice parameters for various metal oxides [2-4] which are found to be fit, and it seems also applicable for other powders of complexes. The first complex refined by Le Bail program was initially reported in 1999 [5] for octahedral $[\text{Co}(\text{NH}_3)_5\text{CO}_3](\text{NO}_3) \cdot \text{H}_2\text{O}$ complex which was found very good result with the figures of merit to be $R_B = 0.053$, $R_p = 0.100$, $R_{wp} = 0.119$. Although the application to other complexes were not continually reported since then it has been applied to some complexes as reported quite recently by Sugiyarto et al. [6], Kusumawardani et al. [7-8] and Sutrisno et al. [9]. Therefore, refining diffractogram of

powder complexes seems to be an alternative way to identify the corresponding lattice parameters. Trifluoroacetate (TFA) of alkali metals have been known to be ionic salts because the corresponding acid, HTFA, is known as a strong acid ($pK_a = 0.23$), being about 100,000 times stronger than that of acetic acid ($pK_a = 4.76$) [10-11]. The highly electronegative fluorine atoms in trifluoromethyl group should weaken the oxygen-hydrogen bond and stabilizes the anionic conjugate base. However, the coordination nature of oxygen atom in acetate group is possible, and with transition metal ions some polynuclear molecular complexes of TFA have been synthesized [12]. The monodentate coordinating with hydrogen bonding of $\text{N}-\text{H} \cdots \text{O}$ has also been observed [13]. Some molecular complexes containing monodentate *pyridine* with TFA, $[\text{M}(\text{py})(\text{CF}_3\text{CO}_2)]$, where $\text{M} = \text{Cu}(\text{II})$, $\text{Ni}(\text{II})$, and $\text{Co}(\text{II})$, have also been characterized [14]. TFA has been considered as weakly coordinating ligand in $[\text{Ni}(\text{o-MeO-dppp})(\text{TFA})_2]$, where $\text{dppp} = 1,3\text{-bis}[\text{di}(\text{o-methoxyphenyl})\text{phosphanyl}]$ propane, as reported to

undergo completely auto-ionized in polar solvents [15], indicating that TFA was no longer to be a ligand in the solution but a counter anion. Therefore, in the presence of relatively strong ligand such as *bipyridine* (*bipy*), the role of TFA might be considered as a counter anion, and the preparation of Ni(II) with *bipy* and TFA should be significantly evident as in this work. Moreover, to the corresponding powder of the complex its cell parameters might be then revealed by Rietica-Le Bail method, and these are the main purpose of this work.

■ EXPERIMENTAL SECTION

Materials

The main reagents, nickel(II) nitrate ($\text{Ni}(\text{NO}_3)_2 \cdot 6\text{H}_2\text{O}$), 2,2'-bipyridine ($\text{C}_{10}\text{H}_8\text{N}_2$), sodium trifluoroacetate (CF_3COONa), ammonium nitrate (NH_4NO_3), calcium chloride (CaCl_2), nickel sulfate (NiSO_4), calcium nitrate ($\text{Ca}(\text{NO}_3)_2$), and aluminium nitrate ($\text{Al}(\text{NO}_3)_3 \cdot 6\text{H}_2\text{O}$), Iron(III) chloride (FeCl_3) were obtained from Aldrich-Sigma, and directly used without special treatment.

Procedure

Procedure for preparation of the complex

The mixture of 0.1 mmol nickel nitrate and 0.32 mmol bipyridine in about 15 mL aqueous solution with drops of ethanol in a 50 mL flask was well stirred and warmed till solution become clear. Saturated aqueous solution of CF_3COONa in excess (0.4 mmol, 5 mL) was then poured to this mixture. The volume was reduced on warming, whereupon the light-pink solid was deposited on cooling while scratching. The precipitate was filtered off, washed with a minimum cold water, and finally dried in exposure.

Instruments and procedure of physical measurements

Magnetism. Magnetic Susceptibility Balance (MSB) of Auto Sherwood Scientific 240V-AC was used to measure the magnetic susceptibility in mass (χ_g) of samples. This instrument was calibrated with $\text{CuSO}_4 \cdot 5\text{H}_2\text{O}$ before running the samples. The powder complex was tightly packed in the Gouy tube till the sign of volume. The difference in mass without and with (electro-)magnet

which reflects the magnetic susceptibility in mass was then recorded. It was converted into molar magnetic susceptibility (χ_M) and then corrected for diamagnetism using Pascal's constant [16] to get corrected molar magnetic susceptibility (χ_M'). The effective magnetic moment (μ_{eff}) was then calculated from the general formula, $\mu_{\text{eff}} = 2.828 \sqrt{\chi_M' \cdot T}$ BM.

UV-Vis electronic and infrared spectra. A spectrophotometer model of Pharmaspec UV 1700 was used to record the UV-VIS electronic spectrum. The sample was spread and pasted with ethanol on a particular thin glass (2×2 cm). The fitting was then set in the cell holder and the spectrum was recorded at 300–800 nm. An Infrared Spectrophotometer of FTIR ABB MB3000 model was used to record the IR-spectrum of sample. The sample which was mixed with KBr was pressed on the cell and then the spectrum was recorded at 600–4000 cm^{-1} .

Metal content and ionic property. An Atomic Absorption Spectrophotometer of PinAAcle 900T Perkin Elmer model was used to record the metal content. A conductometer of Lutron CD-4301 model was used to estimate the conductance property of the complex. It was calibrated with an aqueous solution of 1 M KCl at 25 °C, and some known ionic solutions, NH_4NO_3 , CaCl_2 , $\text{Ca}(\text{NO}_3)_2$, NiSO_4 , MnSO_4 , FeCl_3 , and $\text{Al}(\text{NO}_3)_3$, were also recorded for comparison.

TGA-DTA (Thermogravimetric analysis and differential thermal analysis). The loss of hydrated molecule of water and decomposition of complex was performed on Diamond (Perkin Elmer Instruments), and simultaneous TGA-DTA were obtained by a NETZSCH STA 409C/CO thermal analyzer model with the rate of 10 °C/min.

Powder diffraction. A Rigaku Miniflex 600 40 kW 15 mA Benchtop Diffractometer with $\text{CuK}\alpha$, $\lambda = 1.5406 \text{ \AA}$ was used to record the diffractogram of the complex. The sample was spread on a special glass plate and set on the cell holder. The diffractogram was then recorded in a scan mode at 2–90 degree of 2θ within interval of 0.04 steps per 4 sec for 2 h. The recorded diffractogram was then refined following the Le Bail method of Rietica program within 10–50 degree of 2θ which was run within 75 cycles.

SEM-EDX (Scanning electron microscopy with energy dispersive X-ray). The SEM images of the complex were recorded in JEOL JED-2300 model to confirm the crystallinity as well as the content of main elements in the sample.

■ RESULTS AND DISCUSSION

Conductance, TGA-DTA and Formula of the Complex

The mixture of light-green nickel(II) and colorless bipyridine which produced light-pink color was likely to be the cationic complex, $[\text{Ni}(\text{bipy})_n]^{2+}$. The addition of anionic TFA in excess should force the precipitated complex containing TFA. The conductivity data of the complex and several known ionic compounds in aqueous solution are listed in Table 1. It indicates strongly that the conductance for this complex is clearly in the range for

those compounds containing three ions per molecule, and hence the best possible empirical formula, $[\text{Ni}(\text{bipy})_n](\text{CF}_3\text{COO})_2 \cdot x\text{H}_2\text{O}$, might be proposed for the pink powdered complex.

Estimation of coordination number (n) in the formula of the complex could be worked out by considering the metal content obtained from AAS (calculated 6.81% and found 6.77%), which was then confirmed further by the loss of mass for each of other components indicated in TGA-DTA graph as shown in Fig. 1 and Table 2. In this graph, the first stage of mass loss for about 11.87% at around 100 °C is almost certainly due to the loss of uncoordinated water molecules [9,17-19]. This corresponds to 5.68 H_2O which is close to the calculated percentage of 12.53% for $6\text{H}_2\text{O}$. The next two stages of mass loss in the range of 120–260 °C, could be put together to a total of about 25.71% for decomposition

Table 1. Electrical equivalent conductance of the complex and some known salts in aqueous solutions

Compounds	Equivalent conductance ($\Delta\epsilon$) $\Omega^{-1} \text{cm}^2 \text{mol}^{-1}$	Amount ratio of cation/anion	Number of ions per molecule
$\text{NH}_4 \text{NO}_3$	128.176	1:1	2
NiSO_4	119.55	1:1	2
CaCl_2	196.90	1:2	3
$\text{Ca}(\text{NO}_3)_2$	229.340	1:2	3
$\text{Al}(\text{NO}_3)_3$	510.010	1:3	4
FeCl_3	573.820	1:3	4
$[\text{Ni}(\text{bipy})_n](\text{CF}_3\text{COO})_2 \cdot x\text{H}_2\text{O}$	214.598	1:2	3

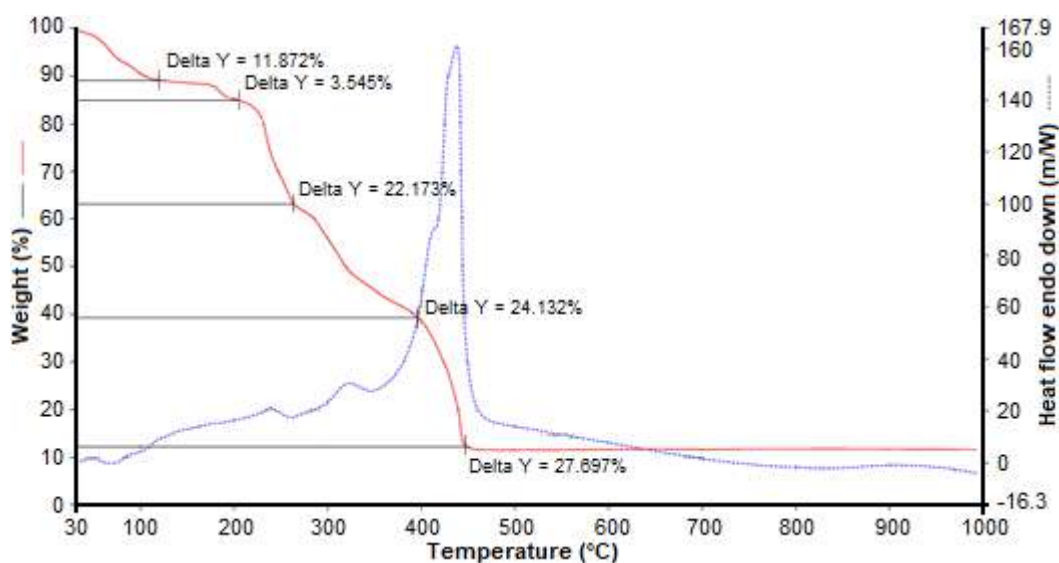


Fig 1. The TGA-DTA of $[\text{Ni}(\text{bipy})_3](\text{CF}_3\text{COO})_2 \cdot 6\text{H}_2\text{O}$ at 30–1000 °C

Table 2. Entity found in $[\text{Ni}(\text{bipy})_3](\text{CF}_3\text{COO})_2 \cdot 6\text{H}_2\text{O}$

Type	Ni	H ₂ O	(CF ₃ COO)	(bipy)	NiO ₂ *
Found	6.77	11.87	25.71	51.83	10.58
Calculated	6.81	12.53	26.24	54.39	10.53
Error (%)	0.58	5.26	2.13	4.72	0.47
Method	AAS	TGA	TGA	TGA	TGA

*NiO (cal. 8.67%) as the residue observed on the graph above 700 °C

of TFA as also observed by Eloussifi et al. [20]. This percentage loss equals 1.96 moles of TFA anions, which is reasonably close to the calculated loss of 26.24% for 2 moles in this complex. The next loss of mass observed in the range 400–450 °C for about 51.83% should be associated with loss of 2.86 moles of bipyridine, though the calculated for 3 moles is 54.39% in this instance. Laishram [21] proposed the loss of bipyridine at 285–476 °C. As Singh et al. suggested [22] the remaining loss observed to be 10.58% approximately refers to NiO₂ which is calculated as 10.53% in mass, before further decomposition to the residue NiO (cal. 8.67%) as indicated by the graph below 700 °C. For those reasons, it can be concluded that the proposed formula, $[\text{Ni}(\text{bipy})_3](\text{CF}_3\text{COO})_2 \cdot 6\text{H}_2\text{O}$, for the complex would be reasonably fit as being expected also from the stoichiometric preparation. The electrolyte nature in aqueous solution for this complex as reflected by conductivity data confirms strongly the ionic property of the TFA rather than the coordinated one [14], and thus, the next particular characterization is described.

Magnetic Property

Based on the complex formula (Table 2), the magnetic susceptibility recorded on the measurements (Table 3) were then worked out to the magnetic moments and for the three separated samples they are in the range 3.13–3.17 BM. It is certainly higher than the spin-only value for the two unpaired electrons (2.83 BM) in the electronic configuration of d^8 -Ni(II), which is commonly observed due to the orbital contribution by ‘mixing in’ of the wave-functions of the higher ³T terms [23–24].

Electronic Spectrum

Electronic spectrum of the powdered complex, $[\text{Ni}(\text{bipy})_3](\text{CF}_3\text{COO})_2 \cdot 6\text{H}_2\text{O}$, was recorded in the range

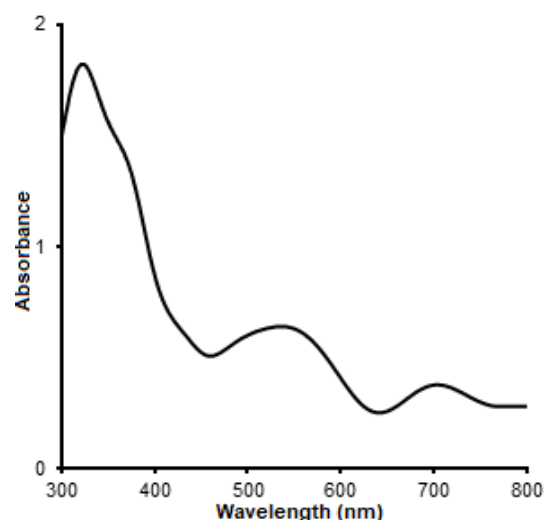
300–800 nm. As displayed in Fig. 2 the two main ligand field bands were well resolved, and centered at about 13700 cm⁻¹ (730 nm) (ν_1) and 18650 cm⁻¹ (536 nm), (ν_2); these are associated with the spin-allowed transitions, $^3\text{A}_{2g} \rightarrow ^3\text{T}_{2g}$, and $^3\text{A}_{2g} \rightarrow ^3\text{T}_{1g}(\text{F})$, respectively. This spectrum is quite similar to that of the tetrafluoroborate recorded by Abramov [25], and the second band being responsible for the pink color. The expected third band, ν_3 ($^3\text{A}_{2g}(\text{F}) \rightarrow ^3\text{T}_{1g}(\text{P})$), as predicted by Tanabe-Sugano to be at higher energy about 26500 cm⁻¹ (278 nm) was not well resolved but as a shoulder due to the masked strong intensity of charge transfer (MLCT) band of 31050 cm⁻¹ (322 nm).

Infrared Spectrum

Infrared spectra of the complex and the TFA-salt were recorded and overlaid as shown in Fig. 3, and thus the assignment seems straight forward. The broad band (Fig. 3(a)-red full line) at about 3400 cm⁻¹ is likely to be -OH stretching of H₂O molecules in the complex as confirmed by TGA-DTA (Fig. 1). Shad et al. observed this

Table 3. Magnetic data of $[\text{Ni}(\text{bipy})_3](\text{CF}_3\text{COO})_2 \cdot 6\text{H}_2\text{O}$ at 291 °C

Sample	$\chi_M' \times 10^{-6}$ (cgs)	μ_{eff} (BM)
1	4.4326	3.15
2	4.3734	3.13
3	4.5128	3.17

**Fig 2.** Electronic spectrum of powder $[\text{Ni}(\text{bipy})_3](\text{CF}_3\text{COO})_2 \cdot 6\text{H}_2\text{O}$

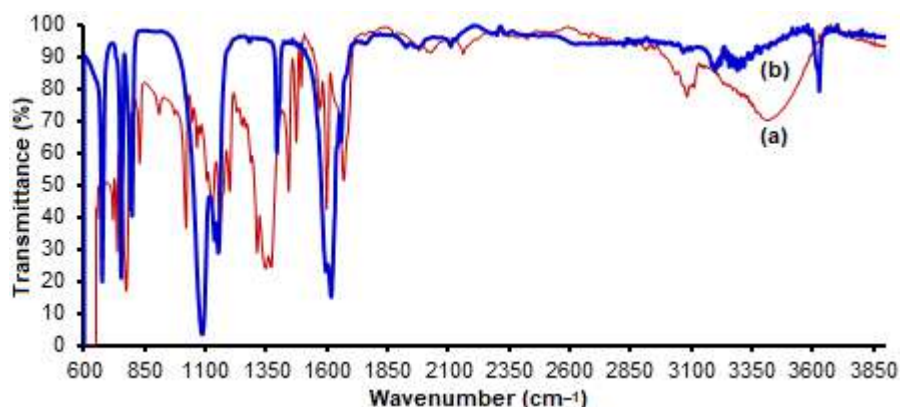


Fig 3. Infrared spectrum of $[\text{Ni}(\text{bipy})_3](\text{CF}_3\text{COO})_2 \cdot 6\text{H}_2\text{O}$ (red, (a)) and $\text{Na CF}_3\text{COO}$ (blue, (b))

assignment at about 3441 cm^{-1} [26], though Kumar et al. [27] also considered C-C aromatic at 3430 cm^{-1} . Another band at 3100 cm^{-1} might be assigned as stretching vibration of C-H bonds as observed by Chen et al. at 3064 cm^{-1} in phenanthroline [28], and Tosonian et al. at $3051\text{--}3068\text{ cm}^{-1}$ [29]. As reported previously, typical vibrations of *bipy* might be shifted due to chelation [1]. Characteristic vibration of bipyridine ($\nu_{\text{C-C}}$ and $\nu_{\text{C-N}}$) are in the range $1650\text{--}1400\text{ cm}^{-1}$ [28,30], and in this instance, they are at 1669 , 1598 , 1498 , 1494 , and 1350 cm^{-1} . Zang et al. [31] suggested that the mode of vibration at 1585 cm^{-1} was to be $\nu_{\text{C-N}}$.

The very strong-sharp peaks at about 1660 and 1160 cm^{-1} are assigned as due to mode of vibrations $\nu_{\text{C=O}}$ and $\nu_{\text{C-O}}$, respectively as observed by Skyranou et al. [32] and Suzuki et al. [33] at 1669 cm^{-1} , and by Osowole et al. [34] at $1192\text{--}1102\text{ cm}^{-1}$. While mode at about 1442 cm^{-1} might be due to $\nu_{\text{C-C}}$ as proposed by Abdelhak et al. [30]. A very strong mode at 1670 cm^{-1} might be due to C=O stretching vibration as compared to that of sodium TFA (Fig. 3(b)-blue line) which was observed at 1669 cm^{-1} [32]. The bands at about 750 and 848 cm^{-1} are deformation asymmetry and symmetry of CF_3 , respectively [7,35-37], as also observed in sodium TFA at 800 and 850 cm^{-1} . The asymmetric CF deformations normally fall in the $500\text{--}625\text{ cm}^{-1}$ region, and O=C-O bending vibration at 700 cm^{-1} [40].

The Powder X-Ray Diffractogram and Its Refinement

Structural data obtained from cationic single crystal of $[\text{Ni}(\text{bipy})_3]^{2+}$ with various counter anions have been established [39-43]. Except for the tetrachloridozincate

salt [43], all adopt the same symmetry, monoclinic, but different in space group, and consequently different cell parameters as described in Table 4. Therefore, structural analysis of powder cation $[\text{Ni}(\text{bipy})_3]^{2+}$ with other counter anion, TFA, should be of interest for this aspect.

The powder X-Ray diffractogram of the complex, $[\text{Ni}(\text{bipy})_3](\text{CF}_3\text{COO})_2 \cdot 6\text{H}_2\text{O}$, together with its refining according to Le Bail method is displayed in Fig. 4. The observed data (+ signs, (a)) are almost coincident to the full line of refinement model (b), and it is confirmed by the almost flat curve (c) reflecting difference between the two. This suggests that the analysis is considered to be fit with low figures of merit: $3.62 (R_p)$, $5.76 (R_{wp})$, $3.48 (R_{exp})$, $2.745 (\text{GOF})$, and $0.05 (\text{Bragg R-Factor})$ as discussed by Toby [44] and found in several of so many reported metal oxides [2-4] and several complexes [5-9]. The detailed lattice parameters of this complex are described in Table 4 along with the corresponding cationic single crystal data of different counter anions, the hexamolybdate [39], the perchlorate [40], the bis(2-thiobarbiturate)-Htba [41], the chloride [42], and the tetrachloridozincate [43]. It is clear that the cell parameters are quite similar to that of hexamolybdate with all parameters are slightly reduced. With the same number of molecules per cell ($Z = 4$) it is readily understood since the size of counter anion-hexamolybdate is greater than that of TFA.

SEM-EDX

Crystallinity of this powder $[\text{Ni}(\text{bipy})_3](\text{CF}_3\text{COO})_2 \cdot 6\text{H}_2\text{O}$ might be reflected by the corresponding

Table 4. Detailed cell parameters of $[\text{Ni}(\text{bipy})_3](\text{X})$, where $\text{X} = (\text{TFA})_2 \cdot 6\text{H}_2\text{O}^*$, $(\text{Mo}_6\text{O}_{19})_2$ [39], $(\text{ClO}_4)_2$ [40], $(\text{Htba})_2 \cdot 6\text{H}_2\text{O}$ [41], and $\text{Cl}_2 \cdot 5.5\text{H}_2\text{O}$ [42], and $[\text{ZnCl}_4]_2$ [43] (*This work was due to Le Bail method of Rietica program)

$[\text{Ni}(\text{bipy})_3](\text{X})$	$(\text{TFA})_2 \cdot 6\text{H}_2\text{O}$ *This work	$(\text{Mo}_6\text{O}_{19})_2$ [39]	$(\text{ClO}_4)_2$ [40]	$(\text{Htba})_2 \cdot 6\text{H}_2\text{O}$ [41]	$\text{Cl}_2 \cdot 5.5\text{H}_2\text{O}$ [42]	$[\text{ZnCl}_4]_2$ [43]
Symmetry	Monoclinic	Monoclinic	Monoclinic	Monoclinic	Monoclinic	Trigonal
Space Grup	$\text{P2}_1/\text{m}$	$\text{P2}_1/\text{n}$	$\text{C2}/\text{c}$	$\text{P2}_1/\text{c}$	$\text{C2}/\text{c}$	R3c
Z	4	4	4	8	4	12
a (Å)	11.6628	12.3549	17.502(2)	13.6618(6)	13.410(2)	13.34.3(2)
b (Å)	17.8225	18.9866	10.777(1)	23.9441(9)	22.509(4)	
c (Å)	16.9786	17.1974	16.092(2)	25.4335(8)	23.781(4)	58.932(12)
β (°)	98.8477	101.114	90.959(2)	93.091(1)	105.390	
V (Å ³)	3487.1950	3958	3034.8(6)	8307.7(5)	6921(2)	9087(3)
Figure of merit:						
R_p	3.62					
R_{wp}	5.76					
R_{exp}	3.48					
Bragg R-Factor	0.05					
GOF	2.745					

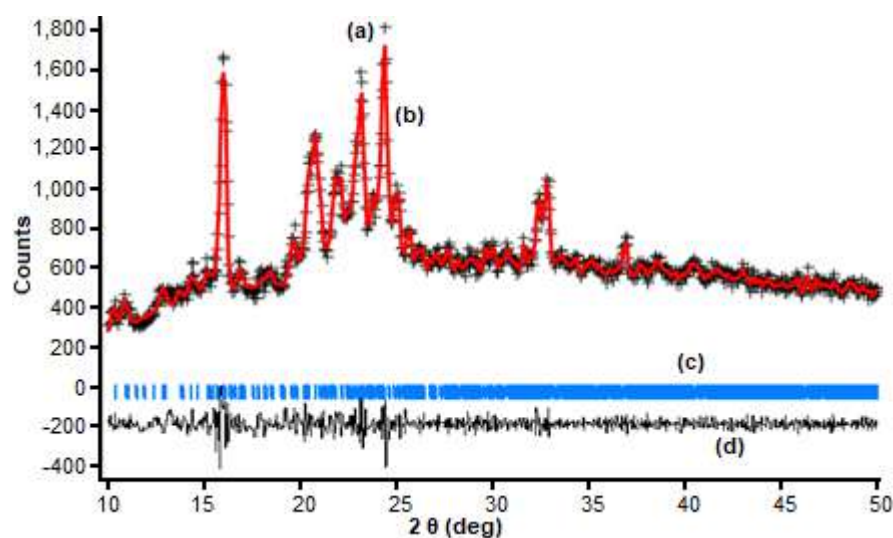


Fig 4. Diffractogram of $[\text{Ni}(\text{bipy})_3](\text{CF}_3\text{COO})_2 \cdot 6\text{H}_2\text{O}$: observed data (sign +, (a)), refined monoclinic space group of $\text{P2}_1/\text{M}$ model (full line, (b)), it's position of 2 theta (c), and the difference between the observed and the refined full line model (d)

SEM images with various magnification depicted in Fig.5 (a-c). Meanwhile, the related energy dispersive X-ray (EDX) analysis result on the selected surface as shown in Fig. 5(d) strongly indicates the presence of all elements contained in the complex except the hydrogen atom. It

should be noted that the percentage ratio of the number of atoms does not represent the empirical formula of the complex, since it is not possible to have homogenous powder as indicated by the SEM images and it's EDX (Fig. 5).

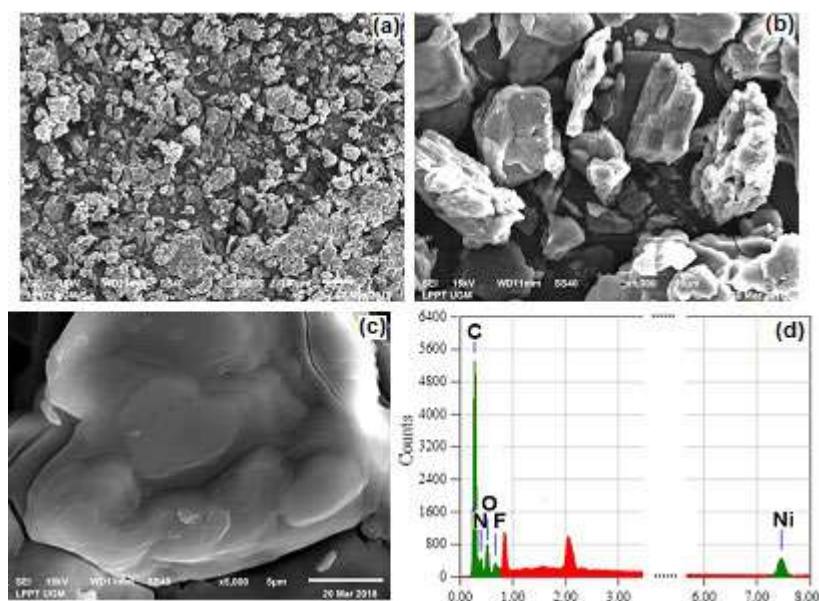


Fig 5. SEM images of $[\text{Ni}(\text{bipy})_3](\text{CF}_3\text{COO})_2 \cdot 6\text{H}_2\text{O}$ at magnification of $100\times$ (a), $1000\times$ (b), $5000\times$ (c) and its EDX analysis result showing the content of elements, Ni-C-F-N-O (d)

CONCLUSION

The complex containing Ni-*bipy*-TFA has been successfully synthesized and its chemical properties have been characterized. The proposed empirical formula of the ionic complex, $[\text{Ni}(\text{bipy})_3](\text{CF}_3\text{COO})_2 \cdot 6\text{H}_2\text{O}$, was estimated by the measurements of electrical equivalent conductance, and metal content (AAS), while the existence of hydrated water molecules, TFA ions, bipyridine molecules, and metal residue were signified by the corresponding TGA-DTA. The presence of elements was confirmed by EDX analysis. The magnetic moment was found to be normal paramagnet corresponding to two unpaired electrons with significant spin-orbit coupling. The UV-VIS spectral property of the complex exhibits the typical two main ligand field bands at the visible areas, and the third ligand field band as well as the charge transfer was observed at much high energy of UV area. The infrared spectrum of the complex shows the typical mode of vibrations of functional groups for bipyridine and the TFA anion. The powder X-Ray diffractogram refined using Le Bail method of Rietica program suggests the complex to adopt monoclinic symmetry of space group, $P2_1/m$.

REFERENCES

- [1] Palmer, R.A., and Piper, T.S., 1966, 2,2'-Bipyridine complexes. I. Polarized crystal spectra of tris(2,2'-bipyridine)copper(II), -nickel(II), -cobalt(II), -iron(II), and -ruthenium(II), *Inorg. Chem.*, 5 (5), 864–878.
- [2] Prijamboedi, Z.B., Nugroho, A.A., and Ismunandar, 2009, Synthesis and structure analysis of aurivillius phases $\text{Pb}_{1-x}\text{Bi}_{4+x}\text{Ti}_{4-x}\text{Mn}_x\text{O}_{15}$, *J. Chin. Chem. Soc.*, 56 (6), 1108–1111.
- [3] Wallwork, K.S., Pring A., Taylor M.R., and Hunter, B.A., 2003, A model for the structure of the hydrated aluminum phosphate, kingite determined by ab initio powder diffraction methods, *Am. Mineral.*, 88 (1), 235–239.
- [4] Wallwork, K.S., James, M., and Carter, M.L., 2006, The crystal chemistry, structure and properties of a synthetic carnotite-type compound, $\text{Ba}_2[\text{UO}_2)_2\text{Ti}_2\text{O}_8]$, *Can. Mineral.*, 44 (2), 433–442.
- [5] Zhu, J.H., Wu, H.X., and Le Bail, A., 1999, Structure of $[\text{Co}(\text{NH}_3)_5\text{CO}_3]\text{NO}_3 \cdot \text{H}_2\text{O}$, *Solid State Sci.*, 1 (1), 55–62.
- [6] Sugiyarto, K.H., Saputra, H.W., Permanasari, L.,

- and Kusumawardani, C., 2017, Structural analysis of powder complex of $[\text{Mn}(\text{phen})_3](\text{CF}_3\text{SO}_3)_2 \cdot 6.5\text{H}_2\text{O}$, *AIP Conf. Proc.*, 1847 (1), 040006.
- [7] Kusumawardani, C., Permanasari, L., Fatonah S.D., and Sugiyarto, K.H., 2017, Structural analysis of powder complex of tris(1,10-phenanthroline) copper(II) trifluoromethane sulfonate dihydrate, *Orient. J. Chem.*, 33 (6), 2841–2847.
- [8] Kusumawardani, C., Kainastiti, F., and Sugiyarto, K.H., 2018, Structural analysis of powder complex of $\text{Cu}(\text{bipy})_3(\text{CF}_3\text{SO}_3)_2(\text{H}_2\text{O})_x$ ($x = 0.5, 1$), *Chiang Mai J. Sci.*, 45 (4), 1944–1952.
- [9] Sutrisno, H., Kusumawardani, C., Rananggana, R.Y., and Sugiyarto, K.H., 2018, Structural analysis of powder tris(phenanthroline)nickel(II) trifluoroacetate, *Chiang Mai J. Sci.*, 45 (7), 2768–2778.
- [10] Anonymous, *Trifluoroacetic acid*, http://www.commonorganicchemistry.com/Common_Reagents/Trifluoroacetic_Acid/Trifluoroacetic_Acid.htm, accessed on April 2019.
- [11] *Table of Acids with Ka and pKa Values*, 2013, Compiled from Appendix 5 Chem 1A, B, C Lab Manual and Zumdahl 6th Ed., The pKa values for organic acids can be found in Appendix II of Bruice 5th Ed., https://www.chem.purdue.edu/docs/exams/2013/April_20_2013_cume.pdf, accessed on April 2019.
- [12] Tokareva, A.O., Tereshchenko, D.S., Boltalin, A.I., and Troyanov, S.I., 2006, Acid Co(II) and Ni(II) trifluoroacetate complexes: Synthesis and crystal structure, *Russ. J. Coord. Chem.*, 32 (9), 663–668.
- [13] Reiß, G.J., and Meyer, M.K., 2010, Synthesis and structural characterization of diisopropylammonium trifluoroacetate and diisopropylammonium pentafluoropropionate, *Z. Naturforsch. B*, 65 (4), 479–484.
- [14] Agambar, C.A., and Orrell, K.G., 1969, Trifluoroacetate complexes of cobalt(II), nickel(II), and copper(II) with pyridine-type ligands. Part I. Metal(II) trifluoroacetates and copper(II) complexes, *J. Chem. Soc. A*, 0, 897–904.
- [15] Angulo, I.M., Bouwman, E., Lok, S.M., Lutz, M., Mul, W.P., and Spek, A.L., 2001, The first low-spin nickel complex with two coordinated water molecules, $[\text{Ni}(o\text{-MeO-dppp})(\text{H}_2\text{O})_2](\text{PF}_6)_2$ -synthesis and structural characterization, *Eur. J. Inorg. Chem.*, 2001 (6), 1465–1473.
- [16] Figgis, B.N., and Lewis, J., 1960, *Modern Coordination Chemistry*, Interscience, New York.
- [17] Sugiyarto, K.H., Kusumawardani, C., Wigati, H., and Sutrisno, H., 2019, Structural study of the powder complex of Cu(II)-1,10-phenanthroline-trifluoroacetate, *Orient. J. Chem.*, 35 (1), 325–331.
- [18] Sugiyarto, K.H., Kusumawardani, C., Sutrisno, H., and Wibowo, M.W.A., 2018, Structural analysis of powdered manganese(II) of 1,10-phenanthroline (phen) as ligand and trifluoroacetate (TFA) as counter anion, *Orient. J. Chem.*, 34 (2), 735–742.
- [19] Chandra, S., and Sangeetika, X., 2004, EPR, magnetic and spectral studies of copper(II) and nickel(II) complexes of Schiff base macrocyclic ligand derived from thiosemicarbazide and glyoxal, *Spectrochim. Acta, Part A*, 60 (1-2), 147–153.
- [20] Eloussifi, H., Farjas J., Roura P., Ricart S., Puig T., Obradors X., and Dammak M., 2013, Thermo analytical study of the decomposition of yttrium trifluoroacetate thin films, *Thin Solid Films*, 545, 200–204.
- [21] Laishram, N.S., 2012, Synthesis, characterization and thermal studies of copper(II) complexes of 2,2'-bipyridyl and 1,10-phenanthroline, *J. Chem. Pharm. Res.*, 4 (9), 4400–4405.
- [22] Singh, V.P., Singh, P., and Singh, A.K., 2011, Synthesis, structural and corrosion inhibition studies on cobalt(II), nickel(II), copper(II) and zinc(II) complexes with 2-acetylthiophene benzoyl hydrazone, *Inorg. Chim. Acta*, 379 (1), 56–63.
- [23] Ferenc, W., Walków-Dziewulska, A., Sarzynski, J., and Paszkowska, B., 2006, Magnetic, thermal and spectral properties of Ni(II) 2,3-, 3,5- and 2,6-dimethoxybenzoates, *Eclat. Quím.*, 31 (3), 53–60.
- [24] Mabbs, F.E., and Machin, D.J., 1973, *Magnetism and Transition Metal Complexes*, Chapman and Hall, London.
- [25] Abramov, V., 2010, New nickel(II) complexes with N-donor ligands and anions as coligands. Structures and optical properties, *Dissertation*,

- Faculty of Mathematics and Natural Sciences, University of Cologne, Deutschland.
- [26] Shad, H.A., Thebo, K.H., Ibupoto, Z.H., Malik, M.A., O'Brien, P., and Raftery, J., 2011, Synthesis, characterization, and crystal structure of a copper(II) complex of 1,10-phenanthroline and succinate, *J. Coord. Chem.*, 64 (13), 2353–2360.
- [27] Kumar, S.P., Suresh, R., Giribabu, K., Manigandan, R., Munusamy, S., Muthamizh, S., and Narayanan, V., 2014, Microwave synthesis of tris-(1,10-phenanthroline) manganese(II) complex and its electrochemical sensing property of catechol, *Int. J. ChemTech Res.*, 6 (6), 3280–3283.
- [28] Chen, H., Xu, X.Y., Gao, J., Yang, X.J., Lu, L.D., and Wang, X., 2006, Study on crystal structure of $[\text{Ni}(\text{phen})_3](\text{ClO}_4)_2$, *Acta Phys. Chim. Sin.*, 22 (7), 856–859.
- [29] Tosonian, S., Ruiz, C.J., Rios, A., Frias, E., and Eichler, J.F., 2013, Synthesis, characterization, and stability of iron (III) complex ions possessing phenanthroline-based ligands, *Open J. Inorg. Chem.*, 3 (1), 7–13.
- [30] Abdelhak, J., Cherni, S.N., and Zid, M.F., 2014, Synthesis, characterization, and crystal structure of new cobalt(III) complex: $[\text{Tris}(1,10\text{-phenanthroline-}\kappa^2\text{N},\text{N}')\text{ cobalt(III)}]\text{ trinitrate monohydrate } [\text{Co}(\text{C}_{12}\text{H}_8\text{N}_2)_3](\text{NO}_3)_3 \cdot \text{H}_2\text{O}$, *Mediterr. J. Chem.*, 3 (1), 738–745.
- [31] Zang, J., Wang, L.X., Zang, L., Chen, Y., and Zang, Q.T., 2013, Co-luminescence properties of terbium ions–benzoic acid–phen complexes doped with europium ions, *Rare Met.*, 32 (6), 599–604.
- [32] Skyrianou, K.C., Perdih, F., Turel, I., Kessissoglou, D.P., and Psomas, G., 2010, Nickel–quinolones interaction. Part 2 – Interaction of nickel(II) with the antibacterial drug oxolinic acid, *J. Inorg. Biochem.*, 104 (2), 161–170.
- [33] Suzuki, H., Takiguchi, T., and Kawasaki, Y., 1978, Synthesis and spectroscopy of acetato and dithiocarbamate complexes of bis(cyclopentadienyl) zirconium(IV), *Bull. Chem. Soc. Jpn.*, 51 (6), 1764–1767.
- [34] Osowole, A.A., Kolawole, G.A., and Fagade, O.E., 2008, Synthesis, characterization and biological studies on unsymmetrical Schiff-base complexes of nickel(II), copper(II) and zinc(II) and adducts with 2,2'-dipyridine and 1,10-phenanthroline, *J. Coord. Chem.*, 61 (7), 1046–1055.
- [35] Sinha, S.P., 1964, 2,2'-Dipyridyl complexes of rare earths. I: Preparation, infrared and some other spectroscopic data, *Spectrochim. Acta*, 20, 879–886.
- [36] Lawrance, G.A., 1986, Coordinated trifluoromethanesulfonate and fluorosulfate, *Chem. Rev.*, 86 (1), 17–33.
- [37] Crowder, G.A., and Jackson, D., 1971, Infrared and Raman spectra of methyl trifluoroacetate, *Spectrochim. Acta, Part A*, 27 (9), 1873–1877.
- [38] Crowder, G.A., 1971, Infrared spectra of trifluoroacetate esters, *J. Fluorine Chem.*, 1 (2), 219–225.
- [39] Fan, L., Wei, P., Pang, S., and Zhang, X., 2010, Tris(2,2'-bipyridine)nickel(II) hexamolybdate, *Acta Crystallogr., Sect. E: Struct. Rep. Online*, 66 (9), m1119.
- [40] Zhou, Y., Li, X., Xu, Y., Cao, R., and Hong, M., 2003, Tris(2,2'-bipyridine)nickel(II) diperchlorate, *Acta Crystallogr., Sect. E: Struct. Rep. Online*, 59 (5), m300–m302.
- [41] Golovnev, N.N., Molokeyev, M.S., Sterkhova, I.V., Lesnikov, M.K., and Samoilo, A.S., 2019, Structure of bis(2-thiobarbiturate)Tris(2,2-bipyridyl)nickel(II) hexahydrate, *J. Struct. Chem.*, 60 (1), 111–116.
- [42] Ruiz-Perez, C., Lorenzo Luis, P.A., Lloret, F., and Julve, M., 2002, Dimensionally controlled hydrogen-bonded nanostructures: Synthesis, structure, thermal, and magnetic behaviour of the tris(chelated) nickel(II) complex $[\text{Ni}(\text{bipy})_3]\text{Cl}_2 \cdot 5.5\text{H}_2\text{O}$ (bipy = 2,2'-bipyridyl), *Inorg. Chim. Acta*, 336, 131–136.
- [43] Lin, S.H., Wang, Z.K., Zhang, B.H., Hu, H.M., and Huang, J.S., 2000, Crystal structure of tris(2,2'-bipyridine)nickel(II) tetrachlorozincate, *Chin. J. Chem.*, 19 (2), 95–98.
- [44] Toby, B.H., 2006, R factors in Rietveld analysis: How good is good enough?, *Powder Diffr.*, 21 (1), 67–70.

Carbonization of Lignin Extracted from Liquid Waste of Coconut Coir Delignification

Widiyastuti Widiyastuti^{1,*}, Mahardika Fahrudin Rois¹, Heru Setyawan¹,
Siti Machmudah¹, and Diky Anggoro²

¹Department of Chemical Engineering, Institut Teknologi Sepuluh Nopember, Kampus ITS Sukolilo, Surabaya 60111, Indonesia

²Department of Physics, Institut Teknologi Sepuluh Nopember, Kampus ITS Sukolilo, Surabaya 60111, Indonesia

* **Corresponding author:**

tel: +62-31-5946240

email: widi@chem-eng.its.ac.id

Received: June 10, 2019

Accepted: October 14, 2019

DOI: 10.22146/ijc.46484

Abstract: Lignin, as a by-product of the pulping process, is less widely used for worth materials. In this study, the utilization of lignin by-product of the soda delignification process of coconut coir converted to the activated carbon by a simple precipitation method followed by the carbonization at various temperatures is presented. The by-product liquor of the soda delignification process having a pH of 13.4 was neutralized by dropping of hydrochloric acid solution to achieve the pH solution of 4, resulting in the lignin precipitation. The precipitated was washed, filtered, and dried. The dried lignin was then carbonized under a nitrogen atmosphere at various temperatures of 500, 700, and 900 °C. The dried lignin and carbonized samples were characterized using SEM, XRD, FTIR, and nitrogen adsorption-desorption analyzer, to examine their morphology, X-Ray diffraction pattern, chemical bonding interaction, and surface area-pore size distribution, respectively. The characterization results showed that the functional groups of lignin mostly disappeared gradually with the increase of temperature approached the graphite spectrum. The XRD patterns confirmed that the carbonized lignin particles were amorphous and assigned as graphitic. All samples had a pore size of 3–4 nm classified as mesoporous particles. This study has shown that the carbonization lignin at a temperature of 700 °C had the highest surface area (i.e., 642.5 m²/g) in which corresponds to the highest specific capacitance (i.e., 28.84 F/g).

Keywords: coconut coir; soda delignification; lignin; carbonization; mesoporous particles

■ INTRODUCTION

Lignin is the most abundant renewable source of aromatic groups in nature and the second most abundant terrestrial biopolymer after cellulose. The pulp and paper industry is the primary producer of cellulose-rich fibers. Besides, cellulosic ethanol facilities are currently coming to resolve the limitation of fossil fuel. Both industries produce lignin as a by-product. The processes of Kraft, sulfite, soda, organosolv, and hydrothermal are some of the delignification methods that use sodium hydroxide and sodium sulfide, sulfur dioxide, sodium hydroxide, an organic solvent, and highly compressed water and temperature, respectively, to separate cellulose fiber by dissolving the lignin. For non-woody lignocellulose sources, soda pulping is widely used for the delignification method [1].

On the other hand, the lignin market is still limited for the valuable application [2]. Therefore, the conversion of lignin to the more valuable functional materials is still a challenge, even though lignin is becoming promising for many future applications [3-5]. As the by-product, lignin liquor is usually treated as liquid wastewater, and then it is concentrated and fired to serve only as fuel producing steam, electricity, and inorganic chemical for internal mill use [6]. Several efforts for extracting lignin from black liquor before further processing are membrane-assisted electrochemical [7] and precipitation through the addition of an acidifying agent of carbon dioxide [8], chloric acid [9], and sulfuric acid [10].

Carbon black is mostly produced from incomplete combustion of fossil fuel. The utilization of agricultural

bio-waste materials directly without separating the components of the bio-waste materials that contain cellulose, hemicellulose, and lignin has also been used for activated carbon sources [11]. The cellulose is separated from lignin for the use of the biofuel process. The utilization of lignin itself to produce carbon black has been attempted, but it is still limited. Macroporous carbon was prepared from lignin by using poly(methyl methacrylate) as the template [12]. Usually, phenolic resin and polystyrene latex were used as the carbon source and template particles, respectively, to generate macroporous carbon nanospheres [13]. The use of lignin from bioethanol co-product using the hydrolysis process for conductive carbon black filler has been studied [14]. Powdered and granular carbon adsorbents are also produced from hydrolysis lignin as the by-product of biofuels [15]. The highest specific surface area was 654 m²/g obtained from the lignin carbonization at a temperature of 900 °C, followed by ball milling. Activated carbon from commercial alkali lignin was synthesized by simultaneous carbonization and alkali hydroxide activation for supercapacitors application [16]. The use of lignin sources and lignin-rich biomass were also compared to the effects of the carbonization process on the activated carbon properties [17]. Alkali lignin purified from papermaking black-liquor was also used to generate a composite of carbon/ZnO for the photocatalytic application [18]. Biomass-based lignin extracted from industrial waste black liquor was carbonized and activated by steam to produce activated carbon [10]. Most of them use lignin from the delignification of wood source, notably pulp and mill industry. Lack of them use non-wood source, and as far as our knowledge, none of them use lignin from the delignification process of coconut coir. The study is needed because different raw material and activation procedure plays an essential role in the characteristics of the generated activated carbon. The microstructure, structure, and electrical characteristics of carbonaceous materials are highly influenced by the lignin feedstock [19].

In this study, the carbonization of lignin extracted from the liquor of coconut coir delignification using the soda-pulping process was introduced with simple precipitation and calcination methods. The effect of the

temperature of carbonization on the characteristics of the generated particles was elucidated. The samples were characterized using scanning electron microscopy (SEM), X-Ray diffraction (XRD), Fourier transform infrared spectrometry (FTIR), and nitrogen adsorption-desorption analyzer to examine the best condition for lignin carbonization derived from coconut coir. The specific capacitance was also measured from the cyclic voltammetry (CV) curve and the correlation with the other particle characteristics was studied.

■ EXPERIMENTAL SECTION

Materials

The liquor obtained from the delignification of coconut coir for cellulose aerogel preparation by the soda process with a pH of 13.4 was used as raw material [20]. The coconut coir was obtained from a traditional market in Keputih, Surabaya, Indonesia. Hydrochloric acid (HCl) 37 wt.% in analytical grade was purchased from Merck.

Instrumentation

The instrumentation used for samples' characterizations were thermogravimetric and differential analysis (TG-DTA, Shimadzu DTG-60H), X-Ray diffraction (XRD, PanAnalytical X'Pert MPD System), Fourier transform infrared spectroscopy (FTIR, Nicolet iS10), scanning electron microscopy (SEM, Hitachi FlexSEM 1000), a nitrogen adsorption-desorption analyzer (Nova 1200e, Quantachrome), and a potentiostat/galvanostat instrument (Metrohm, Autolab PGSTAT302N).

Procedure

Sample preparation

A solution of 1.5 M HCl prepared from HCl 37 wt.% was added drop by drop into the raw material under stirring to decrease the pH liquor of 4 and to precipitate the lignin. The precipitated particles were separated from the liquid by centrifugation and washed ten times to ensure the salt formed did not contaminate the extracted lignin. The precipitated particles were filtered and then dried in the oven at a temperature of 80 °C for 12 h. The dried lignin was calcined in the furnace under the flow of nitrogen with a flow rate of 100 mL/min.

For the sample of carbonized lignin at 500 °C, the dried lignin was gradually heated from 100 °C for 30 min, then at 300 °C for 1 h, and then at 500 °C for 2 h. For the samples of carbonized lignin at 700 and 900 °C, the preliminary treatment was the same with the sample of carbonized lignin 500 °C, and the next step was to continue heating at 700 and 900 °C, respectively, for 2 h.

Sample characterizations

Simultaneous measurement of thermogravimetric and differential analysis was used to examine the weight losses due to lignin decomposition by increasing the temperature. The heating rate was 5 °C/min under the flow of nitrogen. X-Ray diffraction with Cu K α as the radiation source ($\lambda = 0.15406$ nm) was used to evaluate the microstructure of the generated particles. Fourier transform infrared spectroscopy was used to characterize the functional group of the samples. Scanning electron microscopy was used to investigate the morphology of the generated particles. A nitrogen adsorption-desorption analyzer measured at 77 K, the boiling point of nitrogen, was used for surface area and pore characterization. The samples were degassed under the flow of nitrogen at 300 °C for 3 h. The total pore volume of the samples was estimated from the adsorption branch of the isotherm at a relative pressure P/P_0 close to 1. The specific surface area of the samples was calculated by using the multiple-point Brunauer-Emmett-Teller (BET) method at $P/P_0 < 0.3$. The pore size distribution of the samples at the adsorption isotherm using the Barret-Joyner-Halenda (BJH) method was used to determine the diameter and volume of pore samples. The specific capacitance was determined from cyclic voltammetry (CV) at potential applied ranging from -1 to 0 V with a sweep rate of 10 mV/sec using potentiostat/galvanostat instrument. The sample was prepared by mixing the carbon sample and polyvinylidene difluoride (PVdF) at a ratio of 10:1 by weight and transforming the mixture into carbon paste by adding drops of 1-methyl-2-pyrrolidone (NMP). The paste was coated to 1.5 cm² nickel-foam assigned as a working electrode. A platinum foil and Ag/AgCl electrode were used as the counter and reference electrodes, respectively. 100 mL of 0.1 M Na₂S₂O₃ was used as an

electrolyte solution. The specific capacitance (C_s , F/g) was calculated using the following equation:

$$C_s = \frac{1}{mv(V_c - V_a)} \int_{V_a}^{V_c} I(V) dV \quad (1)$$

where v is the potential scan rate (mV/sec), $(V_c - V_a)$ is the applied potential range (V), I is the current response per unit area (mA/cm²), and m is the mass of a sample (g).

RESULTS AND DISCUSSION

The Composition and the Thermal Analysis of the Dried Lignin

The proximate analysis of dried lignin indicated that the volatile matter has the highest composition of 38.03 wt.%, followed by fixed carbon as the second-highest composition of 37.00 wt.%. The ash and the moisture contents of the dried lignin were 21.06 and 3.91 wt.%, respectively. The proximate analysis was supported by gravimetric analysis under the flow of nitrogen, as shown in Fig. 1. The first peak on the DTA graph corresponds to the loss of around 4.5 wt.% moisture content at around 100 °C as indicated by the TG graph. The second peak of the DTA graph occurred at around 416 °C corresponds to around 37 wt.% loss of volatile compounds in the lignin. The clear peak does not indicate the loss of carbon on the DTA graph because of the slow degradation rate of carbon up to the temperature at around 860 °C with the remaining weight at around 21.6 wt.% corresponds to the ash content.

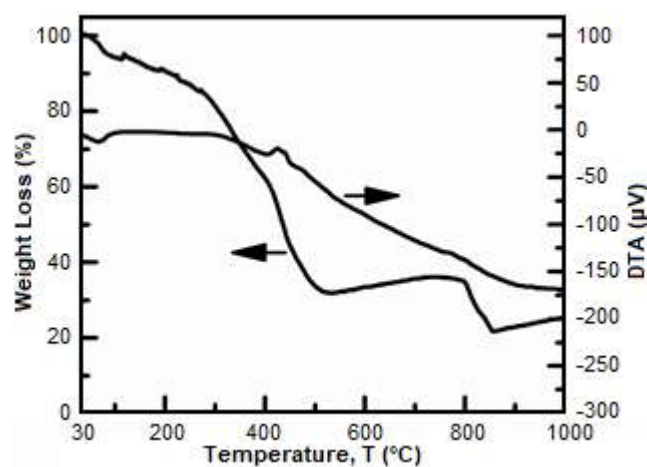


Fig 1. Thermogravimetric analysis of dried lignin using under the flow of nitrogen

The Effect of Carbonization Temperature on the Particle Characteristics

The visual appearance of dried lignin and carbonized lignin at temperatures of 500, 700, and 900 °C are shown in Fig. 2(a-d). The dried lignin has a brownish-red appearance and bulky form. Carbonized lignin is black and shiner with the increase in carbonization temperature caused by the decomposition of the organic compound of some lignin constituents into volatile gases and solid carbon. TG-DTA measurement has confirmed the disappearing of the organic compound during the carbonization by decreasing the weight percentage with increasing the temperature. To investigate further the functional groups existing in the dried lignin and the carbonized lignins in varied temperatures, FTIR analysis is carried out.

Fig. 3 represents the FTIR spectrum of dried lignin and carbonized lignin at temperatures of 500, 700, and 900 °C. The characteristics of FTIR spectrum of dried lignin corresponds to FTIR spectrum at wavenumbers: (1) 3338 cm^{-1} ; (2) 2920 cm^{-1} ; (3) 1695 cm^{-1} ; (4) 1604 cm^{-1} ; (5) 1509 cm^{-1} ; (6) 1420 cm^{-1} ; (7) 1213 cm^{-1} ; (8) 1112 cm^{-1} ; and

(9) 1033 cm^{-1} . These absorption bands in the FTIR spectrum can be assigned to (1) hydroxyl groups in phenolic and aliphatic structures, (2) CH stretching in aromatic methoxyl groups and in aliphatic methyl and methylene groups of side chains, (3) C=O stretching in conjugated *p*-substituted aryl ketones, (4) -C=O of pyruvate, (5) C=C stretching of the aromatic ring (G)CH deformation, (6) C-H asymmetric deformation in -OCH₃, (7) aromatic C-O stretching vibrations, (8) aromatic C-H in-plane deformation, and (9) C_{alkyl}-O ether vibrations methoxyl, respectively [21]. The spectra presented the characteristic peaks of lignin that also reported by others [22-23]. The functional groups of lignin are gradually removed with the increase of carbonization temperature. The pyruvate bond -C=O, the aromatic ring C=C, and the C_{alkyl}-O-ether methoxyl are still observed at the carbonization temperature of 500 °C. Most of the functional groups of lignin disappear at temperatures of 700 and 900 °C and approach the graphite spectrum.

XRD analysis is used to examine the change in the XRD pattern caused by the carbonization temperature.

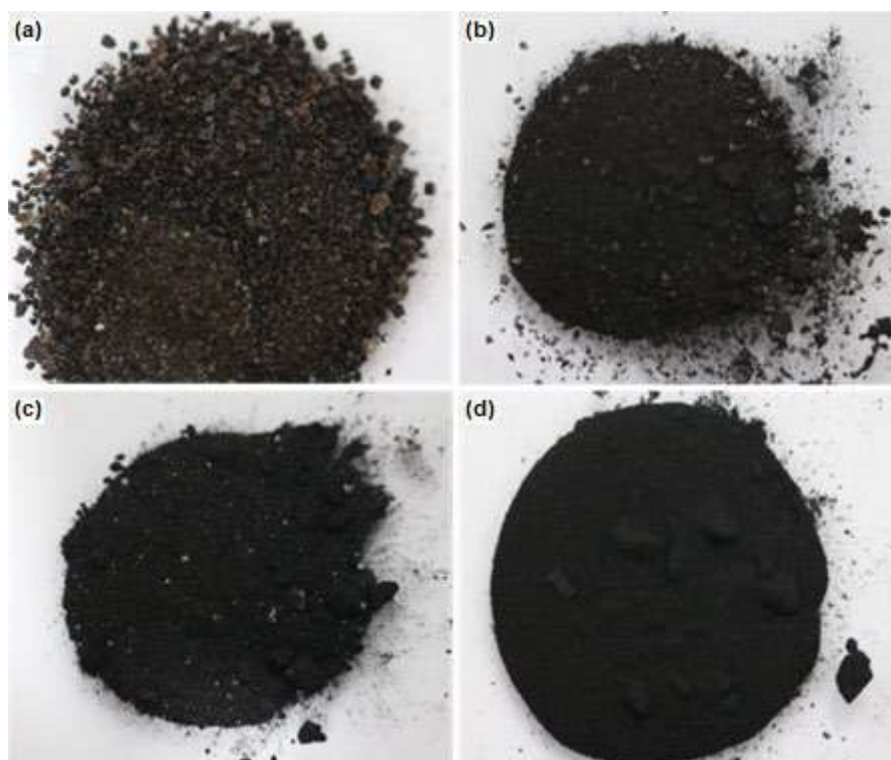


Fig 2. Visual appearances of (a) dried lignin, (b) carbonized lignin at 500 °C, (c) 700 °C, and (d) 900 °C

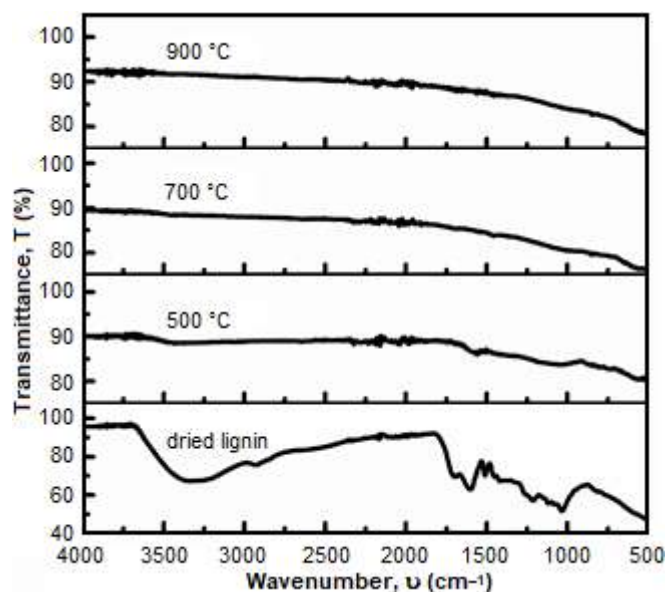


Fig 3. FTIR spectra of dried lignin and carbonized lignins at temperatures of 500, 700, and 900 °C

The XRD pattern of dried lignin and carbonized dried lignin at temperatures of 500, 700, and 900 °C are shown in Fig. 4. The plane of graphite structure (002) at the peak intensity 2θ centered at around 26.5° shows more clearly for carbonized lignin than that of the dried lignin. Increasing the carbonization temperature also slightly shifts the 2θ peak position of the plane (002) to the right position from 21.8° to 25.3° . However, for the carbonization at a temperature of 900 °C, the peak intensity 2θ of the plane (002) shifts back to the left to the position of 23.3° . Another 2θ peak intensity at around 44° is also observed for carbonized lignin and is not found in the dried lignin. The intensity is more apparent with the increase of the carbonization temperature. The same with the peak intensity 2θ of the plane (002), the peak intensity 2θ at around 44° corresponds to the plane (101), which is also assigned to the graphitic sheets. The presences of the broad profiles of the X-ray diffraction patterns represent that the structure of carbon materials is amorphous.

The effect of carbonization temperature on particle morphology is characterized by Scanning Electron Microscopy (SEM). SEM images for dried lignin and carbonized lignin at temperatures of 500, 700, and 900 °C are depicted in Fig. 5 (a-d). For low magnification, all samples exhibit shape irregularly and agglomerated

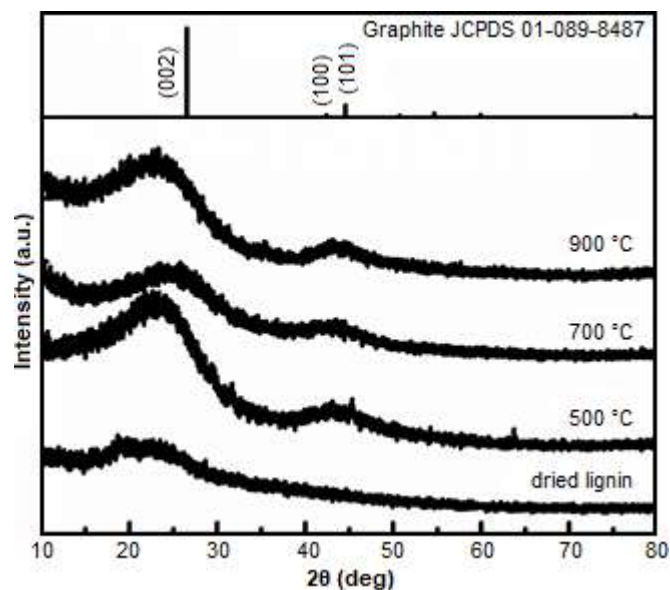


Fig 4. X-ray diffraction patterns of dried lignin and carbonized lignins at temperatures of 500, 700, and 900 °C

particles with the size of a few micrometers. However, for higher magnification (insets Fig. 5(a-d)), the distinct microstructures can be observed. For dried lignin, it can be shown that the agglomerated particles consisted of particles in the scale of nanometers. On the other hand, the size and the number of particle's pore increase with the increase in temperature, as shown in the high magnification SEM images. The increasing carbonization temperature led to the decomposition of more volatile components left behind the micro- and mesoporous carbon particles. The formation of pores for carbonized lignin brings out the increase in the specific surface area that will be explained in the following paragraph.

Table 1 shows the comparison of the specific surface area, pore diameter, and pore volume of lignin without carbonization and with carbonization at various temperatures. The surface area based on BET isotherm analysis of dried lignin extracted from the soda process of coconut coir without followed by carbonization was only $7.037 \text{ m}^2/\text{g}$. The carbonization at temperature of 500 °C increased the specific surface area of the sample to $157.621 \text{ m}^2/\text{g}$. An increase in carbonization temperature to 700 °C could make a 4-fold increase in the specific surface area compared to 500 °C. However, the specific surface area slightly decreased to $541.277 \text{ m}^2/\text{g}$ for the

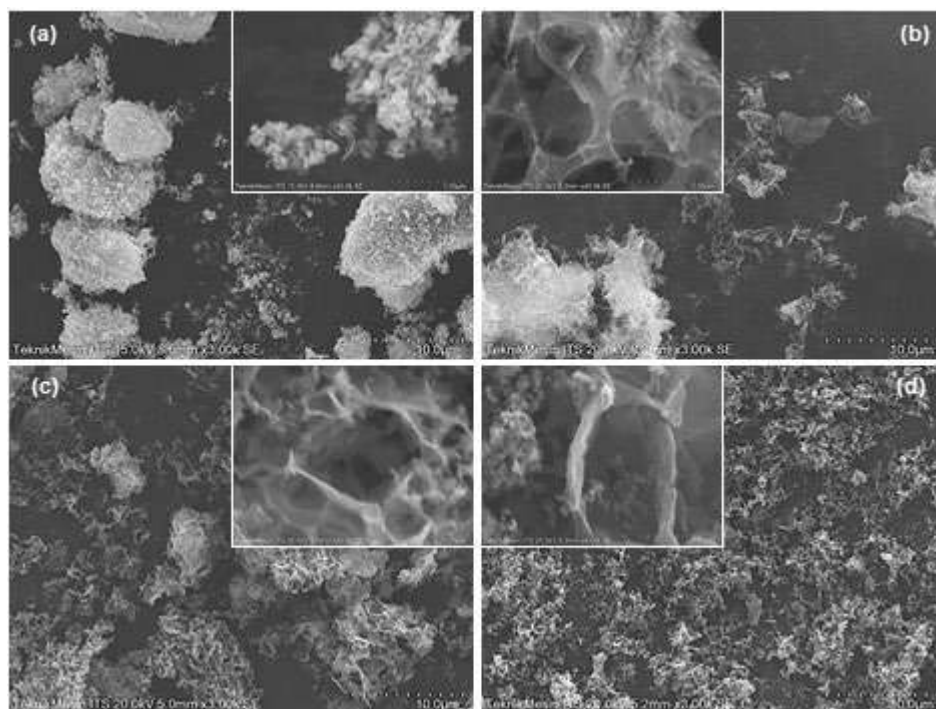


Fig 5. SEM images of (a) dried lignin, (b) carbonized lignins at 500 °C, (c) 700 °C, and (d) 900 °C

Table 1. Specific surface area, pore diameter, and pored volume of dried lignin and carbonized lignin at various temperatures

Sample	Specific surface area (m ² /g)	Pore diameter (nm)	Pore volume (cm ³ /g)
Dried lignin	7.037	3.433	0.002
Carbonized lignin 500 °C	157.621	3.841	0.013
Carbonized lignin 700 °C	642.501	3.387	0.050
Carbonized lignin 900 °C	541.277	3.407	0.084

carbonization at a temperature of 900 °C. The pore size for all samples was not so different, which was in the range of 3–4 nm categorized into mesopore type (2 nm < pore size < 50 nm). The pore volume increased with temperature in which lignin carbonized at 500, 700, and 900 °C had 7, 25, and 42 times more pore volume, respectively, compared to the dried lignin. The decomposition of the most functional group of lignin during carbonization left behind larger pore volume with relatively the same size pore for higher carbonization temperature.

The isothermal adsorption-desorption profiles as a function of the relative pressure of carbonization of lignin at temperatures of 700 and 900 °C are depicted in Fig. 6. Based on the IUPAC 1985 classification, the profiles of carbonized lignin at the temperatures of 700 and 900 °C

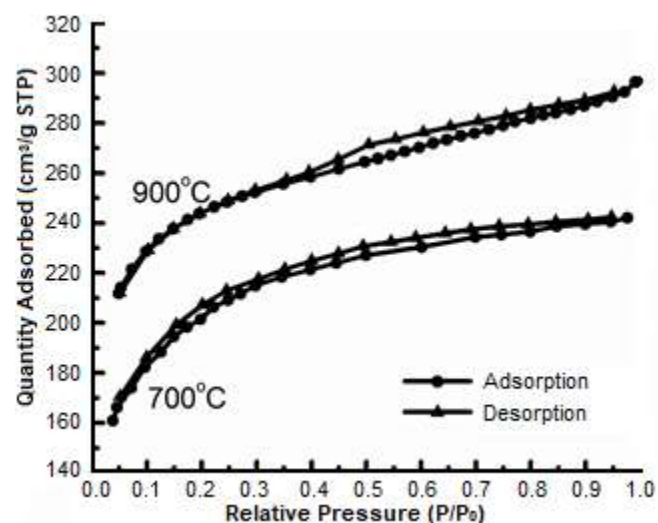


Fig 6. Adsorption and desorption isotherms of the lignin calcined at temperatures of 700 and 900 °C

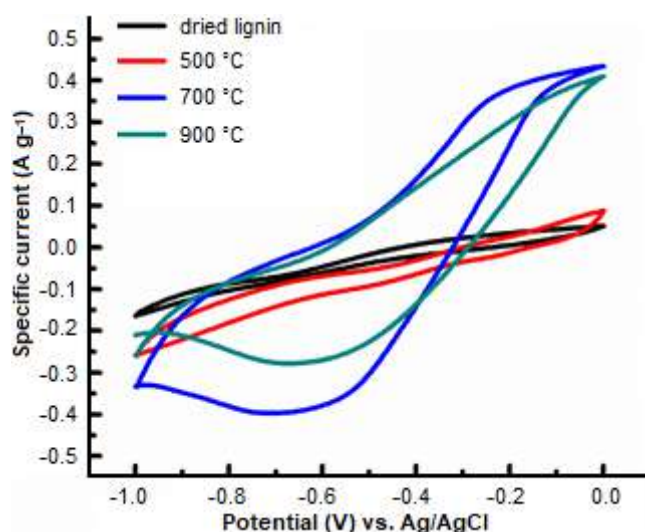


Fig 7. Voltammograms obtained in three-split electrode configuration at 10 mV/sec for dried lignin, carbonized lignin at various temperatures

can be categorized to the Type IV isotherm because there are hysteresis loops [24]. Even though the hysteresis is narrow, the hysteresis is associated with the filling and the emptying of the mesopores by capillary condensation.

The Electrochemical Properties

Fig. 7 shows the cyclic voltammetry curves of the samples at a 10 mV/sec sweep rate. The cyclic voltammetry did not exhibit rectangular curves as the behavior of the double layer capacitive material; however, the symmetry and un-peak curve can be obtained. The specific capacitance calculated using Eq. (1) for dried lignin, carbonized lignin 500 °C, carbonized lignin 700 °C and carbonized lignin 900 °C are 1.96, 4.13, 28.84, and 17.90 F/g, respectively. The carbonized lignin 700 °C gives the highest specific capacitance that correlates with the highest specific surface area. Hu and Hsieh were also reported that the highest surface area and pore volume resulted in the highest specific capacitance and suitable for supercapacitors fabrication [16].

CONCLUSION

Lignin was successfully extracted from the liquid waste of the soda delignification process of coconut coir via neutralization using a hydrochloric acid solution. The extracted lignin was carbonized at various temperatures and characterized using scanning electron microscopy

(SEM), X-Ray diffraction (XRD), Fourier transform infrared spectrometry (FTIR), nitrogen adsorption-desorption analyzer and cyclic voltammetry (CV). The results showed that the carbonization process led to an increase in the specific surface area of the generated carbon particles. The carbonized lignins had mesopores and amorphous graphitic structure with the highest surface area (i.e., 642.5 m²/g) and specific capacitance (i.e., 28.84 F/g) at carbonization temperature of 700 °C.

ACKNOWLEDGMENTS

Research Grant sponsored by Directorate of Research and Community Services, Directorate General of Strengthening Research and Development, Ministry of Research Technology and Higher Education, Republic Indonesia (No. 128/SP2H/PTNBH/DRPM/2018) is gratefully acknowledged. The authors also want to thank Mr. Fahmi Reza Wijanarko and Ms. Deninta Nur Iwana for their assistance in the experiments.

REFERENCES

- [1] Haghdan, S., Rennecker, S., and Smith, G.D., 2016, "Sources of lignin" in *Lignin in Polymer Composites*, Eds. Faruk, O., and Sain, M., Elsevier Inc., Oxford, 1–11.
- [2] Graichen, F.H.M., Grigsby, W.J., Hill, S.J., Raymond, L.G., Sanglard, M., Smith, D.A., Thorlby, G.J., Torr, K.M., and Warnes, J.M., 2017, Yes, we can make money out of lignin and other bio-based resources, *Ind. Crops Prod.*, 106, 74–85.
- [3] Norgren, M., and Edlund, H., 2014, Lignin: Recent advances and emerging applications, *Curr. Opin. Colloid Interface Sci.*, 19 (5), 409–416.
- [4] Naseem, A., Tabasum, S., Zia, K.M., Zuber, M., Ali, M., and Noreen, A., 2016, Lignin-derivatives based polymers, blends and composites: A review, *Int. J. Biol. Macromol.*, 93, 296–313.
- [5] Thakur, V.K., and Thakur, M.K., 2015, Recent advances in green hydrogels from lignin: A review, *Int. J. Biol. Macromol.*, 72, 834–847.
- [6] Laurichesse, S., and Avérous, L., 2014, Chemical modification of lignins: Towards biobased polymers, *Prog. Polym. Sci.*, 39 (7), 1266–1290.

- [7] Jin, W., Tolba, R., Wen, J., Li, K., and Chen, A., 2013, Efficient extraction of lignin from black liquor via a novel membrane-assisted electrochemical approach, *Electrochim. Acta*, 107, 611–618.
- [8] Kouisni, L., Holt-Hindle, P., Maki, K., and Paleologou, M., 2012, The LignoForce System™: A new process for the production of high-quality lignin from black liquor, *J. Sci. Technol. For. Prod. Processes*, 2 (4), 6–10.
- [9] Wang, G., and Chen, H., 2013, Fractionation of alkali-extracted lignin from steam-exploded stalk by gradient acid precipitation, *Sep. Purif. Technol.*, 105, 98–105.
- [10] Kim, D., Cheon, J., Kim, J., Hwang, D., Hong, I., Kwon, O.H., Park, W.H., and Cho, D., 2017, Extraction and characterization of lignin from black liquor and preparation of biomass-based activated carbon therefrom, *Carbon Lett.*, 22, 81–88.
- [11] Yahya, M.A., Al-Qodah, Z., and Ngah, C.W.Z., 2015, Agricultural bio-waste materials as potential sustainable precursors used for activated carbon production: A review, *Renewable Sustainable Energy Rev.*, 46, 218–235.
- [12] Seo, J., Park, H., Shin, K., Baeck, S.H., Rhym, Y., and Shim, S.E., 2014, Lignin-derived macroporous carbon foams prepared by using poly(methyl methacrylate) particles as the template, *Carbon*, 76, 357–367.
- [13] Balgis, R., Widiyastuti, W., Ogi, T., and Okuyama, K., 2017, Enhanced electrocatalytic activity of Pt/3d hierarchical bimodal macroporous carbon nanospheres, *ACS Appl. Mater. Interfaces*, 9 (28), 23792–23799.
- [14] Snowdon, M.R., Mohanty, A.K., and Misra, M., 2014, A study of carbonized lignin as an alternative to carbon black, *ACS Sustainable Chem. Eng.*, 2 (5), 1257–1263.
- [15] Rabinovich, M.L., Fedoryak, O., Dobeles, G., Andersone, A., Gawdzik, B., Lindström, M.E., and Sevastyanova, O., 2016, Carbon adsorbents from industrial hydrolysis lignin: The USSR/Eastern European experience and its importance for modern biorefineries, *Renewable Sustainable Energy Rev.*, 57, 1008–1024.
- [16] Hu, S., and Hsieh, Y.L., 2017, Lignin derived activated carbon particulates as an electric supercapacitor: Carbonization and activation on porous structures and microstructures, *RSC Adv.*, 7 (48), 30459–30468.
- [17] Correa, C.R., Stollovsky, M., Hehr, T., Rauscher, Y., Rolli, B., and Kruse, A., 2017, Influence of the carbonization process on activated carbon properties from lignin and lignin-rich biomasses, *ACS Sustainable Chem. Eng.*, 5 (9), 8222–8233.
- [18] Wang, H., Qiu, X., Liu, W., and Yang, D., 2017, Facile preparation of well-combined lignin-based carbon/ZnO hybrid composite with excellent photocatalytic activity, *Appl. Surf. Sci.*, 426, 206–216.
- [19] Vivekanandhan, S., Misra, M., and Mohanty, A.K., 2015, Microscopic, structural, and electrical characterization of the carbonaceous materials synthesized from various lignin feedstocks, *J. Appl. Polym. Sci.*, 132 (15), 41786.
- [20] Fauziyah, M., Widiyastuti, W., Balgis, R., and Setyawan, H., 2019, Production of cellulose aerogels from coir fibers via an alkali-urea method for sorption applications, *Cellulose*, 26, 9583–9598.
- [21] Raschip, I.E., Hitruc, E.G., and Vasile, C., 2011, Semi-interpenetrating polymer networks containing polysaccharides. II. Xanthan/lignin networks: A spectral and thermal characterization, *High Perform. Polym.*, 23 (3), 219–229.
- [22] do Santos, P.S.B., Erdocia, X., Gatto, D.A., and Labidi, J., 2014, Characterisation of Kraft Lignin Separated by Gradient Acid Precipitation, *Ind. Crops Prod.*, 55, 149–154.
- [23] Toledano, A., Serrano, L., Garcia, A., Mondragon, I., and Labidi, J., 2010, Comparative study of lignin fractionation by ultrafiltration and selective precipitation, *Chem. Eng. J.*, 157 (1), 93–99.
- [24] Rouquerol, J., Rouquerol, F., Llewellyn, P., Maurin, G., and Sing, K., 2014, *Adsorption by Powders and Porous Solids: Principles, Methodology and Applications*, 2nd Ed., Academic Press, London.

Metabolite Profile Evaluation of Indonesian Roasted Robusta Coffees by ^1H NMR Technique and Chemometrics

Nizar Happyana*, Elvira Hermawati, Yana Maolana Syah, and Euis Holisotan Hakim

Organic Chemistry Division, Chemistry Study Program, Faculty of Mathematics and Natural Sciences, Bandung Institute of Technology, Jl. Ganesha No. 10, Bandung 40132, West Java, Indonesia

* **Corresponding author:**

tel: +62-222502103

email: nizar@chem.itb.ac.id

Received: June 10, 2019

Accepted: August 2, 2019

DOI: 10.22146/ijc.46492

Abstract: In this work, ^1H NMR analysis, along with a chemometrics approach, had been applied for investigating metabolite profiles of Indonesian roasted Robusta coffees obtained from Lampung and Aceh. In total, 24 compounds had been successfully detected in the ^1H NMR spectra of the Robusta coffee extracts. Concentrations of some identified metabolites present in the coffees were determined by the quantitative ^1H NMR technique. Orthogonal projection to latent structure-discriminant analysis (OPLSDA) was used as a primary method for the chemometric approach. OPLSDA had classified clearly the Robusta coffee samples corresponding to their origin. Loading plot and S-plot of the OPLSDA revealed characteristic metabolites for each Robusta coffee. The results indicated that quinic acid, mannose, arabinoses, and acetic acid were an important discriminant compound for Lampung Robusta coffees. Meanwhile, lipids, lactic acid, and 5-caffeoylquinic acid were found as characteristic metabolites for Aceh Robusta coffee. This report provided knowledge about the chemical composition of Lampung and Aceh Robusta coffees and shed more light on the diversity of Indonesian Robusta coffees. Furthermore, it confirmed that ^1H NMR analysis coupled with chemometrics was a powerful method for evaluating and classifying metabolite profiles of the roasted Robusta coffees.

Keywords: ^1H NMR; chemometric; roasted Robusta coffee; Indonesia

■ INTRODUCTION

Coffee is one of the most consumed nonalcoholic drinks in the world. The drink is well known for its unique flavors and remarkable aromas. Coffee also possesses physiological and psychological effects [1]. Arabica (*Coffea arabica* L.) and Robusta coffees (*Coffea canephora* P.) are the most consumed coffees worldwide. Arabica coffee is considered having a higher quality than Robusta since it possesses a better taste, an intense aroma, and lower caffeine content [2]. As the second most cultivated coffee after Arabica, Robusta has a more bitter taste and contains more caffeine and chlorogenic acids but fewer sugars [3]. However, Robusta coffee is easier to cultivate since it is more resistant to plant diseases, weather conditions, and able to grow at lower altitudes as well [3].

Literature studies show that many metabolomics and chemometric studies of Robusta coffee focused on the authentication and the differentiation of coffee species [4-

12]. Several measurement methods have been used in these studies, including IR spectroscopies [6,12-13], Raman spectroscopy [7], UV-visible spectroscopy [8], GC [4-5], HPLC [9], GC-MS [11] and NMR [10]. Chemometrics combined with electronic nose and tongue had been used to analyze and classify 7 Chinese Robusta coffee cultivars with different roasting degrees [14]. Furthermore, chemometric approaches, along with GC-MS techniques, had been also applied to discriminate Chinese Robusta coffees based on their geographic origins [15]. Recently, this coupled method had been used to investigate the effects of chemical pre-treatment of Robusta coffee [16].

Indonesia is one of the biggest coffee producers in the world [17]. At least 70% of coffee plants cultivated in Indonesia are Robusta species. This coffee is cultivated in many Indonesian islands, including Sumatera, Java, Sulawesi, Papua, and Sumbawa. Aceh and Lampung that

located in Sumatra, are two popular regions producing Robusta coffee. The taste of Lampung Robusta is unique and different from the taste of Aceh Robusta. From the chemical point of view, the taste differences indicate the distinction of metabolite profiles since the taste of coffee is strongly related to its chemical components. However, the chemical information of Robusta coffees from Indonesia especially Lampung and Aceh, is very limited in the literature.

In this study, Robusta roasted coffees from Lampung and Aceh were analyzed with ^1H NMR technique for investigating their chemical profiles. Chemometric approaches were applied to classify the Robusta coffees based on their origins and to identify their characteristic metabolites. Furthermore, some identified metabolites in the Robusta coffees were successfully quantified by ^1H NMR method.

■ EXPERIMENTAL SECTION

Materials

All coffee samples used in this study were commercially roasted beans of Robusta coffees from Lampung (6 samples) and Aceh (6 samples) and obtained from some coffee companies/suppliers. The detail information of the coffee origins was depicted in Table 1. The extraction solvent used in this work, deuterated water (D_2O), was purchased from Merck (Germany). 3-(trimethylsilyl)-2,2,3,3-tetradeuteropropionic acid sodium salt (TSP) was bought from Merck (Germany). KH_2PO_4 and

K_2HPO_4 that used for making a buffer solution were purchased from Merck (Germany).

Instrumentation

An Encore mill (Baratza, United States) was used to grind the roasted coffee beans. An ultrasonic bath (Krisbow, Indonesia) was used to sonicate the samples. An MC-12 High Speed Microcentrifuge (Benchmark Scientific, United States) were used to centrifuge the samples. A 500 MHz Varian Unity INOVA spectrometer (Agilent Technologies, United States) was used to record ^1H NMR spectra of the Robusta coffees.

Procedure

Sample preparation

The coffee sample preparation was carried out based on the reported works [18-19] with slight modification. The sample was prepared by mixing 200 g of ground Robusta coffee with 1 mL of D_2O containing TSP 1.00 mM in a 2 mL plastic tube. The sample was sonicated at room temperature for 20 min and incubated on a water bath at 90 °C for 30 min. Afterward, the sample was cooled on the water for 10 min, centrifuged for 5 min, and the supernatant was then separated from the precipitate. One hundred microliters of phosphate buffer (pH 5) were added into 400 μL of supernatant and then transferred into a 5 mm NMR tube.

^1H NMR measurement and processing

In the ^1H NMR measurement, the H_2O signals were suppressed by the presaturation method. One hundred

Table 1. Origins of Robusta coffees used in the present study

Sample code	Coffee origin	Company/supplier
A1	Blangkejeren, Gayo Lues, Aceh	Fry Roast
A2	Linge, Aceh Tengah, Aceh	Rebbe Coffee Takengon
A3	Pintu Rime Gayo, Bener Meriah, Aceh	Serenade
A4	Takengon, Aceh Tengah, Aceh	Tampah Kopi Gayo
A5	Takengon, Aceh Tengah, Aceh	Raja Kopi Aceh
A6	Pintu Rime Gayo, Bener Meriah, Aceh	Garasco
L1	Liwa, Lampung Barat, Lampung	Fry Roast
L2	Ulubelu, Tanggamus, Lampung	Hilbrew coffee
L3	Liwa, Lampung Barat, Lampung	Kafein
L4	Liwa, Lampung Barat, Lampung	AKL
L5	Liwa, Lampung Barat, Lampung	AKL
L6	Ulubelu, Tanggamus, Lampung	Halokoffhouse

twenty-eight scans of 64 K data points are recorded with a spectral width of 8012 Hz, the acquisition time of 2.72 s, and a relaxation delay of 2 sec. The free-induction decay (FID) NMR data were processed with ACD/Labs 12.0 software (Advanced Chemistry Development, Inc., Toronto, Canada). This software was also used for referencing, phasing, baseline correction of ^1H NMR spectra. The chemical shifts of ^1H NMR spectra were referenced to the TSP signal. The signal assignments of the components in Robusta coffees were conducted by recognizing the fingerprinting chemical shifts of identified metabolites and comparing the spectra with the reference spectra of corresponding metabolites and with the data in the literature [18].

Multivariate statistical analysis

Alignment and bucketing of the ^1H NMR spectra were performed using ACD/Labs 12.0 software (Advanced Chemistry Development, Inc., Toronto, Canada). Bucketing was carried out by integrating regions of equal width (0.02 ppm) within δ 0.50–10.00 ppm and performed with an intelligent bucketing option as well. The residual water signal at δ 4.73–5.22 ppm were excluded from the multivariate data analysis. The caffeine signals at δ 3.22–3.49 ppm and δ 3.82–3.88 ppm were also excluded for avoiding spurious principal components (PCs) as a consequence of signal shifting [20]. The buckets were normalized to a total integral to avoid dilution effects of the samples. The processed data sets extracted from the ^1H NMR spectra were imported into SIMCA-P version 12.0 (Umetrics, Umeå, Sweden) for the multivariate statistical analysis. The data were then scaled with the Pareto scaling type. The principal component analysis (PCA), an unsupervised pattern-recognition approach, was performed to check intrinsic variation in the data set. Orthogonal projection to latent structure-discriminant analysis (OPLSDA), a supervised pattern-recognition approach, was applied as primary methods for extracting maximum separation among samples. The data sets of the roasted Robusta coffee were divided into 2 groups based on their geographical origins (Lampung and Aceh) and then analyzed with OPLSDA method. The percent of the response variation explained by the models (R2X and R2Y), and the percent of the response variation

predicted by the models according to cross validation (Q2) were computed. Hotelling's T2 regions, shown as an ellipse in the score plot, defined the 95% confidence interval of the modeled variation.

Quantitative ^1H NMR analysis

For evaluating metabolites quantitatively in Lampung and Aceh Robusta coffees, the obtained ^1H NMR data were further processed based on a previous report [21] with slight modifications. TSP signal (1 mM) was used as an internal standard. The quantification was conducted by calculating the relative ratio of the peak area of selected proton signals of the target metabolites to the singlet peak of the TSP signal. The statistical calculation of quantitative ^1H NMR analysis was performed using Microsoft Excel 2013.

RESULTS AND DISCUSSION

Identified Metabolites in the Roasted Robusta Coffees

In this work, metabolites in the roasted Robusta coffee samples (Lampung and Aceh) were recognized by identifying their fingerprint signals in the ^1H NMR spectra and comparing them with the spectra of corresponding reference compounds. The metabolite identification was further confirmed by comparing the spectra with the data reported in the literature [18-19,22]. In total, 24 metabolites were successfully identified in the Robusta coffees, as depicted in the ^1H NMR spectra of the Robusta coffee (Fig. 1). Some molecular structures of the identified metabolites were described in Fig. 2.

Caffeine, as one of the major compounds in the roasted coffee bean, was clearly identified in the ^1H NMR spectra. The strong singlet signals at δ 3.28, 3.45 and 3.88 ppm were assigned as the 3 *N*-methyl of caffeine. Meanwhile, the singlet signal at δ 7.83 ppm was designed as an aromatic proton of caffeine. The intense signals of caffeine in the ^1H NMR spectra of the roasted coffees indicated that the compound is thermally stable during the roasting. Thus, caffeine is an excellent quantitative marker for coffees as proposed by previous reports [18,23]. The proton signals belong to 3 dominant compounds of chlorogenic acids, namely 3-caffeoylquinic

acid, 4-caffeoylquinic acid, and 5-caffeoylquinic acid were also clearly visible in the aliphatic and aromatic regions of the ^1H NMR spectra as shown in Fig. 1. Chlorogenic acids, the ester form of caffeic acid and quinic acid, are major compounds in coffees. However, during the roasting, some chlorogenic acids degrade into quinic acid and γ -quinide since the compounds are unstable thermally [24]. The signals of quinic acid, another major compound in the roasted coffee, were recorded in the ^1H NMR spectra

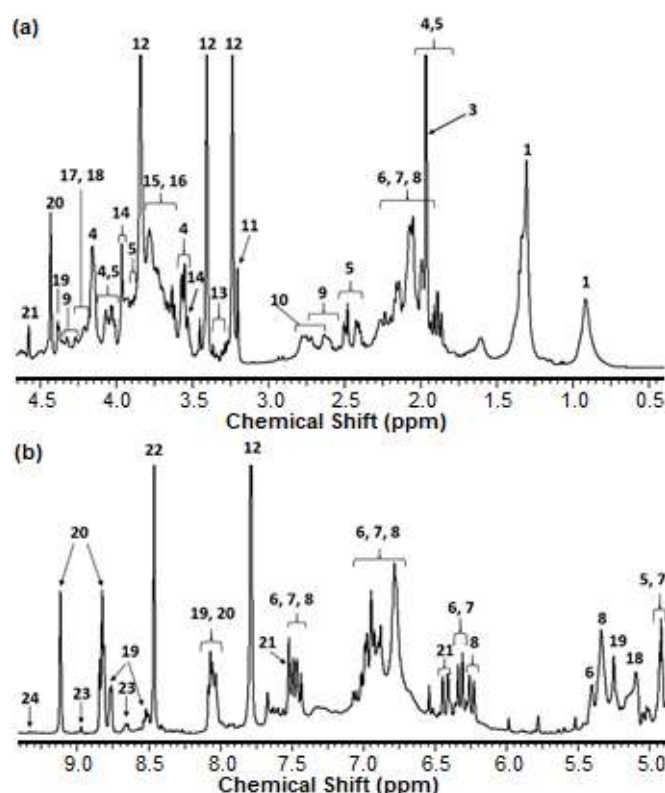


Fig 1. Characteristic signals of the metabolites identified in the ^1H NMR spectrum of the Robusta coffees. (a) Expansion of the ^1H NMR spectrum from 0.4 to 4.6 ppm. (b) Expansion of the ^1H NMR spectrum from 4.8 to 9.4 ppm. 1: lipids; 2: lactic acid; 3: acetic acid; 4: quinic acid; 5: γ -quinide; 6: 3-caffeoylquinic acid; 7: 4-caffeoylquinic acid; 8: 5-caffeoylquinic acid; 9: malic acid; 10: citric acid; 11: choline; 12: caffeine; 13: inositol; 14: β -(1-4)-D-mannopyranose unit; 15: β -(1-4)-D-galactopyranose unit; 16: β -(1-6)-D-galactopyranose unit; 17: α -(1-3)-L-arabinofuranose unit; 18: α -(1-5)-L-arabinofuranose unit; 19: *N*-methyl-pyridinium; 20: trigonelline; 21: 2-furyl-methanol; 22: formic acid; 23: nicotinic acid; 24: 5-(hydroxymethyl) furfural

at δ 4.16, 4.05, 3.57, and in the range 1.88–2.07 ppm. Proton signals belong to γ -quinide, an ester cyclic of quinic acid, were successfully detected at δ 4.91, 4.06, 3.89, and in the range 2.41–2.49 and 1.95–2.14 ppm.

Trigonelline is another major compound in the coffees. This compound was identified in the ^1H NMR spectra by detecting its proton signals at δ 4.44, 8.07, 8.82, 8.84, and 9.12 ppm. Trigonelline is degraded during the roasting process into some compounds including *N*-methyl-pyridinium and nicotinic acid [24]. Both degradation products were also successfully identified in the ^1H NMR spectra of the Robusta coffees. The signals belong to *N*-methyl-pyridinium were recorded at δ 4.37, 8.02, 8.51, and 8.75 ppm. Meanwhile, the proton signals of nicotinic acid were detected at δ 8.27, 8.66 and 8.97 ppm. Sucrose is a major component of green bean coffee. In this work, apparently sucrose had been degraded completely during the roasting; thus, it could not be detected in the ^1H NMR spectra of the roasted Robusta coffees. However, some products of sucrose degradation, including acetic acid, formic acid, lactic acid, 2-furyl-methanol, and 5-hydroxymethylfurfural were successfully identified in the spectra. Proton resonances of acetic acid and formic acid were detected clearly as strong singlet signals in the spectra at δ 1.96 and 8.46 ppm, respectively. The fingerprint signal of lactic acid was recorded at δ 1.36 ppm and the proton resonances belong

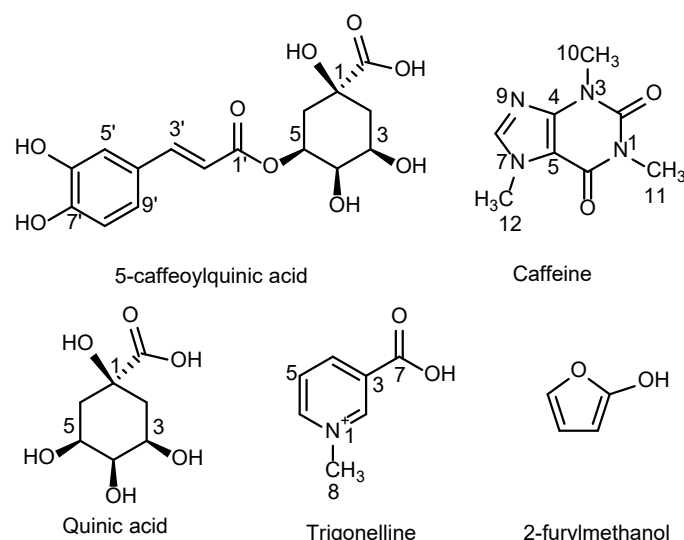


Fig 2. Some molecular structures of identified metabolites in the Robusta coffees

to 2-furylmethanol were recorded at δ 4.56, 6.43, and 7.50 ppm. Meanwhile, the proton resonance of 5-hydroxymethylfurfural has identified at δ 9.38 ppm as a weak signal.

Strong proton signals of lipids were recorded clearly at δ 0.92 and 1.30 ppm and assigned to methyl and methylene protons of fatty acids chains, respectively, as predicted by a previous report [22]. Other organic acids were also successfully identified in the aliphatic region of the ^1H NMR spectra, namely malic acid at δ 2.36 and 2.68 ppm, and then citric acid at δ 2.61 and 2.74 ppm. Further investigation of the aliphatic region revealed the presence of sugar compounds including α -(1-3)-L-arabinofuranose unit (3-arabinose), α -(1-5)-L-arabinofuranose unit (5-arabinose), β -(1-4)-D-mannopyranose unit (mannose), β -(1-4)-D-galactopyranose unit (4-galactose) and β -(1-6)-D-galactopyranose unit (6-galactose). The proton signals belong to the sugar compounds were depicted in Fig. 1. The sugar identification in the roasted Robusta coffees is in accordance with the literature [18-19,24]. Furthermore, a characteristic proton signal corresponding to inositol, sugar alcohol, was detected at δ 3.28 ppm, as shown in Fig. 1. The last identified metabolite found in the spectra was choline. The fingerprint signal of this compound was recorded at δ 3.22 ppm.

^1H NMR Quantitative Analysis

Some identified metabolites in the roasted Robusta coffees were analyzed semi-quantitatively using the ^1H NMR technique. The concentrations of choline, 2-furylmethanol, caffeine, formic acid, *N*-methyl pyridinium, nicotinic acid and trigonelline in Lampung and Aceh roasted Robusta coffees were successfully

determined as shown in Table 2. Compared to the other quantified metabolites, caffeine was found as the most abundant metabolite either in the Aceh Robusta coffees or in the Lampung Robusta coffees. It confirmed that caffeine is the major compound found in the roasted Robusta coffee. The concentration of some quantified metabolites in the Lampung coffees was higher as compared to the Aceh coffees, e.g., the concentration of formic acid in the Lampung coffees was 10.5 mM, while that in the Aceh coffee was 5.4 mM. The opposite case was found for caffeine concentration in the samples. The concentration of caffeine in the Aceh coffees was 25.3 mM and higher as compared to its concentration in the Lampung coffees (22.8 mM). Choline concentration in the Lampung coffees (1.7 mM) was similar to its concentration in the Aceh coffees (1.8 mM).

Discrimination of Metabolite Profiles

The processed data sets obtained from the ^1H NMR spectra were evaluated with multivariate statistical analysis for classifying the roasted Robusta coffees (Lampung and Aceh) based on their geographical origin. In the initial step, the data were analyzed by PCA, an unsupervised pattern-recognition approach performed without using knowledge of the sample class. This approach resulted in a model with 3 principal components (PCs) explaining 80.5% of the total variability (R²X). However, PCA could not provide enough separations (data not shown); thus, the analysis was continued further with OPLSDA method, a supervised pattern-recognition approach. OPLSDA provides a better group separation model and reveals differences among groups since it combines the strengths

Table 2. Relative quantifications of roasted Robusta coffee metabolites

Compound	The concentration of roasted Robusta coffees (mM)	
	Aceh (\pm SD)	Lampung (\pm SD)
Choline (δ 3.19–3.22 ppm)	1.8 \pm 0.1	1.7 \pm 0.1
2-furylmethanol (δ 4.56–4.59 ppm)	3.5 \pm 0.3	4.1 \pm 0.4
Caffeine (δ 7.74–7.84 ppm)	25.3 \pm 1.6	22.8 \pm 0.9
Formic acid (δ 8.44–8.48 ppm)	5.4 \pm 0.5	10.5 \pm 1.2
<i>N</i> -methyl pyridinium (δ 8.49–8.55 ppm)	3.5 \pm 0.1	2.6 \pm 0.2
Nicotinic acid (δ 8.93–8.98 ppm)	0.45 \pm 0.04	0.26 \pm 0.02
Trigonelline (δ 9.09–9.14 ppm)	4.41 \pm 0.5	4.9 \pm 0.3

for each Robusta coffees. Based on the S-plot (Fig. 3(c)) evaluation, Lampung Robusta coffees were characterized by quinic acid (buckets at δ 3.54–3.60, 4.12–4.18, 4.00–4.05 ppm), mannose (bucket at δ 3.92–3.97 ppm), 3-arabinose (bucket at δ 4.18–4.24 ppm) and acetic acid (bucket at δ 1.94–1.98 ppm). Meanwhile, Aceh Robusta coffees were characterized by lipids (buckets at δ 0.89–0.94, 1.27–1.29, 1.29–1.35 ppm), lactic acid (bucket at δ 1.35–1.41 ppm) and 5-caffeoylquinic acid (bucket at δ 5.30–5.36 ppm).

As seen in the S-plot (Fig. 3(c)), some buckets corresponding to quinic acid were located at the edge of the S-plot of the Lampung Robusta coffee zone. It indicated that quinic acid is the most discriminant compound for Lampung Robusta coffees. Meanwhile, the bucket position of lipids at 1.29–1.35 ppm was at the edge of S-plot of Aceh Robusta coffee zone and far enough from the others indicating that lipids were the most discriminant metabolites for Aceh Robusta coffees. Literature reported that the coffee lipids consist of several fatty acids including palmitic, stearic, oleic, vaccenic, linoleic, linolenic and arachidic acids [26]. Furthermore, lipids are surface-active agents contributing to foam and emulsion formations of coffee brew [19] and correlated with the formation of the coffee body [27]. Thus, the high concentration of lipids in the coffees apparently is responsible for the strong body of Aceh Robusta coffees.

■ CONCLUSION

In this report, metabolite profiles of Indonesian roasted Robusta coffees from Lampung and Aceh had been evaluated by the ^1H NMR technique along with the chemometric approach. This technique had successfully identified metabolites present in the roasted Robusta coffees, and some of them had been analyzed semi-quantitatively. The roasted Robusta coffees were clearly differentiated based on their geographic origin by the chemometric approach. Moreover, quinic acid was found as the most discriminant compound for Lampung Robusta coffees, while lipids were discovered as the characteristic metabolites for Aceh Robusta coffees. The results of this study extended our understanding of Indonesian Robusta coffees.

■ ACKNOWLEDGMENTS

This study was funded by the Institute for Research and Community Services, Bandung Institute of Technology, via Riset ITB 2017 Grant under research contract No. 108q/I1.C01/PL/2017.

■ REFERENCES

- [1] Haile, M., and Kang, W.H., 2019, The role of microbes in coffee fermentation and their impact on coffee quality, *J. Food Qual.*, 2019, 4836709.
- [2] Lashermes, P., and Anthony, F., 2007, "Coffee" in *Technical Crops*, Eds. Kole, C., Springer, Berlin, 109–118.
- [3] Farah, A., 2012, "Coffee constituents" in *Coffee: Emerging Health Effects and Disease Prevention*, Eds. Chu, Y.F., John Wiley and Sons Inc., New Jersey, 21–58.
- [4] Alves, M.R., Casal, S., Oliveira, M.B.P.P., and Ferreira, M.A., 2003, Contribution of FA profile obtained by high-resolution GC/chemometric techniques to the authenticity of green and roasted coffee varieties, *J. Am. Oil Chem. Soc.*, 80 (6), 511–517.
- [5] Cossignani, L., Montesano, D., Simonetti, M.S., and Blasi, F., 2016, Authentication of *Coffea arabica* according to triacylglycerol stereospecific composition, *J. Anal. Methods Chem.*, 2016, 7482620.
- [6] Downey, G., and Spengler, B., 1996, Compositional analysis of coffee blends by near infrared spectroscopy, *Ir. J. Agric. Food Res.*, 35 (2), 179–188.
- [7] El-Abassy, R.M., Donfack, P., and Materny, A., 2011, Discrimination between Arabica and Robusta green coffee using visible micro-Raman spectroscopy and chemometric analysis, *Food Chem.*, 126 (3), 1443–1448.
- [8] Suhandy, D., and Yulia, M., 2017, Peaberry coffee discrimination using UV-visible spectroscopy combined with SIMCA and PLS-DA, *Int. J. Food Prop.*, 20, S331–S339.
- [9] Alonso-Salces, R.M., Serra, F., Reniero, F., and Héberger, K., 2009, Botanical and geographical characterization of green coffee (*Coffea arabica* and

- Coffea canephora*): Chemometric evaluation of phenolic and methylxanthine contents, *J. Agric. Food Chem.*, 57 (10), 4224–4235.
- [10] Wei, F., Furihata, K., Koda, M., Hu, F., Kato, R., Miyakawa, T., and Tanokura, M., 2012, ^{13}C NMR-based metabolomics for the classification of green coffee beans according to variety and origin, *J. Agric. Food Chem.*, 60 (40), 10118–10125.
- [11] Zambonin, C.G., Balest, L., De Benedetto, G.E., and Palmisano, F., 2005, Solid-phase microextraction–gas chromatography mass spectrometry and multivariate analysis for the characterization of roasted coffees, *Talanta*, 66 (1), 261–265.
- [12] Okubo, N., and Kurata, Y., 2019, Nondestructive classification analysis of green coffee beans by using Near-Infrared spectroscopy, *Foods*, 8 (2), 82.
- [13] Downey, G., Briandet, R., Wilson, R.H., and Kemsley, E.K., 1997, Near- and mid-infrared spectroscopies in food authentication: Coffee varietal identification, *J. Agric. Food Chem.*, 45 (11), 4357–4361.
- [14] Dong, W., Zhao, J., Hu, R., Dong, Y., and Tan, L., 2017, Differentiation of Chinese Robusta coffees according to species, using a combined electronic nose and tongue, with the aid of chemometrics, *Food Chem.*, 229, 743–751.
- [15] Dong, W., Tan, L., Zhao, J., Hu, R., and Lu, M., 2015, Characterization of fatty acid, amino acid and volatile compound compositions and bioactive components of seven coffee (*Coffea robusta*) cultivars grown in Hainan province, China, *Molecules*, 20 (9), 16687–16708.
- [16] Liu, C., Yang, Q., Linforth, R., Fisk, I.D., and Yang, N., 2019, Modifying Robusta coffee aroma by green bean chemical pre-treatment, *Food Chem.*, 272, 251–257.
- [17] ICO (International Coffee Organization), 2019, *Coffee Report Market April 2019*, <http://www.ico.org/documents/cy2018-19/cmr-0419-e.pdf>, accessed on 17 May 2019.
- [18] Wei, F., Furihata, K., Hu, F., Miyakawa, T., and Tanokura, M., 2011, Two-dimensional ^1H - ^{13}C nuclear magnetic resonance (NMR)-based comprehensive analysis of roasted coffee bean extra, *J. Agric. Food Chem.*, 59 (17), 9065–9073.
- [19] Wei, F., Furihata, K., Miyakawa, T., and Tanokura, M., 2014, A pilot study of NMR-based sensory prediction of roasted coffee bean extracts, *Food Chem.*, 152, 363–369.
- [20] D’Amelio, N., Fontanive, L., Uggeri, F., Suggi-Liverani, F., and Navarini, L., 2009, NMR reinvestigation of the caffeine–chlorogenate complex in aqueous solution and in coffee brews, *Food Biophys.*, 4 (4), 321–330.
- [21] Cagliani, L.R., Pellegrino, G., Giugno, G., and Consonni, R., 2013, Quantification of *Coffea arabica* and *Coffea canephora* var. Robusta in roasted and ground coffee blends, *Talanta*, 106, 169–173.
- [22] Consonni, R., Cagliani, L.R., and Cogliati, C., 2012, NMR based geographical characterization of roasted coffee, *Talanta*, 88, 420–426.
- [23] Tavares, L., and Ferreira, A.G., 2006, Quali- and quantitative analysis of commercial coffee by NMR, *Quím. Nova*, 29 (5), 911–915.
- [24] Wei, F., Furihata, K., Koda, M., Hu, F., Miyakawa, T., and Tanokura, M., 2012, Roasting process of coffee beans as studied by nuclear magnetic resonance: Time course of changes in composition, *J. Agric. Food Chem.*, 60 (4), 1005–1012.
- [25] Bylesjö, M., Rantalainen, M., Cloarec, O., Nicholson, J.K., Holmes, E., and Trygg, J., 2006, OPLS discriminant analysis: Combining the strengths of PLS-DA and SIMCA classification, *J. Chemom.*, 20, 341–351.
- [26] Villarreal, D., Laffargue, A., Posada, H., Bertrand, B., Lashermes, P., and Dussert, S., 2009, Genotypic and environmental effects on coffee (*Coffea arabica* L.) bean fatty acid profile: Impact on variety and origin chemometric determination, *J. Agric. Food Chem.*, 57 (23), 11321–11327.
- [27] Buffo, R.A., and Cardelli-Freire, C., 2004, Coffee flavour: An overview, *Flavour Fragr. J.*, 19 (2), 99–104.

Metabolite Profile Evaluation of Indonesian Roasted Robusta Coffees by ^1H NMR Technique and Chemometrics

Nizar Happyana*, Elvira Hermawati, Yana Maolana Syah, and Euis Holisotan Hakim

Organic Chemistry Division, Chemistry Study Program, Faculty of Mathematics and Natural Sciences, Bandung Institute of Technology, Jl. Ganesha No. 10, Bandung 40132, West Java, Indonesia

* **Corresponding author:**

tel: +62-222502103

email: nizar@chem.itb.ac.id

Received: June 10, 2019

Accepted: August 2, 2019

DOI: 10.22146/ijc.46492

Abstract: In this work, ^1H NMR analysis, along with a chemometrics approach, had been applied for investigating metabolite profiles of Indonesian roasted Robusta coffees obtained from Lampung and Aceh. In total, 24 compounds had been successfully detected in the ^1H NMR spectra of the Robusta coffee extracts. Concentrations of some identified metabolites present in the coffees were determined by the quantitative ^1H NMR technique. Orthogonal projection to latent structure-discriminant analysis (OPLSDA) was used as a primary method for the chemometric approach. OPLSDA had classified clearly the Robusta coffee samples corresponding to their origin. Loading plot and S-plot of the OPLSDA revealed characteristic metabolites for each Robusta coffee. The results indicated that quinic acid, mannose, arabinoses, and acetic acid were an important discriminant compound for Lampung Robusta coffees. Meanwhile, lipids, lactic acid, and 5-caffeoylquinic acid were found as characteristic metabolites for Aceh Robusta coffee. This report provided knowledge about the chemical composition of Lampung and Aceh Robusta coffees and shed more light on the diversity of Indonesian Robusta coffees. Furthermore, it confirmed that ^1H NMR analysis coupled with chemometrics was a powerful method for evaluating and classifying metabolite profiles of the roasted Robusta coffees.

Keywords: ^1H NMR; chemometric; roasted Robusta coffee; Indonesia

■ INTRODUCTION

Coffee is one of the most consumed nonalcoholic drinks in the world. The drink is well known for its unique flavors and remarkable aromas. Coffee also possesses physiological and psychological effects [1]. Arabica (*Coffea arabica* L.) and Robusta coffees (*Coffea canephora* P.) are the most consumed coffees worldwide. Arabica coffee is considered having a higher quality than Robusta since it possesses a better taste, an intense aroma, and lower caffeine content [2]. As the second most cultivated coffee after Arabica, Robusta has a more bitter taste and contains more caffeine and chlorogenic acids but fewer sugars [3]. However, Robusta coffee is easier to cultivate since it is more resistant to plant diseases, weather conditions, and able to grow at lower altitudes as well [3].

Literature studies show that many metabolomics and chemometric studies of Robusta coffee focused on the authentication and the differentiation of coffee species [4-

12]. Several measurement methods have been used in these studies, including IR spectroscopies [6,12-13], Raman spectroscopy [7], UV-visible spectroscopy [8], GC [4-5], HPLC [9], GC-MS [11] and NMR [10]. Chemometrics combined with electronic nose and tongue had been used to analyze and classify 7 Chinese Robusta coffee cultivars with different roasting degrees [14]. Furthermore, chemometric approaches, along with GC-MS techniques, had been also applied to discriminate Chinese Robusta coffees based on their geographic origins [15]. Recently, this coupled method had been used to investigate the effects of chemical pre-treatment of Robusta coffee [16].

Indonesia is one of the biggest coffee producers in the world [17]. At least 70% of coffee plants cultivated in Indonesia are Robusta species. This coffee is cultivated in many Indonesian islands, including Sumatera, Java, Sulawesi, Papua, and Sumbawa. Aceh and Lampung that

located in Sumatra, are two popular regions producing Robusta coffee. The taste of Lampung Robusta is unique and different from the taste of Aceh Robusta. From the chemical point of view, the taste differences indicate the distinction of metabolite profiles since the taste of coffee is strongly related to its chemical components. However, the chemical information of Robusta coffees from Indonesia especially Lampung and Aceh, is very limited in the literature.

In this study, Robusta roasted coffees from Lampung and Aceh were analyzed with ^1H NMR technique for investigating their chemical profiles. Chemometric approaches were applied to classify the Robusta coffees based on their origins and to identify their characteristic metabolites. Furthermore, some identified metabolites in the Robusta coffees were successfully quantified by ^1H NMR method.

■ EXPERIMENTAL SECTION

Materials

All coffee samples used in this study were commercially roasted beans of Robusta coffees from Lampung (6 samples) and Aceh (6 samples) and obtained from some coffee companies/suppliers. The detail information of the coffee origins was depicted in Table 1. The extraction solvent used in this work, deuterated water (D_2O), was purchased from Merck (Germany). 3-(trimethylsilyl)-2,2,3,3-tetra deuteropropionic acid sodium salt (TSP) was bought from Merck (Germany). KH_2PO_4 and

K_2HPO_4 that used for making a buffer solution were purchased from Merck (Germany).

Instrumentation

An Encore mill (Baratza, United States) was used to grind the roasted coffee beans. An ultrasonic bath (Krisbow, Indonesia) was used to sonicate the samples. An MC-12 High Speed Microcentrifuge (Benchmark Scientific, United States) were used to centrifuge the samples. A 500 MHz Varian Unity INOVA spectrometer (Agilent Technologies, United States) was used to record ^1H NMR spectra of the Robusta coffees.

Procedure

Sample preparation

The coffee sample preparation was carried out based on the reported works [18-19] with slight modification. The sample was prepared by mixing 200 g of ground Robusta coffee with 1 mL of D_2O containing TSP 1.00 mM in a 2 mL plastic tube. The sample was sonicated at room temperature for 20 min and incubated on a water bath at 90 °C for 30 min. Afterward, the sample was cooled on the water for 10 min, centrifuged for 5 min, and the supernatant was then separated from the precipitate. One hundred microliters of phosphate buffer (pH 5) were added into 400 μL of supernatant and then transferred into a 5 mm NMR tube.

^1H NMR measurement and processing

In the ^1H NMR measurement, the H_2O signals were suppressed by the presaturation method. One hundred

Table 1. Origins of Robusta coffees used in the present study

Sample code	Coffee origin	Company/supplier
A1	Blangkejeren, Gayo Lues, Aceh	Fry Roast
A2	Linge, Aceh Tengah, Aceh	Rebbe Coffee Takengon
A3	Pintu Rime Gayo, Bener Meriah, Aceh	Serenade
A4	Takengon, Aceh Tengah, Aceh	Tampah Kopi Gayo
A5	Takengon, Aceh Tengah, Aceh	Raja Kopi Aceh
A6	Pintu Rime Gayo, Bener Meriah, Aceh	Garasco
L1	Liwa, Lampung Barat, Lampung	Fry Roast
L2	Ulubelu, Tanggamus, Lampung	Hilbrew coffee
L3	Liwa, Lampung Barat, Lampung	Kafein
L4	Liwa, Lampung Barat, Lampung	AKL
L5	Liwa, Lampung Barat, Lampung	AKL
L6	Ulubelu, Tanggamus, Lampung	Halokoffhouse

twenty-eight scans of 64 K data points are recorded with a spectral width of 8012 Hz, the acquisition time of 2.72 s, and a relaxation delay of 2 sec. The free-induction decay (FID) NMR data were processed with ACD/Labs 12.0 software (Advanced Chemistry Development, Inc., Toronto, Canada). This software was also used for referencing, phasing, baseline correction of ^1H NMR spectra. The chemical shifts of ^1H NMR spectra were referenced to the TSP signal. The signal assignments of the components in Robusta coffees were conducted by recognizing the fingerprinting chemical shifts of identified metabolites and comparing the spectra with the reference spectra of corresponding metabolites and with the data in the literature [18].

Multivariate statistical analysis

Alignment and bucketing of the ^1H NMR spectra were performed using ACD/Labs 12.0 software (Advanced Chemistry Development, Inc., Toronto, Canada). Bucketing was carried out by integrating regions of equal width (0.02 ppm) within δ 0.50–10.00 ppm and performed with an intelligent bucketing option as well. The residual water signal at δ 4.73–5.22 ppm were excluded from the multivariate data analysis. The caffeine signals at δ 3.22–3.49 ppm and δ 3.82–3.88 ppm were also excluded for avoiding spurious principal components (PCs) as a consequence of signal shifting [20]. The buckets were normalized to a total integral to avoid dilution effects of the samples. The processed data sets extracted from the ^1H NMR spectra were imported into SIMCA-P version 12.0 (Umetrics, Umeå, Sweden) for the multivariate statistical analysis. The data were then scaled with the Pareto scaling type. The principal component analysis (PCA), an unsupervised pattern-recognition approach, was performed to check intrinsic variation in the data set. Orthogonal projection to latent structure-discriminant analysis (OPLSDA), a supervised pattern-recognition approach, was applied as primary methods for extracting maximum separation among samples. The data sets of the roasted Robusta coffee were divided into 2 groups based on their geographical origins (Lampung and Aceh) and then analyzed with OPLSDA method. The percent of the response variation explained by the models (R2X and R2Y), and the percent of the response variation

predicted by the models according to cross validation (Q2) were computed. Hotelling's T2 regions, shown as an ellipse in the score plot, defined the 95% confidence interval of the modeled variation.

Quantitative ^1H NMR analysis

For evaluating metabolites quantitatively in Lampung and Aceh Robusta coffees, the obtained ^1H NMR data were further processed based on a previous report [21] with slight modifications. TSP signal (1 mM) was used as an internal standard. The quantification was conducted by calculating the relative ratio of the peak area of selected proton signals of the target metabolites to the singlet peak of the TSP signal. The statistical calculation of quantitative ^1H NMR analysis was performed using Microsoft Excel 2013.

RESULTS AND DISCUSSION

Identified Metabolites in the Roasted Robusta Coffees

In this work, metabolites in the roasted Robusta coffee samples (Lampung and Aceh) were recognized by identifying their fingerprint signals in the ^1H NMR spectra and comparing them with the spectra of corresponding reference compounds. The metabolite identification was further confirmed by comparing the spectra with the data reported in the literature [18-19,22]. In total, 24 metabolites were successfully identified in the Robusta coffees, as depicted in the ^1H NMR spectra of the Robusta coffee (Fig. 1). Some molecular structures of the identified metabolites were described in Fig. 2.

Caffeine, as one of the major compounds in the roasted coffee bean, was clearly identified in the ^1H NMR spectra. The strong singlet signals at δ 3.28, 3.45 and 3.88 ppm were assigned as the 3 *N*-methyl of caffeine. Meanwhile, the singlet signal at δ 7.83 ppm was designed as an aromatic proton of caffeine. The intense signals of caffeine in the ^1H NMR spectra of the roasted coffees indicated that the compound is thermally stable during the roasting. Thus, caffeine is an excellent quantitative marker for coffees as proposed by previous reports [18,23]. The proton signals belong to 3 dominant compounds of chlorogenic acids, namely 3-caffeoylquinic

acid, 4-caffeoylquinic acid, and 5-caffeoylquinic acid were also clearly visible in the aliphatic and aromatic regions of the ^1H NMR spectra as shown in Fig. 1. Chlorogenic acids, the ester form of caffeic acid and quinic acid, are major compounds in coffees. However, during the roasting, some chlorogenic acids degrade into quinic acid and γ -quinide since the compounds are unstable thermally [24]. The signals of quinic acid, another major compound in the roasted coffee, were recorded in the ^1H NMR spectra

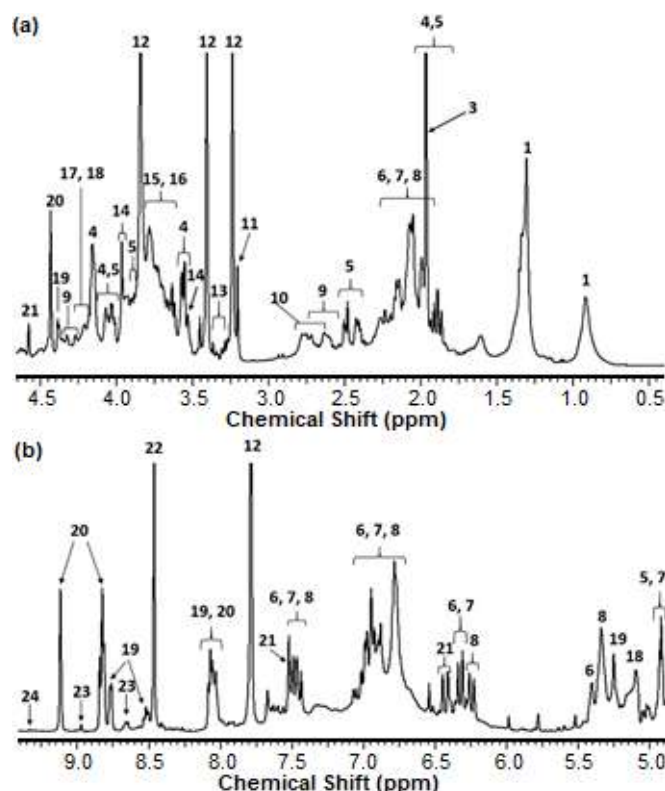


Fig 1. Characteristic signals of the metabolites identified in the ^1H NMR spectrum of the Robusta coffees. (a) Expansion of the ^1H NMR spectrum from 0.4 to 4.6 ppm. (b) Expansion of the ^1H NMR spectrum from 4.8 to 9.4 ppm. 1: lipids; 2: lactic acid; 3: acetic acid; 4: quinic acid; 5: γ -quinide; 6: 3-caffeoylquinic acid; 7: 4-caffeoylquinic acid; 8: 5-caffeoylquinic acid; 9: malic acid; 10: citric acid; 11: choline; 12: caffeine; 13: inositol; 14: β -(1-4)-D-mannopyranose unit; 15: β -(1-4)-D-galactopyranose unit; 16: β -(1-6)-D-galactopyranose unit; 17: α -(1-3)-L-arabinofuranose unit; 18: α -(1-5)-L-arabinofuranose unit; 19: *N*-methyl-pyridinium; 20: trigonelline; 21: 2-furyl-methanol; 22: formic acid; 23: nicotinic acid; 24: 5-(hydroxymethyl) furfural

at δ 4.16, 4.05, 3.57, and in the range 1.88–2.07 ppm. Proton signals belong to γ -quinide, an ester cyclic of quinic acid, were successfully detected at δ 4.91, 4.06, 3.89, and in the range 2.41–2.49 and 1.95–2.14 ppm.

Trigonelline is another major compound in the coffees. This compound was identified in the ^1H NMR spectra by detecting its proton signals at δ 4.44, 8.07, 8.82, 8.84, and 9.12 ppm. Trigonelline is degraded during the roasting process into some compounds including *N*-methyl-pyridinium and nicotinic acid [24]. Both degradation products were also successfully identified in the ^1H NMR spectra of the Robusta coffees. The signals belong to *N*-methyl-pyridinium were recorded at δ 4.37, 8.02, 8.51, and 8.75 ppm. Meanwhile, the proton signals of nicotinic acid were detected at δ 8.27, 8.66 and 8.97 ppm. Sucrose is a major component of green bean coffee. In this work, apparently sucrose had been degraded completely during the roasting; thus, it could not be detected in the ^1H NMR spectra of the roasted Robusta coffees. However, some products of sucrose degradation, including acetic acid, formic acid, lactic acid, 2-furyl-methanol, and 5-hydroxymethylfurfural were successfully identified in the spectra. Proton resonances of acetic acid and formic acid were detected clearly as strong singlet signals in the spectra at δ 1.96 and 8.46 ppm, respectively. The fingerprint signal of lactic acid was recorded at δ 1.36 ppm and the proton resonances belong

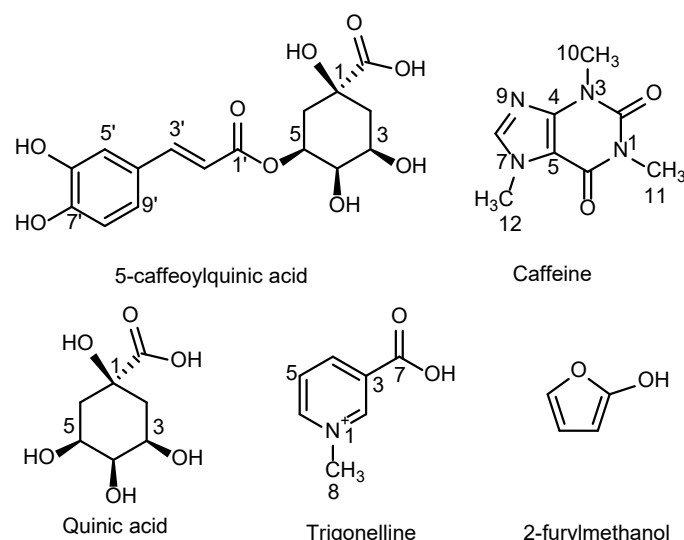


Fig 2. Some molecular structures of identified metabolites in the Robusta coffees

to 2-furylmethanol were recorded at δ 4.56, 6.43, and 7.50 ppm. Meanwhile, the proton resonance of 5-hydroxymethylfurfural has identified at δ 9.38 ppm as a weak signal.

Strong proton signals of lipids were recorded clearly at δ 0.92 and 1.30 ppm and assigned to methyl and methylene protons of fatty acids chains, respectively, as predicted by a previous report [22]. Other organic acids were also successfully identified in the aliphatic region of the ^1H NMR spectra, namely malic acid at δ 2.36 and 2.68 ppm, and then citric acid at δ 2.61 and 2.74 ppm. Further investigation of the aliphatic region revealed the presence of sugar compounds including α -(1-3)-L-arabinofuranose unit (3-arabinose), α -(1-5)-L-arabinofuranose unit (5-arabinose), β -(1-4)-D-mannopyranose unit (mannose), β -(1-4)-D-galactopyranose unit (4-galactose) and β -(1-6)-D-galactopyranose unit (6-galactose). The proton signals belong to the sugar compounds were depicted in Fig. 1. The sugar identification in the roasted Robusta coffees is in accordance with the literature [18-19,24]. Furthermore, a characteristic proton signal corresponding to inositol, sugar alcohol, was detected at δ 3.28 ppm, as shown in Fig. 1. The last identified metabolite found in the spectra was choline. The fingerprint signal of this compound was recorded at δ 3.22 ppm.

^1H NMR Quantitative Analysis

Some identified metabolites in the roasted Robusta coffees were analyzed semi-quantitatively using the ^1H NMR technique. The concentrations of choline, 2-furylmethanol, caffeine, formic acid, *N*-methyl pyridinium, nicotinic acid and trigonelline in Lampung and Aceh roasted Robusta coffees were successfully

determined as shown in Table 2. Compared to the other quantified metabolites, caffeine was found as the most abundant metabolite either in the Aceh Robusta coffees or in the Lampung Robusta coffees. It confirmed that caffeine is the major compound found in the roasted Robusta coffee. The concentration of some quantified metabolites in the Lampung coffees was higher as compared to the Aceh coffees, e.g., the concentration of formic acid in the Lampung coffees was 10.5 mM, while that in the Aceh coffee was 5.4 mM. The opposite case was found for caffeine concentration in the samples. The concentration of caffeine in the Aceh coffees was 25.3 mM and higher as compared to its concentration in the Lampung coffees (22.8 mM). Choline concentration in the Lampung coffees (1.7 mM) was similar to its concentration in the Aceh coffees (1.8 mM).

Discrimination of Metabolite Profiles

The processed data sets obtained from the ^1H NMR spectra were evaluated with multivariate statistical analysis for classifying the roasted Robusta coffees (Lampung and Aceh) based on their geographical origin. In the initial step, the data were analyzed by PCA, an unsupervised pattern-recognition approach performed without using knowledge of the sample class. This approach resulted in a model with 3 principal components (PCs) explaining 80.5% of the total variability (R²X). However, PCA could not provide enough separations (data not shown); thus, the analysis was continued further with OPLSDA method, a supervised pattern-recognition approach. OPLSDA provides a better group separation model and reveals differences among groups since it combines the strengths

Table 2. Relative quantifications of roasted Robusta coffee metabolites

Compound	The concentration of roasted Robusta coffees (mM)	
	Aceh (\pm SD)	Lampung (\pm SD)
Choline (δ 3.19–3.22 ppm)	1.8 \pm 0.1	1.7 \pm 0.1
2-furylmethanol (δ 4.56–4.59 ppm)	3.5 \pm 0.3	4.1 \pm 0.4
Caffeine (δ 7.74–7.84 ppm)	25.3 \pm 1.6	22.8 \pm 0.9
Formic acid (δ 8.44–8.48 ppm)	5.4 \pm 0.5	10.5 \pm 1.2
<i>N</i> -methyl pyridinium (δ 8.49–8.55 ppm)	3.5 \pm 0.1	2.6 \pm 0.2
Nicotinic acid (δ 8.93–8.98 ppm)	0.45 \pm 0.04	0.26 \pm 0.02
Trigonelline (δ 9.09–9.14 ppm)	4.41 \pm 0.5	4.9 \pm 0.3

for each Robusta coffees. Based on the S-plot (Fig. 3(c)) evaluation, Lampung Robusta coffees were characterized by quinic acid (buckets at δ 3.54–3.60, 4.12–4.18, 4.00–4.05 ppm), mannose (bucket at δ 3.92–3.97 ppm), 3-arabinose (bucket at δ 4.18–4.24 ppm) and acetic acid (bucket at δ 1.94–1.98 ppm). Meanwhile, Aceh Robusta coffees were characterized by lipids (buckets at δ 0.89–0.94, 1.27–1.29, 1.29–1.35 ppm), lactic acid (bucket at δ 1.35–1.41 ppm) and 5-caffeoylquinic acid (bucket at δ 5.30–5.36 ppm).

As seen in the S-plot (Fig. 3(c)), some buckets corresponding to quinic acid were located at the edge of the S-plot of the Lampung Robusta coffee zone. It indicated that quinic acid is the most discriminant compound for Lampung Robusta coffees. Meanwhile, the bucket position of lipids at 1.29–1.35 ppm was at the edge of S-plot of Aceh Robusta coffee zone and far enough from the others indicating that lipids were the most discriminant metabolites for Aceh Robusta coffees. Literature reported that the coffee lipids consist of several fatty acids including palmitic, stearic, oleic, vaccenic, linoleic, linolenic and arachidic acids [26]. Furthermore, lipids are surface-active agents contributing to foam and emulsion formations of coffee brew [19] and correlated with the formation of the coffee body [27]. Thus, the high concentration of lipids in the coffees apparently is responsible for the strong body of Aceh Robusta coffees.

■ CONCLUSION

In this report, metabolite profiles of Indonesian roasted Robusta coffees from Lampung and Aceh had been evaluated by the ^1H NMR technique along with the chemometric approach. This technique had successfully identified metabolites present in the roasted Robusta coffees, and some of them had been analyzed semi-quantitatively. The roasted Robusta coffees were clearly differentiated based on their geographic origin by the chemometric approach. Moreover, quinic acid was found as the most discriminant compound for Lampung Robusta coffees, while lipids were discovered as the characteristic metabolites for Aceh Robusta coffees. The results of this study extended our understanding of Indonesian Robusta coffees.

■ ACKNOWLEDGMENTS

This study was funded by the Institute for Research and Community Services, Bandung Institute of Technology, via Riset ITB 2017 Grant under research contract No. 108q/I1.C01/PL/2017.

■ REFERENCES

- [1] Haile, M., and Kang, W.H., 2019, The role of microbes in coffee fermentation and their impact on coffee quality, *J. Food Qual.*, 2019, 4836709.
- [2] Lashermes, P., and Anthony, F., 2007, "Coffee" in *Technical Crops*, Eds. Kole, C., Springer, Berlin, 109–118.
- [3] Farah, A., 2012, "Coffee constituents" in *Coffee: Emerging Health Effects and Disease Prevention*, Eds. Chu, Y.F., John Wiley and Sons Inc., New Jersey, 21–58.
- [4] Alves, M.R., Casal, S., Oliveira, M.B.P.P., and Ferreira, M.A., 2003, Contribution of FA profile obtained by high-resolution GC/chemometric techniques to the authenticity of green and roasted coffee varieties, *J. Am. Oil Chem. Soc.*, 80 (6), 511–517.
- [5] Cossignani, L., Montesano, D., Simonetti, M.S., and Blasi, F., 2016, Authentication of *Coffea arabica* according to triacylglycerol stereospecific composition, *J. Anal. Methods Chem.*, 2016, 7482620.
- [6] Downey, G., and Spengler, B., 1996, Compositional analysis of coffee blends by near infrared spectroscopy, *Ir. J. Agric. Food Res.*, 35 (2), 179–188.
- [7] El-Abassy, R.M., Donfack, P., and Materny, A., 2011, Discrimination between Arabica and Robusta green coffee using visible micro-Raman spectroscopy and chemometric analysis, *Food Chem.*, 126 (3), 1443–1448.
- [8] Suhandy, D., and Yulia, M., 2017, Peaberry coffee discrimination using UV-visible spectroscopy combined with SIMCA and PLS-DA, *Int. J. Food Prop.*, 20, S331–S339.
- [9] Alonso-Salces, R.M., Serra, F., Reniero, F., and Héberger, K., 2009, Botanical and geographical characterization of green coffee (*Coffea arabica* and

- Coffea canephora*): Chemometric evaluation of phenolic and methylxanthine contents, *J. Agric. Food Chem.*, 57 (10), 4224–4235.
- [10] Wei, F., Furihata, K., Koda, M., Hu, F., Kato, R., Miyakawa, T., and Tanokura, M., 2012, ^{13}C NMR-based metabolomics for the classification of green coffee beans according to variety and origin, *J. Agric. Food Chem.*, 60 (40), 10118–10125.
- [11] Zambonin, C.G., Balest, L., De Benedetto, G.E., and Palmisano, F., 2005, Solid-phase microextraction–gas chromatography mass spectrometry and multivariate analysis for the characterization of roasted coffees, *Talanta*, 66 (1), 261–265.
- [12] Okubo, N., and Kurata, Y., 2019, Nondestructive classification analysis of green coffee beans by using Near-Infrared spectroscopy, *Foods*, 8 (2), 82.
- [13] Downey, G., Briandet, R., Wilson, R.H., and Kemsley, E.K., 1997, Near- and mid-infrared spectroscopies in food authentication: Coffee varietal identification, *J. Agric. Food Chem.*, 45 (11), 4357–4361.
- [14] Dong, W., Zhao, J., Hu, R., Dong, Y., and Tan, L., 2017, Differentiation of Chinese Robusta coffees according to species, using a combined electronic nose and tongue, with the aid of chemometrics, *Food Chem.*, 229, 743–751.
- [15] Dong, W., Tan, L., Zhao, J., Hu, R., and Lu, M., 2015, Characterization of fatty acid, amino acid and volatile compound compositions and bioactive components of seven coffee (*Coffea robusta*) cultivars grown in Hainan province, China, *Molecules*, 20 (9), 16687–16708.
- [16] Liu, C., Yang, Q., Linforth, R., Fisk, I.D., and Yang, N., 2019, Modifying Robusta coffee aroma by green bean chemical pre-treatment, *Food Chem.*, 272, 251–257.
- [17] ICO (International Coffee Organization), 2019, *Coffee Report Market April 2019*, <http://www.ico.org/documents/cy2018-19/cmr-0419-e.pdf>, accessed on 17 May 2019.
- [18] Wei, F., Furihata, K., Hu, F., Miyakawa, T., and Tanokura, M., 2011, Two-dimensional ^1H - ^{13}C nuclear magnetic resonance (NMR)-based comprehensive analysis of roasted coffee bean extra, *J. Agric. Food Chem.*, 59 (17), 9065–9073.
- [19] Wei, F., Furihata, K., Miyakawa, T., and Tanokura, M., 2014, A pilot study of NMR-based sensory prediction of roasted coffee bean extracts, *Food Chem.*, 152, 363–369.
- [20] D’Amelio, N., Fontanive, L., Uggeri, F., Suggi-Liverani, F., and Navarini, L., 2009, NMR reinvestigation of the caffeine–chlorogenate complex in aqueous solution and in coffee brews, *Food Biophys.*, 4 (4), 321–330.
- [21] Cagliani, L.R., Pellegrino, G., Giugno, G., and Consonni, R., 2013, Quantification of *Coffea arabica* and *Coffea canephora* var. Robusta in roasted and ground coffee blends, *Talanta*, 106, 169–173.
- [22] Consonni, R., Cagliani, L.R., and Cogliati, C., 2012, NMR based geographical characterization of roasted coffee, *Talanta*, 88, 420–426.
- [23] Tavares, L., and Ferreira, A.G., 2006, Quali- and quantitative analysis of commercial coffee by NMR, *Quím. Nova*, 29 (5), 911–915.
- [24] Wei, F., Furihata, K., Koda, M., Hu, F., Miyakawa, T., and Tanokura, M., 2012, Roasting process of coffee beans as studied by nuclear magnetic resonance: Time course of changes in composition, *J. Agric. Food Chem.*, 60 (4), 1005–1012.
- [25] Bylesjö, M., Rantalainen, M., Cloarec, O., Nicholson, J.K., Holmes, E., and Trygg, J., 2006, OPLS discriminant analysis: Combining the strengths of PLS-DA and SIMCA classification, *J. Chemom.*, 20, 341–351.
- [26] Villarreal, D., Laffargue, A., Posada, H., Bertrand, B., Lashermes, P., and Dussert, S., 2009, Genotypic and environmental effects on coffee (*Coffea arabica* L.) bean fatty acid profile: Impact on variety and origin chemometric determination, *J. Agric. Food Chem.*, 57 (23), 11321–11327.
- [27] Buffo, R.A., and Cardelli-Freire, C., 2004, Coffee flavour: An overview, *Flavour Fragr. J.*, 19 (2), 99–104.

Significance of Oxirane Rings in Epoxidized Palm Oil and Effects on the Coating Performance: Comparison between Epoxidized Unripe Palm Oil and Epoxidized Used Cooking Oil towards Adhesion Performance

Nurul Hazirah Aina Hasnan, Najmiddin Yaakob*, Muhammad Nadzmi Abu Kassim, and Umie Amira Mohd Noh

Faculty of Chemical Engineering, Universiti Teknologi MARA (UiTM), Shah Alam 40450, Selangor, Malaysia

* **Corresponding author:**

tel: +60-194902526

email: najmiddin@uitm.edu.my

Received: June 14, 2019

Accepted: January 8, 2020

DOI: 10.22146/ijc.46619

Abstract: In this study, epoxy coatings made up from petroleum-based epoxy resin mixed with two different types of palm oils were prepared and compared. The commercial epoxy resin based on diglycidyl ether of bisphenol A (DGEBA) were formulated with epoxidized unripe palm oil (EPO) and another one with epoxidized used cooking oil (ECO) at four different ratios (0:100, 10:90, 20:80 and 30:70). The EPO and ECO were prepared through generated in situ of performic acid (HCOOH) and hydrogen peroxide (H₂O₂) by a fixed molar ratio of 1:5:4 mol/mol (EPO/ECO: HCOOH:H₂O₂). The reaction took place at constant temperature (45 °C) with continuous stirring for 150 min to obtain 95.5% oxirane conversion with 90.0% yield. The EPO and ECO were characterized by using Fourier Transform Infrared (FTIR) spectroscopy analysis. X-Cut and Cross-Cut methods were used in the test performance of adhesion strength. The results obtained from adhesion test for EPO were good as the coatings only experienced small trace of peeling. On the other hand, only minimal performances were obtained from the ECO coated metal. This was due to the presence of oxirane in EPO as compared to that of in ECO. EPO has a potential to replace petroleum-based resin in epoxy coating formulation according to its remarkable performances.

Keywords: epoxidized unripe palm oil; epoxidized used cooking oil; epoxy coating; epoxidation; adhesion performance

■ INTRODUCTION

Bio-based materials recently received more attentions in product synthesis and manufacture especially in paint and coating industry. Escalated concern on depletion of fossil fuel and petroleum price has sparked widespread interest in alternative energy. Furthermore, the harm caused to the environment due to excessive use of fossil fuel has also contributes into awareness for more sustainable and environmentally friendly alternatives. Due to this, a research has been made by introducing bio-based materials into epoxy coating formulation in order to minimize or eliminate the dependency towards petroleum-based materials. However, bio-based materials have lower properties than the petroleum-based materials. Thus, in order to sustain the level of mechanical properties, the coating formulation was formulated by

varying the ratio between the bio-based materials and petroleum-based materials.

Epoxy resin is known as the best barrier-coating material in industry due to their toughness, flexibility and high resistance to chemical [1]. Diglycidyl ether of bisphenol A (DGEBA) is a common epoxy resin used in formulating epoxy coating due to their high strength, excellent corrosion protection, and good adhesion to most surfaces [2]. However, DGEBA is carcinogenic that can cause tumor [3] and could affect men reproductive system [4]. The structure of DGEBA is shown in Fig. 1.

Moreover, DGEBA is a petroleum-based product which is poorly biodegradable and usually causing increased in carbon dioxide emissions during the manufacturing process. Therefore, consumers are now turning to eco-friendly ingredient as the main component

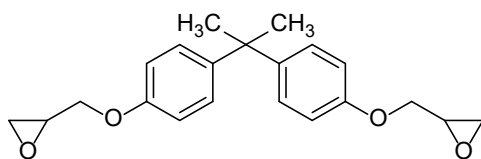


Fig 1. Structure of DGEBA [5]

in their coating material for better environment and health. Bio-based materials such as vegetable oils are safer and more beneficial because they are renewable, easily biodegrade and does not release a significant amount of greenhouse gas during manufacturing process [6].

The past history shows that the utilization of polymers based on vegetable oils such as *Annona squamosa* oil [7], *Mesua ferrea* L. seed oil [8], soybean oil [9], and palm oil [10] drew a great amount of attentions and supports from researchers, technologist, manufacturers and users. Vegetable oils are an excellent choice for the synthesis of bio-based polymers as they are biodegradable, non-toxic, non-depletable, non-volatile and most importantly low-priced and readily available in large quantities. As one of the world's leading producer of palm oil, Malaysia has high availability of palm oil. Palm oil is a type of edible vegetable oil that is produced from palm fruit of oil palm tree. Palm oil mainly consist of triglycerides, vitamin E, carotenoids, phytosterols, phospholipids, free fatty acids, gums, and oxidation products [11-12].

To increase the acceptability of palm oil for human consumption, palm oil undergoes refining process to remove the impurities such as undesirable odor, flavor, and color. The refined palm oil is so-called palm olein. Palm olein is largely use as cooking oil because of its stability at high temperature while at the same time has high antioxidant and limited amounts of unsaturated fatty acids [12]. Palm olein consists of oleic acid (39–45%) and linoleic acid (10–13%). Unsaturated fatty acids and saturated fatty acids also exist in approximately equal proportion in palm olein [13]. Repetition in using cooking oil during cooking and frying can cause deterioration of cooking oil making it no longer usable [14]. Cooking oil eventually is thrown away as waste without proper treatment. The accumulation of disposed used cooking oil polluted the environment and caused

problem to sewage system because at low temperature, the oil will be solidified and clogged the sewage system [15].

In oil palm productions, quality is always be determined by its texture, shape and color. In general, palm fruits turn from dark purple to reddish orange at the apex of their ripening. The rule of thumb for good quality practices is that, only ripe fresh fruit bunch (FFB) of oil palm are harvested and then dispatched to mills within 24 h after harvesting. The problem of poor quality FFB in the market can be minimized if they abide by the rules. However, in the FFB market, this basic principle is not strictly followed. Producers fail to ensure that only ripe FFB are harvested and left them mixed with the unripe FFB. The usual oil extraction rate for a ripe fruits bunches from a mature tree is between 22–24 percent, or 220–240 kg of oil per tonne of fresh fruit bunches [16]. On the contrary, under-ripe fruits bunches contain less oil due to long stalks that soaked up the oil and therefore reduce the oil extraction rate. In order to increase the oil recovery in palm oil mill, the extraction of residual oil from unripe FFB is important. Based on these facts, in this work the used cooking oil and unripe fresh fruit bunch of palm oil is used to develop a new coating material through epoxidation process and subsequently evaluate the resulting coating film's properties and performances.

Epoxidation process is a process where the unsaturated carbon bond present in the palm olein is chemically modified into a value-added product by addition of oxirane ring (Fig. 2). It is desirable to achieve a high oxirane oxygen value and lower iodine value as these criteria are considered to be of better quality [17]. The epoxidation process involves electrophilic addition mechanism as shown in Fig. 3. Epoxidation reaction as

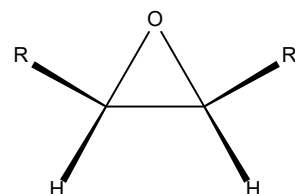


Fig 2. Structure of oxirane ring [10]

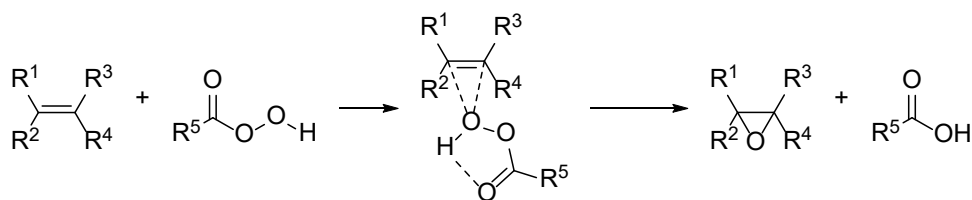


Fig 3. Epoxidation of unsaturated bond [17]

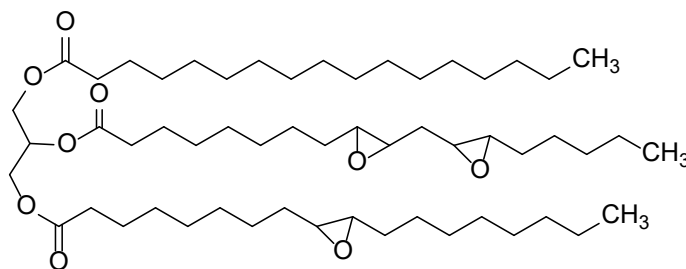


Fig 4. Structure of triglyceride after epoxidation with oxirane highlighted in green

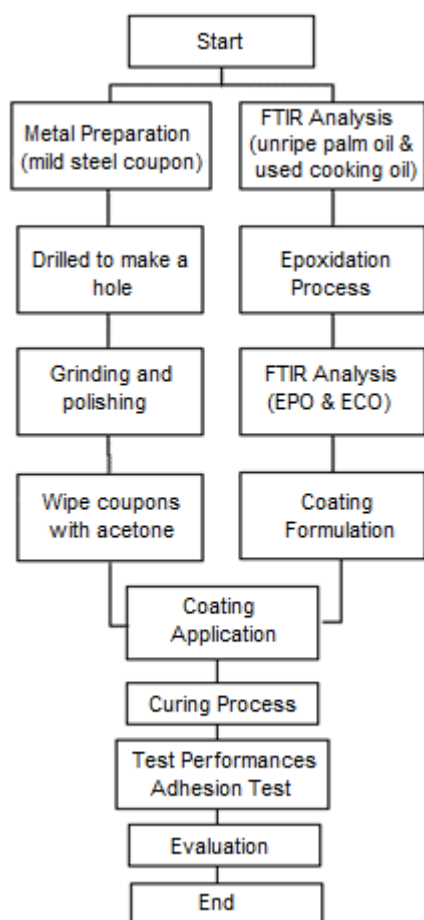


Fig 5. Overall process flow

shown in Fig. 3 takes place in similar way with unsaturated fatty acid structure. Oxirane ring forms at the

unsaturated bond (C=C) to produce an epoxidized palm olein as shown in Fig. 4.

In this research, the epoxidized unripe palm oil (EPO) and epoxidized used cooking oil (ECO) will act as an additional material to reduce the toxicity of the current epoxy coating formulation. The bio-based epoxy coating was produced by varying the formulation into four different ratios (10:90, 20:80, and 30:70) of EPO/ECO to DGEBA. The overall goal is to develop a new coating material based on epoxidized unripe palm oil (EPO)/epoxidized used cooking oil (ECO) and Diglycidyl Ether of Bisphenol A (DGEBA) as well as to evaluate the performance of the new coating material based on their adhesion performance.

■ EXPERIMENTAL SECTION

Test panel for coating performance testing was prepared early before coating application. Unripe palm oil and used cooking oil undergoes epoxidation process before can be used in coating formulation. Observation was made to evaluate the performances for each coating with different formulation. Fig. 5 shows the general steps for this process.

Materials

Formic acid (98–100% purity) and titanium (IV) oxide powder were bought from Merck, Germany. Cycloaliphatic amine adducts (Isophorone diamine with

≥ 99% purity) and diglycidyl ether of bisphenol A were purchased from Sigma-Aldrich, USA. Used cooking oil was obtained from domestic waste. Unripe palm oil was obtained from Prof. Dr. Alawi Sulaiman from Faculty of Plantation and Agrotechnology UiTM Shah Alam. Hydrogen Peroxide (≥ 99% purity) was supplied by the chemistry laboratory in Faculty of Chemical Engineering, UiTM Shah Alam. Riken sandpaper grade 80, 180 and mild steel plate with dimension 60 × 60 × 3 mm were bought from hardware store in Seksyen 7, Shah Alam.

Instrumentation

Fourier Transform Infrared Spectrometer (Brand: Perkin Elmer Model: Spectrum 100), TQC Sheen wet film thickness gauge (Test Kit CC1000) follows ASTM D4414, ASTM D1212 & ISO 2808, DPM-816 digital coating thickness tester, TQC Sheen Cross-Cut cutter, mixer, dip-coater machine, acrylic container, knife, steel ruler and grinding/polishing machine.

Procedure

Epoxidation of unripe palm oil and used cooking oil

A molar ratio of unripe palm oil/used cooking oil:formic acid:hydrogen peroxide (1:5:4 mol/mol) was used in this epoxidation process with the mixture was heated and maintained at 45 °C [17]. Formic acid and hydrogen peroxide were mixed simultaneously in other container before added into the unripe palm oil/cooking oil. During addition of formic acid and hydrogen peroxide into unripe palm oil/used cooking oil, the addition action was done by slowly by adding drop wise of the mixture into the unripe palm oil/used cooking oil. The mixture was mixed homogeneously by using mechanical mixer for 150 min. A sample of unripe palm oil and used cooking oil before and after epoxidized were taken for Fourier Transform Infrared Spectroscopy (FTIR) analysis. The spectrum of unripe palm oil and used cooking oil before and after epoxidized were then compared and analyze for the presence of oxirane ring.

Characterization of palm oils derivatives

Fatty acid profiles of oils were obtained by using a FTIR spectrometer (Perkin Elmer Model; Spectrum 100) equipped with a deuterated triglycine sulphate (DTGS) as a detector and a KBr/germanium as beam splitter,

interfaced to Computer operating under Windows-based, and connected to software of the OMNIC operating system (Version 7.0 Thermo Nicolet). A few drops of each sample were positioned in contact with attenuated total reflectance (ATR) on a multi-bounce plate of crystal at controlled ambient temperature (25 °C). The ATR plate was carefully cleaned in situ by rubbing with acetone and dried with soft tissue before filling in with the next sample, and made it possible to dry the ATR plate. The plate cleanliness was verified by collecting a background spectrum and compared to the previous one. These spectra were recorded as absorbance values at each data point.

Formulation of coating

Blend of epoxidized unripe palm oil/used cooking oil and epoxy resin were prepared with a weight ratio 0:100, 10:90, 20:80, and 30:70 (EPO/ECO:DGEBA) in different beakers. The mixture was mixed using mechanical stirrer at 400 rpm until no phase separation was observed. Then, titanium dioxide powder which act as a pigment was added into all the binder mixture produced at weight ratio of 1:0.5 (Binder:TiO₂). The mixture was then mixed using mechanical mixer at mixer speed of 1010 revolution per minute (rpm) until homogenous phase obtained at approximately 1 h. Finally, cycloaliphatic amine adduct as a crosslinking agent was added at a weight ratio of 1:0.25 (binder:amine). The mixture of binder and amine was then mixed using mechanical mixer at 400 rpm until no phase separation was observed.

Preparation of test panel

Sand paper no. 80 was used to remove any layer of rust and pitting from the surface of test panel. Test panels were then lightly abraded using sandpaper no. 180 and wiped with acetone to remove metal dust that was produced from abrasion before coating application.

Coating application

Coating was applied using Motor-Driven Dip Coater RDC 15 Application as referred to ASTM D823-95. A custom-made acrylic container was used in order to effectively coat the test panel and in the same time without using excessive amount of coating material. The

coating speed was kept constant for all test panels to maintain uniform thickness among all coating. Wet film thickness was measured using TQC Sheen wet film thickness gauge. Three readings were taken at each surface of test panel. Once desired wet film thickness was obtained, the coated test panels were left in laboratory under room temperature and standard condition to let the coating undergoes curing process at ambient temperature for 7 days [10].

Coating performance test

Adhesion test. After the coated test panel cured for 7 days, adhesion performance test was done in order to

determine the degree of adhesion. X-Cut and Cross-Cut Tape Test were used to rate adhesion performance by referring to ASTM D3359-09. The adhesion performance was rated based on classification provided in ASTM D3359-09 in Table 1 and Table 2.

RESULTS AND DISCUSSION

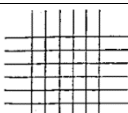
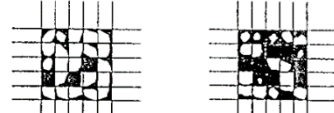
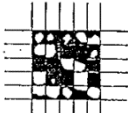
Characterization Tests

Fourier transform infrared spectroscopy (FTIR) technique was performed to identify the chemical bonds existed in the unripe palm oil and used cooking oil before and after epoxidation process.

Table 1. X-Cut Tape Test adhesion classification

Classification	Explanation
5A	No peeling or removal
4A	Trace peeling or removal along incisions or at their intersection
3A	Jagged removal along incisions up to 1.6 mm (1/16 in.) on either side
2A	Jagged removal along most of incisions up to 3.2 mm (1/8 in.) on either side
1A	Removal from most of the area of the X under the tape
0A	Removal beyond the area of the X

Table 2. Cross-Cut Tape Test adhesion classification

Classification	Percent area removed	Surface of Cross-Cut area from which flaking has occurred for six parallel cuts and adhesion range by percent
5B	0% None	
4B	Less than 5%	
3B	5-15%	
2B	15-35%	
1B	35-65%	
0B	Greater than 65%	

The spectrum of unripe palm oil as shown in Fig. 6(a) showed a stretching vibration peak of =CH (3003 cm^{-1}), a stretch of C–H was observed between $2921\text{--}2852\text{ cm}^{-1}$, a carbonyl stretch C=O at 1743 cm^{-1} , and unsaturation peak HC=CH (cis) at wavenumber 1650 cm^{-1} . The peak at 3003 cm^{-1} corresponds to the level of unsaturation that disappears as the double bonds are converted and used; thus, correlating with the epoxide peak at 844 cm^{-1} as shown in Fig. 6(b). The same result generated was also demonstrated in the previous research [17]. The formation of epoxy group in the chemical structure of the epoxidized unripe palm oil indicates that the epoxidation process was successfully done.

Fig. 7(a) shows the spectrum profile of cooking oil before undergoes epoxidation process. A stretch of C–H

was observed between $2921\text{--}2852\text{ cm}^{-1}$. The spectrum shows carbonyl stretch at 1743 cm^{-1} and methyl bending at 1464 cm^{-1} . Presence of nitrogenous compound is shown at 1542 cm^{-1} and methylene group at 721 cm^{-1} . Bending of C–H was observed at 1377 cm^{-1} . Existence of C–O stretching and bending of O–H were found at 1159 cm^{-1} and 1116.95 cm^{-1} respectively.

While, Fig. 7(b) shows the spectrum profile of cooking oil after the epoxidation process. Based on the spectrum profile of ECO, there is no oxirane ring formed in the fatty acid structure from the epoxidation process as the oxirane ring should produce a trough between $833\text{--}841\text{ cm}^{-1}$ [18-19]. Fig. 8 shows the summary of adsorption band of unripe palm oil and used cooking oil before and after epoxidation. Used cooking oil that was

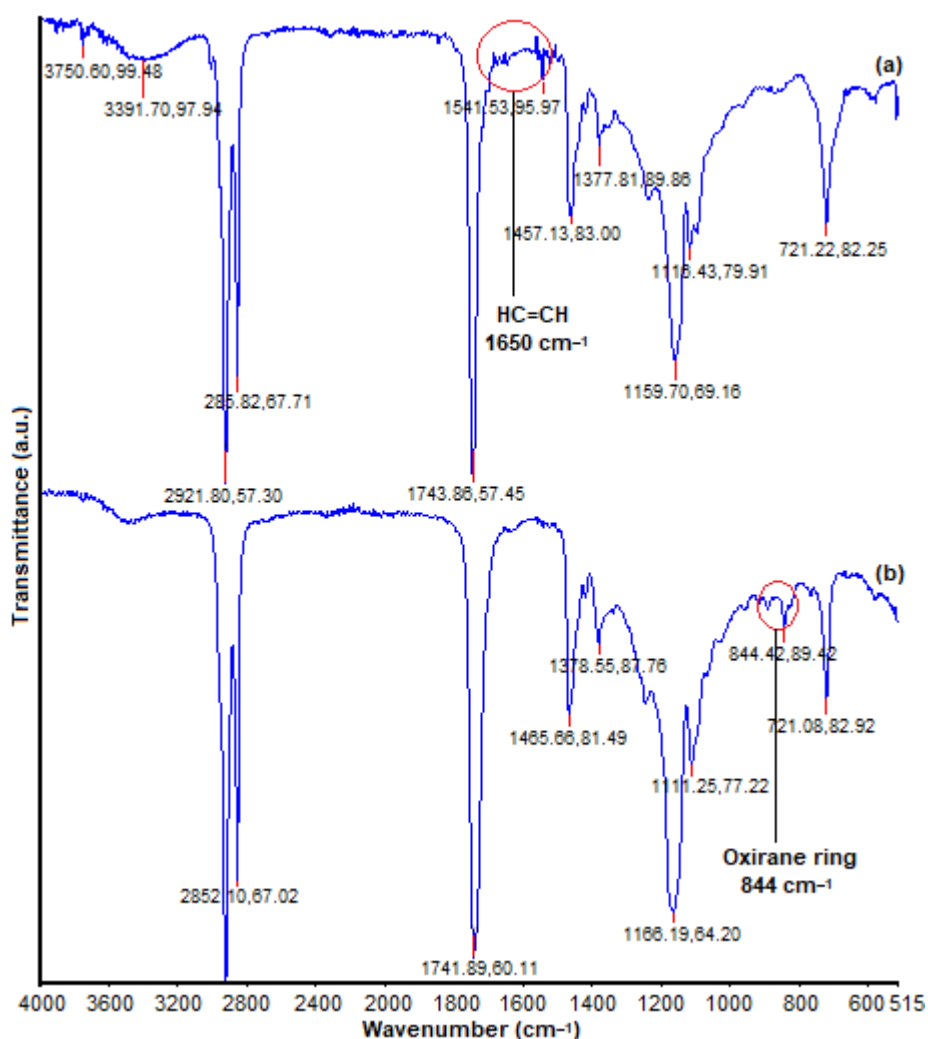


Fig 6. FTIR spectrum of (a) unripe palm oil and (b) epoxidized unripe palm oil

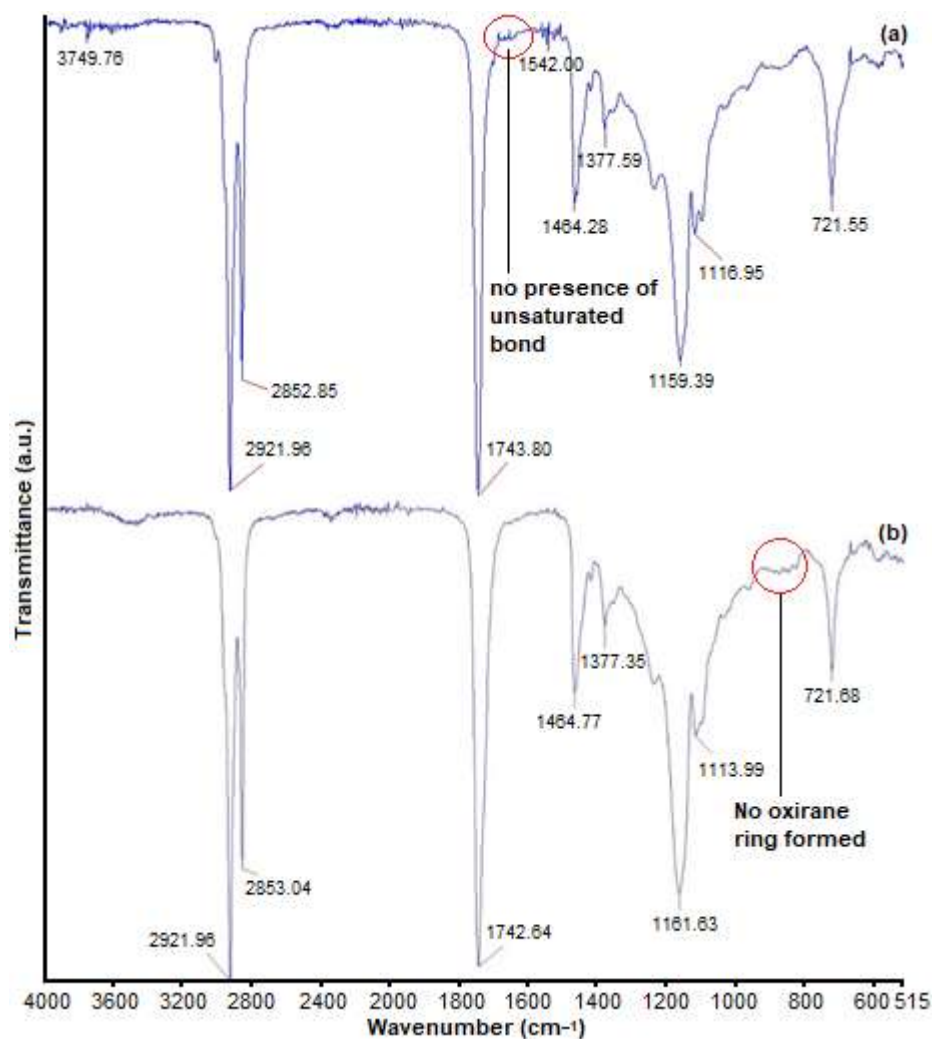


Fig 7. Spectral analysis of (a) used cooking oil and (b) epoxidized used cooking oil

Table 3. Summary of absorption band of unripe palm oil and used cooking oil before and after epoxidation process

Group	Unripe palm oil (cm^{-1})	Epoxidized unripe palm oil (cm^{-1})	Used cooking oil (cm^{-1})	Epoxidized used cooking oil (cm^{-1})
N-H str	3391	3394	3749	-
=CH str	3003	-	2921	2921
HC=CH (cis)	1650	-	-	-
C=O	1743	1741	1743	1742
Oxirane ring	-	844	-	-

collected from domestic household might consist of very low amount of unsaturated fatty acid or none at all. Existence of unsaturated fatty acid in the cooking oil is crucial for epoxidation process because unsaturated fatty acid provide reactive site for epoxidation process to complete [20]. Non-existence of unsaturated fatty acid in

cooking oil is due to decomposition process of unsaturated fatty acid during frying process [14-15].

Adhesion Performance Test

The coated test panel undergoes adhesion performance test in order to determine the degree of

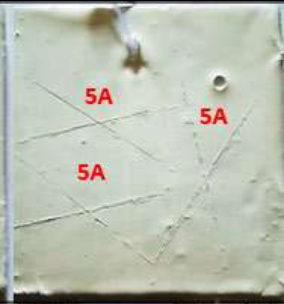
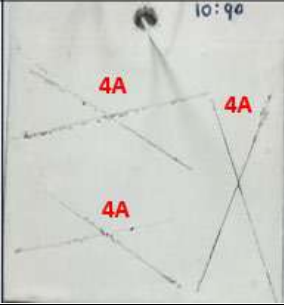
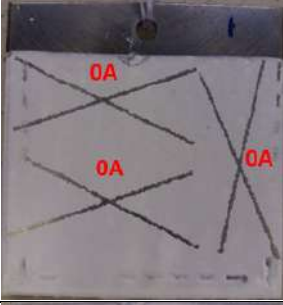
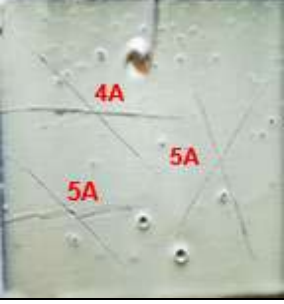
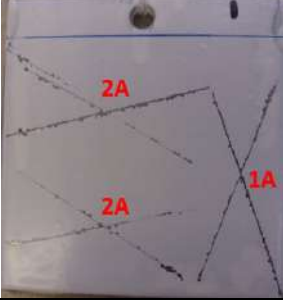
adhesion performance. X-Cut and Cross-Cut Tape Test were used to rate adhesion performance by referring to ASTM D3359-07 [21]. The adhesion performance was rated based on classification provided in Table 1 and 2 as shown earlier.

X-Cut Tape Test

The results obtained from the X-Cut Tape Test for epoxidized unripe palm oil (EPO) coated metals were good as the coatings only experienced small trace of

peeling as seen in Table 4. Formulation 0:100 serves as control which produced best performance with adhesion classification as 5A. Formulation 10:90 and 20:80 are both classified as 4A. Formulation 30:70 also produced the best adhesion classification which is 5A. On the other hand, results from X-Cut Tape Test for ECO coated metals showed that only minimal adhesion performances obtained from ECO coated metal for all formulation. If observed and compared among the coating that was added with ECO in their formulation, 10:90, 20:80 and 30:70,

Table 4. Results of adhesion X-Cut Tape Test of coated metal of EPO and ECO

Ratio	EPO:DGEBA	Classification	ECO:DGEBA	Classification
0:100		5A No peeling or removal		5A No peeling or removal
10:90		4A Trace peeling or removal along incisions or at their intersection		1A Removal from most of the area of the X under the tape
20:80		4A Trace peeling or removal along incisions or at their intersection		0A Removal beyond the area of the X
30:70		5A No peeling or removal		2A Jagged removal along most of incisions up to 3.2 mm (1/8 in.) on either side

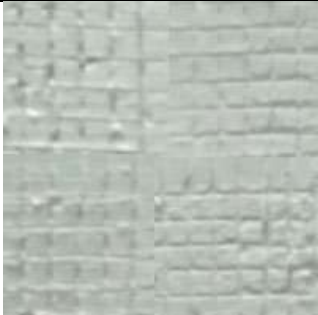
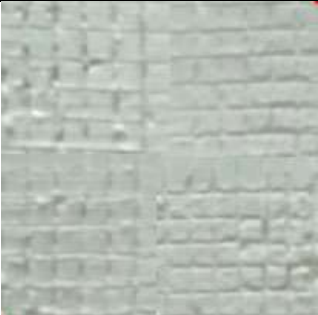
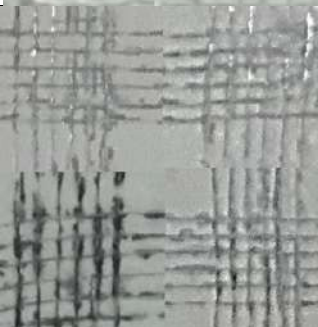
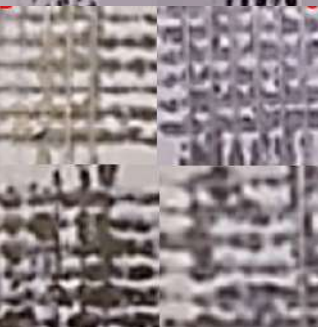
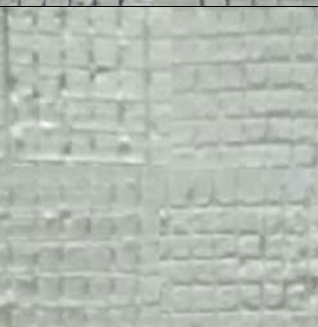
they obtained almost similar adhesion classification. Only formulation 20:80 yielded one rank lower than 10:90 and 30:70. There is no distinctive trend can be observed in result obtained from X-Cut Tape Test.

Cross-Cut Tape Test

Table 5 shows the condition of coated metal of EPO and ECO after being tested with Cross-Cut Tape Test.

The average percent area removed of coated metal was observed and calculated, then classified according to the standard ASTM D3359-09 in Table 2. As can be seen in Fig. 8 and Table 6, formulation 10:90(EPO:DGEBA) was classified as 3B with minimum error bar of 2B, formulation 20:80 was classified as 4B with minimum error bar of 3B and formulation 30:70 was classified as 4B with maximum error bar of 5B. Addition of EPO in the

Table 5. Result of adhesion Cross-Cut Tape Test of coated metal of EPO and ECO

Ratio	EPO:DGEBA	ECO:DGEBA
0:100		
10:90		
20:80		
30:70		

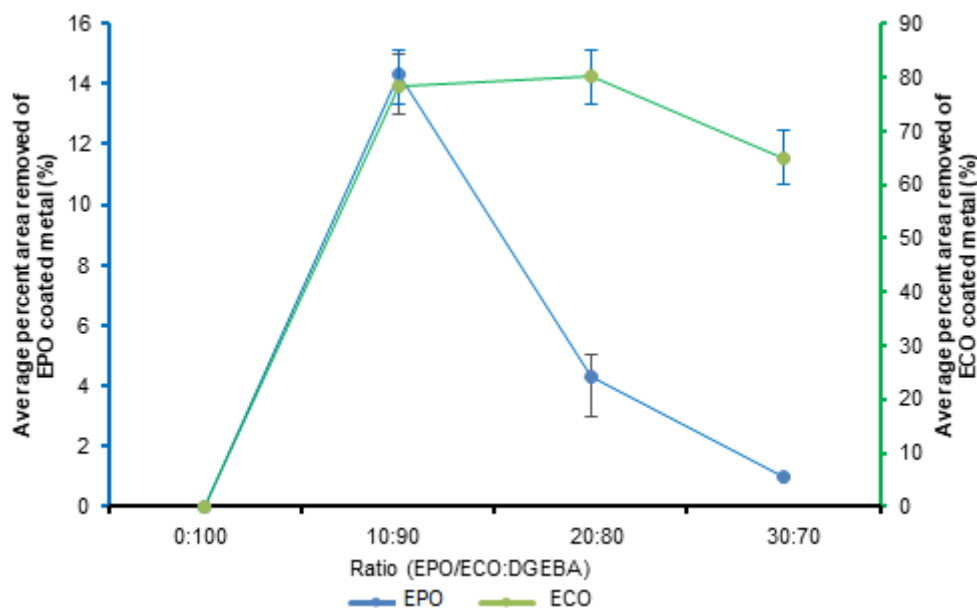


Fig 8. Graph of adhesion performance of developed coating by Cross-Cut Tape Test

Table 6. Summary of Cross-Cut Tape Test adhesion classification

EPO:DGEBA		
Ratio	Average Percent Area Removed (%)	Classification
0:100	0	5B
10:90	14.33	3B
20:80	4.33	4B
30:70	1.0	4B
ECO:DGEBA		
0:100	0	5B
10:90	78.33	0B
20:80	80.0	0B
30:70	65.0	1B

coating formulation have reduced the brittleness of the coating, as the components of EPO in the coating formulation increase, the adhesion performance become better. Meanwhile, only minimal adhesion performance obtained for all formulations of ECO:DGEBA. Both formulations (10:90 and 20:80) which was tested by Cross-Cut tape test were classified as 0B and formulation 30:70 was classified as 1B. These adhesion results support the findings from FTIR analysis of epoxidized cooking oil in Fig. 7(b) that there is non-existence of oxirane ring in the epoxidized cooking oil which is important component to develop a good coating material.

CONCLUSION

In this study, the unripe fruit bunch and used cooking oil was successfully utilized as additional compound in new epoxy formulation. Incorporation of these oils as additional component in formulating new epoxy coating gives oil palm a new area of application and adds value to this renewable resource. Comparison of FTIR analysis on unripe palm oil and used cooking oil before and after epoxidation show different results. Oxirane ring was present at a wavenumber 844 cm^{-1} in EPO whereas the oxirane ring was absent in ECO. The results obtained from the adhesion test from EPO were

good as the coatings only experienced small trace of peeling. Only minimal adhesion performances obtained from ECO coated metal for all formulation. This correlated with absence of oxirane ring from the ECO observed in spectrum profile. Finally, it may be concluded that epoxidized unripe palm oil has a potential to replace petroleum-based resin in coating formulation based on their good performances.

■ ACKNOWLEDGMENTS

This research was funded by Universiti Teknologi MARA (UiTM) under the MITRA PERDANA Grant Scheme, Grant No: 600-IRMI/PERDANA 5/3/MITRA (006/2018)-2.

■ REFERENCES

- [1] Fong, M.N.F., and Salimon, J., 2012, Epoxidation of palm kernel oil fatty acids, *J. Sci. Technol.*, 4 (2), 87–98.
- [2] Kumar, S., Samal, S.K., Mohanty, S., and Nayak, S.K., 2018, Toughening of petroleum based (DGEBA) epoxy resins with various renewable resources based flexible chains for high performance applications: A review, *Ind. Eng. Chem. Res.*, 57 (8), 2711–2726.
- [3] Inadera, H., 2015, *Neurological effects of bisphenol A and its analogues*, *Int. J. Med. Sci.*, 12 (12), 926–936.
- [4] Mínguez-Alarcón, L., Hauser, R., and Gaskins, A.J., 2016, Effects of bisphenol A on male and couple reproductive health: A review, *Fertil. Steril.*, 106 (4), 864–870.
- [5] Parashar, V., and Narula, A.K., 2015, Synthesis and characterization of DGEBA epoxy and novolac epoxy blends and studies on their curing and mechanical behavior, *Knowl. Res.*, 2 (1), 30–36.
- [6] Shi, L., Liu, Z., Li, J., and Qin, Z., 2017, Analysis of edible vegetable oils by infrared absorption spectrometry, *Proceedings of the 2017 2nd International Conference on Electrical, Automation and Mechanical Engineering (EAME 2017)*, 23-24 April 2017, Shanghai, China.
- [7] Ahmad, S., Naqvi, F., Sharmin, E., and Verma, K.L., 2006, Development of amine-acid cured *Annona squamosa* oil epoxy anticorrosive polymeric coatings, *Prog. Org. Coat.*, 55 (3), 268–275.
- [8] Das, G., and Karak, N., 2009, Epoxidized *Mesua ferrea* L. seed oil-based reactive diluent for BPA epoxy resin and their green nanocomposites, *Prog. Org. Coat.*, 66 (1), 59–64.
- [9] Meadows, S.S., Hosur, M.V., Tcherbi-Narteh, A., and Jeelani, S., 2017, Optimization studies on the synthesis and characterization of bio-based epoxidized soybean oil, *The 21st International Conference on Composite Materials (ICCM-21)*, 20–25 August 2017, Xi'an, China.
- [10] Jalil, M.J., Jamaludin, S.K., Azmi, I.S., and Daud, A.R.M., 2017, Characterisation of epoxidation of palm kernel oil based on crude oleic acid, *Ind. Combust.*, 201606.
- [11] Mancini, A., Imperlini, E., Nigro, E., Montagnese, C., Daniele, A., Orrù, S., and Buono, P., 2015, Biological and nutritional properties of palm oil and palmitic acid: Effects on health, *Molecules*, 20 (9), 17339–17361.
- [12] Norhaizan, M.E., Hosseini, S., Gangadaran, S., Lee, S.T., Kapourchali, F.R., and Moghadasian, M.H., 2013, Palm oil: Features and applications, *Lipid Technol.*, 25 (2), 39–42.
- [13] Gunstone, F.D., 2002, *Vegetable Oils in Food Technology: Composition, Properties and Uses*, 1st Ed., Blackwell, Hoboken, New Jersey.
- [14] Omer, N.M.A., Ali, E.M.A., Mariod, A.A., and Mokhtar, M., 2014, Chemical reactions taken place during deep-fat frying and their products: A review, *JNMS*, 16 (1), 1–16.
- [15] Bordin, K., Kunitake, M.T., Aracava, K.K., and Trindade, C.S., 2013, Changes in food caused by deep fat frying – A review, *Arch. Latinoam. Nutr.*, 63 (1), 5–13.
- [16] Donough, C.R., Cock, J., Oberthür, T., Indrasuara, K., Rahmadsyah, Gatot, A.R., and Dolong, T., 2015, Estimating oil content of commercially harvested oil palm fresh fruit bunches – A step towards increasing palm oil yields, *Oil Palm Bull.*, 70, 8–12.
- [17] Derawi, D., Salimon, J., and Ahmed, W.A., 2014, Preparation of epoxidized palm olein as renewable material by using peroxy acids, *Malays. J. Anal. Sci.*, 18 (3), 584–591.

- [18] Fakhari, A., Rahmat, A.R., Wahit, M.U., and Kian, Y.S., 2014, Synthesis of new bio-based thermoset resin from palm oil, *Adv. Mater. Res.*, 931-932, 78–82.
- [19] Tajulruddin, W.N.W., Rahmat, A.R., Yusof, Z.A.M., and Fakhari, A., 2015, Characterization of polyol synthesized from epoxidized palm oil using Fourier transform infra-red and nuclear magnetic resonance, *J. Adv. Res. Appl. Mech.*, 10 (1), 30–35.
- [20] Sudheer, K., Sushanta, K.S., Smita, M., and Sanjay, K.N., 2017, Recent development of bio-based epoxy resins: A review, *Polym. Plast. Technol. Eng.*, 57 (3), 133–155.
- [21] ASTM D3359-07, *Standard Test Methods for Measuring Adhesion by Tape Test*, ASTM International, West Conshohocken, PA, 2007, <https://www.astm.org>.

Fabrication of Superhydrophobic Film on the Surface of Indonesian Bamboo Timber by TiO₂ Deposition and Using Octadecyltrichlorosilane as a Surface Modifier Agent

Diana Vanda Wellia*, Wulandari, Arifah Mustaqimah, Nurul Pratiwi, and Yulia Eka Putri

Department of Chemistry, Faculty of Mathematics and Natural Sciences, Universitas Andalas, Campus Unand Limau Manis, Padang 25163, West Sumatra, Indonesia

* Corresponding author:

email: nandadiana@sci.unand.ac.id

Received: June 18, 2019

Accepted: October 14, 2019

DOI: 10.22146/ijc.46740

Abstract: The tropical bamboo has been widely used in modern society as a potential material for various applications. It is well known that bamboo has low durability due to its hydrophilic properties. To overcome this problem, the superhydrophobic surface on Indonesian bamboo timber had been successfully fabricated via hydrothermal deposition of an anatase TiO₂ and solution immersion of octadecyltrichlorosilane (ODTS), which exhibited a maximum water contact angle (WCA) of 155°. The as-fabricated superhydrophobic bamboo timber not only showed high mechanical resistance against the abrasion of SiC sandpaper but had also been proven to possess high chemical stability after immersion in acidic and basic aqueous solutions. Moreover, the superhydrophobic bamboo timber also demonstrated excellent self-cleaning and flame-resistance properties, in comparison to pure bamboo timber. It is believed that the strategy offered in this study can increase the utilization of bamboo timber for various purposes, especially as a self-cleaning material.

Keywords: superhydrophobic; TiO₂; bamboo; octadecyltrichlorosilane; self-cleaning material

■ INTRODUCTION

Bamboo is a type of woody plant with a hole in the middle which belongs to the grass family (Gramineae), a sub-family of Bambusoideae, consisting of 121 genera and divided into approximately 1,662 species throughout the world [1]. They grow in various countries with various climates, from cold regions to hot tropics, most are located throughout East Asia, from Sakhalin at 51° N in Russia to North Australia, and west to the Himalayas and India [2]. Bamboo is one of the cellulose-based materials that is widely used due to its fast growth and abundant availability [3]. In 3–5 years, the anatomical structure of bamboo becomes stable and mature, resulting in good mechanical strength and utilization properties [4]. As it is widely known, all parts of bamboo have their own application, and the most favored is the bamboo stems [5]. In general, the bamboo stem is arranged in three sections: the outer layer with green color as the skin of the bamboo stem, the middle layer with brown color that is widely known as the bamboo timber, and the inner layer with yellow color [6].

According to the International Network for Bamboo and Rattan (INBAR), Indonesia accounted for 8% of the world exports of bamboo products in 2014 with a value of US\$ 149 million, which ranked as the third largest producer and exporter country of bamboo products in the world. Almost 80% of total Indonesian bamboo usage was for construction material such as buildings, houses, interior and exterior decoration, bridges, scaffolding, ladders, walls, and flooring [7]. The most common Indonesian bamboo that has been reported for housing construction is betung bamboo (*Dendrocalamus asper*). The properties of betung bamboo is different than other types of bamboo, which has the potential to be developed into structural components for construction materials [8].

However, the nature of bamboo timber that consists of unique porous structures and a lot of hydroxyl groups on the surface, support absorbing water and moisture of the surrounding environments, which could later on affect the durability of bamboo products

[9]. Therefore, the most effective and appropriate way to improve the durability of bamboo timber is to modify the chemical properties of its surface.

In recent years, several approaches for the development and improvement of bamboo timber quality have been reported. Fabrication of a superhydrophobic system on the bamboo timber surface could be one of the promising approaches. Li et al. fabricated superhydrophobic bamboo timber by using the hydrothermal mineralization method to synthesize micro/nano CaCO_3 on the bamboo timber surface, then modified by fluoroalkylsilane (FAS) [10]. In another study, Jin et al. successfully prepared a durable, superhydrophobic, superoleophobic and corrosion resistant coating on the surface of bamboo timber by using (heptadecafluoro-1,1,2,2-tetradecyl)trimethoxysilane (FAS-17) as a modifier agent on rose-like ZnO nanoflowers coating [11]. By using the same method, Li et al. also studied the fabrication of durable, self-cleaning and superhydrophobic bamboo timber using the same modifier agent (FAS-17) on anatase TiO_2 film [12]. Based on those works, the deposition of nanoparticles of inorganic materials on bamboo timber plays an important role to improve the physical and chemical properties, like durability and stability. Furthermore, the contribution of the silane compound has been briefly reported as the modifier agent to fabricate the superhydrophobic system on the bamboo timber surface.

In this work, a similar approach was used to fabricate the superhydrophobic system on the surface of Indonesian bamboo timber by using the hydrothermal method through deposition of TiO_2 nanoparticles onto the surface to enhance the roughness of surface, followed by hydrophobization by octadecyltrichlorosilane (ODTS). Furthermore, the physical and chemical properties of the modified bamboo timber were determined and clarified by applying the self-cleaning approach.

■ EXPERIMENTAL SECTION

Materials

All reagents were analytical grade and purchased from Sigma–Aldrich. Indonesian bamboo timber (*Dendrocalamus asper*) with a size of 20 mm × 20 mm × 4 mm was obtained from Universitas Andalas, Padang,

Indonesia. The bamboo slices were washed in deionized water and acetone for 30 min, and dried in the oven at 80 °C for 24 h.

Procedure

Fabrication of TiO_2 particles on the surface of the bamboo timber via hydrothermal method

Two grams of ammonium fluorotitanate and 1.85 g boric acid were dissolved in 100 mL of distilled water under magnetic stirring for 15 min at 25 °C. The pH value of the mixed solution was adjusted to 2 by the addition of hydrochloric acid aqueous solution. Then, 75 mL of this adjusted solution was moved into a 100 mL Teflon-lined autoclave and the bamboo timber was subsequently placed into the reaction solution. The autoclave was placed in an oven at 90 °C for 5 h. Lastly, the sample was separated from the solution, washed with distilled water, and dried at 80 °C for 24 h in an oven [13].

Fabrication of superhydrophobic bamboo timber

Octadecyltrichlorosilane (ODTS) was used to modify the surface of the as-prepared bamboo timber as a layer with low surface energy. The bamboo timber that had a layer of TiO_2 nanoparticles was placed into sealed reactors, with different ratios of ODTS/ethanol solution (1:24, 1:9, 1:4, and 2:3) at ambient temperature for 5 h. Then, the samples were taken out from the reactor, followed by washing with ethanol and drying in an oven [14].

Characterizations

The structures of crystalline were analyzed by X-ray diffraction (XRD, PANalytical CubiX³) with Cu K α radiation ($\lambda = 1.5418 \text{ \AA}$) at a scan rate of 8 (°)/min ranging from 10° to 70°. The morphology of the samples was evaluated using a scanning electron microscope (SEM, JEOL JSM-IT-300) with 300×, 4000× and 6000× magnification. The chemical compositions of the bamboo timber with and without treatments were determined by energy dispersive spectroscopy (EDS, coupled with SEM instrument). FTIR spectra of the samples were recorded using FTIR (Perkin Elmer Company) in the range of 400–4000 cm^{-1} . The thermal properties of the samples (10 mg) were observed by TG-DTA (Perkin Elmer) from

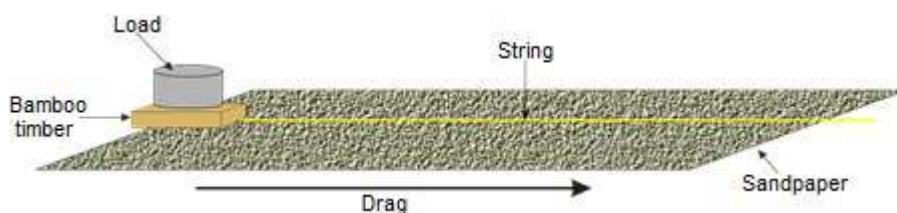


Fig 1. Scheme of the scratch test procedures

25 °C to 575 °C at a rate of 10 °C min⁻¹. The water contact angle (WCA) was captured at ambient temperature by digital microscope-1000× magnification with the droplet volume 5 μL and further analyzed by the image analysis software.

Physical and chemical stability tests

The mechanical stability of the modified bamboo timber was assessed by a scratch test. The procedures of this test were carried out by dragging the modified bamboo timber on the surface of 300 mm length of SiC sandpaper (1500 mesh) under 68 g of the load. The contact angle before and after the scratch test was measured. This analogical procedure is clearly illustrated in Fig. 1 [12]. The chemical stability was tested by measuring the static contact angle of the modified bamboo timber after immersion in the sulfuric acid (pH = 2) and sodium hydroxide (pH = 13) aqueous solution for 6 h, 12 h and 24 h.

Flame retardancy test

The flammability property was determined by counting the time that was used to quench the flame after the modified bamboo timber was burned with an alcohol burner.

Self-cleaning property test

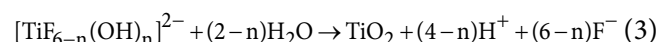
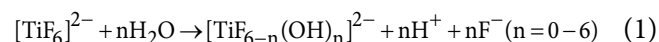
In order to show the self-cleaning ability of the modified bamboo timber, the hydrophilic mud was used as contaminant specimens. The ability of water droplets to remove all of the contaminants on the surface of the modified bamboo timber was observed.

RESULTS AND DISCUSSION

Synthesis of Superhydrophobic Film on the Surface of Bamboo Timber

The superhydrophobic surface of Indonesian bamboo timber was successfully synthesized firstly by

adding TiO₂ on the bamboo timber surface through the hydrothermal method followed by surface modification using ODTs. In the process of hydrothermal, the hydrolysis of (NH₄)₂TiF₆ occurred, which gradually changed the fluorinated titanium complex ions into titanium hydroxide complex ions in an aqueous solution (Eq. (1)) [14]. The resulted fluoro anions from this reaction were removed by boric acid as the fluoride scavenger (Eq. (2)). The H⁺ ions in the solution were increased with the addition of HCl, that accelerated Eq. (2) to move forward. The obtained titanium hydroxide complex ions were further hydrolyzed to form TiO₂ nanoparticles (Eq. (3)). The reaction is described as follows [14]:



The bamboo surface consists of excess hydroxyl groups. The resulting TiO₂ nanoparticles strongly interacted with hydroxyl groups on the bamboo surface due to the presence of high energy and pressure inside the autoclave [14]. The presence of hydroxyl groups resulted in stable TiO₂ nanoparticles on the bamboo timber surface because of the electrostatic adsorption force. The trisilanol groups, resulted from the reaction between ODTs and ethanol will interact with the -OH group and then gradually absorb onto the TiO₂-coated bamboo timber surface (Fig. 2) [14].

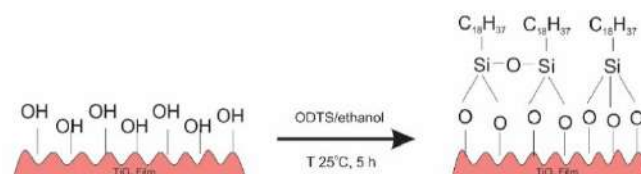


Fig 2. The reaction of superhydrophobic surface fabrication

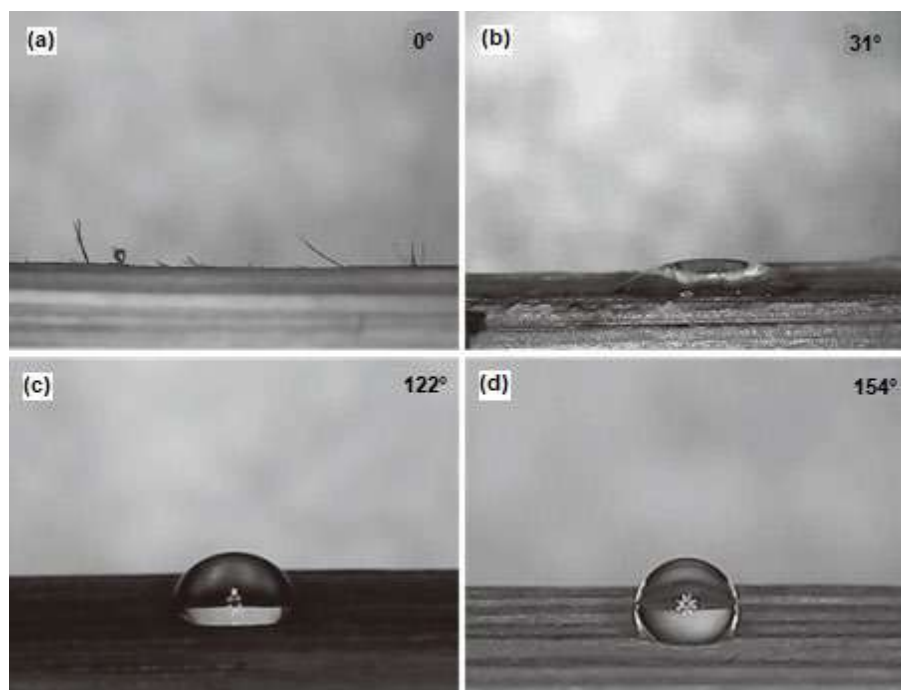


Fig 3. Digital images of the water droplets on the surface of (a) pure bamboo timber, (b) TiO_2 -coated bamboo timber, (c) ODTS-coated bamboo timber, and (d) superhydrophobic bamboo timber

Surface Wettability

The WCA measurements were carried out to determine the chemical properties of the surface of the synthesized samples. Fig. 3(a) shows the photograph of water droplet behavior on the pure bamboo timber surface. Obviously, it demonstrated hydrophilic properties with WCA of 31° . In Fig. 3(b), the bamboo timber had been covered with TiO_2 which exhibited a superhydrophilic performance with WCA of 0° . This phenomenon was due to the excess of hydroxyl groups on the TiO_2 films surface that made the water spread out quickly on the surface of the bamboo timber [12]. On the contrary, when the bamboo timber was coated with ODTS, the surface properties became hydrophobic with a maximum WCA of about 122° (Fig. 3(c)). However, after the modification of ODTS on TiO_2 -coated bamboo timber, the new surface exhibited superhydrophobic properties with WCA of 154° (Fig. 3(d)). The collaboration of surface roughness provided by TiO_2 and low-surface energy layer of ODTS had effectively trapped the air into interspaces of the bamboo timber surface, as the surface properties transformed into superhydrophobic [15].

The Structural Analysis

Fig. 4 shows the XRD patterns of the pure and the TiO_2 -coated bamboo timber. In Fig. 4(a), the characteristic peaks at 15.2° and 21.5° that belonged to (101) and (002) crystal planes, respectively, represented the characteristic of the cellulose crystalline region from pure bamboo timber [14,16]. However, after the hydrothermal process

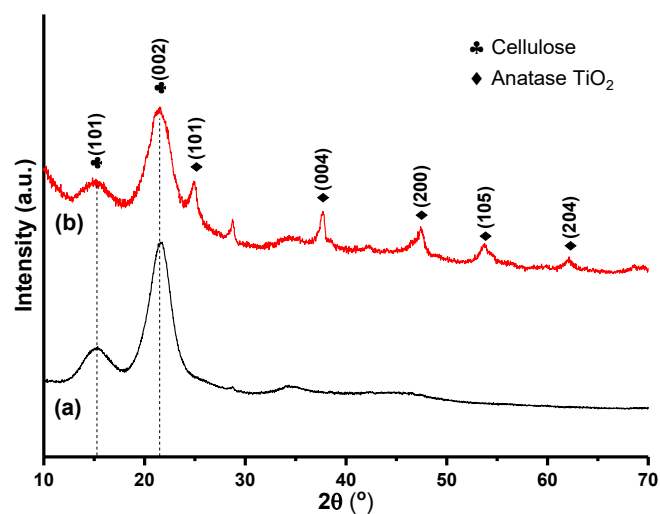


Fig 4. XRD Patterns of (a) the pure bamboo timber, (b) the TiO_2 -coated bamboo timber

(Fig. 4(b)), several new diffraction peaks at 2θ values of 25.0° , 37.6° , 47.5° , 53.8° and 62.2° which corresponded to (101), (004), (200), (105), and (204) planes, respectively, were observed as the characteristic of anatase TiO_2 crystals (JCPDS cards: 21-1272).

The Functional Groups Analysis

The FTIR spectra of the pure bamboo timber, the bamboo timber modified by TiO_2 and the bamboo timber modified by both TiO_2 and ODTs (superhydrophobic bamboo) are shown in Fig. 5. The band at 3333 cm^{-1} (stretching vibrations of O–H groups) in Fig. 5(a) showed higher intensity than in Fig. 5(b, c), indicating that the OH groups were consumed by TiO_2 and ODTs. Respectively, the absorption peaks at 2924 cm^{-1} and 2853 cm^{-1} can be attributed to C–H symmetric and asymmetric stretching vibrations, representing the existence of the long-chain alkyl group from ODTs in the superhydrophobic bamboo [17] and the alkyl groups of cellulose, lignin and hemicellulose in the pure bamboo timber [18-19]. The spectra of superhydrophobic bamboo timber exhibited adsorption peak at 1033 cm^{-1} , which were attributed to the asymmetric stretching vibrations of Si–O–Si due to cross-linked chains between ODTs molecules [14]. Furthermore, the adsorption peaks at 959 cm^{-1} that only appear in the spectra of the TiO_2 -coated bamboo timber and the superhydrophobic bamboo timber, corresponded to the vibration of Ti–O–Si [20]. Thus, we could deduce that the ODTs molecules had grafted on the TiO_2 -coated bamboo timber surface.

Surface Morphologies and Chemical Compositions

SEM-EDX characterization was carried out to observe the surface morphology and determine the chemical composition of the elements on the surface of pure bamboo timber, TiO_2 -coated bamboo timber, and bamboo timber modified by TiO_2 and ODTs (Fig. 6). The morphology of pure bamboo timber is shown in Fig. 6(a), the large pit like tunnel-shapes can be observed. Fig. 6(b) shows the morphology of TiO_2 -coated bamboo timber, which showed that the surface of this sample is rougher compared with pure bamboo timber. This is because TiO_2 aggregation increased the surface roughness of the surface of the bamboo timber [14]. Fig. 6(c) presents the SEM

image of TiO_2 -coated bamboo timber with higher magnification. Clearly, TiO_2 aggregations covered the surface of bamboo timber in order to form a roughness surface. Fig. 6(d) demonstrates the SEM image of the superhydrophobic bamboo surface, which pointed out the combination structure of TiO_2 with the structure of the bamboo timber. Consequently, this structure led to air trapped within the grooves and later formed the superhydrophobic surface.

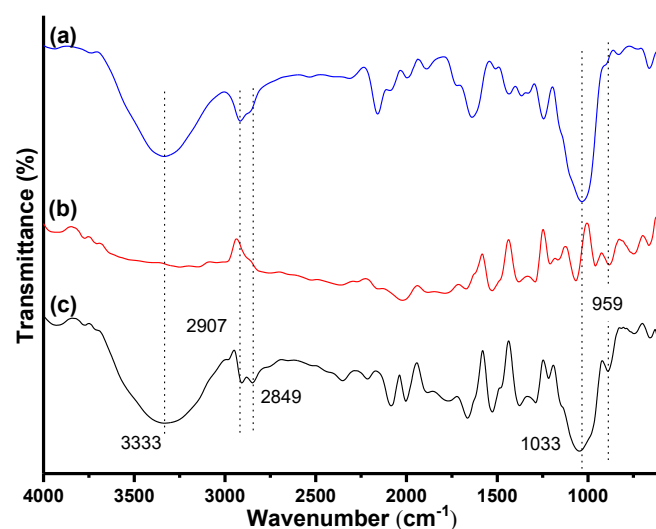


Fig 5. FTIR spectra of (a) the pure bamboo timber, (b) the TiO_2 -coated bamboo timber, and (c) the superhydrophobic bamboo timber

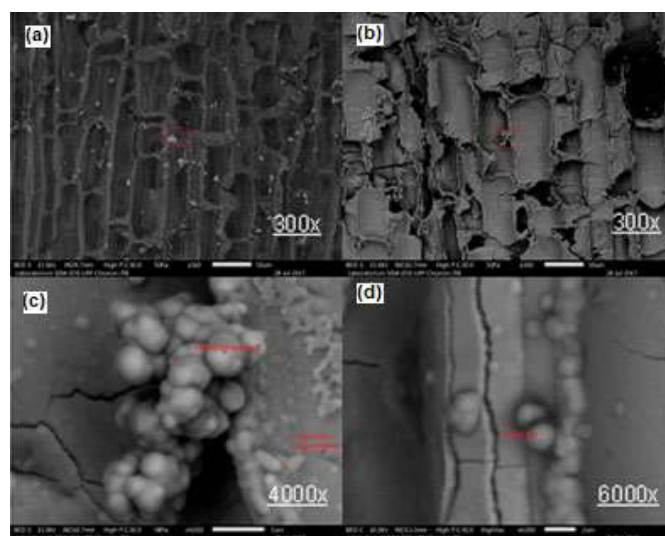


Fig 6. Images SEM of (a) pure bamboo timber (b) TiO_2 -coated bamboo timber (c) high magnification for images b (d) superhydrophobic bamboo timber

EDS was performed to determine the chemical composition of the constituent elements on the surface of pure bamboo timber, TiO₂-coated bamboo timber, and bamboo timber modified by TiO₂ and ODTS. Fig. 7(a) shows the EDS spectrum of pure bamboo timber that is proven by the presence of the C and O elements. The existence of Ti and O elements are shown in Fig. 7(b), which indicated that TiO₂ had been coated on the bamboo timber surface. In Fig. 7(c), the EDS spectrum of bamboo timber modified by TiO₂ and ODTS is shown, which

exhibited the peak of Si, F, Ti and O elements. The appearance of the Si element showed that ODTS had interacted on the surface of the TiO₂-coated bamboo timber. Furthermore, the peak of the F element was observed due to the excess of fluorine ions during the reaction involving TiO₂.

Thermal Stability

The TG/DTA analysis of pure bamboo timber, TiO₂-coated bamboo timber, ODTS-coated bamboo

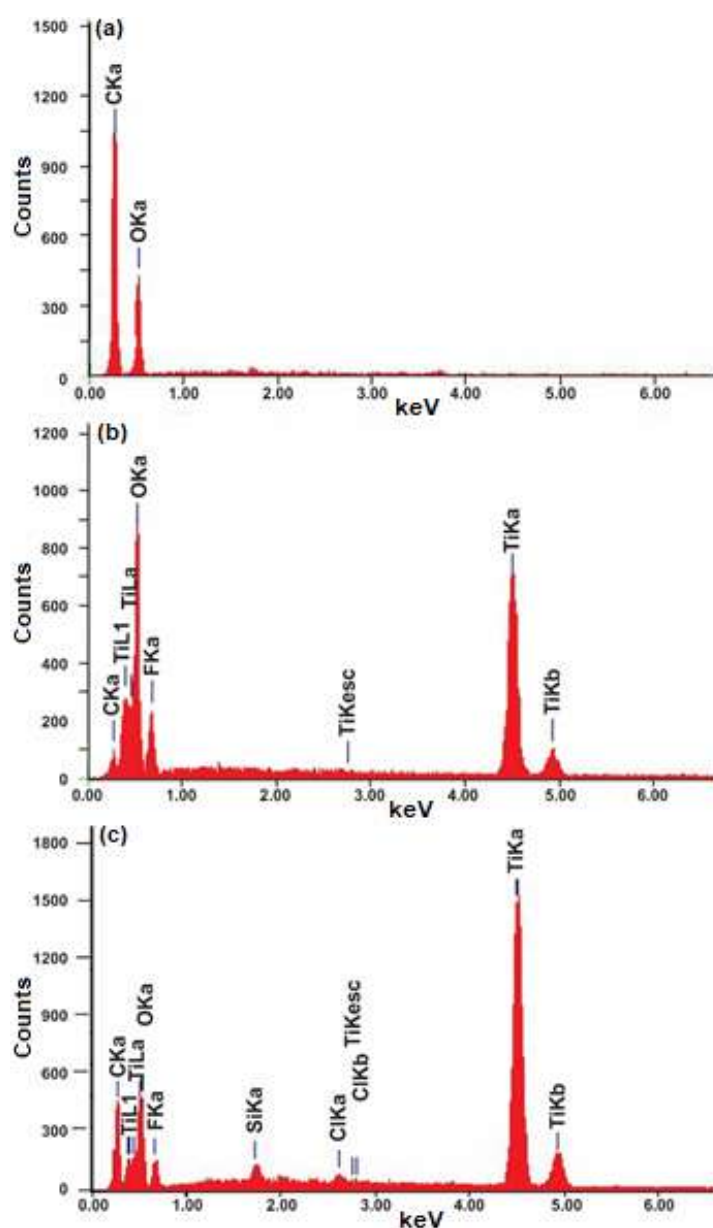


Fig 7. EDS spectrum of (a) the pure bamboo timber, (b) TiO₂-coated bamboo timber, and (C) superhydrophobic bamboo timber

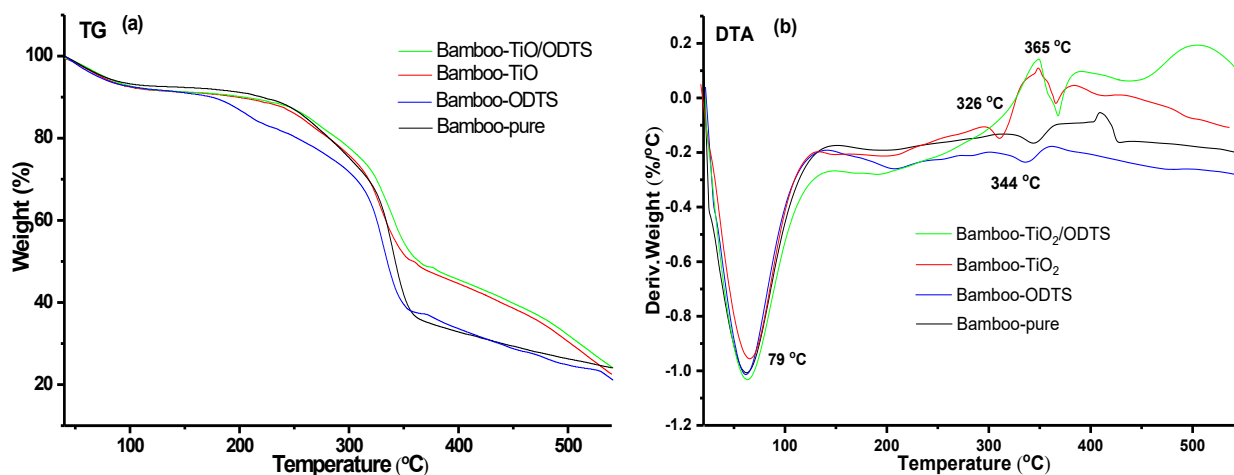


Fig 8. TG-DTA curves of superhydrophobic bamboo timber, TiO_2 -coated bamboo timber, ODTS-coated bamboo timber, and pure bamboo timber

timber, and the bamboo timber modified by TiO_2 and ODTS were shown in Fig. 8. The TG curve (Fig. 8(a)) shows that all samples had a slight weight loss in the range of 60 to 80 °C due to the removal of the absorbed water before pyrolysis [21]. Thermal degradations were also shown in the range 180–250 °C, which is attributed to the partial degradation of hemicellulose [14]. The weight losses in the range of 250–380 °C were continuously due to cellulose and lignin degradation. Furthermore, all of the components of the four samples gradually degraded until the temperature reached 380 °C.

Corresponding to the weight losses of the TG analysis, the DTA curve (Fig. 8(b)) presented wide endothermic peaks at a minimum temperature of 344 °C for pure bamboo timber and ODTS-coated bamboo timber. On the contrary, the sharp endothermic peaks were present at a minimum temperature of 365 °C for the TiO_2 -coated bamboo timber and the bamboo timber modified by TiO_2 and ODTS. The maximum degradation rates of TiO_2 -coated bamboo timber and the bamboo timber modified by TiO_2 and ODTS were lower than of pure bamboo timber and ODTS-coated bamboo timber. This might be attributed to the TiO_2 coating on the surface of the bamboo timber, which inhibited the transfer of oxygen and heat [14].

The total percentage of weight losses during the whole process was about 57.91% for ODTS-coated bamboo timber, 50.04% for pure bamboo timber, 45.03%

for the TiO_2 -coated bamboo timber, and 44.72% for the bamboo timber modified by TiO_2 and ODTS. These results imply that TiO_2 plays a crucial role in thermal stability improvement.

Mechanical and Chemical Stability

The scratch test was carried out to investigate the surface mechanical stability of bamboo timber modified by TiO_2 and ODTS. This investigation could represent the surface properties of the modified bamboo timber in order to survive in harsh conditions. The result showed that the WCA measurement of the modified bamboo timber before and after the scratch test were the same with WCA of 154° (Fig. 9). This result indicated that the modified bamboo timber had good mechanical resistance.

The chemical resistance test was carried out to analogize the corrosive environment. Fig. 10 exhibits the WCA of the modified bamboo timber towards immersing time. In acidic solution, WCA of the modified bamboo

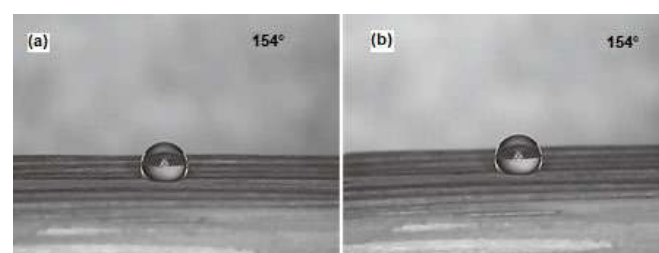


Fig 9. The water contact angle of superhydrophobic bamboo timber (a) before and (b) after the scratch test

timber decreased from 125° to 105° after being immersed for 6 to 24 h. The WCA also decreased from 120° to 95° after the modified bamboo timber was immersed in an alkaline solution for 6 to 24 h. The result shows that the obtained surface of modified bamboo timber was resistant in both acidic and alkaline conditions although the contact angle slightly decreased.

Flammability

In order to explain flammability properties, the pure bamboo timber and bamboo timber modified by TiO₂ and ODTs were burned with an alcohol burner and the time that needed to be burned was counted [14]. Fig. 11 shows digital photos of the pure bamboo timber and the modified bamboo timber when burned with the alcohol burner. The pure bamboo timber was heated with the alcohol burner for 3 sec and became ash in 60 sec (Fig. 11(a-d)). In contrast, modified bamboo timber was not covered with flames at 25 sec and then the flames extinguished itself at 30 sec (Fig. 11(e-h)). These phenomena showed that the modified bamboo timber was more fire resistant than the pure bamboo timber, so it has the potential to be applied as building material.

Based on a reported work, an efficient way to increase

the fire-resistance of synthetic and natural cellulose-based substrates is by modifying the inorganic particles into the structure. In this work, the inorganic material used to improve the flame retardancy properties was TiO₂. It has been verified that the surface of cellulose-based substrates could be modified with TiO₂ as a fire-resistant agent by decreasing the release of total heat, the rate of mass loss, and the effective heat of combustion [14].

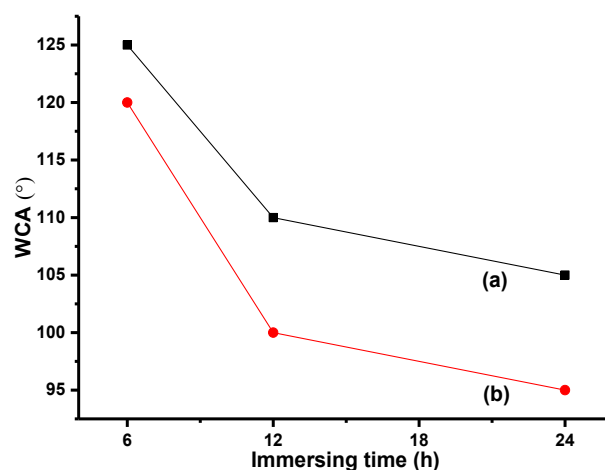


Fig 10. The water contact angle curve of superhydrophobic bamboo timber after immersing in (a) acid and (b) base solution

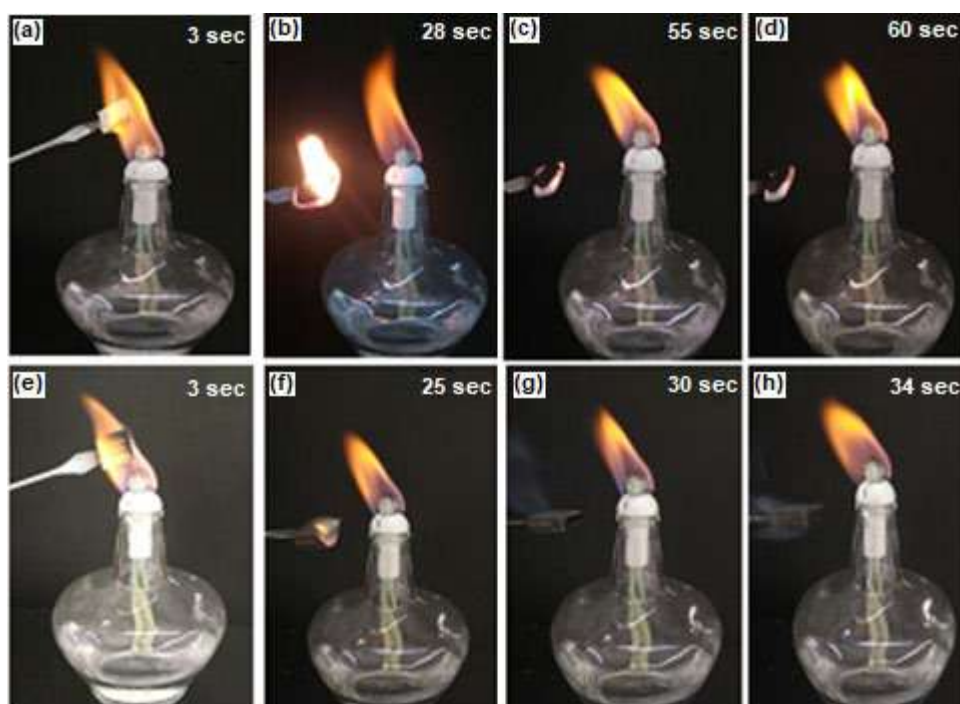


Fig 11. Flammability test of (a-d) pure bamboo timber, and (e-h) superhydrophobic bamboo timber

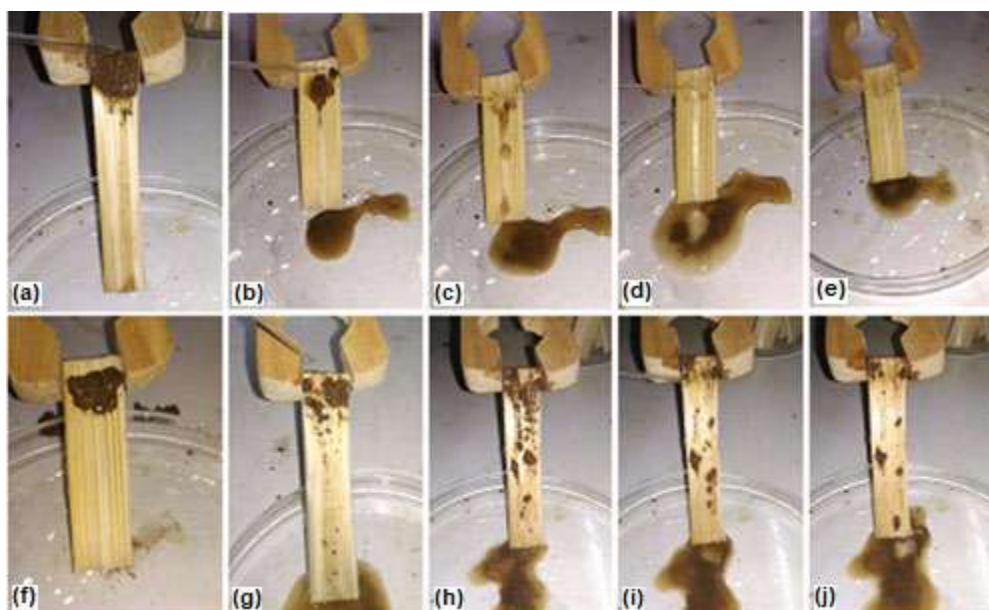


Fig 12. The self-cleaning property test of (a-e) superhydrophobic bamboo timber, and (f-j) pure bamboo timber

Self-Cleaning Property

Fig. 12 shows the process of a self-cleaning system on the pure bamboo timber surface and bamboo timber modified by TiO_2 and ODTs. The procedures of this test were performed by applying the contaminants on the surface of the pure and modified bamboo timber, and then the surface was washed with water. As shown in Fig. 12(a-e), the contaminants were removed easily on the surface of modified bamboo timber by rolling action of a water droplet and then reached a completely clean surface. However, in a similar procedure, the contaminants on the pure bamboo timber surface were not as easily removed as the modified bamboo timber (Fig. 12(f-j)). From the experiments, it can be concluded that the self-cleaning ability of the modified bamboo timber was better than pure bamboo timber. This is because of the nature of the superhydrophobic surface that causes water to be pass easily while carrying the impurities.

CONCLUSION

The superhydrophobic film on the surface of Indonesian bamboo timber with a maximum contact angle of 154° has been successfully fabricated through hydrothermal deposition of TiO_2 combined with octadecyltrichlorosilane (ODTS) modification. This special wettability was contributed by high surface

roughness and low surface energy due to an anatase TiO_2 deposition and a monolayer coating of ODTs, respectively. The treated Indonesian bamboo timber not only exhibited superhydrophobic surface but also mechanical and chemical outstanding stability as well as self-cleaning and flame retardancy properties.

ACKNOWLEDGMENTS

Financial support from the Faculty of Mathematics and Natural Sciences, Universitas Andalas [grant numbers 17/UN.16.03.D/PP/FMIPA/2018] is gratefully acknowledged.

REFERENCES

- [1] Canavan, S., Richardson, D.M., Visser, V., Le Roux, J.J., Vorontsova, M.S., and Wilson, J.R.U., 2016, The global distribution of bamboos: Assessing correlates of introduction and invasion, *AoB Plants*, 9 (1), plw078.
- [2] Yeasmin, L., Ali, M.N., Gantait, S., and Chakraborty, S., 2015, Bamboo: An overview on its genetic diversity and characterization, *3 Biotech*, 5 (1), 1-11.
- [3] Yen, T.M., Ji, Y.J., and Lee, J.S., 2010, Estimating biomass production and carbon storage for a fast-growing makino bamboo (*Phyllostachys makinoi*)

- plant based on the diameter distribution model, *For. Ecol. Manage.*, 260 (3), 339–344.
- [4] He, C., Cui, K., Zhang, J., Duan, A., and Zeng, Y., 2013, Next-generation sequencing-based mRNA and microRNA expression profiling analysis revealed pathways involved in the rapid growth of developing culms in moso bamboo, *BMC Plant Biol.*, 13, 119.
- [5] Sharma, B., Gatóo, A., Bock, M., and Ramage, M., 2015, Engineered bamboo for structural applications, *Constr. Build. Mater.*, 81, 66–73.
- [6] Li, Z., Jiang, Z., Fei, B., Cai, Z., and Pan, X., 2014, Comparison of bamboo green, timber and yellow in sulfite, sulfuric acid and sodium hydroxide pretreatments for enzymatic saccharification, *Bioresour. Technol.*, 151, 91–99.
- [7] Suprapti, S., 2010, Decay resistance of five Indonesian bamboo species against fungi, *J. Trop. For. Sci.*, 22 (3), 287–294.
- [8] Park, S.H., Jang, J.H., Wistara, N.J., Hidayat, W., Lee, M., and Febrianto, F., 2018, Anatomical and physical properties of Indonesian bamboos carbonized at different temperatures, *J. Korean Wood Sci. Technol.*, 46 (6), 656–669.
- [9] Liese, W., and Tang, T.K.H., 2015, “Properties of the bamboo culm” in *Bamboo. Tropical Forestry*, Vol. 10, Eds. Liese, W., and Köhl, M., Springer International Publishing, Cham, Switzerland, 227–256.
- [10] Li, J., Sun, Q., Fan, B., Zheng, H., Yan, C., and Jin, C., 2015, Fabrication of biomimetic superhydrophobic plate-like CaCO_3 coating on the surface of bamboo timber inspired from the biomineralization of nacre in seawater, *Nano Rep.*, 1 (1), 9–14.
- [11] Jin, C., Li, J., Han, S., Wang, J., and Sun, Q., 2014, A durable, superhydrophobic, superoleophobic and corrosion-resistant coating with rose-like ZnO nanoflowers on a bamboo surface, *Appl. Surf. Sci.*, 320, 322–327.
- [12] Li, J., Lu, Y., Wu, Z., Bao, Y., Xiao, R., Yu, H., and Chen, Y., 2016, Durable, self-cleaning and superhydrophobic bamboo timber surfaces based on TiO_2 films combined with fluoroalkylsilane, *Ceram. Int.*, 42 (8), 9621–9629.
- [13] Wellia, D.V., Mustaqimah, A., Wulandari, W., Zulhadjri, Z., Syukri, S., and Pratiwi, N., 2018, Fabrication of hydrophobic Indonesia bamboo modified by octa fluoro 1-pentanol (OFP) based on TiO_2 thin film for self-cleaning application, *J. Pure Appl. Chem. Res.*, 7 (2), 149–159.
- [14] Li, J., Zheng, H., Sun, Q., Han, S., Fan, B., Yao, Q., Yan, C., and Jin, C., 2015, Fabrication of superhydrophobic bamboo timber based on an anatase TiO_2 film for acid rain protection and flame retardancy, *RSC Adv.*, 5 (76), 62265–62272.
- [15] Parkin, I.P., and Palgrave, R.G., 2005, Self-cleaning coatings, *J. Mater. Chem.*, 15 (17), 1689–1695.
- [16] Li, J., Sun, Q., Yao, Q., Wang, J., Han, S., and Jin, C., 2015, Fabrication of robust superhydrophobic bamboo based on ZnO nanosheet networks with improved water-, UV-, and fire-resistant properties, *J. Nanomater.*, 2015, 431426.
- [17] Wang, F., Li, S., and Wang, L., 2017, Fabrication of artificial super-hydrophobic lotus-leaf-like bamboo surfaces through soft lithography, *Colloids Surf., A*, 513, 389–395.
- [18] Li, X., Sun, C., Zhou, B., and He, Y., 2015, Determination of hemicellulose, cellulose and lignin in moso bamboo by near infrared spectroscopy, *Sci. Rep.*, 5, 17210.
- [19] Bao, W., Liang, D., Zhang, M., Jiao, Y., Wang, L., Cai, L., and Li, J., 2017, Durable, high conductivity, superhydrophobicity bamboo timber surface for nanoimprint stamps, *Prog. Nat. Sci. Mater. Int.*, 27 (6), 669–673.
- [20] Chibac, A.L., Buruiana, T., Melinte, V., and Buruiana, E.C., 2017, Photocatalysis applications of some hybrid polymeric composites incorporating TiO_2 nanoparticles and their combinations with $\text{SiO}_2/\text{Fe}_2\text{O}_3$, *Beilstein J. Nanotechnol.*, 8, 272–286.
- [21] Li, J., Sun, Q., Jin, C., and Li, J., 2015, Comprehensive studies of the hydrothermal growth of ZnO nanocrystals on the surface of bamboo, *Ceram. Int.*, 41 (1, Part B), 921–929.

Assessment of Free and Total Cyanide Levels in the Water Environment of Shatt Al-Arab

Zuhair Ali Abdulnabi

Department of Marine Chemistry, Marine Science Center, University of Basrah, Basra, Iraq

* **Corresponding author:**

tel: +96440-7703112882

email: zuhir38@yahoo.com

Received: July 6, 2019

Accepted: September 23, 2019

DOI: 10.22146/ijc.47369

Abstract: The concentration of free and total cyanide in waters was measured by using the colorimetric method through complex formation with pyridine-barbituric acid at the wavelength of 578 nm. Ten stations were selected from water surfaces in the south of Iraq. The samples were distributed among two stations, one was on Euphrates River and the other was on Tigris River (before their confluence and formatting of Shatt Al-Arab) and selected seven stations along Shatt Al-Arab River. All the samples were collected from surface water at depth of 10–15 cm and their pH was adjusted to 12 by using sodium hydroxide. The results showed the highest concentration of free cyanide (0.254 mg/L) in station W₇ and the lowest concentration in stations W₂, W₉ and W₁₀, while the highest and lowest concentration of total cyanide (9.962, 0.207 mg/L) were recorded in station W₇ and W₁ respectively. The standard deviation of all sites (n = 3) of free and total cyanide was calculated and showed 0.007–0.048 and 0.001–0.042 ranges respectively. Furthermore, some of the physico-chemical properties of water were recorded in these stations.

Keywords: colorimetric method; free cyanide; total cyanide; conductometric titration

■ INTRODUCTION

Cyanide has a single negative charge. It consists of carbon and nitrogen atoms with triple covalent bonds $-(C\equiv N)^-$. It refers to the CN groups in cyanide compounds that can be determined as the cyanide ion. Cyanide is a highly reactive compound which readily forms metal cyanide complexes and organic compounds in water. The chemical composition of cyanide in environment samples is affected by factors such as pH, temperature, trace metal content, and the presence of sulfur or sulfur compounds [1-3]. Many cyanide species can exist in aquatic systems such as free cyanide (CN^- , HCN), simple cyanide compounds that can exist in soluble form (NaCN, KCN) and relatively insoluble ($Zn(CN)_2$, $Cu(CN)_2$), weak metal cyanide ($(Zn(CN)_4)^{2-}$, $(Cd(CN)_4)^{2-}$), moderately strong metal-cyanide complexes ($(Cu(CN)_2)^-$, $(Cu(CN)_3)^{2-}$ and $(Ni(CN)_4)^{2-}$) and strong metal cyanide complexes ($(Fe(CN)_6)^{4-}$, $(Co(CN)_6)^{4-}$) [1,4-5]. Moreover, all cyanide compounds have toxic properties especially the free cyanide species [6-7] and their increase causes a lot of risks on the aquatic

system and thus affects human and animal health because they rapidly transfer to all organs and tissues and accumulate via blood. The cyanide concentration is higher in red blood cells than in plasma by a factor of two or three, reflecting cyanide's tendency to bind with methaemoglobin. Cyanide may also accumulate in body cells by binding with metalloproteins or enzymes such as catalyses or cytochrome c oxidase [8-10]. The most important sources of cyanide pollution in the surface water is through mining operations and industrial and agricultural activities [5,10-11]. Thus this study focuses on the evaluation of free and total cyanide levels and their concentrations and distribution in water in order to know the sources of contaminants in the aquatic system.

■ EXPERIMENTAL SECTION

Description of the Study Area

Ten stations were chosen from water surfaces of different regions along the Basra governorate as shown in Fig. 1. The samples were collected from one station on

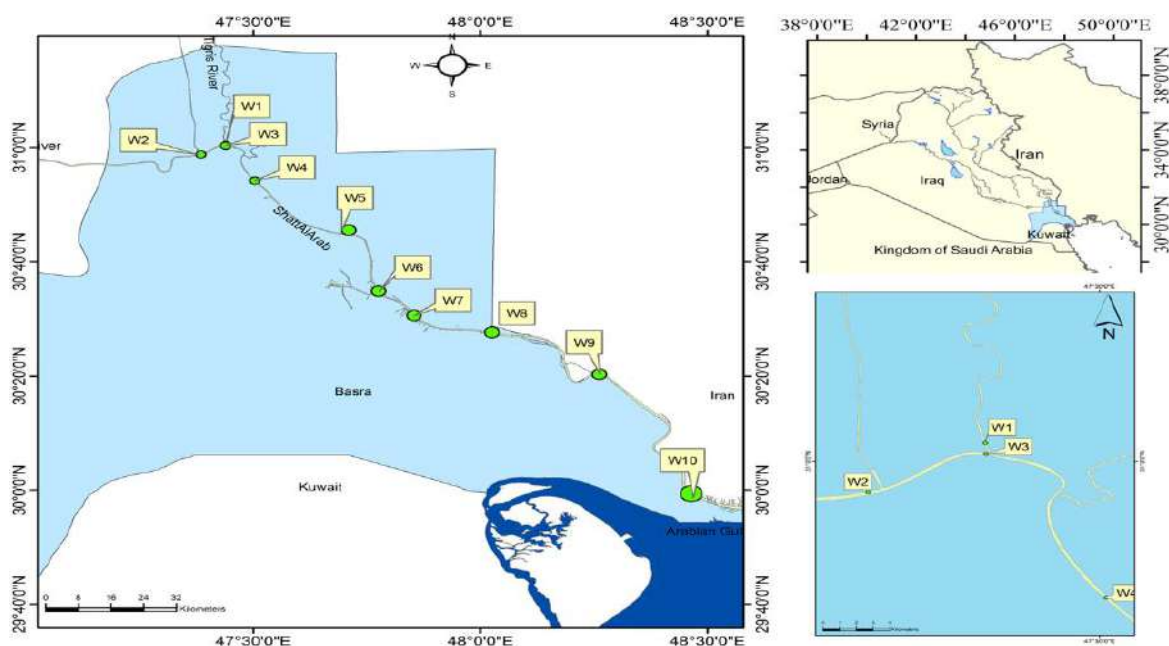


Fig 1. Locations of the samples selected in southern of Iraq

Tigris River (W_1) and two stations on Euphrates river (W_2 , W_3), before the two rivers' confluence and form the Shatt Al-Arab River and another seven selected stations along Shatt Al-Arab River (W_4 - W_{10}). The importance of these regions lies in the various industrial and agricultural activities located along Shatt Al-Arab River as well as some activities like fishing by using toxic materials, navigation in the river and release of urban untreated effluents into the river [1,6]. All samples were collected by water sampler instrument at depth of 10–15 cm in the winter season, February of 2016, in various areas from surface water in low tide time and kept in dark glass bottles. These samples were preserved at pH = 12 by using sodium hydroxide and afterwards all samples were kept under cooling at 6 °C [12] and later transferred to the laboratory for carrying out different operations such as removal of different interferences that affect the accuracy of measurements of cyanide and digestion operations.

Materials

The list of chemical materials used in the procedure such as sodium acetate trihydrate $\text{CH}_3\text{COONa}\cdot 3\text{H}_2\text{O}$ (99%), pyridine $\text{C}_5\text{H}_5\text{N}$ (99%) and sulfuric acid H_2SO_4 (97%) was obtained from J.T. Baker. Glacial acetic acid CH_3COOH (99.8%) and hydrochloric acid HCl (37%) were

supplied by Scharlau. Chloroamine-T $\text{C}_7\text{H}_7\text{ClNNaO}_2\text{S}$ and potassium cyanide KCN were obtained from PubChem. Barbituric acid $\text{C}_4\text{H}_4\text{N}_2\text{O}_3$ and sodium hydroxide NaOH were obtained from Himedia. Sphamic acid $\text{H}_3\text{NO}_3\text{S}$, lead carbonate PbCO_3 and sodium thiosulfate $\text{Na}_2\text{S}_2\text{O}_3$ were supplied by B.D.H. Silver nitrate AgNO_3 , magnesium chloride hexahydrate $\text{MgCl}_2\cdot 6\text{H}_2\text{O}$ (99%), potassium chloride KCl (99.5%) and potassium dichromate $\text{K}_2\text{Cr}_2\text{O}_7$ (99.9%) were supplied by Merck.

Instrumentation

All samples were collected by using a water sampler instrument from the surface water at depth of 10–15 cm in low tide and some physicochemical properties such as pH, conductance, salinity, temperature of water, total dissolved solid TDS were measured directly in the field by multimeter type: WTW (Multi 3410 Set C, Germany). The concentration of free cyanide and total cyanide was measured by UV-Vis instrument type: Shimadzu double-beam UV-Vis spectrophotometer (model 1800 PC, Japan) with 1.0-cm quartz cell.

Procedure

After being collected, the samples were preserved at pH = 12 by using 1.0 M of sodium hydroxide. pH was

adjusted to 12 in order to prevent any interaction between sulfate and cyanide ions that occurs under pH 12 that may later lead to the formation of thiocyanate ions. All samples were kept under cooling at 6 °C in dark glass bottles and then transferred to the laboratory in order to remove the oxidizing agents such as chlorine from the samples by using 0.1 g sodium thiosulfate [2,12].

To determine the free cyanide concentration in all the samples, 40 mL of the alkaline sample was put in a 50 mL volumetric flask (air-tight) and 1 mL of buffer solution was added to it. The buffer solution was prepared from $\text{CH}_3\text{COONa}\cdot 3\text{H}_2\text{O}$ and dissolved in glacial acetic acid. After that, 2 mL of chloroamine-T solution was added to the mixture and was left for 2 min. Then, 5 mL from the mixture of pyridine-barbituric acid (this mixture was prepared by dissolving 15 g barbituric acid in 75 mL pyridine, and adding 15 mL of concentrated HCl and then complementing it to 250 mL with deionized water) were added to the solution and complemented to 50 mL with deionized water and left for 8 min [2,13]. Finishing these steps, the sample was ready for analysis at 578 nm by using the UV-Vis spectrophotometer.

To determine the total cyanide concentration, a digestion operation had to be executed using a distillation method as the one described in the standard method [2]. Several materials such as sulfuric acid, sulphamic acid, lead carbonate and $\text{MgCl}_2\cdot 6\text{H}_2\text{O}$ were used in this method. After completing the digestion of the samples, the described method above was repeated.

In order to determine the concentration of free and total cyanide, the stock solution (1000 mg/L) must be prepared by using KCN and to obtain more accurate results a calibration of KCN standard material should be carried out. In this study the conductometric titration method was used by using silver nitrate, the silver nitrate was calibrated with potassium chloride and the potassium dichromate was used as an indicator. The concentration of AgNO_3 was 880 mg/L after executing the calibration operation with potassium chloride. The calibration curve was obtained through the preparation of a series of 50 mL dilute solutions containing 0, 0.02, 0.1, 0.25, 0.5 mg/L of cyanide concentration and the same procedure was

applied as described before for all the other samples. The result of the standard curve is shown in Fig. 2.

RESULTS AND DISCUSSION

In order to obtain precise results, the conductometric titration method was used through the titration process between silver nitrate and 30 mL of potassium cyanide and measuring their conductivity after each addition of silver nitrate. The results of the conductometric titration method are shown in Fig. 3. This method is important for the calibration operation of the cyanide solution for it enables completing the calibration without using any indicator [14]. The results show that the concentration of the cyanide ion stock solution after carrying out the calibration operation was 997.33 mg/L.

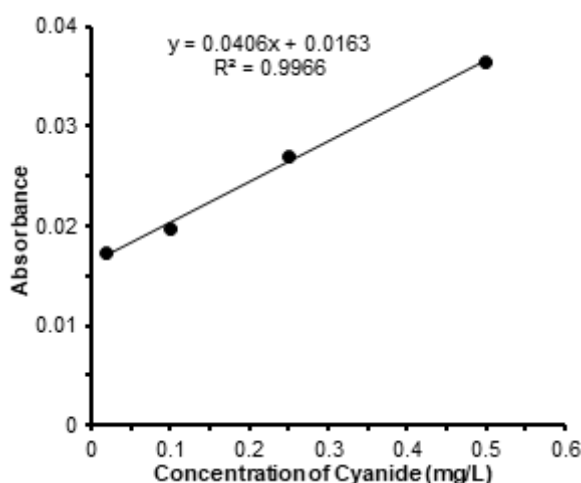


Fig 2. Standard curve of Cyanide solution

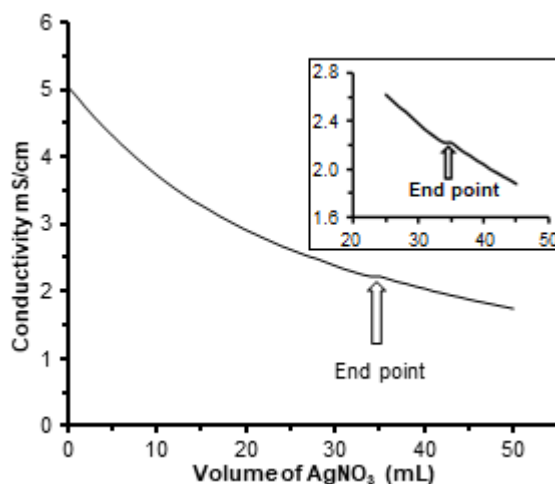


Fig 3. Calibration curve of Cyanide solution

Some physicochemical properties were measured immediately in the field. These parameters are important for determining the quality of water and its effects on the aquatic system. All of the results of the physico-chemical properties measurements are shown in Table 1.

The pH of the water samples from various regions was recorded at 8.096–8.512 range. This refers to the behavior of alkali water due to the existence of different carbon compounds in waters such as carbon dioxide, carbonic acid, bicarbonate ions, and carbonate ions. These parameters are responsible for changing the pH value in aquatic systems. pH results of all the stations along Shatt Al-Arab River were compared between upstream and downstream. The highest pH value was recorded downstream in station W₁₀. This may be due to the increase of concentrations from bicarbonate and carbonate salts in sea waters resulting from tides [2,15], on the other hand, the lowest pH value was recorded upstream in station W₁ because this station has not undergone any anthropogenic activities. Moreover, the pH value was increased from stations W₁ towards W₄ upstream region. This might be attributed to the effect of low and high tide. At the same time, the decreased value of pH was noted in stations W₄ to W₇ due to the increase of the released untreated wastewater into the River [16]. pH results were compared with world regulations and were found to be

within the acceptable limits of WHO 2011, EC 1998, CGL 2014 and the Iraqi standard 2001 for drinking waters [17-20]. The pH results are shown in Table 1.

The electrical conductivity, salinity and total dissolved solid are important for knowing the quality of water and its uses [16]. The measurements results of these parameters are shown in Table 1. The data obtained were in the ranges of 3010–6840 $\mu\text{mhos cm}^{-1}$, 1926.4–4377.6 mg/L and 1.5–3.7 ppt for electrical conductivity, total dissolved solid and salinity, respectively. The results were compared between the upstream and the downstream samples. The downstream samples showed high values, especially in station W₁₀ because these regions are affected by different concentrations of salts from marine water through tide, whereas the upstream samples showed low values, especially in station W₁ because there are no industrial or agricultural activities in this area.

The increase of salts concentration was noted from station W₁ towards W₅, with W₅ having the highest concentration because in this region there are various industrial, agricultural and population activities. Moreover, the increase in salts concentration was also noted from station W₅ towards station W₇ because of the increase in population, industrial and agricultural activities. Additionally, the river navigation was high in

Table 1. Physico-chemical properties of selected water samples

Sampling locations	pH in field	Temperature of water °C in field	Salinity ppt in field	TDS mg/L in field	EC $\mu\text{mhos cm}^{-1}$ in field	EC $\mu\text{mhos cm}^{-1}$ at 25 °C	
Upstream	W ₁	8.096	13.7	1.5	1926.4	3010	3838.5
	W ₂	8.126	13.9	1.6	1971.2	3080	3908.7
	W ₃	8.135	13.8	1.6	1945.6	3040	3867.3
	W ₄	8.369	13.8	1.5	1939.2	3030	3854.6
	W ₅	8.325	14.1	1.8	2214.4	3460	4369.7
Downstream	W ₆	8.267	15.7	3.2	3814.4	5960	7247.3
	W ₇	8.158	15.1	3.6	4288.0	6700	8262.3
	W ₈	8.201	13.7	3.5	4140.8	6470	8250.8
	W ₉	8.280	21.2	1.9	2297.6	3590	3870.9
	W ₁₀	8.512	14.9	3.7	4377.6	6840	8474.9
WHO 2011	6.5-8.5	-	-	1000	-	-	
CGL 2014	6.5-8.5	-	-	500	-	-	
EC 1998	6.5-9.5	20	-	1500	2500	2763.958	
IQS 2001	6.5-8.5	-	-	1000	-	-	

this area because of the commercial port located nearby. Meanwhile, low salts concentration was noted from station W₇ towards W₉ because this region is affected by the flowrate of Karun River towards Shatt Al-Arab [16] in the nearby zone from station W₉. The most important sources of salts concentration in aquatic systems are weathering of rocks, combustion of coal and oil, movement of wind, irrigation and drainage operations, rain water, domestic effluents and industrial waste [15-16].

The free cyanide of all the stations was measured using Uv-Vis spectrophotometer at wavelength 578 nm through complex formation with pyridine-barbituric acid after the chlorination operation was executed by adding chloramine-T and a reddish color solution was formed. Free cyanide is a highly toxic species that can exist in the form CN⁻ or HCN. Moreover, released hydrocyanic acid increases in the aquatic system when the pH value is decreased to a value of about 5–6.5 [4,21]. The increase of cyanide concentration level in the water environment has many risks towards the quality of the aquatic system and thus it will negatively affect the human and animal health, especially in fish because it is able to accumulate in their organs [1,22]. The results of all the cyanide concentration measurements of the samples are shown in Table 2.

The highest value of free cyanide concentration in all the stations was recorded in the downstream regions, especially in station W₇. This might be due to the increase in population, industrial and agricultural activities [6,11]. Furthermore, this particular place is an important region for river navigation because of the commercial port located nearby. Meanwhile, stations W₉ and W₁₀ in the downstream regions and station W₂ from the upstream region had not recorded any value of free cyanide concentration. This might be attributed to the decrease of the population activity in these regions. The concentration of free cyanide was also increased from station W₁ towards W₃ because these stations have undergone an increase of human activities, especially in station W₃, whereas station W₂ did not record any value of free cyanide that might be attributed to the decrease in human activities and increase of agricultural activities. In addition to that, the concentration value of free cyanide decreased in station W₄ when compared with station W₃ and once again the increase of free cyanide concentration was noted in station W₅ because of the high population, industrial and agriculture activities. Likewise, the concentration of free cyanide was compared for all the measurements in the downstream

Table 2. Free and total cyanide concentration of all stations selected from surface water

Sampling locations		Mean (n = 3) of Free cyanide concentration mg/L	Standard Deviation (SD)	Mean (n = 3) of Total cyanide concentration mg/L	Standard Deviation (SD)
Upstream	W ₁	0.036	0.007	0.207	0.010
	W ₂	N.D	-	4.253	0.042
	W ₃	0.222	0.048	0.357	0.031
	W ₄	0.019	0.007	9.022	0.003
	W ₅	0.160	0.031	4.631	0.032
	Average	0.087	0.019	3.694	0.023
Downstream	W ₆	0.013	-	4.234	0.020
	W ₇	0.254	0.027	9.962	0.001
	W ₈	0.109	0.007	6.271	-
	W ₉	N.D	-	3.944	0.004
	W ₁₀	N.D	-	4.758	0.013
	Average	0.075	0.007	5.834	0.007
WHO 2011		0.17	-	-	-
CGL 2014		0.2	-	-	-
EPA 2009		0.2	-	-	-
IQS 2001		0.02	-	-	-

N.D: Not Detected

regions and it was noted that the concentration of free cyanide increased from station W_6 towards W_7 . This might be due to population increase and the increase in industrial and agricultural activities. Additionally, the river navigation also increased in this area. Meanwhile, the concentration of free cyanide decreased from station W_7 towards W_{10} . When compared with other studies carried out in the Shatt Al-Arab environment, the data of this study were found to be consistent [23]. The results of the free cyanide concentration of all the stations were compared with several international regulation regarding permissible cyanide concentrations, namely WHO 2011, CGL 2014, IQS 2001 and EPA 2009 and the results of the current study have shown to be within the acceptable limits of EPA 2009 and CGL 2014. Meanwhile five stations have shown to be within the acceptable limits for IQS 2001. Additionally, two stations, W_3 and W_7 have recorded values that exceed the WHO 2011 allowed limits. The data for all the free cyanide measurements of the selected stations are shown in Table 2.

Total cyanide concentration refers to the sum for all the cyanide ions that are involved in the structure of different compounds such as simple and complex compounds and also organic and inorganic compounds [1,8]. Total cyanide concentration of the selected samples for all the stations were measured through a digestion operation using the distillation method in acidic medium and by gas liberation of hydrocyanic acid. The gas was allocated later in alkaline solution and measured in UV-Vis spectrophotometer [2,12]. The results of all the measurements of the upstream region were in the range of 0.207–9.022 mg/L and the average of the concentrations for this region was 3.694 mg/L. Meanwhile, the stations of the downstream region recorded higher concentrations of the total cyanide when compared with the upstream stations, in the range of 3.944–9.962 mg/L and an average of 5.834 mg/L. This might be attributed to the increase of industrial and population activities and also river navigation in these regions as well as the industrial waste and domestic untreated waste released into the river. The results of the total cyanide concentration are shown in Table 2. Generally, the most important sources that lead to the increase of the cyanide concentrations in water environment are the electroplating industry, gas extraction

stations, combustion of coal and oil, movement of wind, irrigation and drainage operations, wastewater, industrial waste, metal processing, photographic processes, production of synthetic rubber, chemical synthesis, manufacture of plastics, pesticide/rodenticide control, laboratory processes and the manufacture of dyes and pigments [6-8,10,24].

■ CONCLUSION

The current study has shown that cyanide concentration is present in the Shatt Al-Arab River environment that lead to many risks on human and animal's health. The results of the free cyanide concentrations were compared with several international regulations such as WHO 2011, CGL 2014, IQS 2001 and EPA 2009, where it showed values that exceed the permissible values in five stations when compared with IQS 2001 and thus lead to the increase of toxic properties in the aquatic system that can have a negative effect on human and animal's health. The results are consistent with Rasheed and Al-Imara study carried out in the Shatt Al-Arab environment that used cyanide selective electrode method for measurement. Meanwhile the total cyanide concentration has shown the highest values in all stations when compared with all the allowed limits globally.

■ REFERENCES

- [1] Zheng, A., Dzombak, D.A., Luthy, R.G., Sawyer, B., Lazouskas, W., Tata, P., Delaney, M.F., Zilitinkevitch, L., Sebroski, J.R., Swartling, R.S., Drop, S.M., and Flaherty, J.M., 2003, Evaluation and testing of analytical methods for cyanide species in municipal and industrial contaminated waters, *Environ. Sci. Technol.*, 37 (1), 107–115.
- [2] American Public Health Association, American Water Works Association, Water Environment Federation, 1999, *Standard Methods for the examination of water and wastewater*, 20th Ed., APHA, AWWA, WEF, Washington DC.
- [3] Owuamanam, C.I., Iwouno, J.O., Ihediohanma, N.C., and Barber, L.I., 2010, Cyanide reduction, functional and sensory quality of gari as affected by

- pH, temperature and fermentation time, *Pak. J. Nutr.*, 9 (10), 980–986.
- [4] Razanamahandry, L.C., Karoui, H., Andrianisa, H.A., and Yacouba, H., 2017, Bioremediation of soil and water polluted by cyanide: A review, *Afr. J. Environ. Sci. Technol.*, 11 (6), 272–291.
- [5] Chueachot, R., and Chanthai, S., 2014, Spectrophotometric determination of trace cyanide in fruit wines by the catalytic reaction of ninhydrin following micro-distillation, *Orient. J. Chem.*, 30 (1), 119–131.
- [6] Gijzen, H.J., Bernal, E., and Ferrer, H., 2000, Cyanide toxicity and cyanide degradation in anaerobic wastewater treatment, *Water Res.*, 34 (9), 2447–2454.
- [7] Mansfeldt, T., and Biernath, H., 2000, Determination of total cyanide in soils by micro-distillation, *Anal. Chim. Acta*, 406 (2), 283–288.
- [8] Osobamiro, M.T., 2012, Determination of the concentration of total cyanide in waste water of a tobacco company in Southwestern Nigeria, *J. Appl. Sci. Env. Manage.*, 16 (1), 61–63.
- [9] Gensemer, R.W., Deforest, D.K. Cardwell, R.D., Dzombak, D., Santore, R., and Stewart, M., 2006, *Reassessment of cyanide ambient water quality criteria: An integrated approach to the protection of the aquatic environment*, Presentation at the SETAC North America 27th Annual Meeting, Montreal, Canada.
- [10] Obiri, S., Dodoo, D.K., Okai-Sam, F., and Essumang, D.K., 2007, Determination of free cyanide and total cyanide concentrations in surface and underground waters in Bogoso and its surrounding areas in Ghana, *Bull. Chem. Soc. Ethiop.*, 21 (2), 213–220.
- [11] Delaney, M.F., and Blodget, C., 2015, Total cyanide field spikes for industrial wastewater samples verify successful sample integrity, preservation, pre-treatment and testing, *Water Environ. Res.*, 87 (6), 559–566.
- [12] Gautam, S.P., 2011, *Guide manual: Water and wastewater analysis*, Central Pollution Control Board, Ministry of Environment and forests, India.
- [13] United States Environmental Protection Agency (EPA), 1996, *Titrimetric and manual spectrophotometric determinative methods for cyanide*, Method 9014.
- [14] Raj, G., 2008, *Advanced Practical Inorganic Chemistry*, 20th Ed., Krishna Prakashan Media, India.
- [15] Abdalnabi, Z.A., 2016, Assessment of some toxic elements levels in Iraqi marine water, *Mesopot. J. Mar. Sci.*, 31 (1), 85–94.
- [16] Abdalnabi, Z.A., Hassan, W.F., Al-Khuzaie, D.K.K., Saleh, S.M., and Hashim, M.G., 2015, Evaluation of selenium levels for the water surfaces in southern Iraq, *J. Chem. Pharm. Res.*, 7 (10), 495–501.
- [17] WHO, 2011, *Guidelines for drinking water quality*, 4th Ed., Switzerland.
- [18] Directive 98/83/EC, 1998, Council Directive 98/83/EC of 3 November 1998 on the quality of water intended for human consumption, *Official Journal of the European Communities*, L330, 32–54.
- [19] Health Canada, 2014, *Guidelines for Canadian drinking water quality—Summary table*, Water and Air Quality Bureau, Healthy Environments and Consumer Safety Branch, Health Canada, Ottawa, Ontario.
- [20] IQS, 2001, *Standard no. 417 on drinking water and analysis-Standard specification for drinking water*, Central Organization for Quality Control and Standardization, Council of Ministers, Republic of Iraq.
- [21] United States Environmental Protection Agency (EPA), 1980, *Cyanide, total (titrimetric, spectrophotometric)*, Technical Revision, NERL Method 335.2.
- [22] Hassan, D.M.A., and Farghali, M.R.F., 2018, Cyanide pollution in different water sources in Assiut, Egypt: Levels, distributions, and health risk assessment, *Res. J. Environ. Sci.*, 12 (5), 213–219.
- [23] Rasheed, B.A., and Al-Imarah, F.J.M., 2014, Temporal and spatial distribution of cyanide ion in Southern Iraqi waterways, *Int. J. Environ. Water*, 3 (5), 207–212.
- [24] Environment and Climate Change Canada, Health Canada, 2018, *Risk management scope for cyanides*, Government of Canada.

High Oleic Pentaerythritol Tetraester Formation via Transesterification: Effect of Reaction Conditions

Nor Faeqah Idrus^{1,2}, Robiah Yunus^{1,3,*}, Zurina Zainal Abidin¹,
Umer Rashid³, and Norazah Abdul Rahman²

¹Department of Chemical and Environmental Engineering, Engineering Faculty, Universiti Putra Malaysia, 43400 UPM Serdang, Selangor, Malaysia

²Faculty of Chemical Engineering, Universiti Teknologi MARA (UiTM), 40450 Shah Alam, Selangor, Malaysia

³Institute of Advanced Technology, Universiti Putra Malaysia, 43400 UPM Serdang, Selangor, Malaysia

* **Corresponding author:**

tel: +603-89466291

email: robiah@upm.edu.my

Received: July 19, 2019

Accepted: October 17, 2019

DOI: 10.22146/ijc.47891

Abstract: Pentaerythritol tetraoleate esters synthesized from high oleic palm oil methyl ester (POME) have potential as biolubricant base stock. In the present study, the chemical transesterification of POME and pentaerythritol (PE) using sodium methoxide as a catalyst was conducted under vacuum. The effect of operating variables such as reaction temperature, catalyst concentration, the molar ratio of POME to PE, vacuum pressure, and stirring rate on the yield of PE tetraoleate was examined. The ideal conditions for the reaction were at a temperature of 160 °C, 1.25% (w/w) catalyst concentration, the molar ratio of POME to PE at 4.5:1, vacuum pressure at 10 mbar, and stirring speed at 900 rpm. PE tetraoleate with a yield of 36% (w/w), was successfully synthesized under this condition within 2 h of reaction time.

Keywords: transesterification; pentaerythritol tetraester; optimization; biolubricant

■ INTRODUCTION

Pentaerythritol (PE) tetraester can be synthesized from various vegetable oils and fatty acid esters. The synthesis of polyol esters can be carried out via chemical synthesis or enzymatic synthesis. However, enzymatic synthesis is inappropriate for high temperature reaction. Besides, chemical synthesis is a more economical process as the catalyst cost, and catalyst consumption will be much lower, compared to enzymatic synthesis [1]. The chemical synthesis method can be conducted via transesterification and esterification methods. Most of vegetable oil-based lubricants are synthesized via transesterification because of its lower cost and higher conversion at milder operating conditions. High oleic vegetable oils are potential candidates for mineral oil replacement as a base oil for lubricants and synthetic ester due to its excellent oxidative stability. A higher oleic content with relatively low trans and saturated fatty acid contents requires less additional processing steps to improve its oxidative stability. Furthermore, vegetable

oil-based polyol ester lubricants have excellent thermal stability, high viscosity, and biodegradable [2-4].

Previous research by Aziz et al. [5] reported that the highest yield of PE tetraoleate ester obtained via transesterification of palm oil methyl ester (POME) with PE was 37.56%. The reaction was conducted under vacuum to remove the methanol byproduct; thus, minimize the reverse reaction and move the reaction forward. The study also reported the performance parameters for the transesterification to achieve high PE ester conversion. These parameters include reaction temperature, reaction time, catalyst concentration, and the molar ratio of POME to PE. The performance parameter has been optimized with the catalyst concentration, and the molar ratio of POME to PE was found to be the most significant parameter to achieve a high yield of PE tetraoleate ester. Nonetheless, the yield of tetraester is still too low, thus require further studies to deliberate further on how to increase the conversion to tetraester, and thus improve its yield.

Even though the effect of the mixing rate and vacuum pressure plays an important role in increasing the rate of reaction, both parameters have not been investigated. In this reaction, mixing is important to ensure PE is soluble and form a homogeneous mixture with POME. Mixing increases the reaction area between the reactants and not only occurs at the interface; hence, it increases the rate reaction to form a product with the presence of catalyst [6]. Furthermore, the effect of vacuum pressure in transesterification reaction is important for the removal of methanol and to promote the forward reaction [7]. Effective methanol removal may lead to the high formation of the desired yield, which is PE tetraester. Therefore, in this study, the effect of vacuum pressure and mixing rate on the transesterification process of POME and PE via transesterification in batch scale reactions were carried out.

The lubricating properties of the polyol ester depend on the structures of these esters. Thus, it is important to achieve high reaction conversion to obtain high tetraester using the feasible method. The method must be able to produce high conversion to tetraester, simple and economical. Aziz et al. [5] studied the transesterification reaction of PE with palm oil methyl ester (POME) in a batch reactor. The method used sodium methoxide as a catalyst is found to be more feasible, and the reaction time is shorter than the method using an acid catalyst. In this study, the interaction parameters for the transesterification of POME and PE to produce tetraester are elucidated. The effects of reaction parameters such as reaction temperature, catalyst concentration, the molar ratio of POME to PE, vacuum pressure and stirring rate to the formation of products, i.e., PE monooleate (monoester), PE dioleate (diester), PE trioleate (triester) and PE tetraoleate (tetraester) were observed.

■ EXPERIMENTAL SECTION

Materials

Palm oil methyl ester (POME) and pentaerythritol (PE) alcohol were obtained from Solution Engineering (M) Sdn Bhd and Fischer Scientific, respectively. The analytical grade sodium methoxide was used as a catalyst. Transesterification reaction of POME and PE was carried out in the batch reactor.

Reactor Setup

The reactor setup includes 500 mL of the flat bottom three-necked flask as a batch reactor, a reflux condenser, thermometer, a hot plate, and a magnetic stirrer bar. A reactor equipped with a thermometer, a sampling port, and a condenser was immersed in a silicon oil bath and connected to a vacuum pump. A hot plate stirrer was used to provide heat as well as to control the stirring speed of reaction mixture in the reactor. A magnetic bar was used to ensure uniform mixing of the reaction mixture. A thermometer was used to measure the temperature of the reaction, and the reflux condenser was used to condense and return the palm oil methyl ester to the reactor due to its low boiling point. A vacuum pump equipped with a pressure transmitter was connected to the reflux condense to allow for the reaction to take place under various vacuum conditions. An air relief valve was placed in between the reflux condenser and vacuum pump to adjust the vacuum level. The reactor was immersed in a silicon oil bath to ensure uniform temperature reaction throughout the reaction and prevent heat loss.

Procedure

Synthesis of PE esters via transesterification

The reaction conditions were varied based on parameters to be studied, i.e., reaction temperature, catalyst concentration, vacuum pressures, the ratio of POME to PE, and stirring rate. By adapting the optimum reaction conditions obtained by Aziz et al. [5], the effects of reaction parameters on the formation of PE tetraester were examined. The reaction was conducted at temperature of 140 to 170 °C, molar ratio of POME to PE of 4.00:1 to 5.00:1, catalyst concentration of 0.5% (w/w) to 1.5% (w/w) and vacuum pressure ranged from 5 mbar to 50 mbar were employed while stirring rate fixed at 600 rpm and 1.2% catalyst w/w at 600 rpm. For the effect of stirring rate, the experiments were conducted at 300, 600, and 900 rpm, while the other parameters were kept constant at a temperature of 160 °C, the molar ratio of reactant 4.50:1, catalyst concentration 1.25% (w/w) and vacuum pressure of 10 mbar. Product samples were collected at certain time intervals to monitor the ester content. All PE disappeared in 1 h of reaction. However,

the synthesis was prolonged for up to 2 h to ensure complete conversion of PE.

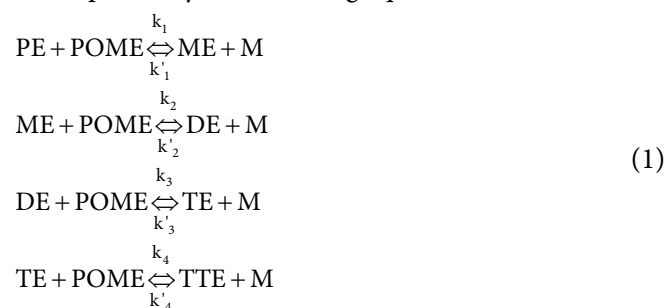
Analysis of the sample

The sampling procedure must be carried out within the possible shortest time to minimize the changes in the reaction system. The product sample was taken from the flask reactor and kept in the vial. The reaction sample was immediately diluted with ethyl acetate and BSTFA and swirled to prevent sample degradation and reverse reactions. The composition of product samples was analyzed using GC analysis method developed by Yunus et al. [8]. DB-HT5 capillary column with $15\text{ m} \times 0.32\text{ mm} \times 0.1\text{ }\mu\text{m}$ i.d., was used to perform the separation in the gas chromatography system. The reaction sample was diluted with 1 mL ethyl acetate and then swirled. Afterward, 0.5 mL of BSTFA was added into the mixture and swirled again. Before being injected into the GC, the prepared samples were heated for 10 min at $50\text{ }^\circ\text{C}$. The oven temperature was set at $80\text{ }^\circ\text{C}$ initially and held for 3 min. Then, it was ramped to $380\text{ }^\circ\text{C}$ at $6\text{ }^\circ\text{C}/\text{min}$ and held for another 6 min. The temperature of the detector and injector was set at 360 and $300\text{ }^\circ\text{C}$, respectively. The carrier gas used was hydrogen with a flow rate of $26.7\text{ mL}/\text{min}$, and the split ratio was done at 1:1.

RESULTS AND DISCUSSION

Transesterification Mechanism of PE Esters

The mechanism of the reaction is proposed to occur via four stepwise series reactions with the formation of intermediates. The reaction began with the formation of intermediate PE monoester, followed by PE diester, then the formation of PE triester, and finally, the product PE tetraester. Fig. 1 shows the overall step of transesterification of pentaerythritol esters. The formation of PE triester and PE tetraester increased significantly in the first 30 min of reaction. The steps can be simplified by the following equations.



The overall reaction is:

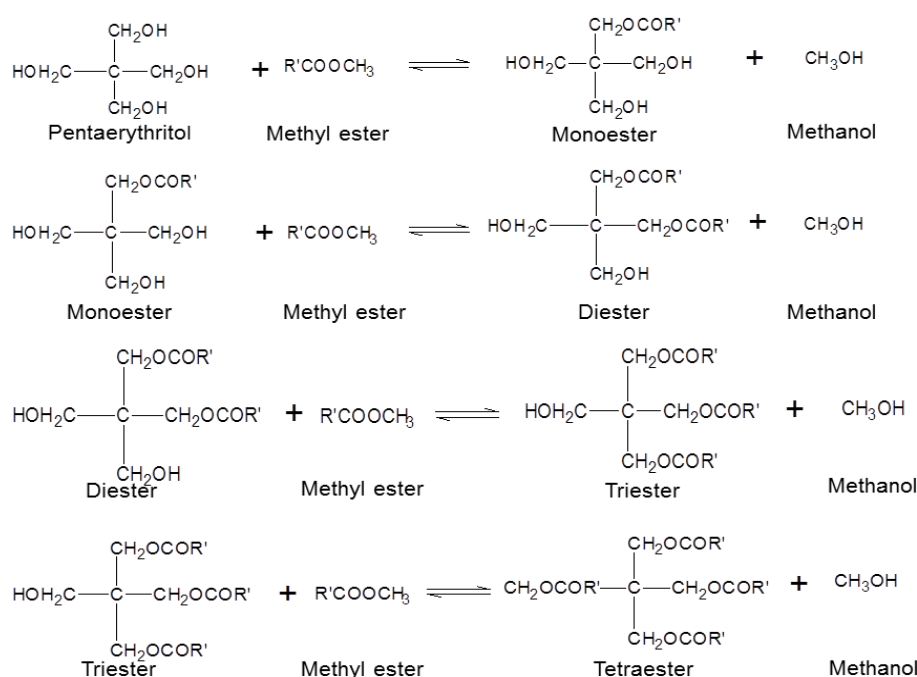


Fig 1. The overall transesterification of palm oil methyl ester with pentaerythritol where R' is C₁₇H₃₃

Fig. 2 shows the distribution curve of PE ester formation after 2 h of reaction at 160 °C and 10 mbar. From the analysis, it is evident that more PE triester and tetraester was formed compared to monoester and diester during the first few minutes of reaction. It indicates that the rate reaction of monoester from pentaerythritol was very fast. Once the monoester formed, it reacts with POME immediately to form diester. The result also indicates that the composition of monoester was maintained below 0.5% throughout the reaction. Lower composition of diester was observed during the first few minutes of reaction, probably due to the competitive reaction to produce triester from diester. After 45 min of reaction, the composition of diester was between 6.0% and 7.0%. Even though almost all monoester was subsequently converted to diester, not all diester was converted to triester, as indicated in the composition of PE ester after 2 h of reaction. Triester compositions were found between 24.0% to 28.0% whereas the composition of tetraester was between 26% to 35% after 45 min of reaction. The lower composition of PE tetraester at the end of the reaction might be due to the lower rate of reaction of triester to form tetraester because of greater steric hindrance of tetraester compared to the triester. In between 60 min to 105 min reaction, the composition of tetraester formed was lower than the triester. This might occur due to the accumulation of methanol in a reaction mixture that drives the PE tetraester reversed back to the triester. The slowest formation of tetraester from the triester also indicates that this step is rate-determining step with forwarding rate reaction constant, k_4 .

Effect of Reaction Time

In this study, the interaction parameters for the transesterification of POME and PE to produce tetraester are elucidated. The effects of reaction parameters such as reaction temperature, catalyst concentration, the molar ratio of POME to PE, vacuum pressure and stirring rate to the formation of products, i.e., PE monooleate (monoester), PE dioleate (diester), PE trioleate (triester) and PE tetraoleate (tetraester) were observed. A preliminary study has been conducted to obtain optimum reaction time, and it indicated that the highest conversion

was achieved after 2 h of reaction. Fig. 3 shows the comparison of product formation at 1 h reaction and 2 h reaction. Pentaerythritol alcohol reactant still exists in the product mixture after a 1 h reaction. However, when the reaction extends up to 2 h, pentaerythritol alcohol completely disappeared and formed PE esters that are PE monoester, PE diester, PE triester, and PE tetraester, and the composition was presented in Table 1. Further increment of reaction time decreased the formation of PE tetraester decreased due to some reverse reactions.

Effect of Reaction Temperature

The reaction temperature was varied from 140, 150, 160 °C, and 170 °C to study the dependency of transesterification reaction on temperature. The other parameters were fixed at constant values; reactants molar ratio of 4.25:1, 1.2% w/w sodium methoxide catalyst,

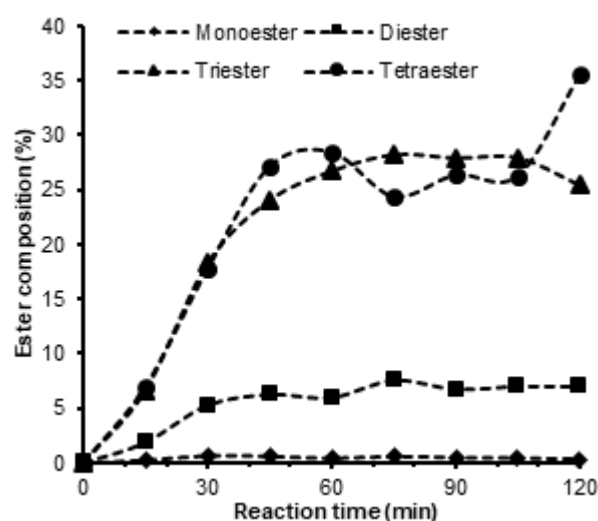


Fig 2. Composition change of PE ester products versus reaction time at 160 °C. (POME:PE, 4.5:1; 10 mbar; 1.25% w/w sodium methoxide; 900 rpm)

Table 1. Composition of PE oleate esters at optimum conditions

Products	Composition (% w/w)
Pentaerythritol monooleate (PE monoester)	0.4%
Pentaerythritol dioleate (PE diester)	6.7%
Pentaerythritol trioleate (PE triester)	25.5%
Pentaerythritol tetraoleate (PE tetraester)	36.0%
Remaining POME	31.4%

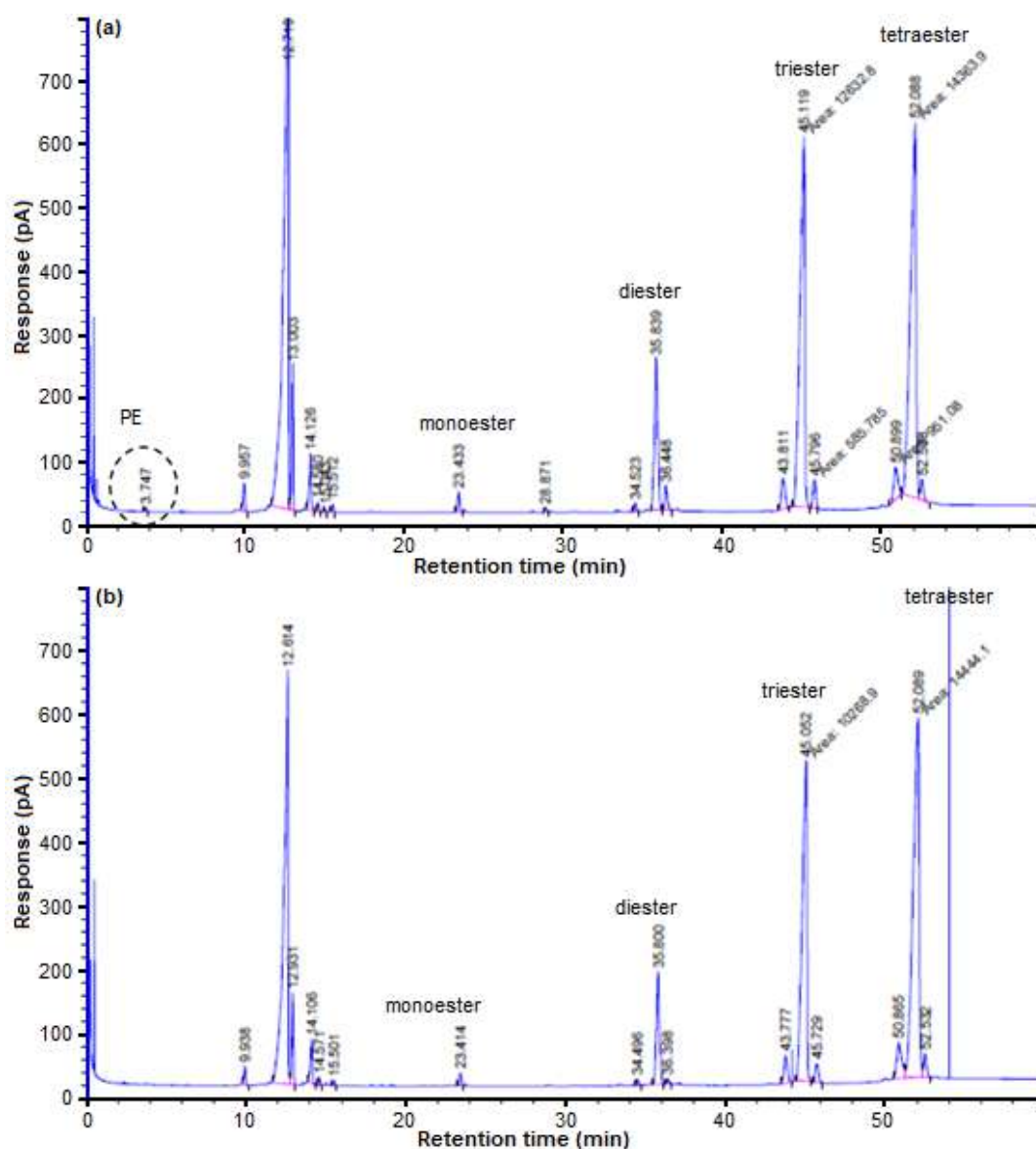


Fig 3. Gas chromatography of PE esters formation at (a) 1 h reaction and (b) 2 h reaction

10 mbar vacuum pressure, and 600 rpm stirring rate. The samples were collected after 1, 2, and 3 h, and then analyzed using the GC to determine the composition of the product. However, it was observed that the reversible reaction occurred after 3 h reaction and most of the PE tetraester reversed back to form triester. Thus, all reactions were stopped after 2 h. Moreover, the synthesis of PE tetraester was performed below 180 °C to avoid sublimation of pentaerythritol. Due to this consideration, the reaction temperature was set in between 140 to 170 °C.

The effect of reaction temperature on the formation of PE esters at 1 h reaction is shown in Fig. 4, and the

formation of PE esters at 2 h reaction is shown in Fig. 5. The yield of PE tetraester at 1 h reaction were 13.4, 24.0, 28.5 and 20.9% at 140, 150, 160 and 170 °C respectively. Fig. 4 shows that the effect of temperature is more obvious after 2 h of reaction. At the same temperature, the composition of PE esters rose to 17.36, 29.43, 36.73, and 20.71%, respectively. The improvement in reaction conversion from 1 to 2 h shows a similar trend with responding to the increase in temperature. The results indicated that the yield of tetraester increased with temperature and the maximum yield was obtained at 160 °C. However, the yield of tetraester was slightly

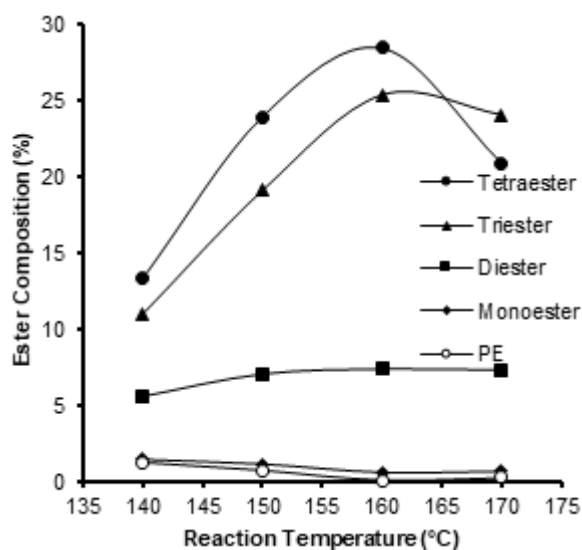


Fig 4. Effect of temperature on PE ester yield at 1 h reaction (POME: PE, 4.5:1; 10 mbar; 1.25%w/w sodium methoxide, 600 rpm)

dropped when the temperature was further increased to 170 °C. This may occur due to a higher rate of the backward reaction that reverses the tetraester back to the triester. These findings concur with similar transesterification reaction of TMP triester reported by Yunus et al. [7] and Koh et al. [9]. At higher temperatures, the rate of reverse reaction of TMP triester to diester was represented by kinetic reaction rate constants, $k_{3,r}$ was significantly larger than $k_{2,r}$ [10].

At higher temperatures, the rate of reaction increases; thus, it increases the yield of PE tetraester. However, the reactant POME can also evaporate at high temperatures, resulting in the occurrence of reverse reaction which reduces the yield of PE tetraester. Hence, it is very important to use cold water in the condenser to condense the evaporating POME and return to the reaction flask. Furthermore, the sublimation of pentaerythritol may also occur. If the reaction temperature is too high, both POME evaporation and pentaerythritol sublimation could take place, resulting in the low yield of PE ester. Therefore, the optimum reaction temperature is proposed at 160 °C which produced the highest yield of tetraester.

Effect of Catalyst Concentration

The use of enzymes as a catalyst for this transesterification reaction is not suitable because of the

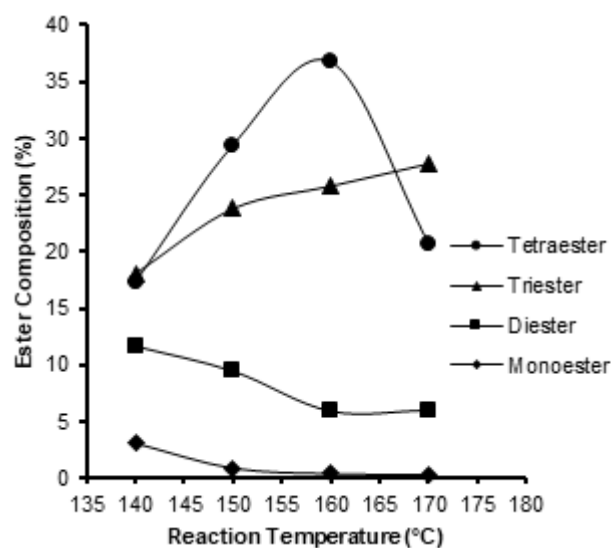


Fig 5. Effect of temperature on PE ester yield at 2 h reaction (POME: PE, 4.5:1; 10 mbar; 1.25%w/w sodium methoxide, 600 rpm)

higher melting point of pentaerythritol, which is at 260 °C. Furthermore, some of the acid catalysts are toxic, and the reaction is longer to obtain high yield. A homogeneous acid catalyst such as sulfuric acid or hydrochloric acid is corrosive, and the main problem is that this hazardous strong acid generates much wastewater during product purification. Furthermore, the reaction with the acid catalyst requires a long reaction time for completion [11].

On the contrary, most of the alkaline catalyst is non-toxic, and the reaction is much faster. Thus, sodium methoxide was used as a catalyst for the transesterification reaction of PE and POME to form PE tetraester. However, sodium methoxide catalyst is easily oxidized in the air; hence, the reaction should be maintained under anhydrous condition [5].

The effect of catalyst concentration on the transesterification reaction was evaluated in the range of 0.5% to 1.5% (w/w), while the other parameters such as temperature, reactants molar ratio, vacuum pressure, and stirring rate were kept constant at 160 °C, 4.25:1, 10 mbar and 600 rpm, respectively. The reaction was carried out for 2 h. Fig. 6 shows the effect of catalyst concentration of the PE ester formed in which the catalyst concentration was varied at 0.5, 0.75, 1.00, 1.25, and 1.5%, respectively. The catalyst concentration has a positive effect on the PE tetraester composition. At the

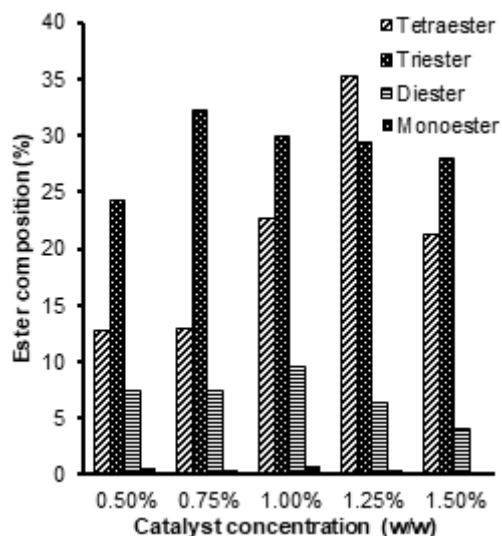


Fig 6. Effect of catalyst concentration on PE ester yield at 2 h reaction (POME: PE, 4.5:1; 10 mbar; 160 °C; 600 rpm)

lowest catalyst concentration, 0.5% w/w, the percentage of tetraester was low at 12.8%. There is no significant effect of catalyst concentration increment from 0.5% to 0.75% w/w on the tetraester composition, which remained at 12.8%. However, when the catalyst was at 1.0% w/w, the composition of tetraester increases to 22.7%. The results are comparable with a transesterification of PE tetraester by Aziz et al. [5], where increasing the catalyst concentration from 0.75% to 1.0% w/w significantly increased the composition of PE tetraester. A similar finding was observed when sodium methoxide used as a catalyst in transesterification of TMP triester, where the highest triester composition was obtained at a catalyst concentration of 1.0% w/w. There is no significant effect on the TMP triester yield increment when the sodium methoxide catalyst used at a concentration between 0.5% w/w to 0.7% w/w [12]. In a transesterification of biodiesel from karanja oil using sodium methoxide, a similar result was observed where the highest composition of karanja oil methyl ester was obtained at a catalyst concentration of 1.0% w/w [13].

In this study, the highest PE tetraester composition, which is 35.2%, was obtained with 1.25% w/w of catalyst. It shows that increasing catalyst concentration will accelerate the reaction and formed more PE esters. On the increasing of catalyst to 1.5% w/w, the composition of tetraester drastically reduced to 21.3%. The amount of

monoester and diester at all catalyst concentration were below 0.5 and 10.0%, respectively. Whereas, the total composition of triester was in the range of 25.0% to 32.0% at all concentrations.

This finding is similar to the PE ester transesterification reaction by Aziz et al. [5] but the highest tetraester composition was obtained in 1 h. However, the reaction was conducted for 2 h in this study to ensure pentaerythritol completely reacted to form PE tetraester. This is because a small amount of pentaerythritol still left in the reaction mixture when the reaction was conducted in 1 h, and only a small amount of PE tetraester was formed. It might be due to a very slow reaction during the first minute due to the mixing and dispersion of reactants and catalysts. Furthermore, the temperature of the reaction mixture slightly reduced about 10 °C to 15 °C as soon as the sodium methoxide catalyst was added. This is because transesterification is an endothermic reaction that adsorbed energy from the surrounding, consequently reduce the temperature of the reaction mixture. Based on the observation, the reaction required 10 min to 15 min to increase to the desired reaction temperature. Therefore, the rate formation was slow at 1 h of reaction, and a lower amount of PE tetraester produced.

The increment of catalyst concentration from 1.25% to 1.5% w/w decreased the amount of PE ester formed. The presence of a large amount of alkaline catalyst in the reaction could lead to the formation of fatty acid soap. The hydrolysis of methyl ester will produce fatty acid and lead to fatty acid soap formation in the presence of metal catalyst [5,14]. Therefore, the formation of PE ester will be affected. The yields of PE ester component were reduced at the highest catalyst concentration 1.5% w/w, as shown in Fig. 6. A similar result was noticed when sodium methoxide was used for transesterification of high oleic TMP triester [12] and transesterification of biodiesel from karanja oil [13], where a higher amount of catalyst reduced the yield of TMP triester and karanja oil methyl ester, respectively. When homogeneous sodium methoxide was employed for transesterification of POME to TMP triester, a low catalyst concentration of 1.0% w/w catalyst was required

to achieve 92.6% TMP triester composition [12]. However, a high catalyst concentration of 1.25% w/w catalyst was required to obtain a high yield of PE tetraester. Therefore, it can be observed as an optimum catalyst concentration for the examined conditions.

Effect of Molar Ratio of POME to PE

The molar ratio of reactants is one of the important parameters that affect the rate of reaction in the transesterification process [1,15-16]. The molar ratio of POME to PE from the stoichiometric is 4 to 1. However, the amount of POME used was in excess to enhance the forward reaction and hinder the backward reaction [16]. The molar ratio of POME to PE was varied at 4:1, 4.25:1, 4.5:1, 4.75:1, and 5:1 to study the effect of the molar ratio of reactants on the PE tetraester formation. The other reaction parameters were kept constant at reaction temperature 160 °C, vacuum pressure at 10 mbar, and 1.25% w/w sodium methoxide. The reaction was carried out up to 2 h at 600 rpm.

The effect of the molar ratio of POME to PE on the formation of PE ester is shown in Fig. 7. The composition of PE tetraester was very low at the stoichiometric ratio of 4:1, which is around 5.0%. The composition of tetraester increased to 19.1 and 35.2% when the ratio of reactants was increased to 4.25:1 and 4.5:1, respectively. However,

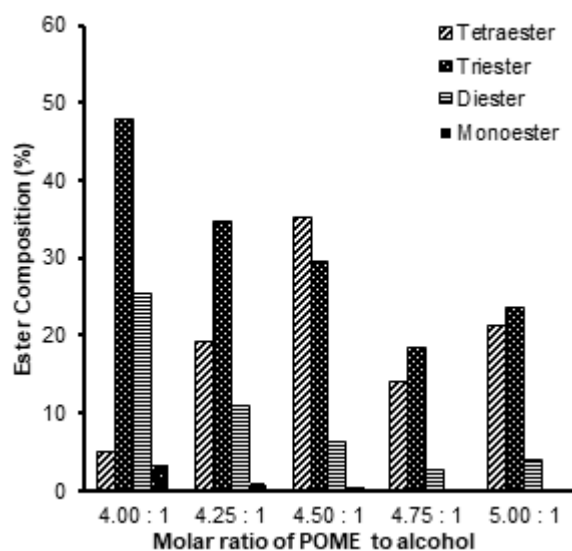


Fig 7. Effect of the molar ratio of POME to PE on PE ester yield at 2 h reaction (10 mbar; 160 °C; 1.25% w/w sodium methoxide, 600 rpm)

the composition of tetraester decreased drastically to 13.9% when the ratio of the reactants was further increased to 4.75:1. At a molar ratio of 5.00:1, the composition of tetraester was slightly increased to 21.2%. At a very high ratio of POME to PE, i.e., at 10:1 and 12:1, the composition of tetraester was markedly decreased to 12.0% and 6.7%, respectively.

There is no significant effect of using the high molar ratio of reactants since the reaction was based on the stoichiometric molar ratio. The highest composition of tetraester was obtained at the molar ratio of 4.5:1. At a molar ratio of 4.00:1 and 4.25:1, the reaction was assumed incomplete since a large proportion of ME and DE still exist. The excess of POME was used to ensure the reaction is complete. When the large excess of POME was used in the reaction, the interaction between the catalyst and the reactants was reduced due to the dilution effect. Thus, the best molar ratio of POME to PE is 4.5:1.

Effect of Vacuum Pressure

The vacuum was used in the reaction to remove the methanol from the process and promote the forward reaction. In order to study the effect of vacuum pressure on the transesterification reaction, the experiments were conducted at 5 mbar, 10 mbar, 20 mbar, and 50 mbar. The other parameters were fixed at a reaction temperature of 160 °C, POME to PE 4.5:1, and at 1.25% w/w sodium methoxide. The reaction was run for 2 h.

The effect of vacuum pressure on the yield of PE esters is shown in Fig. 8. The highest composition of PE tetraester was obtained at 10 mbar, which was at 36.7%. When the vacuum level increased to 20 mbar and 50 mbar, the composition of tetraester drastically decreased to 16.7 and 19.3%, respectively. At low vacuum (high pressure), not all POME was converted to PE esters. For example, 45% of PE esters at 20 mbar and 50 mbar were still in intermediates forms of esters (monoester, diester, and triester). This may occur due to an inadequate vacuum that unable to prevent the backward reaction and reverse the PE esters back to POME. The removal of methanol was slow at a low vacuum; the reaction between methanol with PE esters may have occurred and resulted in the reverse reaction to form POME. It can be seen from the

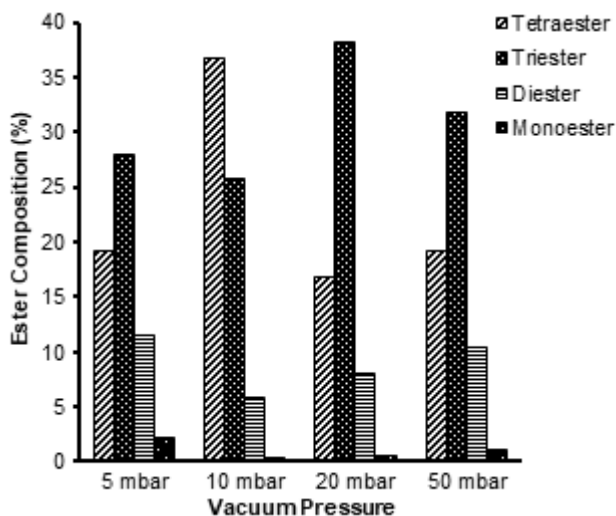


Fig 8. Effect of vacuum pressure on PE ester yield at 2 h reaction (POME: PE, 4.5:1; 160 °C; 1.25% w/w sodium methoxide, 600 rpm)

composition of POME at 20 mbar and 50 mbar, which is higher compared to the composition of POME at 5 mbar and 10 mbar. This observation is similar to previous research on the transesterification reaction of TMP esters conducted by Yunus et al. [7] and Kamil et al. [17].

However, at 5 mbar, the composition of tetraester obtained was reduced to 19.1%. This is because if the vacuum is too high (low pressure), POME will be sucked away together with methanol from the system, resulting in the lower formation of PE esters. POME may evaporate from the reaction system because of lower boiling point properties. Hence, it will change the stoichiometric ratio of reactants in the reaction. The backward reaction may have occurred to reverse the tetraester back to partial esters due to the insufficient quantity of POME. In economic consideration, high vacuum requires high energy and increase the cost of equipment and process.

Therefore, for the transesterification of POME with PE, the optimum vacuum pressure was found to be at 10 mbar for the synthesis temperature between 140 °C to 170 °C. The high yield of PE tetraester was formed under this condition. In contrast with the synthesis of TMP triester using sodium methoxide catalyst, the optimum vacuum pressure was obtained at 20 mbar at a synthesis temperature between 100 °C to 130 °C.

Effect of Stirring Rate

Mixing is very important in transesterification reactions involving POME and PE. PE is solid, and the POME is liquid. In order to make sure PE is soluble and form a homogenous mixture with POME in the presence of a catalyst, good mixing is crucial. This will provide a good mass and heat transfer and maintain uniform conditions in the reaction system. Furthermore, mixing will enhance the mixing of particles or molecules of reactants, thus reduced reaction time [9]. These conditions can be achieved by conducting the reaction in the turbulent flow which can be promoted with the addition of baffles. In a batch system, the reaction can be conducted by providing external mixing using rotary agitation [18]. In a small-scale batch reaction, a stirred batch reactor will be used to conduct the reaction.

In this study, the mixing process in a batch reactor was achieved by providing the stirring of the mixture using magnetic stirrer. The stirring speed played an important role in speeding up the reaction rate. The stirring speed was varied at 300, 600, and 900 rpm, and the other parameters were kept constant at 160 °C, 10 mbar, 1.25% sodium methoxide, and POME to PE at 4.5:1. The sample was taken at 15 min interval, and the reaction was conducted for 2 h. The effect of stirring speed on the composition of PE esters is shown in Fig. 9.

A good mixing between the reactants, i.e., POME, PE, and sodium methoxide catalyst, resulted in effective collisions between the reactants molecules and catalysts. Therefore, enough energy is gained to overcome the potential energy barrier for the reactions to occur and obtain the desired product [9]. Fig. 9 shows that, as the stirring rate increases, the yield of PE tetraester increases. At the lower stirring speed of 300 rpm, the rate formation of PE esters was slow. It can be seen in Fig. 9(a) that the rate of tetraester formation from triester was slow at the beginning, and slightly increased up to 90 min of reaction. At 90 min to 105 min, the rate suddenly increased and thus increased the composition of PE esters. However, the composition of the triester is higher than the tetraester, along with the reaction. It may be

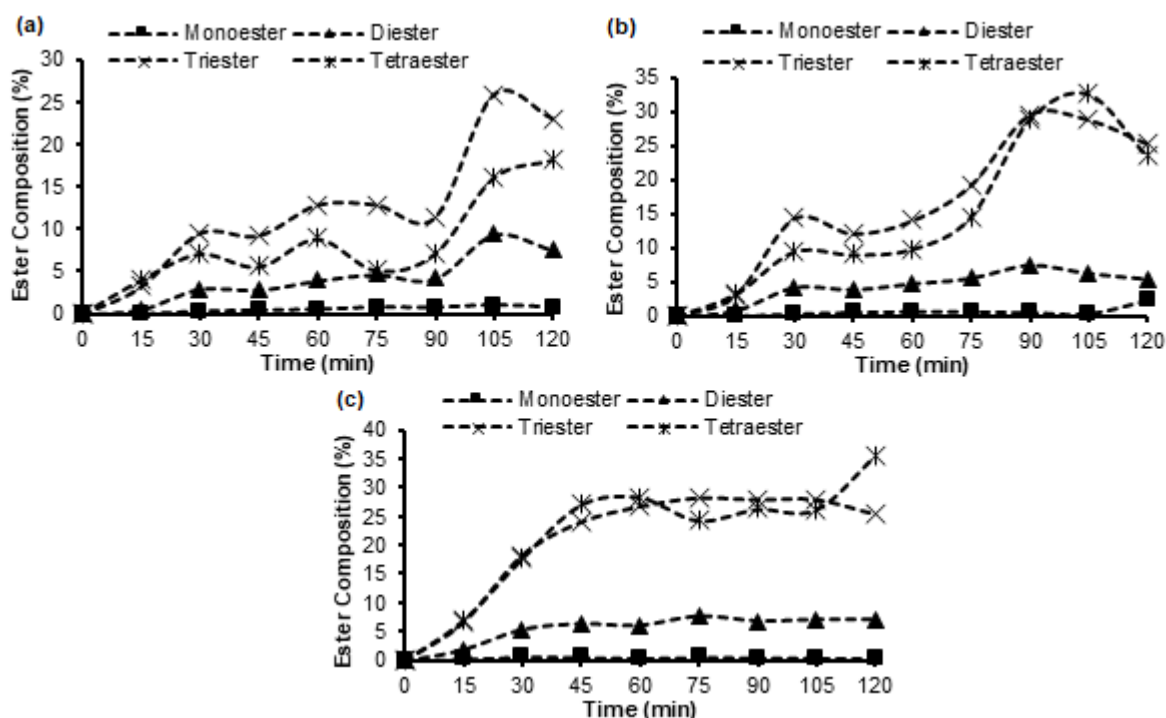


Fig 9. Effect of stirring speed on PE ester yield at 2 h reaction at (a) 300 rpm (b) 600 rpm and (c) 900 rpm (POME: PE, 4.5:1; 160 °C; 10 mbar; 1.25% w/w sodium methoxide)

due to insufficient energy to break the potential energy of triester to convert to tetraester at lower stirring speed. Furthermore, slow mixing may require a longer time to achieve a high composition of desired tetraester [13].

As the stirring speed was increased to 600 rpm, the rate reaction also increased. In the beginning, the composition of the triester is higher than tetraester until 90 min of reaction. The highest tetraester was found after 105 min reaction with tetraester composition at 32.6%. However, the composition of tetraester decreased to 23.5% when the reaction was prolonged to 120 min, as shown in Fig. 9(b). This may occur due to the occurrence of the reverse reaction. Once the reaction achieves its optimum yield, continued stirring will promote the reverse reaction which is competing with the optimality of system kinetics [19].

The highest tetraester composition was obtained when the reaction was conducted at 900 rpm, with a yield of 35.5% after 120 min of reaction. The rate formation of tetraester and triester gradually increased at the early 45 min of reaction. In between 45 min to 105 min, the reaction system produced more tetraester and triester as

shown in Fig. 9(c). Therefore, the stirring rate between 600 rpm to 900 rpm can be regarded as the best mixing speed for the reaction. Under these conditions, a reasonably high yield of PE tetraester can be obtained. Controlling the mixing speed is necessary for the optimum condition of PE esters formation. However, if the stirring speed is too high, it increases the rate of reverse reaction thus reduces the yield of tetraester.

■ CONCLUSION

Based on the results from the optimization study presented, the optimum parameters for the transesterification reaction of POME with PE were found. The temperature of reaction at 160 °C, molar ratio reactants, i.e., POME to PE at 4.5:1, sodium methoxide catalyst concentration at 1.25%, vacuum pressure at 10 mbar and stirring speed at 900 rpm were established as optimum conditions. All reactions were carried out for 2 h in a stirred batch reactor.

The transesterification reaction of POME and PE involved four steps of consecutive reactions to form PE monoester, PE diester, PE triester, and PE tetraester.

Pentaerythritol was not detected in the reaction product and has been fully converted into PE esters. The composition of monoester was below 0.5% at all reaction conditions. The highest composition of PE tetraester was achieved at 36%. The composition of PE tetraester obtained similarly with the previous study by Aziz et al. [5]. It might occur due to the slower rate formation to produce PE tetraester that has a bulky molecule structure. These steric effects would decrease the rate formation of PE tetraester because it has greater steric hindrance with four ester groups as compared to PE triester that consists of three ester groups. The substitution of large methyl oleate group into pentaerythritol by removal of -OH would make the molecule sterically crowded. When more -OH was replaced with methyl ester group, the steric effect would increase, and bulky ester molecule formed [20].

In this study, an efficient chemical synthesis to produce PE esters from palm oil is established. The transesterification reaction system using an alkaline catalyst and equipped with a vacuum system allows for faster reactions and suppress reverse reactions.

■ ACKNOWLEDGMENTS

The authors would like to acknowledge the Department of Chemical and Environmental Engineering, Faculty of Engineering, Universiti Putra Malaysia, which made this study possible.

■ REFERENCES

- [1] Fukuda, H., Kondo, A., and Noda, H., 2001, Biodiesel fuel production by transesterification of oils, *J. Biosci. Bioeng.*, 92 (5), 405–416.
- [2] Reeves, C.J., Menezes, P.L., Jen, T.C., and Lovell, M.R., 2015, The influence of fatty acids on tribological and thermal properties of natural oils as sustainable biolubricants, *Tribol. Int.*, 90, 123–134.
- [3] Arumugam, S., Sriram, G., and Subadhra, L., 2012, Synthesis, chemical modification and tribological evaluation of plant oil as bio-degradable low temperature lubricant, *Procedia Eng.*, 38, 1508–1517.
- [4] Erhan, S.Z., Sharma, B.K., Liu, Z., and Adhvaryu, A., 2008, Lubricant base stock potential of chemically modified vegetable oils, *J. Agric. Food Chem.*, 56 (19), 8919–8925.
- [5] Aziz, N.A.M., Yunus, R., Rashid, U., and Syam, A.M., 2014, Application of response surface methodology (RSM) for optimizing the palm-based pentaerythritol ester synthesis, *Ind. Crops Prod.*, 62, 305–312.
- [6] Ma, F., Clements, L.D., and Hanna, M.A., 1999, The effect of mixing on transesterification of beef tallow, *Bioresour. Technol.*, 69 (3), 289–293.
- [7] Yunus, R., Fakhru'l-Razi, A., Lye, O.T., Iyuke, S.E., and Idris, A., 2003, Development of optimum synthesis method for transesterification of palm oil methyl esters and trimethylolpropane to environmentally acceptable palm oil-based lubricant, *J. Oil Palm Res.*, 15 (2), 35–41.
- [8] Yunus, R., Lye, O.T., Fakhru'l-Razi, A., and Basri, S., 2002, A simple capillary column GC method for analysis of palm oil-based polyol esters, *J. Am. Oil Chem. Soc.*, 79 (11), 1075–1080.
- [9] Koh, M.Y., Mohd. Ghazi, T.I., and Idris, A., 2014, Synthesis of palm based biolubricant in an oscillatory flow reactor (OFR), *Ind. Crops Prod.*, 52, 567–574.
- [10] Hamid, H.A., Yunus, R., Rashid, U., Choong, T.S.Y., and Al-Muhtaseb, A.H., 2012, Synthesis of palm oil-based trimethylolpropane ester as potential biolubricant: Chemical kinetics modeling, *Chem. Eng. J.*, 200-202, 532–540.
- [11] Saifuddin, N., Samiuddin, A., and Kumaran, P., 2015, A review on processing technology for biodiesel production, *Trends Appl. Sci. Res.*, 10 (1), 1–37.
- [12] Hamid, H.A., Yunus, R., Rashid, U., Choong, T.S.Y., Ali, S., and Syam, A.M., 2016, Synthesis of high oleic palm oil-based trimethylolpropane esters in a vacuum operated pulsed loop reactor, *Fuel*, 166, 560–566.
- [13] Sharma, Y.C., Singh, B., and Korstad, J., 2010, High yield and conversion of biodiesel from a nonedible feedstock (*Pongamia pinnata*), *J. Agric. Food Chem.*, 58 (1), 242–247.
- [14] Yunus, R., Fakhru'l-Razi, A., Lye, O.T., Iyuke, S.E., and Idris, A., 2003, Preparation and characterization of trimethylolpropane esters from palm kernel oil methyl esters, *J. Oil Palm Res.*, 15 (2), 42–49.
- [15] Nagendramma, P., and Kaul, S., 2012, Development of ecofriendly/biodegradable lubricants: An

- overview, *Renewable Sustainable Energy Rev.*, 16 (1), 764–774.
- [16] Resul, M.F.M.G., Mohd. Ghazi, T.I., and Idris, A., 2012, Kinetic study of jatropha biolubricant from transesterification of *Jatropha curcas* oil with trimethylolpropane: Effects of temperature, *Ind. Crops Prod.*, 38, 87–92.
- [17] Kamil, R.N.M., Yusup, S., and Rashid, U., 2011, Optimization of polyol ester production by transesterification of jatropha-based methyl ester with trimethylolpropane using Taguchi design of experiment, *Fuel*, 90 (6), 2343–2345.
- [18] Ni, X., Mackley, M.R., Harvey, A.P., Stonestreet, P., Baird, M.H.I., and Rao, N.V.R, 2003, Mixing through oscillations and pulsations—A guide to achieving process enhancements in the chemical and process industries, *Chem. Eng. Res. Des.*, 81 (3), 373–383.
- [19] Rashid, U., Anwar, F., and Knothe, G., 2009, Evaluation of biodiesel obtained from cottonseed oil, *Fuel Process. Technol.*, 90 (9), 1157–1163.
- [20] Daw, G., Regan, A.C., Watt, C.I.F., and Wood, E., 2013, Steric effects and mechanism in the formation of hemi-acetals from aliphatic aldehydes, *J. Phys. Org. Chem.*, 26 (12), 1048–1057.

***In Silico* Study on Interaction and Preliminary Toxicity Prediction of *Eleutherine americana* Components as an Antifungal and Antitoxoplasmosis Candidate**

Sophi Damayanti^{1*}, Nadiyah Athifah Salim Martak¹, Benny Permana¹, Adi Suwandi², Rika Hartati³, and Indra Wibowo⁴

¹Pharmacochemistry Research Group, School of Pharmacy, Institut Teknologi Bandung, Jl. Ganesha No. 10, Bandung 40132, West Java, Indonesia

²Research Center for Nanosciences and Nanotechnology, Institut Teknologi Bandung, Jl. Ganesha No. 10, Bandung 40132, West Java, Indonesia

³Pharmaceutical Biology Research Group, School of Pharmacy, Institut Teknologi Bandung, Jl. Ganesha No. 10, Bandung 40132, West Java, Indonesia

⁴Physiology Animal Development and Biomedical Science, School of Life Science and Technology, Institut Teknologi Bandung, Jl. Ganesha No. 10, Bandung 40132, West Java, Indonesia

* Corresponding author:

tel: +62-22-2504852

email: sophi.damayanti@fa.itb.ac.id

Received: August 8, 2019

Accepted: September 10, 2019

DOI: 10.22146/ijc.48570

Abstract: Red bulbs of *Eleutherine americana* (Aubl.) Merr. ex K. Heyne has been known for its high content of naphthoquinones that have antifungal and antiparasitic activities. In this research, *in silico* interaction study was performed between 31 compounds reported to be found in *E. americana* with the selected target proteins for antifungal and antitoxoplasmosis activity using the molecular docking method. An ORPs (OSBP-related proteins), Osh4 (PDB ID: 1ZHX), and N-myristoyltransferase (Nmt, PDB ID: 1IYL) were used as the antifungal target proteins. *Toxoplasma gondii* purine nucleoside phosphorylase (TgPNP, PDB ID: 3MB8) and calcium-dependent protein kinase-1 (TgCDPK1, PDB ID: 4M84) were used as antitoxoplasmosis target proteins. Three-dimensional structures of the test compounds were made and optimized using GaussView 6.0 and Gaussian 09W. The target proteins were prepared using the Discovery Studio 2016 Program. Aquatic toxicity prediction as the preliminary assessment of the safety of the compounds was performed using ECOSAR v2.0. The results suggest that the compound having both the smallest free binding energy compared with positive control and other test compounds and low predicted toxicity is β -sitosterol with a free binding energy of -11.55 and -11.18 kcal/mol towards Osh4 and Nmt and -8.06 and -10.29 kcal/mol towards TgPNP and TgCDPK1, respectively.

Keywords: fungal infection; toxoplasmosis; *Eleutherine americana*; molecular docking; aquatic toxicity

■ INTRODUCTION

Antifungal is a compound with the activity in destroying or inhibiting the growth of fungi. The development of these compounds is slower compared with antibacterial agents as the similar eukaryotic cell properties of the organisms that the developed targets are more limited [1]. The level of fungal infection has been increased in recent years, and the causes of fungal

infections are also increasingly developing in other fungal species [2]. On the other hand, another emerging infection problem is related to *Toxoplasma gondii*. This parasite can have harmful effects on the fetus, children, and patients with low immune systems [3]. Antitoxoplasmosis is a group of compounds that has the activity to kill or inhibiting the growth of the parasite. Currently, first-line therapy for infection of *T. gondii* is the combination of pyrimethamine and sulfadiazine,

which work synergistically in inhibiting folic acid metabolism of the parasite [4]. However, the combination can cause severe side effects, and lifelong treatment is needed in patients with low immune systems [5]. In addition, the therapy is also contraindicated for the first trimester in pregnancy. These problems result in the demand for the discovery of antifungal and antitoxoplasmosis agents with a better spectrum of activity and safety profile.

Eleutherine americana (Aubl.) Merr. ex K. Heyne is a plant that is well distributed in South America, South Africa, and Southeast Asia. The bulb of the plant has been used in traditional medication for a long time in the treatment of heart disease, breast cancer, diabetes, and hypertension [6]. Furthermore, several kinds of research have reported the antimicrobial activity of the plant using *in silico* method [7-8]. Previous research has also reported that the *E. Americana* bulb is rich in naphthoquinones [7]. The compounds are known to have the activity as antimicrobial and antiparasitic agents [8]. In this research, *in silico* interaction study was carried out between the constituents of the plant with selected target proteins for antifungal and antitoxoplasmosis agents. Aquatic toxicity prediction was also studied to the compounds as the preliminary assessment of their safety profile.

■ EXPERIMENTAL SECTION

Materials

Three-dimensional structures of target proteins were obtained from the Protein Data Bank (<https://www.rcsb.org/>). The targets used for antifungal activity study were an ORPs (OSBP-related proteins), Osh4, and *N*-myristoyltransferase (Nmt). *Toxoplasma gondii* purine nucleoside phosphorylase (TgPNP) and calcium-dependent protein kinase-1 (TgCDPK1) were used in the study of antitoxoplasmosis activity (Table 1 and 2). (1-methylimidazole-2-yl)-[3-methyl-4-[3-(pyridine-3-ylmethylamino) propoxy]-1-benzo-furan-2-yl] methanone (R64) and 25-hydroxycholesterol were used as a positive control in antifungal activity study, while the positive controls used in antitoxoplasmosis activity study were immucillin-H (IMH) and 5-amino-1-tert-butyl-3-(quinolin-2-yl)-1H-pyrazole-4-carboxamide (21E). Research has shown that the NMT gene is essential for vegetative growth and survival of *Candida albicans* and *Cryptococcus neoformans* [9-10]. In addition, NMT is a promising target protein for the development of new fungicidal drugs and has a broad spectrum of antifungal [11]. Osh4 is an important antifungal target protein which plays a role in sterol membrane regulation [12].

Table 1. Three-dimensional structures of proteins used in antifungal activity study

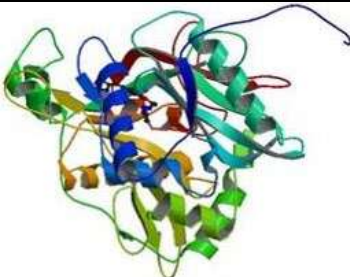
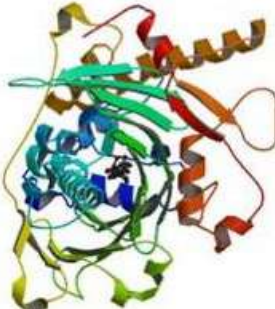
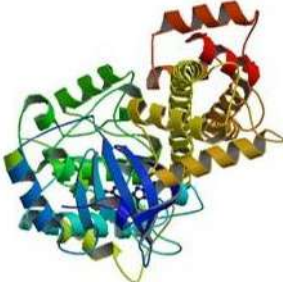
Target Name	Structure	Reference
<i>N</i> -myristoyltransferase (PDB ID: 1IYL)		[14]
Osh4 (PDB ID: 1ZHX)		[15]

Table 2. Three-dimensional structures of proteins used in antitoxoplasmosis activity study

Target Name	Structure	Reference
<i>Purine nucleoside phosphorilase</i> (PDB ID: 3MB8)		[13]
<i>Calcium-dependent protein kinase-1</i> (PDB ID: 4M84)		[5]

For antitoxoplasmosis target proteins, PNP plays an important role in the rescue pathway of nucleotides, and the structure of PNP enzymes in *T. gondii* is different from the structure of PNP in mammals [13]. CDPK1 has a function in the invasive and release of *T. gondii* from its host. In addition, this enzyme is only found in plants and Apicomplexa, but it is not found in humans and animals [5]. The test compounds were 31 molecules that have been reported as the chemical constituents of *E. Americana* (Table 3).

Procedure

Geometry optimization of the test compounds and preparation of the targets

Three-dimensional structures of 31 test compounds were built using GaussView[®] and optimized using Gaussian[®] with Density Functional Theory (DFT) B3LYP method and 6-31G as the basis set. Target protein preparation, including removal of the ligand and water molecules, were carried out using Discovery Studio 2016. Hydrogen atoms were added to the proteins using AutoDock 4.2.6.

In silico interaction study

In silico, an interaction study was carried out by conducting molecular docking of the test compounds

with each target protein using AutoDock 4.2.6. The docking procedures were validated before being used for the test compounds using the root mean square deviation (RMSD) value of the ligand's coordinates after redocking compared with the initial position before being extracted from the protein files. The value of not larger than 2 Å is considered as the acceptance criteria, which indicate that the ligands are back to their original position using the docking procedures [25]. Parameters, such as free energy of binding, inhibition constant and the interaction between the compounds and the residues of the target, were analyzed from the docking results. The data were also compared for the test compounds and the positive controls.

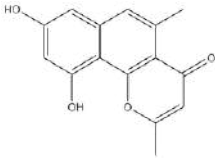
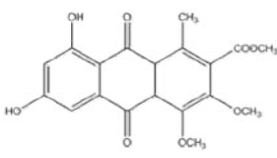
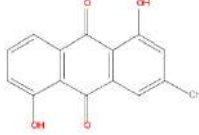
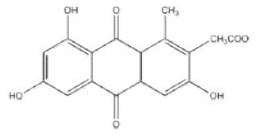
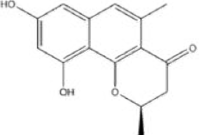
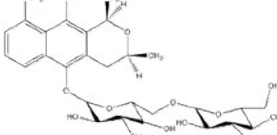
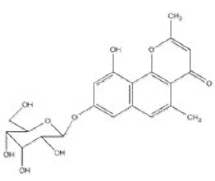
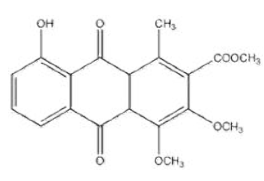
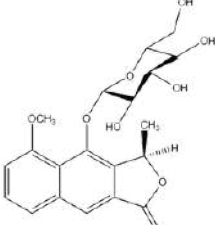
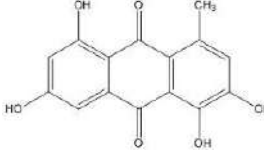
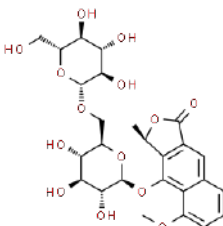
Toxicity prediction using ECOSAR v2.0

The test compound with the best parameter was then subjected to aquatic toxicity prediction using ECOSAR v2.0 [26]. The prediction is including their toxicity towards organisms such as fish, daphnid, and green algae. The procedures involve the submission of SMILES notation of the compounds that were being studied. The results were the value of LC₅₀ for fish and daphnid or EC₅₀ for green algae for acute toxicity and ChV (chronic value) for the three organisms for the chronic toxicity.

Table 3. Chemical constituents of *E. americana* used as the test molecules

No	Compound	Structure	No	Compound	Structure
1	Elecanacin [16]		17	Eleuthinone A [22]	
2	Eleutherin [16]		18	Eleuthraquinone A [22]	
3	Eleutherinon A [17]		19	Eleuthraquinone B [22]	
4	Eleutherinon B [17]		20	Eleucanarol [22]	
5	Eleutherol [18]		21	1,2-dihydroxy-8-methoxy-3-methylantraquinone [16]	
6	Isoeleutherin [16]		22	Eleutherinoside A [23]	
7	Hongconin [19]		23	Eleutherinoside B [23]	
8	Isoeleutherol [16]		24	1,3,6-trihydroxy-8-methylantraquinone [16]	
9	(2S)-1-(3-hydroxy-5-methoxy-1,4-dioxo-1,2,3,4-tetrahydronaphthalen-2-yl)propan-2-yl acetate [16]		25	β -sitosterol [16]	
10	(2R)-1-(3-hydroxy-5-methoxy-1,4-dioxo-1,2,3,4-tetrahydronaphthalen-2-yl)propan-2-yl acetate [16]		26	Kadsuric acid [20]	

Table 3. Chemical constituents of *E. americana* used as the test molecules (Continued)

No	Compound	Structure	No	Compound	Structure
11	Eleutherinol [20]		27	6,8-dihydroxy-3,4-dimethoxy-1-methyl-anthraquinone-2-carboxylic acid methyl ester [24]	
12	1,5-dihydroxy-3-methylanthraquinone [16]		28	2-acetyl-3,6,8-trihydroxy-1-methylanthraquinone [25]	
13	Dihydroeleutherinol [20]		29	Eleuthoside C [16]	
14	2,5-dimethyl-10-hydroxynaphthopyrone 8-O-β-glucopyranoside [16]		30	9,10-dihydro-8-hydroxy-3,4-dimethoxy-9,10-dioxo-2-anthracenecarboxylic acid methyl ester [16]	
15	Eleuthoside A [21]		31	Erythrolaccin [16]	
16	Eleuthoside B [21]				

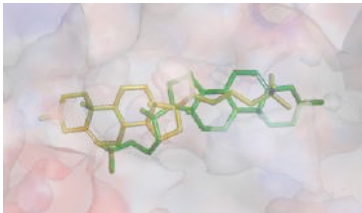
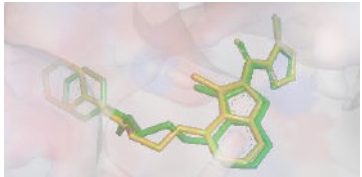
■ RESULTS AND DISCUSSION

In silico Interaction Study

The results of the validation of the molecular docking procedures are shown in Table 4 and 5. It can be seen from the Table 4 and 5 that the docking procedures fulfill the criteria of acceptance for the value of RMSD, indicating that the positions of the ligands were not

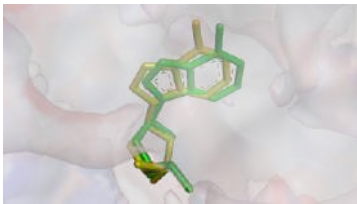
significantly changed after being used in the proposed docking procedures. The docking result of the test compound to each target (Table 6) indicates that all of them have an affinity towards the target protein with negative values of free energy of binding between them and the proteins. The characteristic compounds of *E. Americana* (compound 1, 2, 3, 4, 5 and 11) seem to have

Table 4. Result of the docking procedures validation for antifungal study

Protein	Ligand	Free binding Energy (kcal/mol)	Inhibition Constant (μM)	RMSD (\AA)	Superimposed Ligand Structure*
Osh4	HC3	-11.51	3.67×10^{-3}	1.860	
Nmt	R64	-10.04	4.342×10^{-2}	0.784	

*Superimposing ligand structures before and after redocking with proposed procedures to compare both coordinates. The ligands with the original position are indicated with yellow color while the redocking results are indicated with green.

Table 5. Result of the docking procedures validation for antitoxoplasmosis study

Protein	Ligand	Free binding energy (kcal/mol)	Inhibition Constant (μM)	RMSD (\AA)	Superimposed Ligand Structure*
TgPNP	IMH	-6.93	8.35	0.900	
TgCDPK1	21E	-9.04	2.351×10^{-1}	0.709	

*Superimposing ligand structures before and after redocking with proposed procedures to compare both coordinates. The ligands with the original position are indicated with yellow color while the redocking results are indicated with green.

a weaker affinity to Osh4 and Nmt, with the larger value of the energies and inhibition constants. Compound 25 has a better affinity towards both targets, compared to the positive controls used. The result was also obtained in an antitoxoplasmosis study using TgPNP and TgCDPK1 as the targets. The compound has the lower binding free energy and inhibition constant compared to the positive control and other test compounds. Compound 1, which is a typical compound in the plant, and four other compounds (compound 17, 18, 21, and 26) also have the lower value of both parameters compared to IMH in protein TgPNP.

Docking results to TgCDPK1 show that no typical compound of *E. Americana* which has a better affinity than the positive control. Test compounds having that criteria are compound 25, 26 and 29, with compound 25 has the best affinity among all.

Toxicity Prediction using ECOSAR v2.0.

Aquatic toxicity prediction was carried out as the preliminary assessment of the safety of the compounds. ECOSAR itself has the maximum for the value of $\log K_{ow}$ that indicates that the compound is insoluble that it cannot

Table 6. Docking results of the test compounds to the target proteins

Compound	Free binding energy (kcal/mol)				Inhibition constant (μM)			
	Osh4	Nmt	TgPNP	TgCDPK1	Osh4	Nmt	TgPNP	TgCDPK1
1	-7.59	-7.61	-6.95	-6.73	2.71	2.65	8.06	11.66
2	-7.71	-7.56	-6.16	-7.12	2.22	2.89	30.75	6.09
3	-7.01	-6.68	-5.33	-6.48	7.24	12.68	124.73	17.94
4	-7.1	-6.52	-5.41	-6.31	6.2	16.54	109.16	23.89
5	-6.66	-7.04	-6.02	-6.93	13.03	6.92	38.85	8.27
6	-7.43	-7.41	-6.3	-6.83	3.58	3.69	24.17	9.85
7	-7.18	-6.67	-5.63	-6.93	5.47	12.98	74.65	8.32
8	-6.81	-7.3	-6.52	-6.68	10.24	4.43	16.51	12.72
9	-8.00	-7.28	-6.24	-7.58	1.36	4.59	26.5	2.77
10	-7.62	-7.25	-6.62	-7.38	2.58	4.86	14.01	3.91
11	-7.24	-7.18	-5.61	-6.95	4.96	5.50	76.9	8.05
12	-7.12	-6.63	-6.12	-7.14	6.09	13.7	32.66	5.83
13	-7.44	-7.37	-5.55	-7.02	3.51	3.98	85.29	7.18
14	-8.32	-8.47	-6.18	-8.41	0.800	0.621	29.73	0.686
15	-7.15	-7.54	-5.01	-7.64	5.79	2.95	212.45	2.52
16	-7.54	-7.71	-5.70	-8.58	2.95	2.22	66.69	0.513
17	-7.83	-7.79	-7.46	-7.56	1.83	1.95	3.41	2.85
18	-8.24	-8.33	-7.09	-8.00	0.911	0.781	6.4	1.36
19	-8.02	-8.54	-6.31	-8.22	1.32	0.549	23.71	0.940
20	-6.65	-6.57	-5.77	-6.22	13.28	15.35	58.48	27.39
21	-7.68	-7.35	-7.58	-7.58	2.35	4.12	2.77	2.77
22	-8.25	-7.64	-5.57	-8.03	0.894	2.52	82.53	1.3
23	-7.08	-7.44	-3.61	-6.94	6.43	3.54	$2.25 \cdot 10^3$	8.16
24	-7.56	-7.30	-6.41	-7.80	2.85	4.45	20.13	1.91
25	-11.55	-11.18	-8.06	-10.29	$3.4 \cdot 10^{-3}$	$6.4 \cdot 10^{-3}$	1.24	$2,848 \cdot 10^{-2}$
26	-10.11	-8.02	-7.79	-9.07	0.039	1.33	1.94	$2,238 \cdot 10^{-1}$
27	-8.87	-8.65	-6.68	-7.59	0.315	0.460	12.78	2.74
28	-8.26	-8.6	-6.35	-7.59	0.876	0.495	22.11	2.73
29	-7.6	-8.52	-3.6	-9.64	2.68	0.564	2.28	$8,516 \cdot 10^{-2}$
30	-9.4	-8.47	-6.4	-7.48	0.129	0.619	20.36	3.29
31	-7.15	-7.32	-5.85	-7.45	5.79	4.32	51.64	3.47
Positive controls	-11.51	-10.04	-6.93	-9.04	$3,67 \cdot 10^{-3}$	$4,342 \cdot 10^{-2}$	8.35	$2,351 \cdot 10^{-1}$

develop the toxicity towards the test organism if it has log K_{ow} higher than the limit (Table 7). The program also has a classification of the toxicity (Table 8) that is used by the United States Environmental Protection Agency (US EPA), which consists of high, moderate, and low concern, assessed from the acute and chronic toxicity parameter [27].

The toxicity prediction result (Table 9) shows that the compound 25 and 26 have the value of log K_{ow} which are larger than the maximum limit that they are considered as 'low concern'. Compound 1, 17, and 29 are

also in the same cluster since they have LC_{50} and EC_{50} values larger than 100 mg/L and ChV value larger than 10.0 mg/L. On the other hand, compound 18 and 21 have the value of EC_{50} towards green algae smaller than 1 mg/L that these compounds are considered as 'high concern' toxicity level.

Based on the *in silico* interaction study and the toxicity prediction test, it can be summarized that compound 25 (β -sitosterol) is the most promising compound contained in *E. americana* that predicted to be

Table 7. The maximum limit of log K_{ow} value for aquatic toxicity parameters in ECOSAR*

Fish (LC ₅₀ , 96 h)	Daphnid (LC ₅₀ , 48 h)	Green algae (EC ₅₀ , 96 h)	ChV
5.0	5.0	6.4	8.0

*The values are in ppm. LC₅₀ indicates concentration in water that kills 50% of organism in a continuous exposure. EC₅₀ is concentration that gives decrease of growth of 50% relative to the control in continuous exposure. ChV (chronic value) is a geometric average of NOEC (no observed effect concentration) and LOEC (lowest observed effect concentration) (EPA, 2013)

Table 8. Classification of aquatic toxicity levels

High Concern	Moderate Concern	Low Concern
Any of the 3 acute values are < 1.0 mg/L, or any of the chronic values are < 0.1 mg/L	Any of the 3 acute values are between 1.0 mg/L and 100 mg/L, OR any of the chronic values are between 0.1 mg/L and 10.0 mg/L	All 3 acute values are >100 mg/L, and all three chronic values are >10.0 mg/L, or there are "No Effects at Saturation" (or NES). NES occurs when a chemical is not soluble enough to reach the effect concentration, i.e., the water solubility is lower than an effect concentration, or, for liquids, when K_{ow} criteria are exceeded for an endpoint. For solids, NES is expected if K_{ow} exceeds the specific SAR K_{ow} cutoffs, or the effective concentration is more than one order of magnitude (> 10 X) less than water solubility.

Table 9. Results of prediction of aquatic toxicity

Compound	Molecular weight (g/mol)	Solubility in water (mg/L)	Log K_{ow}	Organism					
				Fish		Daphnid		Green algae	
				LC ₅₀ , 96 h	ChV	LC ₅₀ , 48 h	ChV	EC ₅₀ , 96 h	ChV
1	272.3	728.72	1.62	487.69	45.75	267.44	23.67	172.52	41.81
17	274.28	15,384.22	0.06	498.69	56.38	1,276.11	1,524.82	738.63	100.82
18	312.32	172.81	2.08	5.61	1.48	14.56	0.74	0.4	2.7
21	286.29	871.62	1.44	7.93	3.59	22.15	1.5	0.67	4.82
25	414.72	0	9.65	0	0	0	0	0	0
26	470.7	0	9.28	0	0	0	0	0.01	0.02
29	598.61	6,124.03	-1.16	12,177.76	873.82	1,264.8	79.72	950.84	950.88

*The values are in ppm

the inhibitor of Osh4, Nmt, TgPNP, and TgCDPK1 with better affinity compared to the positive control and other constituents of the plant. In a previous study, it also has been reported that the compound has the activity as an antifungal in an in vitro study [28-29].

Study of Interaction of Compound 25 towards the Target Proteins

Fig. 1 shows the two-dimensional diagram of the interaction between compound 25 and the positive controls with Osh4 and Nmt. The molecular docking result in Fig. 1(a) shows that the compound 25 forms 8

van der Waals interactions with the residues GLN96, ARG100, GLU107, LYS108, LYS109, ASN165, PRO198, and VAL213 of Osh4. Twenty-four of alkyl interactions with the residues TRP10, PHE13, LEU24, LEU27, ALA29, ILE33, LEU39, PHE42, TYR97, PRO110, ILE167, PHE171, LEU177, VAL179, LEU201, ILE203, ILE206 and PRO211, and a hydrogen bond with the residue GLN181 of the target. On the other hand, it is indicated in Fig. 1(b) that the positive control form a similar interaction with the target which consists of 12 van der Waals interactions with TRP10, ALA29, PRO30, LEU39, PHE42, GLU107, LYS108, ILE167, LEU201, ILE206, PRO211 and

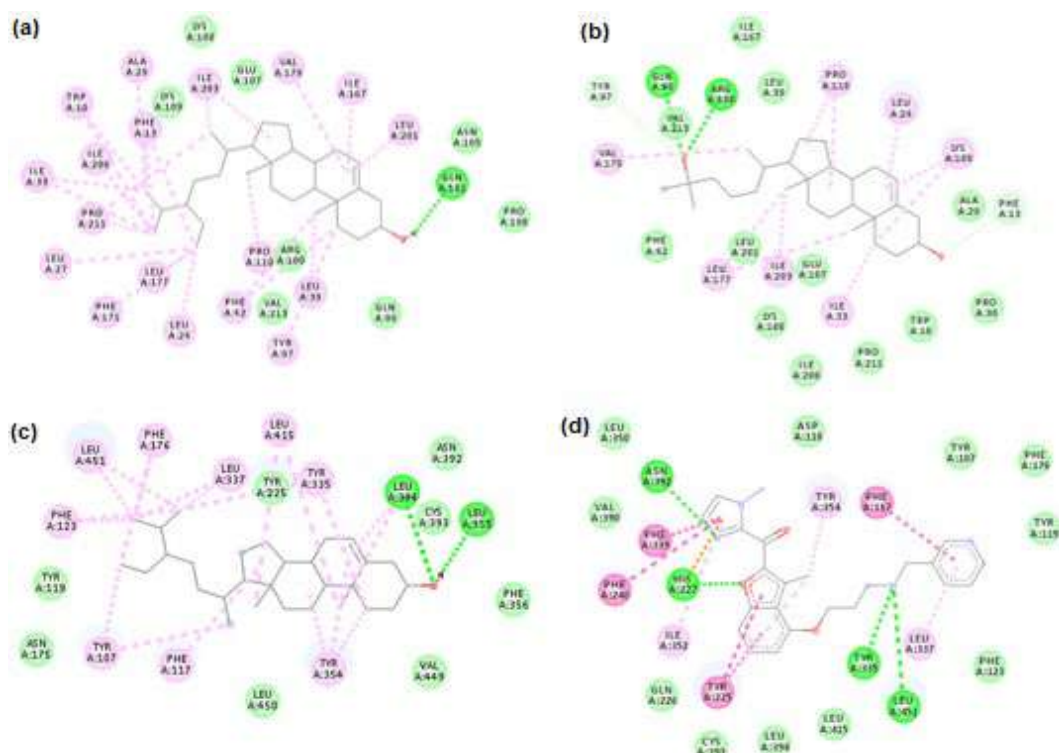


Fig 1. Two-dimensional scheme of interaction between compound 25 and the positive controls with the antifungal target proteins*: (a) compound 25 and Osh4, (b) HC3 and Osh4, (c) compound 25 and Nmt, (d) R64 and Nmt. *alkyl interaction (violet), hydrogen bond (green), van der Waals interaction (light green), pi-pi stacked/pi-pi T-shaped (magenta), pi-cation (orange), and carbon-hydrogen/pi-hydrogen donor (pseudo green)

VAL213, ten alkyl interactions with LEU24, ILE33, LYS109, PRO110, LEU177, VAL179 and ILE203, two hydrogen bonds with GLN96 and ARG100, and 2 phi and hydrogen donor interactions with PHE13 and TYR97 of the target. The same residues are found to be involved in the interaction of the protein with both compounds (PHE13, LEU24, ILE33, TYR97, PRO110, LEU177, VAL179, and ILE203). The interactions of the two ligands with Nmt are shown in Fig. 1(c) and (d). It can be summarized that compound 25 and the protein form 8 van der Waals interactions with the residues of TYR119, ASN175, TYR225, PHE356, ASN392, CYS393, VAL449 and LEU450, twenty alkyl interactions with TYR107, PHE117, PHE123, PHE176, TYR335, LEU337, TYR354, LEU394, LEU415 and LEU451, and 2 hydrogen bonds with LEU355 and LEU394 of Nmt. Meanwhile, the positive control and the protein form 11 van der Waals interactions involving residues TYR107, ASP110, TYR119, PHE123, PHE176, GLN226, LEU350, VAL390,

CYS393, LEU394 and LEU415. Four alkyl interactions are also found between the compound and TYR225, LEU337, ILE352 and TYR354. Other interactions consist of 4 hydrogen bonds with HIS227, TYR335, ASN392 and LEU451, five phi-phi interactions with PHE117, TYR225, PHE240 and PHE339, and a pi-cation interaction with HIS227 of the protein. Same as before, the similar residues are also found to be involved in the interaction of the compounds with the target such as PHE117, TYR335, LEU337, TYR354, and LEU451. The previous study suggested that the residues of PHE117 and TYR354 are involved in the inhibition of the target by ligands [14]. From the diagrams, it can be seen that more alkyl interaction formed by compound 25 and the targets may be the reason for its better affinity parameter in the docking result.

Two-dimensional diagram of interactions between compound 25 and the positive control used with TgPNP and TgCDPK1 is shown in Fig. 2. Fig. 2(a) and (b),

and the positive control with TgPNP, while LEU57, VAL65, ALA78, LYS80, LEU126, and LEU181 are involved in the interaction of the compound and the control with TgCDPK1. Similar to the overall comparison between compound 25 and the control in antifungal interaction study, the more of the alkyl interactions formed between the compound and the target compared with its interaction with the positive control results in the better affinity of the compound 25 towards the two target proteins used in antitoxoplasmosis study.

■ CONCLUSION

The research results suggest that *E. Americana* can be proposed as the candidate of alternatives in the treatment of fungal infection and toxoplasmosis as the constituents of the plant seem to have an affinity to the target used in this study. Compound 25 (β -sitosterol) is the constituent of the plant with a better affinity compared to the positive controls. A preliminary toxicity study suggests that the compound has a low level of aquatic toxicity.

■ ACKNOWLEDGMENTS

This research is supported by the Ministry of Research and Higher Education–PDUPT Dikti 2017-2018.

■ REFERENCES

- [1] Seneviratne, C.J., and Rosa, E.A.R., 2016, Editorial: Antifungal drug discovery: new theories and new therapies, *Front. Microbiol.*, 7, 728.
- [2] Garibotto, F.M., Garro, A.D., Masman, M.F., Rodríguez, A.M., Luiten, P.G.M., Raimondi, M., Zacchino, S.A., Somlai, C., Penke, B., and Enriz, R.D., 2010, New small-size peptides possessing antifungal activity, *Bioorg. Med. Chem.*, 18 (1), 158–167.
- [3] Maldonado, Y.A., and Read, J.S., 2017, Diagnosis, treatment, and prevention of congenital toxoplasmosis in the United States, *Pediatrics*, 139 (2), e20163860.
- [4] Alday, P.H., and Doggett, J.S., 2017, Drugs in development for toxoplasmosis: Advances, challenges, and current status, *Drug Des. Dev. Ther.*, 11, 273–293.
- [5] Zhang, Z., Ojo, K.K., Vidadala, R.S.R., Huang, W., Geiger, J.A., Scheele, S., Choi, R., Reid, M.C., Keyloun, K.R., Rivas, K., Siddaramaiah, L.K., Kenneth, M.C., Robinson, K.P., Merta, P.J., Kifle, L., Hol, W.G.J., Parsons, M., Merritt, E.A., Maly, D.J., Verlinde, C.L.M.J., Voorhis, W.C.V., and Fan, E., 2013, Potent and selective inhibitors of CDPK1 from *T. gondii* and *C. parvum* based on a 5-aminopyrazole-4-carboxamide scaffold, *ACS Med. Chem. Lett.*, 5 (1), 40–44.
- [6] Chen, D.L., Hu, M.G., Liu, Y.Y., Li, R.T., Yu, M., Xu, X.D., and Ma, G.X., 2018, New naphthalene derivatives from the bulbs of *Eleutherine americana* with their protective effect on the injury of HUVECs, *Molecules*, 23 (9), E2111.
- [7] Kuntorini, E.M., and Nugroho, L.H., 2009, Structural development and bioactive content of red bulb plant (*Eleutherine americana*); A traditional medicine for local Kalimantan people, *Biodiversitas*, 11 (2), 102–106.
- [8] Babula, P., Mikelová, R., Potěšil, D., Adam, V., Kizek, R., Havel, L., and Sladký, Z., 2005, Simultaneous determination of 1,4-naphthoquinone, lawsone, juglone and plumbagin by liquid chromatography with UV detection, *Biomed. Pap.*, 149 (Suppl. 1), 25–28.
- [9] Weinberg, R.A., McWherter, C.A., Freeman, S.K., Wood, D.C., Gordon, J.I., and Lee, S.C., 1995, Genetic studies reveal that myristoyl CoA: Protein *N*-myristoyltransferase is an essential enzyme in *Candida albicans*, *Mol. Microbiol.*, 16 (2), 241–250.
- [10] Lodge, J.K., Jackson-Machelski, E., Toffaletti, D.L., Perfect, J.R., and Gordon, J.I., 1994, Targeted gene replacement demonstrates that myristoyl-CoA: Protein *N*-myristoyltransferase is essential for viability of *Cryptococcus neoformans*, *Proc. Natl. Acad. Sci. USA*, 91 (25), 12008–12012.
- [11] Zhong, Y., Han, X., Li, S., Qi, H., Song, Y., and Qiao, X., 2017, Design, synthesis, antifungal activity and molecular docking of thiochroman-4-one derivatives, *Chem. Pharm. Bull.*, 65 (10), 904–910.
- [12] Thenmozhi, M., and Kannabiran, K., 2013, Interaction of *Streptomyces* sp. VITSTK7 compounds with selected antifungal drug target enzymes by *in silico* molecular docking studies, *Interdiscip. Sci.*, 5 (2), 145–149.
- [13] Donaldson, T.M., Cassera, M.B., Ho, M.C., Zhan, C.,

- Merino, E.F., Evans, G.B., Tyler, P.C., Almo, S.C., Schramm, V.L., and Kim, K., 2014, Inhibition and structure of *Toxoplasma gondii* purine nucleoside phosphorylase, *Eukaryot. Cell*, 13 (5), 572–579.
- [14] Sogabe, S., Masubuchi, M., Sakata, K., Fukami, T.A., Morikami, K., Shiratori, Y., Ebiike, H., Kawasaki, K., Aoki, Y., Shimma, N., D'Arcy, A., Winkler, F.K., Banner, D.W., and Ohtsuka, T., 2002, Crystal structures of *Candida albicans* N-myristoyltransferase with two distinct inhibitors, *Chem. Biol.*, 9 (10), 1119–1128.
- [15] Im, Y.J., Raychaudhuri, S., Prinz, W.A., and Hurley, J.H., 2005, Structural mechanism for sterol sensing and transport by OSBP-related proteins, *Nature*, 437 (7055), 154–158.
- [16] Insanu, M., Kusumardiyani, S., and Hartati, R., 2014, Recent studies on phytochemicals and pharmacological effect of *Eleutherine americana* Merr., *Procedia Chem.*, 13, 221–228.
- [17] Alves, T.M.A., Kloos, H., and Zani, C.L., 2003, Eleutherinone, a novel fungitoxic naphthoquinone from *Eleutherine bulbosa* (Iridaceae), *Mem. Inst. Oswaldo Cruz*, 98 (5), 709–712.
- [18] Komura, H., Mizukawa, K., Minakata, H., Huang, H., Qin, G., and Xu, R., 1983, New anthraquinones from *Eleutherine americana*, *Chem. Pharm. Bull.*, 31 (11), 4206–4208.
- [19] Zhengxiong, C., Huizhu, H., Chengrui, W., Yuhui, L., Jianmi, D., Sankawa, U., Noguchi, H., and Itaka, Y., 1986, Hongconin, a new naphthalene derivative from Hong-Cong, the rhizome of *Eleutherine americana* Merr. et Heyne (Iridaceae), *Chem. Pharm. Bull.*, 34 (7), 2743–2746.
- [20] Han, A.R., Min, H.Y., Nam, J.W., Lee, N.Y., Wiryawan, A., Suprpto, W., Lee, S.K., Lee, K.R., and Seo, E.K., 2008, Identification of a new naphthalene and its derivatives from the bulb of *Eleutherine americana* with inhibitory activity on lipopolysaccharide-induced nitric oxide production, *Chem. Pharm. Bull.*, 56 (9), 1314–1316.
- [21] Paramapojn, S., Ganzera, M., Gritsanapan, W., and Stuppner, H., 2008, Analysis of naphthoquinone derivatives in the Asian medicinal plant *Eleutherine americana* by RP-HPLC and LC-MS, *J. Pharm. Biomed. Anal.*, 47 (4-5), 990–993.
- [22] Mahabusarakam, W., Hemtasin, C., Chakthong, S., Voravuthikunchai, S.P., and Olawumi, I.B., 2010, Naphthoquinones, anthraquinones and naphthalene derivatives from the bulbs of *Eleutherine americana*, *Planta Med.*, 76 (4), 345–349.
- [23] Ieyama, T., Gunawan-Puteri, M.D.P.T., and Kawabata, J., 2011, α -Glucosidase inhibitors from the bulb of *Eleutherine americana*, *Food Chem*, 128 (2), 308–311.
- [24] Xu, J., Qiu, F., Duan, W., Qu, G., Wang, N., and Yao, X., 2006, New bioactive constituents from *Eleutherine americana*, *Front. Chem. China*, 1 (3), 320–323.
- [25] Cole, J.C., Murray, C.W., Nissink, J.W.M., Taylor, R.D., and Taylor, R., 2005, Comparing protein-ligand docking programs is difficult, *Proteins Struct. Funct. Bioinf.*, 60 (3), 325–332.
- [26] Mayo-Bean, K., Moran-Bruce, K., Meylan, W., Ranslow, P., Lock, M., Nabholz, J.V., Von Runnen, J., Cassidy, L.M., and Tunkel, J., 2017, *Methodology Document for the ECOlogical Structure-Activity Relationship Model (ECOSAR) Class Program Version 2.0*, U.S. Environmental Protection Agency, Washington DC.
- [27] United States Environmental Protection Agency, 2013, *Interpretive assistance document for assessment of discrete organic chemicals*, U.S. EPA, Washington, 5.
- [28] Kiprono, P.C., Kaberia, F., Keriko, J.M., and Karanja, J.N., 2000, The in vitro anti-fungal and anti-bacterial activities of β -sitosterol from *Senecio lyratus* (Asteraceae), *Z. Naturforsch., C: Biosci.*, 55 (5-6), 485–488.
- [29] Saeidnia, S., Manayi, A., Gohari, A.R., and Abdollahi, M., 2014, The story of beta-sitosterol – A review, *Eur. J. Med. Plants*, 4 (5), 590–609.

Cobalt Doping on Zirconium Titanate as a Potential Photocatalyst with Visible-Light-Response

Emilya Faridatul Sulaikhah, Rian Kurniawan, Mokhammad Fajar Pradipta, Wega Trisunaryanti, and Akhmad Syoufian*

Department of Chemistry, Faculty of Mathematics and Natural Sciences, Universitas Gadjah Mada, Sekip Utara, Yogyakarta 55281, Indonesia

* **Corresponding author:**

email: akhmadsyoufian@ugm.ac.id

Received: September 11, 2019

Accepted: December 16, 2019

DOI: 10.22146/ijc.49459

Abstract: Synthesis of cobalt-doped zirconium titanate (Co-doped $ZrTiO_4$) as a potential photocatalyst with visible-light-response had been conducted. Materials used in this research were titanium tetraisopropoxide (TTIP) as a precursor of TiO_2 , ZrO_2 as another semiconductor for coupling, and $CoSO_4 \cdot 7H_2O$ as the source of cobalt dopant. The composite was prepared by the sol-gel method with various cobalt contents and calcination temperatures. Composites with various Co dopant contents (0, 1, 3, 5, 7, and 9% (Co wt./Ti wt.)) were calcined at 500 °C for 4 h. In addition, the composite with 5% of dopant content was calcined at 700 and 900 °C to observe the influence of calcination temperature. All samples were characterized by using X-ray powder diffraction method (XRD), Fourier-transform infrared spectroscopy (FTIR), specular reflectance UV-Vis spectroscopy (SRUV), and scanning electron microscopy equipped with X-ray energy dispersive spectroscopy (SEM-EDS). Co-doped $ZrTiO_4$ with the lowest bandgap (2.94 eV) was achieved in a sample containing 3% of cobalt content calcined at 500 °C.

Keywords: cobalt; dopant; Co-doped $ZrTiO_4$; photocatalyst; sol-gel

■ INTRODUCTION

The increasing demand for textile products with good coloring quality makes the use of synthetic dyes in the textile industry increasing proportionally [1]. Synthetic dyes are widely used because of their better color, low prices, reusable, and various color choices [2]. Unfortunately, the use of synthetic dyes also has disadvantages, one of which can discharge waste that cannot be decomposed naturally, thus making it dangerous for the environment. Several ways for conventional textile wastewater treatment have been developed, such as chlorination, ozonation, and biodegradation. However, those methods still have several disadvantages, including high operational costs and relatively difficult to execute [3]. Therefore, one alternative for processing textile waste is to use the photocatalytic principle using a photocatalyst [4].

One of the most commonly used photocatalysts is TiO_2 . TiO_2 is a semiconductor with high photocatalytic

activity, non-toxic, relatively inexpensive, and has good stability in aqueous solutions [5]. TiO_2 is a polymorph with large bandgap values of 3.20, 3.02, and 2.96 eV for anatase, rutile, and brookite phases, respectively [6]. Anatase normally exists in the sol-gel product, while brookite is formed as a by-product of precipitation under the acidic condition at low temperature. Pure brookite has a rather difficult preparation method than anatase [7]. Among other polymorphs, anatase phase of TiO_2 is considered to exhibit the best photocatalytic activity based on the dynamics of charge carriers, chemical properties, and activity in photocatalytic degradation of organic compounds [8]. With a bandgap value of 3.20 eV, the maximum wavelength absorption of anatase is at the range of 200–400 nm, in which the UV region included. The sunlight spectrum consists of 5–7% of UV light, 46% of visible light, and 47% of infrared radiation. Therefore, modification of TiO_2 is necessary to shift the absorption to the visible-light region to increase its photocatalytic activity [9].

TiO₂ modification is performed with different methods, including by doping using transition metals [10] and coupling TiO₂ with other semiconductors [11]. TiO₂ doping with Co²⁺ transition metal has a higher photocatalytic activity than pure TiO₂ and shifts the absorption to the direction of visible light [12-13]. The higher content of the Co dopant added to TiO₂ is able to reduce bandgap value from 3.20 to 2.50 eV [14].

Zirconia (ZrO₂) has a good thermal and chemical stability, excellent strength, and high stability against photo-corrosion, thus making it a promising photocatalyst [15]. ZrO₂ coupled with TiO₂ (ZrO₂-TiO₂, ZrTiO₄) can produce a composite with higher photocatalytic activity compared to pure TiO₂, smaller bandgap than pure ZrO₂, and good thermal stability [16]. Syoufian et al. successfully synthesized photo-active zirconium titanate hollow spheres through the sol-gel method using sulfonated polystyrene as the template [17]. Doping of iron and copper into the ZrTiO₄ structure is proven to broaden its absorption spectrum onto visible region [18-19].

In this research, Co-doped ZrTiO₄ was synthesized by the sol-gel method. The sol-gel method was chosen because it offers several advantages, such as an easy process, simple equipment, homogeneous phase, the ability to control the crystal size, nano-sized powder with high purity, and low-temperature condition [20-21]. Various contents of cobalt dopant were applied to study their performance in shifting the absorption of Co-doped ZrTiO₄. Embedding the Co-doped TiO₂ on the surface of ZrO₂ was conducted to inhibit the anatase-to-rutile transformation. Higher calcination temperatures were applied to study the stability of the anatase phase under ZrO₂ presence.

■ EXPERIMENTAL SECTION

Materials

Titanium(IV) tetraisopropoxide (TTIP) (97%, Sigma-Aldrich) was used as the precursor of TiO₂. Zirconia fine powder (Jiaozuo Huasu) and cobalt(II) sulfate heptahydrate (CoSO₄·7H₂O) (Merck) were the source of ZrO₂ matrix and Co dopant, respectively. Absolute ethanol (Merck) and demineralized water (Jaya Sentosa) were chosen as solvents.

Instrumentation

The crystal structure of the material was analyzed by X-ray powder diffractometer (XRD) PANalytical X'Pert PRO MRD instrument with CuKα radiation. Fourier-Transform Infrared Spectrometer (FT-IR) analysis was conducted using Thermo Nicolet iS10. Specular Reflectance UV-Vis spectrophotometer (SRUV) UV1700 Pharmaspec was used to measure the ultraviolet and visible (UV-Vis) absorption of composites. Surface structure was observed with scanning electron microscope equipped with energy dispersive X-ray spectrometer (SEM-EDS) FlexSEM1000.

Procedure

Co-doped ZrTiO₄ was synthesized by the sol-gel method. 2.5 mL of titanium tetraisopropoxide (TTIP) precursor was dissolved in 25 mL of absolute ethanol and stirred for 30 min. 1 g of ZrO₂ powder and a certain amount of CoSO₄·7H₂O with various concentrations (0, 1, 3, 5, 7, and 9% (Co wt./Ti wt.)) were dissolved together in 25 mL of demineralized water. Diluted TTIP was added dropwise into aqueous ZrO₂-CoSO₄·7H₂O suspension. The mixture was further stirred for 30 min and separated by centrifugation at 2000 rpm for 1 h. The obtained solid was aged in the open air for 24 h and then heated at 80 °C for 24 h. Composites with various Co dopant contents were calcined at 500 °C for 4 h. The composite with 5% of dopant content was calcined at 700 and 900 °C to observe the influence of calcination temperature. All samples were characterized by using XRD, FTIR, SEM-EDS, and SRUV spectroscopy.

■ RESULTS AND DISCUSSION

Characterization of the crystalline phase was investigated by comparing the pattern of synthesized materials with references. Fig. 1 shows diffraction patterns of Co-doped ZrTiO₄ with various Co contents calcined at 500 °C. Diffraction patterns of composites show that the highest peaks belong to the two crystal phases, the anatase phase of TiO₂ and the monoclinic phase of ZrO₂. The anatase peaks were observed at 25° and 48°, while the monoclinic peaks were observed at 28° and 31°. Characteristic diffraction peaks of TiO₂ anatase

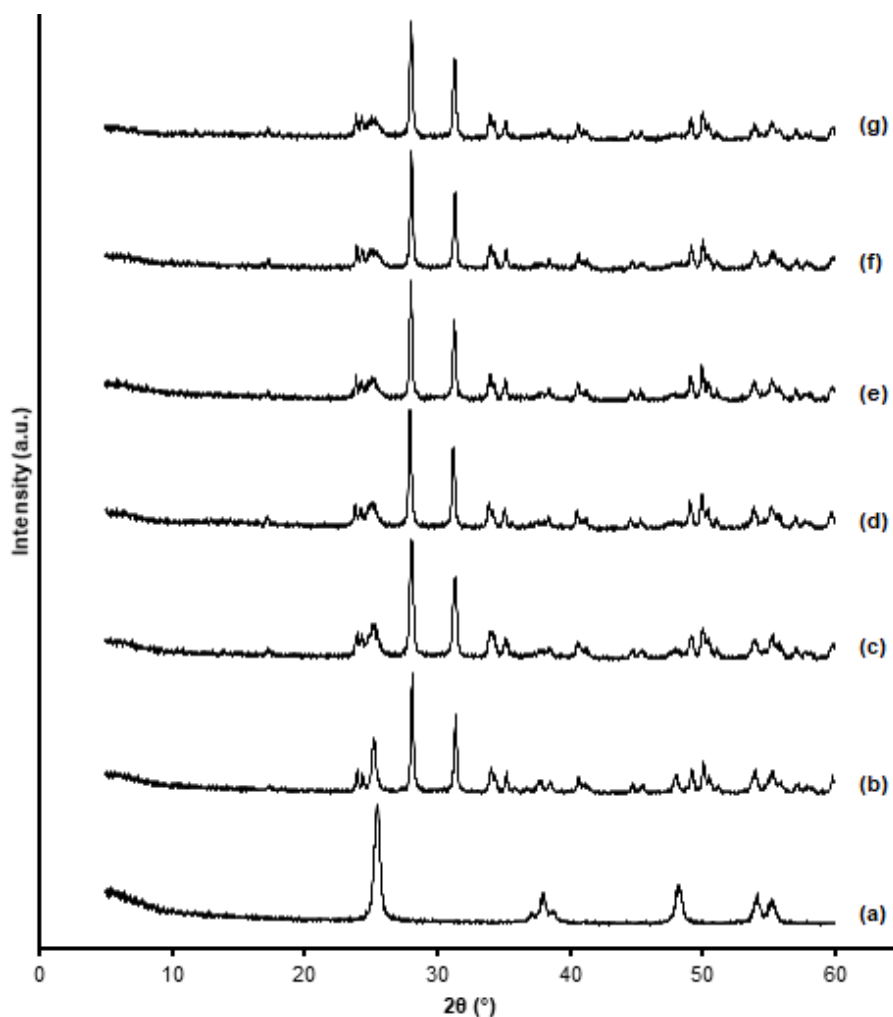


Fig 1. Diffraction patterns of (a) TiO_2 , and Co-doped ZrTiO_4 with (b) 0, (c) 1, (d) 3, (e) 5, (f) 7, and (g) 9% (Co wt./Ti wt.) of Co contents calcined at 500 °C

phase (ICDD: 00-001-0562) appear at 25° (d_{101}), 37° (d_{103}), and 48° (d_{200}). On the other hand, characteristic diffraction peaks of ZrO_2 monoclinic structure (ICDD: 00-036-0420) appear at 28° (d_{101}), 31° (d_{111}), and 34° (d_{002}). There was a decrease in the peak intensity of anatase along with an increase in Co dopant content. The higher contents of Co dopant add more Co atoms entering the crystal lattice. This causes the crystal structures to be irregular and less crystalline.

Fig. 2 shows diffraction patterns of 5% Co-doped ZrTiO_4 with various calcination temperatures and the reference material of TiO_2 calcined at 500 °C. The XRD patterns of TiO_2 and Co-doped ZrTiO_4 calcined at 500 °C show the peaks of two crystalline phases, anatase and monoclinic. The diffraction pattern of Co-doped ZrTiO_4

calcined at 700 °C shows that there was a phase transformation from anatase to rutile, as seen by the appearance of rutile peaks at 27° and 35° (ICDD: 00-004-0551; 27° (d_{110}), 36° (d_{101}), and 54° (d_{211})). The intensity of rutile patterns was higher in Co-doped ZrTiO_4 calcined at 900 °C, which corresponds with the result of previous works [18-19,22]. Anatase peak at 25° was visible with low intensity in the composites calcined at 500 and 700 °C, indicating that the presence of ZrO_2 , which is dominant as supporting material, can inhibit the anatase to rutile transformation [23].

Fig. 3 presents the FTIR spectra of Co-doped ZrTiO_4 with various Co contents and TiO_2 as a reference. All the samples were calcined at 500 °C. The results are in correspond with previous work [24], in which the

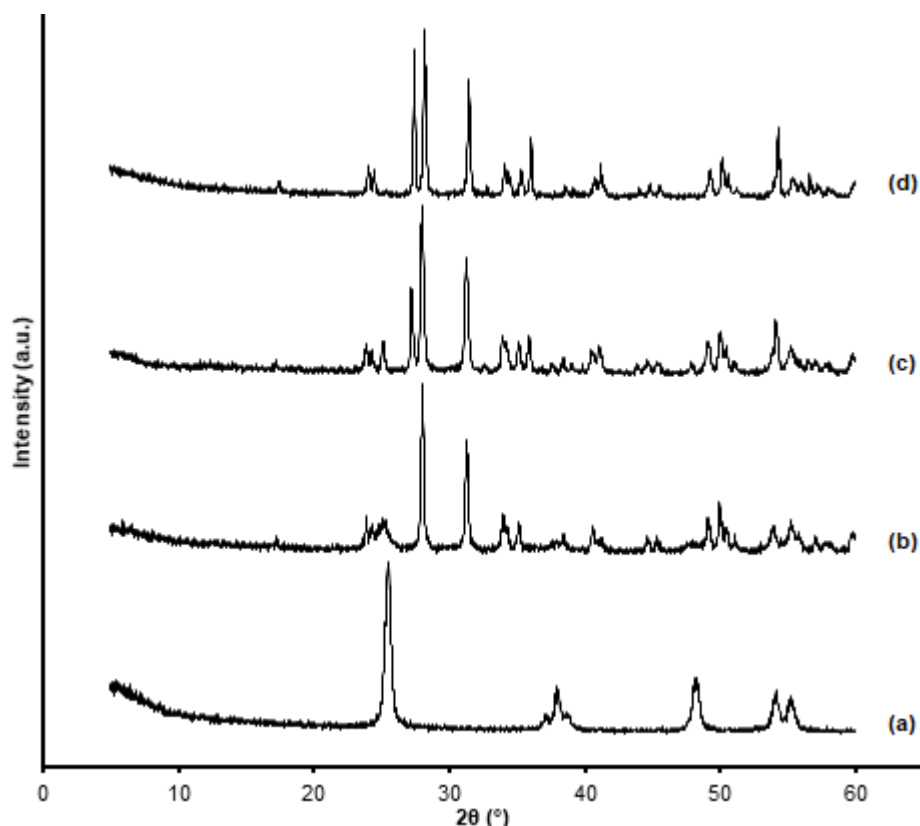


Fig 2. Diffraction patterns of (a) TiO₂ calcined at 500 °C, and 5% Co-doped ZrTiO₄ calcined at (b) 500, (c) 700, and (d) 900 °C

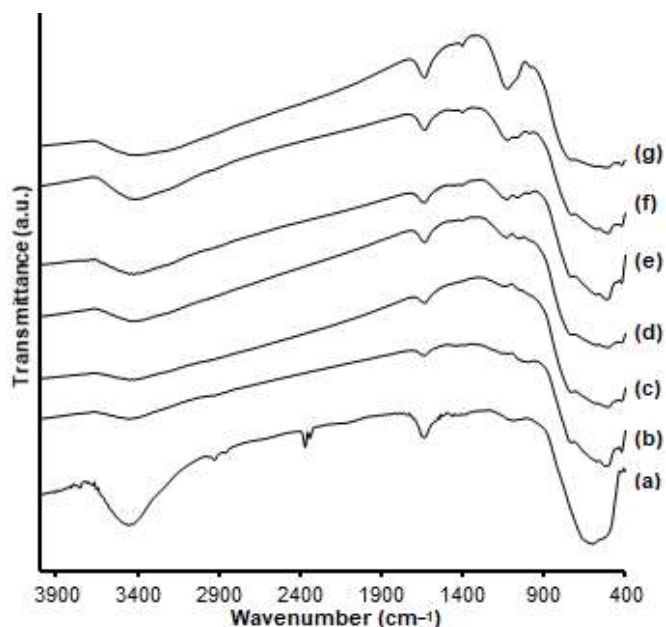


Fig 3. FTIR spectra of (a) TiO₂, and Co-doped ZrTiO₄ with (b) 0, (c) 1 (d) 3, (e) 5, (f) 7, (g) 9% (Co wt./Ti wt.) of Co contents calcined at 500 °C

absorption of the Ti–O–Ti bond at the wavenumber of 400–600 cm⁻¹ tended to weaken as the Co content increased. This indicates that cobalt had been successfully doped on composites. The Ti–O–Ti vibration is hindered by the presence of Co dopant on the ZrTiO₄ structure. Absorption at a wavenumber of 1635 cm⁻¹ shows the –OH bending vibration of H₂O, and the absorption at a wavenumber of 3300–3700 cm⁻¹ belongs to the –OH stretching vibration of H₂O. These are also in correspond with the results of previous work [25]. There was a vibrational band on Co-doped ZrTiO₄ spectra that appeared and elevated around 1100 cm⁻¹ as the cobalt content increased. The band is possibly designated to be either Co–O–Zr or Co–O–Ti vibration, or may even possibly be both.

Fig. 4 presents the FTIR spectra of 5% Co-doped ZrTiO₄ with various calcination temperatures together with TiO₂ calcined at 500 °C as reference. In general, the spectra show that composites with higher calcination

temperatures had decreasing stretching vibration of –OH ($3300\text{--}3700\text{ cm}^{-1}$) and bending vibration of H–O–H (1635 cm^{-1}) in H_2O (the intensity decreased and the peak widened). These are caused by the decrease of water content in the synthesized material due to the high heating temperature during the calcination process. The absorption of the Ti–O–Ti bond also decreased as calcination temperature increased. This is caused by the phase transformation from anatase to rutile. The bond length of the anatase phase is shorter than the rutile phase, thus resulting in different vibrational energy.

The SEM image of doped ZrTiO_4 containing 3% of cobalt content calcined at $500\text{ }^\circ\text{C}$ is shown in Fig. 5, and its corresponding EDS analysis is presented in Table 1. EDS analysis shows that the Co dopant and TiO_2 were successfully embedded on the surface of ZrO_2 . The synthesized composite appears to be in microsize with an estimated particle diameter of around $2\text{--}5\text{ }\mu\text{m}$.

Fig. 6 shows the absorption spectra of Co-doped ZrTiO_4 , whereas the corresponding bandgap values of Co-doped ZrTiO_4 are shown in Table 2. Based on the UV-Vis absorption results, turning points of synthesized materials had already at a wavelength higher than 400 nm (visible range). All synthesized composites show a lower bandgap than TiO_2 . The results are in correspond with the previous work [14], in which Co addition had succeeded in reducing the bandgap value from 3.14 eV to 2.94 eV with the optimum content of 3%. While at Co dopant contents more than 3%, the absorption edge returned to the lower wavelength. The bandgap value increased because of the diminishing doping effect and emerging heterojunction effect. The bandgap of 5% Co-doped ZrTiO_4 calcined at 700 and $900\text{ }^\circ\text{C}$ are lower than that of $500\text{ }^\circ\text{C}$. Based on the diffraction data, the rutile phase of 5% Co-doped ZrTiO_4 emerged as calcination temperature arose. Higher calcination temperatures shift the bandgap

of Co-doped ZrTiO_4 due to the higher content of the rutile phase, which has a lower bandgap than anatase. Our results show that all Co-doped ZrTiO_4 had relatively small bandgap and should be a potential photocatalyst under visible light application.

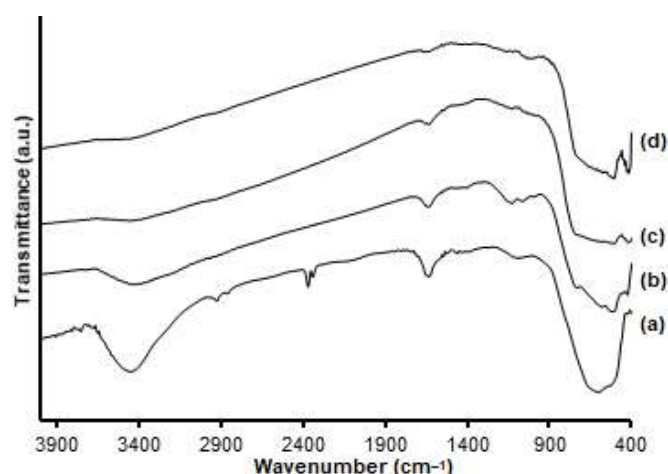


Fig 4. FTIR spectra of (a) TiO_2 calcined at $500\text{ }^\circ\text{C}$, and 5% Co-doped ZrTiO_4 calcined at (b) 500 , (c) 700 , and (d) $900\text{ }^\circ\text{C}$

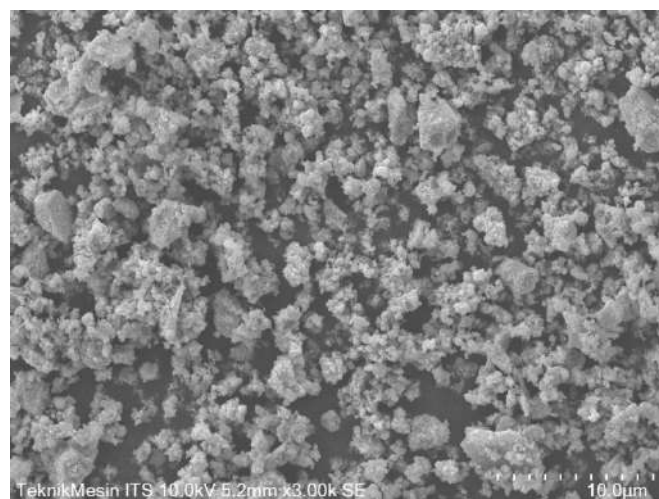


Fig 5. SEM image of 3% Co-doped ZrTiO_4 calcined at $500\text{ }^\circ\text{C}$

Table 1. EDS analysis of 3% Co-doped ZrTiO_4 calcined at $500\text{ }^\circ\text{C}$

Element	Weight %	Atomic %	Net Int.	Error %	K ratio	Z	A	F
O K	42.68	74.91	334.55	9.87	0.0629	1.1622	0.1268	1.0000
Zr L	30.22	9.30	766.97	1.12	0.2486	0.8231	0.9990	1.0012
Ti K	26.14	15.32	782.62	2.05	0.2257	0.9196	0.9301	1.0101
Co K	0.96	0.46	16.23	5.41	0.0086	0.8882	0.9616	1.0454

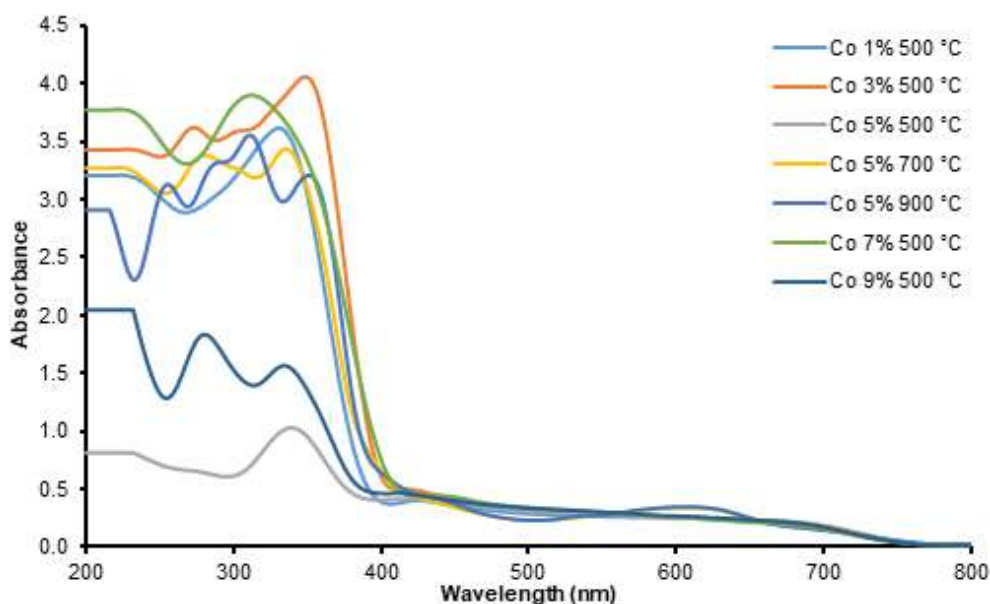


Fig 6. UV-Vis absorption spectra of various Co-doped ZrTiO₄

Table 2. Bandgap data of TiO₂ and Co-doped ZrTiO₄

Composites	E _g (eV)
TiO ₂ 500 °C	3.14
Co-ZrTiO ₄ 1% 500 °C	2.96
Co-ZrTiO ₄ 3% 500 °C	2.94
Co-ZrTiO ₄ 5% 500 °C	3.02
Co-ZrTiO ₄ 5% 700 °C	2.97
Co-ZrTiO ₄ 5% 900 °C	2.94
Co-ZrTiO ₄ 7% 500 °C	3.03
Co-ZrTiO ₄ 9% 500 °C	3.06

CONCLUSION

Synthesis of Co-doped ZrTiO₄ as a potential visible-light responsive photocatalyst by the sol-gel method had been successfully conducted. This was proved by the UV-Vis absorption spectra which show the absorption edge of composites at a wavelength more than 400 nm (visible range). The addition of Co dopants shifts the absorption of ZrTiO₄ to the visible light region. The optimum content of the Co dopant is obtained at 3% (Co wt./Ti wt.) with an optimum calcination temperature of 500 °C to give the bandgap value of 2.94 eV. The presence of ZrO₂ in composites inhibits the phase transformation of anatase to rutile at high temperatures (700 and 900 °C). All materials have displayed visible-light-response as a potential photocatalyst.

ACKNOWLEDGMENTS

We would like to express our gratitude to The Ministry of Research, Technology and Higher Education of the Republic of Indonesia for their support on this work through PDUPT 2019 Grant (2554/UN1.DITLIT/DIT-LIT/LT/2019).

REFERENCES

- [1] dos Santos, A.B., Cervantes, F.J., and van Lier, J.B., 2007, Review paper on current technologies for decolourisation of textile wastewaters: Perspectives for anaerobic biotechnology, *Bioresour. Technol.*, 98 (12), 2369–2385.
- [2] Mirjalili, M., Nazarpour, K., and Karimi, L., 2011, Eco-friendly dyeing of wool using natural dye from weld as co-partner with synthetic dye, *J. Cleaner Prod.*, 19 (9-10), 1045–1051.
- [3] Utubira, Y., Wijaya, K., Triyono, T., and Sugiharto, E., 2006, Preparation and characterization of TiO₂-zeolite and its application to degrade textile wastewater by photocatalytic method, *Indones. J. Chem.*, 6 (3), 231–237.
- [4] Alinsafi, A., Evenou, F., Abdulkarim, E.M., Pons, M.N., Zahraa, O., Benhammou, A., Yaacoubi, A., and Nejmeddine, A., 2007, Treatment of textile

- industry wastewater by supported photocatalysis, *Dyes Pigm.*, 74 (2), 439–445.
- [5] Qamar, M., Saquib, M., and Muneer, M., 2005, Photocatalytic degradation of two selected dye derivatives, chromotrope 2B and amido black 10B, in aqueous suspensions of titanium dioxide, *Dyes Pigm.*, 65 (1), 1–9.
- [6] Wunderlich, W., Oekermann, T., Miao, L., Hue, N.T., Tanemura, S., and Tanemura, M., 2004, Electronic properties of nano-porous TiO₂- and ZnO-thin films-comparison of simulations and experiments, *J. Ceram. Process. Res.*, 5 (4), 343–354.
- [7] Di Paola, A., Bellardita, M., and Palmisano, L., 2013, Brookite, the least known TiO₂ photocatalyst, *Catalysts*, 3 (1), 36–73.
- [8] Li, G., Chen, L., Graham, M.E., and Gray, K.A., 2007, A comparison of mixed phase titania photocatalysts prepared by physical and chemical methods: The importance of the solid-solid interface, *J. Mol. Catal. A: Chem.*, 275 (1-2), 30–35.
- [9] Rehman, S., Ullah, R., Butt, A.M., and Gohar, N.D., 2009, Strategies of making TiO₂ and ZnO visible light active, *J. Hazard. Mater.*, 170 (2-3), 560–569.
- [10] Huo, J., Hu, Y., Jiang, H., Hou, X., and Li, C., 2014, Continuous flame synthesis of near surface nitrogen doped TiO₂ for dye-sensitized solar cells, *Chem. Eng. J.*, 258, 163–170.
- [11] Li, Z., Wnetrzak, R., Kwapinski, W., and Leahy, J.J., 2012, Synthesis and characterization of sulfated TiO₂ nanorods and ZrO₂/TiO₂ nanocomposites for the esterification of biobased organic acid, *ACS Appl. Mater. Interfaces*, 4 (9), 4499–4505.
- [12] Siddhapara, K.S., and Shah, D.V., 2014, Study of photocatalytic activity and properties of transition metal ions doped nanocrystalline TiO₂ prepared by sol-gel method, *Adv. Mater. Sci. Eng.*, 2014, 462198.
- [13] Choi, J., Park, H., and Hoffmann, M.R., 2010, Effects of single metal-ion doping on the visible-light photoreactivity of TiO₂, *J. Phys. Chem. C*, 114 (2), 783–792.
- [14] Siddhapara, K., and Shah, D., 2012, Characterization of nanocrystalline cobalt doped TiO₂ sol-gel material, *J. Cryst. Growth*, 352 (1), 224–228.
- [15] Zhang, X., and Liu, Q., 2008, Visible-light-induced degradation of formaldehyde over titania photocatalyst co-doped with nitrogen and nickel, *Appl. Surf. Sci.*, 254 (15), 4780–4785.
- [16] Kim, J.Y., Kim, C.S., Chang, H.K., and Kim, T.O., 2011, Synthesis and characterization of N-doped TiO₂/ZrO₂ visible light photocatalysts, *Adv. Powder Technol.*, 22 (3), 443–448.
- [17] Syoufian, A., Manako, Y., and Nakashima, K., 2015, Sol-gel preparation of photoactive srilankite-type zirconium titanate hollow spheres by templating sulfonated polystyrene latex particles, *Powder Technol.*, 280, 207–210.
- [18] Andita, K.R., Kurniawan, R., and Syoufian, A., 2019, Synthesis and characterization of Cu-doped zirconium titanate as a potential visible-light responsive photocatalyst, *Indones. J. Chem.*, 19 (3), 761–766.
- [19] Kurniawan, R., Sudiono, S., Trisunaryanti, W., and Syoufian, A., 2019, Synthesis of iron-doped zirconium titanate as a potential visible-light responsive photocatalyst, *Indones. J. Chem.*, 19 (2), 454–460.
- [20] Wellia, D.V., Xu, Q.C., Sk, M.A., Lim, K.H., Lim, T.M., and Tan, T.T.Y., 2011, Experimental and theoretical studies of Fe-doped TiO₂ films prepared by peroxo sol-gel method, *Appl. Catal., A*, 401, 98–105.
- [21] Tomar, L.J., Bhatt, P.J., Desai, R.K., and Chakrabarty, B.S., 2014, Effect of preparation method on optical and structural properties of TiO₂/ZrO₂ nanocomposite, *J. Nanotechnol. Adv. Mater.*, 2 (1), 27–33.
- [22] Samet, L., Nasseur, J.B., Chtourou, R., March, K., and Stephan, O., 2013, Heat treatment effect on the physical properties of cobalt doped TiO₂ sol-gel materials, *Mater. Charact.*, 85, 1–12.
- [23] Nankya, R., and Kim, K.N., 2016, Sol-gel synthesis and characterization of Cu-TiO₂ nanoparticles with enhanced optical and photocatalytic properties, *J. Nanosci. Nanotechnol.*, 16 (11), 11631–11634.
- [24] Choudhury, B., Choudhury, A., Maidul Islam, A.K.M., Alagarsamy, P., and Mukherjee, M., 2011,

Effect of oxygen vacancy and dopant concentration on the magnetic properties of high spin Co^{2+} doped TiO_2 nanoparticles, *J. Magn. Magn. Mater.*, 323 (5), 440–446.

[25] Deng, Q.R., Xia, X.H., Guo, M.L., Gao, Y., and Shao, G., 2011, Mn-doped TiO_2 nanopowders with remarkable visible light photocatalytic activity, *Mater. Lett.*, 65 (13), 2051–2054.

Kinetic Study of HTPB (Hydroxyl Terminated Polybutadiene) Synthesis Using Infrared Spectroscopy

Heri Budi Wibowo^{1,*}, Widhi Cahya Dharmawan¹, Ratih Sanggra Murti Wibowo², and Adi Yulianto²

¹Indonesian National Institute of Aeronautics and Space – LAPAN, Jl. Pemuda Persil No. 1, Jakarta 13220, Indonesia

²Faculty of Engineering, Universitas Gadjah Mada, Jl. Grafika No. 2, Yogyakarta 55281, Indonesia

* Corresponding author:

email: heribw@gmail.com

Received: September 21, 2019

Accepted: December 16, 2019

DOI: 10.22146/ijc.49863

Abstract: A kinetic study of HTPB synthesis by radical polymerization of butadiene with hydrogen peroxide initiator was conducted using infrared spectroscopy. HTPB conversion was determined based on the conjunction termination rate constant, and all polymerization kinetics were evaluated to identify the constant. All polymerization steps (decomposition, initiation, propagation, conjunction, and proportional termination) can be evaluated based on polymer conversion and functionality from data provided by infrared spectroscopy. The investigation variables included the initial molar ratio of initiator to monomer (H_2O_2 /butadiene) and the reaction temperature. These steps were assumed as the first-order reactions, giving constant reaction rates of k_{d_1} , k_{d_2} , k_p , k_t , k_{tc} , and k_{td} . The reaction rates obtained for these constants were $4.2 \times 10^{-5} \text{ sec}^{-1}$, 8.9×10^{-4} , 7.7×10^3 , 8.5×10^7 , 3.2×10^7 and $5.3 \times 10^7 \text{ L mol}^{-1} \text{ sec}^{-1}$, respectively, with activation energy of 7608, 14188, 2247, 105, 87 and 135 kJ mol^{-1} , respectively. The determining step of the reaction rate was identified as the initiation reaction. HTPB conversion can be measured if all polymerization kinetics constants have been evaluated.

Keywords: polymerization; HTPB; butadiene

■ INTRODUCTION

Polyurethane based on hydroxyl-terminated polybutadiene (HTPB), in recent years, has been used as a solid propellant binder for satellite-launcher-motor boosters and ICBM (intercontinental ballistic missile) motors [1-2], because it has good mechanical properties at rocket operating temperatures. Polyurethane based on HTPB is synthesized by copolymerization of HTPB and isocyanates, such as toluene diisocyanate (TDI) or isophorone diisocyanate (IPDI). Research into polyurethane based on HTPB as a propellant binder has been conducted since 1945 [3]. Initially, this research focused on HTPB/isocyanate composition related to its mechanical and viscous-elasticity properties. Subsequent research has focused on the effect of HTPB structures such as chain length, isomers, hydroxyl value, and molecular weight distribution. In the last ten years, research into polyurethane based on HTPB has looked at increasing the energetic properties of the binder by

substituted HTPB with nitro, azide, and oxy functional groups [4-7]. HTPB is a polybutadiene with two chains of hydroxyl groups that have been particularly studied in its use in propellant materials. HTPB can be synthesized by ionic, ionic-coordination, and radical polymerization of butadiene. HTPB produced by ionic and ionic-coordination polymerization has narrow molecular distribution weight, but this type of production requires a highly complex reaction, which is expensive to carry out [3-5]. In contrast, HTPB produced by radical polymerization has broad molecular weight distribution, but its formation reaction is simple and cheap. HTPB is, therefore, generally produced by radical polymerization of butadiene using a hydrogen peroxide initiator [3,8].

The synthesis mechanism for HTPB by radical polymerization of butadiene with hydrogen peroxide initiator is (1) decomposition of hydrogen peroxide producing hydroxyl radicals, (2) monomer initiation by hydroxyl radicals producing radical monomers, (3) propagation of radical monomer growth with

monomers producing radical polymers, (4) termination of radical polymers producing 'dead polymers' [9-10]. Termination steps are simultaneous mechanisms involving both conjunction and disproportional reactions. Conjunction termination would produce HTPB, while disproportional termination would produce mono hydroxyl polybutadiene (HPB) [4]. Given this mechanism, the study of the kinetics of HTPB synthesis requires at least two data sets to be retrieved. The initiation and termination steps are fast reactions [8], and data kinetics are limited by polymer weight and average molecular weight. Therefore, the difficulty is encountered in data retrieval, given the fast reaction rate of the process. For this reason, it is assumed that in the kinetics of HTPB synthesis, termination and initiation rates are the same, and simultaneous conjunction and disproportional termination are ignored [10].

This approach resembles the olefin polymerization kinetics for rubber applications [7-8]. The kinetic of radical polymerization of butadiene and other diene compounds and olefins for rubber applications has been explored since 1940 [11-12]. The polybutadiene in rubber applications has hydrogen-ended functional groups, and polymerization usually uses a peroxide initiator, a redox system, and other strong oxidizers. Wibowo assumes that the ratio of HTPB and mono hydroxyl polybutadiene (HPB) conversion is constant, but this data cannot be satisfied statically [13]. The aim of this research is to explore all the kinetic steps of HTPB synthesis using at least three sets of data retrieved in a manner suitable for fast reaction rates.

The kinetics of radical polymerization can be evaluated based on the presence of increased polymers or decreased monomers. Decreased monomers can be observed from their pressure [14-15], while increased polymers can be evaluated from their weight and chain extent or molecular weight. Unfortunately, decreased monomers and increased polymers cannot be simultaneously identified. The polymer molecular weight can be evaluated via colligative property measurement, viscosity, light scattering, size exclusion chromatography and gel permeation chromatography [16-18]. The polymer extent of a reaction can also be identified by

infrared spectrometry, based on double bond absorption and type of isomer (cis, trans and vinyl isomers) [12,14,19]. Kinetic study of HTPB synthesis by infrared spectroscopy is the most commonly used method because it is fast, cheap and simple to perform.

Infrared spectrometry using adsorption infrared spectra at wavenumber 2250 cm^{-1} can be applied to determine hydroxyl value and functionality of polybutadiene and HTPB [20-22]. The functionality of HTPB is a ratio of average hydroxyl chain to polybutadiene structure. Based on this functionality, the ratio of mono hydroxyl polybutadiene and hydroxyl terminated polybutadiene (HTPB) can be estimated and infrared analysis of polybutadiene can be used to determine the extent of reaction and functionality. All of the constant reaction steps in HTPB synthesis should be evaluated using at least two kinetic data items, and this research, therefore, includes the conjunction and disproportional steps in studying the kinetics of HTPB synthesis via infrared spectroscopy to describe HTPB conversion, average functionality, and molecular weight distribution. Through this approach, all kinetic data for HTPB synthesis can be explored.

In HTPB synthesis by radical polymerization of butadiene using a hydrogen peroxide initiator, butadiene is radically polymerized via initiation, propagation and termination stages [6-7]. The initiation stage involves the dissociation of hydrogen peroxide (H_2O_2) to produce hydroxyl radicals (OH^\bullet) which then react with t monomer butadiene (C_4H_6), producing radical monomer chains with hydroxyl groups ($\text{HO}-\text{C}_4\text{H}_6^\bullet$). The propagation stage involves the growth of the polymer. The active radical monomers ($\text{HO}-\text{C}_4\text{H}_6^\bullet$) react with other monomers to produce radical active dimers ($\text{HO}-(\text{C}_4\text{H}_6)_2^\bullet$). Polymer activity develops by the addition of monomer butadiene to produce higher polymer radical actives ($\text{HO}-(\text{C}_4\text{H}_6)_n^\bullet$). The growth activity of the polymer radicals is terminated by reactions between polymer radicals producing dead polymers, via the active polymer radical ($\text{HO}-(\text{C}_4\text{H}_6)_x$) reacting with the other active radical polymers ($\text{HO}-(\text{C}_4\text{H}_6)_y^\bullet$). The termination can proceed by combinatorial-type reactions producing HTPB with two

end hydroxyl chains ($\text{HO}-(\text{C}_4\text{H}_6)_{x+y}-\text{OH}$) or proportional-type reactions producing two dead polymers, $\text{HO}-(\text{C}_4\text{H}_6)_x$ and $\text{HO}-(\text{C}_4\text{H}_6)_y$, with one of the dead polymers having a double bond. Functionality is identified as the total of dead polymers of both two-hydroxyl-chained (HTPB) and one-hydroxyl-chained (mono hydroxyl polybutadiene) types. Based on the enthalpy of formation, disproportional-type reactions need higher energy than combinatorial-type reactions [8-9]. By means of this kinetic model, all of the kinetic data (rate constants), including the combinatorial and proportional steps, can be effectively evaluated.

■ EXPERIMENTAL SECTION

Materials

Butadiene 98% used in this research was produced by Aneka Gas Co Ltd., Jakarta, Indonesia and was distilled to remove tert-butylcatechol. The hydrogen peroxide used was in pure analysis grade, and the solvent used was toluene.

Instrumentation

The reactor used was an autoclave of 1-L capacity equipped with a stirrer and hot fluid control. A closed FTIR cuvette was connected to the reactor and the solution from the reactor was continuously circulated to it.

The in-situ HTPB product was identified by FTIR (Fourier transform infrared spectrometry). FTIR outputs were measured at ambient conditions at the wavenumber range of $400\text{--}4000\text{ cm}^{-1}$ using an FT-IR spectrometer (Prestige-21). HTPB was identified at wavenumber of $3500, 1700, 710, 790,$ and 910 cm^{-1} for specific absorption of hydroxyl and CH, and cis, trans and vinyl isomers [6]. HTPB was observed for absorption bending vibrations (wagging) of the CH groups in the cis-HTPB unit at a wavenumber of 730 cm^{-1} , for out-of-plane (wagging) vibrations of the CH_2 groups near the double bond of the vinyl-HTPB units at 910 cm^{-1} , and for out-of-plane (wagging) vibrations of the CH groups near the double bonds in trans-HTPB units at 970 cm^{-1} .

The polymer concentration was measured for absorbance at wavenumber 1750 cm^{-1} via bending

vibrations (wagging) of the CH groups, then extrapolated to a standard curve using Beer's law [12]. The standard solution was HTPB in toluene at concentrations of $1.0 \times 10^{-5}, 5.0 \times 10^{-5}, 1.0 \times 10^{-4}, 5.0 \times 10^{-4}$ and $1.0 \times 10^{-3}\text{ mol L}^{-1}$.

The hydroxyl number of HTPB was determined by observing FTIR uptake values at wavenumber 3450 cm^{-1} as specific uptake for hydroxyl groups [1]. The absorbance of hydroxyl groups was then extrapolated with standard alcohol 1,4-butanediol and 1-butanol. In this research, standard alcohol was a mixture of 1,4-butanediol and 1-butanol (mol/mol) at 1.0, 1.1, 1.2, 2.0. The functionality of 1-butanol is 1 and 1,4-butanediol is 2.

Procedure

Butadiene was reacted with hydrogen peroxide in a 1-L autoclave for 60 min in inert nitrogen conditions. The reaction was isothermal and conducted at $100\text{ }^\circ\text{C}$ and 25 bar pressure. The extent of the reaction and functionality was measured by FTIR spectroscopy at wavenumber of $3450, 730, 790$ and 910 cm^{-1} [1,4,7]. Reaction parameters were initiator and reaction temperatures.

The effect of the initiator on polymerization kinetics was studied by adjusting the initial H_2O_2 /butadiene ratio (mol/mol) to 10, 20, 30 and 32%, and the reaction was carried out at $100\text{ }^\circ\text{C}$, 25 bar, and stirrer speed of 100 rpm. The initial butadiene concentration was 1 M. The effect of reaction temperature on polymerization kinetics was studied by adjusting the reaction temperature to 100, 110 and $118\text{ }^\circ\text{C}$ at a pressure of 25 bar, initial H_2O_2 /butadiene ratio of 10%, and stirrer speed of 100 rpm.

Kinetic model

The polymerization of butadiene with hydrogen peroxide initiator occurs through free radical mechanisms [8]. The reaction is started by the dissociation of hydrogen peroxide to form a pair of hydroxyl radicals (OH^\bullet) with dissociation rate constant of k_d . The reaction of hydroxyl radical (OH^\bullet) and monomer butadiene ($\text{H}_2\text{C}=\text{CH}-\text{CH}=\text{CH}_2$) produces the radical-ended monomer $^\bullet\text{H}_2\text{C}-\text{CH}=\text{CH}-\text{CH}_2\text{OH}$ with

adding monomer reaction rate of k_a . The initiation step, therefore, comprises the dissociation of hydrogen peroxide and the adding of monomer reaction. The propagation reaction is started by radical-ended dimer $\bullet(\text{H}_2\text{C}-\text{CH}=\text{CH}-\text{CH}_2)_2\text{OH}$ production from radical-ended monomer $\bullet\text{H}_2\text{C}-\text{CH}=\text{CH}-\text{CH}_2\text{OH}$ and another monomer. The radical-ended dimer then reacts with another monomer to form radical-ended trimer $\bullet(\text{H}_2\text{C}-\text{CH}=\text{CH}-\text{CH}_2)_3\text{OH}$. These propagation reactions occur repeatedly so that the radical-ended polymer acquires a longer chain length $\bullet(\text{H}_2\text{C}-\text{CH}=\text{CH}-\text{CH}_2)_x\text{OH}$. The propagation rate is constant at steady-state and radical-ended polymer reactivity in the chain growth is the same. Individual propagation reactions are identified as rp_1, rp_2, \dots, rp_i , following the extent of the reaction. These propagation reaction steps have the same reaction rates because the activity of the radicals is the same (their activity is not affected by the size of the molecule). The radical-ended polymer reactivity in chain growth is the same. Therefore, all propagation stages can be characterized using the same reaction rate constant of k_p [8-10]. The termination step occurs in simultaneous combinatorial and proportional reactions [7]. $\bullet\text{H}_2\text{C}-\text{CH}=\text{CH}-\text{CH}_2(\text{H}_2\text{C}-\text{CH}=\text{CH}-\text{CH}_2)_x-\text{OH}$ and other polymer-ended radicals produce mono hydroxyl polybutadiene with a double bond, $\text{H}_2\text{C}-\text{C}=\text{H}-\text{CH}=\text{CH}_2(\text{H}_2\text{C}-\text{C}=\text{H}-\text{CH}-\text{CH}_2)_x-\text{OH}$, and another mono hydroxyl polybutadiene with a single bond $\text{H}_3\text{C}-\text{CH}=\text{CH}-\text{CH}_2(\text{H}_2\text{C}-\text{CH}=\text{CH}-\text{CH}_2)_x-\text{OH}$. The junction or combinatorial reaction is a covalent bond reaction of the radical-ended polymer $\bullet(\text{H}_2\text{C}-\text{CH}=\text{CH}-\text{CH}_2)_x-\text{OH}$ and the other radical-ended polymer $\bullet(\text{H}_2\text{C}-\text{CH}=\text{CH}-\text{CH}_2)_y-\text{OH}$ to produce HTPB, $\text{HO}(\text{H}_2\text{C}-\text{CH}=\text{CH}-\text{CH}_2)_{x+y}-\text{OH}$. The combinatorial and proportional termination rate constants are k_{tc} and k_{td} .

The initiator decomposition, initiation, propagation and termination reactions in the radical polymerization of butadiene are simplified as presented in Equations 1 to 5. Compound I is the initiator, R and A are butadiene monomers, RP_i are active polymers with chain length i , and RP_i and RP_jR are stable polymers bound to hydroxyl groups R with chain length j . The initiator decomposition reaction rate constant is k_d , the monomer adding rate

constant is k_a , the propagation rate constant is k_p and the termination rate constant is k_t . The combinatorial reaction rate constant in the termination reaction is k_{td} and the disproportional reaction rate constant in the termination reaction is k_{tc} . These polymerization kinetics are the assumed first order:



The reaction rate equation of initiator dissociation is expressed in Eq. (6). The reaction rate equations of the polymerization steps (initiation, propagation, and termination) are expressed in Eq. (6) to Eq. (10). Polymer concentration comprises all polymers with chain extent from $j = 0$ to $j = n$, $[\text{P}]_0 = \sum_{j=0}^n \text{P}_j$. The active radical concentration $[\text{M}]_0$ comprises all radical polymers with chain extent from $j = 0$ to $j = n$, $[\text{M}]_0 = \sum_{j=0}^n \text{RP}_j$. The termination rate constant is the sum of combination and disproportion rate constants ($k_t = k_{tc} + k_{td}$).

$$R_d = -\frac{d[\text{I}]}{dt} = 2fk_d[\text{I}] \quad (6)$$

$$R_i = -\frac{d[\text{A}]}{dt} = k_a[\text{A}][\text{P}_1] \quad (7)$$

$$R_p = -\frac{d[\text{A}]}{dt} = k_a[\text{A}][\text{P}_1] + k_p[\text{A}][\text{P}_0] \quad (8)$$

$$R_{ap} = \frac{d[\text{P}]_0}{dt} = R_i - 2k_a[\text{P}]_0 \quad (9)$$

$$R_t = -\frac{d[\text{M}]_0}{dt} = (2k_{tc} + k_{td})[\text{P}]_0^2 \quad (10)$$

Monomer A is initiated by hydroxyl radicals forming radical-ended monomers followed by continuous propagation with polymer radicals growing their size/length of chain. Through polymer radical growth, radical concentration is constant (steady-state) until the rate of radical forming is zero ($R_{ap} = 0$). Eq. (9) would express in Eq. (11).

$$[P]_0 = \left(\frac{fk_d[I]}{k_t} \right)^{1/2} \quad (11)$$

The equation of propagation rate would be expressed by substituting Eq. (11) into Eq. (7) to form Eq. (12).

$$R_p = \left(\frac{k_p}{k_t^{1/2}} \right) \left(fk_d[I]^{1/2} \right) [A] \quad (12)$$

Eq. (6) is merged with Eq. (9) then integrated with $\beta = (k_{tc}/k_t)$ and $\alpha = (-k_{td}t)$ to express initial monomer concentration $[A]_0$, expressed in Eq. (13) where M_A is the molecular formula of monomer butadiene [11]. Monomer conversion is $X = [A]/[A]_0$.

$$[A]_0 = (2 - \beta)f[I]_0(1 - \alpha) \quad (13)$$

$$M_n = \frac{([M]_0 - [M])M_A}{([P]_0 + [M]_0)} \quad (14)$$

$$M_n = \frac{A_0 X M_A}{([P]_0 + [M]_0)} \quad (15)$$

Eq. (16) is formed from merging Eq. (10), (12) and (15) and would apply to the calculation of the termination rate constant k_t . The values of k_t and β can be evaluated based on each change of average molecular weight and weight of the polymer.

$$\left(\frac{([A]_0 X M_A) / M_n}{[I]_0 \alpha} \right)^{1/2} = \left(\frac{fk_d}{k_t} \right)^{1/2} + (2 - \beta)(1 - \alpha) \left(\frac{[I]_0}{\alpha} \right)^{1/2} \quad (16)$$

The propagation rate constant k_p is calculated from Eq. (6). The constant $(k_p/k_t^{1/2})$ is calculated as the slope of plotting R_p to R_i or R_p to $(fk_d[I]_0^{1/2}[A]_0)$.

Polymer functionality (f_{OH}) is the equivalent total of hydroxyl groups bonded in the polymer (polybutadiene). Polymers are a mixture of mono hydroxyl polybutadiene (RM_i) and hydroxyl terminated polybutadiene (RM_iR) [9]. The functionality of the polymer is expressed in Eq. (17).

$$f_{OH} = \frac{(2[RM_i] + [RM_iR])}{([RM_i] + [RM_iR])} \quad (17)$$

The total polymer produced is P with $P = 2[RM_i] + [RM_iR]$. RM_i is eliminated from Eq. (17) to become Eq. (18).

$$[RM_i] = 1 - \frac{P}{f_{OH}} \quad (18)$$

The combinatorial termination rate is the increasing rate of polymer RM_iR expressed by Eq. (19). Eq. (20) is the integration of Eq. (19) with the initial condition $[RM_iR]_0 = 0$ and HTPB concentration at time t of $[RM_iR]$.

$$\frac{d[RM_iR]}{dt} = k_{td}[RM_iR] \quad (19)$$

$$\ln[RM_iR] = k_{td}t + \text{constants} \quad (20)$$

Eq. (18) is to be substituted into Eq. (20) to form Eq. (21), which is the relationship equation of the polymer produced (HTPB) and the functionality of the polymer as the time of reaction. The disproportional termination rate constant k_{td} is the slope of plotting $\ln(1 - P/f_{OH})$ as time t . The conjunction termination rate constant k_{tc} is the deviation of k_t and k_{td} ($k_{tc} = k_t - k_{td}$).

$$\ln\left(1 - \frac{P}{f_{OH}}\right) = k_{td}t \quad (21)$$

The polymer concentration was determined by the absorbance of polymers at wavenumber 910 cm^{-1} at the time of reaction.

RESULTS AND DISCUSSION

HTPB was identified by infrared spectroscopy at wavenumber $400\text{--}4000 \text{ cm}^{-1}$ and its infrared spectrum is shown in Fig. 1. The HTPB compound was identified based on infrared absorption at 3450 , 1730 , 710 , 910 , and 970 cm^{-1} , a specific absorption for the hydroxyl group, C-C bond, and C=C bond with cis, trans, and vinyl isomers [12-13]. The presence of a hydroxyl group indicates that the polybutadiene has hydroxyl groups. The

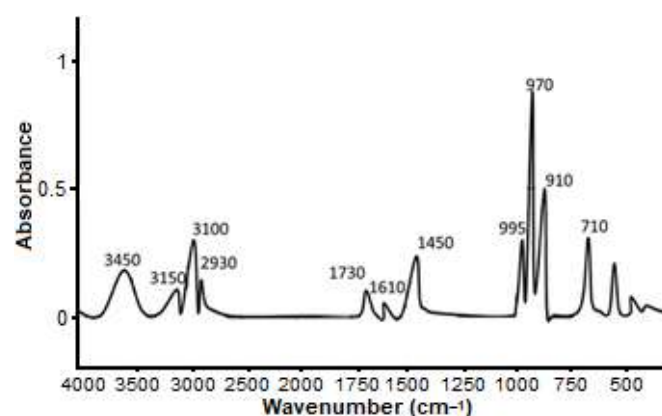


Fig 1. Infrared spectra of polybutadiene

absorbance at wavenumber 710, 910, and 970 cm^{-1} were sharp and strong. The absorption at 930 cm^{-1} implied increasing HTPB. The functionality of HTPB was observed at wavenumber 3450 cm^{-1} .

The absorbance of polybutadiene infrared spectra every ten minutes was observed at wavenumber 910 and 3450 cm^{-1} (Table 1). The HTPB concentration was linear to absorbance (Beer's law) [12]. The HTPB concentration was calculated based on absorbance at 910 cm^{-1} (A_{910}) using Beer's law in Eq. (22) [12]. The functionality of the polymer was measured based on absorbance at 3450 cm^{-1} (A_{3450}) using Eq. (23). The ϵ and b are molar attenuating coefficient or absorptivity of the attenuating species and the optical path length, respectively

$$P = \frac{A_{910}}{\epsilon b} \quad (22)$$

$$[\text{RM}_i] = \frac{A_{3450}}{\epsilon b} \quad (23)$$

The HTPB concentration and functionality every ten minutes are shown in Table 1. Initial condition was

$[\text{A}]_0 = 0.00023 \text{ mol L}^{-1}$ and $[\text{I}]_0 = 0.00002 \text{ mol L}^{-1}$. The polymer produced (XM_A) was calculated from the absorbance of the infrared spectra at 1750 cm^{-1} .

To study the kinetic model, the $([\text{A}]_0 \text{XM}_A / M_n) / ([\text{I}]_0 \alpha)^{1/2}$ was plotted to the $(1-\alpha)([\text{I}]_0 / \alpha)^{1/2}$ and expressed in Fig. 2 based on Eq. (16). The value of $(2-\beta)$ is the slope of this curve. The value of $(fk_d/k_t)^{1/2}$ is the intercept of this curve. The value of $\beta (k_{tc}/k_t)$ and $(fk_d/k_t)^{1/2}$ are 12,001 and $8.5 \times 10^7 \text{ mol L}^{-1} \text{ sec}^{-1}$. The value of fk_d was calculated from the decomposition data of hydrogen peroxide in the various solvents [17]. The dissociation rate constant of hydrogen peroxide in toluene is $4.2 \times 10^{-5} \text{ sec}^{-1}$ [15].

The propagation rate constant k_p was calculated from Eq. (6). The constant $(k_p/k_t^{1/2})$ was calculated as the slope of plotting R_p to R_i or R_p to $(fk_d[\text{I}]_0^{1/2}[\text{A}]_0)$ as expressed in Fig. 3. The value of $(k_p/k_t^{1/2})$ is 4.62 and the value of k_p is $7.7 \times 10^3 \text{ mol L}^{-1} \text{ sec}^{-1}$.

The disproportional termination rate constant (k_{td}) is the slope of curve $\ln(1-P/f_{OH})$ as time t as expressed in

Table 1. HTPB concentration and functionality at 100 °C and pressure of 25 bar

Time (min)	Absorbance at 910 cm^{-1}	Absorbance at 3450 cm^{-1}	C_p (mol L^{-1})	$f_{OH} = [\text{RMR}]/[\text{RM}]$
10	0	0	0	1
20	0.23	0.05	0.00023	1.11111
30	0.35	0.16	0.00035	1.35556
40	0.48	0.31	0.00048	1.68889
50	0.58	0.41	0.00058	1.91111
60	0.62	0.42	0.00062	1.93333

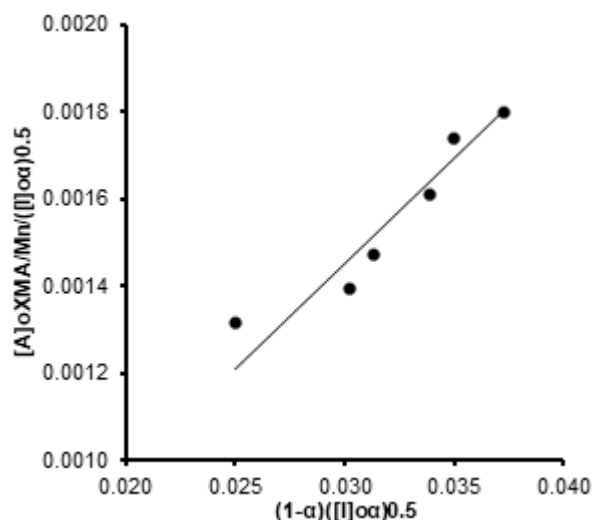


Fig 2. Curve $([\text{A}]_0 \text{XM}_A / M_n) / ([\text{I}]_0 \alpha)^{1/2}$ versus $(1-\alpha)([\text{I}]_0 / \alpha)^{1/2}$

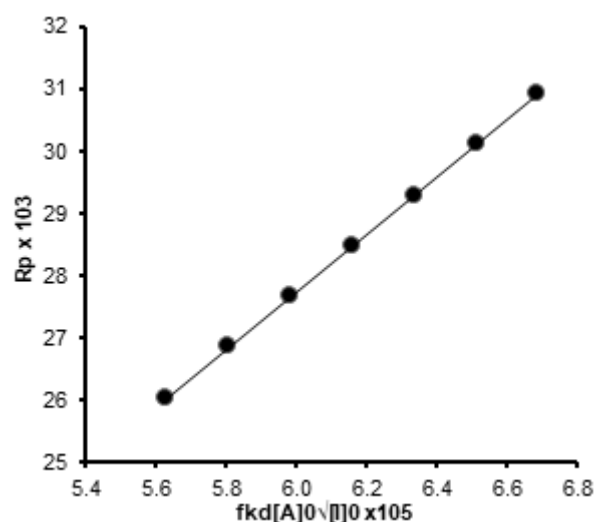


Fig 3. The curve of R_p to $(fk_d[\text{I}]_0^{1/2}[\text{A}]_0)$

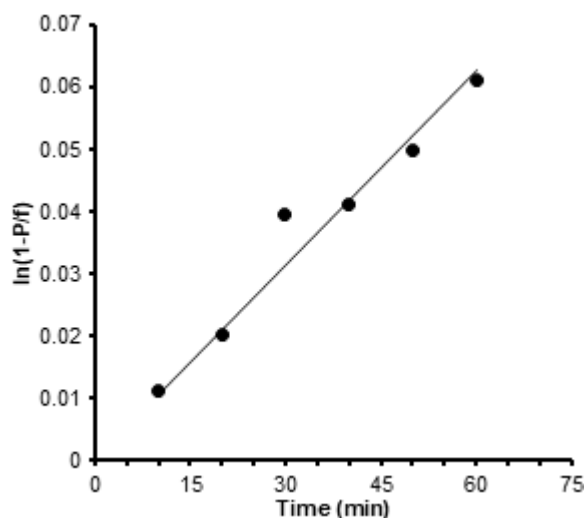


Fig 4. Plotting $\ln(1-P/f_{OH})$ as time t

Fig. 4. The value of (k_t/k_{td}) is 2.5. The conjunction termination rate constant k_{tc} is the deviation of k_t and k_{td} . The value of k_t , k_{td} , and k_{tc} are $8.5 \times 10^7 \text{ mol L}^{-1} \text{ sec}^{-1}$, 3.2×10^7 , and $5.3 \times 10^7 \text{ L mol}^{-1} \text{ sec}^{-1}$.

Based on the radical polymerization mechanism and the value of their rate constant, value of $k_d = 4.2 \times 10^{-5} \text{ sec}^{-1}$, $k_i = 8.9 \times 10^{-4} \text{ L mol}^{-1} \text{ sec}^{-1}$, $k_p = 7.7 \times 10^3 \text{ L mol}^{-1} \text{ sec}^{-1}$, $k_t = 8.5 \times 10^7 \text{ L mol}^{-1} \text{ sec}^{-1}$, $k_{td} = 3.2 \times 10^7 \text{ L mol}^{-1} \text{ sec}^{-1}$, and $k_{tc} = 5.3 \times 10^7 \text{ L mol}^{-1} \text{ sec}^{-1}$. The determining polymerization rate is the lowest step reaction rate. Therefore, the determining polymerization rate is the initiation reaction which has the lowest reaction rate constant ($2.5 \times 10^{-4} \text{ L mol}^{-1} \text{ sec}^{-1}$).

The monomer radical forming rate is faster than the initiator decomposition ($k_i > k_d$) indicating that the monomer radical forming step determines the initiation rate. Every hydroxyl radical formed directly reacts with a butadiene monomer to produce a monomer radical. This phenomenon corresponds to Flory's statement that the speed of initiation in radical polymerization is represented by the reaction of the formation of a radical monomer [13,16].

The k_p value is almost equal to k_i , indicating a competitive reaction, each forming of a monomer radical being followed by the growth of the polymer radical. The overall polymerization reaction rate is an exponential curve as shown in Fig. 4. Initially, the polymerization reaction grows rapidly with the formation of monomer

radicals. When the monomer radical formation reaction is complete, the growth of the polymer will decrease [16-17].

The $(k_p/k_t^{1/2})$ value of 2.56 indicates that the propagation rate is faster than the termination rate. On polymerization, at 100 °C and a pressure of 350 psi the polybutadiene formed has a long chain. The reaction at 90 °C and a pressure of 350 psi obtained $(k_p/k_t^{1/2}) = 0.07$, indicating that the polymer is not formed because all of the growing polymer radicals will directly become dead polymers. Thus, the requirement for polybutadiene formation is a minimum temperature of 100 °C at a pressure of 350 psi.

The value of k_{td} is higher than k_{tc} indicating that more HTPB is produced than monofunctional polybutadiene. The value of k_{td}/k_{tc} of 1.6 indicates that polymer functionality is 1.6. HTPB formation is faster than the formation of mono functional polybutadiene. The results show that the functionality of polymer can be used to study the termination reactions of both disproportional and combinatorial termination in the radical polymerization of butadiene. This result refines the study of butadiene polymerization kinetics by using average molecular weight data and conversion based only on the termination rate [15,17].

According to Eq. (13) and Fig. 2, the polymerization rate (R_p) is directly proportional to $\exp(-k_d t/2)$, $[A][I]_0^{1/2}$, and $k_p/k_t^{1/2}$. The polymerization rate is proportional to $\exp(-k_d t/2)$ indicating that the decomposition rate decreases exponentially as more initiators are used for polymerization. The polymerization rate is directly proportional to $[A][I]_0^{1/2}$, indicating that the polymerization rate is directly proportional to the initial initiator and initial monomer concentration. The overall polymerization rate is directly proportional to the initial initiator concentration. This value is the same as that for the radical polymerization of both olefin and styrene [14]. The polymerization rate is proportional to $(k_p/k_t^{1/2})$ indicating that polymerization will occur if the value of $(k_p/k_t^{1/2})$ is greater than one, so propagation will take place before termination occurs. The calculation results show that the value of $(k_p/k_t^{1/2})$ is 2.56, and so maintained polymerization will take place.

Table 2. Polymerization rate constants of HTPB and TDI

Reaction rate constant	Initial H ₂ O ₂ /butadiene ratio (%mol/mol)			
	10%	20%	30%	32%
k_d (sec ⁻¹)	4.2×10^{-5}	4.2×10^{-5}	4.2×10^{-5}	4.2×10^{-5}
k_a (L mol ⁻¹ sec ⁻¹)	8.9×10^{-4}	8.9×10^{-4}	8.9×10^{-4}	8.9×10^{-4}
k_p (L mol ⁻¹ sec ⁻¹)	7.7×10^3	7.7×10^3	7.7×10^3	7.7×10^3
k_t (L mol ⁻¹ sec ⁻¹)	8.5×10^7	8.5×10^7	8.5×10^7	8.5×10^7
k_{tc} (L mol ⁻¹ sec ⁻¹)	5.3×10^7	5.3×10^7	5.3×10^7	5.3×10^7
k_{td} (L mol ⁻¹ sec ⁻¹)	3.2×10^7	3.2×10^7	3.2×10^7	3.2×10^7

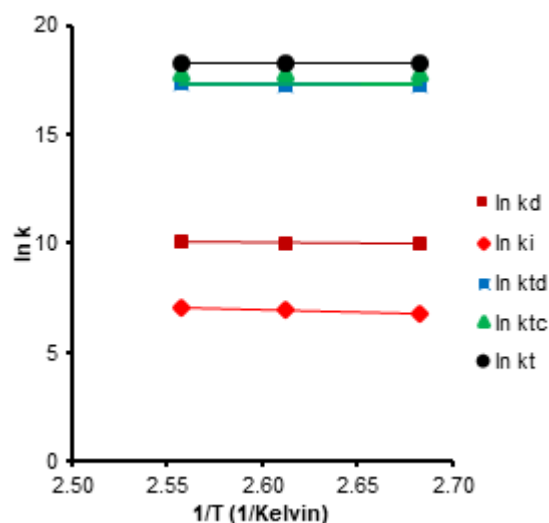
Effect of Initiator

The reaction rate constants k_d , k_a , k_p , k_t , k_{tc} , and k_{td} were calculated using Eq. (16) for different initial H₂O₂/butadiene ratios and the results are presented in Table 2. These results indicate that there is no difference in the polymerization rate if the polymerization steps are the same and that the different initial H₂O₂/butadiene ratio does not change the polymerization rate constants of each step. Based on the calculation of the values of k_d , k_a , k_p , k_t , k_{tc} , and k_{td} , the developed kinetic model had an average error of 1.9% in comparison to experimental data, so the model represents real kinetics for different initial H₂O₂/butadiene ratios. Therefore, the increasing initial concentration of the initiator significantly increases the reaction rate.

Effect of Reaction Temperature

Reaction temperature significantly affects polymerization, following the Arrhenius equation, as presented in Eq. (14). The effect of reaction temperature on polymerization rate constants can be evaluated based on collision frequency factor and reaction activation energy. To calculate these variables, polymerization of butadiene was conducted at various reaction temperatures (100, 110 and 118 °C). After reaction rate constants were calculated, $\ln(k_i)$ was plotted versus $(1/T)$, as can be seen in Fig. 5. According to the Arrhenius equation, the intercept is $\ln(A)$ and the slope is $(-E_i/R)$. The collision frequency factor and reaction activation energy for each reaction rate constant is presented in Table 3.

The activation energy of each reaction step shows the effect of reaction temperature on the reaction rate constant. The initiation reaction needs higher energy than the other reactions. Based on Table 3, the initiation reaction can be

**Fig 5.** The plot of $\ln(k)$ versus $1/T$ **Table 3.** The activation energy for polymerization of butadiene

Reaction steps	E_a (kJ/mol)
Dissociation	7608.1414
Initiation	14188.6724
Propagation	2247.2742
Termination	105.5878
Conjunction termination	87.2970
Disproportional termination	135.5182

identified as the most sensitive to the change of reaction temperature and is, therefore, the determining reaction. This data confirms that the rate of reaction was affected by the reaction temperature increase.

CONCLUSION

The termination of radical polymerization of butadiene using hydrogen peroxide initiator was examined by observing the increase of polymer conversion and functionality. Polymerization of

butadiene was carried at an initial H₂O₂/butadiene ratio of 10%, with hydrogen peroxide 25%, and a reaction temperature of 100 °C. The kinetic constants of polymerization were $4.2 \times 10^{-5} \text{ sec}^{-1}$, $8.9 \times 10^{-4} \text{ L mol}^{-1} \text{ sec}^{-1}$, $7.7 \times 10^3 \text{ L mol}^{-1} \text{ sec}^{-1}$, $8.5 \times 10^7 \text{ L mol}^{-1} \text{ sec}^{-1}$, $3.2 \times 10^7 \text{ L mol}^{-1} \text{ sec}^{-1}$, and $5.3 \times 10^7 \text{ L mol}^{-1} \text{ sec}^{-1}$ for k_D , k_a , k_p , k_t , k_{tc} , and k_{td} , respectively, with activation energy of 7608, 14188, 2247, 105, 87, and 135 kJ/mol, respectively. The determining step of this polymerization was the initiation reaction. This kinetic model shows that the conversion of difunctional polybutadiene (HTPB) had been affected by the reaction temperature.

■ ACKNOWLEDGMENTS

Special thanks are addressed to the National Institute of Aeronautics and Space, LAPAN, Indonesia for its financial support in doing this research via contract No. 082.01.06.3534.001.002.053A.524119.

■ REFERENCES

- [1] Chen, C.Y., Wang, X.F., Gao, L.L., and Zheng, Y.F., 2013, Effect of HTPB with different molecular weights on curing kinetics of HTPB/TDI system, *Chin. J. Energetic Mater.*, 21 (6), 771–776.
- [2] Chen, X., Lai, J., Chang, X., Zhang, Y., Zhang, L., and Wang, C., 2017, Compressive mechanical properties of HTPB propellant at low temperatures and high strain rates, *Results Phys.*, 7, 4079–4084.
- [3] Takahashi, M.F.K., de Lima, M., and Polito, W.L., 1997, Molecular weight determination of HTPB resins by vapor pressure osmometry (VPO) and gel permeation chromatography (GPC): The effect of calibration standards, *Polym. Bull.*, 38, 455–460.
- [4] Flory, P.J., 1969, *Principles of Polymer Chemistry*, Cornell University Press, London, 192–205.
- [5] Gaborieau, M., and Castignolles, P., 2010, Size-exclusion chromatography (SEC) of branched polymers and polysaccharides, *Anal. Bioanal. Chem.*, 399 (4), 1413–1423.
- [6] Hailu, K., Guthausen, G., Becker, W., König, A., Bendfeld, A., and Geissler, E., 2010, In-situ characterization of the cure reaction of HTPB and IPDI by simultaneous NMR and IR measurements, *Polym. Test.*, 29 (4), 513–519.
- [7] Chaturvedi, S., and Dave, P.N., 2019, Solid propellants: AP/HTPB composite propellants, *Arabian J. Chem.*, 12 (8), 2061–2068.
- [8] Kattner, H., and Buback, M., 2017, Termination, transfer, and propagation kinetics of trimethylaminoethyl acrylate chloride radical polymerization in aqueous solution, *Macromolecules*, 50 (11), 4160–4168.
- [9] Krishnan, P.S.G., Ayyaswamy, K., and Nayak, S.K., 2013, Hydroxyl terminated polybutadiene: Chemical modifications and application, *J. Macromol. Sci. Part A Pure Appl. Chem.*, 50 (1), 128–138.
- [10] Lee, S., Choi, C.H., Hong, I.K., and Lee, J.W., 2015, Polyurethane curing kinetics for polymer bonded explosives: HTPB/IPDI binder, *Korean J. Chem. Eng.*, 32 (8), 1701–1706.
- [11] Min, X., Fan, X., and Liu, J., 2018, Utilization of steric hindrance of alkyl lithium-based initiator to synthesize high 1,4 unit-containing hydroxyl-terminated polybutadiene, *R. Soc. Open Sci.*, 5 (5), 180156.
- [12] Moghimi, A., Omrani, I., Nabid, M.R., and Mahmoodi, M., 2013, Quantification of hydroxyl group in polymers containing trace water by 19F NMR spectroscopy, *Eur. Polym. J.*, 49 (1), 228–234.
- [13] Wibowo, H.B., Cahyo, C., and Sanggra, R., 2018, Bulk polymerization kinetics of hydroxyl terminated polybutadiene and toluene diisocyanate with infrared spectroscopy, *Indones. J. Chem.*, 18 (3), 552–560.
- [14] Restasari, A., Ardianingsih, R., Abdillah, L.H., and Hartaya, K., 2015, Effects of toluene diisocyanate's chemical structure on polyurethane's viscosity and mechanical properties for propellant, *Proceedings ISAST III-2015 International Seminar of Aerospace Science and Technology - 2015*, LAPAN, Jakarta, 59–67.
- [15] Toosi, F.S., Shahidzadeh, M., and Ramezanzadeh, B., 2015, An investigation of the effects of prepolymer functionality on the curing behavior

- and mechanical properties of HTPB-based polyurethane, *J. Ind. Eng. Chem.*, 24, 166–173.
- [16] Shokry, S.A., El Morsi, A.K., Sabaa, M.S., Mohamed, R.R., and El Sorogy, H.E., 2015, Synthesis and characterization of polyurethane based on hydroxyl terminated polybutadiene and reinforced by carbon nanotubes, *Egypt. J. Pet.*, 24 (2), 113–232.
- [17] Sikder, B.K., and Jana, T., 2018, Effect of solvent and functionality on the physical properties of hydroxyl-terminated polybutadiene (HTPB)-based polyurethane, *ACS Omega*, 3 (3), 3004–3013.
- [18] Wang, Y., Zeng, X., Li, H., and Guo, J., 2012, Structural characterization of hydroxyl-terminated polybutadiene-bound 2,2-thiobis(4-methyl-6-tert-butylphenol) and its thermo-oxidative aging resistance for natural rubber vulcanizates, *J. Macromol. Sci. Part B Phys.*, 51 (10), 1904–1920.
- [19] Wibowo, H.B., 2018, Current solid propellant research and development in Indonesia and its future direction, *J. Phys. Conf. Ser.*, 1130, 012027.
- [20] Pradel, J.L., Boutevin, B., and Ameduri, B., 2000, Controlled radical polymerization of 1,3-butadiene. II. Initiation by hydrogen peroxide and reversible termination by TEMPO, *J. Polym. Science Part A Polym. Chem.*, 38 (18), 3293–3302.
- [21] Zhou, Q., Jie, S., and Li, B.G., 2014, Preparation of hydroxyl-terminated polybutadiene with high cis-1,4 content, *Ind. Eng. Chem. Res.*, 53 (46), 17884–17893.
- [22] Zhu, X., Fan, X., Zhao, N., Liu, J., Min, X., and Wang, Z., 2018, Comparative study of structures and properties of HTPBs synthesized via three different polymerization methods, *Polym. Test.*, 68, 201–207.

Synthesis, Characterization, and Stability Evaluation of β -Carotene Encapsulated in Starch-Chitosan/Tripolyphosphate Matrices

Agnes Dyah Novitasari Lestari^{1,2,*}, Dwi Siswanta², Ronny Martien³, and Mudasir Mudasir^{2,**}

¹Department of Chemistry, Faculty of Mathematics and Natural Sciences, Universitas Papua, Jl. Gunung Salju, Amban, Manokwari 98314, Indonesia

²Department of Chemistry, Faculty of Mathematics and Natural Sciences, Universitas Gadjah Mada, Sekip Utara, Yogyakarta 55281, Indonesia

³Department of Pharmaceutics, Faculty of Pharmacy, Universitas Gadjah Mada, Sekip Utara, Yogyakarta 55281 Indonesia

* **Corresponding author:**

email: a.dyahnovitasari@gmail.com*; mudasir@ugm.ac.id**

Received: October 8, 2019

Accepted: February 20, 2020

DOI: 10.22146/ijc.50449

Abstract: This study aims to investigate the synthesis and characterization of β -carotene encapsulated in the blending matrices of starch (native and hydrolyzed starch)-chitosan/TPP (tripolyphosphate) by examining the effects of starch-to-chitosan weight ratio, β -carotene addition level, and TPP addition level on the encapsulation efficiency (EE) and loading capacity (LC); and to evaluate their storage stability. The encapsulation was done by the dropwise addition of ethanolic β -carotene dispersion into the blending matrices. The results of XRD analysis show that the encapsulation process significantly decreases the crystallinity of the starches, chitosan, and β -carotene. Scanning electron microscope (SEM) images reveal that the encapsulation products form irregular lumps. The EE and LC tend to increase with the increase in polymer fraction of matrices and β -carotene addition level, and with the decrease in TPP addition level. The addition of chitosan and the replacement of native starch by hydrolyzed starch tend to increase storage stability of β -carotene encapsulated in the starch matrix because chitosan can act as a good film-forming and antioxidant, while hydrolyzed starch contains amylose amylopectin with a short chain which is better in film-forming ability. These results promote the use of the hydrolyzed starch-chitosan/TPP as a matrix to enhance the stability β -carotene via encapsulations.

Keywords: starch; chitosan; TPP; β -carotene; encapsulation

■ INTRODUCTION

Encapsulation of active compounds is an important research topic that has attracted many researchers until recently. Encapsulation is a way to wrap the active substance in order to increase its stability, solubility, bioavailability, and the delivery of the active substance in the body and any desired medium [1-2]. In an encapsulation study, the wrapped material is called the core, while the wrapper is called a matrix. Various matrix materials have been used in the encapsulation process, such as surfactants, synthetic polymers, and natural polymers, including proteins, lipids, and carbohydrates [3].

β -Carotene is one of the main carotenoid compounds and is an active compound that contributes significantly to human health, i.e., as a pro-vitamin A, an antioxidant, and an anticancer agent. Unfortunately, β -carotene is unstable to light, heat, and oxygen [4]. To improve the stability of β -carotene, numerous researchers have tried to encapsulate β -carotene in various matrices to produce liquid or solid products that are easier to be handled. For example, β -Carotene has been encapsulated in the form of oil-in-water (O/W) nano-emulsions with polysorbate tween as an emulsifier using high-pressure homogenization. At 25 °C, the stability of β -carotene decreased after four weeks, with a relatively slight loss of

β -carotene content [5]. In another study, a biosurfactant of egg white protein was applied to improve the physicochemical stability of β -carotene emulsions. The stability of β -carotene found to increase up to approximately 80% on day 30 by using this biosurfactant [6]. Encapsulation using surfactants produced high encapsulation efficiency, but the stability of the encapsulation products is relatively low with regard to temperature and dilution. In addition, certain surfactants have been reported to be toxic at high concentrations [7]. Polymers could be used to replace surfactant, but synthetic polymers show low biocompatibility within the body and had a risk of becoming toxic. Natural polymers have advantages as a matrix of encapsulation since they are biocompatible, biodegradable, and non-toxic, even in high concentrations [8-9]. In the previous study, β -carotene has been encapsulated in natural polymers such as starch, maltodextrin, and modified starch [10]. The use of modified (acid hydrolyzed) starch has been proved to be able to increase the storage stability of β -carotene. A similar result has also been reported in the use of hydrolyzed pinhão (*Araucaria angustifolia* seeds) starch to increase the storage stability of micro-encapsulated β -carotene [11].

Meanwhile, the ability of starch as an encapsulating matrix can also be increased by mixing starch with other compatible polymers. For example, starch could be combined with chitosan to produce a compatible matrix [12-13]. Chitosan and its derivatives have various advantages as matrix materials, as chitosan has antibacterial and antioxidant activities, increases mechanical strength, and tends to be degraded in the small intestine [14-15]. A combination of starch and chitosan polymers could increase composite mechanical strength and resist to high temperatures as well as reduce the rate of amylose release [16]. The polymer combination also produced material that was more resistant to ultraviolet (UV) light in comparison with those using the native starch [17].

The study investigated the effects of the weight ratio of native starch to chitosan on the yield, color, Fourier Infra-Red (FTIR) spectra, optical microscope image, and particle size of the encapsulation products. The

preliminary study showed that β -carotene has been successfully encapsulated in native starch-chitosan/TPP blending matrices producing micro size encapsulation products. Continuing our preliminary research [18], The objectives of this research are (1) to characterize the products of β -carotene encapsulation in the matrices of native starch-chitosan/TPP and acid hydrolyzed starch-chitosan/TPP using Scanning Electron Microscopy (SEM) and X-ray diffractometry (XRD), (2) to study the effect of starch/chitosan weight ratio, β -carotene and TPP addition level on the encapsulation efficiency (EE) and loading capacity (LC), and (3) to investigate the effects of light and heat on the β -carotene stability stored as encapsulation products. As far as we know, our report is original and unique because it is different from the previous reports [10-11]. Here, we have used corn starch, modified the matrix by chitosan addition, studied the effect of the use of hydrolyzed starch instead of native starch, used the solvent displacement method in the synthesis process, and applied freeze-dry in the drying step.

■ EXPERIMENTAL SECTION

Materials

Corn starch, chitosan, TPP, and β -carotene were purchased from Sigma Aldrich. Glacial acetic acid and absolute ethanol were purchased from Merck. All materials were used as received without further purification.

Instrumentation

A Sorvall biofuge primo R refrigerated centrifuge and a Leybold-Heraeus freeze dryer Lyovac GT 2 were used in the preparation of microparticle. The morphology of obtained microparticle was analyzed by using a scanning Electron Microscopy (SEM, JEOL Model JSM-6510LA) and a Transmission electron microscopy (TEM, JEM-1400 JEOL 120 kV). XRD pattern was measured by using a Pananalytical diffractometer with Bragg Brentano geometry and CuK α radiation ($\lambda = 0.1542$ nm, 40 kV, 30 mA). The determination of β -carotene content was performed by measuring the absorbance of β -carotene in hexane using

a Shimadzu UV 1800 spectrophotometer at 450 nm. A storage chamber with a size of $48 \times 37 \times 44 \text{ cm}^3$ which was equipped with two Gaxindo BLB-T5/6W UV Lamps ($\lambda = 365 \text{ nm}$) separated at a distance of 2 cm was used to test the effects of UV light on the storage stability of β -carotene encapsulation.

Procedure

Synthesis of hydrolyzed starch

The synthesis of hydrolyzed starch was carried out in accordance with the previous reports [18-19] as follows. As much as 100 g of starch was added to 500 mL of 0.15 M HCl, and the mixture was stirred by using a magnetic stirrer for 8 h while maintaining a temperature of 50 °C. The hydrolyzed starch was filtered, and the obtained residue was then washed 4 times with distilled water and dried for 48 h at 50 °C [18].

Encapsulation process

The encapsulation process was performed in a similar procedure to our previous work [19] except that the compositions and concentrations of TPP and β -carotene were varied. The matrix mixture of starch-chitosan/TPP was prepared as described in the literature [20] with slight modifications. A certain amount of volume (according to the weight ratio of starch and chitosan) of cationic solution (1% w/v chitosan) was added to the TPP-starch mixture (prepared by adding

water in starch followed by the boiling process) with the compositions as described in Table 1. The encapsulation process was carried out based on the method of the literature [21] with minor modifications. The matrix mixture (220 mL) was heated and stirred in a water bath at 90 °C for 10 min, followed by the addition of 100 mL of a certain amount of ethanolic β -carotene dispersion as given in Table 1 dropwise while continually stirred. The mixtures were then cooled at room temperature and were added with another 100 mL of ethanolic β -carotene dispersion of the same concentration as that used in the previous step. Then, the mixture was centrifuged, dried in freeze-dryer, crushed, and sieved 200 mesh.

Determination of β -carotene content

β -Carotene content in capsules was determined by the method described in the literature [5,22] with slight modifications. A total of 5 mg of sample was dispersed in 1 mL of 2 M HCl, heated in a water bath at 75 °C for 3 min, cooled and added with 2 mL of ethanol and 3 mL of hexane in a test tube. The mixture in the tube was then shaken using vortex until the powder had been bleached. This step was repeated several times and then stopped when all the β -carotene had been extracted. Furthermore, the supernatant was taken, and absorbance of the hexane fraction was measured at 450 nm with a UV-Vis spectrophotometer. The concentration of the β -carotene

Table 1. Sample formulation

Formulation code	Weight ratio of starch to chitosan	Volume of 1% starch dispersion (mL)	Volume of 1% chitosan solution (mL)	β -carotene added in 200 mL ethanol (mg)	TPP added in 20 mL solution (mg)
Fx0	1.00	100	100	0	600
Fx1	0.25	60	140	10	600
Fx2	0.43	40	160	10	600
Fx3	1.00	100	100	10	600
Fx4	2.33	160	40	10	600
Fx5	4.00	140	60	10	600
Fx6	1.00	100	100	5	600
Fx7	1.00	100	100	15	600
Fx8	1.00	100	100	20	600
Fx9	1.00	100	100	10	400
Fx10	1.00	100	100	10	500
Fx11	1.00	100	100	10	700
Fx12	1.00	100	100	10	800

x = N or H, FN = native starch based formulation, FH = hydrolyzed starch based formulation

was determined based on the standard curve of β -carotene that was obtained in the same way as the sample. Loading capacity (LC) and encapsulation efficiency (EE) were calculated by using Eq. (1) and (2).

$$LC \text{ (mg/g)} = \frac{mBC}{mMP} \quad (1)$$

$$EE \text{ (\%)} = \frac{mBC}{mTBC} \times 100 \quad (2)$$

where, mBC = mass of β -carotene encapsulated in the microparticle (mg), mMP = mass of microparticle (g), mTBC = total mass of β -carotene in theoretical loading (mg).

Storage stability test

The storage stability of the encapsulation products was tested according to the literature [11] with slight modifications. The encapsulation products were stored in a dark storage vessel placed in a refrigerator (5 ± 1) °C and in an ambient temperature chamber (30 ± 1) °C. In order to investigate its stability against UV irradiation, the encapsulated β -carotene samples were placed in a UV chamber which furnished with a pair of UV light tube BLB-T5/6W, $\lambda = 365$ nm at ambient temperature. The samples were placed at a distance of 7 cm below the lamps. The concentration of β -carotene was determined once every week for 6 weeks using a UV-Vis spectrophotometer. The storage stability was expressed as the residual rate in a percent: w_t/w_0 , where w_t was the weight of β -carotene after storage during the time interval t , and w_0 was the initial weight of β -carotene.

RESULTS AND DISCUSSION

XRD Analysis

The diffraction patterns of starches, chitosan, TPP, and β -carotene (Fig. 1(a)) show semicrystalline structures, and their characteristic peaks of 2θ are listed in Table 2. The diffraction pattern of hydrolyzed starch shows a slight decrease in crystallinity compared with that of the native starch. This fact may indicate the increase of a shorter chain of amylose in hydrolyzed starch [10,25]. In addition, amylopectin depolymerization resulting from starch hydrolysis increased the quantity of linear chains similar to amylose [26-27]. In X-ray diffractograms of starch, the crystalline regions of the starch are dominated by aggregated double helices of amylopectin chains, while the amorphous regions are greatly composed of amylose. The increase in the quantity of linear chains similar to amylose may increase the amorphous region of hydrolyzed starch. Hence, the shorter chains of amylose and linear chains similar to amylose can participate in double helices with amylopectin, reducing the crystallinity of the starch granules [28].

Moreover, the X-ray diffraction pattern of the blending of starch-chitosan/TPP matrices depicted in Fig. 1(b) clearly shows a significant decline in its crystallinity indicated by the presence of a widening peak at 2θ of 19.89 for native starch-chitosan/TPP and 6.88, 11.82, 18.56, and 34.44 for hydrolyzed starch-chitosan/TPP. The fact that the peaks in the blending

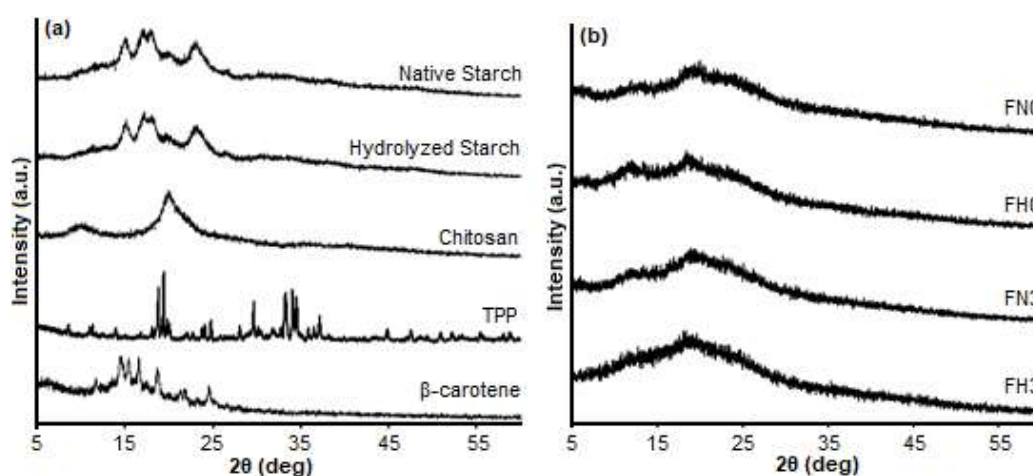


Fig 1. XRD pattern of materials (a) starch, hydrolyzed starch, chitosan, TPP, and β -carotene; (b) blended matrices without β -carotene (FN0 and FH0), and encapsulation products (FN3 and FH3)

Table 2. The 2 θ peaks of materials analyzed by XRD

Materials	2 θ							
Native Starch	9.95	14.88	17.16	18.02	20.09	23.22	26.68	38.37
Hydrolyzed starch	15.12	17.17	18.18	20.07	26.61	30.28		
Chitosan	20.55							
TPP	18.78	19.37	19.78	20.05	24.71	24.78	29.60	33.17
	33.28	34.05	34.49	37.08				
β -carotene	11.07	14.49	15.41	16.61	17.55	18.74	21.38	21.81
	23.17	24.61	27.99	55.26				
FN0	19.89							
FH0	6.88	11.82	18.56	34.44				
FN3	11.83	18.80						
FH3	18.68							

matrices and its encapsulation products decreases suggest that the molecular interaction among starch, chitosan, and TPP [13] exists. Meanwhile, the product of β -carotene encapsulated in native starch-chitosan/TPP matrices also shows broad bands at 2 θ of 11.83 and 18.80, while the one that was encapsulated in hydrolyzed starch-chitosan/TPP matrices shows a broad band at 18.68. From the X-ray diffraction data, it is observed that there is a significant reduction in the number of peaks of β -carotene encapsulated in the hydrolyzed starch-chitosan/TPP (FH3) compared to that of the hydrolyzed starch-chitosan/TPP blended matrix without β -carotene (FH0). In contrast, such significant reductions in the number of peaks of β -carotene are not observed when it is encapsulated in the native starch-chitosan/TPP (FN0 and FN3). This finding indicates that the encapsulation of β -carotene is more effective to be done in hydrolyzed starch-chitosan/TPP than in native starch-chitosan/TPP matrices. These XRD pattern results corroborated the existence of interaction of starch, chitosan, and TPP in agreement with what has been concluded in the previous study [19].

SEM Analysis

The SEM images of the results are presented in Fig. 2. It can be seen that the SEM images/morphology of acid-hydrolyzed starch does not significantly change from that of the native starch. It is observed that there was a slight addition of indentation to that of hydrolyzed starch granules compared with that of native starch (Fig. 2(a) and 2(b)). Similar results in the SEM image of starch

granules after being hydrolyzed were also found in other studies in acid hydrolyzed starch synthesis [26]. The structure of dried particles is influenced by how the particle dried. Spray drying tends to produce spherical particles with a smooth surface, while the freeze-drying process tends to produce non-spherical particles [27].

The SEM images of blending of starch-chitosan/TPP matrices (Fig. 2(d) and 2(e)) and the encapsulation products (Fig. 2(f) and 2(g)) indicate that they are not perfectly spherical but tend to follow the SEM image of chitosan with a non-sharp irregular shape (Fig. 2(c)). These images indicate that starch and chitosan are compatible with each other in blending matrices. Results of SEM analysis support the conclusion of XRD data in this research, as well as the FTIR analysis of our preliminary study [19].

TEM Analysis

TEM analysis was performed to determine the size of the microparticles in a dry state. TEM images of encapsulation products are presented in Fig. 3.

Fig. 3(a) and 3(b) show agglomerated particles, while Fig. 3(c) and 3(d) show single particles of encapsulation products. The single-particle size of FH3 is smaller than FN3. The morphology of encapsulation products is round with clear boundaries that are different from the SEM analysis. This is due to SEM images taken from a dry state deposited on carbon, while TEM images taken from samples are dispersed in distilled water before drying. When dispersed in distilled

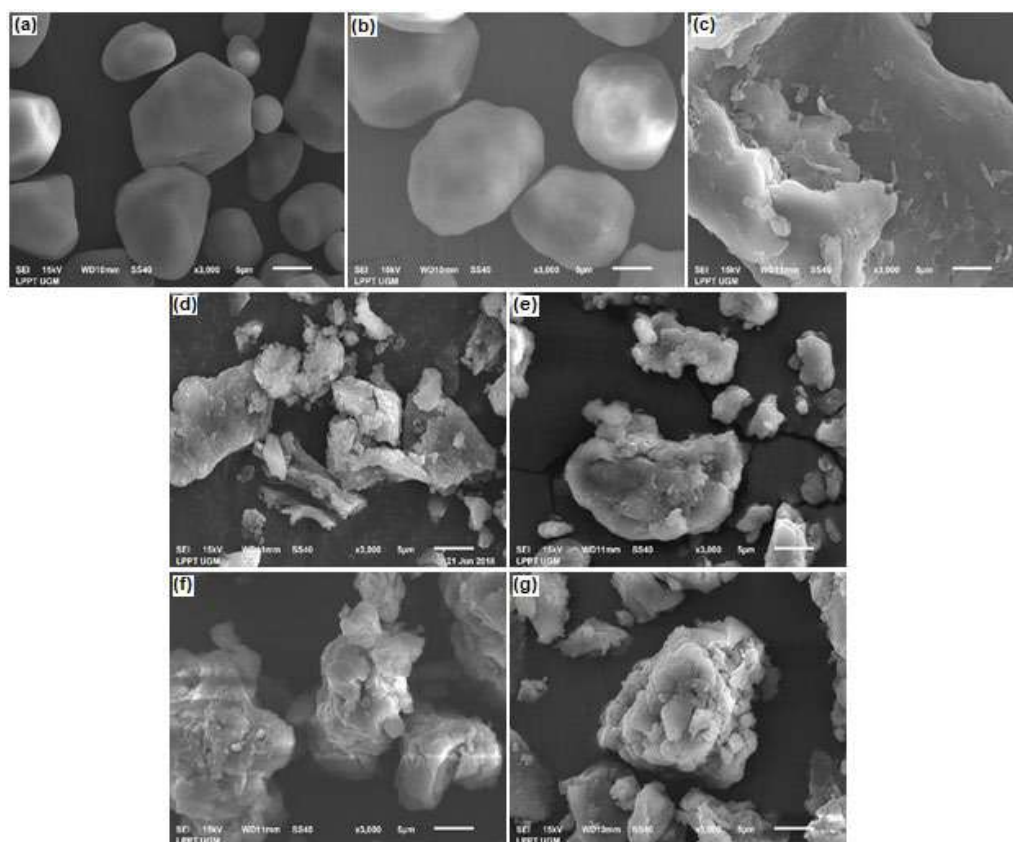


Fig 2. SEM images of matrix materials: (a) starch, (b) hydrolyzed starch, and (c) chitosan; blended matrices without β -carotene: (d) FN0 and (e) FH0; encapsulation products: (f) FN3 and (g) FH3

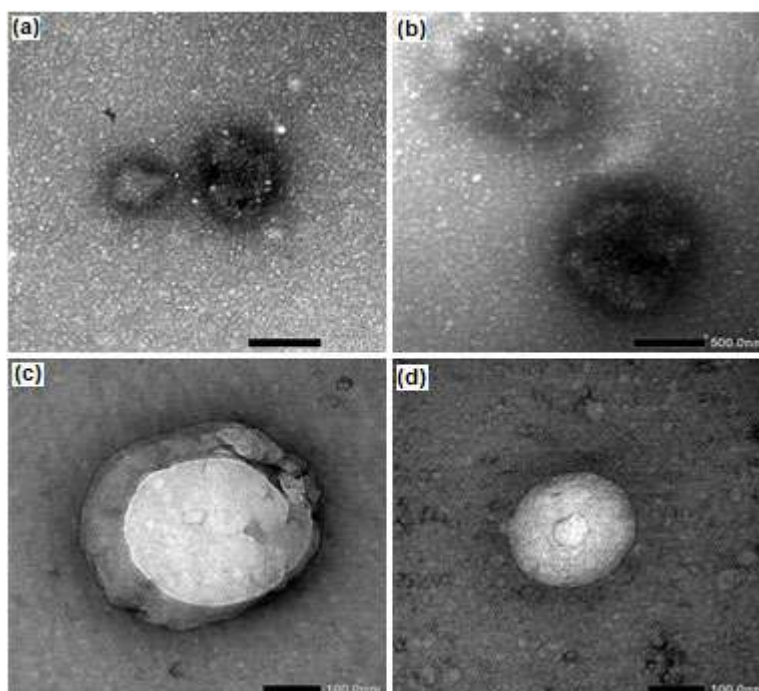


Fig 3. TEM images of encapsulation products: (a) FN3 at 10,000 magnification, (b) FH3 at 10,000 magnification, (c) FN3 at 40,000 magnification, and (d) FH3 at 40,000 magnification

water, the particles separate well and in a state of relaxation, so when dried, they are more rounded. In addition, the obtained SEM images suggest that the particles are agglomerated. In the FN3 and FH3 samples, the darker colored part is the blended starch-chitosan/TPP matrix because this part is more hydrophilic and dense. This proves that β -carotene is successfully encapsulated in the matrix.

The Effects of Weight Ratio of Starch to Chitosan on EE and LC

The effects of starch-to-chitosan weight ratio on EE and LC of β -carotene encapsulated in the matrix of hydrolyzed starch-chitosan/TPP (FH) and the matrix of native starch-chitosan/TPP (FN) are presented in Fig. 4. In this experiment, we have used various weight ratios of starch to chitosan, e.g., 0.25, 0.43, 1.00, 2.33, and 4.00, the constant addition of β -carotene (10 mg), and fixed TPP addition level of 600 mg (Table 1). EE and LC of FH are consistently higher than those of FN (the mean of EE FN 25.94–34.61%, EE FH 27.04–34.64%, LC FN 1.27–1.51 mg/g, and LC FH 1.33–1.70 mg/g). This fact was probably due to the increasing of shorter chains of amylose in hydrolyzed starch [10,25] and the increase of the quantity of linear chains similar to amylose [26-27] as mentioned above. The shorter amylose chains and linear chains similar to amylose have more tendency to dissolve in water and make a continuous network by hydrogen

bonds with itself or with chitosan/TPP, producing a gel structure that traps β -carotene in the structure [10,25]. Loksuwan [10] has also reported that acid modification of starch by spray drying method as a single matrix in β -carotene encapsulation increases the efficiency and loading capacity of β -carotene encapsulation. These results suggest that hydrolyzed starch has a better capability to entrap β -carotene than the native one.

At the weight ratio of starch to chitosan of 0.25–1.00, it is observed that EE and LC of FN and FH have a similar trend, namely the increasing proportion of chitosan in the matrices enhances the EE and LC. Nevertheless, in the ranges of starch-to-chitosan weight ratio of 1.00–4.00, the additional portion of starch increases the EE and LC of FH, but it is not for FN. These results are in good agreement with what has been reported by Subramanian et al. [12] suggesting that the excess portion of the polymer, both starch, and chitosan, in the weight ratio of starch to chitosan up to 1.00 results in the increase of EE and LC.

Effects of β -carotene Addition Level on EE and LC

The effects of the β -carotene addition level on EE and LC of β -carotene encapsulated in the matrix of hydrolyzed starch-chitosan/TPP (FH), and native starch-chitosan/TPP (FN) are presented in Fig. 5. In this part of the experiment, a fixed weight ratio of starch to

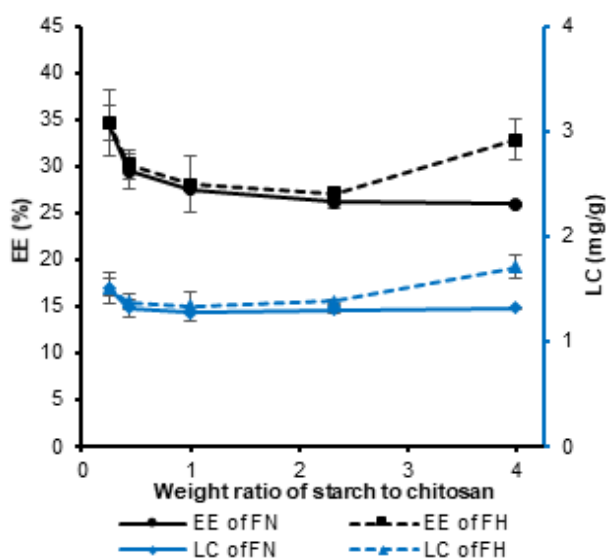


Fig 4. Effects of weight ratio of starch to chitosan on EE and LC

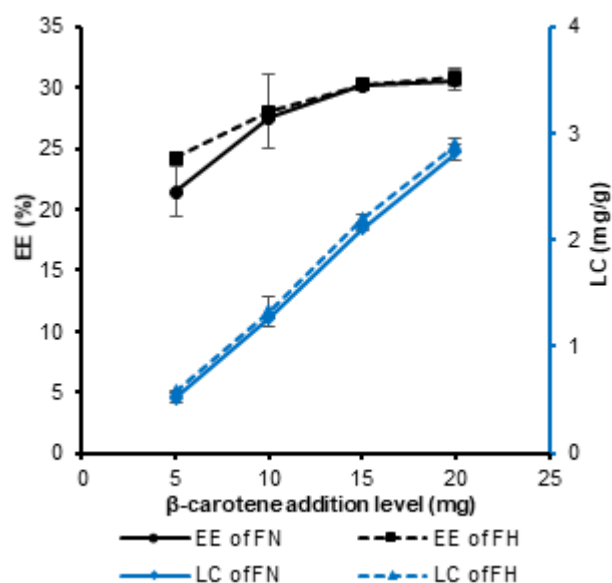


Fig 5. Effects of β -carotene addition level on EE and LC

chitosan of 1.00 and a constant TPP addition level of 600 mg were used, while β -carotene addition level was varied in the range of 5, 10, 15, and 20 mg (Table 1). The trends of data obtained here are in line with those observed for the effect of the weight ratio of starch to chitosan previously discussed, e.g., increasing β -carotene addition gives rise to higher observed EE and LC in FH as compared to those found in FN (the mean of EE FN 21.47–30.59%, EE FH 24.2–29.05%, LC FN 0.52–2.82 mg/g, and LC FH 0.58–2.89 mg/g).

The increase in the β -carotene addition level of 5–10 mg, both in FH and FN, results in significant increases in LC and EE. However, in the β -carotene addition level of 10–20 mg, the significant increase in LC is not accompanied by a significant increase in EE. These results suggest that in the range of 5–20 β -carotene addition levels, the matrices have not reached their saturated condition, and therefore, they are still capable of trapping β -carotene. However, the increase of trapped β -carotene in the matrices resulted from the addition level of β -carotene in the range of 10–20 mg could not enhance its EE. This is probably due to the fact that the higher the addition level of β -carotene in the ethanol, the lower the difference in surface tension between the solvent (ethanol) phase and non-solvent (aqueous) phase [28]. The decrease in surface tension difference between the two phases leads to a weaker Marangoni stress, resulting in the larger droplet of solvent phase [29]. The larger droplets of the solvent phase are more difficult to be entrapped by the matrix system, and it tends to deposit in the outer site of the resulted micro-particle. This gives rise to an undesired condition where some β -carotene can be easily re-released during the washing step using ethanol. In the previous literature [21], it has been reported that in the range of 5–20 mg β -carotene addition level, LC tends to increase, but EE was found to decrease when a similar method was used by using only starch for the matrix. Interestingly, in our results, we observe that the increasing LC in a similar addition level is still accompanied by the increase of EE. This finding clearly reveals the role of the addition of chitosan/TPP in increasing starch capability as a matrix of β -carotene encapsulation.

The Effects of TPP Addition Level on EE and LC

The effects of the TPP addition level in the ranges of 400–800 mg on EE and LC of β -carotene encapsulated in the matrix of hydrolyzed starch-chitosan/TPP (FH) and native starch-chitosan/TPP (FN) are presented in Fig. 6. In this section, the fixed weight ratio of starch to chitosan of 1.00 and constant β -carotene addition level of 10 mg were used, while the TPP addition level was varied in the range of 400, 500, 600, 700, and 800 mg (Table 1). A relatively narrow range of TPP addition levels between 400 and 800 mg/L has been chosen in this study because the additions of TPP with the weight ratio of starch and chitosan lower than 400 mg while keeping the weight ratio of starch to chitosan of 1.00 is not effective as shown by the extremely low yields of the encapsulation products. On the other hand, the addition of TPP larger than 800 mg at the weight ratio of starch to chitosan of 1.00 results in fast agglomeration and precipitation of the matrix mixture even before the β -carotene addition step could be done.

Fig. 6 shows that the EE and LC of FH were slightly higher than FN. Again, this fact supports the previous conclusion that hydrolyzed starch-chitosan/TPP is the better matrix for β -carotene encapsulation (the mean of EE FN 24.44–28.31%, EE FH 27.62–29.05%, LC FN 1.11–1.35 mg/g, and LC FH 1.30–1.37 mg/g). In the range

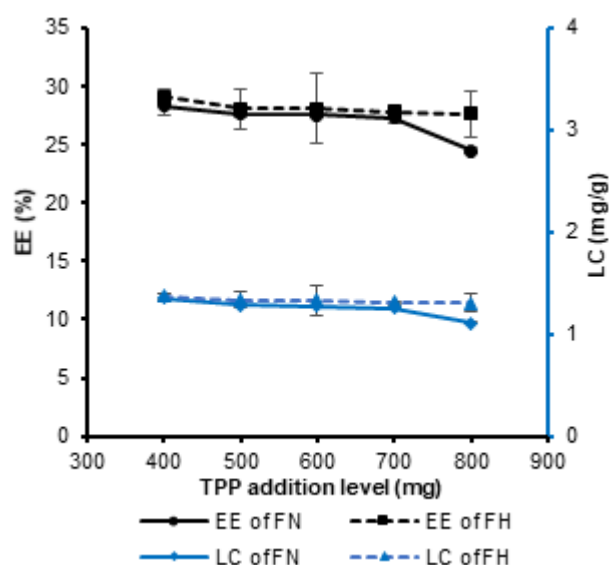


Fig 6. Effects of TPP addition level on EE and LC

of 400–800 mg of the TPP addition level, the increase in the TPP addition level has no significant effect on EE and LC of FH. On the other hand, similar results are found in FN in the range of 400–700 mg. However, in the range of 700–800 mg TPP addition level, a decrease both in EE and LC is observed. The decrease in EE and LC is probably due to the existence of an excess of TPP, which saturates the native starch, causing the matrix to become tighter, and as a result, β -carotene tends to be trapped in the outer surface of the matrix. The trapped β -Carotene in the surface is easily dissolved during the experimental step of ethanol washing after the centrifugation stage. This situation explains the small results of β -carotene found in the encapsulation products. Similar results have also been found in another study [13] suggesting that increasing concentration of TPP in the matrices tends to reduce EE and LC of encapsulation products.

Storage Stability Evaluation

Fig. 7 displays the storage stability of β -carotene encapsulated in the various matrices of native starch only (NS), hydrolyzed starch only (HS), native starch-chitosan/TPP (FN3), and hydrolyzed starch-chitosan/TPP (FH3). It is clearly observed that the storage stability of β -carotene increases when a combination of starch-chitosan/TPP matrix is used compared to those of using starch only, native starch, and hydrolyzed starch. The replacement of native starch with hydrolyzed starch in the matrix of starch-chitosan/TPP slightly increases the stability of β -carotene against UV light (Fig. 7(a)) and heat (Fig. 7(b) and 7(c)). The reaction rate constants and

the half-life of the sample degradation have been determined according to the first-order reaction equation, as presented in Table 3. The reaction kinetics of β -carotene degradation has been found to follow the first-order reaction rate as obviously can be seen from its coefficient of determination (R^2) value, which is in the range of 0.9561 to 0.9976. The longest half-life in every storage condition is shown by the matrix of FH3. The shortest half-life was shown by NS. The enhancement of the stability of β -carotene by modification of starch through hydrolysis reaction has also been reported by Spada et al. [11]. In his paper, he reported that by using hydrolyzed pinhão (*Araucaria angustifolia* seeds) starch as a matrix, the rate constant (k) calculated using first-order kinetic model lower ($k = 0.014$ – 0.017 days $^{-1}$ in the dark at 10–25 °C) than its native starch ($k = 0.048$ – 0.076 days $^{-1}$ in the dark at 10–25 °C). The lower the k , the higher the storage stability of β -carotene. In this research, the storage stability of β -carotene encapsulated in the starch matrices, both native and hydrolyzed starch, increases significantly by the addition of chitosan into the matrix system. The rate constant (k) calculated using first-order kinetic model lower ($k = 0.0072$ – 0.0711 days $^{-1}$ in the dark at 5–30 °C) than its native starch ($k = 0.0107$ – 0.0761 days $^{-1}$ in the dark at 5–30 °C), while in the presence of UV light, the k much higher than in the dark. The half-life of encapsulation product in the order of FH3 > FN3 > HS > NS as reflected from its k . The cause of this result may have been due to the capacity of chitosan in film-forming and antioxidant

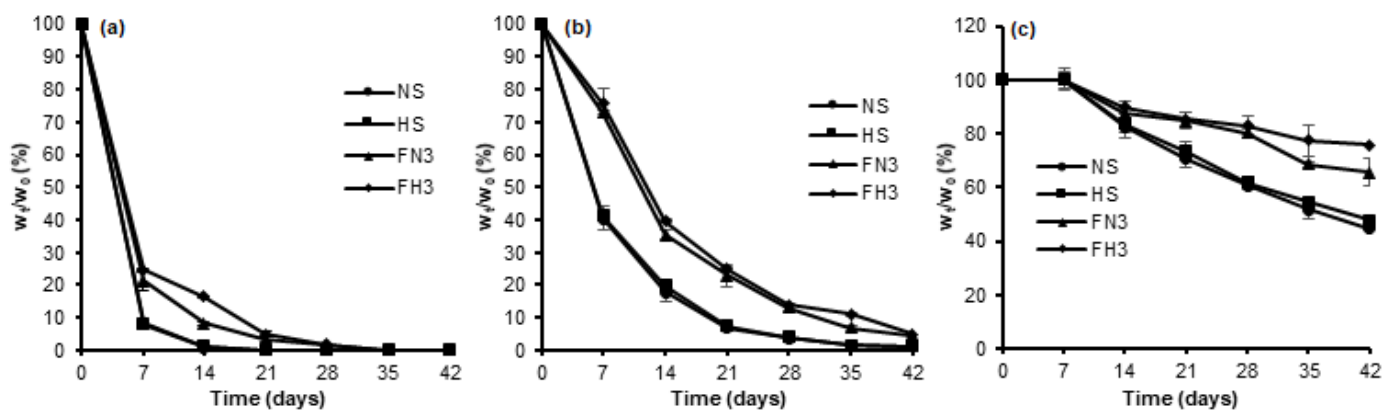


Fig 7. Storage stability of encapsulation products (a) in the presence of UV light at ambient temperature, (b) in the dark at ambient temperature, and (c) in the dark at (5 ± 1) °C

Table 3. Coefficient of determination (R^2) and kinetic parameters in the storage stability test of β -carotene encapsulation products

Sample code	R^2	Regression Equation	k (day ⁻¹)	$t_{0.5}$ (day)
Stored in the presence of UV radiation, ambient temperature				
NS	0.9976	$y = -0.3341x - 0.0665$	0.3341	2.07
HS	0.9961	$y = -0.3221x - 0.0816$	0.3221	2.15
FN3	0.9831	$y = -0.1478x - 0.2683$	0.1478	4.69
FH3	0.9820	$y = -0.1367x - 0.1251$	0.1367	5.07
Stored in the dark, ambient temperature				
NS	0.9835	$y = -0.1088x - 0.1695$	0.109	6.36
HS	0.9836	$y = -0.1078x - 0.1377$	0.1078	6.43
FN3	0.9948	$y = -0.0761x + 0.0842$	0.0761	9.11
FH3	0.9879	$y = -0.0711x + 0.0951$	0.0711	9.75
Stored in the dark, (5 ± 1) °C				
NS	0.9808	$y = -0.0206x + 0.0756$	0.0205	33.80
HS	0.9799	$y = -0.019x + 0.0688$	0.0189	36.67
FN3	0.9561	$y = -0.0108x + 0.0379$	0.0107	64.77
FH3	0.9640	$y = -0.0073x + 0.012$	0.0072	96.25

function, thus, it is able to preserve β -carotene from degradation by light and heat [14].

■ CONCLUSION

It has been shown that the capability of starch as a matrix of β -carotene encapsulation can be enhanced by using hydrolyzed starch and a combination of starch with cross-linked chitosan using TPP as a cross-linker as matrices. The crystallinity of the encapsulation products decreases due to the occurrence of the interaction between starch, chitosan, and TPP. XRD and SEM result has confirmed the good compatibility of the mixture among starch, chitosan, and TPP. The storage stability of β -carotene is enhanced by the encapsulation of β -carotene in the starch-chitosan/TPP matrix. The highest results of EE and LC, as well as the longest storage stability of β -carotene encapsulated in the matrices of hydrolyzed starch-chitosan/TPP, support the potential and promising use of this matrix combination in the encapsulation of other hydrophobic drugs.

■ ACKNOWLEDGMENTS

The authors would like to thank the Directorate General of Higher Education, Ministry of Research, Technology, and Higher Education, The Republic of

Indonesia (*Kemenristekdikti*), for the research funding through the Doctoral Dissertation Research Grant (PDD) with contract number 2885/UN1.DITLIT/DITLIT/LT/2019.

■ REFERENCES

- [1] Chávarri, M., Marañón, I., and Villarán, M.C., 2012, "Encapsulation technology to protect probiotic bacteria" in *Probiotics*, Eds. Rigobelo, E.C., IntechOpen, Rijeka, 501–540.
- [2] Nedovic, V., Kalusevic, A., Manojlovic, V., Levic, S., and Bugarski, B., 2011, An overview of encapsulation technologies for food applications, *Procedia Food Sci.*, 1, 1806–1815.
- [3] Joye, I.J., and McClements, D.J., 2014, Biopolymer-based nanoparticles and microparticles: Fabrication, characterization, and application, *Curr. Opin. Colloid Interface Sci.*, 19 (5), 417–427.
- [4] Gul, K., Tak, A., Singh, A.K., Singh, P., Yousuf, B., and Wani, A.A., 2015, Chemistry, encapsulation, and health benefits of β -carotene - A review, *Cogent Food Agric.*, 1 (1), 1018696.
- [5] Yuan, Y., Gao, Y., Zhao, J., and Mao, L., 2008, Characterization and stability evaluation of β -carotene nanoemulsions prepared by high pressure

- homogenization under various emulsifying conditions, *Food Res. Int.*, 41 (1), 61–68.
- [6] Gu, L., Su, Y., Zhang, M., Chang, C., Li, J., McClements, D.J., and Yang, Y., 2017, Protection of β -carotene from chemical degradation in emulsion-based delivery systems using antioxidant interfacial complexes: Catechin-egg white protein conjugates, *Food Res. Int.*, 96, 84–93.
- [7] Yang, J., Han, S., Zheng, H., Dong, H., and Liu, J., 2015, Preparation and application of micro/nanoparticles based on natural polysaccharides, *Carbohydr. Polym.*, 123, 53–66.
- [8] Fathi, M., Martín, Á., and McClements, D.J., 2014, Nanoencapsulation of food ingredients using carbohydrate based delivery systems, *Trends Food Sci. Technol.*, 39 (1), 18–39.
- [9] Fouladi, E., and Nafchi, A.M., 2014, Effects of acid-hydrolysis and hydroxypropylation on functional properties of sago starch, *Int. J. Biol. Macromol.*, 68, 251–257.
- [10] Lokuwan, J., 2007, Characteristics of microencapsulated β -carotene formed by spray drying with modified tapioca starch, native tapioca starch and maltodextrin, *Food Hydrocolloids*, 21 (5–6), 928–935.
- [11] Spada, J.C., Noreña, C.P.Z., Marczak, L.D.F., and Tessaro, I.C., 2012, Study on the stability of β -carotene microencapsulated with pinhão (*Araucaria angustifolia* seeds) starch, *Carbohydr. Polym.*, 89 (4), 1166–1173.
- [12] Subramanian, S.B., Francis, A.P., and Devasena, T., 2014, Chitosan-starch nanocomposite particles as a drug carrier for the delivery of bis-desmethoxy curcumin analog, *Carbohydr. Polym.*, 114, 170–178.
- [13] Perez, J.J., and Francois, N.J., 2016, Chitosan-starch beads prepared by ionotropic gelation as potential matrices for controlled release of fertilizers, *Carbohydr. Polym.*, 148, 134–142.
- [14] Peng, H., Xiong, H., Li, J., Xie, M., Liu, Y., Bai, C., and Chen, L., 2010, Vanillin cross-linked chitosan microspheres for controlled release of resveratrol, *Food Chem.*, 121 (1), 23–28.
- [15] de Vos, P., Faas, M.M., Spasojevic, M., and Sikkema, J., 2010, Encapsulation for preservation of functionality and targeted delivery of bioactive food components, *Int. Dairy J.*, 20 (4), 292–302.
- [16] Raguzzoni, J.C., Delgadillo, I., and Lopes da Silva, J.A., 2016, Influence of a cationic polysaccharide on starch functionality, *Carbohydr. Polym.*, 150, 369–377.
- [17] Bajer, D., and Kaczmarek, H., 2010, Study of the influence OV UV radiation on biodegradable blends based on chitosan and starch, *Prog. Chem. Appl. Chitin Deriv.*, 15, 17–24.
- [18] Lawal, O.S., and Adebawale, K.O., 2005, Physicochemical characteristics and thermal properties of chemically modified jack bean (*Canavalia ensiformis*) starch, *Carbohydr. Polym.*, 60 (3), 331–341.
- [19] Lestari, A.D.N., Mudasir, Siswanta, D., and Martien, R., 2018, Preliminary study on microprecipitation of β -carotene in starch/chitosan/TPP (tripolyphosphate) matrices: Effects of weight ratio of starch/chitosan, *AIP Conf. Proc.*, 2049, 020045.
- [20] Rampino, A., Borgogna, M., Bellich, B., Blasi, P., Virgilio, F., and Cesàro, A., 2016, Chitosan-pectin hybrid nanoparticles prepared by coating and blending techniques, *Eur. J. Pharm. Sci.*, 84, 37–45.
- [21] Kim, J.Y., and Huber, K.C., 2016, Preparation and characterization of corn starch- β -carotene composites, *Carbohydr. Polym.*, 136, 394–401.
- [22] Rutz, J.K., Borges, C.D., Zambiasi, R.C., da Rosa, C.G., and da Silva, M.M., 2016, Elaboration of microparticles of carotenoids from natural and synthetic sources for applications in food, *Food Chem.*, 202, 324–333.
- [23] Chu, B.S., Ichikawa, S., Kanafusa, S., and Nakajima, M., 2007, Preparation and characterization of β -carotene nanodispersions prepared by solvent displacement technique, *J. Agric. Food Chem.*, 55 (16), 6754–6760.
- [24] Ferranti, V., Marchais, H., Chabenat, C., Orecchioni, A.M., and Lafont, O., 1999, Primidone-loaded poly- ϵ -caprolactone nanocapsules:

- Incorporation efficiency and in vitro release profiles, *Int. J. Pharm.*, 193 (1), 107–111.
- [25] Chen, L., McClements, D.J., Zhang, H., Zhang, Z., Jin, Z., and Tian, Y., 2019, Impact of amylose content on structural changes and oil absorption of fried maize starches, *Food Chem.*, 287, 28–37.
- [26] Ulbrich, M., Beresnewa-Seekamp, T., Walther, W., and Flöter, E., 2016, Acid-thinned corn starch-impact of modification parameters on molecular characteristics and functional properties, *Starch/Stärke*, 68, 399–409.
- [27] Hasani, S., Ojagh, S.M., and Ghorbani, M., 2018, Nanoencapsulation of lemon essential oil in Chitosan-Hicap system. Part 1: Study on its physical and structural characteristics, *Int. J. Biol. Macromol.*, 115, 143–151.
- [28] Hsin, W.L., Sheng, Y.J., Lin, S.Y., and Tsao, H.K., 2004, Surface tension increment due to solute addition, *Phys. Rev. E*, 69 (31), 1–8.
- [29] Blanchette, F., Messio, L., and Bush, J.W.M., 2009, The influence of surface tension gradients on drop coalescence, *Phys. Fluids*, 21 (7), 072107.

pH Dependence on Colorimetric Detection of Hg²⁺ by Histidine-Functionalized Gold Nanoparticles

Dewi Eviane, Dwi Siswanta, and Sri Juari Santosa*

Department of Chemistry, Faculty of Mathematics and Natural Sciences, Universitas Gadjah Mada, Sekip Utara, Yogyakarta 55281, Indonesia

* **Corresponding author:**

tel: +62-8164262984

email: sjuari@ugm.ac.id

Received: November 24, 2019

Accepted: January 20, 2020

DOI: 10.22146/ijc.51824

Abstract: In this study, we successfully developed gold nanoparticles capped with histidine (His-AuNPs) for Hg²⁺ detection using trisodium citrate as the reducing agent. The optimum pH for the detection of Hg²⁺ by His-AuNPs was 12. The addition of Hg²⁺ to the His-AuNPs caused the color change from red to black-blue, which is readily detectable by the naked eye. This color change is followed by a decrease in the intensity of the primary Surface Plasmon Resonance (SPR) peak at a wavelength (λ) of 525 nm and an increase in the secondary peak at $\lambda = 650$ nm. His-AuNPs effectively detected Hg²⁺ with limits of detection and quantitation of 1.77 μ M and 5.89 μ M, respectively. His-AuNPs exhibited good performance for the detection of Hg²⁺ in waste water collected from a steel industrial facility in Banten Province, with a recovery and a percent relative standard deviation of 115% and 1.02%, respectively.

Keywords: AuNPs; histidine; Hg²⁺ detection; synthesis

■ INTRODUCTION

Mercury is a heavy metal that frequently contaminates the environment. Natural environmental mercury is mainly the result of volcanic activity; however, human activities also contribute to the increasing levels of mercury through metal mining, forest fires, solid-waste incineration, and the combustion of fossil fuels (coal, oil, and gas) [1-2]. The divalent mercury ion (Hg²⁺) is the most common form of mercury and is stable when dissolved in water [3]; this mercury species binds easily to amino acids in the body. Mercury is difficult to decompose biologically and persists in ecosystems. The health effects of mercury include damage to the nervous system, heart, kidneys, and bone [4].

Hg²⁺ has usually been analyzed by atomic adsorption spectroscopy (AAS), inductively coupled plasma optical emission spectroscopy (ICP-OES) and mass spectrometry (ICP-MS), high-performance liquid chromatography (HPLC), advanced mercury analysis (AMA), and gas chromatography-atomic fluorescence spectroscopy (GC-AFS) [5-7]. The previous methods are mostly time consuming and require a laboratory. One

alternative method that is fast and simple is colorimetric detection using gold nanoparticles (AuNPs). Colorimetric detection is based on interactions between a target compound and the surfaces of AuNPs, which results in a visually distinct color change.

The major advantage of the use of AuNPs is the ability to functionalize their surfaces with a variety of functional groups. Functional groups on the AuNP surfaces not only stabilize the AuNPs in solution but also provide sites for interactions with metal ions through coordination [8]. The interactions between the functional groups of capping agents and metals affect AuNP stability, which can lead to AuNP aggregation [9]. Aggregation increases the sizes of AuNPs, which results in a red-to-blue color change; a shift and expansion of the surface plasmon resonance (SPR) are also observable by UV-Vis spectroscopy [10].

Various chemicals have been used as capping agents in the synthesis of nanoparticles for metal detection. 4,4-Dipyridine compounds have been used as capping agents in the synthesis of AuNPs for the detection of Hg²⁺ [11]. AuNPs stabilized Tween-20 were used as a probe for the colorimetric detection of Hg²⁺

[12]. However, 4,4-dipyridine and Tween-20 were toxic compounds and not environmentally friendly. Amino acids have been used as capping agents because they were green and biocompatible [14]. The amino acid contains more than one functional group, namely carboxylic acid and amino groups; these functional groups can interact with more than one metal ion [11]. Several amino acids have been used as capping agents for synthesized AuNPs to detect metal ions. Sener et al. showed that AuNPs synthesized using 11-mercaptopundecanoic acid and five amino acids (lysine, cysteine, histidine, tyrosine, and arginine) as capping agents are capable of detecting some toxic heavy-metal ions [12]. In another publication, Sener et al. reported the syntheses of AuNPs for the detection of Hg^{2+} using trisodium citrate as the reducing agent and fourteen types of amino acids as capping agents [13]. Colorimetric detection was only observed when arginine and lysine were used as capping agents, whereas the use of histidine and the eleven other types of amino acids as capping agents did not alter the UV-Vis spectrum of the AuNPs. Liu et al. modified thymine in order to induced AuNPs aggregation in the presence of Hg^{2+} [14]. Chai et al. used l-cysteine-functionalized AuNPs to detect Hg^{2+} [15], while Liu et al. reported the use of AuNPs with cysteine capping agents for the detection of Cu^{2+} [11].

pH plays an important role in AuNP-based metal detection. Guan et al. successfully synthesized AuNPs for the detection of Fe^{3+} at a set pH with histidine as the capping agent [19], while Fu and co-workers adjusted the pH during the synthesis of AuNPs-glutathione for the detection of Ni^{2+} [20]. Inspired by this previous work, in this study, we adjusted the pH during the synthesis of AuNPs using trisodium citrate as the reducing agent and histidine as the capping agent in order to develop a system for the detection of Hg^{2+} . We expect that the developed system can be used to detect Hg^{2+} in wastewater samples.

■ EXPERIMENTAL SECTION

Materials

Solid gold with 99.99% purity was obtained from PT. ANTAM Indonesia. Analytical grade of trisodium citrate, histidine, HNO_3 , $\text{Hg}(\text{NO}_3)_2$ and various standard solutions of $\text{Cd}(\text{NO}_3)_2$, $\text{Zn}(\text{NO}_3)_2$, $\text{Cu}(\text{NO}_3)_2$, $\text{Cr}(\text{NO}_3)_3$,

$\text{Pb}(\text{NO}_3)_2$, $\text{Fe}(\text{NO}_3)_3$, $\text{Co}(\text{NO}_3)_2$, $\text{Ag}(\text{NO}_3)$, $\text{Mg}(\text{NO}_3)_2$, $\text{Ni}(\text{NO}_3)$, $\text{Al}(\text{NO}_3)$, $\text{K}(\text{NO}_3)$, $\text{Na}(\text{NO}_3)$, $\text{Mn}(\text{NO}_3)_2$ were used for this purpose. NaOH and HCl reagents were used to regulate pH. These compounds were obtained from Merck (Germany) and were used without further purification.

Instrumentation

The UV-Vis absorbance spectra were measured using Shimadzu UV-1700 PharmaSpec. The morphologies of the nanoparticles were characterized by Transmission Electron microscopy (TEM, JEOL JEM-1400). The nanoparticles size and zeta potential were determined by Particle Size Analysis (PSA) Horiba SZ-100. The infrared spectra were analyzed by Fourier Transform Infrared (FTIR) using a Shimadzu FTIR Prestige-21. The crystal structures of the nanoparticles were characterized by Shimadzu XRD-6000.

Procedure

Preparation of histidine functionalized AuNPs

Chloroauric acid (HAuCl_4) solution was prepared from 1 g certified gold metal 99.99% which was dissolved in 40 mL of aqua regia. Deionized water was added to increase the volume of the solution to 100 mL. AuNPs were synthesized by the widely used Turkevich method with a few modifications [18]. AuNPs were prepared in a test tube by adding 5 mL of 0.26 mM chloroauric acid solution to 5 mL of 0.02 M sodium citrate solution. The test tube was then placed and heated in a water bath at 95 °C for approximately 15 min. The solution color changed from clear yellow to dark red indicating the formation of AuNPs. To functionalized AuNPs with histidine, 5 mL of 0.1 mM histidine with a pH value of 1 to 13 was added to the synthesized AuNPs solution. The pH of the histidine solution was adjusted using a solution of 0.1 M NaOH and 0.1 M HCl.

Effect of reaction time

The effect of reaction time was determined by reacting 1 mL of the His-AuNPs with 1 mL of a 10 μM Hg^{2+} solution, and the absorbance of the resulting solution was measured using UV-Vis spectrophotometer at 10 min intervals for 120 min.

Detection of Hg²⁺

The 1 mL solution of synthesized His-AuNPs was used as the colorimetric detection. The color change from red to purple to blue-black occurred after the addition of 1 mL of various Hg²⁺ concentrations. Colorimetric detection was carried out on industrial wastewater from Banten Province. Hg²⁺ concentration in wastewater was measured using a mercury analyzer. The collected samples were known to have Hg²⁺ concentrations of 3.55 nM. The samples were spiked with Hg²⁺ standard solution to become 3 and 5 µM. The color changes were observed using a UV-Vis spectrophotometer.

Effect of other cations

The effects of some other ions were investigated by the addition of Cd²⁺, Zn²⁺, Cu²⁺, Cr³⁺, Pb²⁺, Fe³⁺, Co²⁺, Ag⁺, Mg²⁺, Ni²⁺, Al³⁺, K⁺, Na⁺, Mn²⁺. Interference experiments were carried out by adding 0.5 mL of a 10 µM metal solution of the other metal ions to 0.5 mL of 10 µM Hg²⁺, then was added to a 1 mL solution of the synthesized His-AuNPs. Colorimetric changes were observed using a UV-Vis spectrophotometer at wavelength 525 nm. A blank solution devoid of any additional metal cation was also tested.

Characterization

The SPR spectra were acquired at room temperature using a UV-Vis spectrophotometer directly after synthesis using a 1 cm optical path length quartz cuvette and 200–800 nm wavelength range. The morphologies of the AuNPs were characterized by Transmission Electron microscopy (TEM, JEOL JEM-1400). AuNPs for TEM analysis were prepared by immersing the copper grid into AuNPs solution then drying at room temperature. AuNPs size was determined by Particle Size Analysis (PSA, Horiba SZ-100). The zeta potential of the AuNPs solution was assessed using a Horiba SZ-100 Zeta Potential Analyzer. The Particle size and zeta potential were directly measured after synthesis using a 1 cm optical path length cuvette. The crystallinity of AuNPs achieved was investigated by Shimadzu XRD 6000. The interaction between AuNPs, reducing agent, capping agent, and Hg²⁺ was analyzed by FTIR. The sample was prepared by collecting nanoparticle deposits from the centrifugation of the nanoparticle solution.

RESULTS AND DISCUSSION

Effect of Histidine on SPR Peak of AuNPs

pH value is one of the most important factors that influenced the AuNPs system. One of the systems influenced is the SPR peak intensity of AuNPs [20]. In this study, the acidity of histidine solution was affected by the pK_a of histidine; based on its pK_a (α-NH₃⁺: pK_a = 9.2, imidazole group or R: pK_a = 6.0, α-COOH: pK_a = 1.8) [19], His-AuNPs should be more stable under relatively alkaline conditions (pH 8–12). Under these conditions, all of the carboxyl and amino groups in the histidine capping agent are deprotonated, resulting in a negative potential zeta value of -64.4 mV (Table 1). This charge is due to the interactions between the AuNP surfaces and the carboxyl and amino groups of histidine that result in electrostatic repulsion. Fig. 1 shows SPR peak intensity of AuNPs synthesized using trisodium citrate as reducing agent and histidine as capping agent. Fig. 1(a) demonstrates that the addition of histidine at concentrations between 1 µM and 10 mM does not significantly influence the intensity of SPR peak at 525 nm. The addition of 0.1 mM histidine resulted in an increase in SPR peak intensity, but the SPR peak did not shift from 525 nm. His-AuNPs was less stable when the histidine solution was acidic (Fig. 1(b)), as evidenced by a decrease in the SPR peak intensity at 525 nm. Likewise, the His-AuNPs stability was also lower at very alkaline pH, as confirmed by the expanding SPR peak to a higher wavelength (red shift).

Effect of Histidine pH on the Detection of Hg²⁺

Protein probes are strongly influenced by pH [21]. Histidine was added to the AuNPs under a variety of pH in order to ascertain the best conditions for the detection of Hg²⁺. The histidine at the acidic solution is not completely deprotonated; hence interactions between the carboxylate and amine of His-AuNPs and Hg²⁺ were not optimal. All of the amine and carboxyl groups from histidine were deprotonated at pH 13; however, the possible reaction between OH⁻ in histidine solution at pH 13 and Hg²⁺ resulted in fewer interactions between His-AuNPs and Hg²⁺.

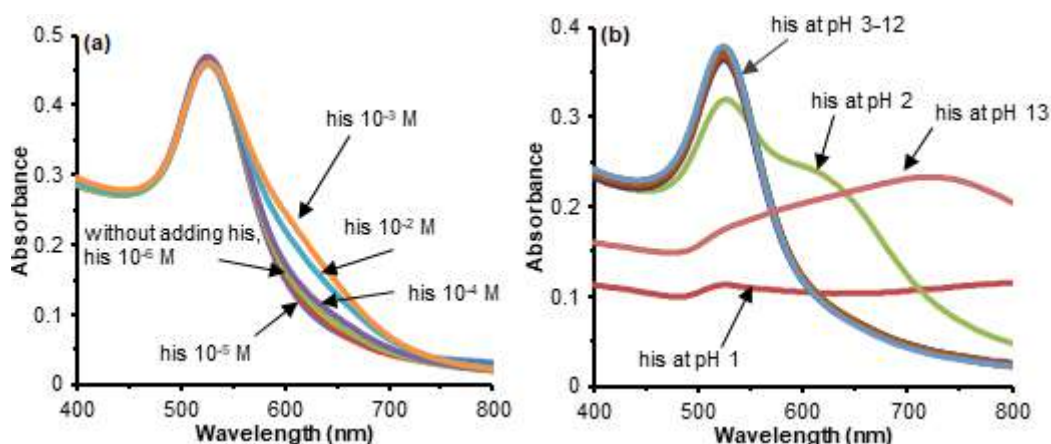


Fig 1. UV-vis spectra of (a) AuNPs with various concentrations of histidine, (b) His-AuNPs prepared with histidine at various acidity

Histidine solution at pH 12 was mixed with AuNPs and was added to Hg^{2+} solution to give a decrease in the intensity of the SPR peak at 525 nm and an appearance of new SPR peak at 650 nm. This corresponds to a red to blue-black color change when the sample was observed with the naked eye as seen in Fig. 2. These results were in line with the previous studies that a specific pH of cysteine as a capping agent could influence the formation of the SPR peak of AuNPs for the detection of glutathione colorimetry [22]. Li et al. reported that cysteine solutions with pH 5.8 affect AuNPs aggregation, resulting in changes in color and changes in SPR peak intensity.

Effect of Interaction Time on the Reaction of His-AuNPs and Hg^{2+}

The reaction time greatly affects the interactions between the His-AuNPs and Hg^{2+} , as shown in Fig. 3(a). The SPR intensity of His-AuNPs at 525 nm was measured every 5 min after the addition of $5 \mu\text{M}$ Hg^{2+} revealing the decrease in the intensity of SPR peak during the observation period to 100 min. The results show that the SPR intensity was stable after 100 min, indicating that the colorimetric detection was optimum after 100 min. Fig. 3(b) reveals that the decrease in the SPR intensity of His-AuNPs-Hg at 525 nm with increasing reaction time 0–120 min is due to red shifting, which indicates that the aggregation of His-AuNPs-Hg in the colloidal solution occurred. Furthermore, the addition of Hg^{2+} to His-AuNPs resulted in a new SPR peak at 650 nm, which was

red-shifted to 700 nm with increasing reaction time. This observation is consistent with the formation of the larger size of nanoparticles through aggregation. This was confirmed by PSA that the His-AuNPs-Hg particles were larger than those of His-AuNPs (Table 1).

Colorimetric Detection Mechanism

Prior to the addition of Hg^{2+} ions, the AuNP and His-AuNPs solutions were red in color when viewed by the naked eye. The addition of Hg^{2+} to His-AuNPs resulted in a red to blue-black color change, which occurred within a few seconds after the addition of Hg^{2+} indicating a decrease in nanoparticle stability. This change was confirmed by UV-Vis spectroscopy, which revealed a decrease in the intensity of the original SPR

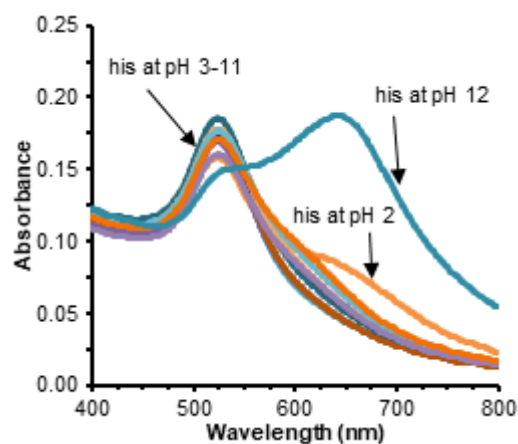


Fig 2. UV-Vis spectra of His-AuNPs with histidine prepared at various pH and added Hg^{2+}

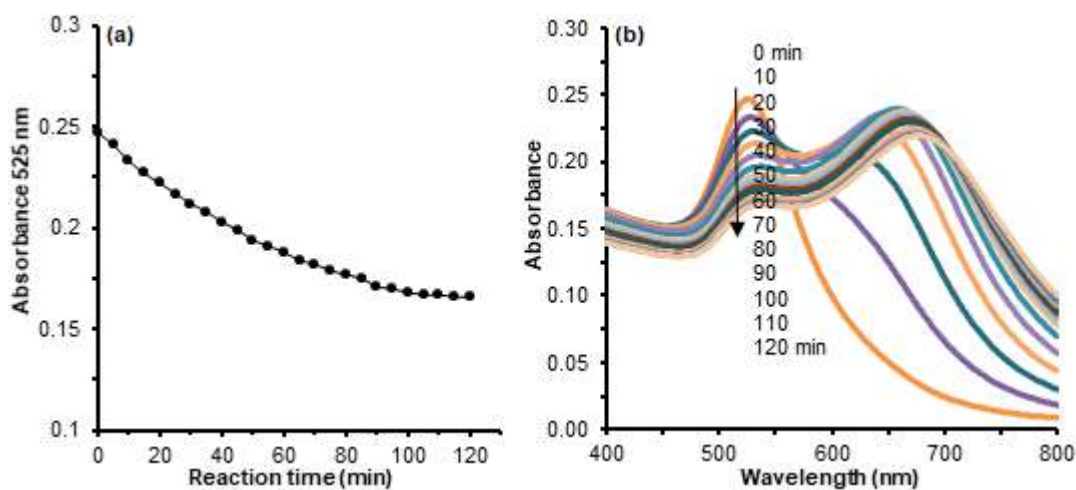


Fig 3. (a) The effect of reaction time between His-AuNPs and Hg^{2+} on the SPR peak at 525 nm. (b) The wavelength (400–800 nm) as a function of reaction time

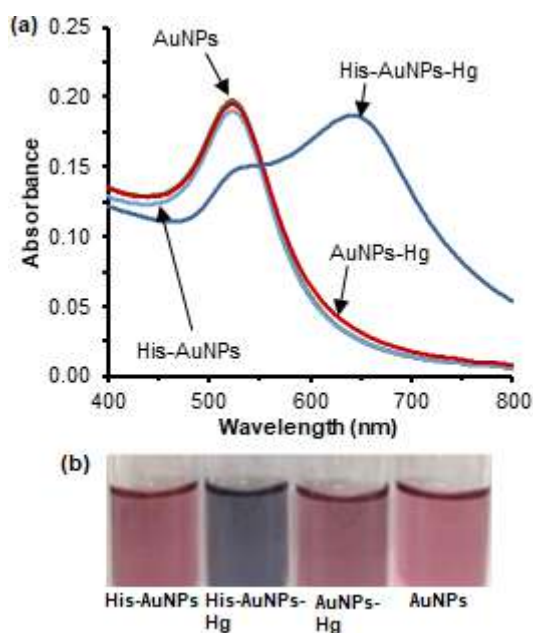


Fig 4. Colorimetric responses: (a) Spectra SPR of AuNPs, His-AuNPs, AuNPs-Hg, and His-AuNPs-Hg (b) picture of AuNPs, His-AuNPs, AuNPs-Hg, and His-AuNPs-Hg

peak at 525 nm and the formation of a new SPR peak above 650 nm (Fig. 4); this new SPR peak is ascribable to His-AuNPs aggregation. In addition, nanoparticles aggregation caused color changing and SPR peak widening [23]. This result is consistent with other studies that using AuNPs with thymine as a capping agent which showed the formation of new SPR peak UV-Vis spectra at around 650 nm after Hg^{2+} addition [20]. The color change

of AuNPs colloid could be seen in Fig. 4(b).

Sener et al. predicted that aggregation between Hg^{2+} and lysine/arginine occurs because these two amino acids have two remaining amino group molecules that can interact with more than one Hg^{2+} to form bridges between particles [13]. Du et al. synthesized AuNPs using thymine as capping agents for colorimetric sensors of Hg^{2+} based on thymine coordination chemistry, resulting in aggregation of AuNPs [20]. Based on the report, we concluded that the mechanism for this colorimetric response was involving one amino group of histidine that is used to interact with AuNPs surface and two remaining amino groups belonging to histidine are used to provide a strong coordination interaction with Hg^{2+} . Fig. 5 showed the illustration of colorimetric sensors that occur between His-AuNPs and Hg^{2+} was based on histidine coordination chemistry.

Zeta Potential Analysis

Zeta Potential was determined at optimum conditions and room temperature. Zeta potential was measured by adding 5 mL of various Hg^{2+} concentrations to 5 mL His-AuNPs. The zeta potential is a surface-charge parameter of colloidal particles [24]. Colloidal particles with zeta potential values of more than +30 mV or less than -30mV are stable colloids due to strong electrostatic repulsion between particles thereby preventing aggregation [25]. The zeta potential

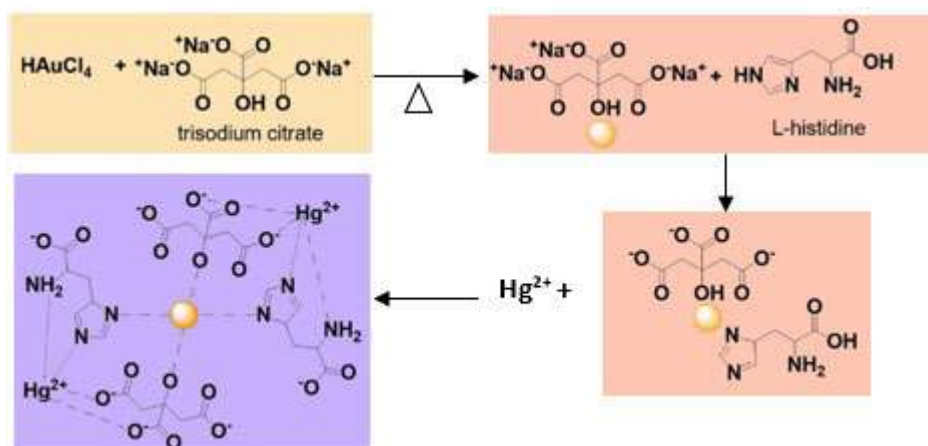


Fig 5. Schematic illustration Hg^{2+} detection by His-AuNPs

was used to indicate if the interactions between Hg^{2+} and His-AuNPs exist. The synthesized AuNPs have negative surface charges (Table 1), and the zeta potential of His-AuNPs was found to be more negative than that of the AuNPs, which indicates that the AuNPs solution is more stable after the addition of histidine. Interactions between the amino groups and the AuNP surface can result in a more-negative zeta potential of the colloid [26]. In our study, the existence of deprotonated amine and carboxylate from histidine that are on the surface of AuNPs will increase electrostatic repulsion, thereby increasing stability. Meanwhile, the addition of Hg^{2+} to His-AuNPs reduced the stability promoting an aggregation as indicated by the nanoparticle zeta potential being closer to zero. This means that the addition of Hg^{2+} to His-AuNPs affects the zeta potential. The higher the concentration of Hg^{2+} added, the closer the zeta potential of the His-AuNPs-Hg solution to zero. The stability of AuNPs after the addition of histidine and Hg^{2+} was confirmed with the observation of the particle size.

Addition of histidine to AuNPs resulted in a decrease in the size of His-AuNPs, while addition of Hg^{2+} caused aggregation of His-AuNPs followed by increased size of His-AuNPs. The size of the nanoparticles was confirmed by PSA as shown in Table 1.

Effect of Other Cations to the Hg^{2+} Detection

Our work tested fourteen other cations (K^+ , Co^{2+} , Na^+ , Ag^+ , Cu^{2+} , Mg^{2+} , Zn^{2+} , Mn^{2+} , Al^{3+} , Fe^{3+} , Cr^{3+} , Ni^{2+} , Pb^{2+} , and Cd^{2+}) to determine the effect of the other cations to the colorimetric Hg^{2+} detection. Fig. 6(a) shows that the SPR intensity at 525 nm only decreased with the addition of Hg^{2+} . The addition of fourteen other cations to His-AuNPs did not significantly reduce the SPR intensity at 525 nm. However, the addition of Ag^+ resulted in a slight increase of the SPR intensity of AuNPs since Ag^+ is stabilized by citrate [27]. Interference experiments were carried out by adding 0.5 mL of a 5 μM one of 14 cations to 0.5 mL of a 5 μM Hg^{2+} . The mixture of two cations was added to the 1 mL His-AuNPs. The addition

Table 1. Zeta potential and particle size of AuNPs, His-AuNPs and His-AuNPs-Hg

Sample	Zeta Potential (mV)	PSA (nm)
AuNPs	-34.8	Monodisperse 38.6
His-AuNPs	-64.4	Monodisperse 32.1
His-AuNPs-Hg 5 μM	-11.5	Monodisperse 252.8
His-AuNPs-Hg 7 μM	-10	
His-AuNPs-Hg 9 μM	-6.3	
His-AuNPs-Hg 11 μM	-2.1	

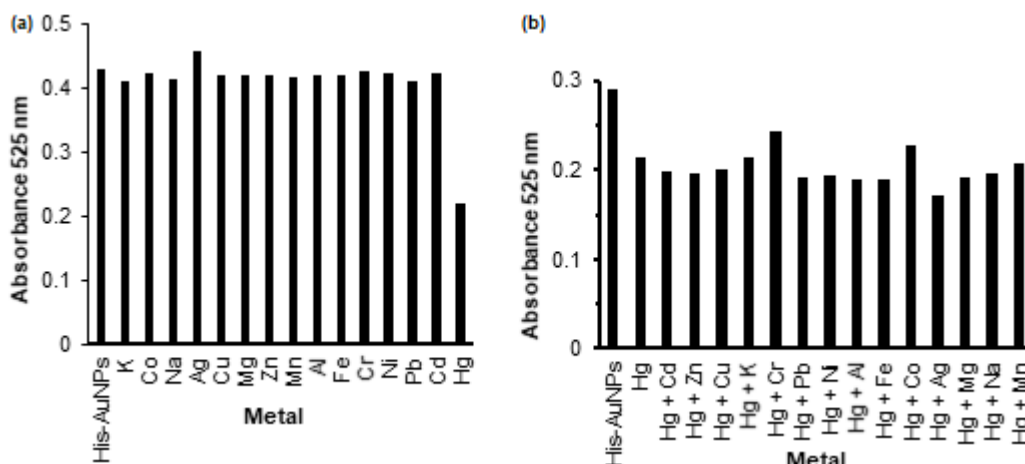


Fig 6. SPR intensity of His-AuNPs in the presence of (a) one cation (b) two cations (Hg^{2+} with one other cation) on 525 nm

of other cations to the Hg^{2+} had essentially no effect on the His-AuNPs detection-response to Hg^{2+} . A visual color change from red to blue-black was noted and was confirmed by UV-Vis spectroscopy (Fig. 6(b)).

Detection of Hg^{2+}

In this work, we have successfully synthesized His-AuNPs using trisodium citrate as a reducing agent and histidine as a capping agent for Hg^{2+} detection. Hg^{2+} at different concentrations were tested to determine the sensitivity of the colorimetric-detection method, and the change in the absorbance at 525 nm (ΔA_{525}) was plotted as a function of Hg^{2+} concentration (Fig. 7). Linearity determination was done by adding 5 mL Hg^{2+} to 5 mL His-AuNPs. ΔA_{525} was found to be linearly related to Hg^{2+} in the 9–16 μM concentration range ($R = 0.909$), with the limit of detection (LoD) and limit of quantitation (LoQ) for Hg^{2+} of 1.77 μM and 5.89 μM , respectively. The LoD

was calculated by the equation $\text{LoD} = 3 S_0/K$ and $\text{LoQ} = 10 S_0/K$, where S_0 was the standard deviation of the blank ($n = 7$) and K was the slope of the calibration line. The lowest detectable Hg^{2+} concentration in this work was 1.77 μM , which is above the allowed Hg^{2+} concentration limit (15.43 nM) in the environment defined by the Indonesian government (Indonesian Government Regulation number 82/2001). This assay could be used to determine mercury in the environment in accordance with the LOD and linearity range. Table 2 showed the comparison of the present method with the other reported values.

His-AuNPs was used to detect Hg^{2+} in real wastewater samples collected from an industrial site in Banten Province. Wastewater was filtered to remove any solids before testing. The concentration of Hg^{2+} in collected wastewater was 3.55 nM tested by using mercury analyzer. A recovery testing was performed by

Table 2. Performance of some typical colorimetric methods for the detection of Hg^{2+} .

Methods	Linear range	LOD	Ref
Colorimetric Lysine-AuNPs	1–60 nM	10 nM	[13]
Colorimetric Histidine-AuNPs	-	-	[13]
Colorimetric Thymine derivative-AuNPs	50-250 nM	0.8 nM	[20]
Colorimetric Cysteamine-AuNPs	0.05–3 μM	30 μM	[28]
Colorimetric Thiocetic acid-AuNPs	0.01–1 μM	10 μM	[29]
Colorimetric Polyethyleneimine-AuNPs	0.003–5 μM	1.72 nM	[30]
Colorimetric 8-hydroxyquinolines and oxalates-AuNPs	10 nM to 100 mM	10 nM	[31]
Colorimetric Histidine-AuNPs	9–16 μM	1.77 μM	This work

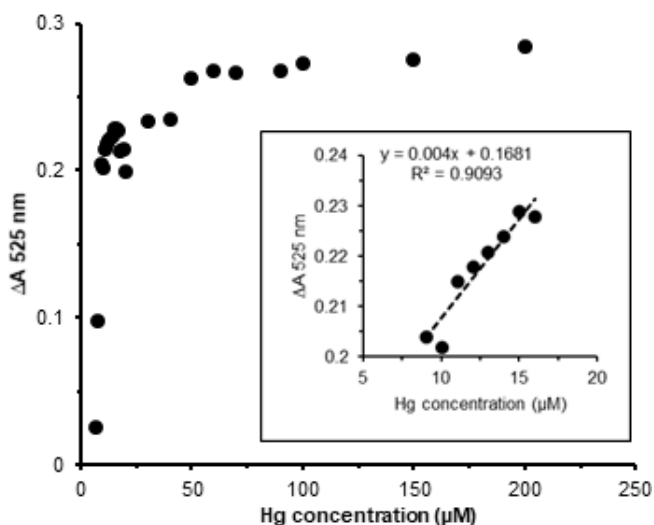


Fig 7. Response (ΔA_{525}) of the colorimetric assay against increasing Hg^{2+} concentrations

spiking to concentrations of 3 and 5 μM , with the recovery value determined to be $115 \pm 2\%$ ($n = 3$). Repeatedly measuring the concentration of the 10 μM Hg^{2+} sample resulted in a percent relative standard deviation (%RSD)

of 1.02%. These experimental results confirm the effectiveness of this detection method for quantifying Hg^{2+} in the waste water.

Characterization of AuNPs

The addition of a capping agent to the AuNPs affects both the particle size and distribution. The AuNPs exhibited a non-uniform nanoparticle size distribution with an average size of 38.6 nm with 82.9% of the nanoparticles were smaller than 100 nm and had monodispersed spherical morphologies. AuNPs with various sizes can be obtained when synthesized using the citrate reduction method, depending on the reactant molar ratio [26,32]. The size distribution of AuNPs was confirmed using PSA measurement (Fig. 8(a)) to give 97.5% of the nanoparticles smaller than 100 nm with an average size of 32.1 nm (Fig. 8(b)). The spherical morphologies of these nanoparticles were also characterized by TEM. Fig. 9(a) shows TEM images of AuNPs synthesized using trisodium citrate as the reducing

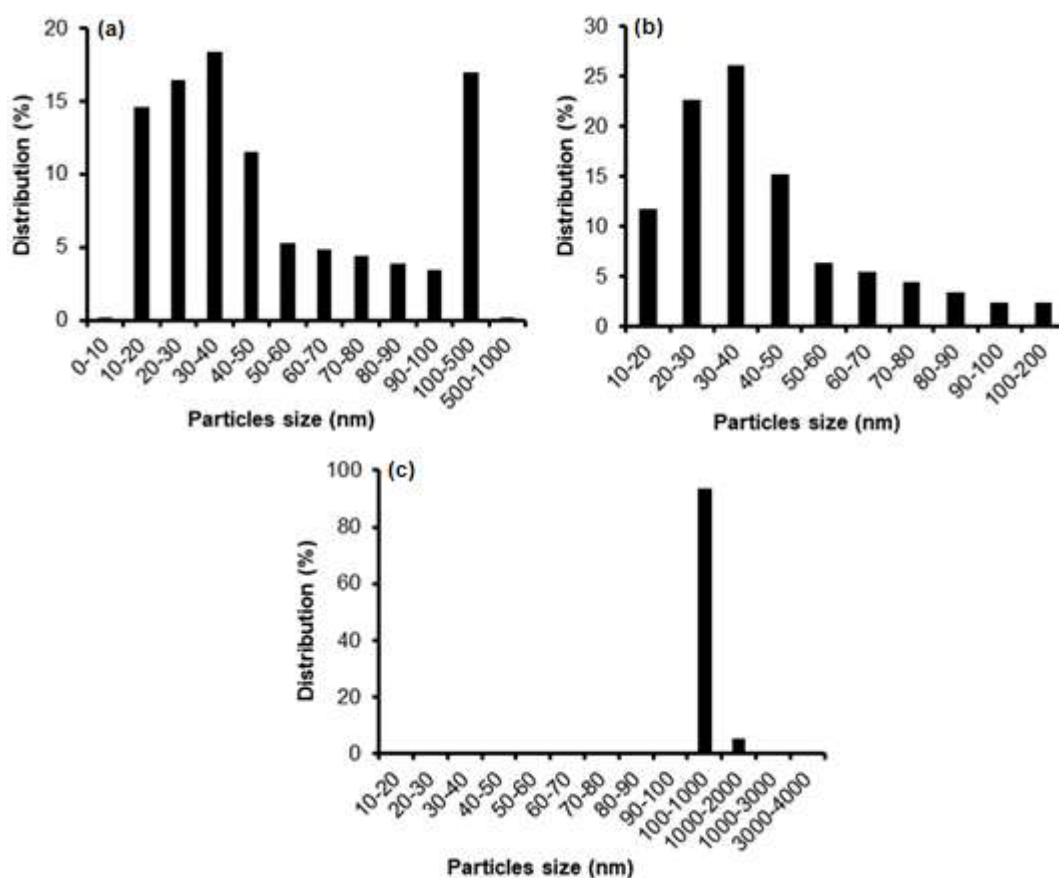


Fig 8. Particle-size distributions of (a) AuNPs (b) His-AuNPs, and (c) His-AuNPs-Hg

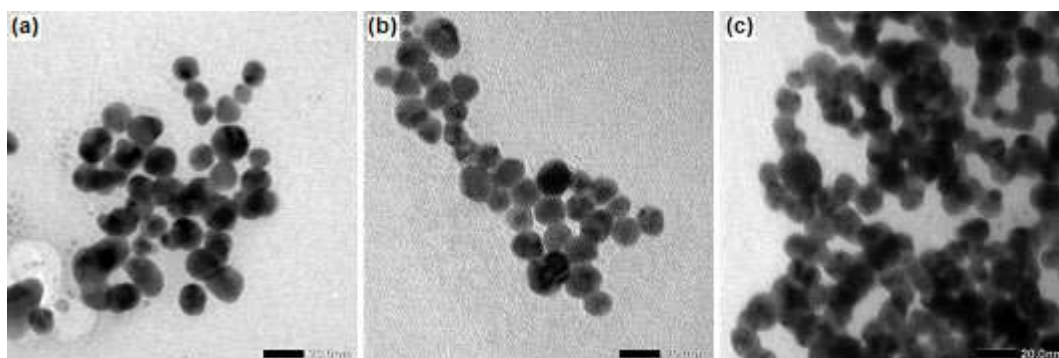


Fig 9. TEM images of (a) AuNPs, (b) His-AuNPs, and (c) His-AuNPs-Hg

agent. The addition of histidine to the AuNPs resulted in smaller and relatively uniformly distributed nanoparticles (Fig. 9(b)). We conclude that the addition of histidine as a stabilizing agent affects nanoparticle size. Fig. 9(c) shows that the addition of $10 \mu\text{M}$ Hg^{2+} resulted in larger nanoparticles due to aggregation. The average size of the His-AuNPs particles after the addition of Hg^{2+} was 252.8 nm.

Characterization using FTIR showed the differences between AuNPs before and after the addition of histidine and Hg^{2+} as shown in (Fig. 10). The AuNPs FTIR spectra showed OH stretching bands around 3448 cm^{-1} and OH bending at 1635 cm^{-1} . The C-O vibration band is shown at 1381 cm^{-1} . The C=O band was found at wavenumbers 1651 and 1558 cm^{-1} . The characteristic band of AuNPs shows the functional group on trisodium citrate around Au(0). His-AuNPs FTIR spectra show bands around the wave number 3448 cm^{-1} which are sharper than AuNPs because of the stretching contribution of -NH. The

interaction of AuNPs with histidine causes the vibration of band stretching C=O to shift from 1651 and 1658 cm^{-1} to 1627 and 1573 cm^{-1} , and the sharpening of the C-O peak at the wavenumber 1381 cm^{-1} . FTIR spectra changes were evident that His-AuNPs interact with Hg^{2+} . The His-AuNPs-Hg spectra showed a reduction in the band at a wavelength of 3448 cm^{-1} which was possible because of the interaction of the amine group on His-AuNPs with Hg^{2+} . The interaction of his-AuNPs with Hg^{2+} causes vibration band stretching of C=O at wavenumbers of 1627 cm^{-1} experienced a shift to 1589 cm^{-1} .

XRD measurement was conducted to determine the phase composition and crystal structure of AuNPs. Peaks from AuNPs and His-AuNPs reveal the formation of gold nanoparticles due to diffraction (111), (200), (220), (311), and (222) with face centered cubic crystal shapes (fcc) (Fig. 11). XRD AuNPs and His-AuNPs patterns are consistent with the results of previous studies [19,33]. The XRD pattern between AuNPs and His-AuNPs has a

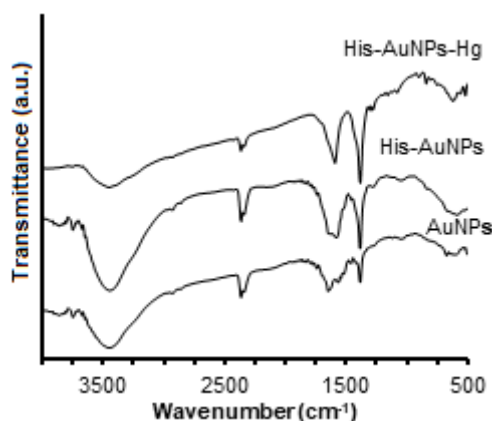


Fig 10. FTIR spectra of AuNPs, His-AuNPs, and His-AuNPs-Hg

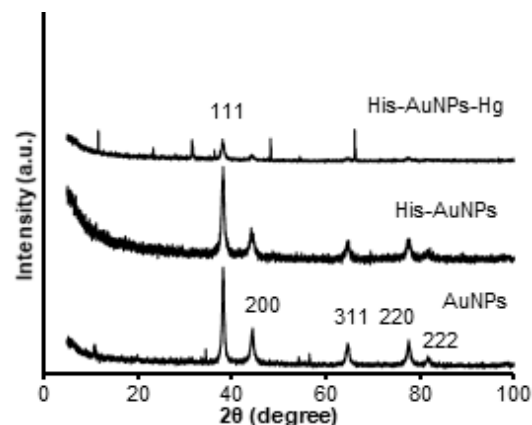


Fig 11. XRD patterns of the AuNPs, His-AuNPs, and His-AuNPs-Hg

similar crystallinity according to their intensity. These results are based on the reference of the Joint Committee on Powder Diffraction Standard (JCPDS 04-0784), which suggests that the crystalline gold nanoparticles were formed. However, the addition of Hg^{2+} causes a decrease in peak intensity in the XRD diffraction pattern (111), (200), (220), (311), which is probably due to the aggregation of nanoparticles as evidenced in the TEM image. This result is in line with Tripathy et al. which reported that the aggregation of AuNPs due to the addition of Fe^{3+} caused a decrease in the peak XRD intensity characteristic of AuNPs [34].

■ CONCLUSION

In this study, colorimetric detection of Hg^{2+} using His-AuNPs has successfully been done by adjusting the pH of the histidine solution that significantly affected the aggregation of His-AuNPs. UV-Vis spectroscopy revealed that the addition of Hg^{2+} to His-AuNPs resulted in a decrease in absorbance at 525 nm only when histidine solution at pH 12 was used, with new peaks observed at wavelengths of around 650 nm. The change in color from red to blue-black was readily observed with the naked eye. This mercury detection method showed a good selectivity with limits of detection and quantitation for Hg^{2+} of 1.77 μM and 5.89 μM , respectively.

■ REFERENCES

- [1] Apilux, A., Siangproh, W., Praphairaksit, N., and Chailapakul, O., 2012, Simple and rapid colorimetric detection of Hg(II) by a paper-based device using silver nanoplates, *Talanta*, 97, 388–394.
- [2] Brasca, R., Onaindia, M.C., Goicoechea, H.C., de la Peña, A.M., and Culzoni, M.J., 2016, Highly selective and ultrasensitive turn-on luminescence chemosensor for mercury(II) determination based on the rhodamine 6G derivative FC1 and Au nanoparticles, *Sensors*, 16 (10), 1652.
- [3] Du, J., Liu, M., Lou, X., Zhao, T., Wang, Z., Xue, Y., Zhao, J., and Xu, Y., 2012, Highly sensitive and selective chip-based fluorescent sensor for mercuric ion: Development and comparison of turn-on and turn-off systems, *Anal. Chem.*, 84 (18), 8060–8066.
- [4] Miretzky, P., and Cirelli, A.F., 2009, Hg(II) removal from water by chitosan and chitosan derivatives: A review, *J. Hazard. Mater.*, 167 (1-3), 10–23.
- [5] Xie, Z.J., Bao, X.Y., and Peng, C.F., 2018, Highly sensitive and selective colorimetric detection of methylmercury based on DNA functionalized gold nanoparticles, *Sensors*, 18 (8), 2679.
- [6] Suvarapu, L.N., and Baek, S.O., 2017, Recent studies on the speciation and determination of mercury in different environmental matrices using various analytical techniques, *Int. J. Anal. Chem.*, 2017, 3624015.
- [7] Azemard, S., and Vassileva, E., 2015, Determination of methyl mercury in marine biota samples with advanced mercury analyzer: Method validation, *Food Chem.*, 176, 367–375.
- [8] Oliveira, E., Núñez, C., Santos, H.M., Fernández-Lodeiro, J., Fernández-Lodeiro, A., Capelo, J.L., and Lodeiro, C., 2015, Revisiting the use of gold and silver functionalised nanoparticles as colorimetric and fluorometric chemosensors for metal ions, *Sens. Actuators, B*, 212, 297–328.
- [9] Lou, T., Wang, Y., Li, J., Peng, H., Xiong, H., and Chen, L., 2011, Rapid detection of melamine with 4-mercaptopyridine-modified gold nanoparticles by surface-enhanced Raman scattering, *Anal. Bioanal. Chem.*, 401, 333–338.
- [10] Priyadarshini, E., and Pradhan, N., 2017, Chemical gold nanoparticles as efficient sensors in colorimetric detection of toxic metal ions: A review, *Sens. Actuators, B*, 238, 888–902.
- [11] Liu, J.M., Wang, H.F., and Yan, X.P., 2011, A gold nanorod based colorimetric probe for the rapid and selective detection of Cu^{2+} ions, *Analyst*, 136 (19), 3904–3910.
- [12] Sener, G., Uzun, L., and Denizli, A., 2014, Colorimetric sensor array based on gold nanoparticles and amino acids for identification of toxic metal ions in water, *ACS Appl. Mater. Interfaces*, 6 (21), 18395–18400.
- [13] Sener, G., Uzun, L., and Denizli, A., 2014, Lysine-promoted colorimetric response of gold nanoparticles: A simple assay for ultrasensitive

- mercury(II) detection, *Anal. Chem.*, 86 (1), 514–520.
- [14] Liu, X., Cheng, X., Bing, T., Fang, C., and Shangguan, D., 2010, Visual detection of Hg^{2+} with high selectivity using thymine modified gold nanoparticles, *Anal. Sci.*, 26 (11), 1169–1172.
- [15] Chai, F., Wang, C., Wang, T., Ma, Z., and Su, Z., 2009, L-cysteine functionalized gold nanoparticles for the colorimetric detection of Hg^{2+} induced by ultraviolet light, *Nanotechnology*, 21 (2), 025501.
- [16] Guan, J., Jiang, L., Li, J., and Yang, W., 2008, pH-dependent aggregation of histidine-functionalized Au nanoparticles induced by Fe^{3+} ions, *J. Phys. Chem. C*, 112, 3267–3271.
- [17] Fu, R., Li, J., and Yang, W., 2012, Aggregation of glutathione-functionalized Au nanoparticles induced by Ni^{2+} ions, *J. Nanopart. Res.*, 14, 929.
- [18] Turkevich, J., Stevenson, P.C., and Hiller, J., 1951, A study of the nucleation and growth processes in the synthesis of colloidal gold, *Discuss. Faraday Soc.*, 11, 55–75.
- [19] Liu, Z., Zu, Y., Fu, Y., Meng, R., Guo, S., Xing, Z., and Tan, S., 2010, Hydrothermal synthesis of histidine-functionalized single-crystalline gold nanoparticles and their pH-dependent UV absorption characteristic, *Colloids Surf., B*, 76 (1), 311–316.
- [20] Du, J., Wang, Z., Fan, J., and Peng, X., 2015, Chemical gold nanoparticle-based colorimetric detection of mercury ion via coordination chemistry, *Sens. Actuators, B*, 212, 481–486.
- [21] Poornima, V., Alexandar, V., Iswariya, S., Perumal, P.T., and Uma, T.S., 2016, Gold nanoparticle-based nanosystems for the colorimetric detection of Hg^{2+} ion contamination in the environment, *RSC Adv.*, 6 (52), 46711–46722.
- [22] Li, J.F., Huang, P.C., and Wu, F.Y., 2017, Specific pH effect for selective colorimetric assay of glutathione using anti-aggregation of label-free gold nanoparticles, *RSC Adv.*, 7, 13426–13432.
- [23] Annur, S., Santosa, S.J., Aprilita, N.H., Phuong, N.T., and Phuoc, N.V., 2018, Rapid Synthesis of Gold Nanoparticles without Heating Process, *Asian J. Chem.*, 30 (11), 2399–2403.
- [24] Bhattacharjee, S., 2016, DLS, and zeta potential – What they are and what they are not ?, *J. Controlled Release*, 235, 337–351.
- [25] Yoosaf, K., Ipe, B.I., Suresh, C.H., and Thomas, K.G., 2007, In situ synthesis of metal nanoparticles and selective naked-eye detection of lead ions from aqueous media, *J. Phys. Chem. C*, 111 (34), 12839–12847.
- [26] Zakaria, H.M., Shah, A., Konieczny, M., Hoffmann, J.A., Nijdam, A.J., and Reeves, M.E., 2013, Small molecule- and amino acid-induced aggregation of gold nanoparticles, *Langmuir*, 29 (25), 7661–7673.
- [27] Wang, G.L., Zhu, X.Y., Jiao, H.J., Dong, Y.M., and Li, Z.J., 2012, Ultrasensitive and dual functional colorimetric sensors for mercury(II) ions and hydrogen peroxide based on catalytic reduction property of silver nanoparticles, *Biosens. Bioelectron.*, 31 (1), 337–342.
- [28] Ma, Y., Jiang, L., Mei, Y., Song, R., Tian, D., and Huang, H., 2013, Colorimetric sensing strategy for mercury(II) and melamine utilizing cysteamine-modified gold nanoparticles, *Analyst*, 138 (18), 5338–5343.
- [29] Su, D., Yang, X., Xia, Q., Chai, F., Wang, C., and Qu, F., 2013, Colorimetric detection of Hg^{2+} using thioctic acid functionalized gold nanoparticles, *RSC Adv.*, 3 (46), 24618–24624.
- [30] Kim, K.M., Nam, Y.S., Lee, Y., and Lee, K.B., 2018, A highly sensitive and selective colorimetric Hg^{2+} ion probe using gold nanoparticles functionalized with polyethyleneimine, *J. Anal. Methods Chem.*, 2018, 1206913.
- [31] Gao, Y., Li, X., Li, Y., Li, T., Zhao, Y., and Wu, A., 2014, A simple visual and highly selective colorimetric detection of Hg^{2+} based on gold nanoparticles modified by 8-hydroxyquinolines and oxalates, *Chem. Commun.*, 50 (49), 6447–6450.
- [32] Kumar, S., Gandhi, K.S., and Kumar, R., 2007, Modeling of formation of gold nanoparticles by citrate method, *Ind. Eng. Chem. Res.*, 46 (10), 3128–3136.
- [33] Halder, A., Das, S., Bera, T., and Mukherjee, A.,

2017, Rapid synthesis for monodispersed gold nanoparticles in kaempferol and anti-leishmanial efficacy against wild and drug resistant strains, *RSC Adv.*, 7 (23), 14159–14167.

[34] Tripathy, S.K., Woo, J.Y., and Han, C.S., 2013, Colorimetric detection of Fe(III) ions using label-free gold nanoparticles and acidic thiourea mixture, *Sens. Actuators, B*, 181, 114–118.

Short Communication:**Structure-Based Design and Molecular Dynamics Simulations of Pentapeptide AEYTR as a Potential Acetylcholinesterase Inhibitor**Vivitri Dewi Prasasty¹ and Enade Perdana Istyastono^{2,*}¹Faculty of Biotechnology, Atma Jaya Catholic University of Indonesia, Jakarta 12930, Indonesia²Faculty of Pharmacy, Sanata Dharma University, Paingan, Maguwoharjo, Depok, Sleman, Yogyakarta 55282, Indonesia*** Corresponding author:**

email: enade@usd.ac.id

Received: May 28, 2019

Accepted: July 25, 2019

DOI: 10.22146/ijc.46329

Abstract: Structure-based virtual screening protocol to identify potent acetylcholinesterase inhibitors was retrospectively validated. The protocol could be employed to examine the potential of designed compounds as novel acetylcholinesterase inhibitors. In a research project designing short peptides as acetylcholinesterase inhibitors, peptide AEYTR emerged as one of the potential inhibitors. This article presents the design of AEYTR assisted by the validated protocol and guided by literature reviews followed by molecular dynamics studies to examine the interactions of the pentapeptide in the binding pocket of the acetylcholinesterase enzyme. The molecular dynamics simulations were performed using YASARA Structure in Google Cloud Platform. The peptide AEYTR was identified *in silico* as a potent acetylcholinesterase inhibitor with the average free energy of binding (ΔG) of -19.138 kcal/mol.

Keywords: acetylcholinesterase; pentapeptide; molecular dynamics; YASARA Structure; Google Cloud Platform

■ INTRODUCTION

The approval of potent acetylcholinesterase inhibitors (AChEIs) to treat Alzheimer's Disease (AD) has shown benefits both medically and economically [2], since the approval of tacrine in 1993 [1]. For example, the cost saving of the medication use of AChEI donepezil (AriceptTM) could reach \$2408 in 1 year during 1997–1999 [2]. Recent studies reported that the continuing use of donepezil for treating AD was more cost-effective than discontinuation [3]. The studies also reported that the use of donepezil alone is not less cost-effective compared to the use of donepezil-memantine combined [3]. On the other hand, it is predicted that the number of people with dementia will increase in the coming years [4]. Targeting acetylcholinesterase (AChE) to develop novel drugs to treat AD has therefore, become of considerable interest [1,5] despite the expiration of the AriceptTM patent in November 2010.

Current advances in computational medicinal chemistry can significantly increase the efficiency of drug

discovery [6]. Integration of available and accessible computational tools is highly encouraged to avoid pitfalls in computer-aided drug discovery [6-11]. One of the suggested integration is the “focused integration”, which employs filtering molecules to compile a focused library that contains only compatible and favorable molecules to be screened subsequently [10-12]. Molecular interaction fingerprints play an important role in this integration [10,12-16]. Combined with other docking scores, molecular interaction fingerprints could produce an ensemble-based scoring function to increase the prediction ability of the developed method [6], e.g., the use of ensemble Protein-Ligand Interaction Fingerprints (ensPLIF) to increase the prediction ability of structure-based virtual screening (SBVS) protocols targeting estrogen receptor alpha [17] and AChE [18]. The structure-based approach to discover new AChEIs was developed to publicly provide a computer-aided protocol to predict the activity of designed compounds as potent AChEIs [18]. The *F*-measure value of the SBVS

protocol to identify potent AChEIs is 0.413 [18], which is higher than the reference SBVS protocol (F -measure = 0.226) [19].

In this article, a structure-based *de novo* design of a pentapeptide as a potential AChEI guided by literature [20] and assisted by a validated SBVS protocol [18] is presented. Following the design, molecular dynamics (MD) simulations of the selected peptide in the binding pocket of AChE using YASARA Structure [21] have been performed to obtain more insights into the enzyme-inhibitor interactions. Due to current issues of energy efficiency in green computing [22], we were tempted to perform the MD simulations in Google Cloud Platform (<https://cloud.google.com/>). The usage of this platform has not been reported yet in running MD simulation before. The design led to the identification of pentapeptide AEYTR as a potential AChEI, which was confirmed by the production run of the MD simulations resulting in the average free energy of binding (ΔG) of -19.138 kcal/mol.

■ COMPUTATIONAL DETAILS

Materials

All 400 SMILES formats of tetrapeptides starting with AE as the two first amino acids were provided by Prasasty et al. [20]. Module *molconvert* (Molecule File Converter) version 17.13.0 from ChemAxon Ltd. (<https://chemaxon.com/>) was used to build the SMILES format of the designed pentapeptides from their one-letter-code amino acid sequences. The retrospectively validated SBVS protocol developed by Riswanto et al. [18] installed in a gold package of virtual private server provided by Rumahweb Indonesia (<https://www.rumahweb.com/vps-indonesia/>) was used to perform *in silico* tests on the designed peptides. Molecular dynamics simulations were performed by employing YASARA Structure [21] version 19.5.5 in a virtual machine with 8 virtual central processing units (CPUs), 30 GB memory, 20 GB persistent disk and Ubuntu 16.04 LTS as the operating system provided by Google Cloud Platform (<https://cloud.google.com/>). A working station with Intel® Pentium® Silver N5000 as the CPU and 4 GB memory and Windows 10 Home as the operating system were used as

the computer client to communicate and to control the virtual servers.

Procedure

Design and in silico tests of peptides

The SMILES formats of all 400 tetrapeptides starting with AE as the first two amino acids were objected to previously published SBVS protocol to identify potent AChEIs [18,20]. Based on the results of the virtual screening and guided by literature reviews [20], some pentapeptides were designed. The list of one-letter-code amino acid sequences of the designed compounds was then converted to their SMILES forms by employing module *molconverter* and virtually screened by employing the SBVS protocol [18].

Molecular dynamics simulations

The pentapeptide identified as a potential AChEIs was subjected to MD simulations by using YASARA Structure. The best pose of the hit in the virtual screening was selected and later prepared in a scene mode in YASARA Structure using the default mode. The scene mode was then subjected to MD simulations using the default settings of YASARA Structure macro for MD run (http://www.yasara.org/md_run.mcr) [21], except for the length of MD and the intervals of taking snapshots. In this research, the length of the MD run was 10 ns, and the snapshots were taken at every 10 ps intervals [23]. The production runs were analyzed in the last 5 ns of the simulations, and the equilibrium states were considered reached if the average deviation of the root-mean-squared distances (RMSD) value of the backbone atoms was less than 1 Å [23]. The free energy of binding (ΔG) of the value of each snapshot of the enzyme-ligand binding in the last 5 ns of the MD simulations was also calculated by employing VINA [24] local search in YASARA structure after the enzyme and peptides atoms were fixed [21].

■ RESULTS AND DISCUSSION

This research aimed to design a pentapeptide as a potential AChEI, where the retrospectively validated SBVS protocol [18] was employed, and literature reviews were performed [20]. Molecular dynamics simulations

of the designed pentapeptide in the binding pocket of AChE were also performed to gain insights for further drug discovery processes. To explore the applicability of Google Cloud Platform as a cloud computing service, the MD simulations were performed in a virtual machine in the platform.

The virtual screening of all 400 tetrapeptides starting with amino acids AE resulted in 4 peptides identified as potent AChEIs. The identified tetrapeptides were AEKY, AERW, AEYQ, and AEYT (Fig. 1). The starting AE amino acids were selected since the most potent peptide as AChEI extracted from human was AEFHRWSSYMVHWK [20]. Additional K amino acid at the beginning of AEFHRWSSYMVHWK was reported detrimental for the activity [20]. The literature review reported that the shortest peptides as AChEIs were pentapeptides and the

5th amino acid in the most potent peptide from human as AChEI and in the most potent AChI colivelin, SALLRSIPAPAGASRLLLLTGEIDL was R [20]. Following the findings resulted from the *in silico* tests and equipped by the information about the 5th amino acid, pentapeptides AEKYR, AERWR, AEYQR, and AEYTR were constructed and virtually tested [18].

The pentapeptide AEYTR (Fig. 1) was the only pentapeptide identified as the potent AChEI in the *in silico* tests. The peptide showed ensPLIF #302 value ≥ 0.878 (0.952), ensPLIF #365 value < 0.678 (0.460), and ensPLIF #208 value ≥ 0.164 (0.312) which were the 1st key to be identified as potent AChEI [18]. These ensPLIFs #302, #365, and #208 represent hydrophobic interaction to F³³¹, hydrophobic interaction to G⁴⁴¹, and hydrogen bond to S²⁰⁰, respectively, in the binding pocket

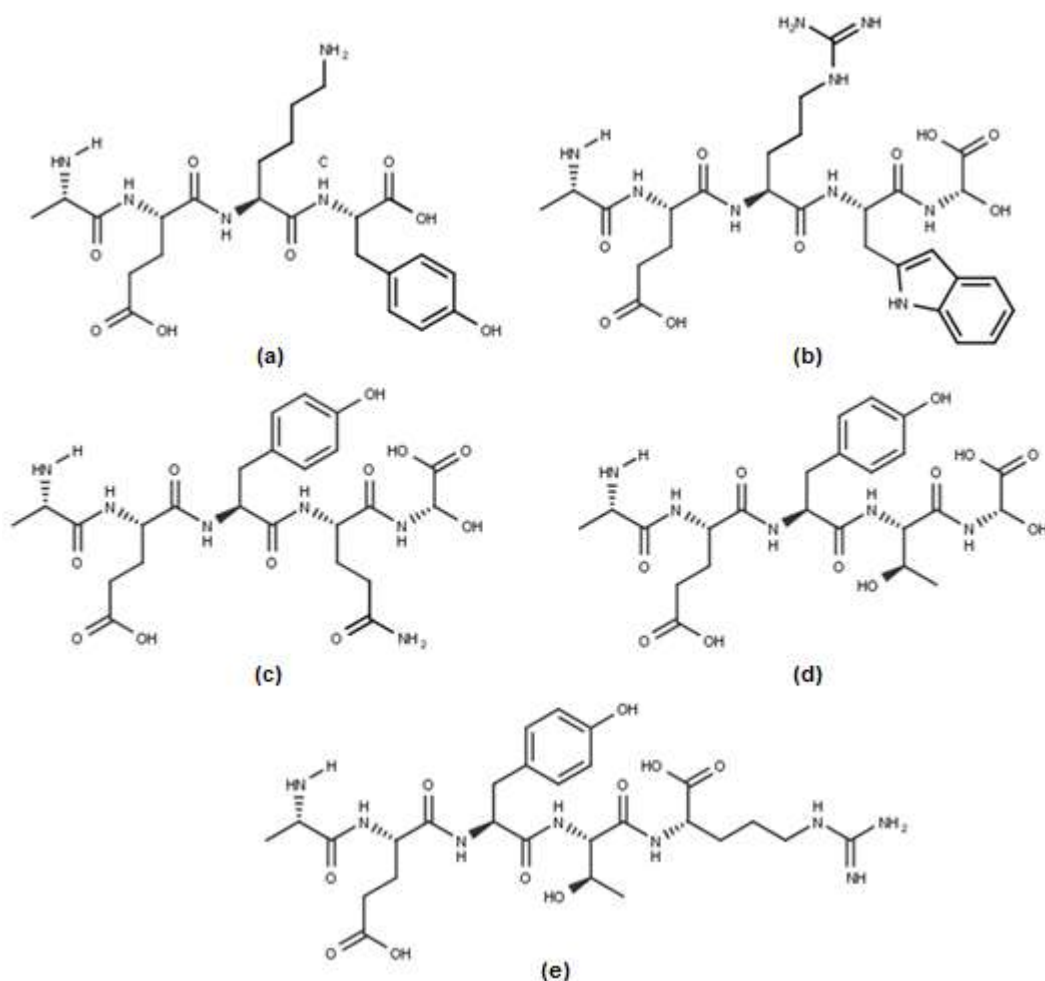


Fig 1. The two-dimensional structures of the AChE inhibitors identified in the virtual screening campaigns: AEKY (a), AERW (b), AEYQ (c), AEYT (d), and AEYTR (e)

of AChE (Fig. 2(a)) [18,25]. In the point of view of the endogenous substrate acetylcholine, the AE amino acids could act as the bioisostere of the acetyl moiety, while the R amino acid could serve as the bioisostere of choline. The additional YT amino acids in the sequence numbers 3 and 4 increase the probabilities to have a hydrophobic interaction to F³³¹ and a hydrogen bond to S²⁰⁰ in the binding pocket of AChE.

Molecular dynamics simulations by employing the best pose of AEYTR in AChE resulted from the previous SBVS campaigns as the initial point were then performed to examine the stability of the enzyme-inhibitor binding [23]. The average deviation value of the RMSD of the backbone atoms of the enzyme during the production run

was 0.204 Å with a standard deviation value of 0.089 Å (Fig. 3(a)). It indicated that the equilibrium had been reached before 5 ns in the MD simulations. These results are in line with those suggested by Liu et al. based on their examination on 10 ns MD simulations of 120 protein-ligand complexes [23]. Therefore, the stability of the AEYTR binding to AChE could be analyzed, and the ΔG could be calculated.

The RMSD values of the AEYTR in the production run of the MD simulations ranged from 2.068 Å to 2.539 Å. The average deviation value of the RMSD was 0.223 Å with a standard deviation value of 0.070 Å (Fig. 3(a)). This small shift reduced the chance to have a hydrogen bond to S²⁰⁰, but the chance of the hydrophobic interaction

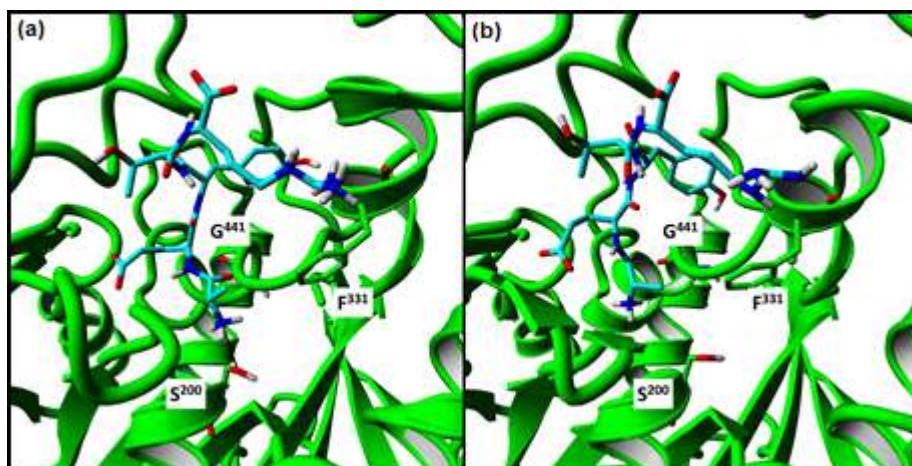


Fig 2. The pentapeptide AEYTR (depicted as sticks with carbon atoms colored with cyan) in the binding pocket of AChE (depicted as cartoon with carbon atoms colored green) resulted from the SVBS campaigns and used as the initial point of the MD simulations (a) and the pose of the MD simulations at 10 ns (b). The residues S²⁰⁰, F³³¹, and G⁴⁴¹ are shown since these residues are the important residues in the identification of AEYTR as a potent AChEI. Nitrogen, oxygen, and hydrogen atoms are colored with blue, red and white respectively. The black line represents the hydrogen bond. For the sake of clarity, non-polar hydrogens and residues 275 to 300 are not shown

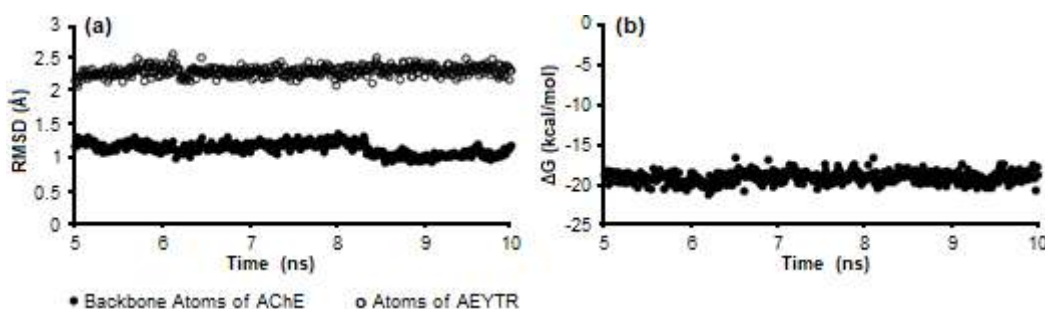


Fig 3. The RMSD values of the backbone atoms of AChE and the atoms of pentapeptide AEYTR during production run (a); The free energy of binding (ΔG) values of AChE-AEYTR during production run (b)

to F³³¹, as the most important interaction in this enzyme-inhibitor case, and the hydrophobic interaction to G⁴⁴¹ [18], remained high (Fig. 2(b)). Although the poses of AEYTR was not stable during equilibrium processes indicated by RMSD values of more than 2.0 Å, the poses remained stable in the production run of the MD simulations [23]. The ΔG calculations were, therefore, valid for the poses in the production run [21,23]. The calculation of ΔG was still considered underdeveloped in YASARA Structure [21]. Fortunately, the ΔG calculation could be performed by employing Autodock VINA [24] in YASARA Structure. The docking simulations employed the macro *dock_runlocal.mcr* with VINA as the docking software in YASARA Structure [21]. The enzyme AChE and the peptide AEYTR from each snapshot of the MD's production run were converted to pdb files and were subsequently fixed to avoid the pose searching phase in the docking simulations. These resulted in the average ΔG value of -19.138 kcal/mol with a standard deviation value of 0.701 kcal/mol (Fig. 3(b)). These values were equal to inhibition constant (K_i) values in subpicomolar [21] indicating that the pentapeptide AEYTR was a potent AChEI. *In vitro* tests will be performed as the ultimate confirmation of the *in silico* results [18,26] and discussed elsewhere.

The MD simulations took 1,575 min in Google Cloud Platform. The platform for the simulations cost circa 203.55 Indonesian Rupiah (IDR) or 0.015 US Dollar (USD)/min. Thus, the computational cost of the MD simulations was about 320,584.14 IDR or 22.91 USD in total. It was considered efficient, especially for research groups that do not have access or have limited access to high performance computing facilities. Besides green computing issues [22], this affordable price in using cloud computing platform could serve as a pivotal strategy in computer-aided drug discovery and development in the near future.

■ CONCLUSION

The pentapeptide AEYTR was identified as a potential hit to be developed as AChEI by employing the retrospectively validated SBVS protocol. The subsequent MD simulations using YASARA Structure in Google Cloud Platform showed that the AChE was stable during

the production run. Vice versa, the AEYTR poses in the binding pocket of AChE were also stable in the production run. Moreover, the ΔG values of the AChE-AEYTR indicated that the pentapeptide could serve as a potent AChEI. However, this finding should be confirmed by *in vitro* tests.

■ ACKNOWLEDGMENTS

This research was financially supported by the Directorate of Research and Community Services, Ministry of Research, Technology and Higher Education, the Republic of Indonesia (Research Grant No. 2/AKM/MONOPNT/2019).

■ REFERENCES

- [1] Mehta, M., Adem, A., and Sabbagh, M., 2012, New acetylcholinesterase inhibitors for Alzheimer's disease, *Int. J. Alzheimers Dis.*, 2012, 728983.
- [2] Fillit, H., and Hill, J., 2005, Economics of dementia and pharmacoeconomics of dementia therapy, *Am. J. Geriatr. Pharmacother.*, 3 (1), 39–49.
- [3] Knapp, M., King, D., Romeo, R., Adams, J., Baldwin, A., Ballard, C., Banerjee, S., Barber, R., Bentham, P., Brown, R.G., Burns, A., Denning, T., Findlay, D., Holmes, C., Johnson, T., Jones, R., Katona, C., Lindesay, J., Macharouthu, A., McKeith, I., McShane, R., O'Brien, J.T., Phillips, P.P.J., Sheehan, B., and Howard, R., 2017, Cost-effectiveness of donepezil and memantine in moderate to severe Alzheimer's disease (the DOMINO-AD trial), *Int. J. Geriatr. Psychiatry*, 32 (12), 1205–1216.
- [4] Ahmadi-Abhari, S., Guzman-Castillo, M., Bandosz, P., Shipley, M.J., Muniz-Terrera, G., Singh-Manoux, A., Kivimäki, M., Steptoe, A., Capewell, S., O'Flaherty, M., and Brunner, E.J., 2017, Temporal trend in dementia incidence since 2002 and projections for prevalence in England and Wales to 2040: Modelling study, *BMJ*, 358, j2856.
- [5] Murray, A.P., Faraoni, M.B., Castro, M.J., Alza, N.P., and Cavallaro, V., 2013, Natural AChE inhibitors from plants and their contribution to Alzheimer's disease therapy, *Curr. Neuropharmacol.*, 11 (4), 388–413.

- [6] Macalino, S.J.Y., Gosu, V., Hong, S., and Choi, S., 2015, Role of computer-aided drug design in modern drug discovery, *Arch. Pharmacol Res.*, 38 (9), 1686–1701.
- [7] Tanrikulu, Y., Proschak, E., Werner, T., Geppert, T., Todoroff, N., Klenner, A., Kottke, T., Sander, K., Schneider, E., Seifert, R., Stark, H., Clark, T., and Schneider, G., 2009, Homology model adjustment and ligand screening with a pseudoreceptor of the human histamine H4 receptor, *ChemMedChem*, 4 (5), 820–827.
- [8] Sirci, F., Istyastono, E.P., Vischer, H.F., Kooistra, A.J., Nijmeijer, S., Kuijjer, M., Wijtmans, M., Mannhold, R., Leurs, R., de Esch, I.J.P., and de Graaf, C., 2012, Virtual fragment screening: Discovery of histamine H(3) receptor ligands using ligand-based and protein-based molecular fingerprints, *J. Chem. Inf. Model.*, 52 (12), 3308–3324.
- [9] Istyastono, E.P., Nurrochmad, A., and Yuniarti, N., 2016, Structure-Based virtual screening campaigns on curcuminoids as potent ligands for histone deacetylase-2, *Orient. J. Chem.*, 32 (1), 275–282.
- [10] Istyastono, E.P., Kooistra, A.J., Vischer, H., Kuijjer, M., Roumen, L., Nijmeijer, S., Smits, R., de Esch, I.J.P., Leurs, R., and de Graaf, C., 2015, Structure-based virtual screening for fragment-like ligands of the G protein-coupled histamine H4 receptor, *Med. Chem. Commun.*, 6 (6), 1003–1017.
- [11] Kiss, R., Kiss, B., Könczöl, A., Szalai, F., Jelinek, I., László, V., Noszál, B., Falus, A., and Keseru, G.M., 2008, Discovery of novel human histamine H4 receptor ligands by large-scale structure-based virtual screening, *J. Med. Chem.*, 51 (11), 3145–3153.
- [12] de Graaf, C., Kooistra, A.J., Vischer, H.F., Katritch, V., Kuijjer, M., Shiroishi, M., Iwata, S., Shimamura, T., Stevens, R.C., de Esch, I.J.P., and Leurs, R., 2011, Crystal structure-based virtual screening for fragment-like ligands of the human histamine H(1) receptor, *J. Med. Chem.*, 54 (23), 8195–8206.
- [13] Marcou, G., and Rognan, D., 2007, Optimizing fragment and scaffold docking by use of molecular interaction fingerprints, *J. Chem. Inf. Model.*, 47 (1), 195–207.
- [14] Radifar, M., Yuniarti, N., and Istyastono, E.P., 2013, PyPLIF-assisted redocking indomethacin-(R)-alpha-ethyl-ethanolamide into cyclooxygenase-1, *Indones. J. Chem.*, 13 (3), 283–286.
- [15] Radifar, M., Yuniarti, N., and Istyastono, E.P., 2013, PyPLIF: Python-based protein-ligand interaction fingerprinting, *Bioinformatics*, 9 (6), 325–328.
- [16] Schultes, S., Nijmeijer, S., Engelhardt, H., Kooistra, A.J., Vischer, H.F., de Esch, I.J.P., Haaksma, E.E.J., Leurs, R., and de Graaf, C., 2013, Mapping histamine H4 receptor–ligand binding modes, *Med. Chem. Commun.*, 4 (1), 193–204.
- [17] Istyastono, E.P., Yuniarti, N., Hariono, M., Yuliani, S.H., and Riswanto, F.D.O., 2017, Binary quantitative structure-activity relationship analysis in retrospective structure based virtual screening campaigns targeting estrogen receptor alpha, *Asian J. Pharm. Clin. Res.*, 10 (12), 206–211.
- [18] Riswanto, F.D.O., Hariono, M., Yuliani, S.H., and Istyastono, E.P., 2017, Computer-aided design of chalcone derivatives as lead compounds targeting acetylcholinesterase, *Indonesian J. Pharm.*, 28 (2), 100–111.
- [19] Mysinger, M.M., Carchia, M., Irwin, J.J., and Shoichet, B.K., 2012, Directory of useful decoys, enhanced (DUD-E): Better ligands and decoys for better benchmarking, *J. Med. Chem.*, 55 (14), 6582–6594.
- [20] Prasasty, V., Radifar, M., and Istyastono, E.P., 2018, Natural peptides in drug discovery targeting acetylcholinesterase, *Molecules*, 23 (9), 2344.
- [21] Krieger, E., and Vriend, G., 2015, New ways to boost molecular dynamics simulations, *J. Comput. Chem.*, 36 (13), 996–1007.
- [22] Chen, H., Zhu, X., Guo, H., Zhu, J., Qin, X., and Wu, J., 2015, Towards energy-efficient scheduling for real-time tasks under uncertain cloud computing environment, *J. Syst. Software*, 99, 20–35.
- [23] Liu, K., Watanabe, E., and Kokubo, H., 2017, Exploring the stability of ligand binding modes to proteins by molecular dynamics simulations, *J. Comput.-Aided Mol. Des.*, 31 (2), 201–211.

- [24] Trott, O., and Olson, A.J., 2010, AutoDock Vina: Improving the speed and accuracy of docking with a new scoring function, efficient optimization, and multithreading, *J. Comput. Chem.*, 31 (2), 455–461.
- [25] Dvir, H., Wong, D.M., Harel, M., Barril, X., Orozco, M., Luque, F.J., Munoz-Torrero, D., Camps, P., Rosenberry, T.L., Silman, I., and Sussman, J.L., 2002, 3D structure of *Torpedo californica* acetylcholinesterase complexed with huprine X at 2.1 Å resolution: Kinetic and molecular dynamic correlates, *Biochemistry*, 41 (9), 2970–2981.
- [26] Yuniarti, N., Mungkasi, S., Yuliani, S.H., and Istyastono, E.P., 2019, Development of a graphical user interface application to identify marginal and potent ligands for estrogen receptor alpha, *Indones. J. Chem.*, 19 (2), 531–537.